Dredging Processes The Cutting of Sand, Clay & Rock Cutting Theory

by

Dr.ir. Sape A. Miedema

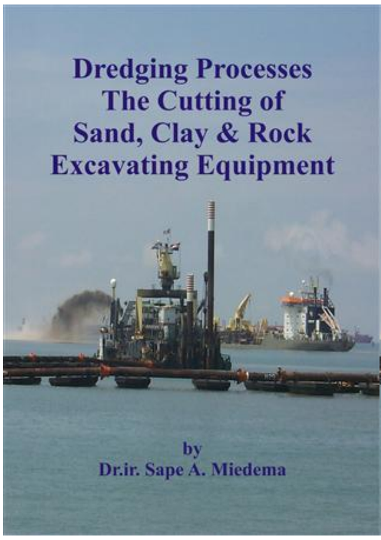
Dredging Processes
The Cutting of
Sand, Clay & Rock
Excavating Equipment
by
Dr.ir. Sape A. Miedema

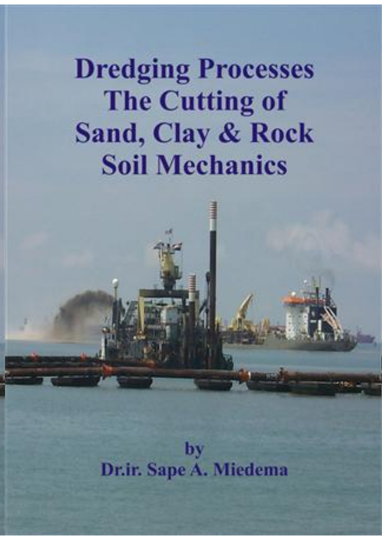
Dredging Processes
The Cutting of
Sand, Clay & Rock
Soil Mechanics
by
Dr.ir. Sape A. Miedema

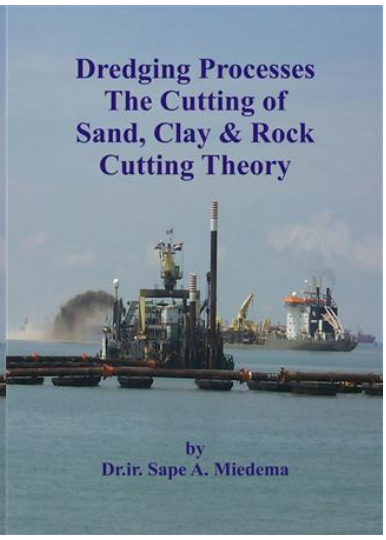
Dredging Processes
The Cutting of
Sand, Clay & Rock
Cutting Theory
by
Dr.ir. Sape A. Miedema

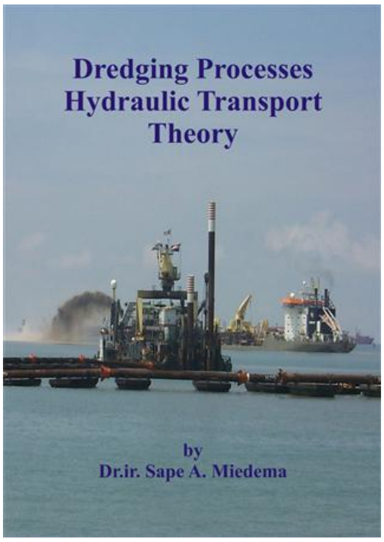
Dredging Processes
Hydraulic Transport
Theory
by
Dr.ir. Sape A. Miedema

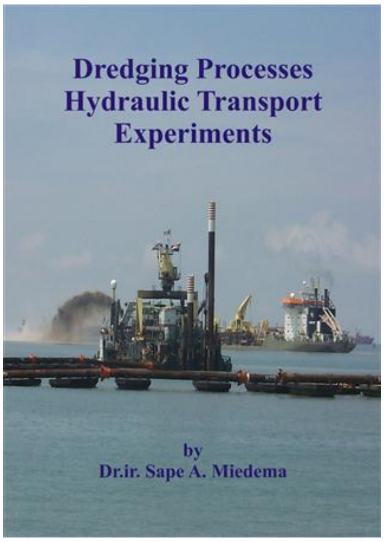
Dredging Processes
Hydraulic Transport
Experiments
by
Dr.ir. Sape A. Miedema

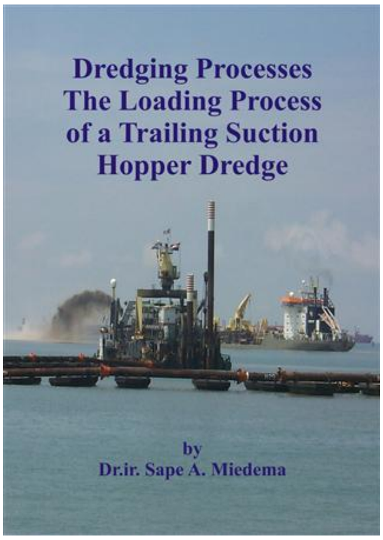
Dredging Processes
The Loading Process
of a Trailing Suction
Hopper Dredge
by
Dr.ir. Sape A. Miedema

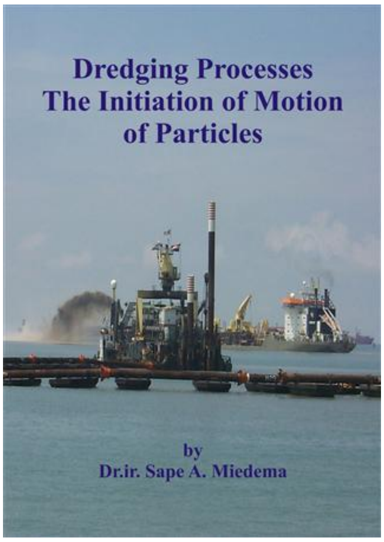
Dredging Processes
The Initiation of Motion
of Particles
by
Dr.ir. Sape A. Miedema

Dredging Processes
The Cutting of Sand, Clay & Rock
Theory

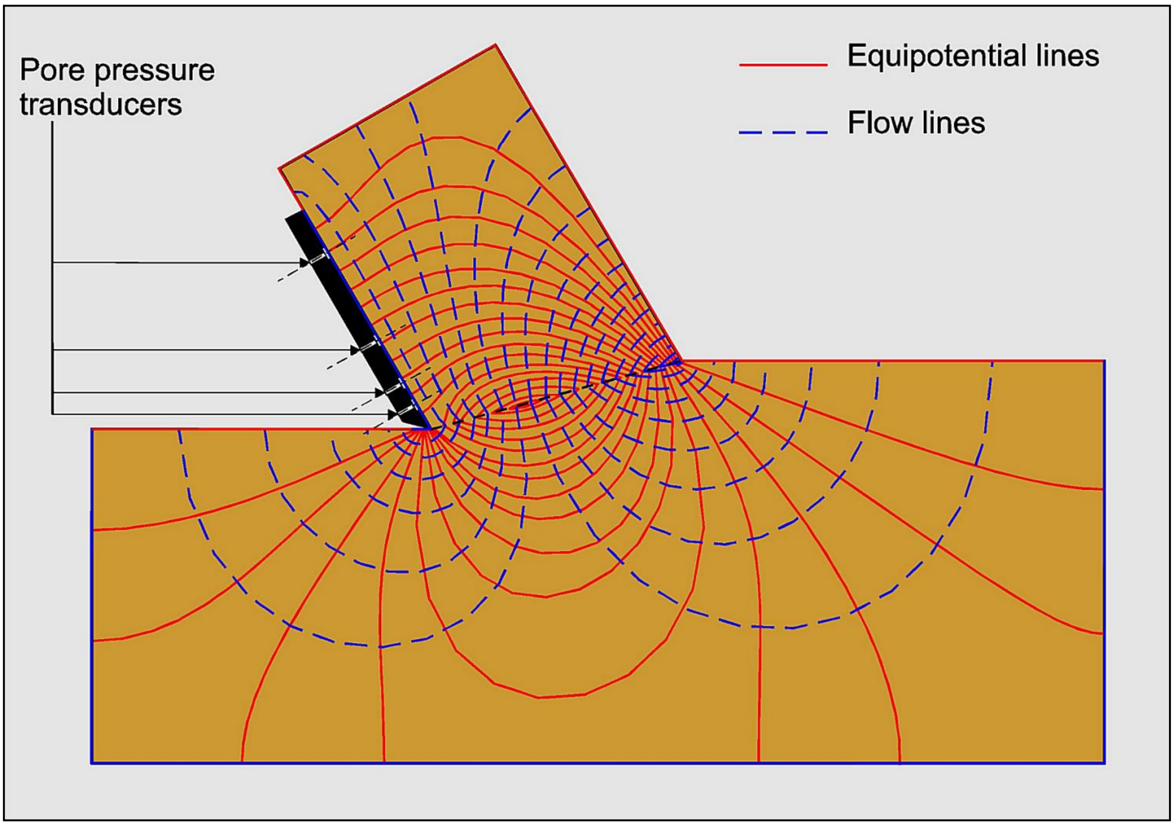

By

Dr.ir. Sape A. Miedema

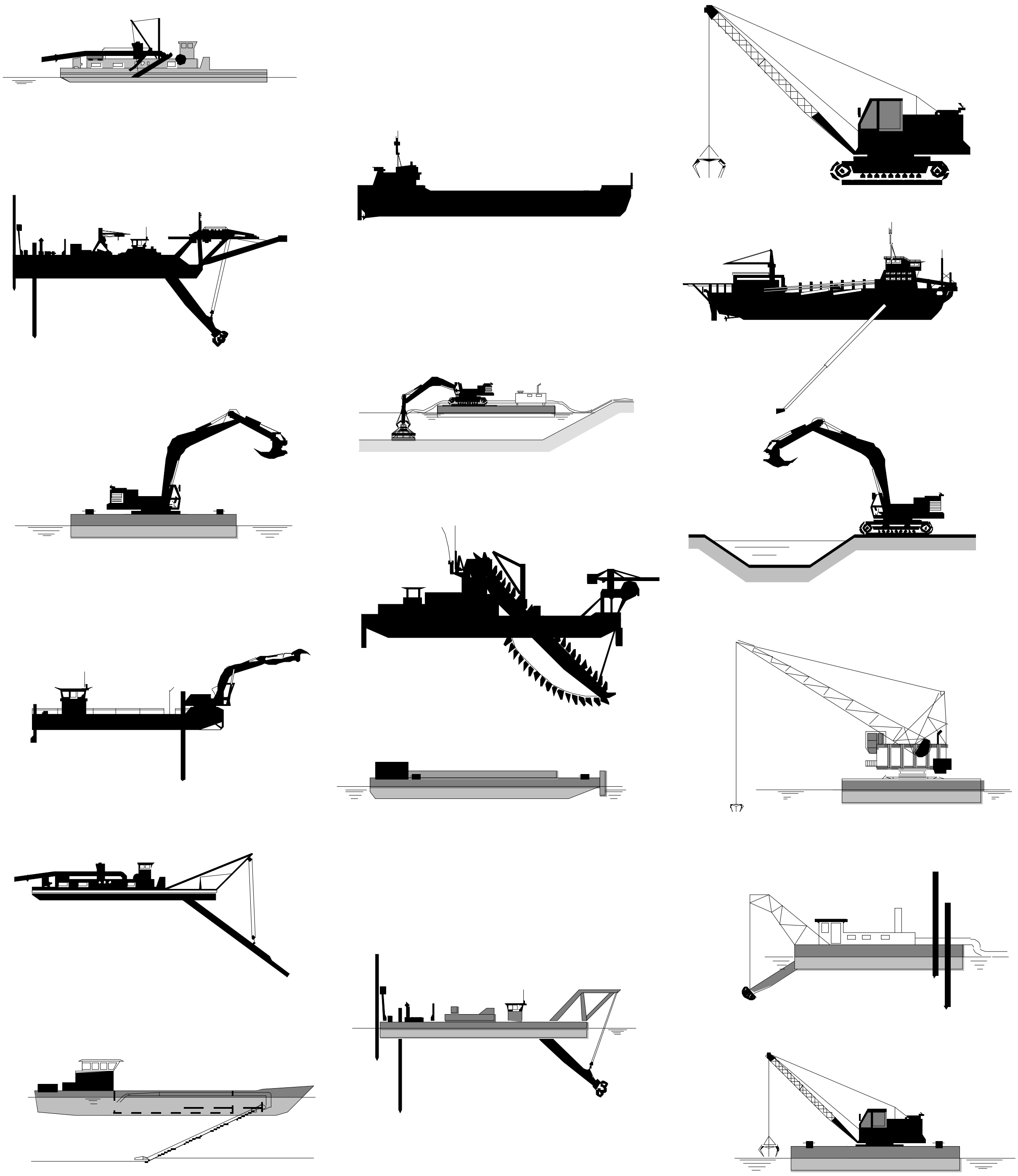

Dredging Processes
The Cutting of Sand, Clay & Rock
Theory

This book is dedicated to my grandson Tijmen

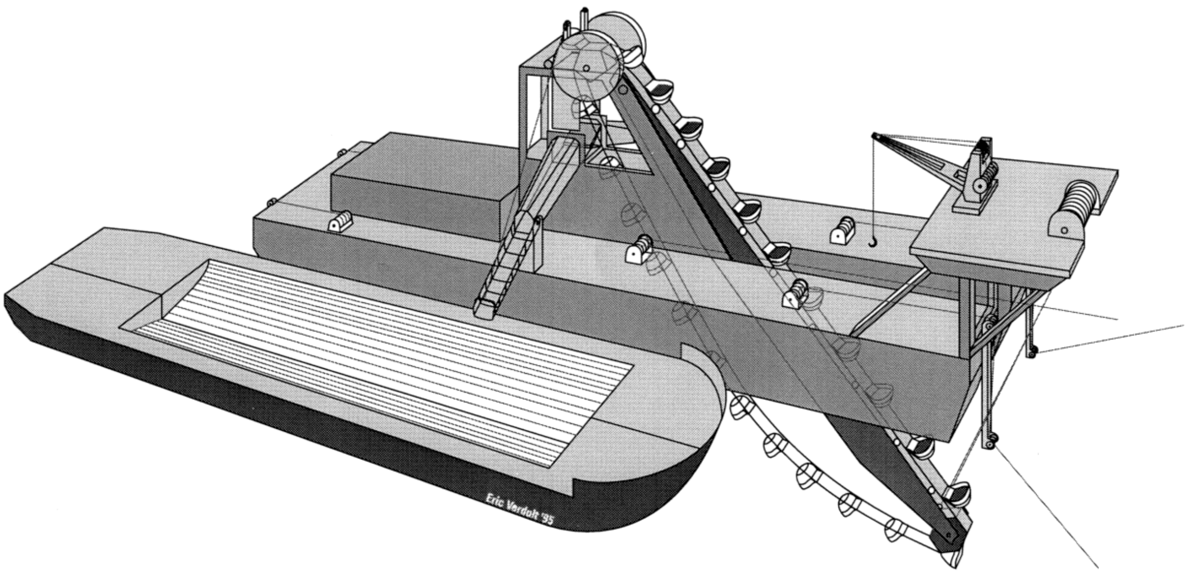

Design & Production: Dr.ir. S.A. Miedema

ISBN Book: 978-94-6186-249-5

ISBN EBook: 978-94-6186-252-5

Preface

Lecture notes for the course OE4626 Dredging Processes, for the MSc program Offshore & Dredging Engineering, at the Delft University of Technology.

By Dr.ir. Sape A. Miedema, Thursday, November 28, 2013

In dredging, trenching, (deep sea) mining, drilling, tunnel boring and many other applications, sand, clay or rock has to be excavated. The productions (and thus the dimensions) of the excavating equipment range from mm^3/sec - cm^3/sec to m^3/sec. In oil drilling layers with a thickness of a magnitude of 0.2 mm are cut, while in dredging this can be of a magnitude of 0.1 m with cutter suction dredges and meters for clamshells and backhoe's. Some equipment is designed for dry soil, while others operate under water saturated conditions. Installed cutting powers may range up to 10 MW. For both the design, the operation and production estimation of the excavating equipment it is important to be able to predict the cutting forces and powers. After the soil has been excavated it is usually transported hydraulically as a slurry over a short (TSHD's) or a long distance (CSD's). Estimating the pressure losses and determining whether or not a bed will occur in the pipeline is of great importance. Fundamental processes of sedimentation, initiation of motion and ersosion of the soil particles determine the transport process and the flow regimes. In TSHD's the soil has to settle during the loading process, where also sedimentation and erosion will be in equilibrium. In all cases we have to deal with soil and high density soil water mixtures and its fundamental behavior.

Publications of the author on the cutting processes:

1. Miedema, S.A., "The soil reaction forces on a crown cutter head on a swell compensated ladder". LaO/81/97, Delft University of Technology, 1981, 36 pages.
2. Miedema, S.A., "Computer program for the determination of the reaction forces on a cutter head, resulting from the motions of the cutter head". Delft Hydraulics, 1981, 82 pages.
3. Miedema, S.A., "The mathematical modeling of the soil reaction forces on a cutter head and the development of the computer program DREDMO". CO/82/125, Delft University of Technology, 1982, with appendices 600 pages.
4. Miedema, S.A., "The Interaction between Cutter head and Soil at Sea" (In Dutch). Proc. Dredging Day November 19th, Delft University of Technology 1982.
5. Koning, J. de, Miedema, S.A., & Zwartbol, A., "Soil/Cutter head Interaction under Wave Conditions ". Proc. WODCON X, Singapore 1983.
6. Miedema, S.A., "Mathematical Modeling of a Seagoing Cutter Suction Dredge" (In Dutch). Published: The Hague, 18-9-1984, KIVI Lectures, Section Under Water Technology.
7. Miedema, S.A., "The Cutting of Densely Compacted Sand under Water ". Terra et Aqua No. 28, October 1984 pp. 4-10.
8. Miedema, S.A., "Mathematical Modeling of the Cutting of Densely Compacted Sand Under Water". Dredging & Port Construction, July 1985, pp. 22-26.
9. Miedema, S.A., "Derivation of the Differential Equation for Sand Pore Pressures". Dredging & Port Construction, September 1985, pp. 35.
10. Miedema, S.A., "The Application of a Cutting Theory on a Dredging Wheel ". Proc. WODCON XI, Brighton 1986.
11. Miedema, S.A., "Underwater Soil Cutting: a Study in Continuity". Dredging & Port Construction, June 1986, pp. 47-53.
12. Miedema, S.A., "The cutting of water saturated sand, laboratory research" (In Dutch). Delft University of Technology, 1986, 17 pages.
13. Miedema, S.A., "The forces on a trenching wheel, a feasibility study" (In Dutch). Delft, 1986, 57 pages + software.
14. Miedema, S.A., "Calculation of the Cutting Forces when Cutting Water Saturated Sand ". Basic Theory and Applications for 3-D Blade Movements and Periodically Varying Velocities for, in Dredging Commonly used Excavating Means. Ph.D. Thesis, Delft University of Technology, September 15th 1987.
15. Bakker, A. & Miedema, S.A., "The Specific Energy of the Dredging Process of a Grab Dredge". Delft University of Technology, 1988, 30 pages.
16. Miedema, S.A., "On the Cutting Forces in Saturated Sand of a Seagoing Cutter Suction Dredge". Proc. WODCON XII, Orlando, Florida, USA, April 1989. This paper was given the IADC Award for the best technical paper on the subject of dredging in 1989.

17. Miedema, S.A., "On the Cutting Forces in Saturated Sand of a Seagoing Cutter Suction Dredge". Terra et Aqua No. 41, December 1989, Elseviers Scientific Publishers.
18. Miedema, S.A., "New Developments of Cutting Theories with respect to Dredging, the Cutting of Clay". Proc. WODCON XIII, Bombay, India, 1992.
19. Miedema, S.A. & Journee, J.M.J. & Schuurmans, S., "On the Motions of a Seagoing Cutter Dredge, a Study in Continuity". Proc. WODCON XIII, Bombay, India, 1992.
20. Becker, S. & Miedema, S.A. & Jong, P.S. de & Wittekoek, S., "On the Closing Process of Clamshell Dredges in Water Saturated Sand". Proc. WODCON XIII, Bombay, India, 1992. This paper was given the IADC Award for the best technical paper on the subject of dredging in 1992.
21. Becker, S. & Miedema, S.A. & Jong, P.S. de & Wittekoek, S., "The Closing Process of Clamshell Dredges in Water Saturated Sand". Terra et Aqua No. 49, September 1992, IADC, The Hague.
22. Miedema, S.A., "Modeling and Simulation of Dredging Processes and Systems". Symposium "Zicht op Bagger processen", Delft University of Technology, Delft, The Netherlands, 29 October 1992.
23. Miedema, S.A. & Becker, S., "The Use of Modeling and Simulation in the Dredging Industry, in Particular the Closing Process of Clamshell Dredges", CEDA Dredging Days 1993, Amsterdam, Holland, 1993.
24. Miedema, S.A., "On the Snow-Plough Effect when Cutting Water Saturated Sand with Inclined Straight Blades". ASCE Proc. Dredging 94, Orlando, Florida, USA, November 1994.
25. Miedema, S.A., "Production Estimation Based on Cutting Theories for Cutting Water Saturated Sand". Proc. WODCON IV, November 1995, Amsterdam, The Netherlands 1995.
26. Miedema, S.A. & Zhao Yi, "An Analytical Method of Pore Pressure Calculations when Cutting Water Saturated Sand". Texas A&M 33nd Annual Dredging Seminar, June 2001, Houston, USA 2001.
27. Zhao Yi, & Miedema, S.A., "Finite Element Calculations To Determine The Pore Pressures When Cutting Water Saturated Sand At Large Cutting Angles". CEDA Dredging Day 2001, November 2001, Amsterdam, the Netherlands.
28. Miedema, S.A., & Ma, Y., "The Cutting of Water Saturated Sand at Large Cutting Angles". Proc. Dredging02, May 5-8, Orlando, Florida, USA.
29. Miedema, S.A., & He, Y., "The Existence of Kinematic Wedges at Large Cutting Angles". Proc. WEDA XXII Technical Conference & 34th Texas A&M Dredging Seminar, June 12-15, Denver, Colorado, USA.
30. Miedema, S.A., Frijters, D., "The Mechanism of Kinematic Wedges at Large Cutting Angles - Velocity and Friction Measurements". 23rd WEDA Technical Conference & 35th TAMU Dredging Seminar, Chicago, USA, June 2003.
31. Miedema, S.A., "The Existence of Kinematic Wedges at Large Cutting Angles". CHIDA Dredging Days, Shanghai, China, November 2003.
32. Miedema, S.A. & Frijters, D.D.J., "The wedge mechanism for cutting of water saturated sand at large cutting angles". WODCON XVII, September 2004, Hamburg Germany.
33. Miedema, S.A., "THE CUTTING MECHANISMS OF WATER SATURATED SAND AT SMALL AND LARGE CUTTING ANGLES". International Conference on Coastal Infrastructure Development - Challenges in the 21st Century. Hong Kong, November 2004.
34. He, J., Miedema, S.A. & Vlasblom, W.J., "FEM Analyses Of Cutting Of Anisotropic Densely Compacted and Saturated Sand", WEDAXXV & TAMU37, New Orleans, USA, June 2005.
35. Miedema, S.A., "The Cutting of Water Saturated Sand, the FINAL Solution". WEDAXXV & TAMU37, New Orleans, USA, June 2005.
36. Miedema, S.A., "THE CUTTING OF WATER SATURATED SAND, THE SOLUTION". CEDA African Section: Dredging Days 2006 - Protection of the coastline, dredging sustainable development, Nov. 1-3, Tangiers, Morocco.
37. Miedema, S.A. & Vlasblom, W.J., "THE CLOSING PROCESS OF CLAMSHELL DREDGES IN WATER-SATURATED SAND". CEDA African Section: Dredging Days 2006 - Protection of the coastline, dredging sustainable development, Nov. 1-3, Tangiers, Morocco.
38. Miedema, S.A. "THE CUTTING OF WATER SATURATED SAND, THE SOLUTION". The 2nd China Dredging Association International Conference & Exhibition, themed 'Dredging and Sustainable Development' and in Guangzhou, China, May 17-18 2006.
39. Ma, Y, Ni, F. & Miedema, S.A., "Calculation of the Blade Cutting Force for small Cutting Angles based on MATLAB". The 2nd China Dredging Association International Conference & Exhibition, themed 'Dredging and Sustainable Development' and in Guangzhou, China, May 17-18 2006.
40. Miedema, S.A. , Kerkvliet, J., Strijbis, D., Jonkman, B., Hatert, M. v/d, "THE DIGGING AND HOLDING CAPACITY OF ANCHORS". WEDA XXVI AND TAMU 38, San Diego, California, June 25-28, 2006.
41. Ma Yasheng, Ni Fusheng, S.A. Miedema, "Mechanical Model of Water Saturated Sand Cutting at Blade Large Cutting Angles", Journal of Hohai University Changzhou, ISSN 1009-1130, CN 32-1591, 2006.

42. Miedema, S.A., Lager, G.H.G., Kerkvliet, J., "An Overview of Drag Embedded Anchor Holding Capacity for Dredging and Offshore Applications". WODCON, Orlando, USA, 2007.
43. Miedema, S.A., "A Sensitivity Analysis Of The Production Of Clamshells". WEDA XXVIII & Texas A&M 39. St. Louis, USA, June 8-11, 2008.
44. Miedema, S.A., "A Sensitivity Analysis Of The Production Of Clamshells". WEDA Journal of Dredging Engineering, December 2008.
45. Miedema, S.A., "New Developments Of Cutting Theories With Respect To Dredging, The Cutting Of Clay And Rock". WEDA XXIX & Texas A&M 40. Phoenix Arizona, USA, June 14-17 2009.
46. Miedema, S.A., "New developments of cutting theories with respect to offshore applications, the cutting of sand, clay and rock". ISOPE 2010, Beijing China, June 2010.
47. Miedema, S.A., "The influence of the strain rate on cutting processes". ISOPE 2010, Beijing China, June 2010.
48. Abdeli, M., Miedema, S.A., Schott, D., Alvarez Grima, M., "The application of discrete element modeling in dredging". WODCON XIX, Beijing China, September 2010.
49. Rahman, M., Schott, D.L., Miedema, S.A., Lodewijks, G., "Simulation of cutting process by hybrid granular and multi-body dynamics software". 3rd International Conference on Bulk solids. Glasgow, Scotland, September 9-10, 2010.
50. Rahman, M., Abdeli, M., Miedema, S.A., Schott, D., "Simulation of passive soil failure & cutting processes in sand. OMAE 2011 ASME, June 19-24, Rotterdam, the Netherlands.
51. Miedema, S.A., "Soil cutting processes, the cutting of water saturated sand". OMAE 2011 ASME, June 19-24, Rotterdam, the Netherlands.
52. Miedema, S.A., "THE BULLDOZER EFFECT WHEN CUTTING WATER SATURATED SAND". OMAE 2012 ASME, June 10-15, Rio de Janeiro, Brazil.
53. Miedema, S.A., Zijsling, D., "HYPERBARIC ROCK CUTTING". OMAE 2012 ASME, June 10-15, Rio de Janeiro, Brazil.

This book gives an overview of cutting theories. It starts with a generic model, which is valid for all types of soil (sand, clay and rock) after which the specifics of dry sand, water saturated sand, clay, rock and hyperbaric rock are covered. For each soil type small blade angles and large blade angles, resulting in a wedge in front of the blade, are discussed. The failure mechanism of sand, dry and water saturated, is the so called Shear Type. The failure mechanism of clay is the so called Flow Type, but under certain circumstances also the Curling Type and the Tear Type are possible. Rock will usually fail in a brittle way. This can be brittle tensile failure, the Tear Type, for small blade angles, but it can also be brittle shear failure, which is of the Shear Type of failure mechanism for larger blade angles. Under hyperbaric conditions rock may also fail in a more ductile way according to the Flow Type of failure mechanism.

For each case considered, the equations/model for the cutting forces, power and specific energy are given. The models are verified with laboratory research, mainly at the Delft University of Technology, but also with data from literature.

Dr.ir. Sape A. Miedema
Delft University of Technology
Delft, the Netherlands
Thursday, November 28, 2013

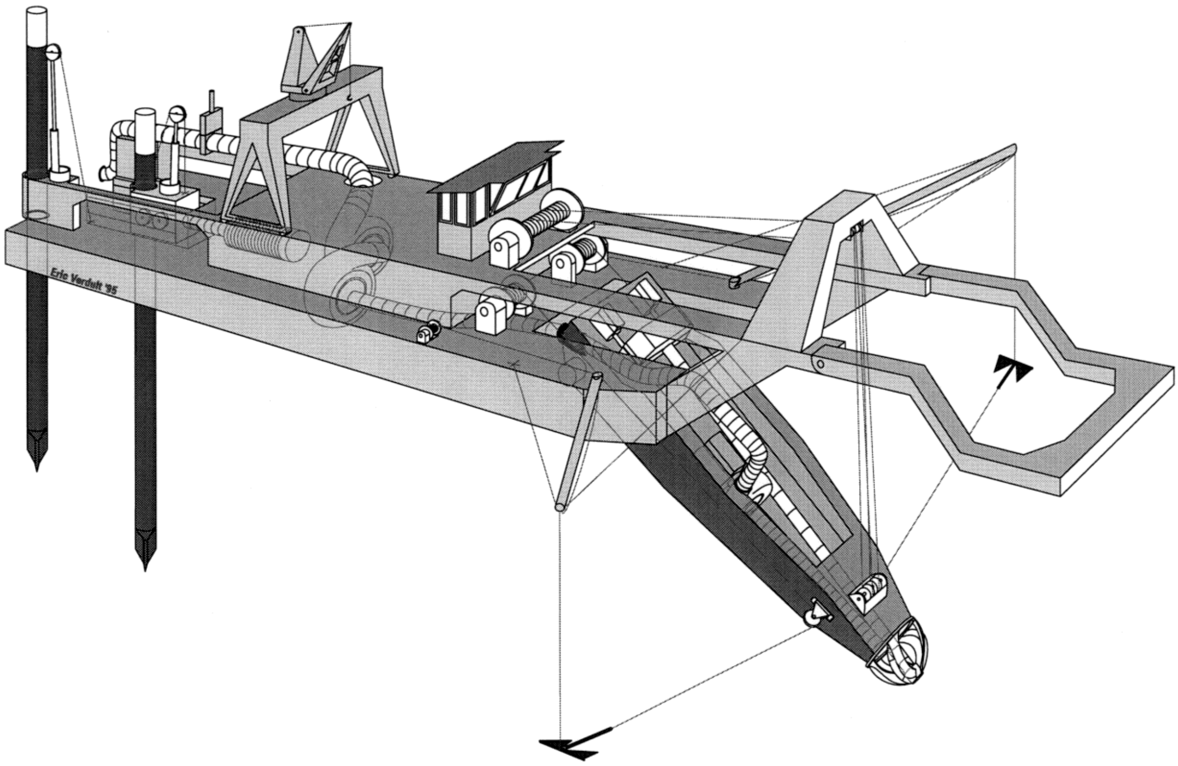
Eric Verdult '95

Table of Contents

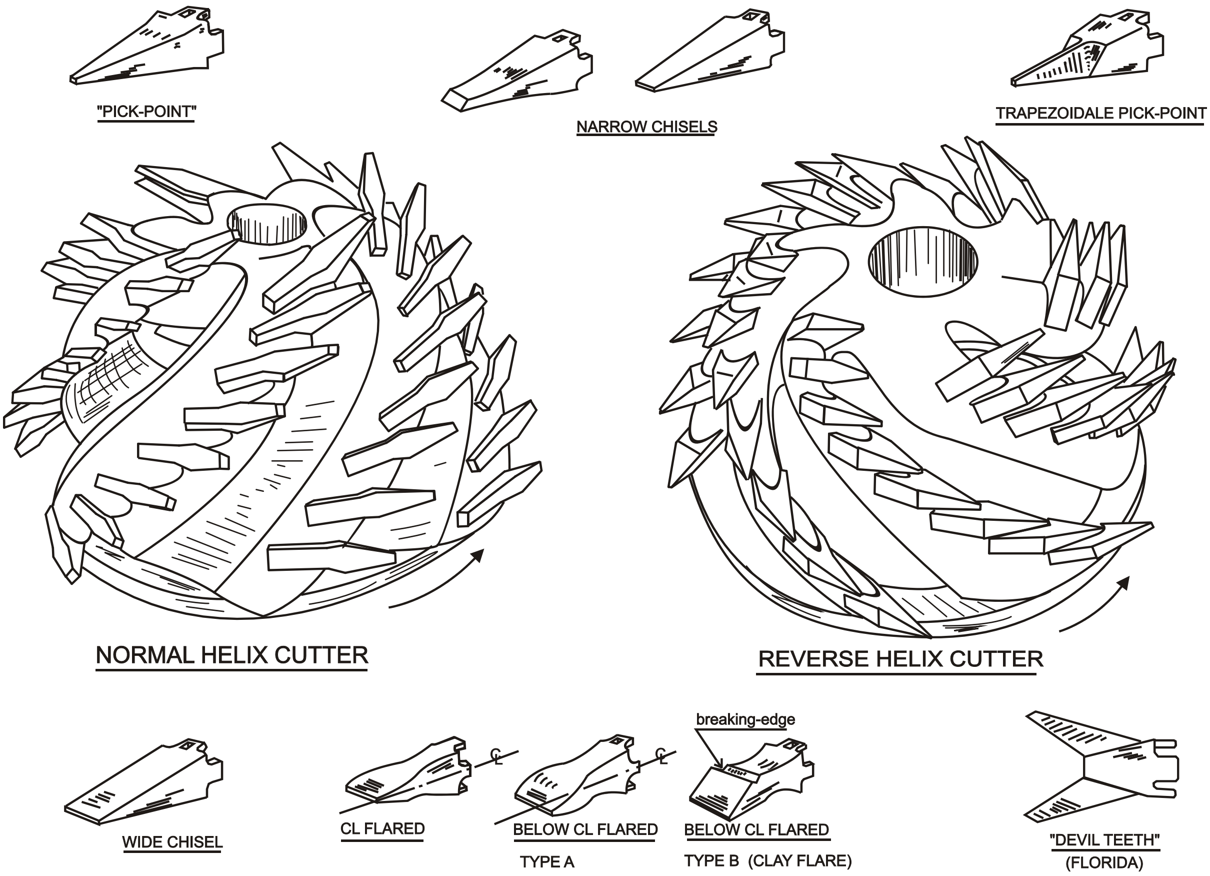
"PICK-POINT"
NARROW CHISELS
TRAPEZOIDALE PICK-POINT
NORMAL HELIX CUTTER
REVERSE HELIX CUTTER
breaking-edge
WIDE CHISEL
CL FLARED
BELOW CL FLARED
TYPE A
BELOW CL FLARED
TYPE B (CLAY FLARE)
"DEVIL TEETH"
(FLORIDA)

Chapter 1: Some Basic Soil Mechanics

1.1. Introduction

Cutting processes of soil distinguish from the classical soil mechanics in civil engineering in the fact that:

Classical soil mechanics assume:
1. Small to very small strain rates.
2. Small to very small strains.
3. A very long time span, years to hundrets of years.
4. Structures are designed to last forever.

Cutting processes assume:
1. High to very high strain rates.
2. High to very high strains and deformations in general.
3. A very short time span, following from very high cutting velocities.
4. The soil is supposed to be excavated, the coherence has to be broken.

For the determination of cutting forces, power and specific energy the criterion for failure has to be known. In this book the failure criterion of Mohr-Coulomb will be applied in the mathematical models for the cutting of sand, clay and rock. The Mohr–Coulomb theory is named in honour of Charles-Augustin de Coulomb and Christian Otto Mohr. Coulomb's contribution was a 1773 essay entitled "*Essai sur une application des règles des maximis et minimis à quelques problèmes de statique relatifs à l'architecture*". Mohr developed a generalised form of the theory around the end of the 19th century. To understand and work with the Mohr-Coulomb failure criterion it is also necessary to understand the so called Mohr circle. The Mohr circle is a two dimensional graphical representation of the state of stress at a point. The absissa, $\boldsymbol{\sigma}$, and ordinate, $\boldsymbol{\tau}$, of each point on the circle are the normal stress and shear stress components, respectively, acting on a particular cut plane under an angle $\boldsymbol{\alpha}$ with the horizontal. In other words, the circumference of the circle is the locus of points that represent the state of stress on individual planes at all their orientations. In this book a plane strain situation is considered, meaning a two-dimensional cutting process. The width of the blades considered $\mathbf{w}$ is always much bigger than the layer thickness $\mathbf{h_i}$ considered. In geomechanics (soil mechanics and rock mechanics) compressive stresses are considered positive and tensile stresses are considered to be negative, while in other engineering mechanics the tensile stresses are considered to be positive and the compressive stresses are considered to be negative. Here the geomechanics approach will be applied. There are two special stresses to be mentioned, the so called principal stresses. Principal stresses occur at the planes where the shear stress is zero. In the plane strain situation there are two principal stresses, which are always under an angle of 90º with each other.

1.2. The Mohr Circle

In the derivation of the Mohr circle the vertical stress $\boldsymbol{\sigma_v}$ and the horizontal stress $\boldsymbol{\sigma_h}$ are assumed to be the principal stresses, but in reality these stresses could have any orientation. It should be noted here that the Mohr circle approach is valid for the stress situation in a point in the soil.Now consider an infinitisimal element of soil under plane strain conditions as is shown in Figure 1-1. On the element a vertical stress $\boldsymbol{\sigma_v}$ and a horizontal stress $\boldsymbol{\sigma_h}$ are acting. On the horizontal and vertical planes the shear stresses are assumed to be zero. Now the question is? What would the normal stress $\boldsymbol{\sigma}$ and shear stress $\boldsymbol{\tau}$ be on a plane with an angle $\boldsymbol{\alpha}$ with the horizontal direction? To solve this problem, the horizontal and vertical equilibria of forces will be derived. Equilibria of stresses do not exist, by the way. One should consider that the surfaces of the triangle drawn in Figure 1-1 are not equal. If the surface (or length) of the surface under the angle $\boldsymbol{\alpha}$ is considered to be 1, then the surface (or length) of the horizontal side is **cos(α)** and the vertical side **sin(α)**. The stresses have to be multiplied with their surface in order to get forces and forces are required for the equilibria of forces. The derivation of the Mohr circle is also an excersise for the derivation of many equations in this book where equilibria of forces and moments are applied.

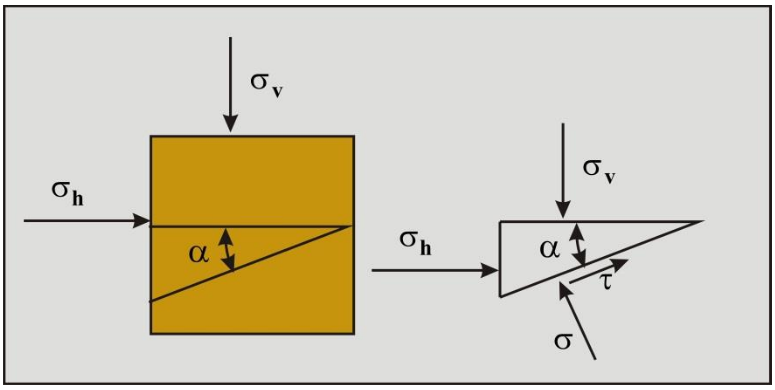

Figure 1-1: The stresses on a soil element.

The equilibrium of forces in the horizontal direction:

$$\sigma_h \cdot \sin(\alpha) = \sigma \cdot \sin(\alpha) - \tau \cdot \cos(\alpha) \tag{1-1}$$

The equilibrium of forces in the vertical direction:

$$\sigma_v \cdot \cos(\alpha) = \sigma \cdot \cos(\alpha) + \tau \cdot \sin(\alpha) \tag{1-2}$$

Equations (1-1) and (1-2) form a system of two equations with two unknowns' $\boldsymbol{\sigma}$ and $\boldsymbol{\tau}$. The normal stresses $\boldsymbol{\sigma_h}$ and $\boldsymbol{\sigma_v}$ are considered to be known variables. To find a solution for the normal stress $\boldsymbol{\sigma}$ on the plane considered, equation (1-1) is multiplied with **sin(α)** and equation (1-2) is multiplied with **cos(α)**, this gives:

$$\sigma_h \cdot \sin(\alpha) \cdot \sin(\alpha) = \sigma \cdot \sin(\alpha) \cdot \sin(\alpha) - \tau \cdot \cos(\alpha) \cdot \sin(\alpha) \tag{1-3}$$

$$\sigma_v \cdot \cos(\alpha) \cdot \cos(\alpha) = \sigma \cdot \cos(\alpha) \cdot \cos(\alpha) + \tau \cdot \sin(\alpha) \cdot \cos(\alpha) \tag{1-4}$$

Adding up equations (1-3) and (1-4) eliminates the terms with $\boldsymbol{\tau}$ and preserves the terms with $\boldsymbol{\sigma}$, giving:

$$\sigma_v \cdot \cos^2(\alpha) + \sigma_h \cdot \sin^2(\alpha) = \sigma \tag{1-5}$$

Using some basic rules from trigonometry:

$$\cos^2(\alpha) = \frac{1 + \cos(2 \cdot \alpha)}{2} \tag{1-6}$$

$$\sin^2(\alpha) = \frac{1 - \cos(2 \cdot \alpha)}{2} \tag{1-7}$$

Giving for the normal stress **σ** on the plane considered:

$$\sigma = \left(\frac{\sigma_v + \sigma_h}{2}\right) + \left(\frac{\sigma_v - \sigma_h}{2}\right) \cdot \cos(2 \cdot \alpha) \qquad \textbf{(1-8)}$$

To find a solution for the shear stress τ on the plane considered, equation (1-1) is multiplied with **-cos(α)** and equation (1-2) is multiplied with **sin(α)**, this gives:

$$-\sigma_h \cdot \sin(\alpha) \cdot \cos(\alpha) = -\sigma \cdot \sin(\alpha) \cdot \cos(\alpha) + \tau \cdot \cos(\alpha) \cdot \cos(\alpha) \qquad \textbf{(1-9)}$$

$$\sigma_v \cdot \cos(\alpha) \cdot \sin(\alpha) = \sigma \cdot \cos(\alpha) \cdot \sin(\alpha) + \tau \cdot \sin(\alpha) \cdot \sin(\alpha) \qquad \textbf{(1-10)}$$

Adding up equations (1-9) and (1-10) eliminates the terms with **σ** and preserves the terms with **τ**, giving:

$$(\sigma_v - \sigma_h) \cdot \sin(\alpha) \cdot \cos(\alpha) = \tau \qquad \textbf{(1-11)}$$

Using the basic rules from trigonometry, equations (1-6) and (1-7), gives for **τ** on the plane considered:

$$\tau = \left(\frac{\sigma_v - \sigma_h}{2}\right) \cdot \sin(2 \cdot \alpha) \qquad \textbf{(1-12)}$$

Squaring equations (1-8) and (1-12) gives:

$$\left(\sigma - \left(\frac{\sigma_v + \sigma_h}{2}\right)\right)^2 = \left(\frac{\sigma_v - \sigma_h}{2}\right)^2 \cdot \cos^2(2 \cdot \alpha) \qquad \textbf{(1-13)}$$

And:

$$\tau^2 = \left(\frac{\sigma_v - \sigma_h}{2}\right)^2 \cdot \sin^2(2 \cdot \alpha) \qquad \textbf{(1-14)}$$

Adding up equations (1-13) and (1-14) gives:

$$\left(\sigma - \left(\frac{\sigma_v + \sigma_h}{2}\right)\right)^2 + \tau^2 = \left(\frac{\sigma_v - \sigma_h}{2}\right)^2 \cdot \left(\sin^2(2 \cdot \alpha) + \cos^2(2 \cdot \alpha)\right) \qquad \textbf{(1-15)}$$

This can be simplified to the following circle equation:

$$\left(\sigma - \left(\frac{\sigma_v + \sigma_h}{2}\right)\right)^2 + \tau^2 = \left(\frac{\sigma_v - \sigma_h}{2}\right)^2 \qquad \textbf{(1-16)}$$

If equation (1-16) is compared with the general circle equation from mathematics, equation (1-17):

$$(x - x_C)^2 + (y - y_C)^2 = R^2 \qquad \textbf{(1-17)}$$

The following is found:

$$x = \sigma$$
$$x_C = \left(\frac{\sigma_v + \sigma_h}{2}\right)$$
$$y = \tau \qquad \textbf{(1-18)}$$
$$y_C = 0$$

$$\mathbf{R} = \left(\frac{\sigma_v - \sigma_h}{2} \right)$$

Figure 1-2 shows the resulting Mohr circle with the Mohr-Coulomb failure criterion:

$$\tau = c + \sigma \cdot \tan(\varphi) \qquad \textbf{(1-19)}$$

The variable **c** is the cohesion or internal shear strength of the soil. In Figure 1-2 it is assumed that the cohesion **c=0**, which describes the behavior of a cohesionless soil, sand. Further it is assumed that the vertical stress σ_v (based on the weight of the soil above the point considered) is bigger than the horizontal stress σ_h. So in this case the horizontal stress at failure follows the vertical stress. The angle α of the plane considered, appears as an angle of $2\cdot\alpha$ in the Mohr circle.
Figure 1-3: Shows how the internal friction angle can be determined from a number of tri-axial tests for a cohesionless soil (sand). The 3 circles in this figure will normally not have the failure line as a tangent exactly, but one circle will be a bit to big and another a bit to small. The failure line found will be a best fit.
Figure 1-4 and Figure 1-5 show the Mohr circles for a soil with an internal friction angle and cohesion. In such a soil, the intersection point of the failure line with the vertical axis is considered to be the cohesion.

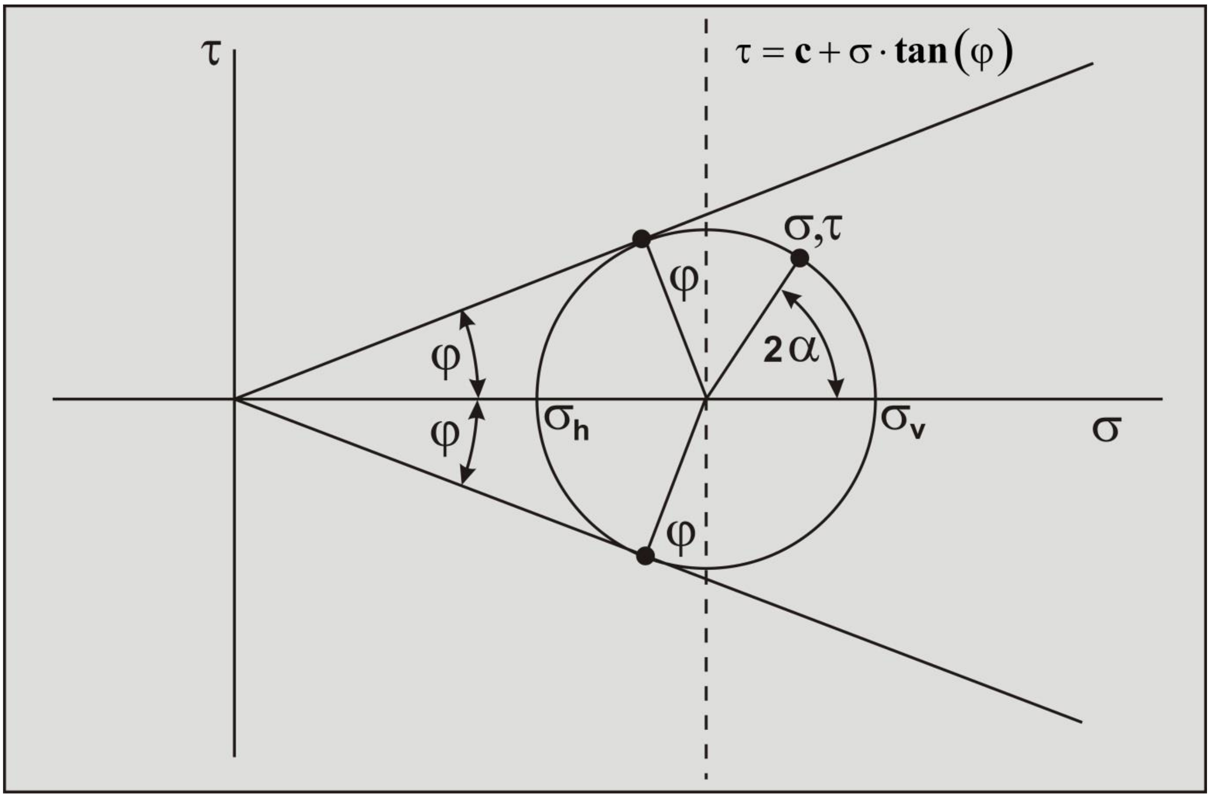

Figure 1-2: The resulting Mohr circle for cohesionless soil.

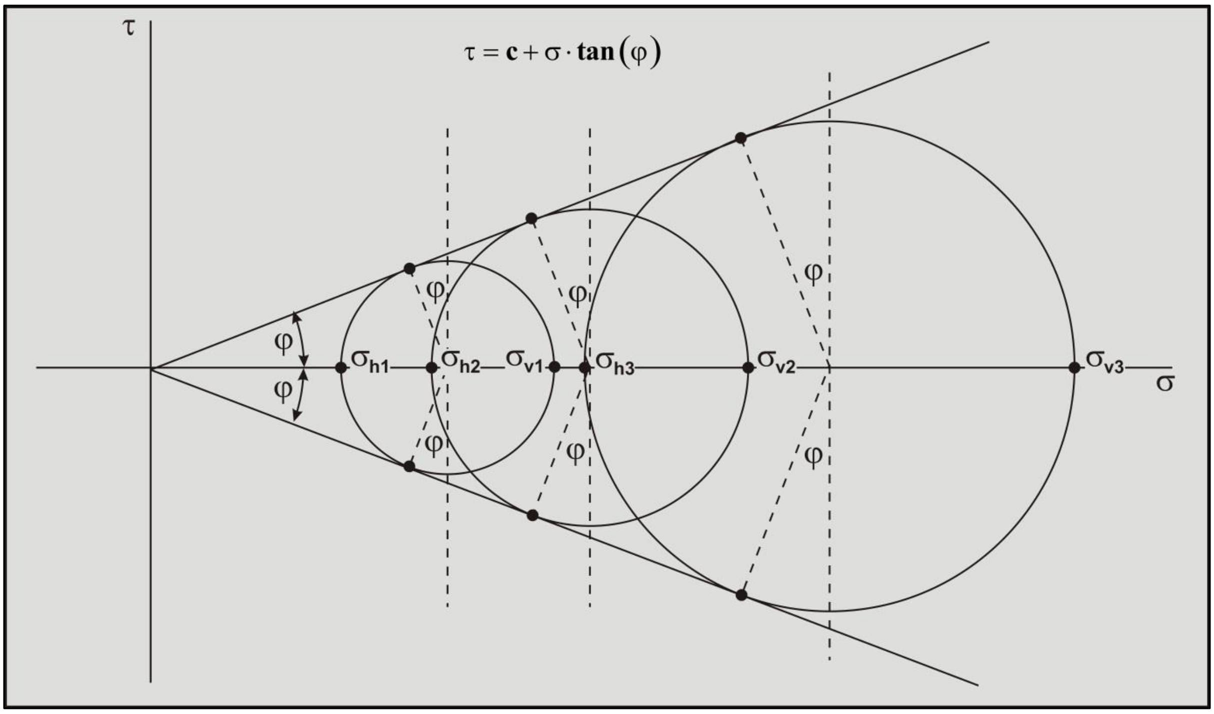

Figure 1-3: Determining the angle of internal friction from tri-axial tests of cohesionless soil.

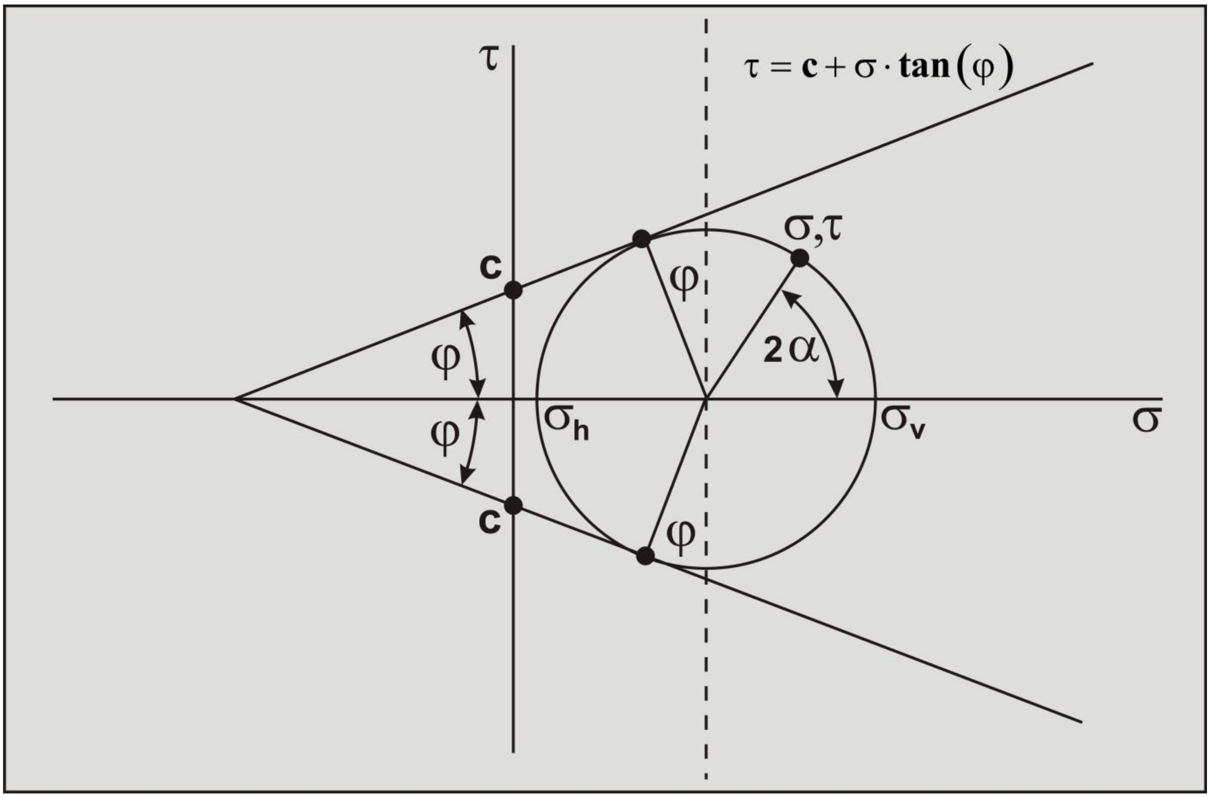

Figure 1-4: The Mohr circle including cohesion.

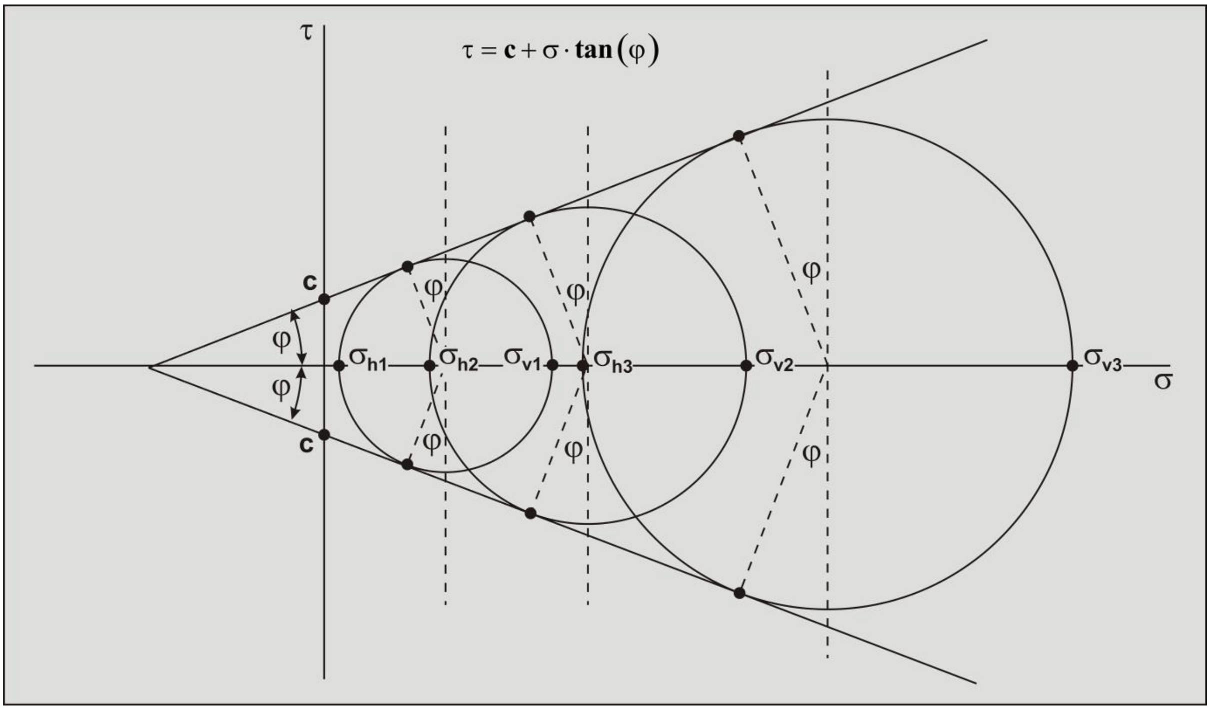

Figure 1-5: Determining the angle of internal friction from tri-axial tests of soil with cohesion.

1.3. Active Soil Failure

Active soil failure is failure of the soil where the soil takes action, normally because of gravity. The standard example of active soil failure is illustrated by the retaining wall example. A retaining wall has to withstand the forces exerted on it by the soil, in this case a sand with an internal friction angle **φ**. The retaining wall has to be strong enough to withstand the maximum possible occuring force. The height of the reaining wall is **h**. The problem has 4 unknowns; the force on the retaining wall **F**, the normal force on the shear plane **N**, the shear force on the shear plane **S** and the angle of the shear plane with the horizontal **β**. To solve this problem, 4 conditions (equations) have to be defined. The first equation is the relation between the normal force **N** and the shear force **S**. The second and third equations follow from the horizontal and vertical equilibrium of forces on the triangular wedge that will move downwards when the retaining wall fails to withstand the soil forces. The fourth condition follows from the fact that we search for the maximum possible force, a maximum will occur if the derivative of the force with respect to the angle of the shear plane is zero and the double derivative is negative. It should be mentioned that the directon of the shear force is always opposite to the possible direction of motion of the soil. Since the soil will move downwards because of gravity, the shear force is directed upwards.

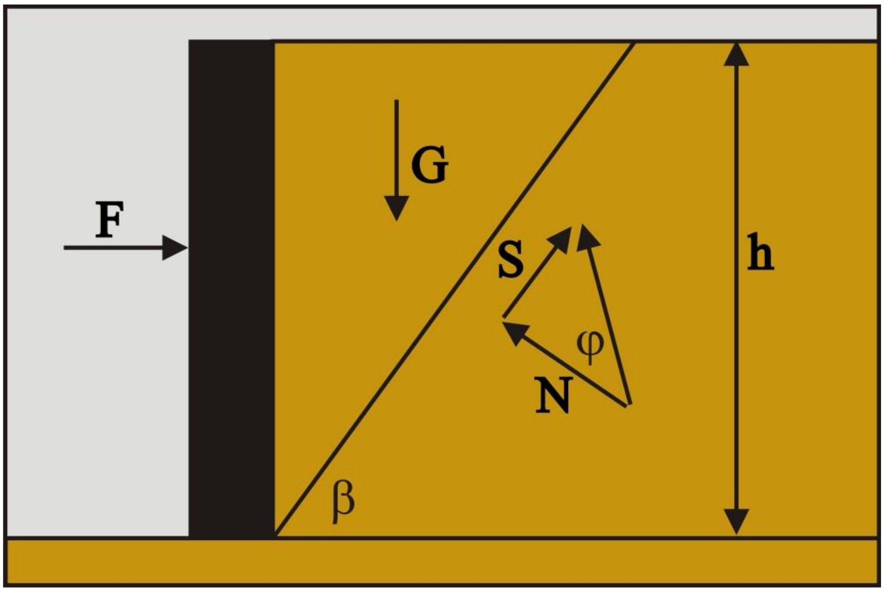

Figure 1-6: Active soil failure.

To start solving the problem, first the weight of the triangular wedge of soil is determined according to:

$$\mathbf{G = \frac{1}{2} \cdot \rho_s \cdot g \cdot h^2 \cdot cot(\beta)} \tag{1-20}$$

The first relation necessary to solve the problem, the relation between the normal force and the shear force on the shear plane is:

$$\mathbf{S = N \cdot tan(\varphi)} \tag{1-21}$$

Further it is assumed that the soil consists of pure sand without cohesion and adhesion and it is assumed that the retaining wall is smooth, so no friction between the sand and the wall.

$$\begin{aligned} &\textbf{No cohesion} \Rightarrow \mathbf{c=0} \\ &\textbf{No adhesion} \Rightarrow \mathbf{a=0} \\ &\textbf{Smooth wall} \Rightarrow \mathbf{\delta=0} \end{aligned} \tag{1-22}$$

This gives for the horizontal and vertical equilibrium equations on the triangular wedge:

$$\begin{aligned} &\textbf{Horizontal} \Rightarrow \mathbf{F + S \cdot cos(\beta) - N \cdot sin(\beta) = 0} \\ &\textbf{Vertical} \Rightarrow \mathbf{G - N \cdot cos(\beta) - S \cdot sin(\beta) = 0} \end{aligned} \tag{1-23}$$

Solving the first 3 equations with the first 3 unknowns gives for the force on the retaining wall:

$$\mathbf{F = -G \cdot \tan(\varphi - \beta)} \tag{1-24}$$

With the equation for the weight of the sand.

$$\mathbf{G = \frac{1}{2} \cdot \rho_s \cdot g \cdot h^2 \cdot \cot(\beta)} \tag{1-25}$$

The equation for the force on the retaining wall is found.

$$\mathbf{F = -\frac{1}{2} \cdot \rho_s \cdot g \cdot h^2 \cdot \frac{\cos(\beta) \cdot \sin(\varphi - \beta)}{\sin(\beta) \cdot \cos(\varphi - \beta)}} \tag{1-26}$$

This equation still contains the angle of the shear plane as an unknown. Since we are looking for the maximum possible force, a value for **β** has to be found where this force reaches a maximum. The derivative of the force and the double derivative have to be determined.

$$\mathbf{\frac{dF}{d\beta} = 0} \tag{1-27}$$

$$\mathbf{\frac{d^2F}{d\beta^2} < 0} \tag{1-28}$$

Since the equation of the force on the retaining wall contains this angle both in the nominator and the denominator, determining the derivative may be complicated. It is easier to simplify the equation with the following trick:

$$\begin{gathered}\mathbf{-\frac{\cos(\beta) \cdot \sin(\varphi - \beta)}{\sin(\beta) \cdot \cos(\varphi - \beta)} = -\frac{\cos(\beta) \cdot \sin(\varphi - \beta)}{\sin(\beta) \cdot \cos(\varphi - \beta)} - 1 + 1 =} \\ \mathbf{-\frac{\cos(\beta) \cdot \sin(\varphi - \beta)}{\sin(\beta) \cdot \cos(\varphi - \beta)} - \frac{\sin(\beta) \cdot \cos(\varphi - \beta)}{\sin(\beta) \cdot \cos(\varphi - \beta)} + 1 = 1 - \frac{\sin(\varphi)}{\sin(\beta) \cdot \cos(\varphi - \beta)}}\end{gathered} \tag{1-29}$$

Substituting this result in the equation for the force on the retaining wall gives:

$$\mathbf{F = \frac{1}{2} \cdot \rho_g \cdot g \cdot h^2 \cdot \left(1 - \frac{\sin(\varphi)}{\sin(\beta) \cdot \cos(\varphi - \beta)}\right)} \tag{1-30}$$

When the denominator in the term between brackets has a maximum, also the whole equation has a maximum. So we have to find the maximum of this denominator.

$$\mathbf{f = \sin(\beta) \cdot \cos(\beta - \varphi) \;\Rightarrow\; F\ maximum\ if\ f\ maximum} \tag{1-31}$$

The first derivative of this denominator with respect to the shear angle is:

$$\mathbf{\frac{df}{d\beta} = \cos(2 \cdot \beta - \varphi)} \tag{1-32}$$

The second derivative of this denominator with respect to the shear angle is:

$$\mathbf{\frac{d^2f}{d\beta^2} = -2 \cdot \sin(2 \cdot \beta - \varphi)} \tag{1-33}$$

The first derivative is zero when the shear angle equals 45 degrees plus half the internal friction angle:

$$\frac{df}{d\beta} = 0 \Rightarrow \beta = \frac{\pi}{4} + \frac{1}{2} \cdot \varphi \tag{1-34}$$

Substituting this solution in the equation for the double derivative gives a negative double derivative which shows that a maximum has been found.

$$\frac{d^2 f}{d\beta^2} = -2 \text{ for } \beta = \frac{\pi}{4} + \frac{1}{2} \cdot \varphi \tag{1-35}$$

Substituting this solution for the shear plane angle in the equation for the force on the retaining wall gives:

$$F = \frac{1}{2} \cdot \rho_s \cdot g \cdot h^2 \cdot \left(\frac{1 - \sin(\varphi)}{1 + \sin(\varphi)} \right) = \frac{1}{2} \cdot \rho_s \cdot g \cdot h^2 \cdot K_a \tag{1-36}$$

The factor $\mathbf{K_a}$ is often referred to as the coefficient of active failure, which is smaller than 1. In the case of a 30 degrees internal friction angle, the value is 1/3.

$$K_A = \frac{1 - \sin\varphi}{1 + \sin\varphi} = \tan^2(45 - \varphi / 2) \tag{1-37}$$

The horizontal stresses equal the vertical stresses times the factor of active failure, which means that the horizontal stresses are smaller than the vertical stresses.

$$\sigma_h = K_A \cdot \sigma_v \tag{1-38}$$

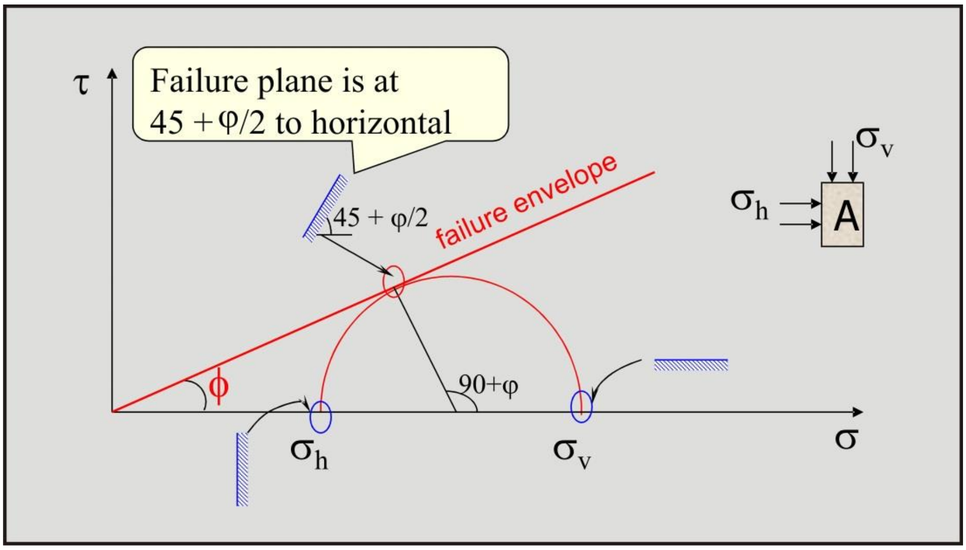

Figure 1-7: The Mohr circle for active soil failure.

1.4. Passive Soil Failure

Passive soil failure is failure of the soil where the outside world takes action, for example a bulldozer. The standard example of passive soil failure is illustrated by the retaining wall example. A retaining wall has to push to supercede the forces exerted on it by the soil, in this case a sand with an internal friction angle **φ**. The retaining wall has to push strong enough to overcome the minimum possible occuring force. The height of the reaining wall is **h**. The problem has 4 unknowns; the force on the retaining wall **F**, the normal force on the shear plane **N**, the shear force on the shear plane **S** and the angle of the shear plane with the horizontal **β**. To solve this problem, 4 conditions (equations) have to be defined. The first equation is the relation between the normal force **N** and the shear force **S**. The second and third equations follow from the horizontal and vertical equilibrium of forces on the triangular wedge that will move upwards when the retaining wall pushes and the soil fails. The fourth condition follows from the fact that we search for the minimum possible force, a minimum will occur if the derivative of the force with respect to the angle of the shear plane is zero and the double derivative is positive. It should be mentioned that the directon of the shear force is always opposite to the possible direction of motion of the soil. Since the soil will move upwards because of the pushing retaining wall, the shear force is directed downwards.

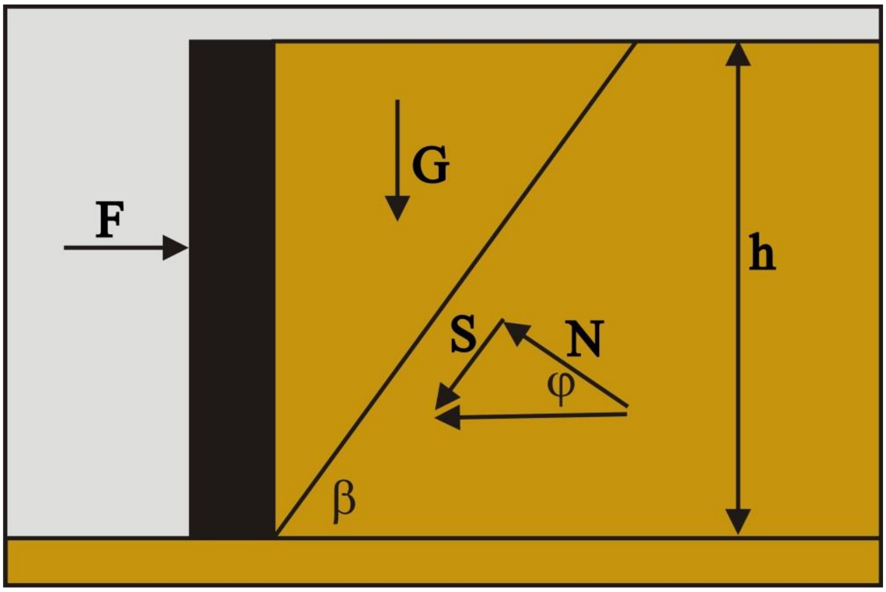

Figure 1-8: Passive soil failure.

To start solving the problem, first the weight of the triangular wedge of soil is determined according to:

$$G = \frac{1}{2} \cdot \rho_g \cdot g \cdot h^2 \cdot \cot(\beta) \tag{1-39}$$

The first relation necessary to solve the problem, the relation between the normal force and the shear force on the shear plane is:

$$S = N \cdot \tan(\varphi) \tag{1-40}$$

Further it is assumed that the soil consists of pure sand without cohesion and adhesion and it is assumed that the retaining wall is smooth, so no friction between the sand and the wall.

$$\begin{aligned} &\text{No cohesion} \Rightarrow c=0 \\ &\text{No adhesion} \Rightarrow a=0 \\ &\text{Smooth wall} \Rightarrow \delta=0 \end{aligned} \tag{1-41}$$

This gives for the horizontal and vertical equilibrium equations on the triangular wedge:

$$\begin{aligned} &\text{Horizontal} \Rightarrow F - S \cdot \cos(\beta) - N \cdot \sin(\beta) = 0 \\ &\text{Vertical} \Rightarrow G - N \cdot \cos(\beta) + S \cdot \sin(\beta) = 0 \end{aligned} \tag{1-42}$$

Solving the first 3 equations with the first 3 unknowns gives for the force on the retaining wall:

$$\mathbf{F = G \cdot \tan(\varphi + \beta)} \tag{1-43}$$

With the equation for the weight of the sand.

$$\mathbf{G = \frac{1}{2} \cdot \rho_g \cdot g \cdot h^2 \cdot \cot(\beta)} \tag{1-44}$$

The equation for the force on the retaining wall is found.

$$\mathbf{F = \frac{1}{2} \cdot \rho_g \cdot g \cdot h^2 \cdot \frac{\cos(\beta) \cdot \sin(\varphi + \beta)}{\sin(\beta) \cdot \cos(\varphi + \beta)}} \tag{1-45}$$

This equation still contains the angle of the shear plane as an unknown. Since we are looking for the minimum possible force, a value for **β** has to be found where this force reaches a minimum. The derivative of the force and the double derivative have to be determined.

$$\mathbf{\frac{dF}{d\beta} = 0} \tag{1-46}$$

$$\mathbf{\frac{d^2F}{d\beta^2} > 0} \tag{1-47}$$

Since the equation of the force on the retaining wall contains this angle both in the nominator and the denominator, determining the derivative may be complicated. It is easier to simplify the equation with the following trick:

$$\begin{gathered}\mathbf{\frac{\cos(\beta) \cdot \sin(\varphi + \beta)}{\sin(\beta) \cdot \cos(\varphi + \beta)} = \frac{\cos(\beta) \cdot \sin(\varphi + \beta)}{\sin(\beta) \cdot \cos(\varphi + \beta)} - 1 + 1 = \frac{\cos(\beta) \cdot \sin(\varphi + \beta)}{\sin(\beta) \cdot \cos(\varphi + \beta)} - \frac{\sin(\beta) \cdot \cos(\varphi + \beta)}{\sin(\beta) \cdot \cos(\varphi + \beta)} + 1 =} \\ \mathbf{\frac{\cos(-\beta) \cdot \sin(\varphi + \beta)}{\sin(\beta) \cdot \cos(\varphi + \beta)} + \frac{\sin(-\beta) \cdot \cos(\varphi + \beta)}{\sin(\beta) \cdot \cos(\varphi + \beta)} + 1 = 1 + \frac{\sin(\varphi)}{\sin(\beta) \cdot \cos(\varphi + \beta)}}\end{gathered} \tag{1-48}$$

Substituting this result in the equation for the force on the retaining wall gives:

$$\mathbf{F = \frac{1}{2} \cdot \rho_g \cdot g \cdot h^2 \cdot \left(1 + \frac{\sin(\varphi)}{\sin(\beta) \cdot \cos(\varphi + \beta)}\right)} \tag{1-49}$$

When the denominator in the term between brackets has a maximum, also the whole equation has a minimum. So we have to find the maximum of this denominator.

$$\mathbf{f = \sin(\beta) \cdot \cos(\beta + \varphi) \;\; \Rightarrow \;\; F \text{ minimum if } f \text{ maximum}} \tag{1-50}$$

The first derivative of this denominator with respect to the shear angle is:

$$\mathbf{\frac{df}{d\beta} = \cos(2 \cdot \beta + \varphi)} \tag{1-51}$$

The second derivative of this denominator with respect to the shear angle is:

$$\mathbf{\frac{d^2f}{d\beta^2} = -2 \cdot \sin(2 \cdot \beta + \varphi)} \tag{1-52}$$

The first derivative is zero when the shear angle equals 45 degrees minus half the internal friction angle:

$$\frac{df}{d\beta}=0 \Rightarrow \beta=\frac{\pi}{4}-\frac{1}{2}\cdot\varphi \tag{1-53}$$

Substituting this solution in the equation for the double derivative gives a negative double derivative which shows that a maximum has been found.

$$\frac{d^2f}{d\beta^2}=-2 \text{ for } \beta=\frac{\pi}{4}-\frac{1}{2}\cdot\varphi \tag{1-54}$$

Substituting this solution for the shear plane angle in the equation for the force on the retaining wall gives:

$$F=\frac{1}{2}\cdot\rho_g\cdot g\cdot h^2\cdot\left(\frac{1+\sin(\varphi)}{1-\sin(\varphi)}\right)=\frac{1}{2}\cdot\rho_g\cdot g\cdot h^2\cdot K_p \tag{1-55}$$

The factor K_p is often referred to as the coefficient of passive failure, which is larger than 1. In the case of a 30 degrees internal friction angle, the value is 3.

$$K_p=\frac{1+\sin\varphi}{1-\sin\varphi}=\tan^2(45+\varphi/2) \tag{1-56}$$

The horizontal stresses equal the vertical stresses times the factor of passive failure, which means that the horizontal stresses are larger than the vertical stresses.

$$\sigma_h=K_p\cdot\sigma_v \tag{1-57}$$

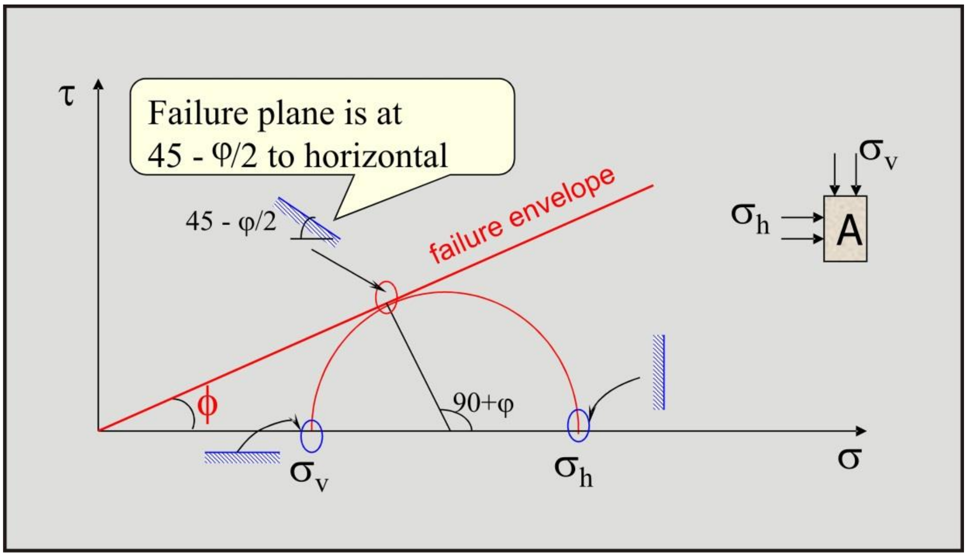

Figure 1-9: The Mohr circle for passive soil failure.

1.5. Summary

Figure 1-10 gives a summary of the Mohr circles for **Active** and **Passive** failure of a cohesionless soil.

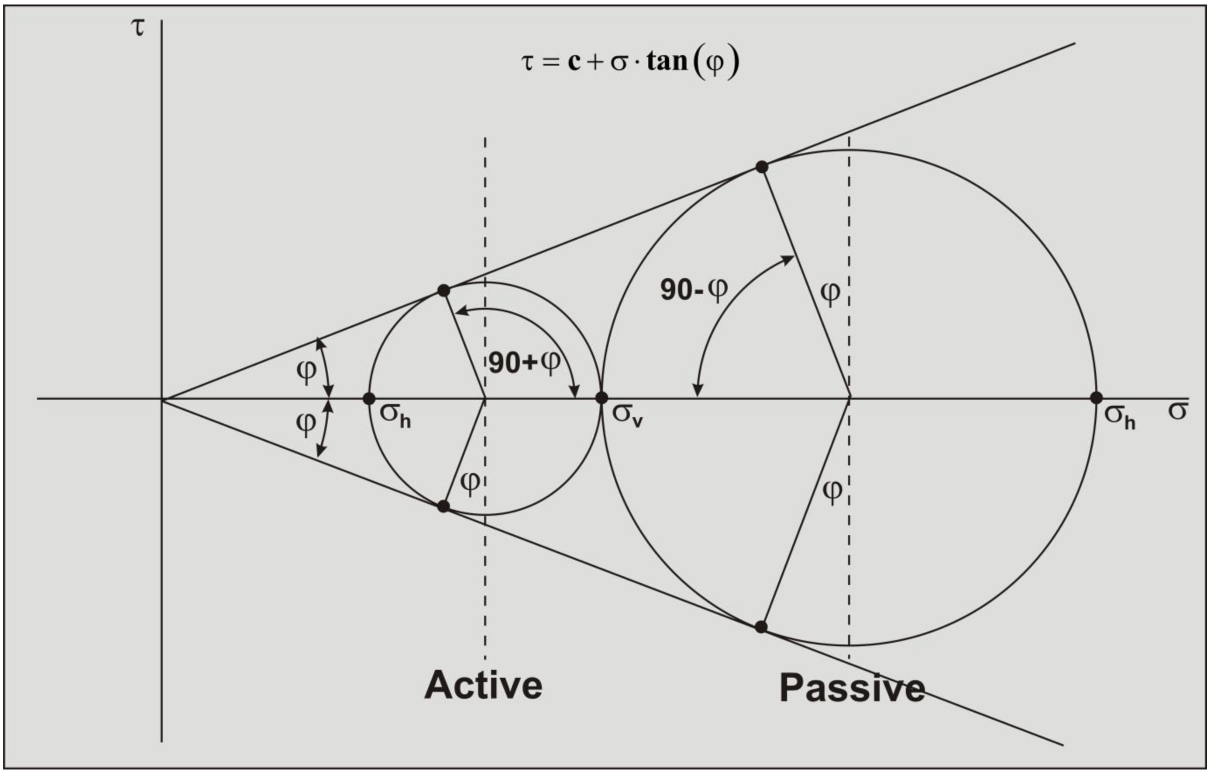

Figure 1-10: The Mohr circles for active and passive failure for a cohesionless soil.

Some equations for a cohesionless soil in the active state:

Failure will occur if:

$$\sin(\varphi) = \frac{\frac{1}{2} \cdot (\sigma_v - \sigma_h)}{\frac{1}{2} \cdot (\sigma_v + \sigma_h)} \tag{1-58}$$

This can also be written as:

$$\left(\frac{\sigma_v - \sigma_h}{2}\right) - \left(\frac{\sigma_v + \sigma_h}{2}\right) \cdot \sin(\varphi) = 0 \tag{1-59}$$

Using this equation the value of $\boldsymbol{\sigma_h}$ can be expressed into $\boldsymbol{\sigma_v}$:

$$\sigma_h = \sigma_v \frac{1 - \sin(\varphi)}{1 + \sin(\varphi)} = K_a \cdot \sigma_v \tag{1-60}$$

On the other hand, the value of $\boldsymbol{\sigma_v}$ can also be expressed into $\boldsymbol{\sigma_h}$:

$$\sigma_v = \sigma_h \frac{1 + \sin(\varphi)}{1 - \sin(\varphi)} = K_p \cdot \sigma_h \tag{1-61}$$

For the passive state the stresses $\boldsymbol{\sigma_v}$ and $\boldsymbol{\sigma_h}$ should be reversed.

Figure 1-11 gives a summary of the Mohr circles for **Active** and **Passive** failure for a soil with cohesion.

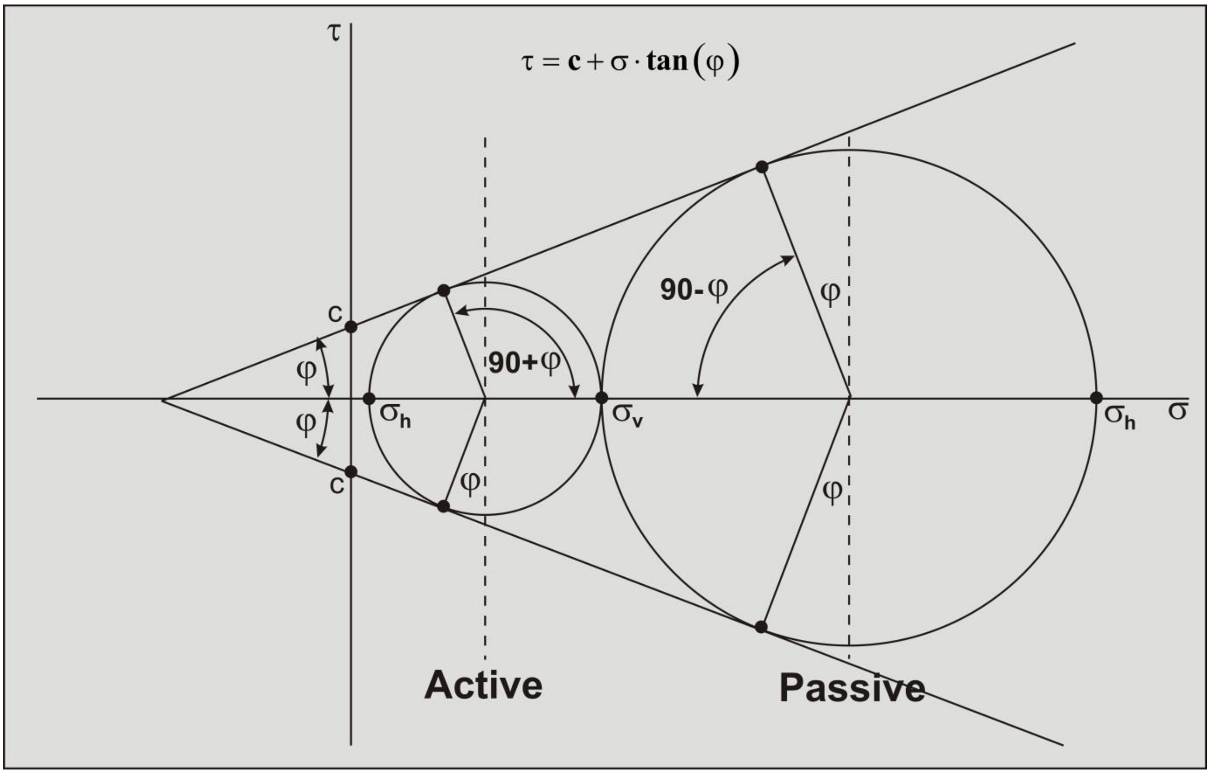

Figure 1-11: The Mohr circles for active and passive failure for a soil with cohesion.

Some equations for a soil with cohesion in the active state:

Failure will occur if:

$$\sin(\varphi) = \frac{\frac{1}{2}\cdot(\sigma_v - \sigma_h)}{c\cdot\cot(\varphi) + \frac{1}{2}\cdot(\sigma_v + \sigma_h)} \tag{1-62}$$

This can also be written as:

$$\left(\frac{\sigma_v - \sigma_h}{2}\right) - \left(\frac{\sigma_v + \sigma_h}{2}\right)\cdot\sin(\varphi) - c\cdot\cos(\varphi) = 0 \tag{1-63}$$

Using this equation the value of $\boldsymbol{\sigma_h}$ can be expressed into $\boldsymbol{\sigma_v}$:

$$\sigma_h = \sigma_v \frac{1-\sin(\varphi)}{1+\sin(\varphi)} - 2\cdot c\cdot\frac{\cos(\varphi)}{1+\sin(\varphi)} = K_a\cdot\sigma_v - 2\cdot c\cdot\sqrt{K_a} \tag{1-64}$$

On the other hand, the value of $\boldsymbol{\sigma_v}$ can also be expressed into $\boldsymbol{\sigma_h}$:

$$\sigma_v = \sigma_h \frac{1+\sin(\varphi)}{1-\sin(\varphi)} + 2\cdot c\cdot\frac{\cos(\varphi)}{1-\sin(\varphi)} = K_p\cdot\sigma_h + 2\cdot c\cdot\sqrt{K_p} \tag{1-65}$$

For the passive state the stresses $\boldsymbol{\sigma_v}$ and $\boldsymbol{\sigma_h}$ should be reversed.

1.6. Cohesion/Adhesion versus Internal/External Friction

To avoid confusion between cohesion and adhesion on one side and internal and external friction on the other side, internal and external friction, also named Coulomb friction, depend linearly on normal stresses, internal friction depends on the normal stress between the sand grains and external friction on the normal stress between the sand grains and another material, for example steel. In civil engineering internal and external friction are denoted by the angle of internal friction and the angle of external friction, also named the soil/interface friction angle. In mechanical engineering the internal and external friction angles are denoted by the internal and external friction coefficient. If there is no normal stress, there is no shear stress resulting from normal stress, so the friction is zero. Adhesion and cohesion are considered to be the sticky effect between two surfaces. Cohesion is the sticky effect between two surfaces of the same material before any failure has occurred and adhesion is the sticky effect between two different materials, for example adhesive tape. Adhesion and cohesion could be named the external and internal shear strength which are independent from normal stresses. The equations for the resulting shear stresses are:

$$\tau_{in} = \tau_c + \sigma_{in} \cdot \tan(\varphi) \quad \text{or} \quad \tau_{in} = \tau_c + \sigma_{in} \cdot \mu_{in} \qquad (1\text{-}66)$$

$$\tau_{ex} = \tau_a + \sigma_{ex} \cdot \tan(\delta) \quad \text{or} \quad \tau_{ex} = \tau_a + \sigma_{ex} \cdot \mu_{ex} \qquad (1\text{-}67)$$

Or

$$\tau_{in} = c + \sigma_{in} \cdot \tan(\varphi) \quad \text{or} \quad \tau_{in} = c + \sigma_{in} \cdot \mu_{in} \qquad (1\text{-}68)$$

$$\tau_{ex} = a + \sigma_{ex} \cdot \tan(\delta) \quad \text{or} \quad \tau_{ex} = a + \sigma_{ex} \cdot \mu_{ex} \qquad (1\text{-}69)$$

With:

$$\mu_{in} = \tan(\varphi) \qquad (1\text{-}70)$$

$$\mu_{ex} = \tan(\delta) \qquad (1\text{-}71)$$

The values of the internal friction angle **φ** and the external friction angle **δ** not only depend on the soil properties like the density and the shape of the particles, but may also depend on the deformation history.

1.7. Nomenclature Chapter 1:

a, τ_a	Adhesion or external shear strength	kPa
c, τ_c	Cohesion or internal shear strength	kPa
f	Function	-
F	Horizontal force	kN
g	Gravitational constant (9.81)	m/s^2
G	Gravitational vertical force	kN
h	Height of the dam/soil	m
K_a	Coefficient of active failure	-
K_p	Coefficient of passive failure	-
N	Force normal to the shear plane	kN
S	Shear force on the shear plane	kN
α	Orientation of shear plane (Mohr circle)	rad
β	Angle of the shear plane (active & passive failure)	rad
δ	External friction angle or soil/interface friction angle	rad
φ	Internal friction angle	rad
σ	Normal stress	kPa
σ_h	Horizontal normal stress (principal stress)	kPa
σ_v	Vertical normal stress (principal stress)	kPa
σ_{in}	Internal normal stress	kPa
σ_{ex}	External normal stress or soil interface normal stress	kPa
τ	Shear stress	kPa
τ_{in}	Internal shear stress	kPa
τ_{ex}	External shear stress or soil interface shear stress	kPa
ρ_g	Density of the soil	ton/m^3
μ_{in}	Internal friction coefficient	-
μ_{ex}	External friction coefficient	-

Chapter 2: The General Cutting Process

2.1. Cutting Mechanisms

Hatamura and Chijiiwa (1975), (1976), (1976), (1977) and (1977) distinguished three failure mechanisms in soil cutting. The "shear type", the "flow type" and the “tear type”. The "flow type" and the "tear type" occur in materials without an angle of internal friction. The "shear type" occurs in materials with an angle of internal friction like sand. A fourth failure mechanism can be distinguished (Miedema (1992)), the "curling type", as is known in metal cutting. Although it seems that the curling of the chip cut is part of the flow of the material, whether the "curling type" or the "flow type" occurs depends on several conditions. The curling type in general will occur if the adhesive force on the blade is large with respect to the normal force on the shear plane. Whether the curling type results in pure curling or buckling of the layer cut giving obstruction of the flow depends on different parameters.

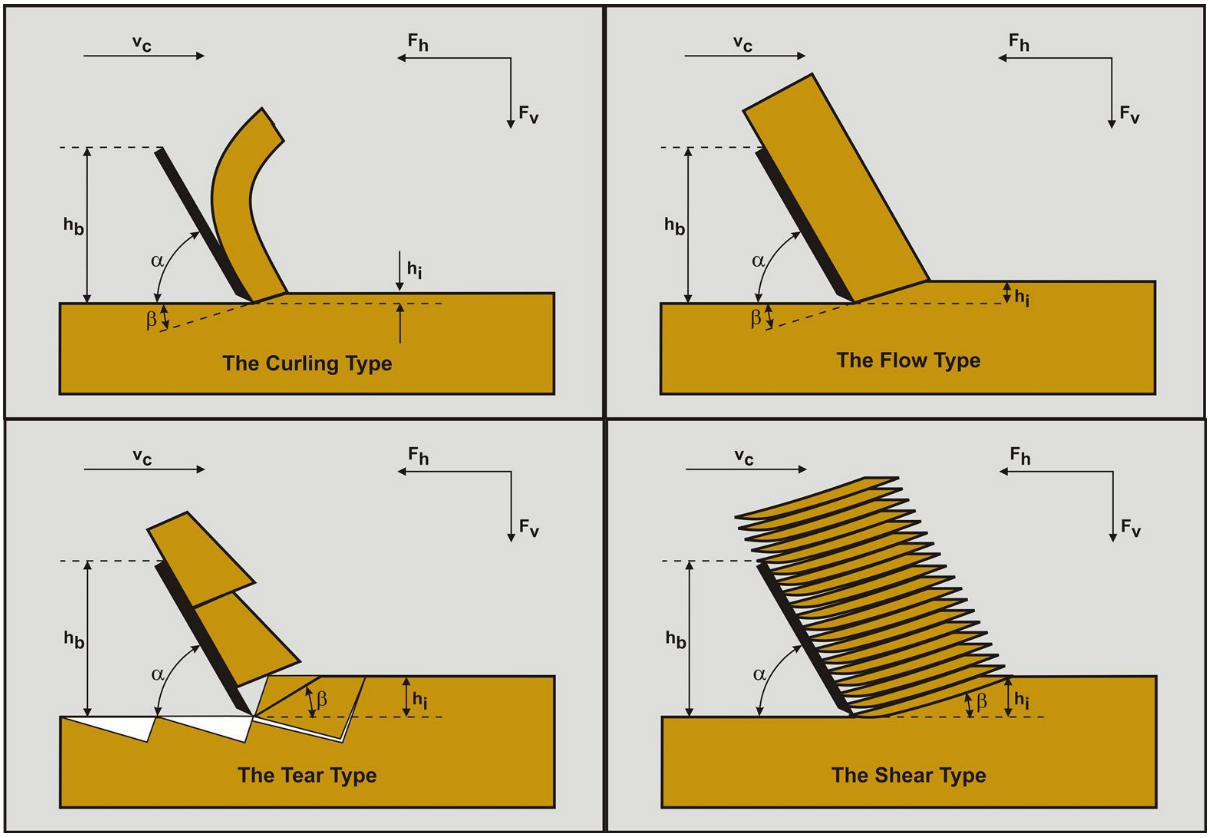

Figure 2-1: The Curling Type, the Flow Type, the Tear Type and the Shear Type.

Figure 2-1 illustrates the curling type, the flow type mechanism as they might occur when cutting clay or rock, the tear type and the shear type mechanism as they might occur when cutting clay or rock (the tear type) or cutting sand (the shear type). To predict which type of failure mechanism will occur under given conditions with specific soil, a formulation for the cutting forces has to be derived. The derivation is made under the assumption that the stresses on the shear plane and the blade are constant and equal to the average stresses acting on the surfaces. Figure 2-2 gives some definitions regaring the cutting process. The line A-B is considered to be the shear plane, while the line A-C is the contact area between the blade and the soil. The blade angle is named $\boldsymbol{\alpha}$ and the shear angle $\boldsymbol{\beta}$. The blade is moving from left to right with a cutting velocity $\mathbf{v_c}$. The thickness of the layer cut is $\mathbf{h_i}$ and the vertical height of the blade $\mathbf{h_b}$. The horizontal force on the blade $\mathbf{F_h}$ is positive from right to left always opposite to the direction of the cutting velocity $\mathbf{v_c}$. The vertical force on the blade $\mathbf{F_v}$ is positive downwards. Since the vertical force is perpendicular to the cutting velocity, the vertical force does not contribute to the cutting power, which is equal to:

$$\mathbf{P_c = F_h \cdot v_c} \tag{2-1}$$

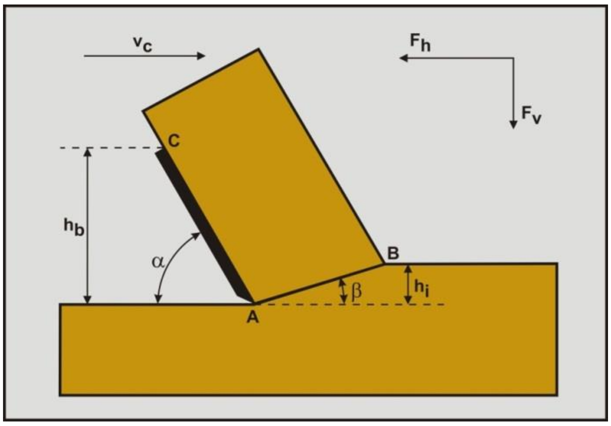

Figure 2-2: The cutting process.

2.2. The Basic Cutting Mechanism: The Flow Type/Shear Type

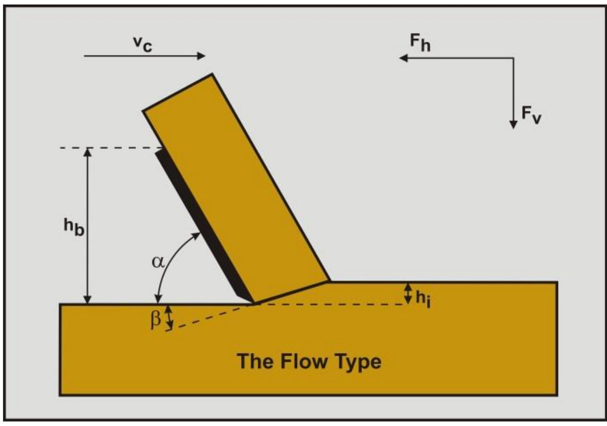

Figure 2-3: The Flow Type

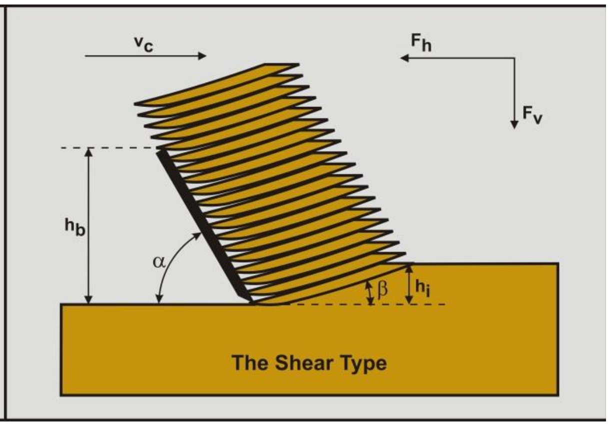

Figure 2-4: The Shear Type

Figure 2-3 and Figure 2-4 show the **Flow Type** and the **Shear Type** of cutting process. The **Shear Type** is modeled as the **Flow Type**. The difference is that in dry soil the forces calculated for the **Flow Type** are constant forces because the process is ductile. For the **Shear Type** the forces are the peak forces, because the process is assumed to be brittle (shear). The average forces can be determined by multiplying the peak forces with a factor of ¼ to ½.

2.2.1. The Equilibrium of Forces

Figure 2-5 illustrates the forces on the layer of soil cut. The forces shown are valid in general. The forces acting on this layer are:

1 A normal force acting on the shear surface $\mathbf{N_1}$ resulting from the effective grain stresses.
2 A shear force $\mathbf{S_1}$ as a result of internal fiction $\mathbf{N_1 \cdot tan(\phi)}$.
3 A force $\mathbf{W_1}$ as a result of water under pressure in the shear zone.
4 A shear force **C** as a result of pure cohesion τ_c. This force can be calculated by multiplying the cohesive shear strength τ_c with the area of the shear plane.
5 A gravity force **G** as a result of the (under water) weight of the layer cut.
6 An inertial force **I**, resulting from acceleration of the soil.
7 A force normal to the blade $\mathbf{N_2}$, resulting from the effective grain stresses.
8 A shear force $\mathbf{S_2}$ as a result of the external friction angle $\mathbf{N_2 \cdot tan(\delta)}$.
9 A shear force **A** as a result of pure adhesion between the soil and the blade τ_a. This force can be calculated by multiplying the adhesive shear strength τ_a of the soil with the contact area between the soil and the blade.
10 A force $\mathbf{W_2}$ as a result of water under pressure on the blade

The normal force $\mathbf{N_1}$ and the shear force $\mathbf{S_1}$ can be combined to a resulting grain force $\mathbf{K_1}$.

$$\mathbf{K_1 = \sqrt{N_1^2 + S_1^2}} \tag{2-2}$$

The forces acting on a straight blade when cutting soil, can be distinguished as:

11. A force normal to the blade $\mathbf{N_2}$, resulting from the effective grain stresses.
12. A shear force $\mathbf{S_2}$ as a result of the external friction angle $\mathbf{N_2 \cdot tan(\delta)}$.
13. A shear force **A** as a result of pure adhesion between the soil and the blade τ_a. This force can be calculated by multiplying the adhesive shear strength τ_a of the soil with the contact area between the soil and the blade.
14. A force $\mathbf{W_2}$ as a result of water under pressure on the blade.

These forces are shown in Figure 2-6. If the forces $\mathbf{N_2}$ and $\mathbf{S_2}$ are combined to a resulting force $\mathbf{K_2}$ and the adhesive force **A** and the water under pressures forces $\mathbf{W_1}$ and $\mathbf{W_2}$ are known, then the resulting force $\mathbf{K_2}$ is the unknown force on the blade. By taking the horizontal and vertical equilibrium of forces an expression for the force $\mathbf{K_2}$ on the blade can be derived.

$$\mathbf{K_2 = \sqrt{N_2^2 + S_2^2}} \tag{2-3}$$

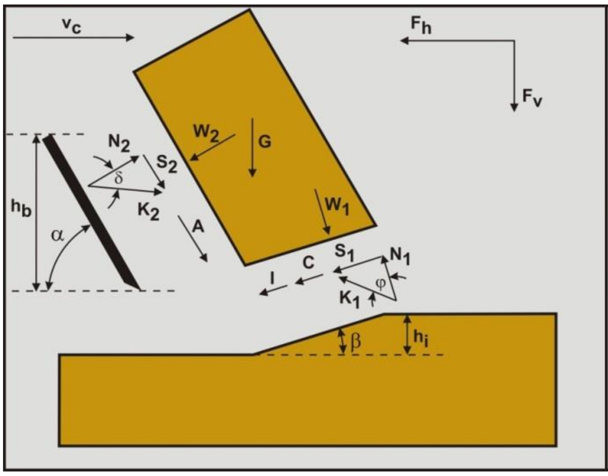

Figure 2-5: The forces on the layer cut.

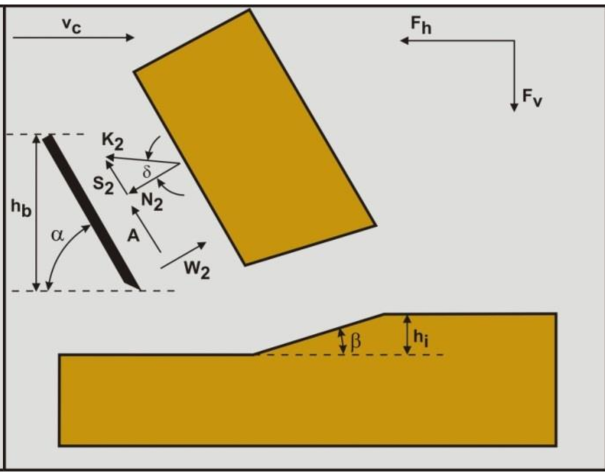

Figure 2-6: The forces on the blade.

The horizontal equilibrium of forces:

$$\sum F_h = K_1 \cdot \sin(\beta+\varphi) - W_1 \cdot \sin(\beta) + C \cdot \cos(\beta) + I \cdot \cos(\beta) - A \cdot \cos(\alpha) + W_2 \cdot \sin(\alpha) - K_2 \cdot \sin(\alpha+\delta) = 0 \tag{2-4}$$

The vertical equilibrium of forces:

$$\sum F_v = -K_1 \cdot \cos(\beta+\varphi) + W_1 \cdot \cos(\beta) + C \cdot \sin(\beta) + I \cdot \sin(\beta) + G + A \cdot \sin(\alpha) + W_2 \cdot \cos(\alpha) - K_2 \cdot \cos(\alpha+\delta) = 0 \tag{2-5}$$

The force $\mathbf{K_1}$ on the shear plane is now:

$$K_1 = \frac{W_2 \cdot \sin(\delta) + W_1 \cdot \sin(\alpha+\beta+\delta) + G \cdot \sin(\alpha+\delta) - I \cdot \cos(\alpha+\beta+\delta) - C \cdot \cos(\alpha+\beta+\delta) + A \cdot \cos(\delta)}{\sin(\alpha+\beta+\delta+\varphi)} \tag{2-6}$$

The force $\mathbf{K_2}$ on the blade is now:

$$K_2 = \frac{W_2 \cdot \sin(\alpha+\beta+\varphi) + W_1 \cdot \sin(\varphi) + G \cdot \sin(\beta+\varphi) + I \cdot \cos(\varphi) + C \cdot \cos(\varphi) - A \cdot \cos(\alpha+\beta+\varphi)}{\sin(\alpha+\beta+\delta+\varphi)} \tag{2-7}$$

From equation (2-7) the forces on the blade can be derived. On the blade a force component in the direction of cutting velocity $\mathbf{F_h}$ and a force perpendicular to this direction $\mathbf{F_v}$ can be distinguished.

$$F_h = -W_2 \cdot \sin(\alpha) + K_2 \cdot \sin(\alpha+\delta) + A \cdot \cos(\alpha) \tag{2-8}$$

$$F_v = -W_2 \cdot \cos(\alpha) + K_2 \cdot \cos(\alpha+\delta) - A \cdot \sin(\alpha) \tag{2-9}$$

The normal force on the shear plane is now:

$$N_1 = \frac{W_2 \cdot \sin(\delta) + W_1 \cdot \sin(\alpha+\beta+\delta) + G \cdot \sin(\alpha+\delta) - I \cdot \cos(\alpha+\beta+\delta) - C \cdot \cos(\alpha+\beta+\delta) + A \cdot \cos(\delta)}{\sin(\alpha+\beta+\delta+\varphi)} \cdot \cos(\varphi) \tag{2-10}$$

The normal force on the blade is now:

$$N_2 = \frac{W_2 \cdot \sin(\alpha+\beta+\varphi) + W_1 \cdot \sin(\varphi) + G \cdot \sin(\beta+\varphi) + I \cdot \cos(\varphi) + C \cdot \cos(\varphi) - A \cdot \cos(\alpha+\beta+\varphi)}{\sin(\alpha+\beta+\delta+\varphi)} \cdot \cos(\delta) \tag{2-11}$$

If the equations (2-10) and (2-11) give a positive result, the normal forces are compressive forces. It can be seen from these equations that the normal forces can become negative, meaning that a tensile rupture might occur, depending on values for the adhesion and cohesion and the angles involved. The most critical direction where this might occur can be found from the Mohr circle.

2.2.2. The Individual Forces

If there is no cavitation the water pressures forces W_1 and W_2 can be written as:

$$W_1 = \frac{p_{1m} \cdot \rho_w \cdot g \cdot v_c \cdot \varepsilon \cdot h_i^2 \cdot w}{(a_1 \cdot k_i + a_2 \cdot k_{max}) \cdot \sin(\beta)} = \frac{p_{1m} \cdot \rho_w \cdot g \cdot v_c \cdot \varepsilon \cdot h_i^2 \cdot w}{k_m \cdot \sin(\beta)} \qquad \textbf{(2-12)}$$

$$W_2 = \frac{p_{2m} \cdot \rho_w \cdot g \cdot v_c \cdot \varepsilon \cdot h_i \cdot w}{(a_1 \cdot k_i + a_2 \cdot k_{max}) \cdot \sin(\alpha)} = \frac{p_{2m} \cdot \rho_w \cdot g \cdot v_c \cdot \varepsilon \cdot h_i \cdot w}{k_m \cdot \sin(\alpha)} \qquad \textbf{(2-13)}$$

In case of cavitation W_1 and W_2 become:

$$W_1 = \frac{\rho_w \cdot g \cdot (z+10) \cdot h_i \cdot w}{\sin(\beta)} \qquad \textbf{(2-14)}$$

$$W_2 = \frac{\rho_w \cdot g \cdot (z+10) \cdot h_b \cdot w}{\sin(\alpha)} \qquad \textbf{(2-15)}$$

Wismer and Luth (1972A) and (1972B) investigated the inertia forces term **I** of the total cutting forces. The following equation is derived:

$$I = \rho_g \cdot v_c^2 \cdot \frac{\sin(\alpha)}{\sin(\alpha+\beta)} \cdot h_i \cdot w \qquad \textbf{(2-16)}$$

The cohesive and the adhesive forces **C** and **A** can be determined with soil mechanical experiments. For the cohesive and adhesive forces the following equations are valid:

$$C = \frac{c \cdot h_i \cdot w}{\sin(\beta)} \qquad \textbf{(2-17)}$$

$$A = \frac{a \cdot h_b \cdot w}{\sin(\alpha)} \qquad \textbf{(2-18)}$$

The gravitation force **G** (mass) follows from:

$$G = (\rho_g - \rho_w) \cdot g \cdot h_i \cdot w \cdot \frac{\sin(\alpha+\beta)}{\sin(\beta)} \cdot \left\{ \frac{(h_b + h_i \cdot \sin(\alpha))}{\sin(\alpha)} + \frac{h_i \cdot \cos(\alpha+\beta)}{2 \cdot \sin(\beta)} \right\} \qquad \textbf{(2-19)}$$

This is in accordance with the area that is used for the water pore pressure calculations in the case of water saturated sand (see Figure 5-6).

2.3. The Curling Type

In some soils it is possible that the **Curling Type** of cutting mechanism occurs. This will happen when the layer cut is relatively thin and there is a force on the blade of which the magnitude depends on the blade height, like the adhesive force or the pore pressure force in the case of a cavitating cutting process. In soils like clay and loam, but also in rock under hyperbaric conditions this may occur. Figure 2-7 shows this **Curling Type**. The question now is, what is the effective blade height **h'_b** where the soil is in contact with the blade.

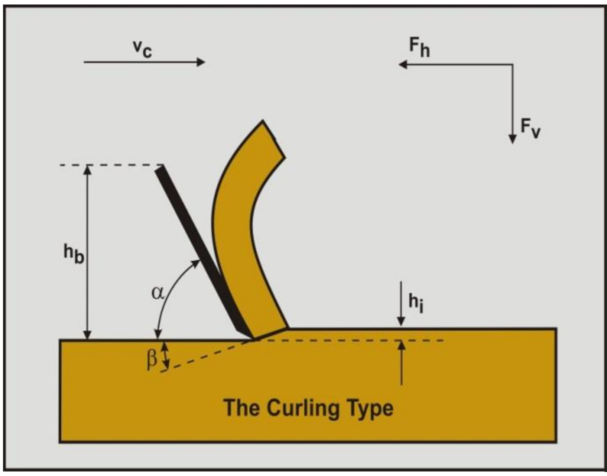

Figure 2-7: The Curling Type of cutting mechanism.

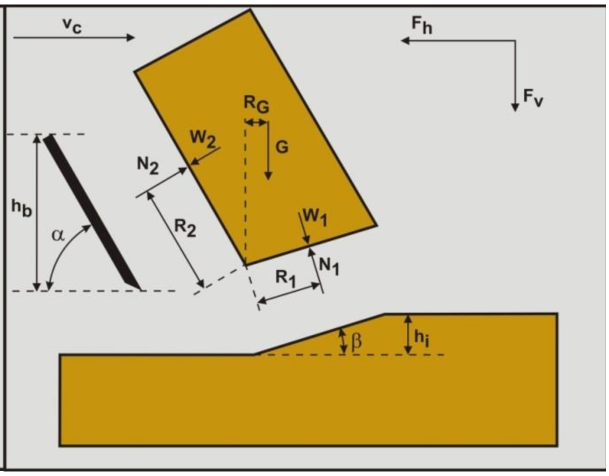

Figure 2-8: The general equilibrium of moments.

To solve this problem, an additional equation is required. There is only one equation available and that is the equilibrium equation of moments on the layer cut. Figure 2-8 shows the moments acting on the layer cut. In the case of clay, loam or hyperbaric rock, the contribution of gravity can be neglected.

The equilibrium of moments when the gravity moment is neglected is:

$$(N_1 - W_1)\cdot R_1 = (N_2 - W_2)\cdot R_2 \tag{2-20}$$

The arms of the 2 moments are:

$$R_1 = \frac{\lambda_1 \cdot h_i}{\sin(\beta)}, \; R_2 = \frac{\lambda_2 \cdot h'_b}{\sin(\alpha)} \tag{2-21}$$

This gives the equilibrium equation of moments on the layer cut:

$$\begin{gathered}\left(\frac{W_2\cdot\sin(\delta)+W_1\cdot\sin(\alpha+\beta+\delta)-C\cdot\cos(\alpha+\beta+\delta)+A\cdot\cos(\delta)}{\sin(\alpha+\beta+\delta+\varphi)}\cdot\cos(\varphi)-W_1\right)\cdot\frac{\lambda_1\cdot h_i}{\sin(\beta)}\\ =\\ \left(\frac{W_2\cdot\sin(\alpha+\beta+\varphi)+W_1\cdot\sin(\varphi)+C\cdot\cos(\varphi)-A\cdot\cos(\alpha+\beta+\varphi)}{\sin(\alpha+\beta+\delta+\varphi)}\cdot\cos(\delta)-W_2\right)\cdot\frac{\lambda_2\cdot h'_b}{\sin(\alpha)}\end{gathered} \tag{2-22}$$

When the equations for **W_1**, **W_2**, **C** and **A** as mentioned before are substituted, the resulting equation is a second degree equation with **h'_b** as the variable. This can be solved using the following set of equations:

$$A \cdot x^2 + B \cdot x + C = 0$$

$$h_b' = x = \frac{-B - \sqrt{B^2 - 4 \cdot A \cdot C}}{2 \cdot A}$$

$$A = \frac{\lambda_2 \cdot p_{2m} \cdot \sin(\alpha+\beta+\delta+\varphi) - \lambda_2 \cdot p_{2m} \cdot \sin(\alpha+\beta+\varphi) \cdot \cos(\delta) + a \cdot \lambda_2 \cdot \cos(\alpha+\beta+\varphi) \cdot \cos(\delta)}{\sin(\alpha) \cdot \sin(\alpha)} \tag{2-23}$$

$$B = \frac{\lambda_1 \cdot p_{2m} \cdot \sin(\delta) \cdot \cos(\varphi) - \lambda_2 \cdot p_{1m} \cdot \cos(\delta) \cdot \sin(\varphi) - c \cdot \lambda_2 \cdot \cos(\delta) \cdot \cos(\varphi) + a \cdot \lambda_1 \cdot \cos(\varphi) \cdot \cos(\delta)}{\sin(\alpha) \cdot \sin(\beta)} \cdot h_i$$

$$C = \frac{\lambda_1 \cdot p_{1m} \cdot \sin(\alpha+\beta+\delta) \cdot \cos(\varphi) - \lambda_1 \cdot p_{1m} \cdot \sin(\alpha+\beta+\delta+\varphi) - c \cdot \lambda_1 \cdot \cos(\alpha+\beta+\delta) \cdot \cos(\varphi)}{\sin(\beta) \cdot \sin(\beta)} \cdot h_i \cdot h_i$$

$$\begin{aligned} &\text{if } h_b' < h_b \text{ then use } h_b' \\ &\text{if } h_b' \geq h_b \text{ then use } h_b \end{aligned} \tag{2-24}$$

2.4. The Tear Type

The **Tear Type** of cutting process has a failure mechanism based on tensile failure. For such a failure mechanism to occur it is required that negative stresses may occur. In sand this is not the case, because in sand the failure lines according to the Mohr-Coulomb criterion will pass through the origin as is shown in Figure 1-2 and Figure 1-3. For the failure lines not to pass through the origin it is required that the soil has a certain cohesion or shear strength like with clay and rock. In clay and rock, normally, the inertial forces and the gravity can be neglected and also the water pore pressures do no play a role. Only with hyperbaric rock cutting the water pore pressures will play a role, but there the **Tear Type** will not occur. This implies that for the **Tear Type** a soil with cohesion and adhesion and internal and external friction will be considered.

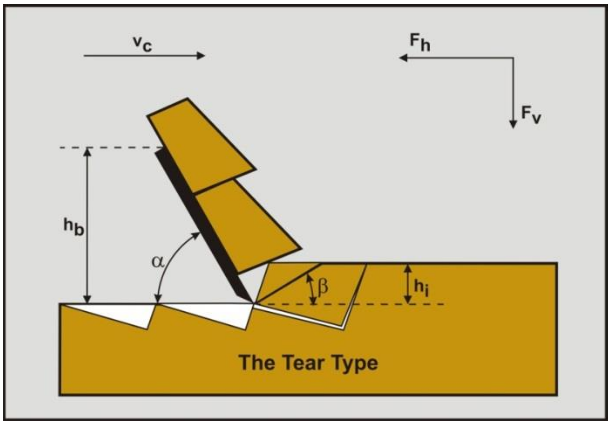

Figure 2-9: The Tear Type cutting mechanism in rock.

If clay or rock is considered, the following condition can be derived with respect to tensile rupture:

With the relations for the cohesive force **C**, the adhesive force **A** and the adhesion/cohesion ratio **r** (the ac ratio **r**):

$$C = \frac{\lambda \cdot c \cdot h_i \cdot w}{\sin(\beta)} \tag{2-25}$$

$$A = \frac{\lambda \cdot a \cdot h_b \cdot w}{\sin(\alpha)} \tag{2-26}$$

$$r = \frac{a \cdot h_b}{c \cdot h_i} \tag{2-27}$$

The horizontal $\mathbf{F_h}$ and vertical $\mathbf{F_v}$ cutting forces can be determined according to:

$$F_h = \lambda \cdot c \cdot h_i \cdot w \cdot \frac{\frac{\sin(\alpha+\delta)}{\sin(\beta)} \cdot \cos(\varphi) + r \cdot \frac{\sin(\beta+\varphi)}{\sin(\alpha)} \cdot \cos(\delta)}{\sin(\alpha+\beta+\delta+\varphi)} \tag{2-28}$$

$$F_v = \lambda \cdot c \cdot h_i \cdot w \cdot \frac{\frac{\cos(\alpha+\delta)}{\sin(\beta)} \cdot \cos(\varphi) - r \cdot \frac{\cos(\beta+\varphi)}{\sin(\alpha)} \cdot \cos(\delta)}{\sin(\alpha+\beta+\delta+\varphi)} \tag{2-29}$$

The shear angle β is determined in the case where the horizontal cutting force F_h is at a minimum, based on the minimum energy principle.

$$\frac{\partial F_h}{\partial \beta}=\frac{r\cdot\cos(\delta)\cdot\sin(2\cdot\beta+\varphi)\cdot\sin(\alpha)\cdot\sin(\beta)\cdot\sin(\alpha+\beta+\delta+\varphi)}{\sin^2(\alpha+\beta+\delta+\varphi)\cdot\sin^2(\alpha)\cdot\sin^2(\beta)}$$

$$\frac{-\sin(\alpha)\cdot\sin(\alpha+2\cdot\beta+\delta+\varphi)\cdot\left(\sin(\alpha)\cdot\sin(\alpha+\delta)\cdot\cos(\varphi)+r\cdot\sin(\beta)\cdot\sin(\beta+\varphi)\cdot\cos(\delta)\right)}{\sin^2(\alpha+\beta+\delta+\varphi)\cdot\sin^2(\alpha)\cdot\sin^2(\beta)}=0 \tag{2-30}$$

In the special case where there is no adhesion, $r=0$, the shear angle is:

$$\frac{\partial F_h}{\partial \beta}=\frac{-\sin(\alpha+2\cdot\beta+\delta+\varphi)\cdot\sin(\alpha+\delta)\cdot\cos(\varphi)}{\sin^2(\alpha+\beta+\delta+\varphi)\cdot\sin^2(\beta)}=0 \tag{2-31}$$

So:

$$\sin(\alpha+2\cdot\beta+\delta+\varphi)=0 \text{ for } \alpha+2\cdot\beta+\delta+\varphi=\pi \text{ giving } \beta=\frac{\pi}{2}-\frac{\alpha+\delta+\varphi}{2} \tag{2-32}$$

The cohesion **c** can be determined from the UCS value and the angle of internal friction **φ** according to (as is shown in Figure 2-10):

$$c=\frac{UCS}{2}\cdot\left(\frac{1-\sin(\varphi)}{\cos(\varphi)}\right) \tag{2-33}$$

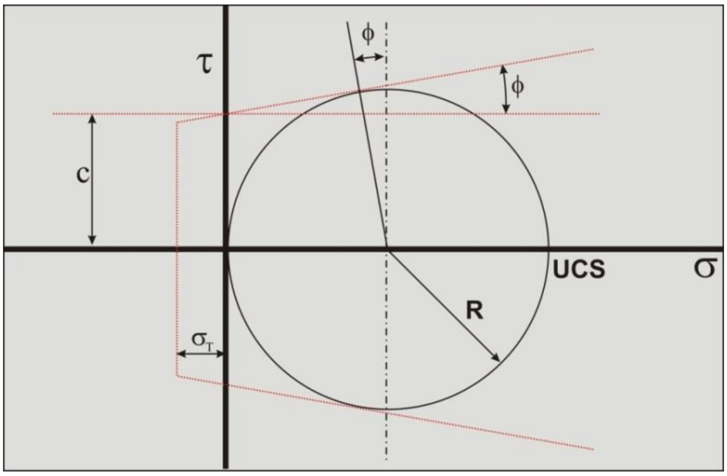

Figure 2-10: The Mohr circle for UCS and cohesion.

According to the Mohr-Coulomb failure criterion, the following is valid for the shear stress on the shear plane, as is shown in Figure 2-11.

$$\tau_{S1}=c+\sigma_{N1}\cdot\tan(\varphi) \tag{2-34}$$

The average stress condition on the shear plane is now $\boldsymbol{\sigma_{N1}}$, $\boldsymbol{\tau_{S1}}$ as is show in Figure 2-11. A Mohr circle (Mohr circle 1) can be drawn through this point, resulting in a minimum stress $\boldsymbol{\sigma_{min}}$ which is negative, so tensile. If this minimum normal stress is smaller than the tensile strength $\boldsymbol{\sigma_T}$ tensile fracture will occur, as is the case in the figure. Now Mohr circle 1 can never exist, but a smaller circle (Mohr circle 2) can, just touching the tensile strength $\boldsymbol{\sigma_T}$. The question is now, how to get from Mohr circle 1 to Mohr circle 2. To find Mohr circle 2 the following steps have to be taken.

The radius **R** of the Mohr circle 1 can be found from the shear stress $\boldsymbol{\tau_{S1}}$ by:

$$\mathbf{R} = \frac{\tau_{S1}}{\cos(\varphi)} \tag{2-35}$$

The center of the Mohr circle 1, σ_C, now follows from:

$$\sigma_C = \sigma_{N1} + R \cdot \sin(\varphi) = \sigma_{N1} + \tau_{S1} \cdot \tan(\varphi) = \sigma_{N1} + c \cdot \tan(\varphi) + \sigma_{N1} \cdot \tan^2(\varphi) \tag{2-36}$$

The normal force N_1 on the shear plane is now:

$$N_1 = \frac{-C \cdot \cos(\alpha+\beta+\delta) + A \cdot \cos(\delta)}{\sin(\alpha+\beta+\delta+\varphi)} \cdot \cos(\varphi) = \lambda \cdot c \cdot h_i \cdot w \cdot \frac{-\dfrac{\cos(\alpha+\beta+\delta)}{\sin(\beta)} + r \cdot \dfrac{\cos(\delta)}{\sin(\alpha)}}{\sin(\alpha+\beta+\delta+\varphi)} \cdot \cos(\varphi) \tag{2-37}$$

The normal stress σ_{N1} on the shear plane is:

$$\sigma_{N1} = \frac{N_1 \cdot \sin(\beta)}{h_i \cdot w} = \lambda \cdot c \cdot \frac{-\dfrac{\sin(\beta) \cdot \cos(\alpha+\beta+\delta)}{\sin(\beta)} + r \cdot \dfrac{\sin(\beta) \cdot \cos(\delta)}{\sin(\alpha)}}{\sin(\alpha+\beta+\delta+\varphi)} \cdot \cos(\varphi) \tag{2-38}$$

The minimum principal stress σ_{min} equals the normal stress in the center of the Mohr circle σ_C minus the radius of the Mohr circle **R**:

$$\sigma_{min} = \sigma_C - R = \sigma_{N1} + c \cdot \tan(\varphi) + \sigma_{N1} \cdot \tan^2(\varphi) - \frac{c}{\cos(\varphi)} - \frac{\sigma_{N1} \cdot \tan(\varphi)}{\cos(\varphi)} \tag{2-39}$$

Rearranging this gives:

$$\sigma_{min} = \sigma_{N1} \cdot \left(1 + \tan^2(\varphi) - \frac{\tan(\varphi)}{\cos(\varphi)}\right) + c \cdot \left(\tan(\varphi) - \frac{1}{\cos(\varphi)}\right) \tag{2-40}$$

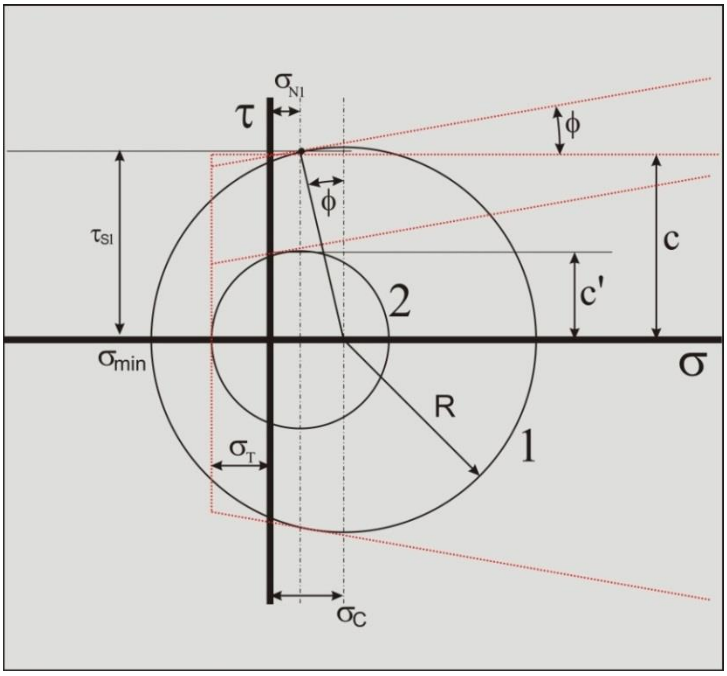

Figure 2-11: The Mohr circles of the Tear Type.

$$\sigma_{min} = \frac{\sigma_{N1}}{\cos(\varphi)} \cdot \left(\frac{\cos^2(\varphi) + \sin^2(\varphi) - \sin(\varphi)}{\cos(\varphi)} \right) - c \cdot \left(\frac{1 - \sin(\varphi)}{\cos(\varphi)} \right) = \left(\frac{\sigma_{N1}}{\cos(\varphi)} - c \right) \cdot \left(\frac{1 - \sin(\varphi)}{\cos(\varphi)} \right) \tag{2-41}$$

Now ductile failure will occur if the minimum principal stress $\boldsymbol{\sigma_{min}}$ is bigger than then tensile strength $\boldsymbol{\sigma_T}$, thus:

$$\sigma_{min} > \sigma_T \tag{2-42}$$

If equation (2-42) is true, ductile failure will occur. Keep in mind however, that the tensile strength $\boldsymbol{\sigma_T}$ is a negative number. Of course if the minimum normal stress σ_{min} is positive, brittle failure can never occur. Substituting equation (2-38) for the normal stress on the shear plane gives the following condition for the **Tear Type**:

$$c \cdot \left(\frac{r \cdot \dfrac{\sin(\beta) \cdot \cos(\delta)}{\sin(\alpha)} - \cos(\alpha + \beta + \delta) - \sin(\alpha + \beta + \delta + \varphi)}{\sin(\alpha + \beta + \delta + \varphi)} \right) \cdot \left(\frac{1 - \sin(\varphi)}{\cos(\varphi)} \right) > \sigma_T \tag{2-43}$$

In clay it is assumed that the internal and external friction angles are zero, while in rock it is assumed that the adhesion is zero. This will be explained in detail in the chapters on clay and rock cutting.

The ratio's between the pore pressures and the cohesive shear strength, in the case of hyperbaric rock cutting, can be found according to:

$$r = \frac{a \cdot h_b}{c \cdot h_i}, \; r_1 = \frac{p_{1m} \cdot h_i}{c \cdot h_i} \quad \text{or} \quad r_1 = \frac{\rho_w \cdot g \cdot (z + 10) \cdot h_i}{c \cdot h_i}, \; r_2 = \frac{p_{2m} \cdot h_b}{c \cdot h_i} \quad \text{or} \quad r_2 = \frac{\rho_w \cdot g \cdot (z + 10) \cdot h_b}{c \cdot h_i} \tag{2-44}$$

Equation (2-45) can be derived for the occurrence of tensile failure under hyperbaric conditions. Under hyperbaric conditions equation (2-45) will almost always be true, because of the terms with $\mathbf{r_1}$ and $\mathbf{r_2}$ which may become very big (positive). So tensile failure will not be considered for hyperbaric conditions.

$$c \cdot \left(\frac{r \cdot \dfrac{\sin(\beta) \cdot \cos(\delta)}{\sin(\alpha)} + r_2 \cdot \dfrac{\sin(\beta) \cdot \sin(\delta)}{\sin(\alpha)} + r_1 \cdot \sin(\alpha + \beta + \delta) - \cos(\alpha + \beta + \delta) - \sin(\alpha + \beta + \delta + \varphi)}{\sin(\alpha + \beta + \delta + \varphi)} \right) \cdot \left(\frac{1 - \sin(\varphi)}{\cos(\varphi)} \right) > \sigma_T \tag{2-45}$$

Analysing equations (2-43) and (2-45) gives the following conclusions:

1. The first term of equations (2-43) and (2-45) is always positive.
2. If the sum of $\boldsymbol{\alpha+\beta+\delta>\pi/2}$, in the second term of equation (2-43) and the fourth term of equation (2-45), these terms are positive, which will be the case for normal cutting angles.
3. The second and third terms of equation (2-45) are always positive.
4. The last term in equations (2-43) and (2-45) is always negative.
5. Equation (2-43) may become negative and fulfill the condition for the **Tear Type**.
6. Equation (2-45) will never become negative under normal conditions, so under hyperbaric conditions the **Tear Type** will never occur.
7. The **Tear Type** may occur with clay and rock under atmospheric conditions.

2.5. The Snow Plough Effect

2.5.1. The Normal and Friction Forces on the Shear Surface and on the Blade

On a cutterhead, the blades can be divided into small elements, at which a two dimensional cutting process is considered. However, this is correct only when the cutting edge of this element is perpendicular to the direction of the velocity of the element. For most elements this will not be the case. The cutting edge and the absolute velocity of the cutting edge will not be perpendicular. This means the elements can be considered to be deviated with respect to the direction of the cutting velocity. A component of the cutting velocity perpendicular to the cutting edge and a component parallel to the cutting edge can be distinguished. This second component results in a deviation force on the blade element, due to the friction between the soil and the blade. This force is also the cause of the transverse movement of the soil, the snowplough effect.

To predict the deviation force and the direction of motion of the soil on the blade, the equilibrium equations of force will have to be solved in three directions. Since there are four unknowns, three forces and the direction of the velocity of the soil on the blade, one additional equation is required. This equation follows from an equilibrium equation of velocity between the velocity of grains in the shear zone and the velocity of grains on the blade. Since the four equations are partly non-linear and implicit, they have to be solved iteratively. The results of solving these equations have been compared with the results of laboratory tests on sand. The correlation between the two was very satisfactory, with respect to the magnitude of the forces and with respect to the direction of the forces and the flow of the soil on the blade.

Although the normal and friction forces as shown in Figure 2-12 are the basis for the calculation of the horizontal and vertical cutting forces, the approach used, requires the following equations to derive these forces by using equations (2-8) and (2-9). The index 1 points to the shear surface, while the index 2 points to the blade.

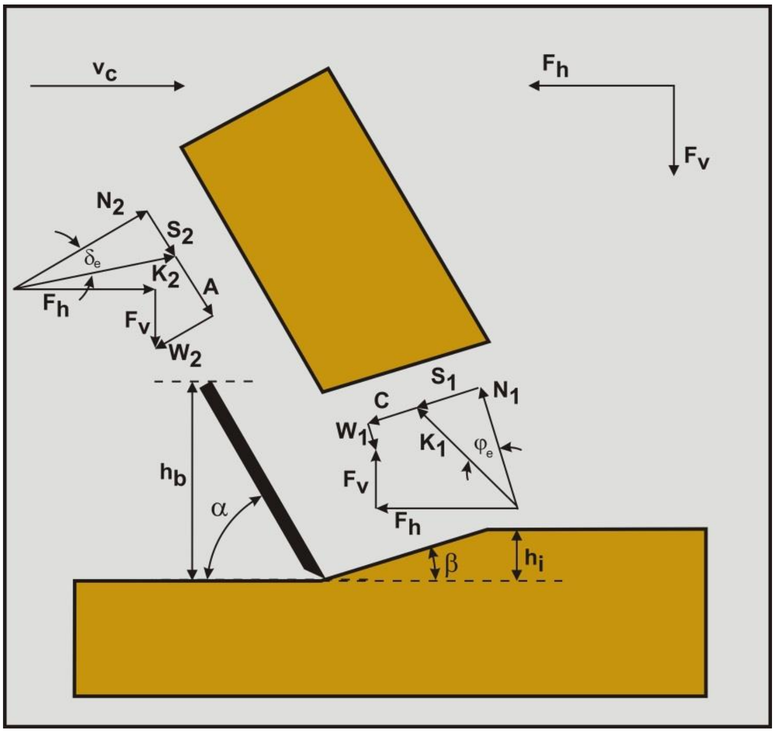

Figure 2-12: The forces on the layer cut.

$$\mathbf{F_{n1} = F_h \cdot \sin(\beta) - F_v \cdot \cos(\beta)} \quad \textbf{(2-46)}$$

$$\mathbf{F_{f1} = F_h \cdot \cos(\beta) + F_v \cdot \sin(\beta)} \quad \textbf{(2-47)}$$

$$\mathbf{F_{n2} = F_h \cdot \sin(\alpha) + F_v \cdot \cos(\alpha)} \quad \textbf{(2-48)}$$

$$\mathbf{F_{f2} = F_h \cdot \cos(\alpha) - F_v \cdot \sin(\alpha)} \quad \textbf{(2-49)}$$

2.5.2. The 3D Cutting Theory

The previous paragraphs summarized the two-dimensional cutting theory. However, as stated in the introduction, in most cases the cutting process is not two-dimensional, because the drag velocity is not perpendicular to the cutting edge of the blade. Figure 2-13 shows this phenomenon. As with snow-ploughs, the soil will flow to one side while the blade is pushed to the opposite side. This will result in a third cutting force, the deviation force $\mathbf{F_d}$. To determine this force, the flow direction of the soil has to be known. Figure 2-14 shows a possible flow direction.

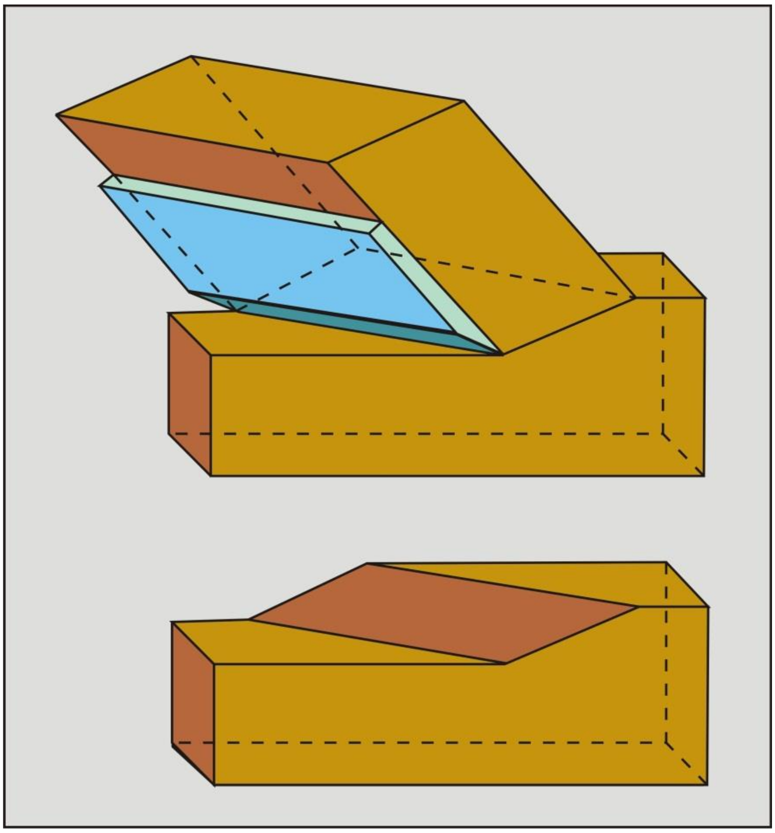

Figure 2-13: The 3D cutting process.

2.5.3. Velocity Conditions

For the velocity component perpendicular to the blade $\mathbf{v_c}$, if the blade has a deviation angle ι and a drag velocity $\mathbf{v_d}$ according to Figure 2-14, it yields:

$$v_c = v_d \cdot \cos(\iota) \tag{2-50}$$

The velocity of grains in the shear surface perpendicular to the cutting edge $\mathbf{v_{r1}}$ is now:

$$v_{r1} = v_c \cdot \frac{\sin(\alpha)}{\sin(\alpha + \beta)} \tag{2-51}$$

The relative velocity of grains with respect to the blade $\mathbf{v_{r2}}$, perpendicular to the cutting edge is:

$$v_{r2} = v_c \cdot \frac{\sin(\beta)}{\sin(\alpha + \beta)} \tag{2-52}$$

The grains will not only have a velocity perpendicular to the cutting edge, but also parallel to the cutting edge, the deviation velocity components $\mathbf{v_{d1}}$ on the shear surface and $\mathbf{v_{d2}}$ on the blade.

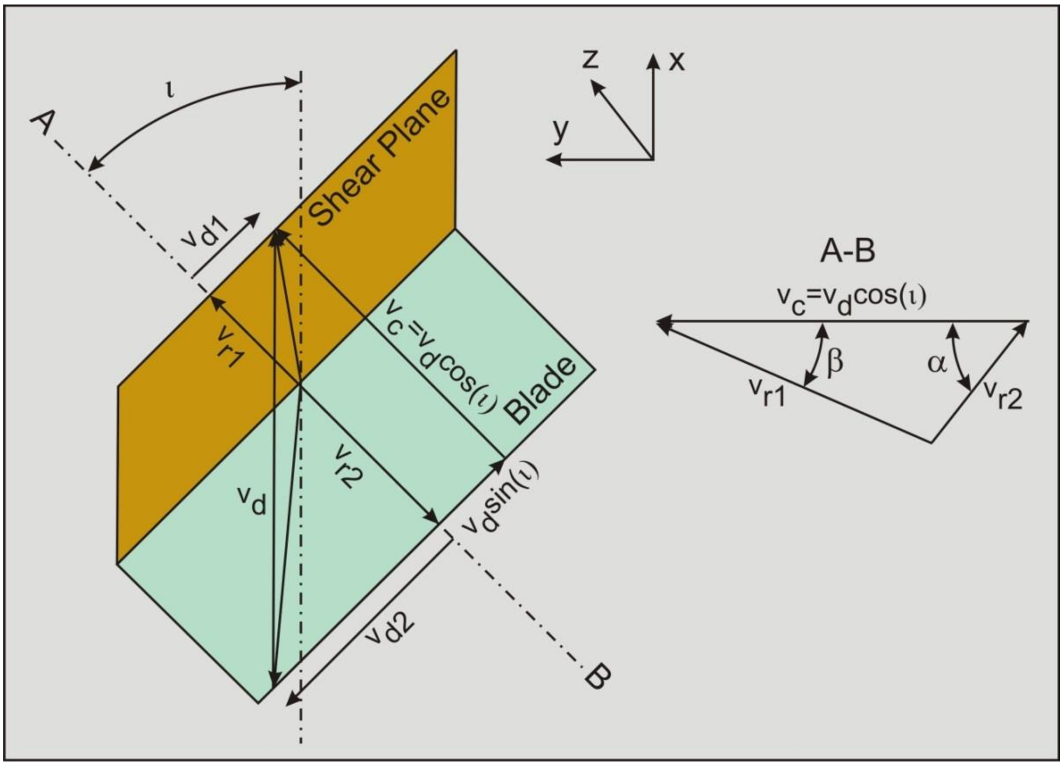

Figure 2-14: Velocity conditions.

The velocity components of a grain in **x**, **y** and **z** direction can be determined by considering the absolute velocity of grains in the shear surface, this leads to:

$$\overrightarrow{\mathbf{v}_{r2}}+\overrightarrow{\mathbf{v}_{d2}}+\overrightarrow{\mathbf{v}_{d}}=\overrightarrow{\mathbf{v}_{r1}}+\overrightarrow{\mathbf{v}_{d1}} \quad \textbf{(2-53)}$$

$$\mathbf{v_{x1}=v_{r1}\cdot\cos(\beta)\cdot\cos(\iota)+v_{d1}\cdot\sin(\iota)} \quad \textbf{(2-54)}$$

$$\mathbf{v_{y1}=v_{r1}\cdot\cos(\beta)\cdot\sin(\iota)-v_{d1}\cdot\cos(\iota)} \quad \textbf{(2-55)}$$

$$\mathbf{v_{z1}=v_{r1}\cdot\sin(\beta)} \quad \textbf{(2-56)}$$

The velocity components of a grain can also be determined by a summation of the drag velocity of the blade and the relative velocity between the grains and the blade, this gives:

$$\mathbf{v_{x2}=v_{d}-v_{r2}\cdot\cos(\alpha)\cdot\cos(\iota)-v_{d2}\cdot\sin(\iota)} \quad \textbf{(2-57)}$$

$$\mathbf{v_{y2}=-v_{r2}\cdot\cos(\alpha)\cdot\sin(\iota)+v_{d2}\cdot\cos(\iota)} \quad \textbf{(2-58)}$$

$$\mathbf{v_{z2}=v_{r2}\cdot\sin(\alpha)} \quad \textbf{(2-59)}$$

Since both approaches will have to give the same resulting velocity components, the following condition for the transverse velocity components can be derived:

$$\mathbf{v_{x1}=v_{x2}\;===>\;v_{d1}+v_{d2}=v_{d}\cdot\sin(\iota)} \quad \textbf{(2-60)}$$

$$\mathbf{v_{y1}=v_{y2}\;===>\;v_{d1}+v_{d2}=v_{d}\cdot\sin(\iota)} \quad \textbf{(2-61)}$$

$$\mathbf{v_{z1}=v_{z2}} \quad \textbf{(2-62)}$$

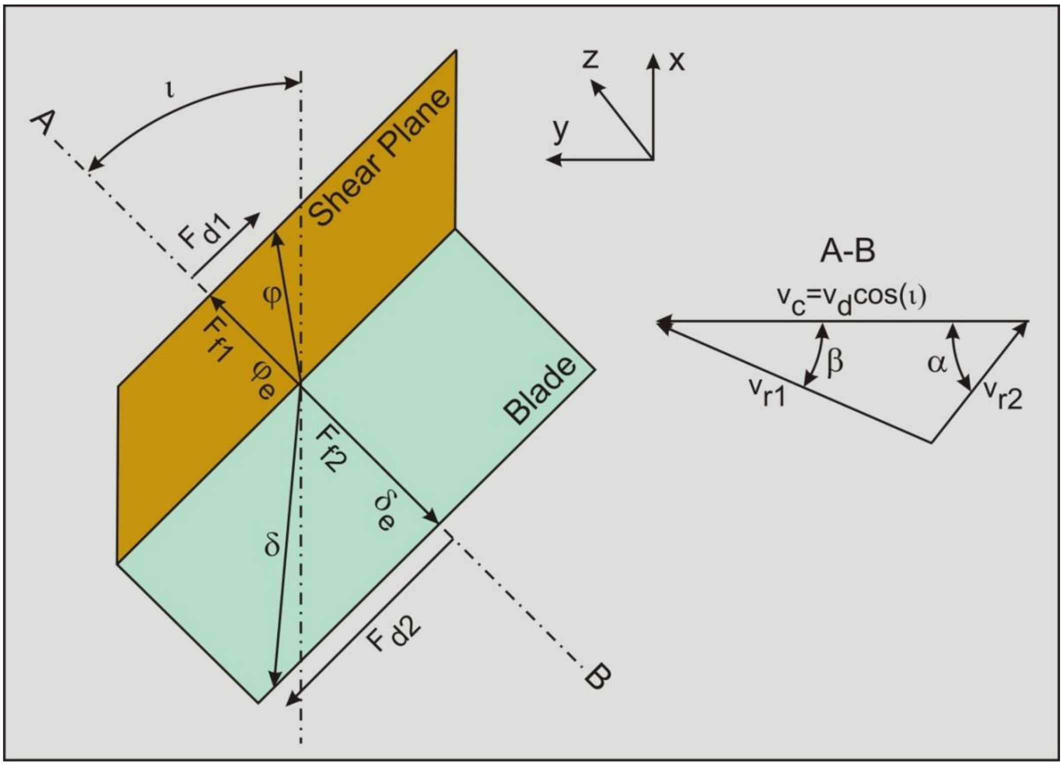

Figure 2-15: Force directions.

2.5.4. The Deviation Force

Since a friction force always has a direction matching the direction of the relative velocity between two bodies, the fact that a deviation velocity exists on the shear surface and on the blade, implies that also deviation forces must exist. To match the direction of the relative velocities, the following equations can be derived for the deviation force on the shear surface and on the blade (Figure 2-15):

$$\mathbf{F_{d1} = F_{f1} \cdot \frac{v_{d1}}{v_{r1}}} \qquad \textbf{(2-63)}$$

$$\mathbf{F_{d2} = F_{f2} \cdot \frac{v_{d2}}{v_{r2}}} \qquad \textbf{(2-64)}$$

Since perpendicular to the cutting edge, an equilibrium of forces exists, the two deviation forces must be equal in magnitude and have opposite directions.

$$\mathbf{F_{d1} = \left|F_{d2}\right|} \qquad \textbf{(2-65)}$$

By substituting equations (2-63) and (2-64) in equation (2-65) and then substituting equations (2-47) and (2-49) for the friction forces and equations (2-51) and (2-52) for the relative velocities, the following equation can be derived, giving a second relation between the two deviation velocities:

$$\boldsymbol{\lambda = \frac{v_{d1}}{v_{d2}} = \left(\frac{F_{f2}}{F_{f1}}\right) \cdot \left(\frac{v_{r1}}{v_{r2}}\right) = \left(\frac{F_h \cdot \cos(\alpha) - F_v \cdot \sin(\alpha)}{F_h \cdot \cos(\beta) + F_v \cdot \sin(\beta)}\right) \cdot \left(\frac{\sin(\alpha)}{\sin(\beta)}\right)} \qquad \textbf{(2-66)}$$

To determine $\mathbf{F_h}$ and $\mathbf{F_v}$ perpendicular to the cutting edge, the angle of internal friction $\boldsymbol{\varphi_e}$ and the external friction angle $\boldsymbol{\delta_e}$ mobilized perpendicular to the cutting edge, have to be determined by using the ratio of the transverse velocity and the relative velocity, according to:

$$\mathbf{\tan(\varphi_e) = \tan(\varphi) \cdot \cos\left(atn\left(\frac{v_{d1}}{v_{r1}}\right)\right)} \qquad \textbf{(2-67)}$$

$$\tan\left(\delta_e\right) = \tan\left(\delta\right)\cdot\cos\left(\mathrm{atn}\left(\frac{v_{d2}}{v_{r2}}\right)\right) \quad \text{(2-68)}$$

For the cohesion **c** and the adhesion **a** this gives:

$$c_e = c\cdot\cos\left(\mathrm{atn}\left(\frac{v_{d1}}{v_{r1}}\right)\right) \quad \text{(2-69)}$$

$$a_e = a\cdot\cos\left(\mathrm{atn}\left(\frac{v_{d2}}{v_{r2}}\right)\right) \quad \text{(2-70)}$$

2.5.5. The Resulting Cutting Forces

The resulting cutting forces in **x**, **y** and **z** direction can be determined once the deviation velocity components are known. However, it can be seen that the second velocity condition equation (2-66) requires the horizontal and vertical cutting forces perpendicular to the cutting edge, while these forces can only be determined if the mobilized internal and external friction angles and the mobilized cohesion and adhesion (equations (2-67), (2-68), (2-69) and (2-70)) are known. This creates an implicit set of equations that will have to be solved by means of an iteration process. For the cutting forces on the blade the following equation can be derived:

$$F_{x2} = F_h\cdot\cos\left(\iota\right) + F_{d2}\cdot\sin\left(\iota\right) \quad \text{(2-71)}$$

$$F_{y2} = F_h\cdot\sin\left(\iota\right) - F_{d2}\cdot\cos\left(\iota\right) \quad \text{(2-72)}$$

$$F_{z2} = F_v \quad \text{(2-73)}$$

The problem of the model being implicit can be solved in the following way:

A new variable **λ** is introduced in such a way that:

$$v_{d1} = \frac{\lambda}{1+\lambda}\cdot v_d\cdot\sin\left(\iota\right) \quad \text{(2-74)}$$

$$v_{d2} = \frac{1}{1+\lambda}\cdot v_d\cdot\sin\left(\iota\right) \quad \text{(2-75)}$$

This satisfies the condition from equations (2-60) and (2-61) for the sum of these 2 velocities:

$$v_{d1} + v_{d2} = v_d\cdot\sin\left(\iota\right) \quad \text{(2-76)}$$

The procedure starts with a starting value for **λ=1**. Based on the velocities found with equations (2-74), (2-75), (2-51) and (2-52), the mobilized internal $\boldsymbol{\varphi_e}$ and external $\boldsymbol{\delta_e}$ friction angles and the cohesion $\mathbf{c_e}$ and adhesion $\mathbf{a_e}$ can be determined with the equations (2-67), (2-68), (2-69) and (2-70). Once these are known, the horizontal $\mathbf{F_h}$ and vertical $\mathbf{F_v}$ cutting forces in the plane perpendicular to the cutting edge can be determined with equations (2-8) and (2-9). With the equations (2-47), (2-49), (2-63) and (2-64) the friction and deviation forces on the blade and the shear plane can be determined. Now with equation (2-66) the value of the variable **λ** can be determined and if the starting value is correct, this value should be found. In general this will not be the case after one iteration. But repeating this procedure 3 or 4 times should give enough accuracy.

Start:	
Labda = 1	
'In case of deviation angle	(2-51)
If Iota <> 0 Then	(2-52)
Vr1 = Vd * cos(Iota) * sin(Alpha) / sin(Alpha + Beta)	(2-74)
Vr2 = Vd * cos(Iota) * sin(Beta) / sin(Alpha + Beta)	(2-75)
Vd1 = Vd * sin(Iota) * Labda / (1 + Labda)	
Vd2 = Vd * sin(Iota) / (1 + Labda)	(2-67)
'So Vd1+Vd2 = Vd * sin(Iota)	(2-68)
Phi_e = atn(Tan(Phi) * cos(atn(Vd1 / Vr1)))	(2-69)
Delta_e = atn(Tan(Delta) * cos(atn(Vd2 / Vr2)))	(2-70)
Cohesion_e = Cohesion * cos(atn(Vd1 / Vr1))	
Adhesion_e = Adhesion * cos(atn(Vd2 / Vr2))	
End If	
Insert here the force calculation (F_h and F_v)	
'In case of deviation angle	(2-47)
If Iota <> 0 Then	(2-49)
Ff1 = Fh * cos(Beta) + Fv * sin(Beta)	(2-63)
Ff2 = Fh * cos(Alpha) - Fv * sin(Alpha)	(2-64)
Fd1 = abs(Ff1 * (Vd1 / Vr1))	(2-66)
Fd2 = abs(Ff2 * (Vd2 / Vr2))	Some additional accuracy at the end
Labda2 = (Vr1 / Vr2) * (Ff2 / Ff1)	(2-71)
Fd = (Fd1 + Fd2) / 2	(2-72)
Fx2 = Fh * cos(Iota) + Fd * sin(Iota)	(2-73)
Fy2 = Fh * sin(Iota) - Fd * cos(Iota)	
Fz2 = Fv	
End If	
If Abs(Labda – Labda2) > 0.001 Then Goto Start	

Figure 2-16: A piece of a program showing the iteration scheme.

2.6. Nomenclature Chapter 2:

a_1, a_2	Coefficients for weighted permeability	-
a, τ_a	Adhesion or external shear strength	kPa
A	Adhesive force on the blade	kN
c, τ_c	Cohesion or internal shear strength	kPa
C, C_1	Force due to cohesion in the shear plane	kN
C_2	Force due to cohesion on the front of the wedge	kN
C_3	Force due to cohesion at the bottom of the wedge	kN
F_h	Horizontal cutting force	kN
F_{f1}	Friction force on the shear surface	kN
F_{f2}	Friction force on the blade	kN
F_{n1}	Normal force on the shear surface	kN
F_{n2}	Normal force on the blade	kN
F_v	Vertical cutting force	kN
F_{d1}	Deviation force on the shear surface	kN
$F_{d, d2}$	Deviation force on the blade	kN
$F_{x1, 2}$	Cutting force in x-direction	kN
$F_{y1, 2}$	Cutting force in y-direction	kN
$F_{z1, 2}$	Cutting force in z-direction	kN
g	Gravitational constant (9.81)	m/s^2
G, G_1	Gravitational force on the layer cut	kN
G_2	Gravitational force on the wedge	kN
h_i	Initial thickness of layer cut	m
h_b	Height of blade	m
h'_b	Effective height of the blade in case **Curling Type**	m
I	Inertial force on the shear plane	kN
k_i	Initial permeability	m/s
k_{max}	Maximum permeability	m/s
k_m	Average permeability	m/s
K_1	Grain force on the shear plane	kN
K_2	Grain force on the blade or the front of the wedge	kN
K_3	Grain force on the bottom of the wedge	kN
K_4	Grain force on the blade (in case a wedge exists)	kN
n_i	Initial porosity	%
n_{max}	Maximum porosity	%
N_1	Normal force on the shear plane	kN
N_2	Normal force on the blade or the front of the wedge	kN
N_3	Normal force on the bottom of the wedge	kN
N_4	Normal force on the blade (in case a wedge exists)	kN
p_{1m}	Average pore pressure on the shear surface	kPa
p_{2m}	Average pore pressure on the blade	kPa
P_c	Cutting power	kW
R_1	Acting point of resulting forces on the shear plane	m
R_2	Acting point of resulting forces on the blade	m
R_3	Acting point of resulting forces on the bottom of the wedge	m
R_4	Acting point of resulting forces on the blade (in case a wedge exists)	m
S_1	Shear force due to friction on the shear plane	kN
S_2	Shear force due to friction on the blade or the front of the wedge	kN
S_3	Shear force due to friction at the bottom of the wedge	kN
S_4	Shear force due to friction on the blade (in case a wedge exists)	kN
v_c	Cutting velocity component perpendicular to the blade	m/s
v_d	Cutting velocity, drag velocity	m/s
v_{r1}	Velocity of grains in the shear surface	m/s

v_{r2}	Relative velocity of grains on the blade	m/s
v_{d1}	Deviation velocity of grains in the shear surface	m/s
v_{d2}	Deviation velocity of grains on the blade	m/s
$v_{x1,2}$	Velocity of grains in the x-direction	m/s
$v_{y1,2}$	Velocity of grains in the y-direction	m/s
$v_{z1,2}$	Velocity of grains in the z-direction	m/s
w	Width of blade	m
W_1	Force resulting from pore underpressure on the shear plane	kN
W_2	Force resulting from pore underpressure on the blade or on the front of the wedge	kN
W_3	Force resulting from pore underpressure on the bottom of the wedge	kN
W_4	Force resulting from pore underpressures on the blade (in case a wedge exists)	
z	Water depth	m
α	Cutting angle blade	rad
β	Shear angle	rad
ε	Dilatation	-
ϕ	Angle of internal friction	rad
ϕ_e	Angle of internal friction perpendicular to the cutting edge	rad
λ	Angle of internal friction on the front of the wedge	rad
λ_1	Acting point factor for resulting forces on the shear plane	-
λ_2	Acting point factor for resulting forces on the blade or front of wedge	-
λ_3	Acting point factor for resulting forces on the bottom of the wedge	-
λ_4	Acting point factor for resulting forces on the blade	-
δ	External friction angle	rad
δ_e	External friction angle perpendicular to the cutting edge	rad
ι	Deviation angle blade	rad
ρ_g	Density of the soil	ton/m³
ρ_w	Density water	ton/m³
θ	Wedge angle	rad

Chapter 3: Which Equation and Which Cutting Mechanism for Which Kind of Soil?

3.1. Cutting Dry Sand

In dry sand the cutting processes are governed by gravity and by inertial forces. Pore pressure forces, cohesion and adhesion are not present or can be neglected. Internal and external friction are present. The cutting process is of the **Shear Type** with discrete shear planes, but this can be modeled as the **Flow Type**, according to Merchant (1944). This approach will give an estimate of the maximum cutting forces. The average cutting forces may be 30%-50% of the maximum cutting forces.

3.2. Cutting Water Saturated Sand

From literature it is known that, during the cutting process, the sand increases in volume. This increase in volume is accredited to dilatancy. Dilatancy is the change of the pore volume as a result of shear in the sand package. This increase of the pore volume has to be filled with water. The flowing water experiences a certain resistance, which causes sub-pressures in the pore water in the sand package. As a result the grain stresses increase and therefore the required cutting forces. The rate of the increase of the pore volume in the dilatancy zone, the volume strain rate, is proportional to the cutting velocity. If the volume strain rate is high, there is a chance that the pore pressure reaches the saturated water vapor pressure and cavitation occurs. A further increasing volume strain rate will not be able to cause a further decrease of the pore pressure. This also implies that, with a further increasing cutting velocity, the cutting forces cannot increase as a result of the dilatancy properties of the sand. The cutting forces can, however, still increase with an increasing cutting velocity as a result of the inertia forces and the flow resistance.

The cutting process can be subdivided in 5 areas in relation with the cutting forces:

- Very low cutting velocities, a quasi-static cutting process. The cutting forces are determined by the gravitation, cohesion and adhesion.
- The volume strain rate is high in relation to the permeability of the sand. The volume strain rate is however so small that inertia forces can be neglected. The cutting forces are dominated by the dilatancy properties of the sand.
- A transition region, with local cavitation. With an increasing volume strain rate, the cavitation area will increase so that the cutting forces increase slightly as a result of dilatancy.
- Cavitation occurs almost everywhere around and on the blade. The cutting forces do not increase anymore as a result of the dilatancy properties of the sand.
- Very high cutting velocities. The inertia forces part in the total cutting forces can no longer be neglected but form a substantial part.

Under normal conditions in dredging, the cutting process in sand will be governed by the effects of dilatation. Gravity, inertia, cohesion and adhesion will not play a role.

3.3. Cutting Clay

In clay the cutting processes are dominated by cohesion and adhesion (internal and external shear strength). Because of the $\varphi=0$ concept, the internal and external friction angles are set to 0. Gravity, inertial forces and pore pressures are also neglected. This simplifies the cutting equations. Clay however is subject to strengthening, meaning that the internal and external shear strength increase with an increasing strain rate. The reverse of strengthening is creep, meaning that under a constant load the material will continue deforming with a certain strain rate.
Under normal circumstances clay will be cut with the flow mechanism, but under certain circumstances the curling type or the tear type may occur.
The curling type will occur when the blade height is big with respect to the layer thickness, h_b/h_i, the adhesion is high compared to the cohesion **a/c** and the blade angle α is relatively big.
The tear type will occur when the blade height is small with respect to the layer thickness, h_b/h_i, the adhesion is small compared to the cohesion **a/c** and the blade angle α is relatively small.

3.4. Cutting Rock Atmospheric

Rock is the collection of materials where the grains are bonded chemically from very stiff clay, sandstone to very hard basalt. It is difficult to give one definition of rock or stone and also the composition of the material can differ strongly. Still it is interesting to see if the model used for sand and clay, which is based on the Coulomb model, can be used for rock as well. Typical parameters for rock are the compressive strength UCS and the tensile strength BTS and specifically the ratio between those two, which is a measure for how fractured the rock is. Rock also has shear strength and because it consists of bonded grains it will have an internal friction angle and an external friction angle. It can be assumed that the permeability of the rock is very low, so initially the pore pressures do no play a role or cavitation will always occur under atmospheric conditions. But since the absolute hydrostatic pressure, which would result in a cavitation under pressure of the same magnitude can be neglected with respect to the compressive strength of the rock; the pore pressures are usually neglected. This results in a material where gravity, inertia, pore pressures and adhesion can be neglected.

3.5. Cutting Rock Hyperbaric

In the case of hyperbaric rock cutting, the pore pressures cannot be neglected anymore. Gravity and inertial forces can still be neglected. Usually rock has no adhesion.

3.6. Summary

	Gravity	Inertia	Pore Pressure	Cohesion	Adhesion	Friction
Dry sand						
Saturated sand						
Clay						
Atmospheric rock						
Hyperbaric rock						

3.7. Nomenclature Chapter 3:

a	Adhesion or external shear strength	kPa
c	Cohesion or internal shear strength	kPa
h_i	Thickness of the layer cut	m
h_b	Height of the blade	m
α	Blade angle	rad
φ	Angle of internal friction	rad

Chapter 4: Dry Sand Cutting

4.1. Introduction

In dry sand the cutting processes are governed by gravity and by inertial forces. Pore pressure forces, cohesion and adhesion are not present or can be neglected. Internal and external friction are present. The cutting process is of the **Shear Type** with discrete shear planes (see Figure 4-1), but this can be modeled as the **Flow Type** (see Figure 4-2), according to Merchant (1944). This approach will give an estimate of the maximum cutting forces. The average cutting forces may be 30%-50% of the maximum cutting forces.

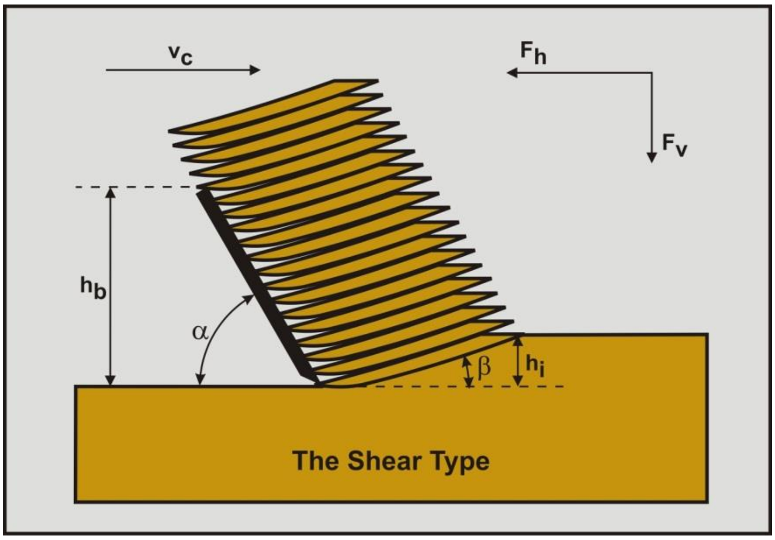

Figure 4-1: The cutting mechanism in dry sand, the Shear Type.

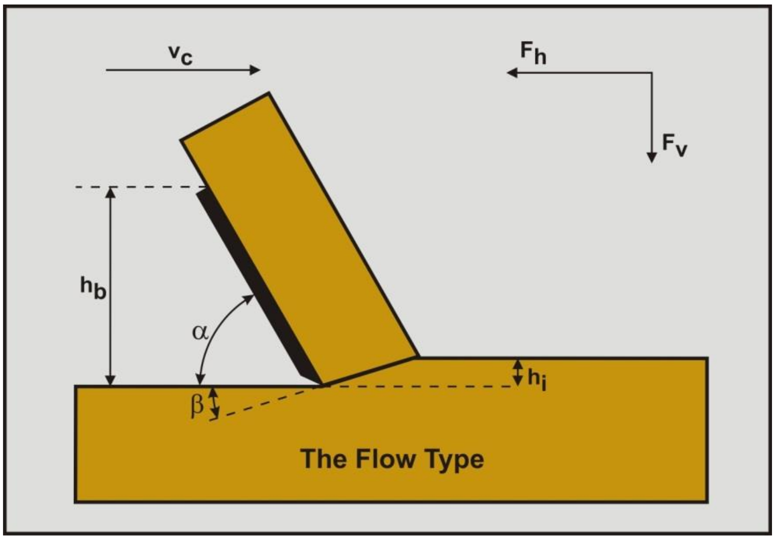

Figure 4-2: Dry sand modeled according to the Flow Type.

4.2. The Force Balance

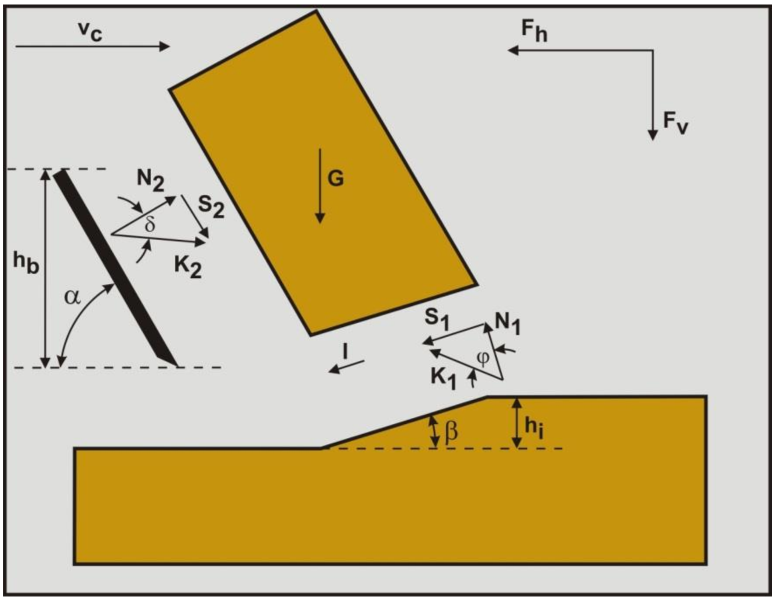

Figure 4-3: The forces on the layer cut in dry sand.

Figure 4-3 illustrates the forces on the layer of soil cut. The forces shown are valid in general. The forces acting on this layer are:

1. A normal force acting on the shear surface $\mathbf{N_1}$, resulting from the effective grain stresses.
2. A shear force $\mathbf{S_1}$ as a result of internal fiction, $\mathbf{N_1 \cdot tan(\phi)}$.
3. A gravity force **G** as a result of the weight of the layer cut.
4. An inertial force **I**, resulting from acceleration of the soil.
5. A force normal to the blade $\mathbf{N_2}$, resulting from the effective grain stresses.
6. A shear force $\mathbf{S_2}$ as a result of the soil/steel friction $\mathbf{N_2 \cdot tan(\delta)}$.

The normal force $\mathbf{N_1}$ and the shear force $\mathbf{S_1}$ can be combined to a resulting grain force $\mathbf{K_1}$.

$$\mathbf{K_1 = \sqrt{N_1^2 + S_1^2}} \qquad \mathbf{(4\text{-}1)}$$

The forces acting on a straight blade when cutting soil, can be distinguished as:

7. A force normal to the blade $\mathbf{N_2}$, resulting from the effective grain stresses.
8. A shear force $\mathbf{S_2}$ as a result of the soil/steel friction $\mathbf{N_2 \cdot tan(\delta)}$.

These forces are shown in Figure 4-4. If the forces $\mathbf{N_2}$ and $\mathbf{S_2}$ are combined to a resulting force $\mathbf{K_2}$ and the adhesive force and the water under pressures are known, then the resulting force $\mathbf{K_2}$ is the unknown force on the blade. By taking the horizontal and vertical equilibrium of forces an expression for the force $\mathbf{K_2}$ on the blade can be derived.

$$\mathbf{K_2 = \sqrt{N_2^2 + S_2^2}} \qquad \mathbf{(4\text{-}2)}$$

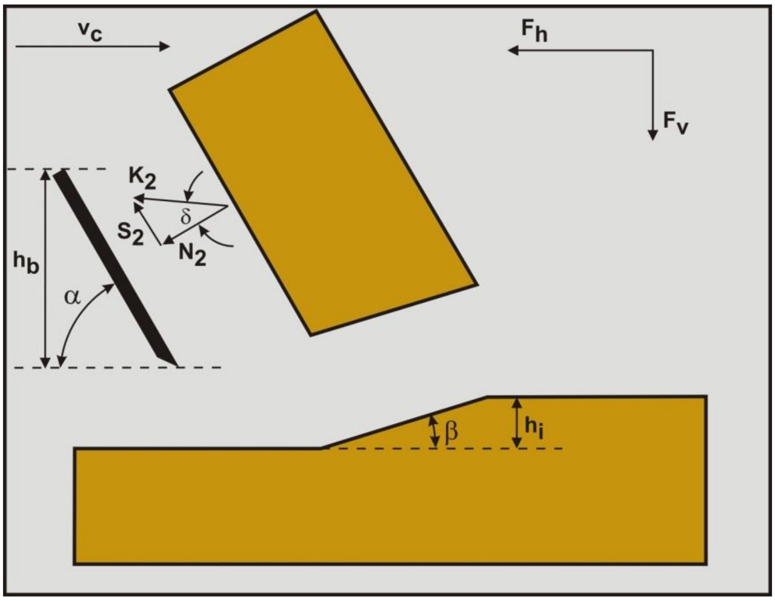

Figure 4-4: The forces on the blade in dry sand.

Pure sand is supposed to be cohesion less, meaning it does not have shear strength or the shear strength is zero and the adhesion is also zero. The shear stresses, internal and external, depend completely on the normal stresses. In dry sand the pores between the sand grains are filled with air and although dilatation will occur due to shearing, Miedema (1987 September), there will be hardly any generation of pore under pressures because the permeability for air flowing through the pores is high. This means that the cutting forces do not depend on pore pressure forces, nor on adhesion and cohesion, but only on gravity and inertia, resulting in the following set of equations:

The horizontal equilibrium of forces:

$$\sum F_h = K_1 \cdot \sin(\beta + \varphi) + I \cdot \cos(\beta) - K_2 \cdot \sin(\alpha + \delta) = 0 \tag{4-3}$$

The vertical equilibrium of forces:

$$\sum F_v = -K_1 \cdot \cos(\beta + \varphi) + I \cdot \sin(\beta) + G - K_2 \cdot \cos(\alpha + \delta) = 0 \tag{4-4}$$

The force $\mathbf{K_1}$ on the shear plane is now:

$$K_1 = \frac{G \cdot \sin(\alpha + \delta) - I \cdot \cos(\alpha + \beta + \delta)}{\sin(\alpha + \beta + \delta + \varphi)} \tag{4-5}$$

The force $\mathbf{K_2}$ on the blade is now:

$$K_2 = \frac{G \cdot \sin(\beta + \varphi) + I \cdot \cos(\varphi)}{\sin(\alpha + \beta + \delta + \varphi)} \tag{4-6}$$

Wismer and Luth (1972A) and (1972B) researched the inertia forces part of the total cutting forces. The following equation is derived:

$$I = \rho_g \cdot v_c^2 \cdot \frac{\sin(\alpha)}{\sin(\alpha + \beta)} \cdot h_i \cdot w \tag{4-7}$$

The gravitation force (mass) follows from:

$$G = (\rho_s - \rho_w) \cdot g \cdot h_i \cdot w \cdot \frac{\sin(\alpha + \beta)}{\sin(\beta)} \cdot \left\{ \frac{(h_b + h_i \cdot \sin(\alpha))}{\sin(\alpha)} + \frac{h_i \cdot \cos(\alpha + \beta)}{2 \cdot \sin(\beta)} \right\} \tag{4-8}$$

From equation (4-6) the forces on the blade can be derived. On the blade a force component in the direction of cutting velocity $\mathbf{F_h}$ and a force perpendicular to this direction $\mathbf{F_v}$ can be distinguished.

$$\mathbf{F_h = K_2 \cdot \sin(\alpha + \delta)} \tag{4-9}$$

$$\mathbf{F_v = K_2 \cdot \cos(\alpha + \delta)} \tag{4-10}$$

The normal force on the shear plane is now:

$$\mathbf{N_1 = \frac{G \cdot \sin(\alpha + \delta) - I \cdot \cos(\alpha + \beta + \delta)}{\sin(\alpha + \beta + \delta + \varphi)} \cdot \cos(\varphi)} \tag{4-11}$$

The normal force on the blade is now:

$$\mathbf{N_2 = \frac{G \cdot \sin(\beta + \varphi) + I \cdot \cos(\varphi)}{\sin(\alpha + \beta + \delta + \varphi)} \cdot \cos(\delta)} \tag{4-12}$$

Equations (4-11) and (4-12) show that the normal force on the shear plane $\mathbf{N_1}$ can become negative at very high velocities, which are physically impossible, while the normal force on the blade $\mathbf{N_2}$ will always be positive. Under normal conditions the sum of $\boldsymbol{\alpha+\beta+\delta}$ will be greater than 90 degrees in which case the cosine of this sum is negative, resulting in a normal force on the shear plane that is always positive. Only in the case of a small blade angle $\boldsymbol{\alpha}$, shear angle $\boldsymbol{\beta}$ and angle of external friction $\boldsymbol{\delta}$, the sum of these angles could be smaller than 90°, but still close to 90° degrees. For example a blade angle of 30° would result in a shear angle of about 30°. Loose sand could have an external friction angle of 20°, so the sum would be 80°. But this is a lower limit for $\boldsymbol{\alpha+\beta+\delta}$. A more realistic example is a blade with an angle of 60°, resulting in a shear angle of about 20° and a medium to hard sand with an external friction angle of 30°, resulting in $\boldsymbol{\alpha+\beta+\delta=110°}$. So for realistic cases the normal force on the shear plane $\mathbf{N_1}$ will always be positive. In dry sand, always the shear type of cutting mechanism will occur.

4.3. Nomenclature Chapter 4:

F_h	Horizontal cutting force	kN
F_v	Vertical cutting force	kN
g	Gravitational constant (9.81)	m/s^2
G	Gravitational force on the layer cut	kN
h_i	Initial thickness of layer cut	m
h_b	Height of blade	m
I	Inertial force on the shear plane	kN
K_1	Grain force on the shear plane	kN
K_2	Grain force on the blade or the front of the wedge	kN
N_1	Normal force on the shear plane	kN
N_2	Normal force on the blade or the front of the wedge	kN
P_c	Cutting power	kW
S_1	Shear force due to friction on the shear plane	kN
S_2	Shear force due to friction on the blade or the front of the wedge	kN
v_c	Cutting velocity component perpendicular to the blade	m/s
w	Width of blade	m
W_1	Force resulting from pore underpressure on the shear plane	kN
W_2	Force resulting from pore underpressure on the blade or on the front of the wedge	kN
α	Cutting angle blade	rad
β	Shear angle	rad
ϕ	Angle of internal friction	rad
δ	External friction angle	rad
ρ_g	Density of the soil	ton/m^3
ρ_w	Density water	ton/m^3

Chapter 5: Water Saturated Sand Cutting

5.1. Introduction

Although calculation models for the determination of the cutting forces for dry soil, based on agriculture, were available for a long time (Hettiaratchi & Reece (1965), (1966), (1967A), (1967B), (1974), (1975) and Hatamura & Chiiwa (1975), (1976), (1976), (1977) and (1977)) it is only since the seventies and the eighties that the cutting process in saturated sand is extensively researched at the Delft Hydraulics Laboratory, at the Delft University of Technology and at the Mineraal Technologisch Instituut (MTI, IHC).

First the process is described, for a good understanding of the terminology used in the literature discussion.

From literature it is known that, during the cutting process, the sand increases in volume (see Figure 5-6). This increase in volume is accredited to dilatancy. Dilatancy is the change of the pore volume as a result of shear in the sand package. This increase of the pore volume has to be filled with water. The flowing water experiences a certain resistance, which causes sub-pressures in the pore water in the sand package. As a result the grain stresses increase and therefore the required cutting forces. The rate of the increase of the pore volume in the dilatancy zone, the volume strain rate, is proportional to the cutting velocity. If the volume strain rate is high, there is a chance that the pore pressure reaches the saturated water vapor pressure and cavitation occurs. A further increasing volume strain rate will not be able to cause a further decrease of the pore pressure. This also implies that, with a further increasing cutting velocity, the cutting forces cannot increase as a result of the dilatancy properties of the sand. The cutting forces can, however, still increase with an increasing cutting velocity as a result of the inertia forces and the flow resistance.

The cutting process can be subdivided in 5 areas in relation with the cutting forces:

- Very low cutting velocities, a quasi-static cutting process. The cutting forces are determined by the gravitation, cohesion and adhesion.
- The volume strain rate is high in relation to the permeability of the sand. The volume strain rate is however so small that inertia forces can be neglected. The cutting forces are dominated by the dilatancy properties of the sand.
- A transition region, with local cavitation. With an increasing volume strain rate, the cavitation area will increase so that the cutting forces increase slightly as a result of dilatancy.
- Cavitation occurs almost everywhere around and on the blade. The cutting forces do not increase anymore as a result of the dilatancy properties of the sand.
- Very high cutting velocities. The inertia forces part in the total cutting forces can no longer be neglected but form a substantial part.

Under normal conditions in dredging, the cutting process in sand will be governed by the effects of dilatation. Gravity, inertia, cohesion and adhesion will not play a role.

5.2. Cutting theory literature

In the seventies extensive research is carried out on the forces that occur while cutting sand under water. A conclusive cutting theory has however not been published in this period. However qualitative relations have been derived by several researchers, with which the dependability of the cutting forces with the soil properties and the blade geometry are described (Joanknecht (1974), van Os (1977A), (1976) and (1977B)).

A process that has a lot of similarities with the cutting of sand as far as water pressure development is concerned, is the, with uniform velocity, forward moving breach. Meijer and van Os (1976) and Meijer (1981) and (1985) have transformed the storage equation for the, with the breach, forward moving coordinate system.

$$\left|\frac{\partial^2 \mathbf{p}}{\partial \mathbf{x}^2}\right| + \left|\frac{\partial^2 \mathbf{p}}{\partial \mathbf{y}^2}\right| = \frac{\rho_\mathbf{w} \cdot \mathbf{g} \cdot \mathbf{v_c}}{\mathbf{k}} \cdot \left|\frac{\partial \mathbf{e}}{\partial \mathbf{x}}\right| - \frac{\rho_\mathbf{w} \cdot \mathbf{g}}{\mathbf{k}} \cdot \left|\frac{\partial \mathbf{e}}{\partial \mathbf{t}}\right| \tag{5-1}$$

In the case of a stationary process, the second term on the right is zero, resulting:

$$\left|\frac{\partial^2 p}{\partial x^2}\right| + \left|\frac{\partial^2 p}{\partial y^2}\right| = \frac{\rho_w \cdot g \cdot v_c}{k} \cdot \left|\frac{\partial e}{\partial x}\right| \tag{5-2}$$

Van Os (1977A), (1976) and (1977B) describes the basic principles of the cutting process, with special attention for the determination of the water sub-pressures and the cavitation. Van Os uses the non-transformed storage equation for the determination of the water sub-pressures.

$$\left|\frac{\partial^2 p}{\partial x^2}\right| + \left|\frac{\partial^2 p}{\partial y^2}\right| = \frac{\rho_w \cdot g}{k} \cdot \left|\frac{\partial e}{\partial t}\right| \tag{5-3}$$

The average volume strain rate has to be substituted in the term **∂e/∂t** on the right. The average volume strain rate is the product of the average volume strain of the sand package and the cutting velocity and arises from the volume balance over the shear zone. Van Os gives a qualitative relation between the water sub-pressures and the average volume strain rate:

$$p :: \frac{v_c \cdot h_i \cdot \varepsilon}{k} \tag{5-4}$$

The problem of the solution of the storage equation for the cutting of sand under water is a mixed boundary value problem, for which the water sub-pressures along the boundaries are known (hydrostatic).

Joanknecht (1973) and (1974) assumes that the cutting forces are determined by the sub-pressure in the sand package. A distinction is made between the parts of the cutting force caused by the inertia forces, the sub-pressure behind the blade and the soil mechanical properties of the sand. The influence of the geometrical parameters gives the following qualitative relation:

$$F_{ci} :: v_c \cdot h_i^2 \cdot w \tag{5-5}$$

The cutting force is proportional to the cutting velocity, the blade width and the square of the initial layer-thickness. A relation with the pore percentage and the permeability is also mentioned. A relation between the cutting force and these soil mechanical properties is however not given. It is observed that the cutting forces increase with an increasing blade angle.

In the eighties research has led to more quantitative relations. Van Leussen and Nieuwenhuis (1984) discuss the soil mechanical aspects of the cutting process. The forces models of Miedema (1984B), (1985B), (1985A), (1986B) and (1987 September), Steeghs (1985A) and (1985B) and the CSB (Combinatie Speurwerk Baggertechniek) model (van Leussen en van Os (1987 December)) are published in the eighties.

Brakel (1981) derives a relation for the determination of the water sub-pressures based upon, over each other rolling, round grains in the shear zone. The force part resulting from this is added to the model of Hettiaratchi and Reece (1974).

Miedema (1984B) has combined the qualitative relations of Joanknecht (1973) and (1974) and van Os (1976), (1977A) and (1977B) to the following relation:

$$F_{ci} :: \frac{\rho_w \cdot g \cdot v_c \cdot h_i^2 \cdot w \cdot \varepsilon}{k_m} \tag{5-6}$$

With this basic equation calculation models are developed for a cutter head and for the periodical moving cutter head in the breach. The proportionality constants are determined empirically.
Van Leussen and Nieuwenhuis (1984) discuss the soil mechanical aspects of the cutting process. Important in the cutting process is the way shear takes place and the shape or angle of the shear plane, respectively shear zone. In literature no unambiguous image could be found. Cutting tests along a windowpane gave an image in which the shape of the shear plane was more in accordance with the so-called "stress characteristics" than with the so-called "zero-extension lines". Therefore, for the calculation of the cutting forces, the "stress characteristics method" is used (Mohr-Coulomb failure criterion). For the calculation of the water sub-pressures, however, the "zero-

extension lines" are used, which are lines with a zero linear strain. A closer description has not been given for both calculations.

Although the cutting process is considered as being two-dimensional, Van Leussen and Nieuwenhuis found, that the angle of internal friction, measured at low deformation rates in a triaxial apparatus, proved to be sufficient for dredging processes. Although the cutting process can be considered as a two-dimensional process and therefore it should be expected that the angle of internal friction has to be determined with a "plane deformation test". A sufficient explanation has not been found.

Little is known about the value of the angle of friction between sand and steel. Van Leussen and Nieuwenhuis don't give an unambiguous method to determine this soil mechanical parameter. It is, however, remarked that at low cutting velocities (0.05 mm/s), the soil/steel angle of friction can have a statistical value which is 1.5 to 2 times larger than the dynamic soil/steel angle of friction. The influence of the initial density on the resulting angle of friction is not clearly present, because loose packed sand moves over the blade. The angles of friction measured on the blades are much larger than the angles of friction measured with an adhesion cell, while also a dependency with the blade angle is observed.

With regard to the permeability of the sand, Van Leussen and Nieuwenhuis found that no large deviations of Darcy's law occur with the water flow through the pores. The found deviations are in general smaller than the accuracy with which the permeability can be determined in situ.

The size of the area where $\partial e/\partial t$ from equation (5-5) is zero can be clarified by the figures published by van Leussen and Nieuwenhuis. The basis is formed by a cutting process where the density of the sand is increased in a shear band with a certain width. The undisturbed sand has the initial density while the sand after passage of the shear band possesses a critical density. This critical density appeared to be in good accordance with the wet critical density of the used types of sand. This implies that outside the shear band the following equation (Biot (1941)) is valid:

$$\left|\frac{\partial^2 \mathbf{p}}{\partial \mathbf{x}^2}\right| + \left|\frac{\partial^2 \mathbf{p}}{\partial \mathbf{y}^2}\right| = \mathbf{0} \tag{5-7}$$

Values for the various densities are given for three types of sand. Differentiation of the residual density as a function of the blade angle is not given. A verification of the water pressures calculations is given for a 60° blade with a blade-height/layer-thickness ratio of 1.

Miedema (1984A) and (1984B) gives a formulation for the determination of the water sub-pressures. The deformation rate is determined by taking the volume balance over the shear zone, as van Os (1977A), (1976) and (1977B) did. The deformation rate is modeled as a boundary condition in the shear zone , while the shear zone is modeled as a straight line instead of a shear band as with van Os (1976), (1977A), (1977B), van Leussen and Nieuwenhuis (1984) and Hansen (1958). The influence of the water depth on the cutting forces is clarified. Steeghs (1985A) and (1985B) developed a theory for the determination of the volume strain rate, based upon a cyclic deformation of the sand in a shear band. This implies that not an average value is taken for the volume strain rate but a cyclic, with time varying, value, based upon the dilatancy angle theory.

Miedema (1985A) and (1985B) derives equations for the determination of the water sub-pressures and the cutting forces, based upon Miedema (1982), (1984A) and (1984B). The water sub-pressures are determined with a finite element method. Explained are the influence of the permeability of the disturbed and undisturbed sand and the determination of the shear angle. The derived theory is verified with model tests. On basis of this research $\mathbf{n_{max}}$ is chosen for the residual pore percentage instead of the wet critical density.

Steeghs (1985A) and (1985B) derives equations for the determination of the water sub-pressures according to an analytical approximation method. With this approximation method the water sub-pressures are determined with a modification of equation (5-4) derived by van Os (1976), (1977A), (1977B) and the storage equation (5-7). Explained is how cutting forces can be determined with the force equilibrium on the cut layer. Also included are the gravity force, the inertia forces and the sub-pressure behind the blade. For the last influence factor no formulation is given. Discussed is the determination of the shear angle. Some examples of the cutting forces are given as a function of the cutting velocity, the water depth and the sub-pressure behind the blade. A verification of this theory is not given.

Miedema (1986A) develops a calculation model for the determination of the cutting forces on a cutter-wheel based upon (1985A) and (1985B). This will be discussed in the appropriate section. Also nomograms are published with which the cutting forces and the shear angle can be determined in a simple way. Explained is the determination of the weighted average permeability from the permeability of the disturbed and undisturbed sand. Based upon the calculations it is concluded that the average permeability forms a good estimation.

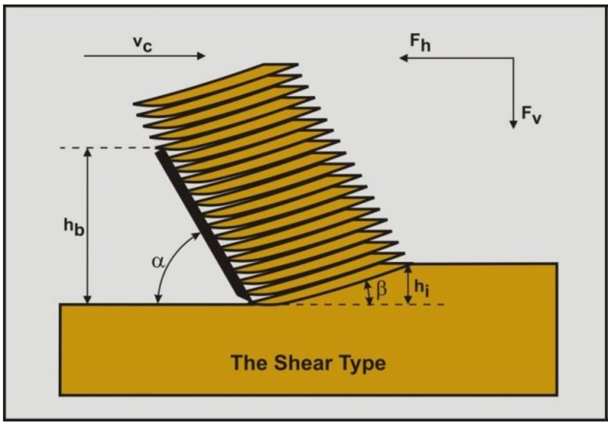

Figure 5-1: The cutting mechanism in water saturated sand, the Shear Type.

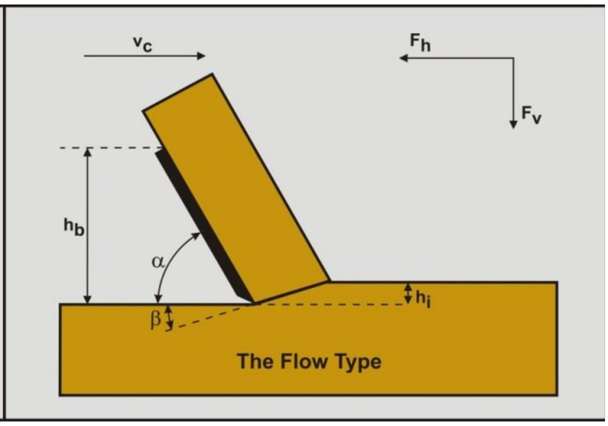

Figure 5-2: Water saturated sand modeled according to the Flow Type.

Miedema (1986B) extends the theory with adhesion, cohesion, inertia forces, gravity, and sub-pressure behind the blade. The method for the calculation of the coefficients for the determination of a weighted average permeability are discussed. It is concluded that the additions to the theory lead to a better correlation with the tests results.

Van Os and van Leussen (1987 December) summarize the publications of van Os (1976), (1977A), (1977B) and of Van Leussen and Nieuwenhuis (1984) and give a formulation of the theory developed in the early seventies at the Waterloopkundig Laboratorium. Discussed are the water pressures calculation, cavitation, the weighted average permeability, the angle of internal friction, the soil/steel angle of friction, the permeability, the volume strain and the cutting forces. Verification is given of a water pressures calculation and the cutting forces. The water sub-pressures are determined with equation (5-4) derived by van Os (1976), (1977A) and (1977B). The water pressures calculation is performed with the finite difference method, in which the height of the shear band is equal to the mesh width of the grid. The size of this mesh width is considered to be arbitrary. From an example, however, it can be seen that the shear band has a width of 13% of the layer-thickness. Discussed is the determination of a weighted average permeability. The forces are determined with Coulomb's method.

5.3. The Equilibrium of Forces

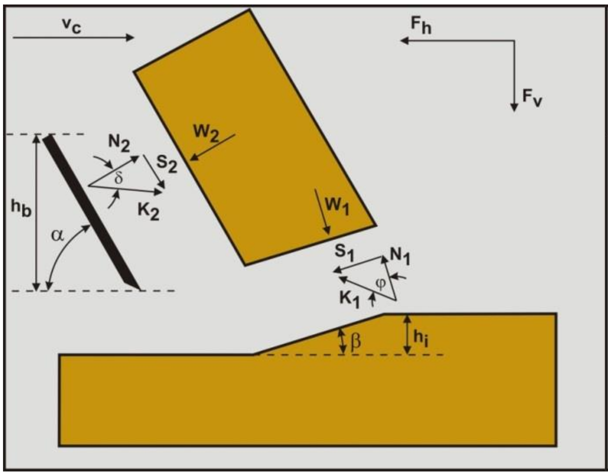

Figure 5-3: The forces on the layer cut in water saturated sand.

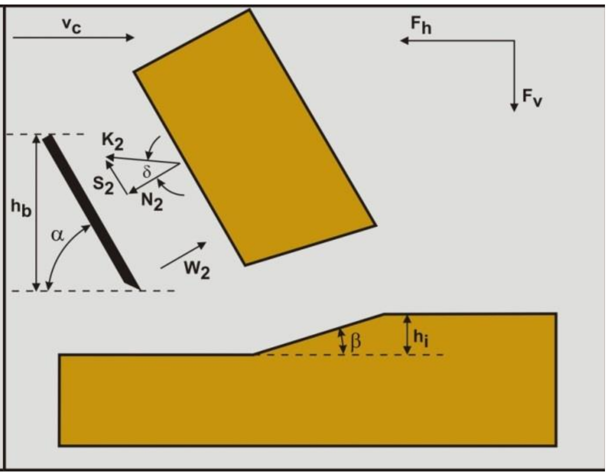

Figure 5-4: The forces on the blade in water saturated sand.

Figure 5-3 illustrates the forces on the layer of soil cut. The forces shown are valid in general. The forces acting on this layer are:

1. A normal force acting on the shear surface $\mathbf{N_1}$.
2. A shear force $\mathbf{S_1}$ as a result of internal fiction $\mathbf{N_1 \cdot tan(\phi)}$.
3. A force $\mathbf{W_1}$ as a result of water under pressure in the shear zone.
4. A force normal to the blade $\mathbf{N_2}$.
5. A shear force $\mathbf{S_2}$ as a result of the soil/steel friction $\mathbf{N_2 \cdot tan(\delta)}$.
6. A force $\mathbf{W_2}$ as a result of water under pressure on the blade.

The normal force $\mathbf{N_1}$ and the shear force $\mathbf{S_1}$ can be combined to a resulting grain force $\mathbf{K_1}$.

$$K_1 = \sqrt{N_1^2 + S_1^2} \quad \textbf{(5-8)}$$

The forces acting on a straight blade when cutting soil, can be distinguished as:

7. A force normal to the blade $\mathbf{N_2}$.
8. A shear force $\mathbf{S_2}$ as a result of the soil/steel friction $\mathbf{N_2 \cdot tan(\delta)}$.
9. A force $\mathbf{W_2}$ as a result of water under pressure on the blade.

These forces are shown in Figure 5-4. If the forces $\mathbf{N_2}$ and $\mathbf{S_2}$ are combined to a resulting force $\mathbf{K_2}$ and the adhesive force and the water under pressures are known, then the resulting force $\mathbf{K_2}$ is the unknown force on the blade. By taking the horizontal and vertical equilibrium of forces an expression for the force $\mathbf{K_2}$ on the blade can be derived.

$$K_2 = \sqrt{N_2^2 + S_2^2} \quad \textbf{(5-9)}$$

Water saturated sand is also cohesion less, although in literature the phenomenon of water under pressures is sometimes referred to as apparent cohesion. It should be stated however that the water under pressures have nothing to do with cohesion or shear strength. The shear stresses still follow the rules of Coulomb friction. Due to dilatation, a volume increase of the pore volume caused by shear stresses, under pressures develop around the shear plane as described by Miedema (1987 September), resulting in a strong increase of the grain stresses. Because the permeability of the flow of water through the pores is very low, the stresses and thus the forces are dominated by the phenomenon of dilatancy and gravitation, inertia, adhesion and cohesion can be neglected.

The horizontal equilibrium of forces is:

$$\sum F_h = K_1 \cdot \sin(\beta + \varphi) - W_1 \cdot \sin(\beta) + W_2 \cdot \sin(\alpha) - K_2 \cdot \sin(\alpha + \delta) = 0 \quad \textbf{(5-10)}$$

The vertical equilibrium of forces is:

$$\sum F_v = -K_1 \cdot \cos(\beta + \varphi) + W_1 \cdot \cos(\beta) + W_2 \cdot \cos(\alpha) - K_2 \cdot \cos(\alpha + \delta) = 0 \quad \textbf{(5-11)}$$

The force $\mathbf{K_1}$ on the shear plane is now:

$$K_1 = \frac{W_2 \cdot \sin(\delta) + W_1 \cdot \sin(\alpha + \beta + \delta)}{\sin(\alpha + \beta + \delta + \varphi)} \quad \textbf{(5-12)}$$

The force $\mathbf{K_2}$ on the blade is now:

$$K_2 = \frac{W_2 \cdot \sin(\alpha + \beta + \varphi) + W_1 \cdot \sin(\varphi)}{\sin(\alpha + \beta + \delta + \varphi)} \quad \textbf{(5-13)}$$

From equation (5-13) the forces on the blade can be derived. On the blade a force component in the direction of cutting velocity $\mathbf{F_h}$ and a force perpendicular to this direction $\mathbf{F_v}$ can be distinguished.

$$F_h = -W_2 \cdot \sin(\alpha) + K_2 \cdot \sin(\alpha + \delta) \quad \textbf{(5-14)}$$

$$F_v = -W_2 \cdot \cos(\alpha) + K_2 \cdot \cos(\alpha + \delta) \quad \textbf{(5-15)}$$

The normal force on the shear plane is now:

$$N_1 = \frac{W_2 \cdot \sin(\delta) + W_1 \cdot \sin(\alpha + \beta + \delta)}{\sin(\alpha + \beta + \delta + \varphi)} \cdot \cos(\varphi) \tag{5-16}$$

The normal force on the blade is now:

$$N_2 = \frac{W_2 \cdot \sin(\alpha + \beta + \varphi) + W_1 \cdot \sin(\varphi)}{\sin(\alpha + \beta + \delta + \varphi)} \cdot \cos(\delta) \tag{5-17}$$

Equations (5-16) and (5-17) show, that the normal forces on the shear plane and the blade are always positive. Positive means compressive stresses. In water saturated sand, always the shear type of cutting mechanism will occur. Figure 5-5 shows these forces on the layer cut.

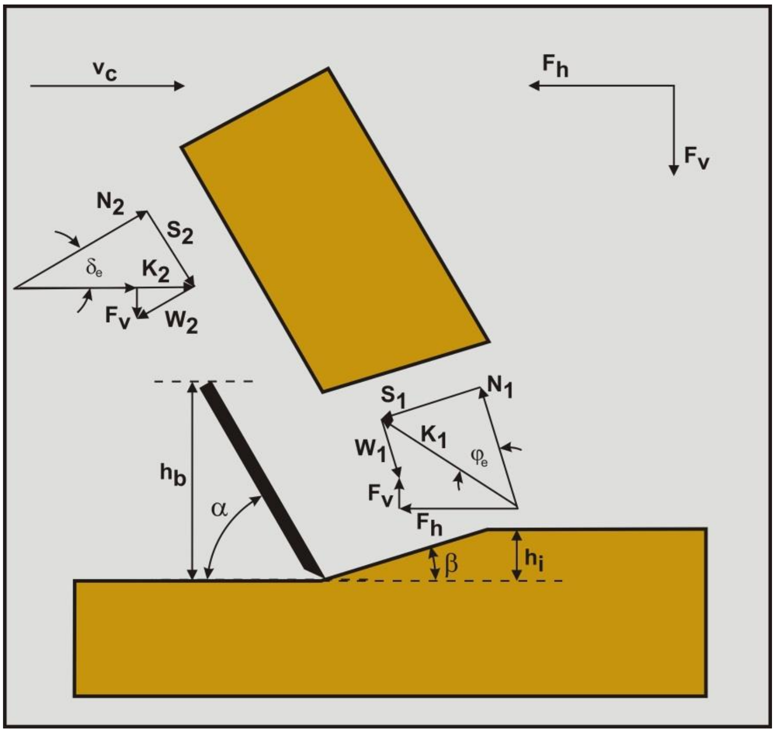

Figure 5-5: The forces on the blade when cutting water saturated sand.

5.4. Determination of the Under-Pressure around the Blade

The cutting process can be modeled as a two-dimensional process, in which a straight blade cuts a small layer of sand (Figure 5-6). The sand is deformed in the shear zone, also called deformation zone or dilatancy zone. During this deformation the volume of the sand changes as a result of the shear stresses in the shear zone. In soil mechanics this phenomenon is called dilatancy. In hard packed sand the pore volume is increased as a result of the shear stresses in the deformation zone. This increase in the pore volume is thought to be concentrated in the deformation zone, with the deformation zone modeled as a straight line. Water has to flow to the deformation zone to fill up the increase of the pore volume in this zone. As a result of this water flow the grain stresses increase and the water pressures decrease. Therefore there are water under-pressures.

This implies that the forces necessary for cutting hard packed sand under water will be determined for an important part by the dilatancy properties of the sand. At low cutting velocities these cutting forces are also determined by the gravity, the cohesion and the adhesion for as far as these last two soil mechanical parameters are present in the sand. Is the cutting at high velocities, than the inertia forces will have an important part in the total cutting forces especially in dry sand.

If the cutting process is assumed to be stationary, the water flow through the pores of the sand can be described in a blade motions related coordinate system. The determination of the water under-pressures in the sand around the blade is then limited to a mixed boundary conditions problem. The potential theory can be used to solve this problem. For the determination of the water under-pressures it is necessary to have a proper formulation of the boundary condition in the shear zone. Miedema (1984B) derived the basic equation for this boundary condition.

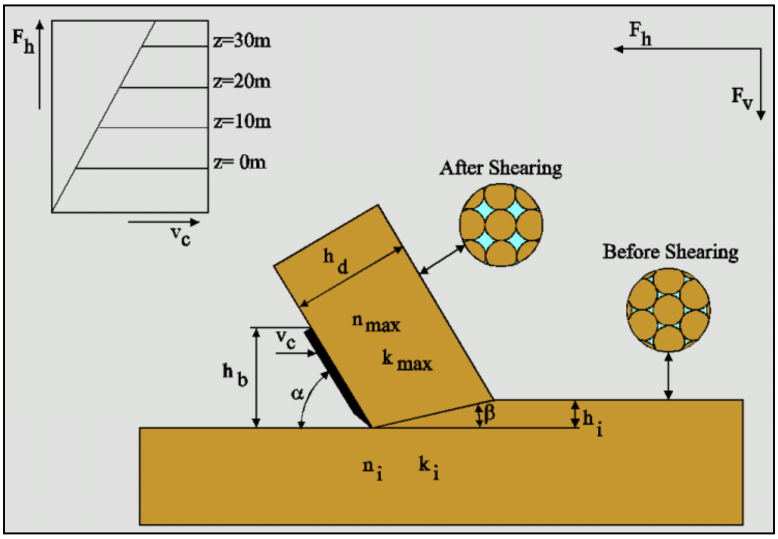

Figure 5-6: The cutting process modeled as a continuous process.

In (1985A) and (1985B) a more extensive derivation is published by Miedema. If it is assumed that no deformations take place outside the deformation zone, then the following equation applies for the sand package around the blade:

$$\left|\frac{\partial^2 p}{\partial x^2}\right| + \left|\frac{\partial^2 p}{\partial y^2}\right| = 0 \tag{5-18}$$

The boundary condition is in fact a specific flow rate (Figure 5-7) that can be determined with the following hypothesis. For a sand element in the deformation zone, the increase in the pore volume per unit of blade length is:

$$\Delta V = \varepsilon \cdot \Delta A = \varepsilon \cdot \Delta x \cdot \Delta h_i = \varepsilon \cdot \Delta x \cdot \Delta l \cdot \sin(\beta) \tag{5-19}$$

$$\varepsilon = \frac{n_{max} - n_i}{1 - n_{max}} \tag{5-20}$$

It should be noted that in this book the symbol **ε** is used for the dilatation, while in previous publications the symbol **e** is often used. This is to avoid confusion with the symbol **e** for the void ratio.
For the residual pore percentage $\mathbf{n_{max}}$ is chosen on the basis of the ability to explain the water under-pressures, measured in laboratory tests. The volume flow rate flowing to the sand element is equal to:

$$\Delta Q = \frac{\partial V}{\partial t} = \varepsilon \cdot \frac{\partial x}{\partial t} \cdot \Delta l \cdot \sin(\beta) = \varepsilon \cdot v_c \cdot \Delta l \cdot \sin(\beta) \tag{5-21}$$

With the aid of Darcy's law the next differential equation can be derived for the specific flow rate perpendicular to the deformation zone:

$$q = \frac{\partial Q}{\partial l} = q_1 + q_2 = \frac{k_i}{\rho_w \cdot g} \cdot \left|\frac{\partial p}{\partial n}\right|_1 + \frac{k_{max}}{\rho_w \cdot g} \cdot \left|\frac{\partial p}{\partial n}\right|_2 = \varepsilon \cdot v_c \cdot \sin(\beta) \tag{5-22}$$

The partial derivative **∂p/∂n** is the derivative of the water under-pressures perpendicular on the boundary of the area, in which the water under-pressures are calculated (in this case the deformation zone). The boundary conditions on the other boundaries of this area are indicated in Figure 5-7. A hydrostatic pressure distribution is assumed on the boundaries between sand and water. This pressure distribution equals zero in the calculation of the water under-pressures, if the height difference over the blade is neglected.

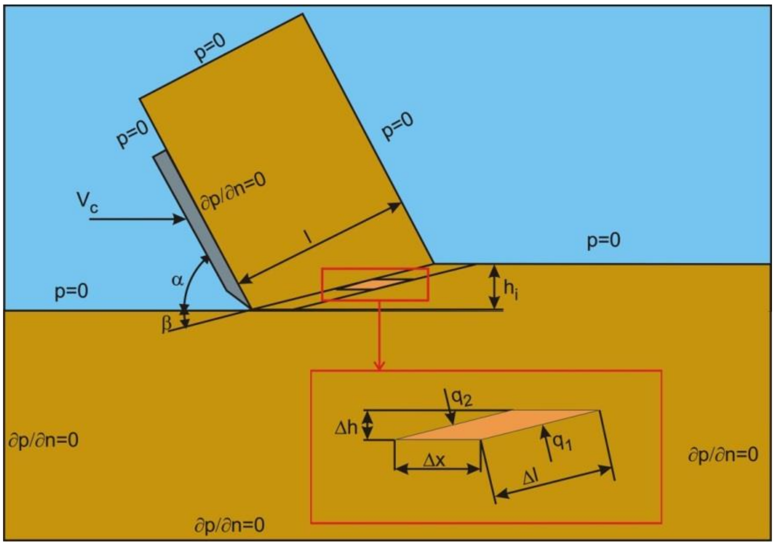

Figure 5-7: The volume balance over the shear zone.

The boundaries that form the edges in the sand package are assumed to be impenetrable. Making equation (5-22) dimensionless is similar to that of the breach equation of Meijer and van Os (1976). In the breach problem the length dimensions are normalized by dividing them by the breach height, while in the cutting of sand they are normalized by dividing them by the cut layer thickness.
Equation (5-22) in normalized format:

$$\frac{k_i}{k_{max}} \cdot \left|\frac{\partial p}{\partial n'}\right|_1 + \left|\frac{\partial p}{\partial n'}\right|_2 = \frac{\rho_w \cdot g \cdot v_c \cdot \varepsilon \cdot h_i \cdot \sin(\beta)}{k_{max}} \quad \text{with:} \quad n' = \frac{n}{h_i} \tag{5-23}$$

This equation is made dimensionless with:

$$\left|\frac{\partial p}{\partial n}\right|' = \frac{\left|\frac{\partial p}{\partial n'}\right|}{\rho_w \cdot g \cdot v_c \cdot \varepsilon \cdot h_i / k_{max}} \tag{5-24}$$

The accent indicates that a certain variable or partial derivative is dimensionless. The next dimensionless equation is now valid as a boundary condition in the deformation zone:

$$\frac{k_i}{k_{max}} \cdot \left|\frac{\partial p}{\partial n}\right|_1' + \left|\frac{\partial p}{\partial n}\right|_2' = \sin(\beta) \tag{5-25}$$

The storage equation also has to be made dimensionless, which results in the next equation:

$$\left|\frac{\partial^2 p}{\partial x^2}\right|' + \left|\frac{\partial^2 p}{\partial y^2}\right|' = 0 \tag{5-26}$$

Because this equation equals zero, it is similar to equation (5-18). The water under-pressures distribution in the sand package can now be determined using the storage equation and the boundary conditions. Because the calculation of the water under-pressures is dimensionless the next transformation has to be performed to determine the real water under-pressures. The real water under-pressures can be determined by integrating the derivative of the water under-pressures in the direction of a flow line, along a flow line, so:

$$P_{calc} = \int_{s'} \left|\frac{\partial p}{\partial s}\right|' \cdot ds' \tag{5-27}$$

This is illustrated in Figure 5-8. Using equation (5-30) this is written as:

$$\mathbf{P_{real}} = \int_{s} \left| \frac{\partial \mathbf{p}}{\partial \mathbf{s}} \right| \cdot \mathbf{ds} = \int_{s'} \frac{\rho_w \cdot \mathbf{g} \cdot \mathbf{v_c} \cdot \varepsilon \cdot \mathbf{h_i}}{\mathbf{k_{max}}} \cdot \left| \frac{\partial \mathbf{p}}{\partial \mathbf{s}} \right|' \cdot \mathbf{ds'} \tag{5-28}$$

$$\mathbf{s'} = \frac{\mathbf{s}}{\mathbf{h_i}}$$

This gives the next relation between the real emerging water under-pressures and the calculated water under-pressures:

$$\mathbf{P_{real}} = \frac{\rho_w \cdot \mathbf{g} \cdot \mathbf{v_c} \cdot \varepsilon \cdot \mathbf{h_i}}{\mathbf{k_{max}}} \cdot \mathbf{P_{calc}} \tag{5-29}$$

To be independent of the ratio between the initial permeability $\mathbf{k_i}$ and the maximum permeability $\mathbf{k_{max}}$, $\mathbf{k_{max}}$ has to be replaced with the weighted average permeability $\mathbf{k_m}$ before making the measured water under-pressures dimensionless.

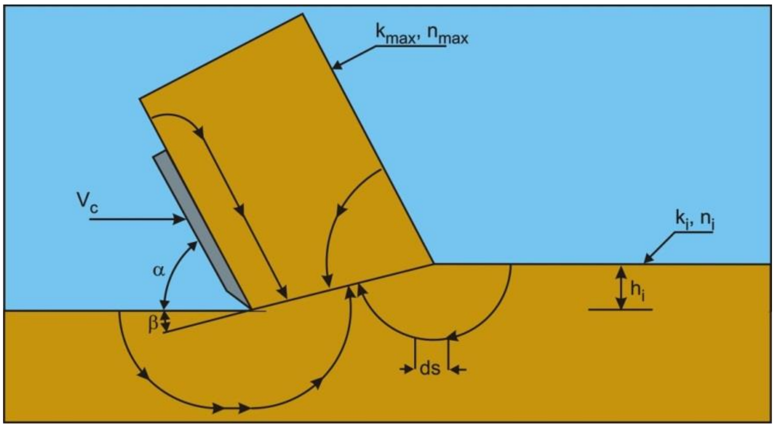

Figure 5-8: Flow of the pore water to the shear zone.

5.5. Numerical Water Pore Pressure Calculations

The water under-pressures in the sand package on and around the blade are numerically determined using the finite element method. The solution of such a calculation is however not only dependent on the physical model of the problem, but also on the next points:

1. The size of the area in which the calculation takes place.
2. The size and distribution of the elements
3. The boundary conditions

The choices for these three points have to be evaluated with the problem that has to be solved in mind. These calculations are about the values and distribution of the water under-pressures in the shear zone and on the blade. A variation of the values for point 1 and 2 may therefore not influence this part of the solution. This is achieved by on the one hand increasing the area in which the calculations take place in steps and on the other hand by decreasing the element size until the variation in the solution was less than 1%. The distribution of the elements is chosen such that a finer mesh is present around the blade tip, the shear zone and on the blade, also because of the blade tip problem. A number of boundary conditions follow from the physical model of the cutting process, these are:

1. The boundary condition in the shear zone. This is described by equation (5-23).
2. The boundary condition along the free sand surface. The hydrostatic pressure at which the process takes place, can be chosen, when neglecting the dimensions of the blade and the layer in relation to the hydrostatic pressure head. Because these calculations are meant to obtain the difference between the water under-pressures and the hydrostatic pressure it is valid to take a zero pressure as the boundary condition.

The boundary conditions, along the boundaries of the area where the calculation takes place that are located in the sand package are not determined by the physical process. For this boundary condition there is a choice between:

1. A hydrostatic pressure along the boundary.
2. A boundary as an impenetrable wall.
3. A combination of a known pressure and a known specific flow rate.

None of these choices complies with the real process. Water from outside the calculation area will flow through the boundary. This also implies, however, that the pressure along this boundary is not hydrostatic. If, however, the boundary is chosen with enough distance from the real cutting process the boundary condition may not have an influence on the solution. The impenetrable wall is chosen although this choice is arbitrary. Figure 5-7 gives an impression of the size of the area and the boundary conditions, while Figure 5-9 shows the element mesh. Figure 5-11 shows the two-dimensional distribution of the water under-pressures. A table with the dimensionless pore pressures can be found in Miedema (1987 September), Miedema & Yi (2001) and in 0 and Appendix Q:.

The following figures give an impression of how the FEM calculations are carried out:
Figure 5-9 and Figure 5-10: Show how the mesh has been varied in order to get a 1% accuracy.
Figure 5-11: Shows both the equipotential lines and the flow lines (stream function).
Figure 5-13 and Figure 5-14: Show the equi-potential lines both as lines and as a color plot. This shows clearly where the largest underpressures occur on the shear plane.

Figure 5-12 shows the pressure distribution on both the shear plane and the blade. From these pressure distributions the average dimensionless pressures $\mathbf{p_{1m}}$ and $\mathbf{p_{2m}}$ are determined.
Figure 5-15 and Figure 5-16: Show the steamlines both as lines and as a color plot. This shows the paths of the pore water flow.

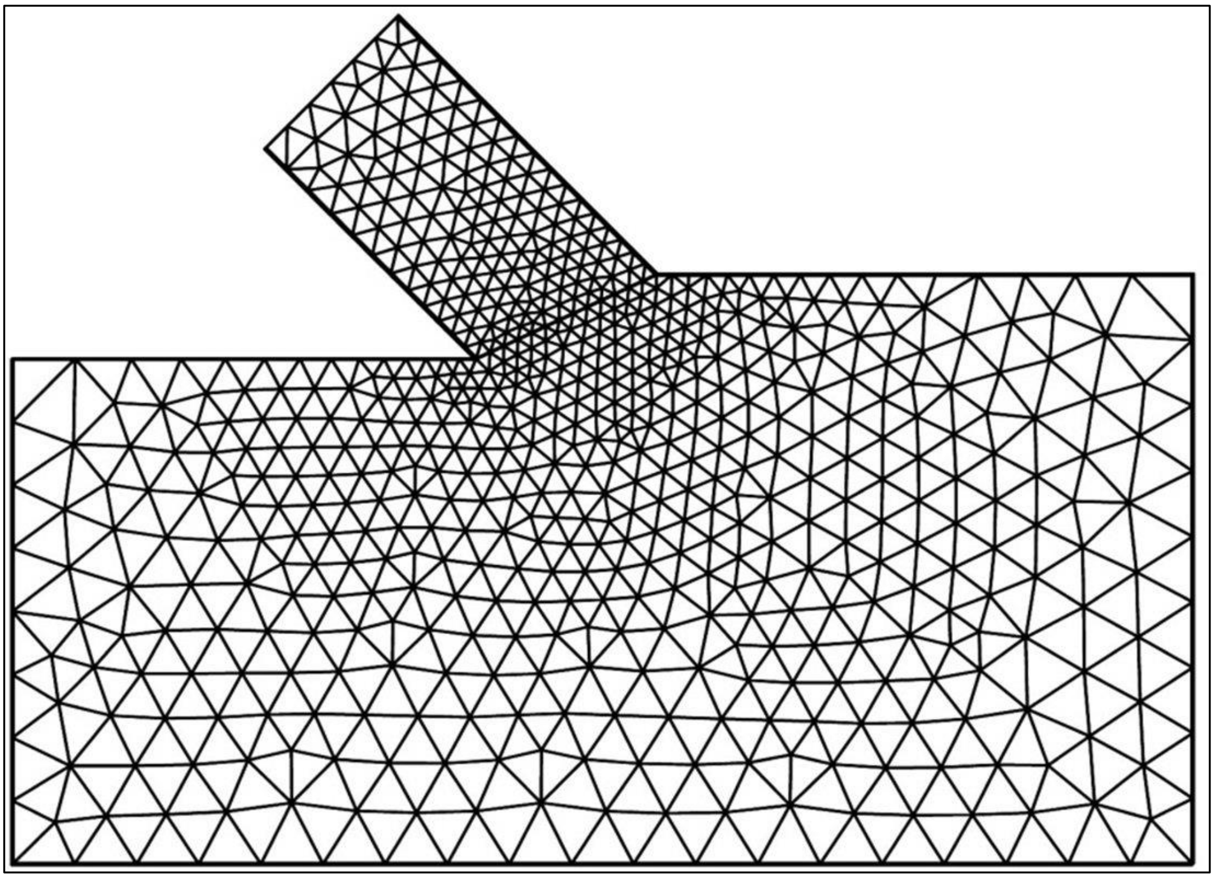

Figure 5-9: The coarse mesh as applied in the pore pressure calculations.

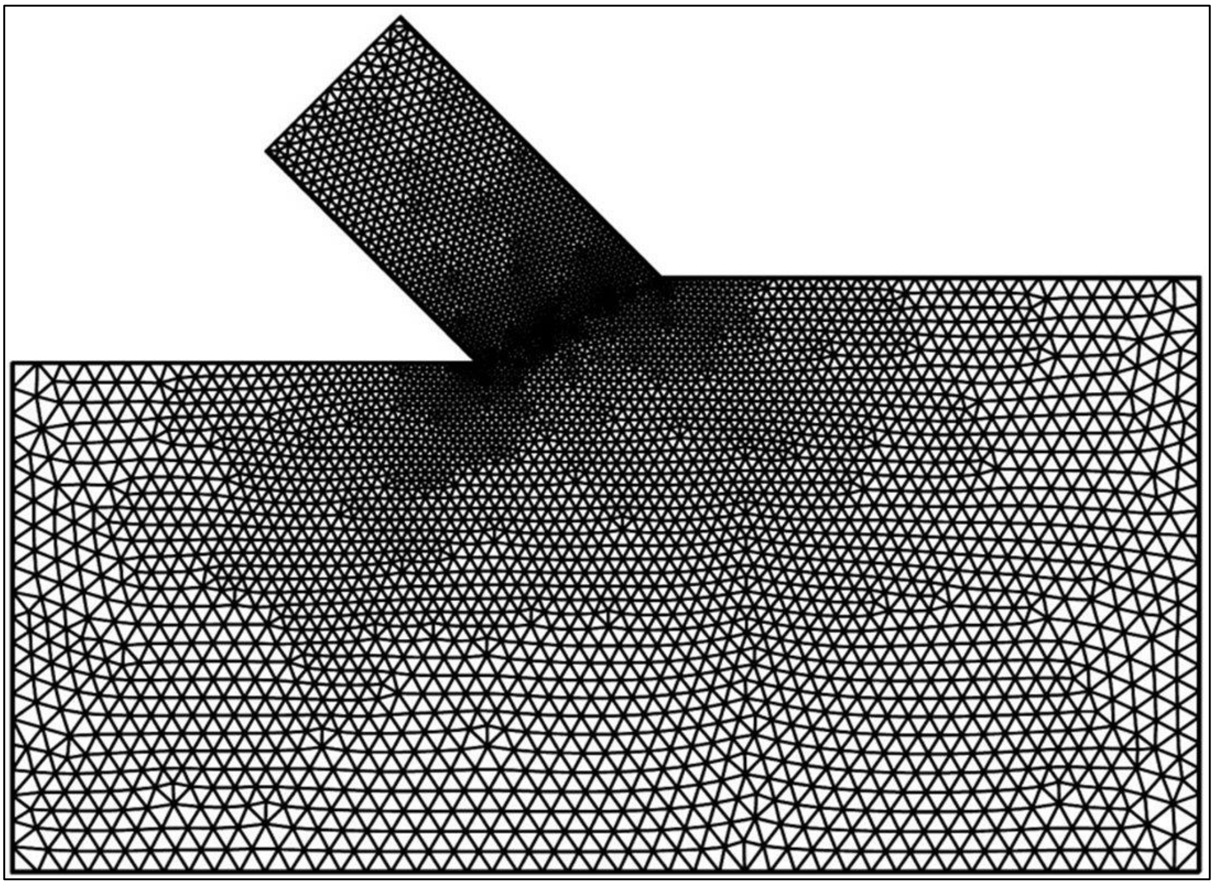

Figure 5-10: The fine mesh as applied in the pore pressure calculations.

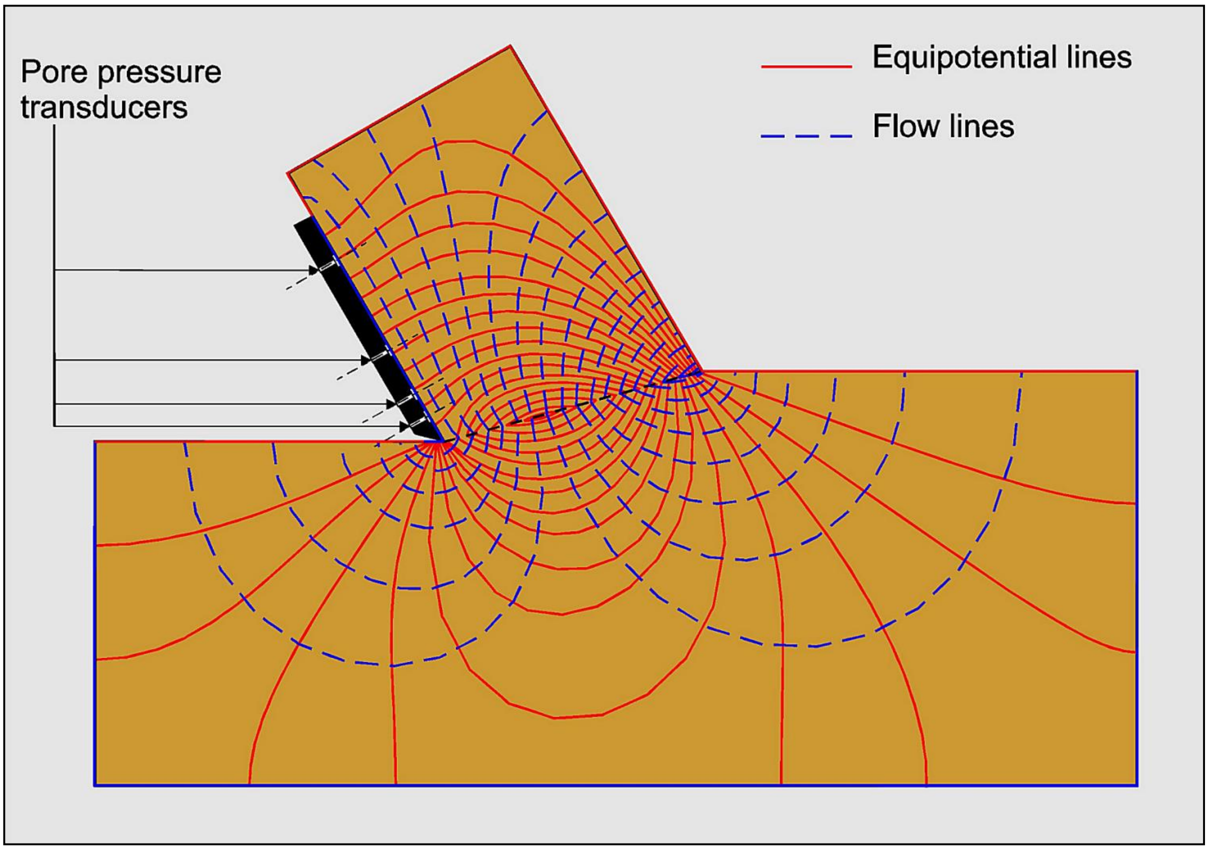

Figure 5-11: The water under-pressures distribution in the sand package around the blade.

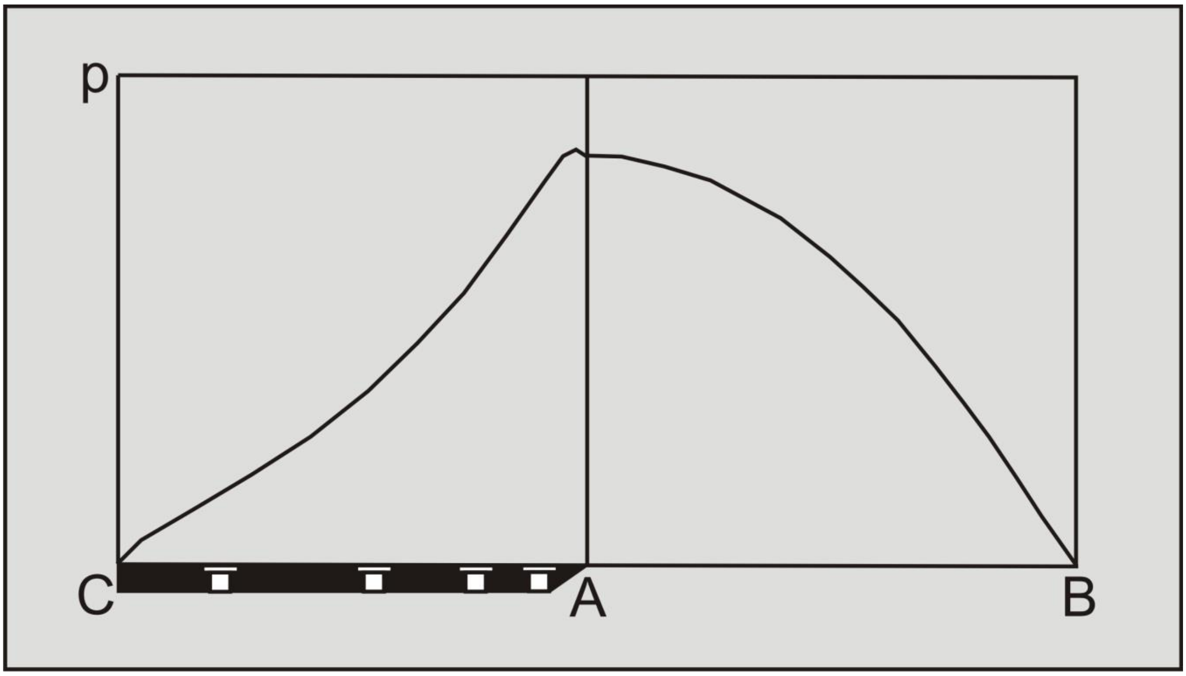

Figure 5-12: The pore pressure distribution on the blade A-C and in the shear zone A-B.

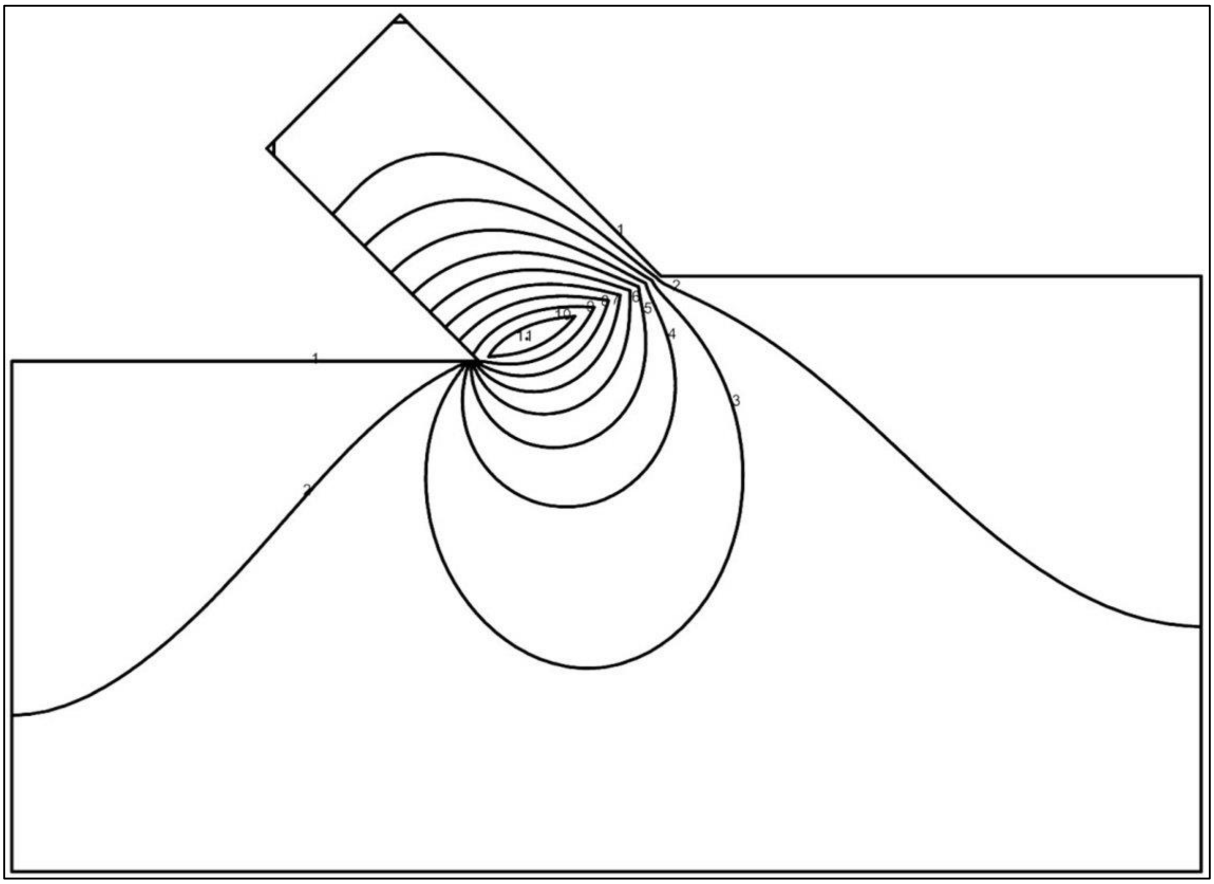

Figure 5-13: The equipotential lines.

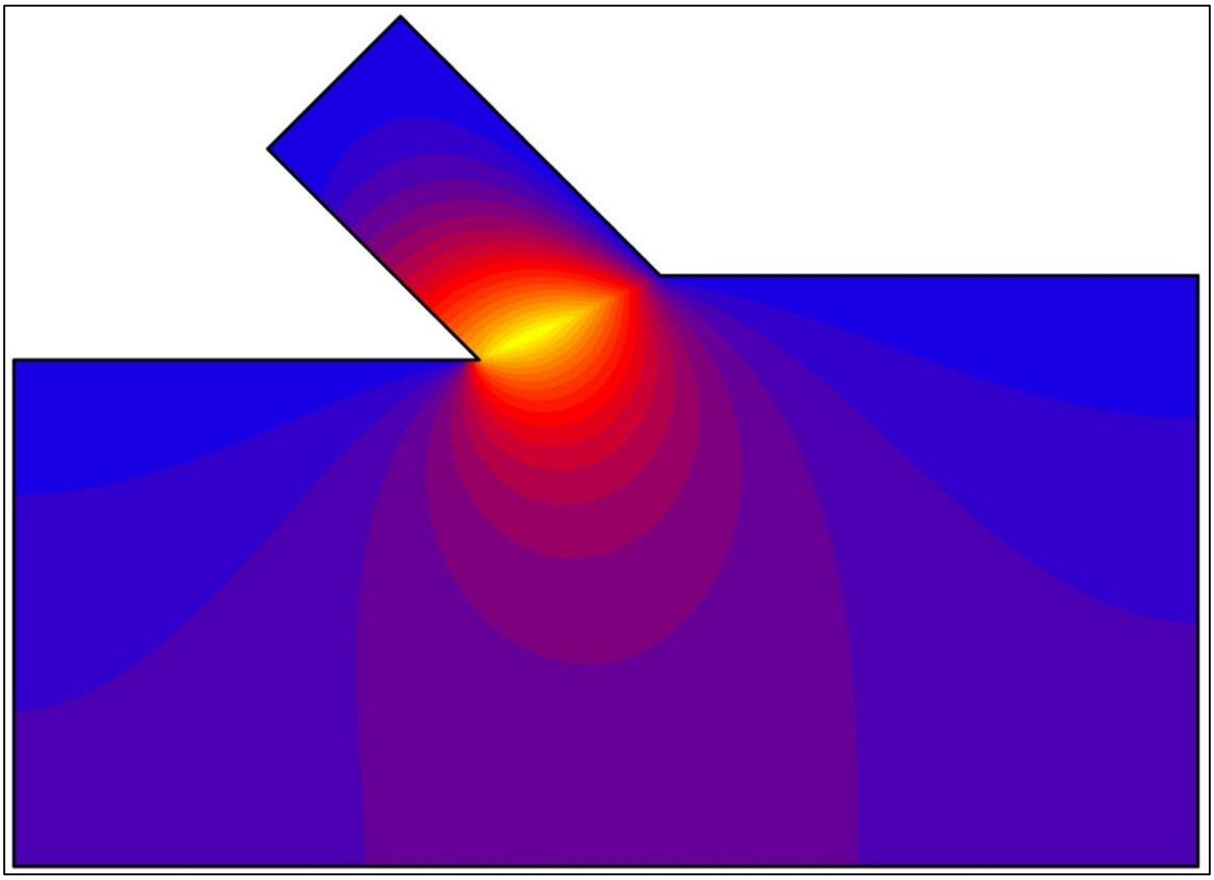

Figure 5-14: The equipotential lines in color.

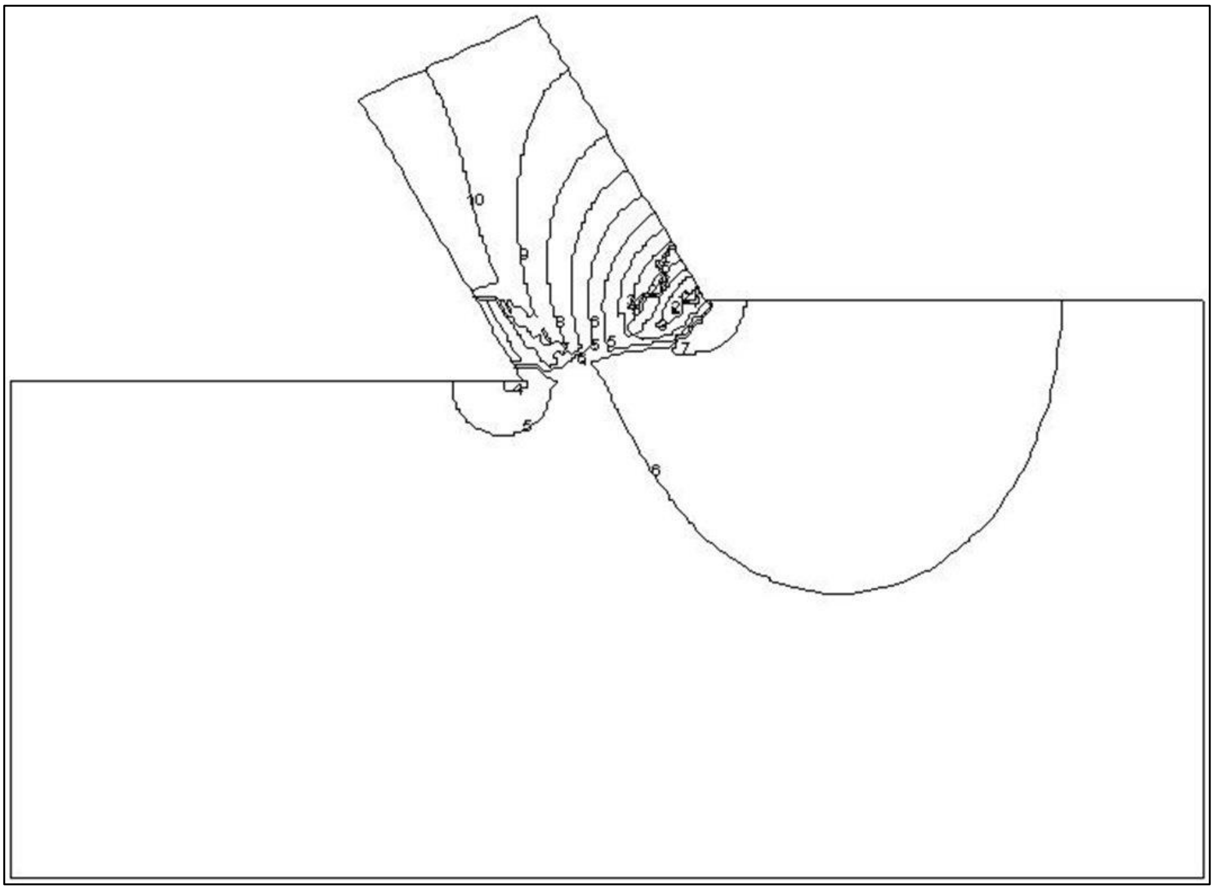

Figure 5-15: Flow lines or stream function.

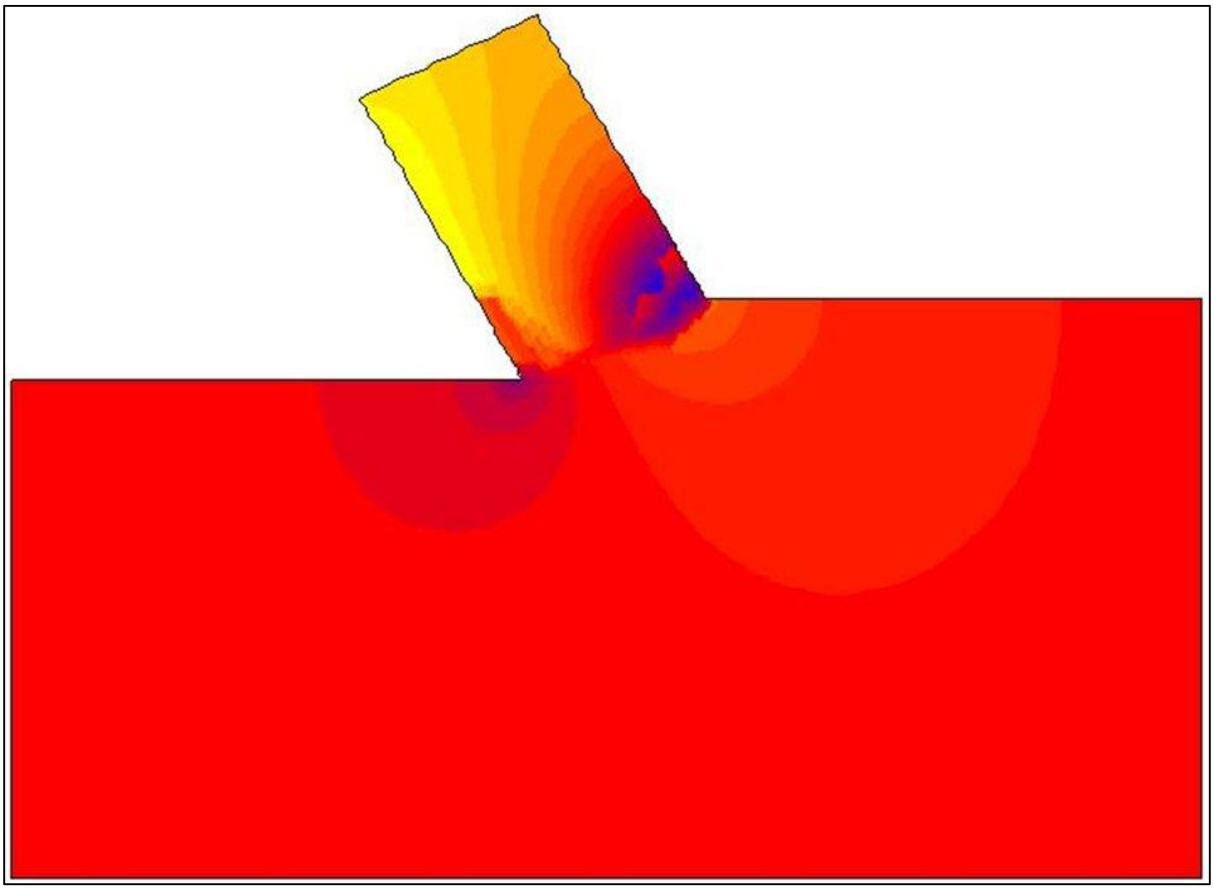

Figure 5-16: The stream function in colors.

5.6. The Blade Tip Problem

During the physical modeling of the cutting process it has always been assumed that the blade tip is sharp. In other words, that in the numerical calculation, from the blade tip, a hydrostatic pressure can be introduced as the boundary condition along the free sand surface behind the blade. In practice this is never valid, because of the following reasons:

1. The blade tip always has a certain rounding, so that the blade tip can never be considered really sharp.
2. Through wear of the blade a flat section develops behind the blade tip, which runs against the sand surface (clearance angle ≤ zero)
3. If there is also dilatancy in the sand underneath the blade tip it is possible that the sand runs against the flank after the blade has passed.
4. There will be a certain under-pressure behind the blade as a result of the blade speed and the cutting process.

A combination of these factors determines the distribution of the water under-pressures, especially around the blade tip. The first three factors can be accounted for in the numerical calculation as an extra boundary condition behind the blade tip. Along the free sand surface behind the blade tip an impenetrable line element is put in, in the calculation. The length of this line element is varied with $\mathbf{0.0 \cdot h_i}$, $\mathbf{0.1 \cdot h_i}$ and $\mathbf{0.2 \cdot h_i}$. It showed from these calculations that especially the water under-pressures on the blade are strongly determined by the choice of this boundary condition as indicated in Figure 5-17 and Figure 5-18.

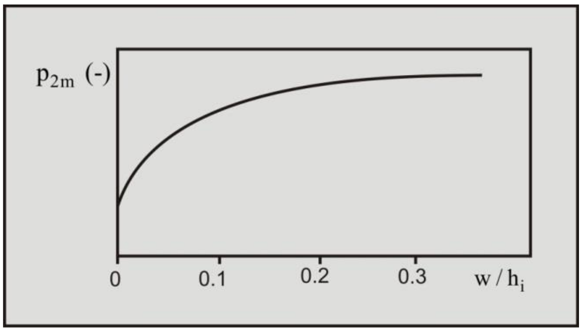

Figure 5-17: The water pore pressures on the blade as function of the length of the wear section w.

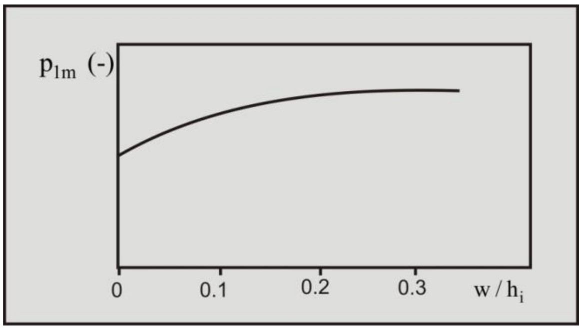

Figure 5-18: The water pore pressure in the shear zone as function of the length of the wear section w.

It is hard to estimate to what degree the influence of the under-pressure behind the blade on the water under-pressures around the blade tip can be taken into account with this extra boundary condition. Since there is no clear formulation for the under-pressure behind the blade available, it will be assumed that the extra boundary condition at the blade tip describes this influence.

If there is no cavitation the water pressures forces $\mathbf{W_1}$ and $\mathbf{W_2}$ can be written as:

$$\mathbf{W_1 = \frac{p_{1m} \cdot \rho_w \cdot g \cdot v_c \cdot \varepsilon \cdot h_i^2 \cdot w}{\left(a_1 \cdot k_i + a_2 \cdot k_{max}\right) \cdot \sin(\beta)}} \tag{5-30}$$

and

$$\mathbf{W_2 = \frac{p_{2m} \cdot \rho_w \cdot g \cdot v_c \cdot \varepsilon \cdot h_i \cdot h_b \cdot w}{\left(a_1 \cdot k_i + a_2 \cdot k_{max}\right) \cdot \sin(\alpha)}} \tag{5-31}$$

In case of cavitation $\mathbf{W_1}$ and $\mathbf{W_2}$ become:

$$\mathbf{W_1 = \frac{\rho_w \cdot g \cdot (z+10) \cdot h_i \cdot w}{\sin(\beta)}} \tag{5-32}$$

and

$$W_2 = \frac{\rho_w \cdot g \cdot (z+10) \cdot h_b \cdot w}{\sin(\alpha)} \tag{5-33}$$

5.7. Analytical Water Pore Pressure Calculations

As is shown in Figure 5-8, the water can flow from 4 directions to the shear zone where the dilatancy takes place. Two of those directions go through the sand which has not yet been deformed and thus have a permeability of $\mathbf{k_i}$, while the other two directions go through the deformed sand and thus have a permeability of $\mathbf{k_{max}}$. Figure 5-11 shows that the flow lines in 3 of the 4 directions have a more or less circular shape, while the flow lines coming from above the blade have the character of a straight line. If a point on the shear zone is considered, then the water will flow to that point along the 4 flow lines as mentioned above. Along each flow line, the water will encounter a certain resistance. One can reason that this resistance is proportional to the length of the flow line and reversibly proportional to the permeability of the sand, the flow line passes. Figure 5-19 shows a point on the shear zone and it shows the 4 flow lines. The length of the flow lines can be determined with the equations (5-34), (5-35), (5-36) and (5-37). The variable $\mathbf{L_{max}}$ in these equations is the length of the shear zone, which is equal to $\mathbf{h_i/\sin(\beta)}$, while the variable **L** starts at the free surface with a value zero and ends at the blade tip with a value $\mathbf{L_{max}}$.

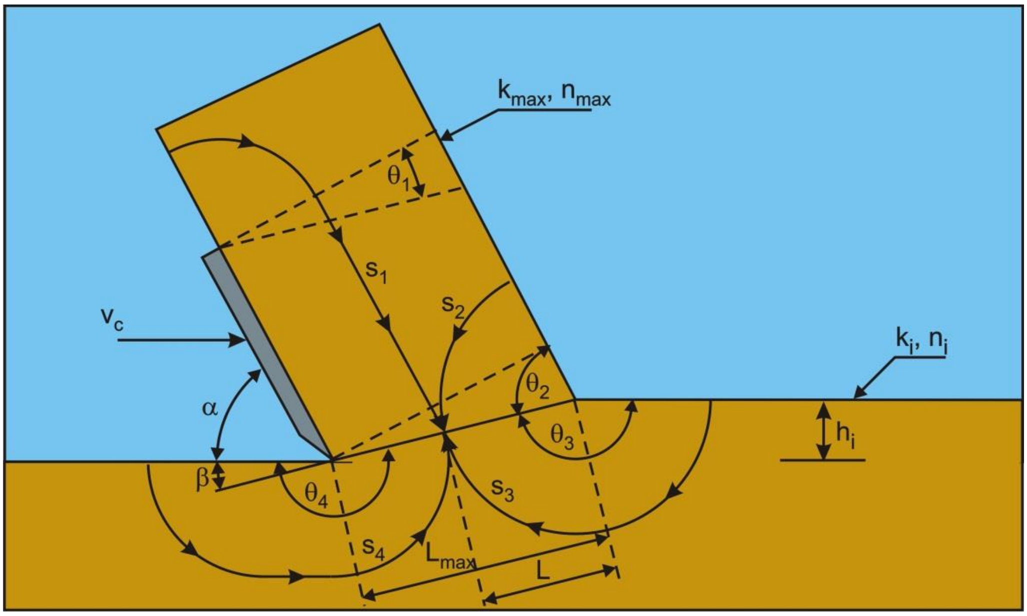

Figure 5-19: The flow lines used in the analytical method.

For the lengths of the 4 flow lines:

$$s_1 = \left(L_{max} - L\right) \cdot \left(\frac{\pi}{2} + \theta_1\right) + \frac{h_b}{\sin(\alpha)} \tag{5-34}$$

$$\text{With: } \theta_1 = \frac{\pi}{2} - (\alpha + \beta)$$

$$s_2 = L \cdot \theta_2 \tag{5-35}$$

$$\text{With: } \theta_2 = \alpha + \beta$$

$$s_3 = L \cdot \theta_3 \tag{5-36}$$

$$\text{With: } \theta_3 = \pi - \beta$$

$$s_4 = (L_{max} - L) \cdot \theta_4 + 0.2 \cdot h_i \cdot \pi$$

$$\text{With: } \theta_4 = \pi + \beta \tag{5-37}$$

The total resistance on the flow lines can be determined by dividing the length of a flow line by the permeability of the flow line. The equations (5-38), (5-39), (5-40) and (5-41) give the resistance of each flow line.

$$R_1 = \frac{s_1}{k_{max}} \tag{5-38}$$

$$R_2 = \frac{s_2}{k_{max}} \tag{5-39}$$

$$R_3 = \frac{s_3}{k_i} \tag{5-40}$$

$$R_4 = \frac{s_4}{k_i} \tag{5-41}$$

Since the 4 flow lines can be considered as 4 parallel resistors, the total resulting resistance can be determined according to the rule for parallel resistors. Equation (5-42) shows this rule.

$$\frac{1}{R_t} = \frac{1}{R_1} + \frac{1}{R_2} + \frac{1}{R_3} + \frac{1}{R_3} \tag{5-42}$$

The resistance $\mathbf{R_t}$ in fact replaces the $\mathbf{h_i/k_{max}}$ part of the equations (5-23), (5-24), (5-28) and (5-29), resulting in equation (5-43) for the determination of the pore vacuum pressure of the point on the shear zone.

$$\Delta p = \rho_w \cdot g \cdot v_c \cdot \varepsilon \cdot \sin(\beta) \cdot R_t \cdot \sin(\alpha)^{0.2} \tag{5-43}$$

The average pore vacuum pressure on the shear zone can be determined by summation or integration of the pore vacuum pressure of each point on the shear zone. Equation (5-44) gives the average pore vacuum pressure by summation.

$$p_{1m} = \frac{1}{n} \cdot \sum_{i=0}^{n} \Delta p_i \quad \text{with: } L_i = i \cdot \frac{L}{n} \tag{5-44}$$

The determination of the average pore vacuum pressure on the blade cannot be carried out by integration or summation, because the calculation only gives the pore vacuum pressure at the tip (edge) of the blade. It is known that the pore vacuum pressure at the top of the blade equals zero, because the sand at that point is in direct contact with the surrounding water. If the pore vacuum pressure distribution on the blade is considered linear, then the average pore vacuum pressure equals 50% of the pore vacuum pressure at the blade edge.

$$p_{2m} = \frac{\Delta p_n}{2} \cdot f \cdot \left(1 + \left(\frac{k_i}{k_{max}}\right) \cdot \sin(\alpha)\right) \tag{5-45}$$

However Figure 5-12 (left graph) shows that this distribution is not linear. Going from the tip (edge) of the blade to the top of the blade, first the pore vacuum pressure increases until it reaches a maximum and then it decreases (non-linear) until it reaches zero at the top of the blade. In this graph, the top of the blade is left and the tip of the blade is right. The graph on the right side of Figure 5-12 shows the pore vacuum pressure on the shear zone. In this graph, the tip of the blade is on the left side, while the right side is the point where the shear zone reaches the free water surface. Thus the pore vacuum pressure equals zero at the free water surface (most right point of the graph).

Because the distribution of the pore vacuum pressure is non-linear, a shape factor has to be used. From the FEM calculations of Miedema (1987 September) and Yi (2000) it is known, that the shape of the pore vacuum pressure distribution on the blade depends strongly on the ratio of the length of the shear zone and the length of the blade, and on the length of the flat wear zone (as shown in Figure 5-17 and Figure 5-18). A high ratio should result in a shape factor higher then 2, while a low ratio should result in a factor smaller then 0.5. Equation (5-46) gives the ratio in a modified form. The value of the power has been determined by trial and error.

$$\mathbf{f}=\left(\frac{\mathbf{h_i}}{\mathbf{h_b}}\right)^{\pi/2-1.35\cdot\alpha}\cdot\frac{\sin(\alpha+\beta)\cdot\sin(\alpha)^{0.5}}{2\cdot\sin(\beta)} \tag{5-46}$$

In the past decades many research has been carried out into the different cutting processes. The more fundamental the research, the less the theories can be applied in practice. The analytical method as described here, gives a method to use the basics of the sand cutting theory in a very practical and pragmatic way.
One has to consider that usually the accuracy of the output of a complex calculation is determined by the accuracy of the input of the calculation, in this case the soil mechanical parameters. Usually the accuracy of these parameters is not very accurate and in many cases not available at all. The accuracy of less then 10% of the analytical method described here is small with regard to the accuracy of the input. This does not mean however that the accuracy is not important, but this method can be applied for a quick first estimate.
By introducing some shape factors to the shape of the streamlines, the accuracy of the analytical model can be improved.

Table 5-1: A comparison between the numerical and analytical dimensionless pore vacuum pressures.

k_i/k_{max}=0.25	p_{1m}	p_{2m}	p_{1m} (analytical)	p_{2m} (analytical)
α=30°, β=30°, h_b/h_i=2	0.294	0.085	0.333	0.072
α=45°, β=25°, h_b/h_i=2	0.322	0.148	0.339	0.140
α=60°, β=20°, h_b/h_i=2	0.339	0.196	0.338	0.196

Table 5-1 was determined by Miedema & Yi (2001). Since then the algoritm has been improved slightly, resulting in the program listing of Figure 5-20.

```
Teta1 = Pi - Alpha - Beta
Teta2 = Alpha + Beta
Teta3 = Pi - Beta
Teta4 = Pi + Beta

L1 = Hi / Sin(Beta)
L2 = Hb / Sin(Alpha)
L3 = 0.2 * Hi / Sin(Alpha)

N = 100
Lmax =L1
StepL = Lmax / N
P = 0
DPMax = RhoW * G * (Z + 10)
Flag = False

For I = 0 To N
  L = I * StepL + 0.0000000001

  S1 = (Lmax - L) * Teta1 + L2
  S2 = L * Teta2
  S3 = L * Teta3
  S4 = (Lmax - L) * Teta4 + L3

  R1 = S1 / Kmax
  R2 = S2 / Kmax
  R3 = S3 / Ki
  R4 = S4 / Ki
  Rt = 1 / (1 / R1 + 1 / R2 + 1 / R3 + 1 / R4)

  DP = RhoW * G * Vc * E * Sin(Beta) * Rt
  DP = DP * Sin(Teta) ^ 0.2
  If I = N Then DP0 = DP
  If DP > PMax Then PMax = DP
  P0 = P0 + DP
  If DP > DPMax Then
    DP = DPMax
    Flag = True
  End If
  P = P + DP
Next I

P1m = (P - DP / 2) / N
P0 = (P0 - DP0 / 2) / N
Factor = (Hi / Hb) ^ (Pi / 2 - Teta * 1.35) * Sin(Teta + Beta) * Sin(Teta) ^ 0.5 / Sin(Beta) / 2
If Flag Then
  Argument = -2 * Factor * (P0 - P1m) / P1m
  Factor = Factor * Exp(Argument) + (1 - Exp(Argument))
End If
P2m = DP * Factor * (1 + (Ki / Kmax) ^ 2 * Sin(Teta))
If P2m > DPMax Then
  P2m = DPMax
End If
```

Figure 5-20: A small program to determine the pore pressures.

Figure 5-20 shows a program listing to determine the pore pressures with the analytical method. The program already takes into account that the pore pressures cannot exceed the water vapor pressure and corrects for that.

5.8. Determination of the Shear Angle β

The equations are derived with which the forces on a straight blade can be determined according the method of Coulomb (see Verruyt (1983)). Unknown in these equations is the shear angle **β**. In literature several methods are used to determine this shear angle.

The oldest is perhaps the method of Coulomb (see Verruyt (1983)). This method is widely used in sheet pile wall calculations. Since passive earth pressure is the cause for failure here, it is necessary to find the shear angle at which the total, on the earth, exerted force by the sheet pile wall is at a minimum.
When the water pressures are not taken into account, an analytical solution for this problem can be found.

Another failure criterion is used by Hettiaratchi and Reece (1966), (1967A), (1967B), (1974) and (1975). This principle is based upon the cutting of dry sand. The shear plane is not assumed to be straight as in the method of Coulomb, but the shear plane is composed of a logarithmic spiral from the blade tip that changes into a straight shear plane under an angle of **45º - φ/2** with the horizontal to the sand surface. The straight part of the shear plane is part of the so-called passive Rankine zone. The origin of the logarithmic spiral is chosen such that the total force on the blade is minimal.

There are perhaps other failure criterions for sheet pile wall calculations known in literature, but these mechanisms are only suited for a one-time failure of the earth. In the cutting of soil the process of building up stresses and next the collapse of the earth is a continuous process.

Another criterion for the collapse of earth is the determination of those failure conditions for which the total required strain energy is minimal. Rowe (1962) and Josselin de Jong (1976) use this principle for the determination of the angle under which local shear takes place. From this point of view it seems plausible to assume that those failure criterions for the cutting of sand have to be chosen, for which the cutting work is minimal. This implies that the shear angle **β** has to be chosen for which the cutting work and therefore the horizontal force, exerted by the blade on the soil, is minimal. Miedema (1985B) and (1986B) and Steeghs (1985A) and (1985B) have chosen this method.
Assuming that the water pressures are dominant in the cutting of packed water saturated sand, and thus neglecting adhesion, cohesion, gravity, inertia forces, flow resistance and under-pressure behind the blade, the force $\mathbf{F_h}$ (equation (5-14)) becomes for the non-cavitating situation:

$$\mathbf{F_h}=\left(\begin{array}{l}-\mathbf{p_{2m}}\cdot\mathbf{h_b}\cdot\dfrac{\sin(\alpha)}{\sin(\alpha)}+\mathbf{p_{2m}}\cdot\mathbf{h_b}\cdot\dfrac{\sin(\alpha+\beta+\varphi)\cdot\sin(\alpha+\delta)}{\sin(\alpha+\beta+\delta+\varphi)\cdot\sin(\alpha)}\\ \\ +\mathbf{p_{1m}}\cdot\mathbf{h_i}\cdot\dfrac{\sin(\varphi)\cdot\sin(\alpha+\delta)}{\sin(\alpha+\beta+\delta+\varphi)\cdot\sin(\beta)}\end{array}\right)\cdot\frac{\rho_w\cdot\mathbf{g}\cdot\mathbf{v_c}\cdot\varepsilon\cdot\mathbf{h_i}\cdot\mathbf{w}}{(\mathbf{a_1}\cdot\mathbf{k_i}+\mathbf{a_2}\cdot\mathbf{k_{max}})} \tag{5-47}$$

With the following simplification:

$$\mathbf{F_h'}=\frac{\mathbf{F_h}}{\dfrac{\rho_w\cdot\mathbf{g}\cdot\mathbf{v_c}\cdot\varepsilon\cdot\mathbf{h_i}\cdot\mathbf{w}}{(\mathbf{a_1}\cdot\mathbf{k_i}+\mathbf{a_2}\cdot\mathbf{k_{max}})}} \tag{5-48}$$

Since the value of the shear angle **β**, for which the horizontal force is minimal, has to be found, equations (5-49) and (5-52) are set equal to zero. It is clear that this problem has to be solved iterative, because an analytical solution is impossible.
The Newton-Rhapson method works very well for this problem. In Miedema (1987 September) and Appendix C: and Appendix G: the resulting shear angles **β**, calculated with this method, can be found for several values of **δ**, **φ**, **α**, several ratios of $\mathbf{h_b/h_i}$ and for the non-cavitating and cavitating cutting process.

Interesting are now the results if another method is used. To check this, the shear angles have also been determined according Coulomb's criterion: there is failure at the shear angle for which the total force, exerted by the blade on the soil, is minimal. The maximum deviation of these shear angles with the shear angles according Miedema (1987

September) has a value of only 3° at a blade angle of 15°. The average deviation is approximately 1.5° for blade angles up to 60°.

The forces have a maximum deviation of less than 1%. It can therefore be concluded that it does not matter if the total force, exerted by the soil on the blade, is minimized, or the horizontal force. Next these calculations showed that the cutting forces, as a function of the shear angle, vary only slightly with the shear angles, found using the above equation. This sensitivity increases with an increasing blade angle. Figure 5-21 shows this for the following conditions:
The forces are determined by minimizing the specific cutting energy and minimizing the total cutting force $\mathbf{F_t}$. **(**$\boldsymbol{\alpha}$ **= 15°**, **30°**, **45°** and **60°**, $\boldsymbol{\delta}$ **= 24°**, $\boldsymbol{\varphi}$ **= 42°**, $\mathbf{h_b/h_i = 1}$ and a non-cavitating cutting process).
The derivative of the force $\mathbf{F'_h}$ to the shear angle $\boldsymbol{\beta}$ becomes:

$$\begin{aligned}\frac{\partial F_h^{'}}{\partial \beta} &= -p_{1m} \cdot h_i \cdot \frac{\sin(\varphi)\cdot\sin(\alpha+2\cdot\beta+\delta+\varphi)\cdot\sin(\alpha+\delta)}{\sin^2(\beta)\cdot\sin(\alpha+\beta+\delta+\varphi)^2} \\ &+ p_{2m}\cdot h_b \cdot \frac{\sin(\delta)\cdot\sin(\alpha+\delta)}{\sin(\alpha)\cdot\sin(\alpha+\beta+\delta+\varphi)^2} \\ &+ \frac{\partial p_{1m}}{\partial \beta}\cdot h_i \cdot \frac{\sin(\varphi)\cdot\sin(\alpha+\delta)}{\sin(\beta)\cdot\sin(\alpha+\beta+\delta+\varphi)} \\ &+ \frac{\partial p_{2m}}{\partial \beta}\cdot h_b \cdot \left\{\frac{\sin(\alpha+\beta+\varphi)\cdot\sin(\alpha+\delta)}{\sin(\alpha)\cdot\sin(\alpha+\beta+\delta+\varphi)} - 1\right\} = 0\end{aligned} \tag{5-49}$$

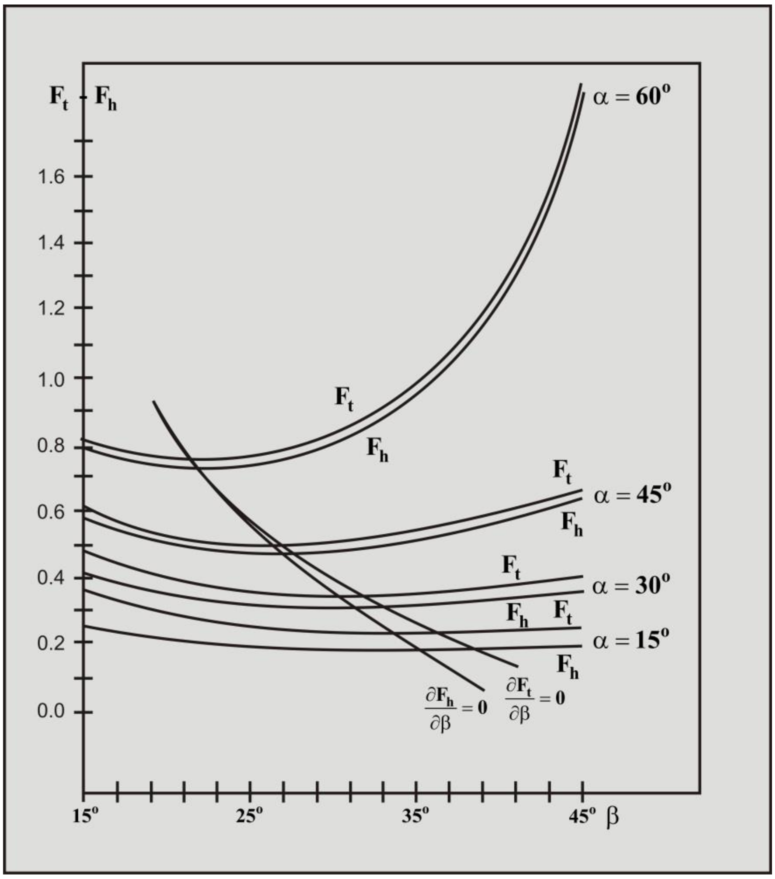

Figure 5-21: The forces $\mathbf{F_h}$ and $\mathbf{F_t}$ as function of the shear angle $\boldsymbol{\beta}$ and the blade angle $\boldsymbol{\alpha}$.

For the cavitating situation this gives for the force $\mathbf{F_h}$:

$$F_h = \left(\begin{array}{l} -h_b \cdot \dfrac{\sin(\alpha)}{\sin(\alpha)} + h_b \cdot \dfrac{\sin(\alpha+\beta+\varphi)\cdot\sin(\alpha+\delta)}{\sin(\alpha+\beta+\delta+\varphi)\cdot\sin(\alpha)} \\ \\ +h_i \cdot \dfrac{\sin(\varphi)\cdot\sin(\alpha+\delta)}{\sin(\alpha+\beta+\delta+\varphi)\cdot\sin(\beta)} \end{array} \right) \cdot \rho_w \cdot g \cdot (z+10) \cdot w \tag{5-50}$$

With the following simplification:

$$F_h^{'} = \frac{F_h}{\rho_w \cdot g \cdot (z+10) \cdot w} \tag{5-51}$$

The derivative of the force **F'ₕ** to the shear angle **β** becomes:

$$\frac{\partial F_h^{'}}{\partial \beta} = -h_i \cdot \frac{\sin(\varphi)\cdot\sin(\alpha+2\cdot\beta+\delta+\varphi)\cdot\sin(\alpha+\delta)}{\sin^2(\beta)\cdot\sin(\alpha+\beta+\delta+\varphi)^2} + h_b \cdot \frac{\sin(\delta)\cdot\sin(\alpha+\delta)}{\sin(\alpha)\cdot\sin(\alpha+\beta+\delta+\varphi)^2} = 0 \tag{5-52}$$

For the cavitating cutting process equation (5-52) can be simplified to:

$$h_b \cdot \sin(\delta)\cdot\sin^2(\beta) = h_i \cdot \sin(\alpha)\cdot\sin(\phi)\cdot\sin(\alpha+2\cdot\beta+\delta+\varphi) \tag{5-53}$$

The iterative results can be approximated by:

$$\beta = 61.29^{\circ} + 0.345 \cdot \frac{h_b}{h_i} - 0.3068\cdot\alpha - 0.4736\cdot\delta - 0.248\cdot\varphi \tag{5-54}$$

5.9. The Coefficients a_1 and a_2

In the derivation of the calculation of the water under-pressures around the blade for the non-cavitating cutting process, resulting in equations (5-30) and (5-31), it already showed that the water under-pressures are determined by the permeability of the undisturbed sand $\mathbf{k_i}$ and the permeability of the disturbed sand $\mathbf{k_{max}}$. Equation (5-25) shows this dependence. The water under-pressures are determined for several ratios of the initial permeability of the undisturbed sand to the maximum permeability of the disturbed sand:

$\mathbf{k_i/k_{max} = 1}$

$\mathbf{k_i/k_{max} = 0.5}$

$\mathbf{k_i/k_{max} = 0.25}$

The average water under-pressures $\mathbf{p_{1m}}$ en $\mathbf{p_{2m}}$ can be put against the ratio $\mathbf{k_i/k_{max}}$, for a certain shear angle **β**. A hyperbolic relation emerges between the average water under-pressures and the ratio of the permeability's. If the reciprocal values of the average water under-pressures are put against the ratio of the permeability's a linear relation emerges.

The derivatives of $\mathbf{p_{1m}}$ and $\mathbf{p_{2m}}$ to the ratio $\mathbf{k_i/k_{max}}$ are, however, not equal to each other. This implies that a relation for the forces as a function of the ratio of permeability's cannot be directly derived from the found average water under-pressures.

This is in contrast with the method used by Van Leussen and Van Os (1987 December). They assume that the average pore pressure on the blade has the same dependability on the ratio of permeability's as the average pore pressure in the shear zone. No mathematical background is given for this assumption.

For the several ratios of the permeability's it is possible with the shear angles determined, to determine the dimensionless forces $\mathbf{F_h}$ and $\mathbf{F_v}$. If these dimensionless forces are put against the ratio of the permeability's, also a hyperbolic relation is found (Miedema (1987 September)), shown in Figure 5-22 and Figure 5-23.

A linear relation can therefore also be found if the reciprocal values of the dimensionless forces are taken. This relation can be represented by:

$$\frac{1}{F_h}=a+b\cdot\frac{k_i}{k_{max}} \tag{5-55}$$

With the next transformations an equation can be derived for a weighted average permeability $\mathbf{k_m}$:

$$a_1=\frac{b}{a+b} \quad \& \quad a_2=\frac{a}{a+b} \tag{5-56}$$

So:

$$k_m=a_1\cdot k_i+a_2\cdot k_{max} \quad \text{with: } a_1+a_2=1 \tag{5-57}$$

Since the sum of the coefficients $\mathbf{a_1}$ en $\mathbf{a_2}$ is equal to 1 only coefficient $\mathbf{a_1}$ is given in Miedema (1987) and Appendix F:. It also has to be remarked that this coefficient is determined on the basis of the linear relation of $\mathbf{F_h}$ (dimensionless $\mathbf{c_1}$), because the horizontal force gives more or less the same relation as the vertical force, but has besides a much higher value. Only for the 60° blade, where the vertical force is very small and can change direction, differences occur between the linear relations of the horizontal and the vertical force as function of the ratio of the permeability's.
The influence of the undisturbed soil increases when the blade-height/layer-thickness ratio increases. This can be explained by the fact that the water that flows to the shear zone over the blade has to cover a larger distance with an increasing blade height and therefore has to overcome a higher resistance. Relatively more water will have to flow through the undisturbed sand to the shear zone with an increasing blade height.

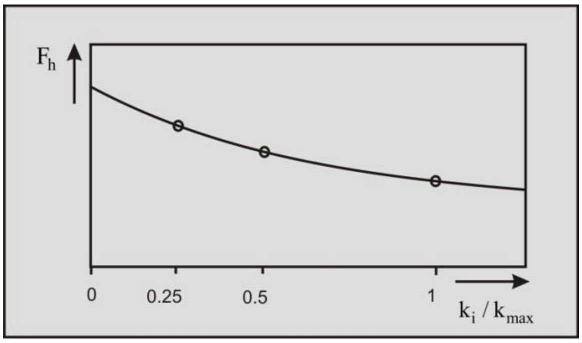

Figure 5-22: The force F_h as function of the ratio between k_i and k_{max}.

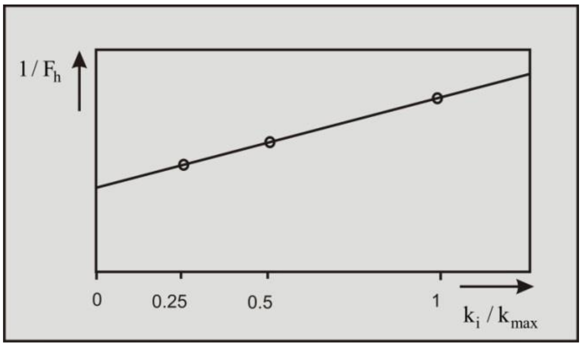

Figure 5-23: The reciprocal of the force F_h as function of the ratio between k_i and k_{max}.

5.10. Determination of the Coefficients c_1, c_2, d_1 and d_2.

If only the influence of the water under-pressures on the forces that occur with the cutting of saturated packed sand under water is taken in to account, equations (5-14) and (5-15) can be applied. It will be assumed that the non-cavitating process switches to the cavitating process for that cutting velocity $\mathbf{v_c}$, for which the force in the direction of the cutting velocity $\mathbf{F_h}$ is equal for both processes. In reality, however, there is a transition region between both processes, where locally cavitation starts in the shear zone. Although this transition region starts at about 65% of the cutting velocity at which, theoretically, full cavitation takes place, it shows from the results of the cutting tests that for the determination of the cutting forces the existence of a transition region can be neglected. In the simplified equations the coefficients $\mathbf{c_1}$ en $\mathbf{d_1}$ represent the dimensionless horizontal force (or the force in the direction of the cutting velocity) in the non-cavitating and the cavitating cutting process. The coefficients $\mathbf{c_2}$ and $\mathbf{d_2}$ represent the dimensionless vertical force or the force perpendicular to the direction of the cutting velocity in the non-cavitating and the cavitating cutting process. For the non-cavitating cutting process:

$$\mathbf{F_{ci}} = \frac{\mathbf{c_i \cdot \rho_w \cdot g \cdot v_c \cdot h_i^2 \cdot \varepsilon \cdot w}}{\mathbf{k_m}} \tag{5-58}$$

In which:

$$\mathbf{c_1} = \frac{\left(\mathbf{p_{1m}} \cdot \frac{\sin(\phi)}{\sin(\beta)} + \mathbf{p_{2m}} \cdot \frac{\mathbf{h_b}}{\mathbf{h_i}} \cdot \frac{\sin(\alpha+\beta+\phi)}{\sin(\alpha)}\right) \cdot \sin(\alpha+\delta)}{\sin(\alpha+\beta+\delta+\phi)} - \mathbf{p_{2m}} \cdot \frac{\mathbf{h_b}}{\mathbf{h_i}} \cdot \frac{\sin(\alpha)}{\sin(\alpha)} \tag{5-59}$$

And:

$$\mathbf{c_2} = \frac{\left(\mathbf{p_{1m}} \cdot \frac{\sin(\phi)}{\sin(\beta)} + \mathbf{p_{2m}} \cdot \frac{\mathbf{h_b}}{\mathbf{h_i}} \cdot \frac{\sin(\alpha+\beta+\phi)}{\sin(\alpha)}\right) \cdot \cos(\alpha+\delta)}{\sin(\alpha+\beta+\delta+\phi)} - \mathbf{p_{2m}} \cdot \frac{\mathbf{h_b}}{\mathbf{h_i}} \cdot \frac{\cos(\alpha)}{\sin(\alpha)} \tag{5-60}$$

And for the cavitating cutting process:

$$\mathbf{F_{ci}} = \mathbf{d_i \cdot \rho_w \cdot g \cdot (z+10) \cdot h_i \cdot w} \tag{5-61}$$

In which:

$$\mathbf{d_1} = \frac{\left(\frac{\sin(\phi)}{\sin(\beta)} + \frac{\mathbf{h_b}}{\mathbf{h_i}} \cdot \frac{\sin(\alpha+\beta+\phi)}{\sin(\alpha}\right) \cdot \sin(\alpha+\delta)}{\sin(\alpha+\beta+\delta+\phi)} - \frac{\mathbf{h_b}}{\mathbf{h_i}} \cdot \frac{\sin(\alpha)}{\sin(\alpha)} \tag{5-62}$$

And:

$$\mathbf{d_2} = \frac{\left(\frac{\sin(\phi)}{\sin(\beta)} + \frac{\mathbf{h_b}}{\mathbf{h_i}} \cdot \frac{\sin(\alpha+\beta+\phi)}{\sin(\alpha)}\right) \cdot \cos(\alpha+\delta)}{\sin(\alpha+\beta+\delta+\phi)} - \frac{\mathbf{h_b}}{\mathbf{h_i}} \cdot \frac{\cos(\alpha)}{\sin(\alpha)} \tag{5-63}$$

The values of the 4 coefficients are determined by minimizing the cutting work that is at that shear angle $\boldsymbol{\beta}$ where the derivative of the horizontal force to the shear angle is zero. The coefficients $\mathbf{c_1}$, $\mathbf{c_2}$, $\mathbf{d_1}$ en $\mathbf{d_2}$ are given in Miedema (1987 September) and in Appendix D: and Appendix E: for the non-cavitating cutting process and Appendix H: and Appendix I: for the cavitating cutting process as functions of $\boldsymbol{\alpha}$, $\boldsymbol{\delta}$, $\boldsymbol{\varphi}$ and the ratio $\mathbf{h_b/h_i}$.

5.11. Specific Cutting Energy

In the dredging industry, the specific cutting energy is described as:

The amount of energy, that has to be added to a volume unit of soil (e.g. sand) to excavate the soil.

The dimension of the specific cutting energy is: kN/m² or kPa for sand and clay, while for rock often MN/m^2 or MPa is used.

Adhesion, cohesion, gravity and the inertia forces will be neglected in the determination of the specific cutting energy. For the case as described above, cutting with a straight blade with the direction of the cutting velocity perpendicular to the blade (edge of the blade) and the specific cutting energy can be written:

$$\mathbf{E_{sp} = \frac{F_h \cdot v_c}{h_i \cdot w \cdot v_c} = \frac{F_h}{h_i \cdot w}} \quad \textbf{(5-64)}$$

The method, with which the shear angle β is determined, is therefore equivalent with minimizing the specific cutting energy, for certain blade geometry and certain soil mechanical parameters. For the specific energy, for the non-cavitating cutting process, it can now be derived from equations (5-58) and (5-64), that:

$$\mathbf{E_{gc} = c_1 \cdot \rho_w \cdot g \cdot v_c \cdot h_i \cdot \frac{\varepsilon}{k_m}} \quad \textbf{(5-65)}$$

For the specific energy, for the fully cavitating cutting process, can be written from equations (5-61) and (5-64):

$$\mathbf{E_{ca} = d_1 \cdot \rho_w \cdot g \cdot (z + 10)} \quad \textbf{(5-66)}$$

From these equations can be derived that the specific cutting energy, for the non-cavitating cutting process is proportional to the cutting velocity, the layer-thickness and the volume strain and inversely proportional to the permeability. For the fully cavitating process the specific cutting energy is only dependent on the water depth.

Therefore it can be posed, that the specific cutting energy, for the fully cavitating cutting process is an upper limit, provided that the inertia forces, etc., can be neglected. At very high cutting velocities, however, the specific cutting energy, also for the cavitating process will increase as a result of the inertia forces and the water resistance.

5.11.1. Specific Energy and Production in Sand

As discussed previously, the cutting process in sand can be distinguished in a non-cavitating and a cavitating process, in which the cavitating process can be considered to be an upper limit to the cutting forces. Assuming that during an SPT test in water-saturated sand, the cavitating process will occur, because of the shock wise behavior during the SPT test, the SPT test will give information about the cavitating cutting process. Whether, in practice, the cavitating cutting process will occur, depends on the soil mechanical parameters, the geometry of the cutting process and the operational parameters. The cavitating process gives an upper limit to the forces, power and thus the specific energy and a lower limit to the production and will therefore be used as a starting point for the calculations. For the specific energy of the cavitating cutting process, the following equation can be derived according to Miedema (1987 September):

$$\mathbf{E_{sp} = \rho_w \cdot g \cdot (z + 10) \cdot d_1} \quad \textbf{(5-67)}$$

The production, for an available power $\mathbf{P_a}$, can be determined by:

$$\mathbf{Q = \frac{P_a}{E_{sp}} = \frac{P_a}{\rho_w \cdot g \cdot (z + 10) \cdot d_1}} \quad \textbf{(5-68)}$$

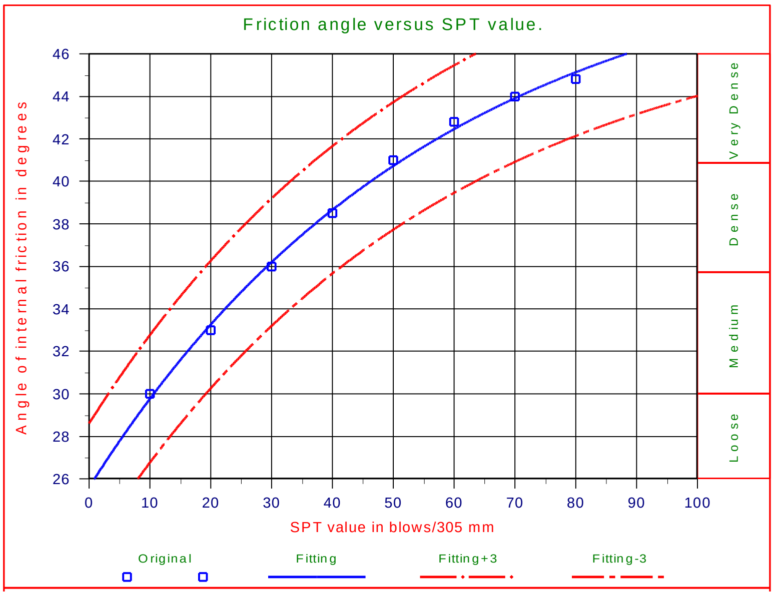

Figure 5-24: Friction angle versus SPT value (Lambe & Whitman (1979), page 148) and Miedema (1995)).

The coefficient $\mathbf{d_1}$ is the only unknown in the above equation. A relation between $\mathbf{d_1}$ and the SPT value of the sand and between the SPT value and the water depth has to be found. The dependence of $\mathbf{d_1}$ on the parameters $\boldsymbol{\alpha}$, $\mathbf{h_i}$ en $\mathbf{h_b}$ can be estimated accurately. For normal sands there will be a relation between the angle of internal friction and the soil interface friction. Assume blade angles of 30, 45 and 60 degrees, a ratio of 3 for $\mathbf{h_b / h_i}$ and a soil/interface friction angle of 2/3 times the internal friction angle. For the coefficient $\mathbf{d_1}$ the following equations are found by regression:

$$\mathbf{d_1 = -0.185 + 0.666 \cdot e^{0.0444 \cdot \varphi}} \quad (\alpha = 30 \text{ degrees}) \tag{5-69}$$

$$\mathbf{d_1 = +0.304 + 0.333 \cdot e^{0.0597 \cdot \varphi}} \quad (\alpha = 45 \text{ degrees}) \tag{5-70}$$

$$\mathbf{d_1 = +0.894 + 0.154 \cdot e^{0.0818 \cdot \varphi}} \quad (\alpha = 60 \text{ degrees}) \tag{5-71}$$

With: $\boldsymbol{\varphi}$ = the angle of internal friction in degrees.

Lambe & Whitman (1979), page 78) and Miedema (1995) give the relation between the SPT value, the relative density and the hydrostatic pressure in two graphs, see Figure 5-25. With some curve-fitting these graphs can be summarized with the following equation:

$$\mathbf{SPT = \left(1.82 + 0.221 \cdot (z + 10)\right) \cdot 10^{-4} \cdot RD^{2.52}} \tag{5-72}$$

Lambe & Whitman (1979), page 148) and Miedema (1995) give the relation between the SPT value and the angle of internal friction, also in a graph, see Figure 5-24. This graph is valid up to 12 m in dry soil. With respect to the internal friction, the relation given in the graph has an accuracy of 3 degrees. A load of 12 m dry soil with a density of 1.67 ton/m^3 equals a hydrostatic pressure of 20 m.w.c. An absolute hydrostatic pressure of 20 m.w.c. equals 10 m of water depth if cavitation is considered. Measured SPT values at any depth will have to be reduced to the value that would occur at 10 m water depth. This can be accomplished with the following equation (see Figure 5-26):

$$\mathbf{SPT_{10} = \frac{1}{(0.646 + 0.0354 \cdot z)} \cdot SPT_z} \tag{5-73}$$

With the aim of curve-fitting, the relation between the SPT value reduced to 10 m water depth and the angle of internal friction can be summarized to:

$$\varphi = 54.5 - 25.9 \cdot e^{-0.01753 \cdot SPT_{10}} \text{ (+ 3 degrees value)} \tag{5-74}$$

For water depths of 0, 5, 10, 15, 20, 25 and 30 m and an available power of 100 kW the production is shown graphically for SPT values in the range of 0 to 100 SPT. Figure 5-27 shows the specific energy and Figure 5-28 the production for a 45 degree blade angle.

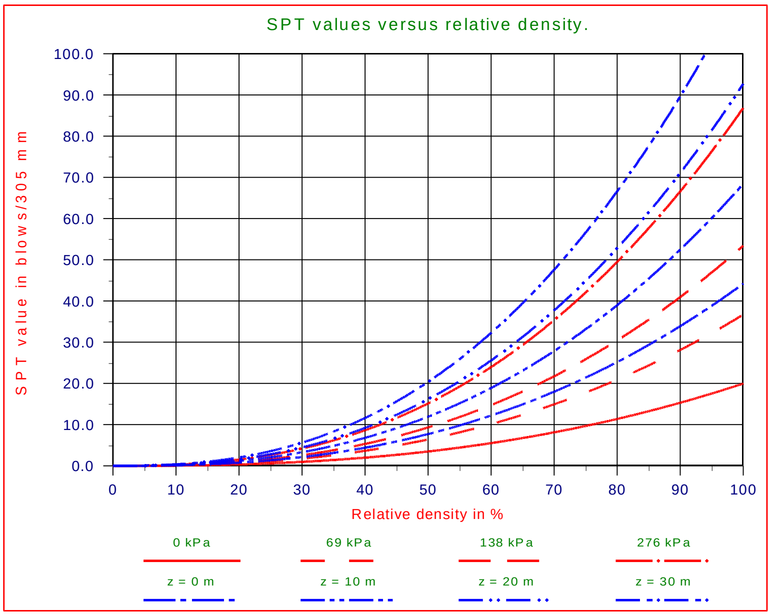

Figure 5-25: SPT values versus relative density (Lambe & Whitman (1979), page 78) and Miedema (1995)).

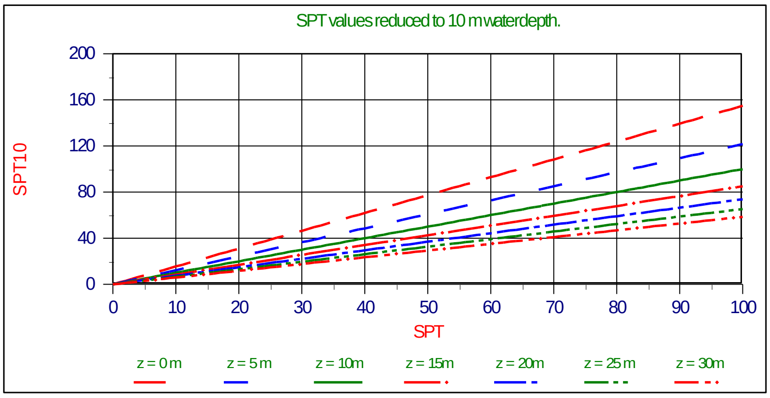

Figure 5-26: SPT values reduced to 10m water depth.

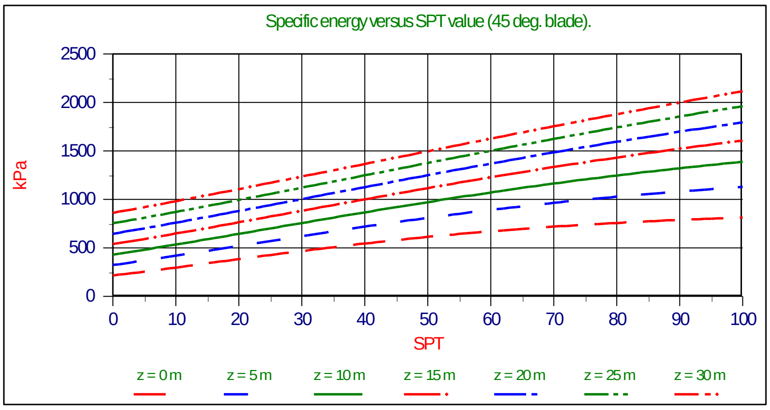

Figure 5-27: Specific energy versus SPT value (45 deg. blade).

5.11.2. The Transition Cavitating/Non-Cavitating

Although the SPT value only applies to the cavitating cutting process, it is necessary to have a good understanding of the transition between the non-cavitating and the cavitating cutting process. Based on the theory in Miedema (1987 September), an equation has been derived for this transition. If this equation is valid, the cavitating cutting process will occur.

$$\frac{\mathbf{d_1 \cdot (z+10) \cdot k_m}}{\mathbf{c_1 \cdot v_c \cdot h_i \cdot \varepsilon}} < 1 \qquad \textbf{(5-75)}$$

The ratio $\mathbf{d_1/c_1}$ appears to have an almost constant value for a given blade angle, independent of the soil mechanical properties. For a blade angle of 30 degrees this ratio equals 11.9. For a blade angle of 45 degrees this ratio equals 7.72 and for a blade angle of 60 degrees this ratio equals 6.14. The ratio $\mathbf{\varepsilon/k_m}$ has a value in the range of 1000 to 10000 for medium to hard packed sands. At a given layer thickness and water depth, the transition cutting velocity can be determined using the above equation. At a given cutting velocity and water depth, the transition layer thickness can be determined.

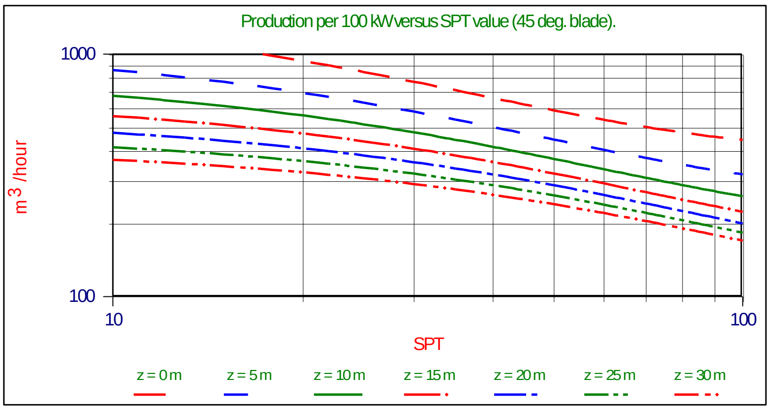

Figure 5-28: Production per 100kW versus SPT value (45 deg. blade).

5.11.3. Conclusions Specific Energy

To check the validity of the above derived theory, research has been carried out in the laboratory of the chair of Dredging Technology of the Delft University of Technology. The tests are carried out in hard packed water saturated sand, with a blade of 0.3 m by 0.2 m. The blade had cutting angles of 30, 45 and 60 degrees and deviation angles of 0, 15, 30 and 45 degrees. The layer thicknesses were 2.5, 5 and 10 cm and the drag velocities 0.25, 0.5 and 1 m/s. Figure 5-53 shows the results with a deviation angle of 0 degrees, while Figure 5-54 shows the results with a deviation angle of 45 degrees. The lines in this figure show the theoretical forces. As can be seen, the measured forces match the theoretical forces well. Based on two graphs from Lambe & Whitman (1979) and an equation for the specific energy from Miedema (1987 September) and (1995), relations are derived for the SPT value as a function of the hydrostatic pressure and of the angle of internal friction as a function of the SPT value. With these equations also the influence of water depth on the production can be determined. The specific energies as measured from the tests are shown in Figure 5-53 and Figure 5-54. It can be seen that the deviated blade results in a lower specific energy. These figures also show the upper limit for the cavitating cutting process. For small velocities and/or layer thicknesses, the specific energy ranges from 0 to the cavitating value. The tests are carried out in sand with an angle of internal friction of 40 degrees. According to Figure 5-24 this should give an SPT value of 33. An SPT value of 33 at a water depth of about 0 m, gives according to Figure 5-27, a specific energy of about 450-500 kPa. This matches the specific energy as shown in Figure 5-53.

All derivations are based on a cavitating cutting process. For small SPT values it is however not sure whether cavitation will occur. A non-cavitating cutting process will give smaller forces and power and thus a higher production. At small SPT values however the production will be limited by the bull-dozer effect or by the possible range of the operational parameters such as the cutting velocity.
The calculation method used remains a lower limit approach with respect to the production and can thus be considered conservative. For an exact prediction of the production all of the required soil mechanical properties will have to be known. As stated, limitations following from the hydraulic system are not taken into consideration.

More specific energy graphs can be found in Appendix N: Specific Energy .
More measurements can be found in Appendix M: The Snow Plough Effect.

5.12. Wear and Side Effects

In the previous chapters the blades are assumed to have a reasonable sharp blade tip and a positive clearance angle. A two dimensional cutting process has also been assumed. In dredging practice these circumstances are hardly encountered. It is however difficult to introduce a concept like wear in the theoretical model, because for every wear stage the water pressures have to be determined numerically again.

Also not clear is, if the assumption that the sand shears along a straight line will also lead to a good correlation with the model tests with worn blades. Only for the case with a sharp blade and a clearance angle of -1° a model test is performed.

It is however possible to introduce the wear effects and the side effects simply in the theory with empirical parameters. To do this the theoretical model is slightly modified. No longer the horizontal and the vertical forces are used, but the total cutting force and its angle with the direction of the velocity component perpendicular to the blade edge. Figure 5-29 shows the dimensionless forces $\mathbf{c_1}$, $\mathbf{c_2}$, en $\mathbf{c_t}$ for the non-cavitating cutting process and the dimensionless forces $\mathbf{d_1}$, $\mathbf{d_2}$ en $\mathbf{d_t}$ for the cavitating process.
For the total dimensionless cutting forces it can be written:

non-cavitating **cavitating**

$$\mathbf{c_t = \sqrt{\left(c_1 \cdot c_1 + c_2 \cdot c_2\right)}} \qquad \mathbf{d_t = \sqrt{\left(d_1 \cdot d_1 + d_2 \cdot d_2\right)}} \qquad \textbf{(5-76)}$$

For the angle the force makes with the direction of the velocity component perpendicular to the blade edge:

$$\boldsymbol{\theta_t = \mathrm{atn}\left(\frac{c_2}{c_1}\right)} \qquad \boldsymbol{\Theta_t = \mathrm{atn}\left(\frac{d_2}{d_1}\right)} \qquad \textbf{(5-77)}$$

It is proposed to introduce the wear and side effects, introducing a wear factor $\mathbf{c_s}$ ($\mathbf{d_s}$) and a wear angle $\boldsymbol{\theta_s}$ ($\boldsymbol{\Theta_s}$), according to:

$$\mathbf{c_{ts} = c_t \cdot c_s} \qquad \mathbf{d_{ts} = d_t \cdot d_s} \qquad \textbf{(5-78)}$$

and

$$\boldsymbol{\theta_{ts} = \theta_t + \theta_s} \qquad \boldsymbol{\Theta_{ts} = \Theta_t + \Theta_s} \qquad \textbf{(5-79)}$$

For the side effects, introducing a factor $\mathbf{c_r}$ ($\mathbf{d_r}$) and an angle $\boldsymbol{\theta_r}$ ($\boldsymbol{\Theta_r}$), we can now write:

$$\mathbf{c_{tr} = c_t \cdot c_r} \qquad \mathbf{d_{tr} = d_t \cdot d_r} \qquad \textbf{(5-80)}$$

and

$$\boldsymbol{\theta_{tr} = \theta_t + \theta_r} \qquad \boldsymbol{\Theta_{tr} = \Theta_t + \Theta_r} \qquad \textbf{(5-81)}$$

In particular the angle of rotation of the total cutting force as a result of wear, has a large influence on the force needed for the haul motion of cutter-suction and cutter-wheel dredgers. Figure 5-30 and Figure 5-31 give an impression of the expected effects of the wear and the side effects.

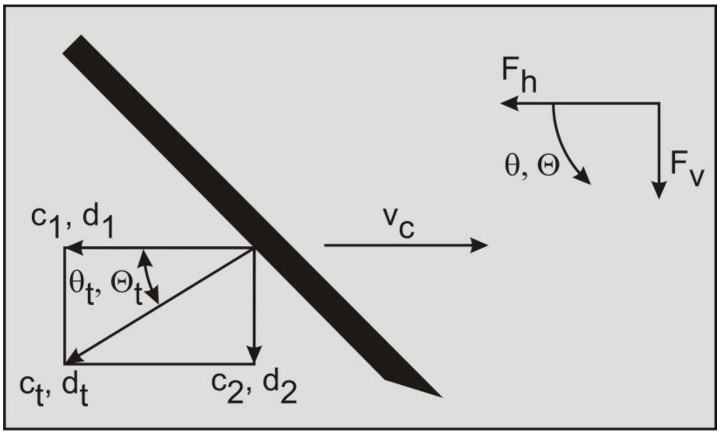

Figure 5-29: The total dimensionless cutting force c_t, d_t.

Tthe angle the forces make with the velocity direction $\boldsymbol{\theta_t}$, $\boldsymbol{\Theta_t}$, where this angle is positive when directed downward.

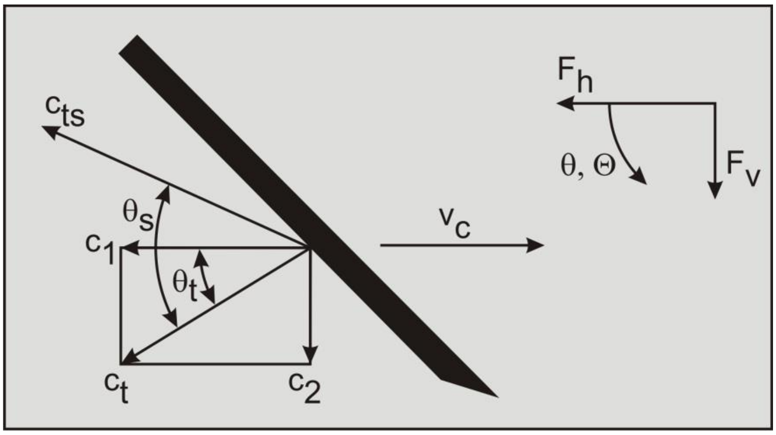

Figure 5-30: The influence of wear.

The influence of wear on the magnitude and the direction of the dimensionless cutting forces $\boldsymbol{c_t}$ or $\boldsymbol{d_t}$ for the non-cavitating cutting process.

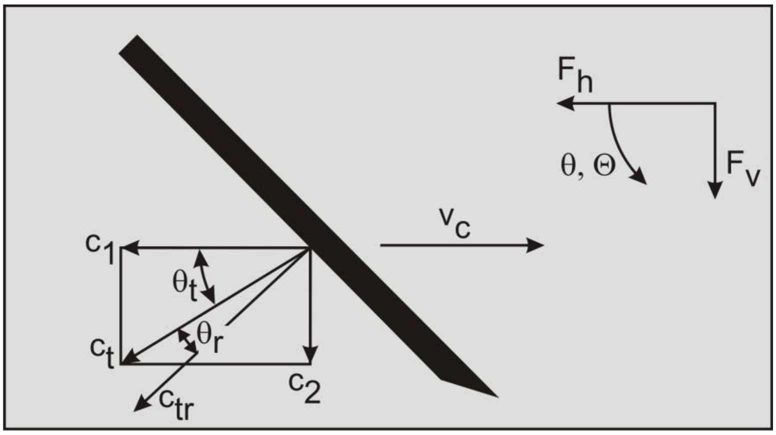

Figure 5-31: The influence of side effects.

The influence of side effects on the magnitude and the direction of the dimensionless cutting forces $\boldsymbol{c_t}$ or $\boldsymbol{d_t}$ for the non-cavitating cutting process.

5.13. Experiments

5.13.1. Description of the Test Facility

The tests with the straight blades are performed on two locations:

1. The old laboratory of Dredging Engineering, which will be called the old laboratory DE.

2. The new laboratory of Dredging Engineering, which will be called the new laboratory DE.

The test stand in the old laboratory DE consists of a concrete tank, 30 m long, 2.5 m wide and 1.35 m high, filled with a layer of 0.5 m sand with a $\mathbf{d_{50}}$ of 200 μm and above the sand 0.6 m water. The test stand in the new laboratory DE consists of a concrete tank, 33 m long, 3 m wide and internally 1.5 m high, with a layer of 0.7 m sand with a $\mathbf{d_{50}}$ of 105 μm and above the sand 0.6 m water. In both laboratories a main carriage can ride over the full length of the tank, pulled by two steel cables. These steel cables are winded on the drums of a hydraulic winch, placed in the basement and driven by a squirrel-cage motor of 35 kW in the old laboratory DE and 45 kW in the new laboratory DE.

In the old laboratory DE the velocity of the carriage could be infinitely variable controlled from 0.05 m/s to 2.50 m/s, with a pulling force of 6 kN. In the new laboratory DE the drive is equipped with a hydraulic two-way valve, which allows for the following speed ranges:

1. A range from 0.05 m/s to 1.40 m/s, with a maximum pulling force of 15 kN.

2. A range from 0.05 m/s to 2.50 m/s, with a maximum pulling force of 7.5 kN.

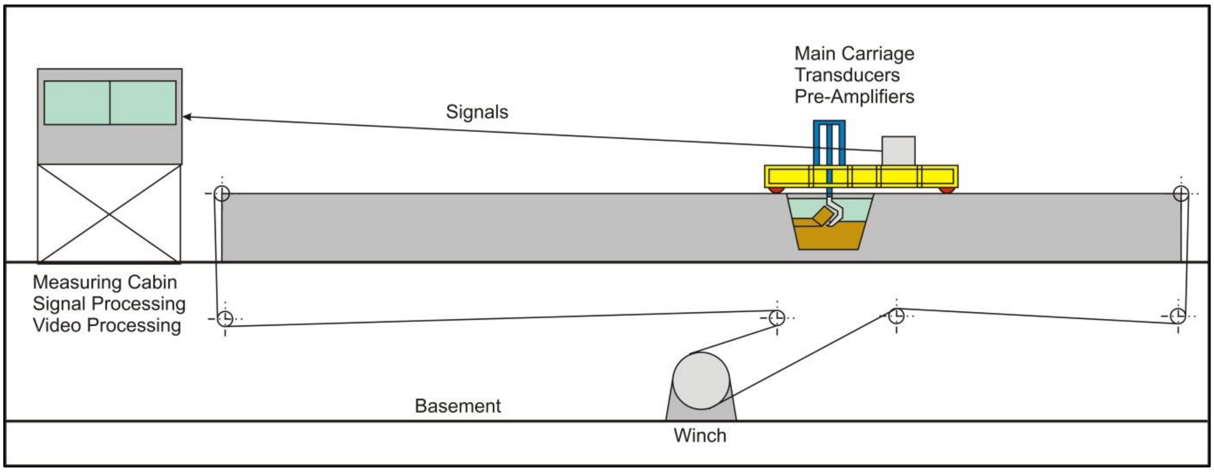

Figure 5-32: Side view of the old laboratory.

An auxiliary carriage, on which the blades are mounted, can be moved transverse of the longitudinal direction on the main carriage. Hydraulic cylinders are used to adjust the cutting depth and to position the blades in the transverse direction of the tank. Figure 5-32 shows a side view of the concrete tank with the winch drive in the basement and Figure 5-33 shows a cross section with the mounting of cutterheads or the blades underneath the auxiliary carriage (in the new laboratory DE). The main difference between the two laboratories is the side tank, which was added to dump the material excavated. This way the water stays clean and under water video recordings are much brighter. After a test the material excavated is sucked up by a dustpan dredge and put back in the main tank. The old laboratory DE was removed in 1986, when the new laboratory was opened for research. Unfortunately, the new laboratory stopped existing in 2005. Right now there are two such laboratories in the world, one at Texas A&M University in College Station, Texas, USA and one at Hohai University, Changzhou, China. Both laboratories were established around 2005.
Figure 5-34 and Figure 5-35 give an overview of both the old and the new laboratories DE, while Figure 5-36 shows a side view of the carriage, underneath which the blades are mounted.

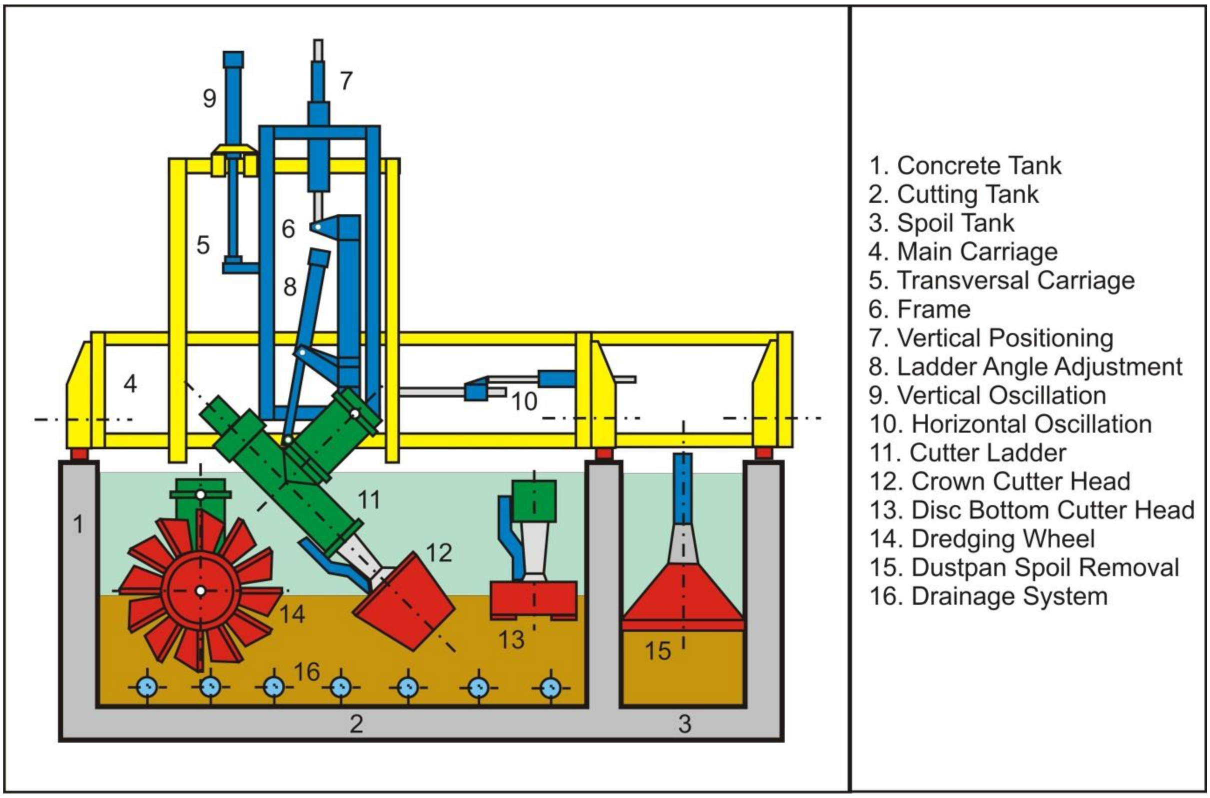

Figure 5-33: The cross section of the new laboratory DE.

Removing the spoil tank (3) from this figure gives a good impression of the cutting tank in the old laboratory DE. Instead of a cutterhead, blades are mounted under the frame (6) during the cutting tests.

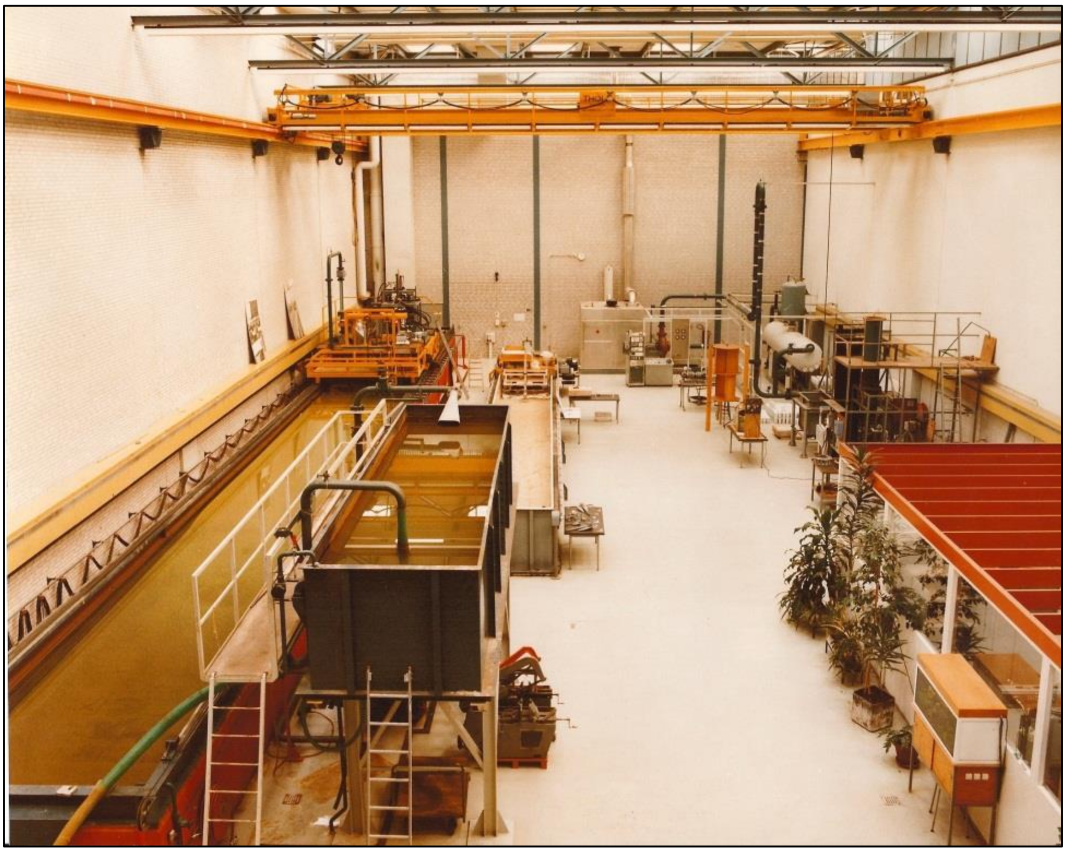

Figure 5-34: An overview of the old laboratory DE.

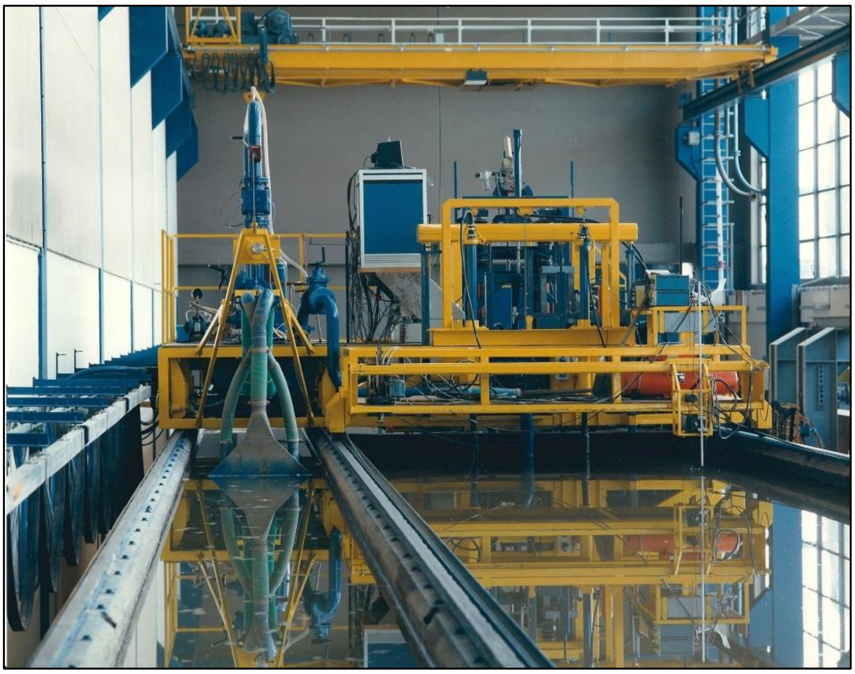

Figure 5-35: An overview of the new laboratory DE.

Figure 5-36: A side view of the carriage.

The tests are carried out using a middle blade, flanked on both sides by a side blade, in order to establish a two-dimensional cutting process on the middle blade. The middle blade (center blade) is mounted on a dynamometer, with which the following loads can be measured:

1. The horizontal force
2. The vertical force
3. The transverse force
4. The bending moment

The side blades are mounted in a fork-like construction, attached to some dynamometers, with which the following loads can be measured:

1. The horizontal force
2. The vertical force

Figure 5-37 and Figure 5-38 show the mounting construction of the blades.

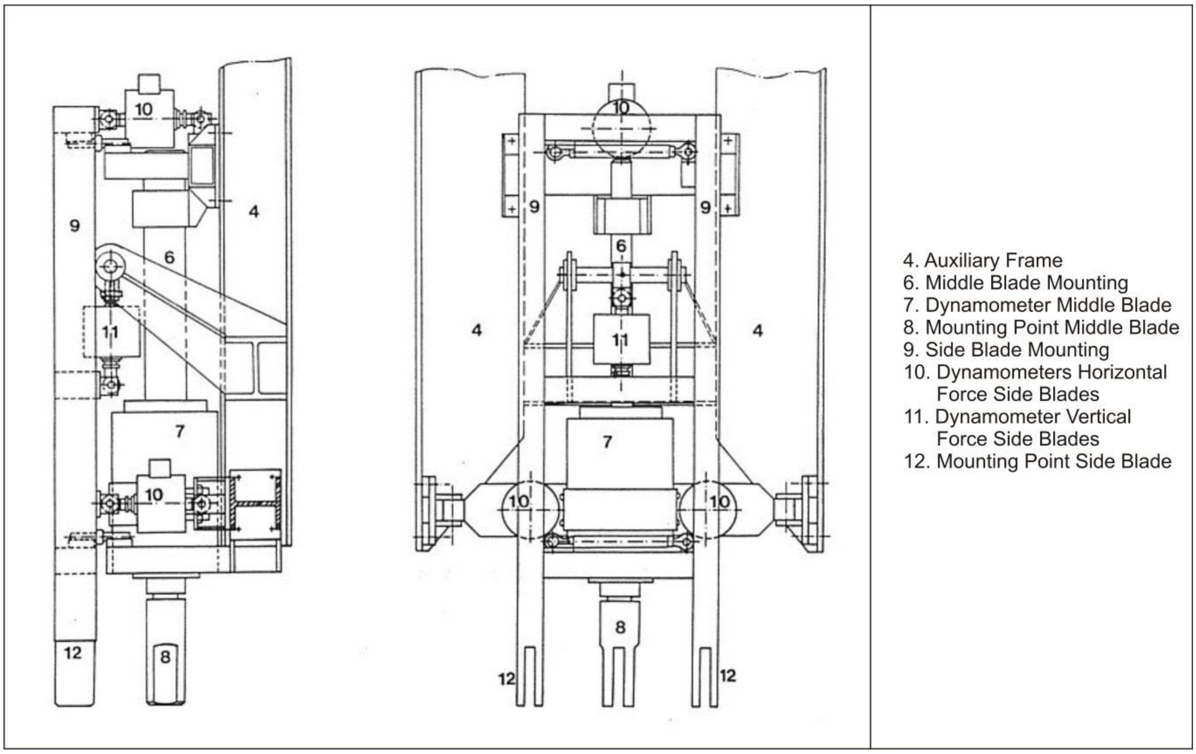

Figure 5-37: The construction in which the blades are mounted.

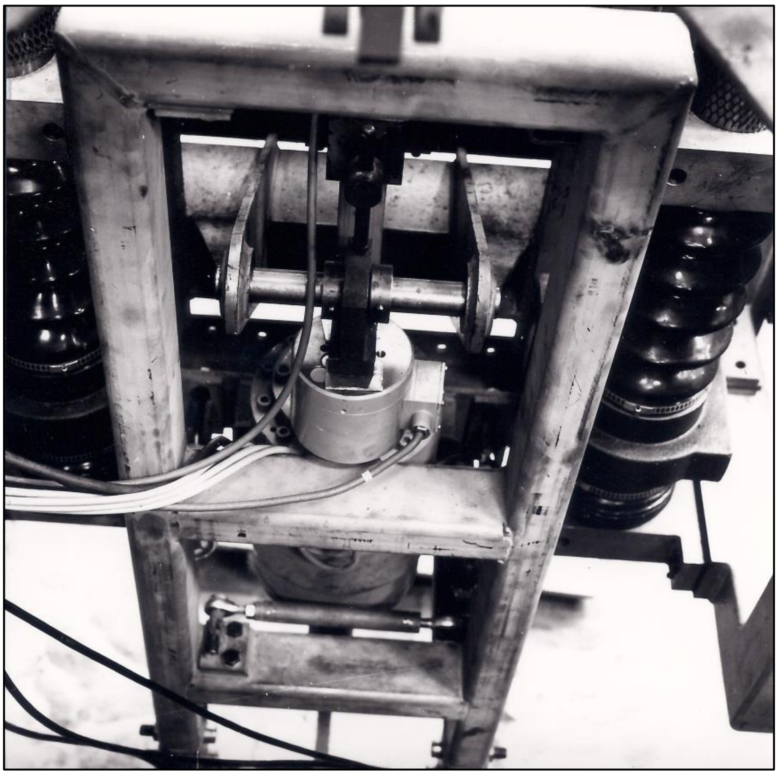

Figure 5-38: The blades are mounted in a frame with force and torque transducers.

In the middle blade, four pore pressure transducers are mounted, with which the pore pressure distribution on the blade can be measured. However no tests are performed in which the forces on the side blades and the pore pressures are measured at the same time. The measuring signals of the dynamometers and the pressure transducers are transmitted to a measurement compartment through pre-amplifiers on the main carriage. In this measurement compartment the measuring signals are suited by 12 bit, 400 Hz A/D converters for processing on a P.C. (personal computer), after which the signals are stored on a flexible disk. Next to the blades, under water, an under water video camera is mounted to record the cutting process. This also gave a good impression of the shear angles occuring.

Figure 5-39 shows how a blade is mounted under the carriage in the new laboratory DE, in this case for so called snow-plough research.Figure 5-40 shows the center blade and the two side blades mounted under the carriage in the old laboratory DE. In the center blade the 4 pore pressure transducers can be identified (the white circles) with which the pore pressures are measured.

Figure 5-43 shows the signal processing unit on the carriage, including pre-amplifiers and filters. The pre-amplifiers are used to reduce the noise on the signals that would occur transporting the signals over long distance to the measurement cabin.

Figure 5-42 shows the device used to measure the cone resistance of the sand before every experiment. The cone resistance can be related to the porosity of the sand, where the porosity relates to both the internal and external friction angle and to the permeability.

Figure 5-44 shows the measurement cabin with a PC for data processing and also showing the video screen and the tape recorder to store the video images of all the experiments.

Figure 5-41 shows a side view of the center blades. These blades could also be equipped with a wear flat to measure the influence of worn blades.

Figure 5-39: A blade mounted under the carriage in the new laboratory DE.

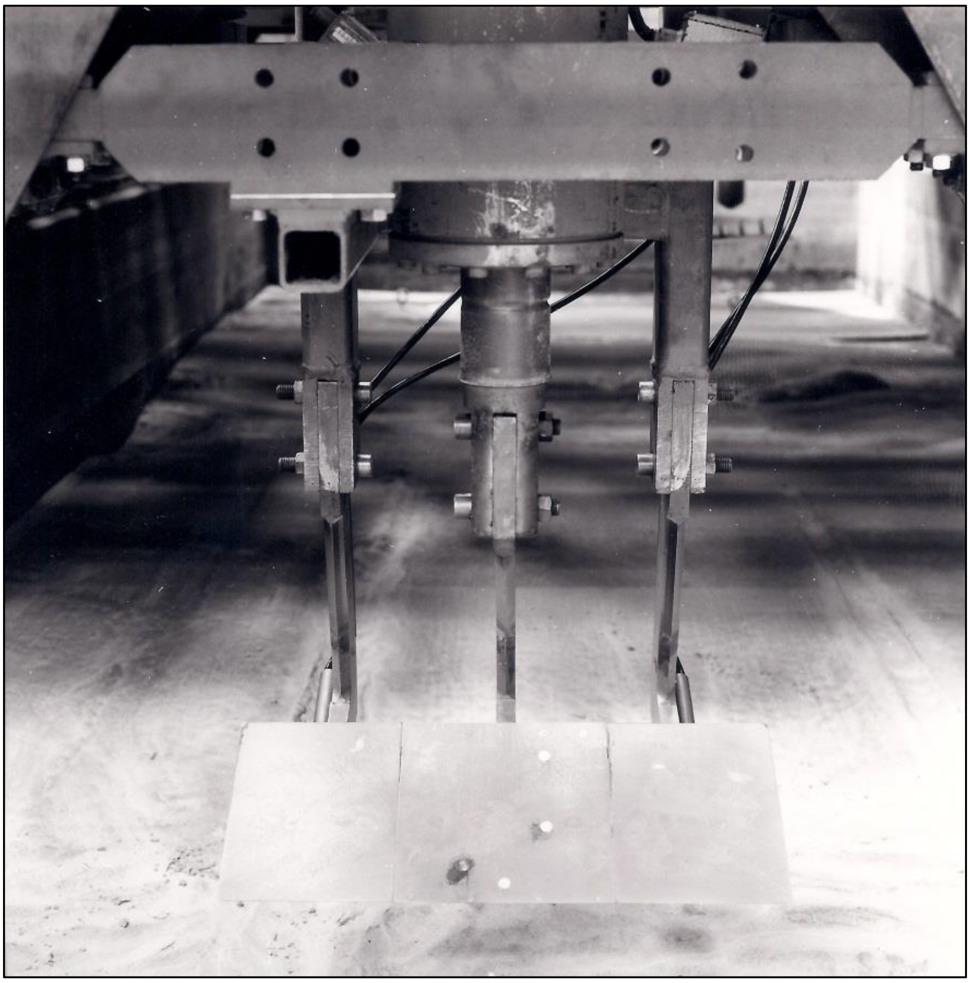

Figure 5-40: The center blade and the side blades, with the pore pressure transducers in the center blade.

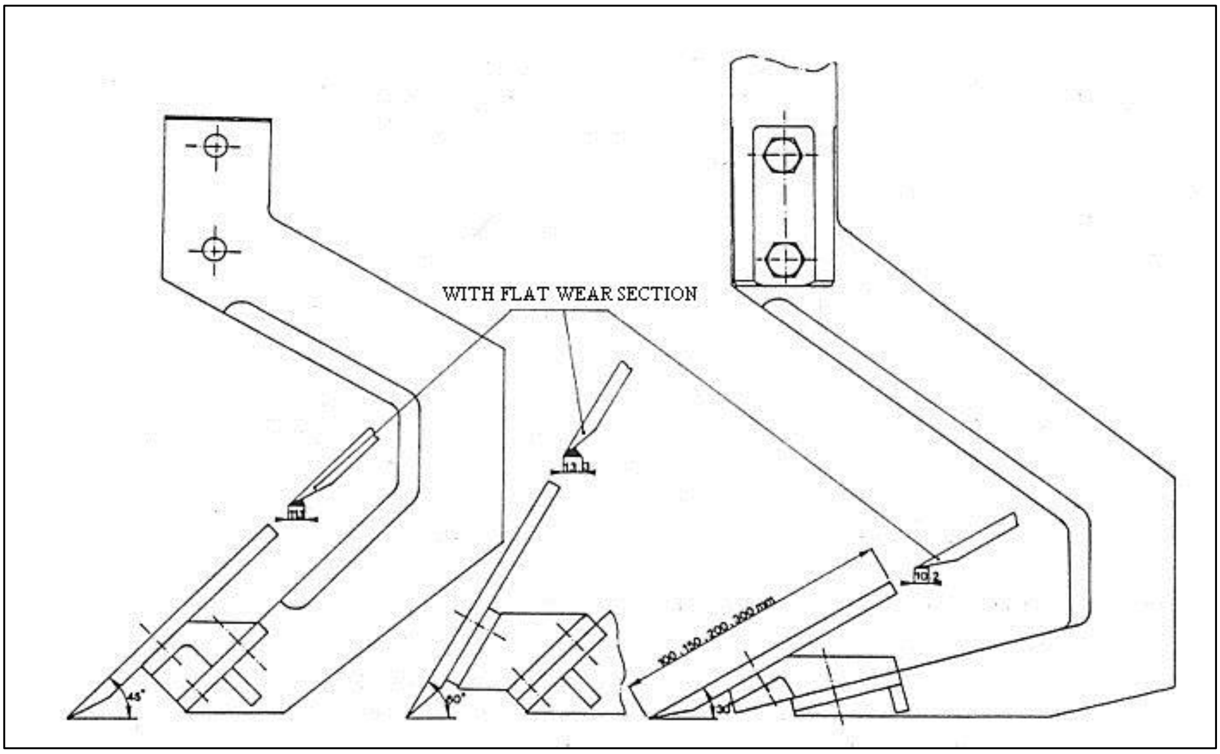

Figure 5-41: The center blade of 30º, 45º and 60º, with and without wear flat.

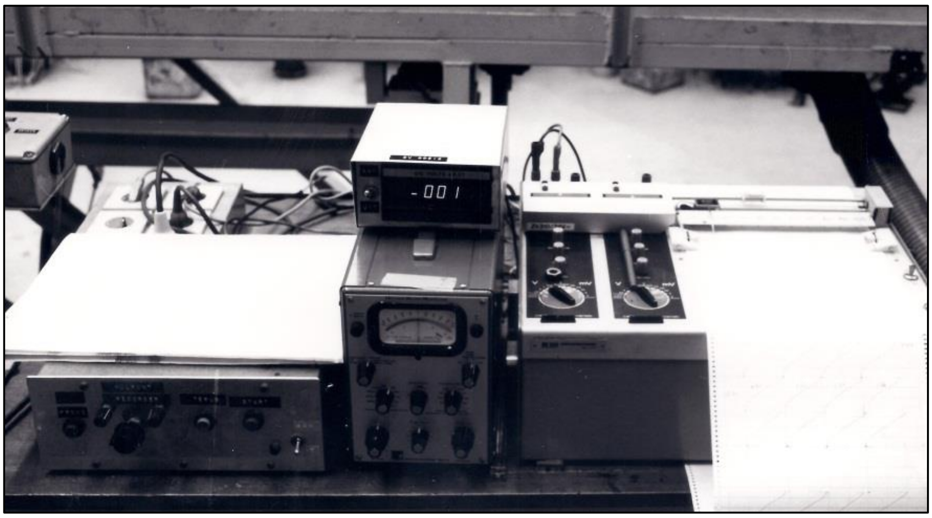

Figure 5-42: Measuring the cone resistance of the sand.

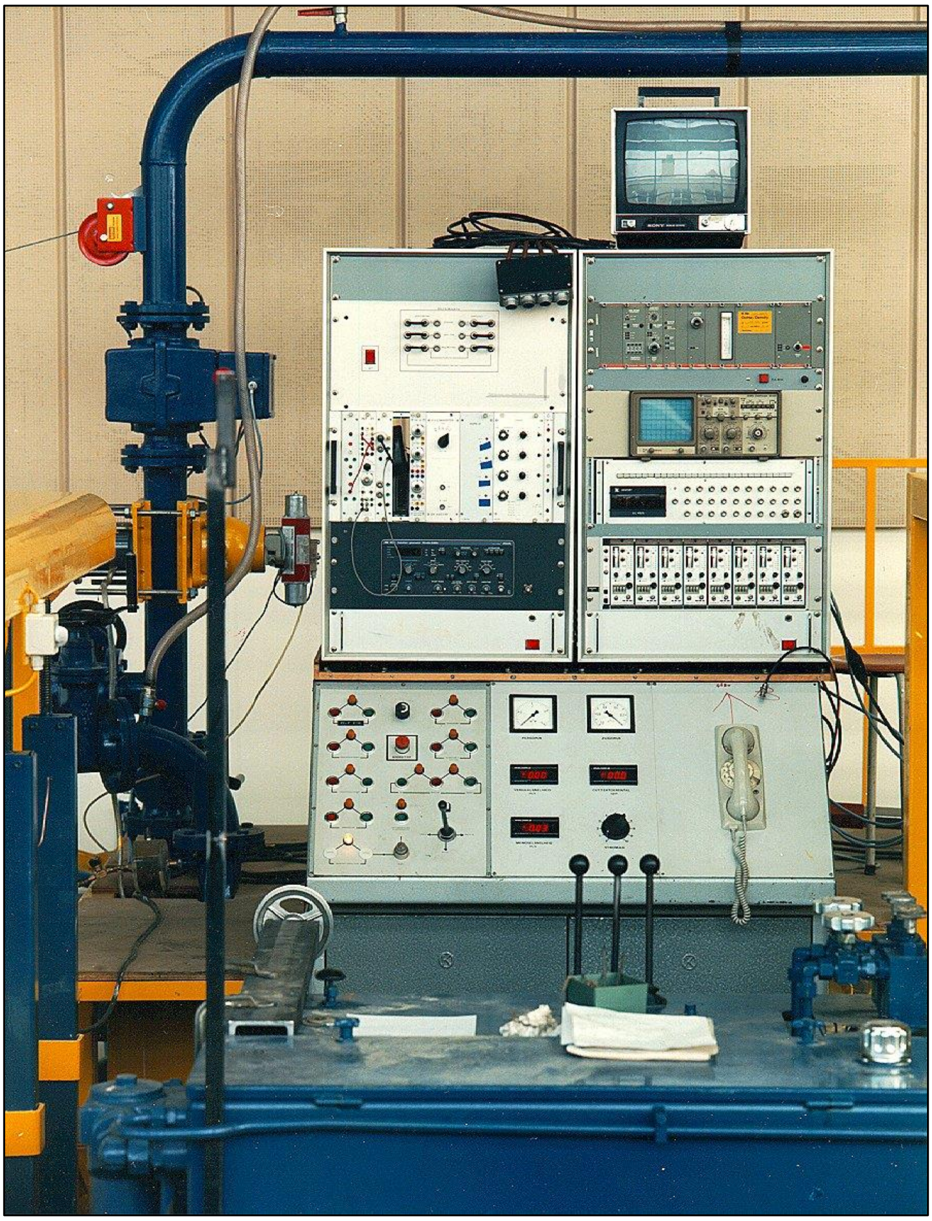

Figure 5-43: The pre-amplifiers and filters on the carriage.

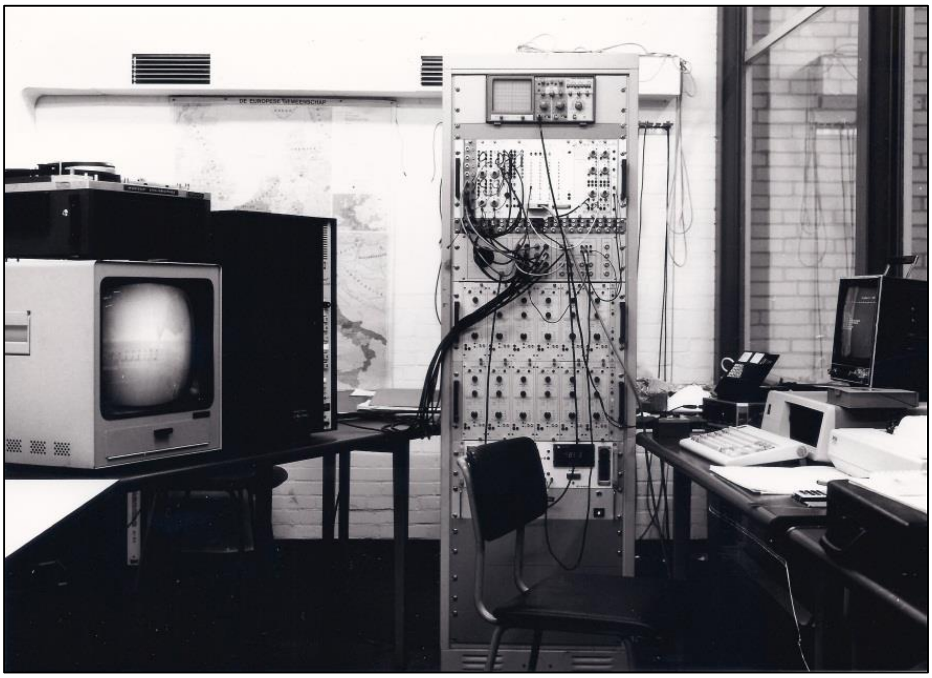

Figure 5-44: A view of the measurement cabin.

5.13.2. Test Program

The theory for the determination of the forces that occur during the cutting of fully water saturated sand with straight blades is verified in two types of sand, sand with a $\mathbf{d_{50}}$ of 200 μm and sand with a $\mathbf{d_{50}}$ of 105 μm. The soil mechanical parameters of these two types of sand can be found in Appendix J: and Appendix K:.

The research can be subdivided in a number of studies:

1. Research of the water resistance of the blades
2. Research of the accuracy of the assumed two-dimensional character of the cutting process on the middle blade by varying the width of the middle blade with a total width of the middle blade and the side blades of 520 mm. This research is performed in the 200 μm sand.
3. Research of the quantitative character of the side effects in relation to the size and the direction of the cutting forces. This research is performed in the 200 μm sand.
4. Research of the in the theory present scale rules. This research is performed in the 200 μm sand.
5. Research of the accuracy of the theory of the cutting forces and the water sub-pressures in the non-cavitating cutting process. This research is performed in the 200 μm sand.
6. Research of the accuracy of the theory of the forces and the water sub-pressures in the non-cavitating and the partly cavitating cutting process. This research is performed in the 105 μm sand.

From points 4 and 5 it has also been established that the maximum pore percentage of the sand can be chosen for the residual pore percentage. In the 200 μm the dry critical density, the wet critical density and the minimal density are determined, while in the 105 μm sand the wet critical density and the minimal density are determined. These pore values can be found in Appendix J: and Appendix K:.

For both type of sand only the minimal density (maximum pore percentage n_{max}) gave a large enough increase in volume to explain the measured water sub-pressures. This in contrast to Van Leussen and Nieuwenhuis (1984) and Van Leussen and Van Os (1987 December), where for the residual density the wet critical density is chosen.

5.13.3. Water Resistance

The water resistance is investigated under circumstances comparable with the cutting tests as far as scale; blade width and cutting velocity are concerned. Since the water resistance during all these tests could be neglected in comparison with the cutting forces, performed under the same conditions (maximum 2%), the water resistance terms are neglected in the further verification. The water resistance could however be more significant at higher cutting velocities above 2 m/s. It should be noted that at higher cutting velocities also the cutting forces will be higher, especially for the non-cavitating cutting process. Further, the inertial force, which is neglected in this research, may also play a role at very high cutting velocities.

5.13.4. The Influence of the Width of the Blade

The blade on which the cutting forces are measured is embedded between two side blades. These side blades have to take care of the three-dimensional side effects, so that on the middle blade a two-dimensional cutting process takes place. The question now is how wide the side blades need to be, at a certain cutting depth, to avoid a significant presence of the side effects on the middle blade. Essential is, that at the deepest cutting depth the side effects on the middle blade are negligible.

For this research the following blade configurations are used:

1. A middle blade of 150 mm and two side blades of 185 mm each.
2. A middle blade of 200 mm and two side blades of 160 mm each.
3. A middle blade of 250 mm and two side blades of 135 mm each.

The total blade width in each configuration is therefore 520 mm. The results of this research are, scaled to a middle blade of 200 mm wide, shown in Table 5-2, in which every value is the average of a number of tests. In this table the forces on the 0.20 m and the 0.25 m wide blade are listed in proportion to the 0.15 m wide blade. The change of the direction of the forces in relation to the 0.15 m wide blade is also mentioned.

From this table the following conclusions can be drawn:

1 There is no clear tendency to assume that the side effects influence the cutting forces in magnitude.

2 The widening of the middle blade and thus narrowing the side blades, gives slightly more downward aimed forces on the middle blade at a blade angle of 30°. At a blade angle of 45° this tendency can be seen at a blade-height/layer-thickness ratio of 1 and 2, while at a blade-height/ layer-thickness ratio of 3 the forces are just slightly aimed upward. The 60° blade angle gives the same image as the 45° blade angle, however with smaller differences in proportion to the 0.15 m wide blade.

Table 5-2: The influence of the width ratio between the center blade and the side blades.

		w=0.20 m (2)		**w=0.25 m (3)**	
α	**h_b/h_i**	**c_{t2}/c_{t1}**	**$\theta_{t2}-\theta_{t1}$**	**c_{t3}/c_{t1}**	**$\theta_{t3}-\theta_{t1}$**
30°	**1**	0.95	+1.0°	1.02	+1.0°
30°	**2**	1.10	+2.0°	0.93	+4.0°
30°	**3**	0.96	+5.0°	1.05	+7.0°
45°	**1**	1.08	+3.0°	1.01	+5.0°
45°	**2**	0.93	+3.0°	0.93	+5.0°
45°	**3**	0.93	-8.0°	1.07	-5.0°
60°	**1**	1.09	+0.0°	1.00	+1.0°
60°	**2**	0.90	+1.0°	0.92	+2.0°
60°	**3**	1.04	-5.0°	0.99	-4.0°

The total measured cutting force $\mathbf{c_t}$ and the force direction $\boldsymbol{\theta_t}$, at a blade width of .20 m ($\mathbf{c_{t2}}$, $\boldsymbol{\theta_{t2}}$) (2) and a blade width of .25 m ($\mathbf{c_{t3}}$, $\boldsymbol{\theta_{t3}}$) (3) in proportion to the total cutting force and direction at a blade width of 0.15 m ($\mathbf{c_{t1}}$, $\boldsymbol{\theta_{t1}}$) (1), according the blade configurations mentioned here.

5.13.5. Side Effects

On the outside of the side blades a three-dimensional cutting process acts, in a sense that the shear zone here is three-dimensional, but on top of that the water flows three-dimensional to the shear zone. This makes the cutting forces differ, in magnitude and direction, from the two-dimensional cutting process. Additionally it is imaginable that also forces will act on the blade in the transversal direction (internal forces in the blade). The influence of the side effects is researched by measuring the forces on both the middle blade as on the side blades. Possible present transversal forces are researched by omitting one side blade in order to be able to research the transversal forces due to the three-dimensional side effects.

For this research the following blade configurations are used:

1. A middle blade of 150 mm and two side blades of 185 mm each.
2. A middle blade of 200 mm and two side blades of 160 mm each.
3. A middle blade of 250 mm and two side blades of 135 mm each.
4. A middle blade of 200 mm and one side blade of 160 mm

The results of this research can be found in Table 5-3, where every value represents the average of a number of tests. The cutting forces in this table are scaled to the 200 mm blade to simulate a middle blade without side blades.

Table 5-3: The cutting forces on the side blades.

		w=.15 m (1)		w=.20 m (2)		w=.25 m (3)		w=.20 m (4)	
α	**h_b/h_i**	**c_r**	**θ_r**	**c_r**	**θ_r**	**c_r**	**θ_r**	**c_r**	**θ_r**
30°	**1**	1.06	+26°	1.23	+14°	1.17	+11°	1.01	+13°
30°	**2**	0.78	+18°	0.87	+16°	0.83	+10°	1.14	+10°
30°	**3**	0.74	+22°	0.56	+22°	0.53	+11°	1.45	+ 6°
45°	**1**	1.13	+23°	1.10	+14°	1.26	+ 9°	1.04	+ 5°
45°	**2**	0.94	+19°	0.94	+11°	0.93	+ 7°	0.92	+ 7°
45°	**3**	0.79	+14°	1.10	+17°	0.98	+11°	0.85	+ 6°
60°	**1**	1.10	+ 8°	1.10	+ 6°	1.10	+ 5°	1.04	+ 2°
60°	**2**	0.94	+12°	1.10	+ 8°	1.06	+ 6°	0.91	+ 2°
60°	**3**	0.77	+ 8°	0.99	+15°	1.02	+11°	0.86	+ 3°

The cutting force on the side blades in ratio to the cutting force on the middle blade $\mathbf{c_r}$, assuming that the cutting process on the middle blade is two-dimensional. Also shown is the change of direction of the total cutting force $\boldsymbol{\theta_r}$. The cutting forces are scaled to the width of the middle blade for the blade widths .15 m (1), .20 m (2) en .25 m (3). The second column for w=.20 m (4) contains the results of the tests with only one side blade to measure the side effects on the middle blade. The measured cutting forces are compared to the similar tests where two side blades are used. The blade configurations are according to chapter 5.13.4.

From this research the following conclusions can be drawn:

1. For all blade angles the cutting force on the edge is larger than follows from the two-dimensional process, for a blade-height / layer-thickness ratio of 1.
2. A blade-height / layer-thickness ratio of 2 or 3 shows a somewhat smaller cutting force with a tendency to smaller forces with a higher blade-height / layer-thickness ratio.
3. The direction of the cutting force is, for all four blade configurations, aimed more downwards on the sides than in the middle, where the differences with the middle blade decrease with a wider middle blade and therefore less wide side blades. This implies that, with the widening of the middle blade, the influence of the three-dimensional cutting process on the middle blade increases with a constant total blade width. This could be expected. It also explains that the cutting force in the middle blade is directed more downwards with an increasing middle blade width.
4. Blade configuration 4 differs slightly, as far as the magnitude of the forces is concerned, from the tendency seen in the other three configurations with the 30° blade. The direction of the cutting forces match with the other configurations. It has to be remarked that in this blade configuration the side effects occur only on one side of the blade, which explains the small change of the cutting forces.
5. The measured transverse forces for blade configuration 4 are in the magnitude of 1% of the vector sum of the horizontal and the vertical cutting forces and therefore it can be concluded that the transverse forces are negligible for the used sand.

The conclusions found are in principle only valid for the sand used. The influence of the side effects on the magnitude and the direction of the expected cutting forces will depend on the ratio between the internal friction of the sand and the soil/steel friction. This is because the two-dimensional cutting process is dominated by both angles of friction, while the forces that occur on the sides of the blade, as a result of the three-dimensional shear plane, are dominated more by the internal friction of the sand.

5.13.6. Scale Effects

The soil mechanical research showed that the density of the sand increases slightly with the depth. Since both the permeability and the volume strain, and less significant the other soil mechanical parameters, are influenced by the density, it is important to know the size of this influence on the cutting forces (assuming that the two-dimensional cutting theory is a valid description of the process). If the two-dimensional cutting theory is a valid description of the process, the dimensionless cutting forces will have to give the same results for similar geometric ratios, independent of the dimensions and the layer-thickness, according the equations for the non-cavitating cutting process and the cavitating cutting process.

The following blade configurations are used to research the scaling influence:

1. A blade with a width of 150 mm wide and a height of 100 mm.
2. A blade with a width of 150 mm wide and a height of 150 mm.
3. A blade with a width of 150 mm wide and a height of 200 mm.
4. A blade with a width of 150 mm wide and a height of 300 mm.

The results of this research can be found in Table 5-4, where every value represents the average value of a number of tests.

Table 5-4: Influence of the scale factor.

Configuration		**1**	**2**	**3**	**4**
α	**h_b/h_i**	**h = 0.10**	**0.15**	**0.20**	**0.30**
30°	**1**	0.93	1.00	0.94	1.18
30°	**2**	1.23	1.00	1.06	1.13
30°	**3**	----	1.00	0.89	0.90
45°	**1**	0.95	1.00	1.13	----
45°	**2**	0.89	1.00	1.05	1.30
45°	**3**	----	1.00	1.02	1.13
60°	**1**	0.91	1.00	----	----
60°	**2**	0.90	1.00	1.19	1.04
60°	**3**	1.02	1.00	1.13	1.21

The total cutting force $\mathbf{c_t}$ with blade heights of .10 m (1), .15 m (2), .20 m (3) and .30 m (4) in proportion to the cutting force at a blade height .15 m (2). The blade configurations are according chapter 5.13.4.
Because the influences of the gravity and inertia forces can disturb the character of the dimensionless forces compared to Appendix C: to Appendix I:, the measured forces are first corrected for these influences. The forces in the table are in proportion to the forces that occurred with blade configuration 2.

The following conclusions can be drawn from the table:

1. There is a slight tendency to larger dimensionless forces with increasing dimensions of the blades and the layer-thickness, which could be expected with the slightly increasing density.
2. For a blade angle of 30° and a blade-height / layer-thickness ratio of 2, large dimensionless forces are measured for blade configuration 1. These are the tests with the thinnest layer-thickness of 25 mm. A probable cause can be that the rounding of the blade tip in proportion with the layer-thickness is relatively large, leading to a relatively large influence of this rounding on the cutting forces. This also explains the development of the dimensionless forces at a blade angle of 30° and a blade-height / layer-thickness ratio of 3.

5.13.7. Comparison of Measurements versus Theory

The results of the preceding three investigations are collected in Table 5-5, compared with the theory. Every value is the average of a number of tests. In the table it can be found:

1. The dimensionless forces, the average from the several scales and blade widths.
2. As 1, but corrected for the gravity and inertia forces.
3. The theoretical dimensionless forces according to Appendix C: to Appendix I:.

Table 5-5: The total cutting force measured.

		measured				calculated	
		not-corrected		corrected		theoretical	
α	**h_b/h_i**	c_t	θ_t	c_t	θ_t	c_t	θ_t
30°	**1**	0.52	+13.3°	0.48	+17.1°	0.39	+28.3°
30°	**2**	0.56	+17.0°	0.53	+20.1°	0.43	+27.4°
30°	**3**	0.56	+24.8°	0.53	+28.2°	0.43	+27.3°
45°	**1**	0.71	+ 4.9°	0.63	+ 7.5°	0.49	+12.9°
45°	**2**	0.75	+ 6.0°	0.66	+ 8.0°	0.57	+10.7°
45°	**3**	0.76	+ 5.1°	0.70	+ 6.9°	0.61	+ 9.9°
60°	**1**	1.06	+ 1.2°	0.88	+ 1.9°	0.69	- 0.7°
60°	**2**	1.00	- 2.4°	0.84	- 3.4°	0.83	- 3.2°
60°	**3**	0.99	- 3.4°	0.85	- 4.2°	0.91	- 4.6°

The total cutting force measured (not-corrected and corrected for the gravity and inertia forces) and the theoretical total cutting forces (all dimensionless). The theoretical values for $\mathbf{c_t}$ and $\boldsymbol{\theta_t}$ are based on an angle of internal friction of 38°, a soil/steel angle of friction of 30° and a weighed average permeability of approximately .000242 m/s dependent on the weigh factor a_1. The total cutting force $\mathbf{c_t}$ and the force direction $\boldsymbol{\theta_t}$ are determined according chapter 5.12.

The following conclusions can be drawn from this table:

1. The measured and corrected cutting forces are larger than the, according to the theory, calculated cutting forces, at blade angles of 30° and 45°. The differences become smaller with an increase in the blade angle and when the blade-height / layer-thickness ratio increases.
2. For a blade angle of 60° the corrected measure forces agree well with the calculated forces.
3. The tendency towards larger forces with a larger blade-height / layer-thickness ratio (theory) is clearly present with blade angles 30° and 45°.
4. At a blade angle of 60° the forces seem to be less dependent of the blade-height / layer-thickness ratio.
5. The direction of the measured cutting forces agrees well with the theoretical determined direction. Only at the blade angle of 30° the forces are slightly aimed more upward for the blade-height / layer-thickness ratios 1 and 2.
6. Neglecting the inertia forces, gravity, etc. introduces an error of at least 15% within the used velocity range. This error occurs with the 60° blade, where the cutting velocity is the lowest of all cutting tests and is mainly due to the gravity.

Considering that the sand, in the course of the execution of the tests, as a result of segregation, has obtained a slightly coarser grain distribution and that the tests are performed with an increasing blade angle, can be concluded that the test results show a good correlation with the theory. It has to be remarked, however, that the scale and side effects can slightly disturb the good correlation between the theory and the measurements.

5.13.8. Location of the Resulting Cutting Force

A quantity that is measured but has not been integrated in the theory is the location of the resulting cutting force. This quantity can be of importance for the determination of the equilibrium of a drag head. The locations, of the in this chapter performed tests, are listed in Table 5-6. Table 5-7 lists the dimensionless locations of the resulting cutting force, in relation with the layer-thickness.

Table 5-6: The location of the resulting cutting force.

Configuration		1	2	3	4
α	**h_b/h_i**	**h = 0.10**	**0.15**	**0.20**	**0.30**
30°	**1**	51.25	63.1	96.7	157.2
30°	**2**	76.00	55.7	61.3	84.8
30°	**3**	----	50.5	54.3	71.5
45°	**1**	66.38	87.5	128.0	----
45°	**2**	55.13	56.9	73.4	128.6
45°	**3**	----	62.0	56.0	82.1
60°	**1**	69.88	99.5	----	----
60°	**2**	50.00	68.4	86.1	123.9
60°	**3**	46.25	55.0	66.3	95.1

The location of the resulting cutting force in mm from the blade tip, for the blade configurations of chapter 5.13.4.

Table 5-7: The location of the resulting cutting force.

Configuration		1	2	3	4
α	**h_b/h_i**	**h = 0.10**	**0.15**	**0.20**	**0.30**
30°	**1**	0.51	0.42	0.48	0.59
30°	**2**	1.52	0.75	0.61	0.56
30°	**3**	----	1.01	0.82	0.71
45°	**1**	0.67	0.58	0.64	----
45°	**2**	1.11	0.76	0.63	0.73
45°	**3**	----	1.25	0.84	0.83
60°	**1**	0.70	0.66	----	----
60°	**2**	1.01	0.91	0.86	0.83
60°	**3**	1.38	1.11	0.99	0.95

The location of the resulting cutting force from the blade tip, along the blade, made dimensionless by dividing with the layer-thickness, for the blade configurations of chapter 5.13.4.

From these tables the following conclusions can be drawn:
1. The location of the resulting cutting force is closer to the blade tip with larger blade dimensions.
2. The location of the resulting cutting force is closer to the blade tip with a smaller blade-height / layer-thickness ratio.

The first conclusion can be based upon the fact that a possible present adhesion, on a larger scale (and therefore layer-thickness) causes, in proportion, a smaller part of the cutting force. For the second conclusion this can also be a cause, although the blade-height / layer-thickness ratio must be seen as the main cause.

5.13.9. Verification of Forces & Water Pore Pressures in 200 μm Sand

The linear cutting theory is researched on three points:

The distribution of the water sub-pressures on the blade for a blade with a radius of rounding of 1 mm.
The distribution of the water sub-pressures on the blade for a blade with a flat wear face of approximately 10 mm and a clearance angle of 1°.
The correlation between the measured cutting forces and the theoretical cutting forces.

The dimensions of the blades and the wear faces can be found in Figure 5-41. In Table 5-10 the ratios of the wear face length and the layer-thickness are listed. In the preceding paragraph already a few conclusions are drawn upon the correlation between the measured and the calculated cutting forces. In this research both the forces and the water pressures are measured to increase the knowledge of the accuracy of the theory. Also it has to be mentioned that the soil mechanical parameters are determined during this research.

In Figure 5-52 the results of a test are shown. The results of the whole research of the forces are listed in Table 5-8 for the blade with the radius of rounding of 1 mm and in Table 5-9 for the blade with the wear flat. The dimensionless measured water sub-pressures are shown in Appendix L: Experiments in Water Saturated Sand, in which the theoretical distribution is represented by the solid line. The water sub-pressures are made dimensionless, although the weighed average permeability $\mathbf{k_m}$ is used instead of the permeability $\mathbf{k_{max}}$ used in the equations.

From this research the following conclusions can be drawn:

1. The measured forces and water sub-pressures show, in general, a good correlation with the theory.
2. The tendency towards increasing and more upward aimed forces with increasing blade angles can be observed clearly in the
3. Table 5-8 and Table 5-9.
4. The ratio between the measured and calculated forces becomes smaller when the blade angle and the blade-height / layer-thickness ratio increase.
5. The cutting forces on the blade with the wear face are almost equal to the cutting forces on the blade with the radius of rounding, but are slightly aimed more upward.
6. The ratio between the measured and calculated water sub-pressures is, in general, smaller than the ratio between the measured and calculated cutting forces.
7. The measured water sub-pressures on the blade with the wear face and the blade with the radius of rounding differ slightly (Table 5-10) from the water sub-pressures on the blade with the radius of rounding. On the 30° and the 45° blade, the water sub-pressures tend to smaller values for the blade with the wear face, although the differences are very small. On the 60° blade these water sub-pressures are slightly higher. Therefore it can be concluded that, for water pressures calculations, the wear-section-length / layer-thickness ratio w/h_i has to be chosen dependent of the blade angle. Which was already clear during the tests because the clearance angle increased with a larger blade angle. For the determination of Appendix C: to Appendix I:, however, the ratio used was $w/h_i=0.2$, which is a good average value.

Table 5-8: Measured dimensionless forces.

		measured				**calculated**	
		not-corrected		**corrected**		**theoretical**	
α	**h_b/h_i**	c_t	θ_t	c_t	θ_t	c_t	θ_t
30°	**1**	0.54	+29.3°	0.49	+29.0°	0.39	+28.3°
30°	**2**	0.48	+27.5°	0.46	+27.2°	0.43	+27.4°
30°	**3**	0.49	+27.6°	0.46	+27.3°	0.43	+27.3°
45°	**1**	0.78	+15.1°	0.58	+13.9°	0.49	+12.9°
45°	**2**	0.64	+12.3°	0.59	+11.6°	0.57	+10.7°
45°	**3**	0.60	+11.0°	0.55	+10.5°	0.61	+ 9.9°
60°	**1**	1.16	+ 0.7°	0.77	- 0.6°	0.69	+ 0.7°
60°	**2**	0.95	- 1.4°	0.79	- 2.2°	0.83	- 3.2°
60°	**3**	0.93	- 3.4°	0.82	- 4.0°	0.91	- 4.6°
60°	**6**	0.70	- 4.8°	0.64	- 5.7°	1.14	- 7.4°

Measured dimensionless forces, not-corrected and corrected for gravity and inertia forces and theoretical values according to Appendix C: to Appendix I: for the blade with the radius of rounding and the sub-pressure behind the blade. The theoretical values for $\mathbf{c_t}$ en $\boldsymbol{\theta_t}$ are determined based on values for the angle of internal friction of

38°, a soil/steel angle of friction of 30° and a weighed average permeability of 0.000242 m/s, dependent on the weigh factor $\mathbf{a_1}$.

Table 5-9: Measured dimensionless forces.

		measured				calculated	
		not-corrected		corrected		theoretical	
α	h_b/h_i	c_t	θ_t	c_t	θ_t	c_t	θ_t
30°	**1**	0.53	+26.2°	0.48	+25.9°	0.39	+28.3°
30°	**2**	0.48	+24.0°	0.46	+23.7°	0.43	+27.4°
30°	**3**	0.49	+24.7°	0.46	+24.3°	0.43	+27.3°
45°	**1**	0.72	+11.9°	0.57	+11.0°	0.49	+12.9°
45°	**2**	0.66	+ 8.8°	0.60	+ 8.3°	0.57	+10.7°
45°	**3**	0.63	+ 7.8°	0.60	+ 7.3°	0.61	+ 9.9°
60°	**1**	-----	-----	-----	-----	-----	-----
60°	**2**	0.90	- 5.6°	0.80	- 6.2°	0.83	- 3.2°
60°	**3**	0.95	- 7.3°	0.87	- 8.0°	0.91	- 4.6°
60°	**6**	0.70	- 9.2°	0.64	-10.1°	1.14	- 7.4°

Measured dimensionless forces, not-corrected and corrected for gravity and inertia forces and theoretical values according to Appendix C: to Appendix I: for the blade with the flat wear face and the sub-pressure behind the blade. The theoretical values for $\mathbf{c_t}$ en $\mathbf{\theta_t}$ are determined according chapter 5.12. They are based on values for the angle of internal friction of 38°, a soil/steel angle of friction of 30° and a weighed average permeability of 0.000242 m/s, dependent on the weigh factor $\mathbf{a_1}$.

Table 5-10: Average dimensionless pore pressures on the blade.

α	h_b/h_i	w	h_i	w/h_i	p_{2ma}	p_{2ms}	p_{2m}	p_{2ms}/p_{2ma}
30°	**1**	10.2	100	0.102	0.076	0.073	0.076	0.96
30°	**2**	10.2	50	0.204	0.051	0.050	0.049	0.98
30°	**3**	10.2	33	0.308	0.034	0.030	0.034	0.88
45°	**1**	11.1	141	0.079	0.090	0.080	0.097	0.89
45°	**2**	11.1	70	0.159	0.069	0.068	0.082	0.99
45°	**3**	11.1	47	0.236	0.052	0.051	0.065	0.98
60°	**1**	13.3	173	0.077	0.107	-----	0.091	----
60°	**2**	13.3	87	0.153	0.083	0.090	0.100	1.08
60°	**3**	13.3	58	0.229	0.075	0.081	0.094	1.08
60°	**6**	13.3	30	0.443	0.035	0.038	0.061	1.09

The average dimensionless pore pressures on the blade, on the blade with the radius of rounding $\mathbf{p_{2ma}}$ and the blade with the wear face $\mathbf{p_{2ms}}$, the theoretical values $\mathbf{p_{2m}}$ and the ratio between the sub-pressures $\mathbf{p_{2ms}}$ en $\mathbf{p_{2ma}}$, as a function of the length of the wear face **w** (mm), the layer-thickness $\mathbf{h_i}$ (mm) and the wear-section-length / layer-thickness ratio.

5.13.10. Verification of Forces & Water Pore Pressures in a 105 mm Sand

The linear cutting theory for the 105 μm is investigated on three points:

1. The distribution of the water sub-pressures on the blade in a non-cavitating cutting process.
2. The distribution of the water sub-pressures on the blade in the transition region between the non-cavitating and the cavitating cutting process.
3. The correlation between the measured cutting forces and the theoretical calculated cutting forces.

The dimensions of the blades can be found in Figure 5-41. In this research only a 30° blade with a layer-thickness of 100 mm, a 45° blade with a layer-thickness of 70 mm and a 60° with a layer-thickness of 58 mm, are used, at a blade height h of 200 mm. The soil mechanical parameters of the used sand are listed in Appendix K:. The results of the research regarding the cutting forces can be found in Table 5-11.

Table 5-11: Measured dimensionless forces.

		measured				calculated	
α	h_b/h_i	c_t	θ_t	c_t	θ_t	c_t	θ_t
no cavitation		**not-corrected**		**corrected**		**theoretical**	
30°	**1**	.45	+16.5°	.45	+25.6°	.41	+25.1°
45°	**2**	.50	- 3.5°	.47	+ 7.2°	.62	+ 7.6°
60°	**3**	.60	- 8.8°	.58	- 6.3°	1.02	- 7.5°
cavitation		**not-corrected**		**corrected**		**theoretical**	
30°	**1**	3.4	+13.1°	3.4	+24.2°	3.3	+21.6°
45°	**2**	4.7	-10.3°	4.2	+ 5.7°	4.6	+ 2.6°
60°	**3**	4.9	- 9.0°	4.8	- 7.8°	6.8	-12.1°

Measured dimensionless forces, not-corrected and corrected for gravity and inertia forces and the theoretical values according to Appendix C: to Appendix F: for the non-cavitating cutting process and according to Appendix G: to Appendix I: for the cavitating cutting process, calculated with a sub-pressure behind the blade. The values of $\mathbf{c_t}$ and $\boldsymbol{\theta_t}$ are calculated according chapter 5.12. They are based on values for the angle of internal friction of 38°, a soil/steel angle of friction of 30° and a weighed average permeability between 0.00011 m/s and 0.00012 m/s, dependent on the weigh factor $\mathbf{a_1}$ and the initial pore percentage of the sandbed.

The dimensionless measured water sub-pressures of the non-cavitating cutting process are presented in Appendix L:, in which the solid line represents the theoretical distribution. The dimensionless measured water sub-pressures in the transition region are also presented in Appendix L:. The figures in Appendix L: show the measured horizontal forces $\mathbf{F_h}$, in which the solid line represents the theoretical distribution. Other figures show the measured vertical forces $\mathbf{F_v}$, in which the solid line represents the theoretical distribution. Also shown in is the distribution of the forces, for several water depths, during a fully cavitating cutting process (the almost horizontal lines). From this research the following conclusions can be drawn:

1. The tests with the 30° blade give a good correlation with the theory, both for the forces as for the water sub-pressures. For the 45° blade both the forces and the water sub-pressures are lower than the theoretical calculated values with even larger deviations for the 60° blade. For the 60° blade the forces and the water sub-pressures values are approximately 60% of the calculated values.
2. The direction of the cutting forces agrees reasonably well with the theory for all blade angles, after correction for the gravity and the inertia forces.
3. The figures in Appendix L: show that the profile of the water sub-pressures on the blade, clearly changes shape when the peak stress close to the blade tip (sub-pressure) has a value of approximately 65% of the absolute pressure. An increase of the cutting velocity results in a more flattening profile, with a translation of the peak to the middle of the blade. No cavitation is observed but rather an asymptotic approach of the cavitation pressure with an increasing cutting velocity. For the 60° blade the flattening only appears near the blade tip. This can be explained with the large blade-height / layer-thickness ratio. This also explains the low cutting forces in the range where cavitation is expected. There is some cavitation but only locally in the shear zone; the process is not yet fully cavitated.
4. Since, according to the theory, the highest sub-pressures will appear in the shear zone, cavitation will appear there first. The theoretical ratio between the highest sub-pressure in the shear zone and the highest sub-pressure on the blade is approximately 1.6, which is in accordance with conclusion 3. Obviously there is cavitation in the shear zone in these tests, during which the cavitation spot expands to above the blade and higher above the blade with higher cutting velocities.

In Appendix L: the pore pressure graphs show this relation between the cavitation spot and the water pressures profile on the blade. The water sub-pressures will become smaller where the cavitation spot ends. This also implies that the measurements give an impression of the size of the cavitation spot.

As soon as cavitation occurs locally in the sand package, it becomes difficult to determine the dimensionless coefficients $\mathbf{c_1}$ and $\mathbf{c_2}$ or $\mathbf{d_1}$ and $\mathbf{d_2}$. This is difficult because the cutting process in the transition region varies between a cavitating and a non-cavitating cutting process. The ratio between the average water pressure in the shear zone and the average water pressure on the blade surface changes continuously with an increasing cutting velocity. On top of that the shape and the size of the area where cavitation occurs are unknown. However, to get an impression of the cutting process in the transition region, a number of simplifications regarding the water flow through the pores are carried out.

1. The flow from the free sand surface to the shear zone takes place along circular flow lines (see equations (5-35) and (5-36)), both through the packed sand as through the cut sand. With this assumption the distance from the free sand surface to the cavitation area can be determined, according:

$$\xi_0 = \frac{(z+10)}{v_c \cdot \varepsilon \cdot \sin(\beta)} \cdot \left(\frac{k_{max}}{\alpha+\beta} + \frac{k_i}{\pi - \beta} \right) \cdot \sin(\alpha+\beta) \tag{5-82}$$

2. The flow in the cut sand is perpendicular to the free sand surface, from the breakpoint where the shear plane reaches the free sand surface. This flow fills the water vapor bubbles with water. The distance from the free sand surface to the cavitating area can now be determined, under the assumption that the volume flow rate of the vapor bubbles equals the volume flow rate of the dilatancy, according:

$$\frac{k_{max} \cdot (z+10)}{\xi} \cdot d\psi = v_c \cdot \varepsilon \cdot \frac{\sin(\beta)}{\sin(\alpha+\beta)} \cdot d\xi \tag{5-83}$$

   In which the right term represents the volume flow rate of the vapor bubbles from the dilatancy zone, while the left term represents the supply of water from the free sand surface. This is shown in Appendix L: the pore pressure graphs. With the initial value from equation (5-82) the following solution can be found:

$$\xi = \sqrt{\xi_0^2 + 2 \cdot \frac{k_{max} \cdot (z+10)}{\left(v_c \cdot \frac{\sin(\beta)}{\sin(\alpha+\beta)} \cdot \varepsilon \right)} \cdot \psi} \tag{5-84}$$

3. The distance from the blade to the cavitation spot is considered to be constant over the blade. The magnitude of this distance is however unknown.

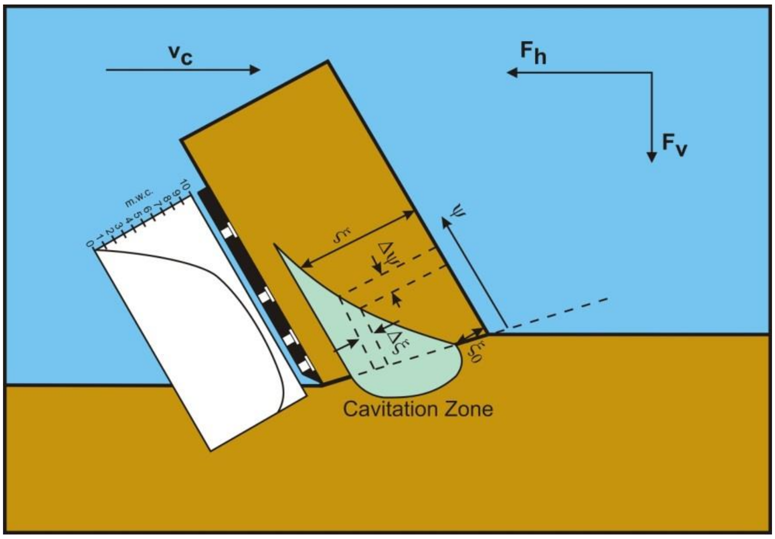

Figure 5-45: The development of cavitation over the blade.

The relation between the dimensions of the cavitation spot, and the water pressure profile on the blade.
The progressive character of the cavitation spot development results from equation (5-84). If, at a certain cutting velocity, cavitation occurs locally in the cavitation zone, then the resulting cavitation spot will always expand immediately over a certain distance above the blade as a result of the fact that a certain time is needed to fill the volume flow rate of the vapor bubbles. The development of the water sub-pressures will, in general, be influenced by the ever in the pore water present dissolved air. As soon as water sub-pressures are developing as a result of the increase in volume in the shear zone, part of the dissolved air will form air bubbles. Since these air bubbles are compressible, a large part of the volume strain will be taken in by the expansion of the air bubbles, which results in a less fast increase of the water sub-pressures with an increasing cutting velocity. The maxima of the water sub-pressures will also be influenced by the present air bubbles. This can be illustrated with the following example:

Assume the sand contains 3 volume percent air, which takes up the full volume strain in the dilatancy zone. With a volume strain of 16%, this implies that after expansion, the volume percentage air is 19%. Since it is a quick process, it may be assumed that the expansion is adiabatic, which amounts to maximum water sub-pressures of 0.925 times the present hydrostatic pressure. In an isothermal process the maximum water sub-pressures are 0.842 times the present hydrostatic pressure. From this simple example can be concluded that the in the pore water present, either dissolved or not, air has to be taken into account. In the verification of the water sub-pressures, measured during the cutting tests in the 105 μm sand, the possibility of a presence of dissolved air is recognized but it appeared to be impossible to quantify this influence. It is however possible that the maximum water sub-pressures reached (Appendix L: the pore pressure graphs) are limited by the in the pore water present dissolved air.

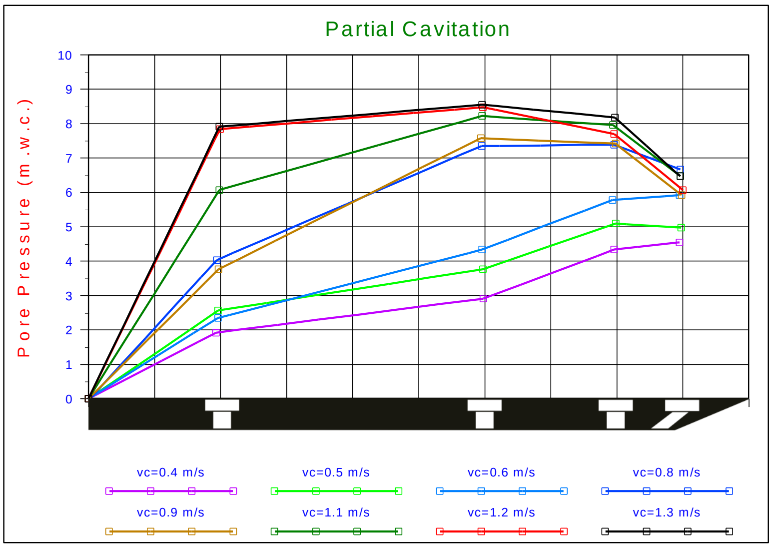

Figure 5-46: Partial cavitation limited by dissolved air, α=45º, h_i=7cm.

5.13.11. Determination of φ and δ from Measurements

The soil/steel friction angle **δ** and the angle of internal friction **φ** can be determined from cutting tests. Sand without cohesion or adhesion is assumed in the next derivations, while the mass of the cut layer has no influence on the determination of the soil/steel friction angle. In Figure 5-47 it is indicated which forces, acting on the blade, have to be measured to determine the soil/steel friction angle **δ**.

The forces $\mathbf{F_h}$ and $\mathbf{F_v}$ can be measured directly. Force $\mathbf{W_2}$ results from the integration of the measured water pressures on the blade. From this figure the normal force on the blade, resulting from the grain stresses on the blade, becomes:

$$\mathbf{F_n = W_2 - W_3 + F_h \cdot \sin(\alpha) + F_v \cdot \cos(\alpha)} \quad \textbf{(5-85)}$$

The friction force, resulting from the grain stresses on the blade, becomes:

$$\mathbf{F_w = F_h \cdot \cos(\alpha) - F_v \cdot \sin(\alpha)} \quad \textbf{(5-86)}$$

The soil/steel angle of friction now becomes:

$$\boldsymbol{\delta} = \mathbf{arctan}\left(\frac{\mathbf{F_w}}{\mathbf{F_n}}\right) \quad \textbf{(5-87)}$$

Determination of the angle of internal friction from the cutting tests is slightly more complicated. In Figure 5-48 it is indicated which forces, acting on the cut layer, have to be measured to determine this angle. Directly known are the measured forces $\mathbf{F_h}$ and $\mathbf{F_v}$. The force $\mathbf{W_1}$ is unknown and impossible to measure. However from the numerical water pressures calculations the ratio between $\mathbf{W_1}$ and $\mathbf{W_2}$ is known. By multiplying the measured force $\mathbf{W_2}$ with this ratio an estimation of the value of the force $\mathbf{W_1}$ can be obtained, so:

$$\mathbf{W_1 = \left(\frac{W_1}{W_2}\right)_{calc} \cdot W_{2mean}} \tag{5-88}$$

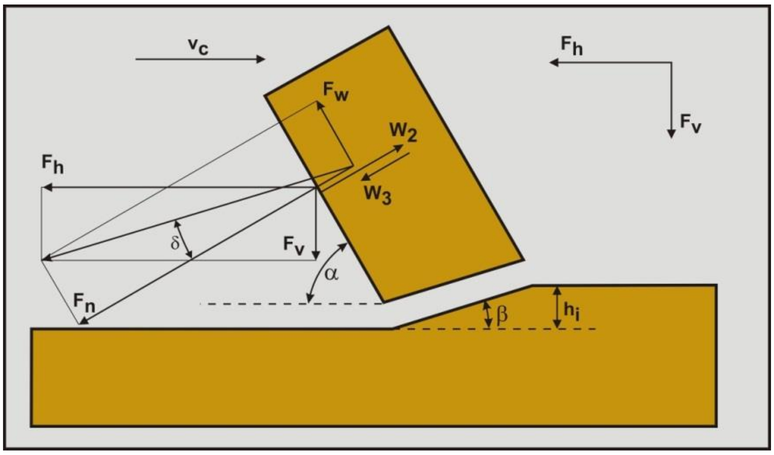

Figure 5-47: The forces from which the soil/steel friction angle δ can be determined.

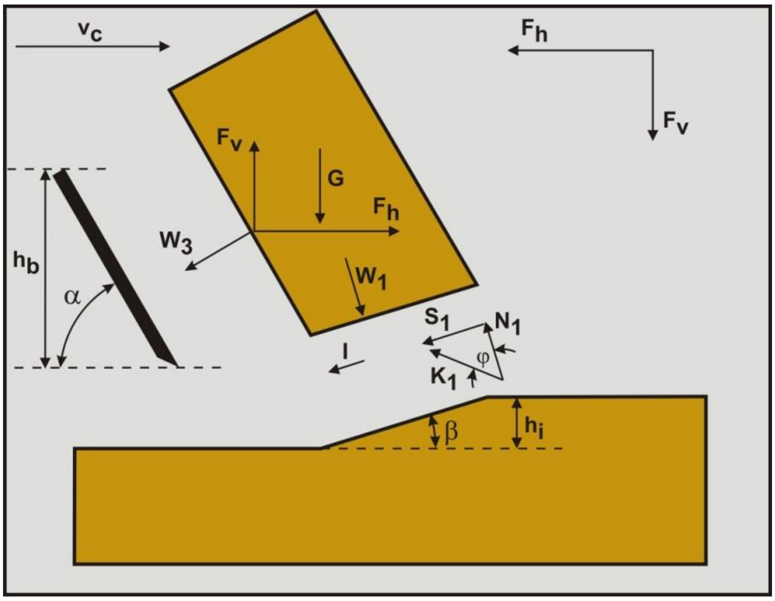

Figure 5-48: The forces from which the angle of internal friction φ of the sand can be determined.

For the horizontal and the vertical force equilibrium of the cut layer can now be written:

$$\mathbf{F_h - W_3 \cdot \sin(\alpha) = K_1 \cdot \sin(\beta + \phi) - W_1 \cdot \sin(\beta) + I \cdot \cos(\beta)} \tag{5-89}$$

$$\mathbf{F_v - W_3 \cdot \cos(\alpha) = -K_1 \cdot \cos(\beta + \phi) + W_1 \cdot \cos(\beta) + I \cdot \sin(\beta) + G} \tag{5-90}$$

The angle of internal friction:

$$\mathbf{\phi = \arctan\left(\frac{F_h - W_3 \cdot \sin(\alpha) + W_1 \cdot \sin(\beta) - I \cdot \cos(\beta)}{-F_v + W_3 \cdot \cos(\alpha) + W_1 \cdot \cos(\beta) + I \cdot \sin(\beta) + G}\right) - \beta} \tag{5-91}$$

The equations derived (5-87) and (5-91) are used to determine the values of φ and δ from the cutting tests carried out. The soil/steel friction angle can quite easily be determined, with the remark that the side and wear effects can influence the results from this equation slightly. The soil/steel friction angle, determined with this method, is therefore a gross value. This value, however, is of great practical importance, because the side and wear effects that occur in practice are included in this value.

The soil/steel friction angle **δ**, determined with this method, varied between 24° and 35°, with an average of approximately 30°. For both types of sand almost the same results where found for the soil/steel friction angle. A clear tendency towards stress or blade angle dependency of the soil/steel angle of friction is not observed. This in contrast to Van Leussen and Nieuwenhuis (1984), who found a blade angle dependency according Hettiaratchi and Reece (1974).

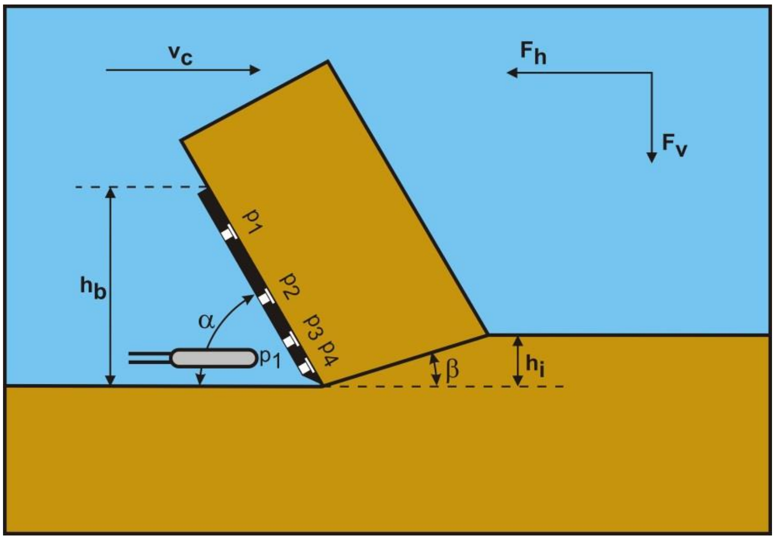

Figure 5-49: The location of the pressure transducer behind the blade.

Harder to determine is the angle of internal friction. The following average values for the angle of internal friction are found, for the 200 μm sand:

- **α = 30° » φ = 46.7°**
- **α = 45° » φ = 45.9°**
- **α = 60° » φ = 41.0°**

These values are high above the angle of internal friction that is determined with soil mechanical research according to Appendix J:, for a pore percentage of 38.5%. From equation (5-91) it can be derived that the presence of sub-pressure behind the blade makes the angle of internal friction smaller and also that this reduction is larger when the blade angle is smaller. Within the test program space is created to perform experiments where the sub-pressure is measured both on and behind the blade (Figure 5-49). Pressure transducer p_1 is removed from the blade and mounted behind the blade tip. Although the number of measurements was too limited to base an theoretical or empirical model on, these measurements have slightly increased the understanding of the sub-pressure behind the blade. Behind the blade tip sub-pressures are measured, with a value of 30% to 60% of the peak pressure on the blade. The highest sub-pressure behind the blade was measured with the 30° blade. This can be explained by the wedge shaped space behind the blade. The following empirical equation gives an estimate of the force $\mathbf{W_3}$ based on these measurements:

$$\mathbf{W_3 = 0.3 \cdot cot(\alpha) \cdot W_2} \tag{5-92}$$

The determination of the angle of internal friction corrected for under pressure behind the blade $\mathbf{W_3}$ led to the following values:

- **α = 30° » φ = 36.6°**
- **α = 45° » φ = 39.7°**
- **α = 60° » φ = 36.8°**

For the verification of the cutting tests an average value of 38° for the internal angle of friction is assumed. These values are also more in accordance with the values of internal friction mentioned in Appendix J:, where a value of approximate 35° can be found with a pore percentage of 38.5%.

The same phenomena are observed in the determination of the angle of internal friction of the 105 μm sand. The assumption of a hydrostatic pressure behind the blade resulted also in too large values for the angle of internal friction, analogously to the calculations of the 200 μm sand. Here the following values are determined:

- **α = 30° » φ = 46.2°**
- **α = 45° » φ = 38.7°**
- **α = 60° » φ = 40.3°**

The determination of the angle of internal friction corrected for under pressure behind the blade $\mathbf{W_3}$ led to the following values:

- **α = 30° » φ = 38.7°**
- **α = 45° » φ = 34.0°**
- **α = 60° » φ = 38.4°**

The low value of the angle of internal friction for the 45° blade can be explained by the fact that these tests are performed for the first time in the new laboratory DE in a situation where the sand was not homogenous from top to bottom. For the verification of the cutting forces and the water pressures is, for both sand types, chosen for a soil/steel friction angle of 30° and an angle of internal friction of 38°, as average values.

5.14. General Conclusions

From the performed research the following general conclusions can be drawn:

1. Both the measured cutting forces as the measured water sub-pressures agree reasonably with the theory. For both sand types is observed that the cutting forces and the water sub-pressures become smaller in comparison with the theory, when the blade angle becomes larger. For the 30° blade the cutting forces and the water sub-pressures are larger or equal to theoretical derived values, while for the 60° blade the theory can overestimate the measurements with a factor 1.6. This can be explained by assuming that with an increasing blade angle the cutting process becomes more discontinuous and therefore decreases the average volume strain rate. Slices of sand shear off with dilatancy around the shear planes, while the dilatancy is less in the sand between the shear planes. The theory can still be pretty useful since in dredging practice the used blade angles are between 30° and 45°.
2. Side effects can considerably influence the direction of the cutting forces, although the magnitude of the cutting forces is less disturbed. As a result of the side effects the cutting forces are aimed more downward.
3. Wear effects can also influence the direction of the cutting forces considerably, while also the magnitude of the cutting forces is less disturbed. As a result of the wear the cutting forces are, however, aimed more upwards.

5.15. The Snow Plough Effect

To check the validity of the above derived theory, research has been carried out in the new laboratory DE. The tests are carried out in hard packed water saturated sand, with a blade of 0.3 m by 0.2 m. The blade had a cutting angle of 45 degrees and inclination angles of 0, 15, 30 and 45 degrees. The layer thicknesses were 2.5, 5 and 10 cm and the drag velocities 0.25, 0.5 and 1 m/s. Figure 5-53 and Figure 5-54 show the results with and without an inclination angle of 45 degrees. The lines in this figure show the theoretical forces. As can be seen, the measured forces match the theoretical forces well. Since the research is still in progress, further publications on this subject will follow.

More measurements can be found in Appendix M: The Snow Plough Effect.

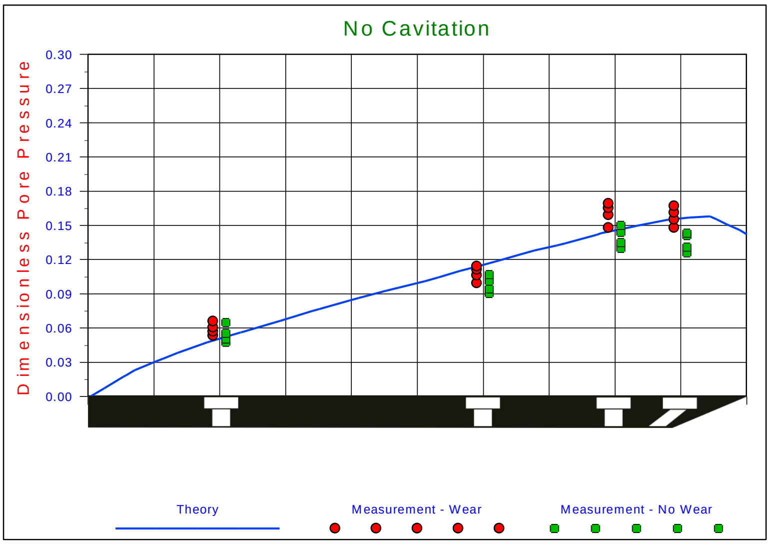

Figure 5-50: An example of pore pressure measurements versus the theory.

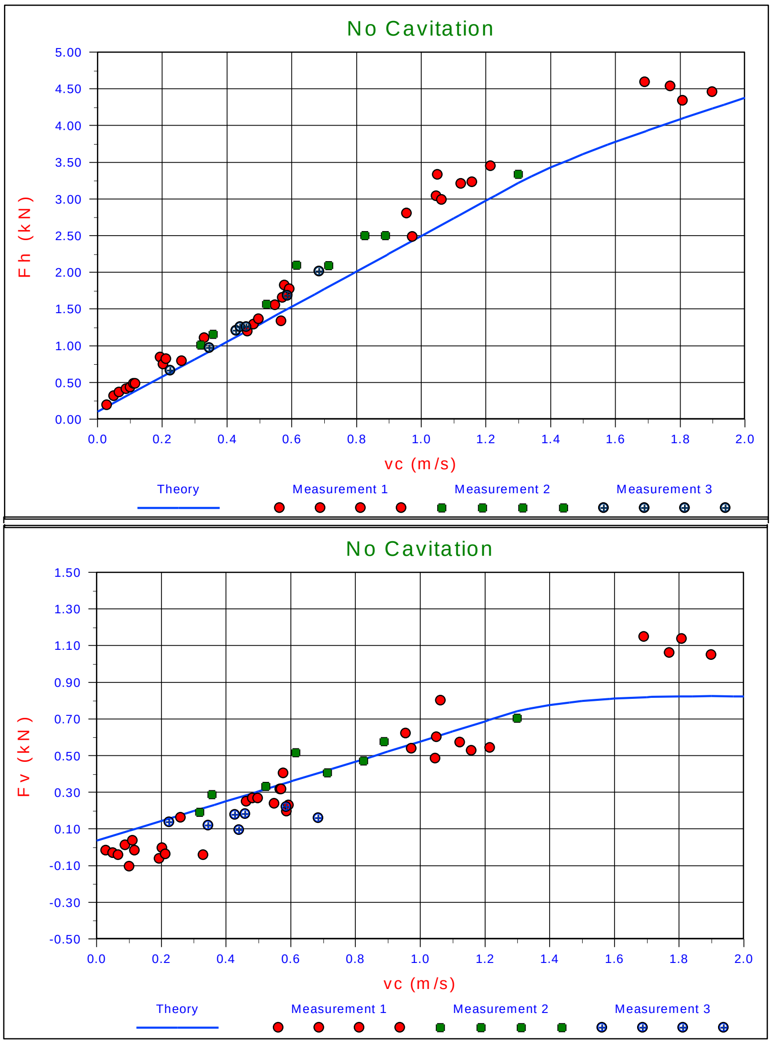

Figure 5-51: An example of the forces measured versus the theory.

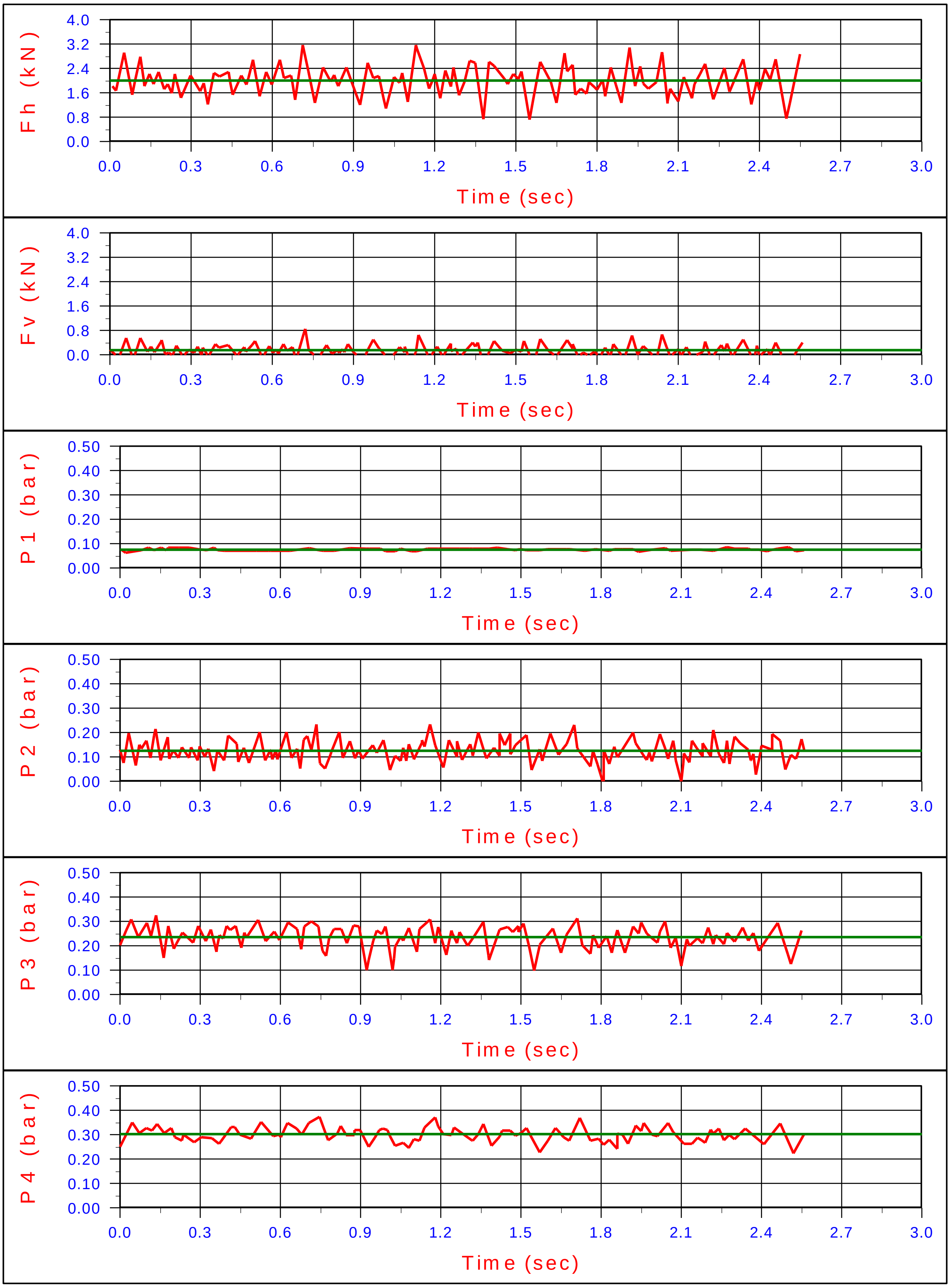

Figure 5-52: An example of the measured signals (forces and pore pressures).

The result of a cutting test graphically. In this figure the horizontal force $\mathbf{F_h}$, the vertical force $\mathbf{F_v}$ and the water pore-pressures on the blade **P1, P2, P3** and **P4** are shown. The test is performed with a blade angle α of 45°, a layer thickness $\mathbf{h_i}$ of 70 mm and a cutting velocity $\mathbf{v_c}$ of 0.68 m/s in the 200 μm sand.

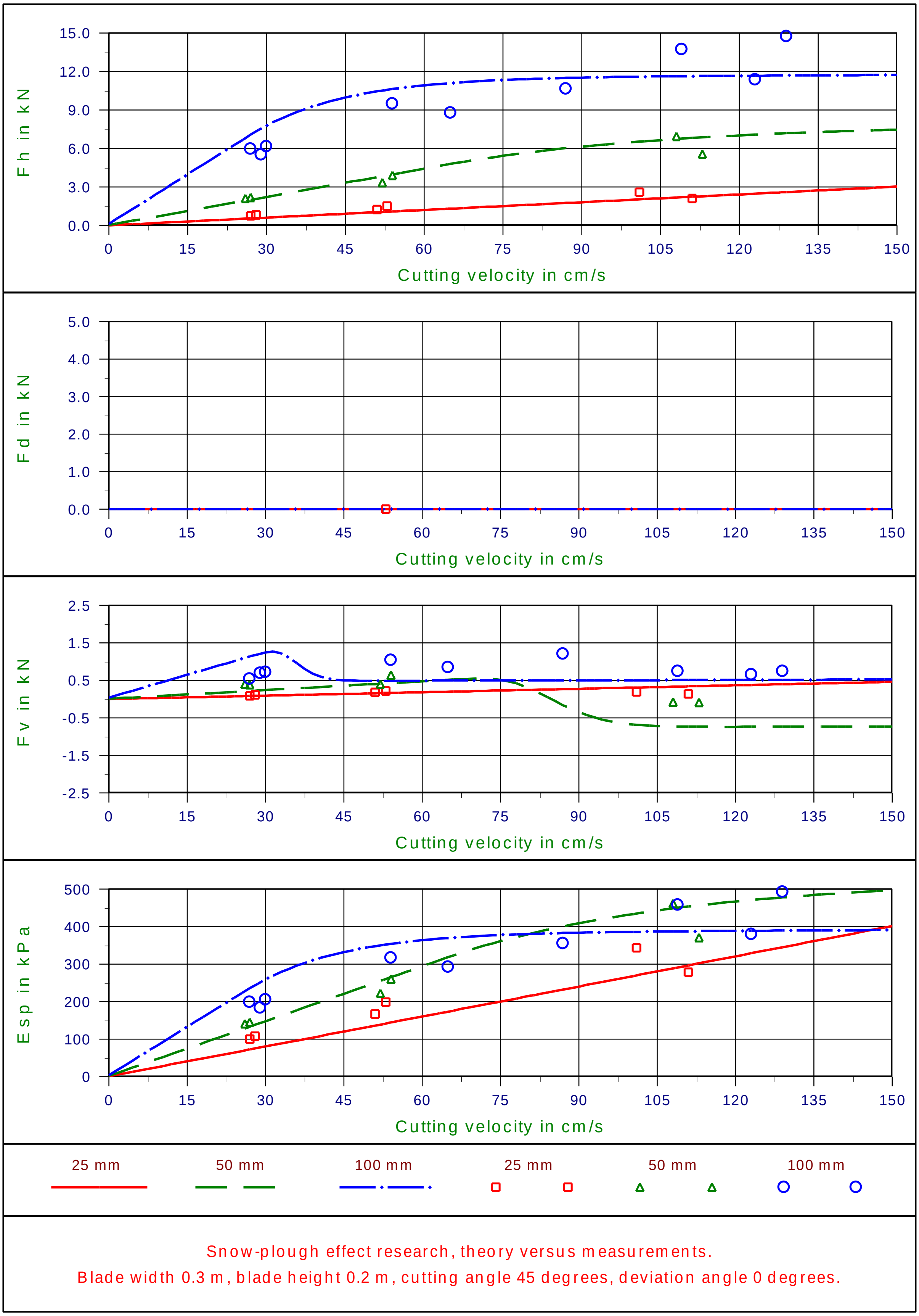

Figure 5-53: F_h, F_v, F_d and E_{sp} as a function of the cutting velocity and the layer thickness, without deviation.

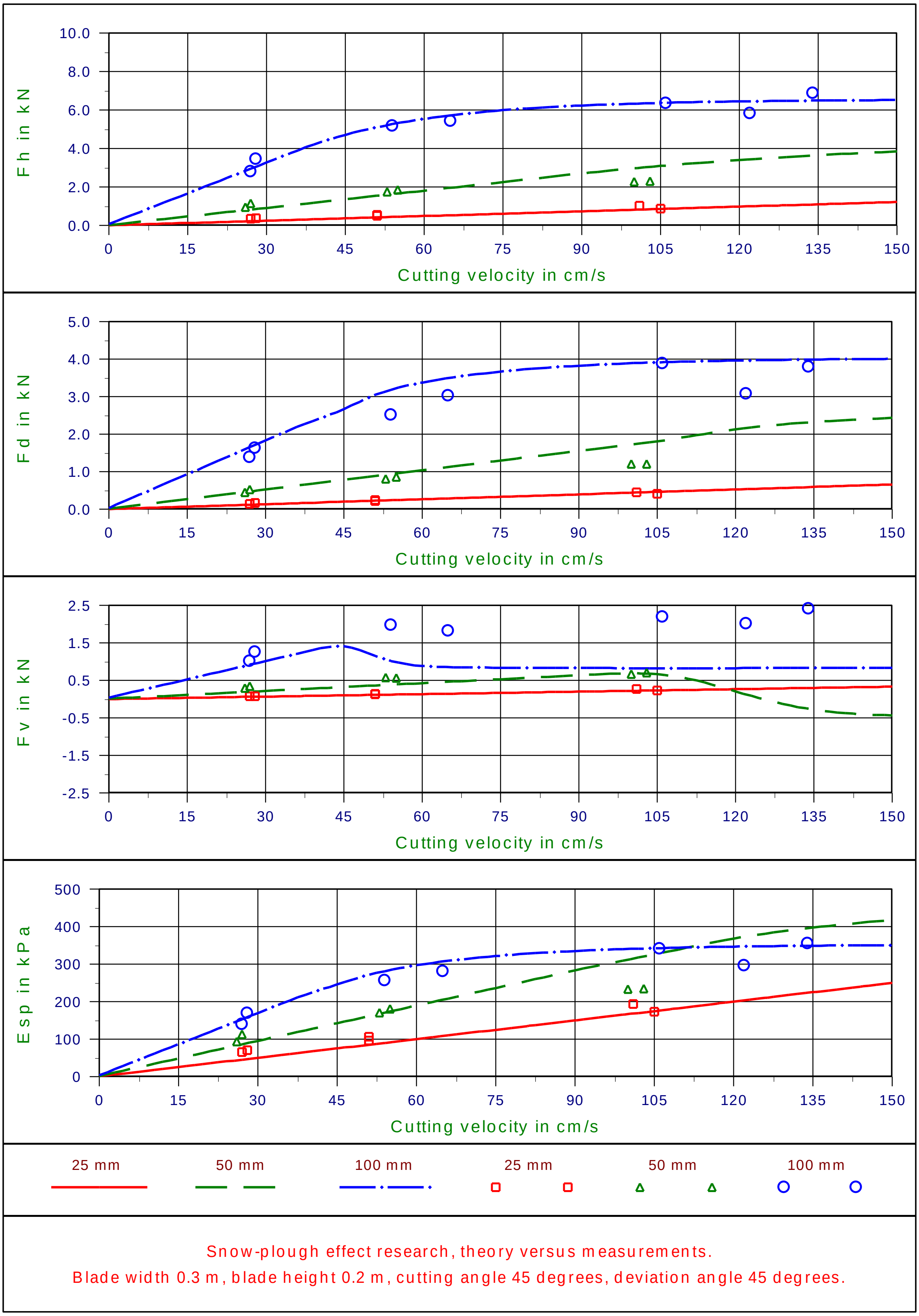

Figure 5-54: F_h, F_v, F_d and E_{sp} as a function of the cutting velocity and the layer thickness, with deviation.

More results of measurements can be found in Appendix L: Experiments in Water Saturated Sand and Appendix M: The Snow Plough Effect

5.16. Nomenclature Chapter 5:

a_1, a_2	Weight factors k-value (permeability)	-
A	Surface	m^2
b_{pr}	Projected width of the blade perpendicular to the velocity direction	m
c_i, c_1, c_2	Coefficients (non-cavitating cutting process)	-
c_r	Coefficient side effects	-
c_s	Wear coefficient	-
c_t	Coefficient total cutting force (non-cavitating cutting process)	-
c_{ts}	Coefficient total cutting force including wear effects	-
c_{tr}	Coefficient total cutting force including side effects	-
d_i, d_1, d_2	Coefficients (cavitating cutting process)	-
d_r	Coefficient side effects	-
d_s	Wear coefficient	-
d_t	Coefficient total cutting force (cavitating cutting process)	-
d_{ts}	Coefficient total cutting force including wear	-
d_{tr}	Coefficient total cutting force including side effects	-
E_{sp}	Specific cutting energy	kN/m^2
E_{gc}	Specific cutting energy (no cavitation)	kN/m^2
E_{ca}	Specific cutting energy (full cavitation)	kN/m^2
F_{ci}	Cutting force (general)	kN
F_{cit}	Total cutting force (general)	kN
F_h	Horizontal cutting force (parallel to the cutting speed)	kN
F_l	Cutting force parallel to the edge of the blade	kN
F_n	Normal force	kN
F_v	Vertical cutting force (perpendicular to the cutting velocity)	kN
F_w	Friction force	kN
F_x	Cutting force in x-direction (longitudinal)	kN
F_{xt}	Total cutting force in x-direction (longitudinal)	kN
F_y	Cutting force in y-direction (transversal)	kN
F_{yt}	Total cutting force in y-direction (transversal)	kN
F_z	Cutting force in z-direction (vertical)	kN
g	Gravitational acceleration	m/s^2
h_i	Initial layer thickness	m
h_b	Blade height	m
k	Permeability	m/s
k_i	Initial permeability	m/s
k_{max}	Maximum permeability	m/s
k_m	Effective permeability	m/s
K_1	Grain force on the shear zone	kN
K_2	Grain force on the blade	kN
l	Length of the shear zone	m
n	Normal on an edge	m
n	Porosity	-
n_i	Initial pore percentage	%
n_{max}	Maximum pore percentage	%
N_1	Normal force on the shear zone	kN
N_2	Normal force on the blade	kN
p	Number of blades excavating element	-
p	Pressure (water pressure)	kPa
p_{atm}	Atmosferic pressure	kPa

p_{calc}	Calculated dimensionless pressure (water pore pressure)	-
p_{damp}	Saturated water pore pressure (12 cm w.k.)	kPa
p_{real}	Real pore pressure (water pore pressure)	kPa
p_{1m}	Average pore pressure in the shear zone	-
p_{2m}	Average pore pressure on the blade	-
P_c	Drive power excavating element	kW
q, q_1, q_2	Specific flow	m/s
Q	Flow per unit of blade width	m^2/s
s	Length of a stream line	m
s	Measure for the layer thickness	m
S_1	Shear force on the shear zone	kN
S_2	Shear force on the blade	kN
v_c	Cutting velocity perpendicular to the edge of the blade	m/s
V	Volume strain per unit of blade width	m^2
w	Width of blade of blade element	m
W_1	Pore pressure force on the shear zone	kN
W_2	Pore pressure force on the blade	kN
x	Coordinate	m
y	Coordinate	m
z	Coordinate	m
z	Water depth	m
α	Blade angle	rad
β	Shear angle	rad
ε	Volume strain	-
φ	Angle of internal friction	rad
δ	Soil/steel interface friction angle	rad
ρ_g	Wet density of the sand	ton/m^3
ρ_s	Dry density of the sand	ton/m^3
ρ_w	Density of water	ton/m^3
θ_r	Angular displacement force vector as a result of side effects	rad
θ_s	Angular displacement force vector as a result of wear	rad
θ_t	Angle force vector angle in relation to cutting velocity vector	rad
θ_{ts}	Angle force vector angle in relation to velocity vector including wear	rad
θ_{tr}	Angle force vector angle in relation to velocity vector including side effects	rad
Θ_r	Angular displacement force vector as a result of side effects	rad
Θ_s	Angular displacement force vector as a result of wear	rad
Θ_t	Angle force vector angle in relation to cutting velocity vector	rad
Θ_{ts}	Angle force vector angle in relation to velocity vector including wear	rad
Θ_{tr}	Angle force vector angle in relation to velocity vector including side effects	rad

Chapter 6: Clay Cutting

6.1. Introduction

Hatamura and Chijiiwa (1975), (1976), (1976), (1977) and (1977) distinguished three failure mechanisms in soil cutting. The "shear type", the "flow type" and the “tear type”. The "flow type" and the "tear type" occur in materials without an angle of internal friction. The "shear type" occurs in materials with an angle of internal friction like sand. A fourth failure mechanism can be distinguished (Miedema (1992)), the "curling type", as is known in metal cutting. Although it seems that the curling of the chip cut is part of the flow of the material, whether the "curling type" or the "flow type" occurs depends on several conditions. The curling type in general will occur if the adhesive force on the blade is large with respect to the normal force on the shear plane. Whether the curling type results in pure curling or buckling of the layer cut giving obstruction of the flow depends on different parameters.

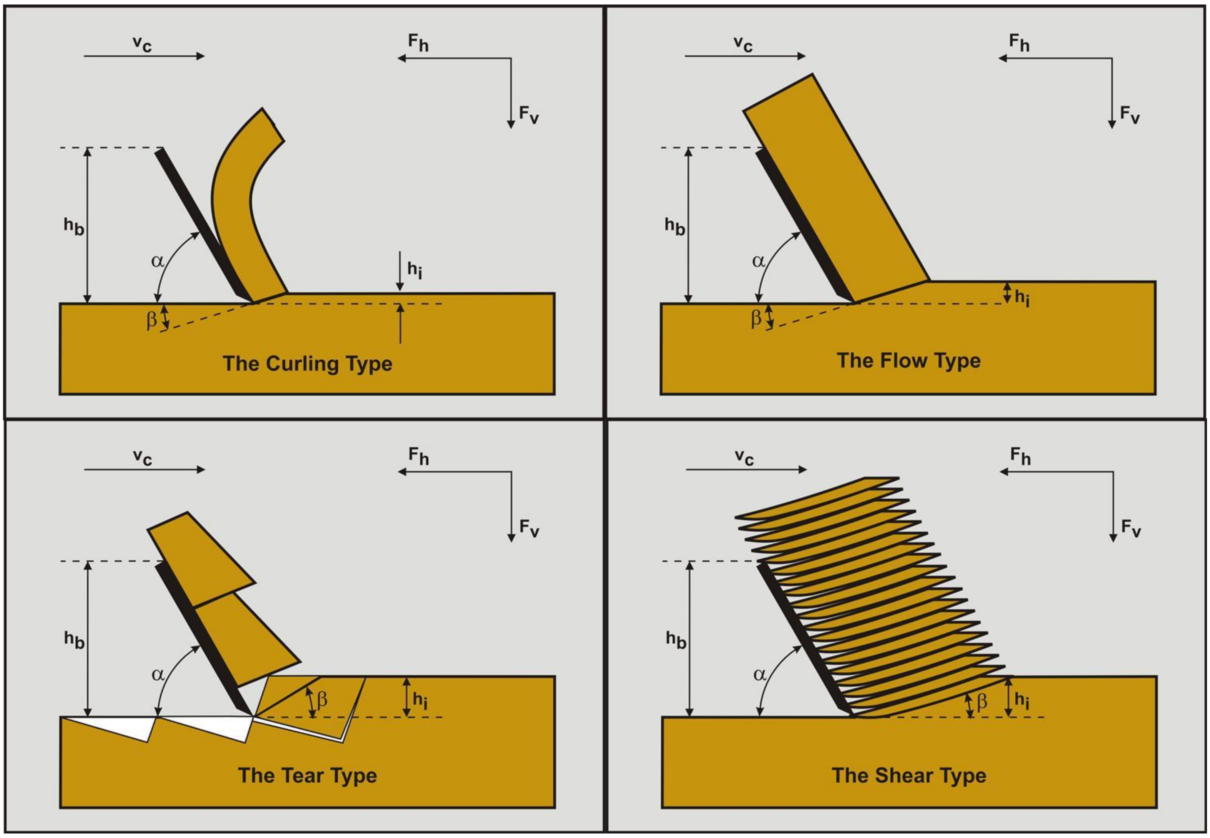

Figure 6-1: The Curling Type, the Flow Type, the Tear Type and the Shear Type.

Figure 6-1 illustrates the curling type, the flow type mechanism as they might occur when cutting clay or rock, the tear type and the shear type mechanism as they might occur when cutting clay or rock (the tear type) or cutting sand (the shear type). To predict which type of failure mechanism will occur under given conditions with specific soil, a formulation for the cutting forces has to be derived. The derivation is made under the assumption that the stresses on the shear plane and the blade are constant and equal to the average stresses acting on the surfaces. Figure 6-2 gives some definitions regarding the cutting process. The line A-B is considered to be the shear plane, while the line A-C is the contact area between the blade and the soil. The blade angle is named $\boldsymbol{\alpha}$ and the shear angle $\boldsymbol{\beta}$. The blade is moving from left to right with a cutting velocity $\mathbf{v_c}$. The thickness of the layer cut is $\mathbf{h_i}$ and the vertical height of the blade $\mathbf{h_b}$. The horizontal force on the blade $\mathbf{F_h}$ is positive from right to left always opposite to the direction of the cutting velocity $\mathbf{v_c}$. The vertical force on the blade $\mathbf{F_v}$ is positive downwards. Since the vertical force is perpendicular to the cutting velocity, the vertical force does not contribute to the cutting power, which is equal to:

$$\mathbf{P_c = F_h \cdot v_c} \quad \mathbf{(6\text{-}1)}$$

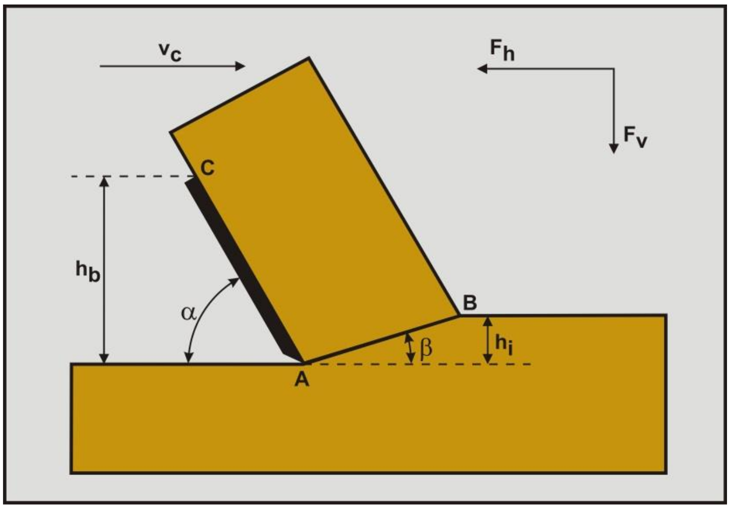

Figure 6-2: Clay cutting definitions.

In clay the cutting processes are dominated by cohesion and adhesion (internal and external shear strength). Because of the **φ=0** concept, the internal and external friction angles are set to 0. Gravity, inertial forces and pore pressures are also neglected. This simplifies the cutting equations. Clay however is subject to strengthening, meaning that the internal and external shear strength increase with an increasing strain rate. The reverse of strengthening is creep, meaning that under a constant load the material will continue deforming with a certain strain rate.
Under normal circumstances clay will be cut with the flow mechanism, but under certain circumstances the curling type or the tear type may occur.
The curling type will occur when the blade height is big with respect to the layer thickness, $\mathbf{h_b/h_i}$, the adhesion is high compared to the cohesion **a/c** and the blade angle **α** is relatively big.
The tear type will occur when the blade height is small with respect to the layer thickness, $\mathbf{h_b/h_i}$, the adhesion is small compared to the cohesion **a/c** and the blade angle **α** is relatively small.

This chapter is based on Miedema (1992), (2009) and (2010).

6.2. The Influence of the Strain Rate on the Cutting Process

6.2.1. Introduction

Previous researchers, especially Mitchell (1976), have derived equations for the strain rate dependency of the cohesion based on the "rate process theory". However the resulting equations did not allow pure cohesion and adhesion. In many cases the equations derived resulted in a yield stress of zero or minus infinity for a material at rest. Also empirical equations have been derived giving the same problems.
Based on the "rate process theory" with an adapted Boltzman probability distribution, the Mohr-Coulomb failure criteria will be derived in a form containing the influence of the deformation rate on the parameters involved. The equation derived allows a yield stress for a material at rest and does not contradict the existing equations, but confirms measurements of previous researchers. The equation derived can be used for silt and for clay, giving both materials the same physical background. Based on the equilibrium of forces on the chip of soil cut, as derived by Miedema (1987 September) for soil in general, criteria are formulated to predict the failure mechanism when cutting clay. A third failure mechanism can be distinguished, the "curling type". Combining the equation for the deformation rate dependency of cohesion and adhesion with the derived cutting equations, allows the prediction of the failure mechanism and the cutting forces involved. The theory developed has been verified by using data obtained by Hatamura and Chijiiwa (1975), (1976), (1976), (1977) and (1977) with respect to the adapted rate process theory and data obtained by Stam (1983) with respect to the cutting forces. However since the theory developed confirms the work carried out by previous researchers its validity has been proven in advance. In this chapter simplifications have been applied to allow a clear description of the phenomena involved.
The theory in this chapter has been published by Miedema (1992) and later by Miedema (2009) and (2010).

6.2.2. The Rate Process Theory

It has been noticed by many researchers that the cohesion and adhesion of clay increase with an increasing deformation rate. It has also been noticed that the failure mechanism of clay can be of the "flow type" or the "tear type", similar to the mechanisms that occur in steel cutting. The rate process theory can be used to describe the phenomena occurring in the processes involved. This theory, developed by Glasstone, Laidler and Eyring (1941) for the modeling of absolute reaction rates, has been made applicable to soil mechanics by Mitchell (1976). Although there is no physical evidence of the validity of this theory it has proved valuable for the modeling of many processes such as chemical reactions. The rate process theory, however, does not allow strain rate independent stresses such as real cohesion and adhesion. This connects with the starting point of the rate process theory that the probability of atoms, molecules or particles, termed flow units having a certain thermal vibration energy is in accordance with the Boltzman distribution (Figure 6-3):

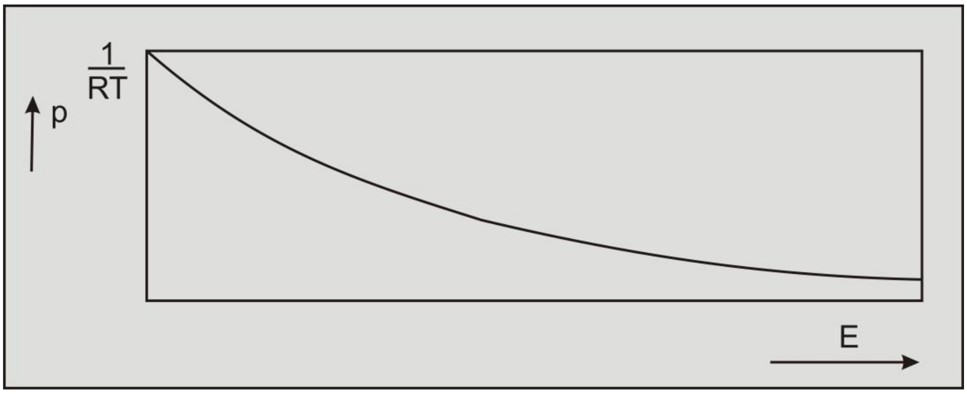

Figure 6-3: The Boltzman probability distribution.

$$\mathbf{p(E) = \frac{1}{R \cdot T} \cdot \exp\left(\frac{-E}{R \cdot T}\right)} \qquad \textbf{(6-2)}$$

The movement of flow units participating in a time dependent flow is constrained by energy barriers separating adjacent equilibrium positions. To cross such an energy barrier, a flow unit should have an energy level exceeding certain activation energy $\mathbf{E_a}$. The probability of a flow unit having an energy level greater than a certain energy level $\mathbf{E_a}$ can be calculated by integrating the Boltzman distribution from the energy level $\mathbf{E_a}$ to infinity, as depicted in Figure 6-4, this gives:

$$p_{E>E_a} = \exp\left(\frac{-E_a}{R\cdot T}\right) \tag{6-3}$$

The value of the activation energy $\mathbf{E_a}$ depends on the type of material and the process involved. Since thermal vibrations occur at a frequency given by **kT/h**, the frequency of activation of crossing energy barriers is:

$$\nu = \frac{k.T}{h}\cdot\exp\left(\frac{-E_a}{R\cdot T}\right) \tag{6-4}$$

In a material at rest the barriers are crossed with equal frequency in all directions. If however a material is subjected to an external force resulting in directional potentials on the flow units, the barrier height in the direction of the force is reduced by (**f•λ/2**) and raised by the same amount in the opposite direction. Where f represents the force acting on a flow unit and **λ** represents the distance between two successive equilibrium positions. From this it can be derived that the net frequency of activation in the direction of the force **f** is as illustrated in Figure 6-5:

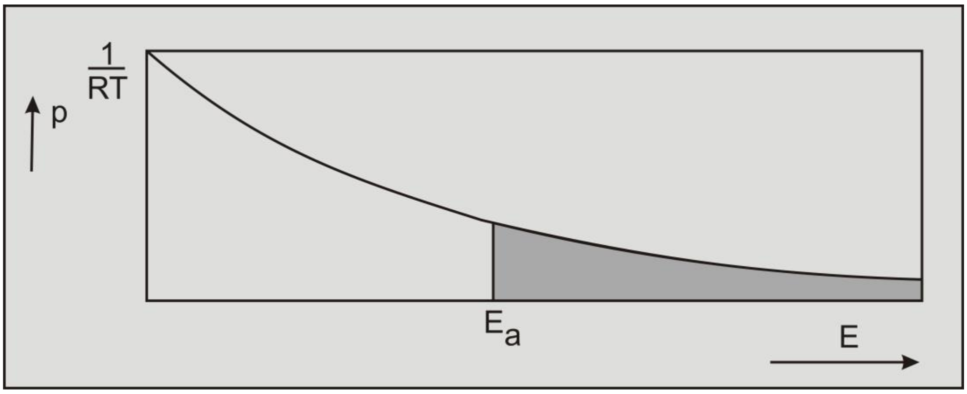

Figure 6-4: The probability of exceeding an energy level Ea.

$$\nu = \frac{k\cdot T}{h}\cdot\exp\left(\frac{-E_a}{R\cdot T}\right)\cdot\left\{\exp\left(\frac{+f\cdot\lambda}{2\cdot k\cdot T}\right)-\exp\left(\frac{-f\cdot\lambda}{2\cdot k\cdot T}\right)\right\} \tag{6-5}$$

If a shear stress **τ** is distributed uniformly along **S** bonds between flow units per unit area then **f=τ/S** and if the strain rate is a function **X** of the proportion of successful barrier crossings and the displacement per crossing according to **dε/dt=X·ν** then:

$$\dot{\varepsilon} = 2\cdot X\cdot\frac{k\cdot T}{h}\cdot\exp\left(\frac{-E_a}{R\cdot T}\right)\cdot\sinh\left(\frac{\tau\cdot\lambda\cdot N}{2\cdot S\cdot R\cdot T}\right) \qquad \text{with} : R = N\cdot k \tag{6-6}$$

From this equation, simplified equations can be derived to obtain dashpot coefficients for theological models, to obtain functional forms for the influences of different factors on strength and deformation rate, and to study deformation mechanisms in soils. For example:

$$\text{if}\quad\left(\frac{\tau\cdot\lambda\cdot N}{2\cdot S\cdot R\cdot T}\right)<1\quad\text{then}\quad\sinh\left(\frac{\tau\cdot\lambda\cdot N}{2\cdot S\cdot R\cdot T}\right)\approx\left(\frac{\tau\cdot\lambda\cdot N}{2\cdot S\cdot R\cdot T}\right) \tag{6-7}$$

Resulting in the mathematical description of a Newtonian fluid flow, and:

$$\text{if}\quad\left(\frac{\tau\cdot\lambda\cdot N}{2\cdot S\cdot R\cdot T}\right)>1\quad\text{then}\quad\sinh\left(\frac{\tau\cdot\lambda\cdot N}{2\cdot S\cdot R\cdot T}\right)\approx\frac{1}{2}\cdot\exp\left(\frac{\tau\cdot\lambda\cdot N}{2\cdot S\cdot R\cdot T}\right) \tag{6-8}$$

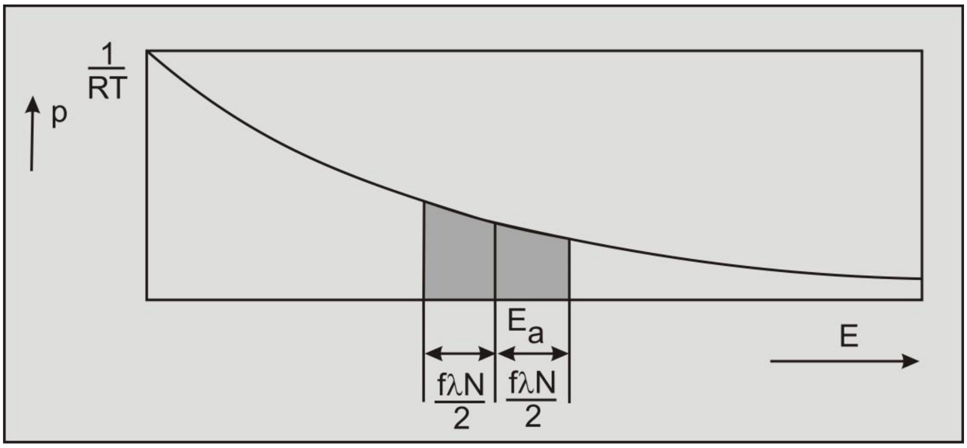

Figure 6-5: The probability of net activation in direction of force.

Resulting in a description of the Mohr-Coulomb failure criterion for soils as proposed by Mitchell et al. (1968). Zeng and Yao (1988) and (1991) used the first simplification (6-7) to derive a relation between soil shear strength and shear rate and the second simplification (6-8) to derive a relation between soil-metal friction and sliding speed.

6.2.3. Proposed Rate Process Theory

The rate process theory does not allow for shear strength if the deformation rate is zero. This implies that creep will always occur since any material is always exposed to its own weight. This results from the starting point of the rate process theory, the Boltzman distribution of the probability of a flow unit exceeding a certain energy level of thermal vibration. According to the Boltzman distribution there is always a probability that a flow unit exceeds an energy level, between an energy level of zero and infinity, this is illustrated in Figure 6-4.
Since the probability of a flow unit having an infinite energy level is infinitely small, the time-span between the occurrences of flow units having an infinite energy level is also infinite, if a finite number of flow units is considered. From this it can be deduced that the probability that the energy level of a finite number of flow units does not exceed a certain limiting energy level in a finite time-span is close to 1. This validates the assumption that for a finite number of flow units in a finite time-span the energy level of a flow unit cannot exceed a certain limiting energy level $\mathbf{E_l}$. The resulting adapted Boltzman distribution is illustrated in Figure 6-6. The Boltzman distribution might be a good approximation for atoms and molecules but for particles consisting of many atoms and/or molecules the distribution according to Figure 6-6 seems more reasonable, since it has never been noticed that sand grains in a layer of sand at rest, start moving because of their internal energy. In clay some movement of the clay particles seems probable since the clay particles are much smaller than the sand particles. Since particles consist of many atoms, the net vibration energy in any direction will be small, because the atoms vibrate thermally with equal frequency in all directions.

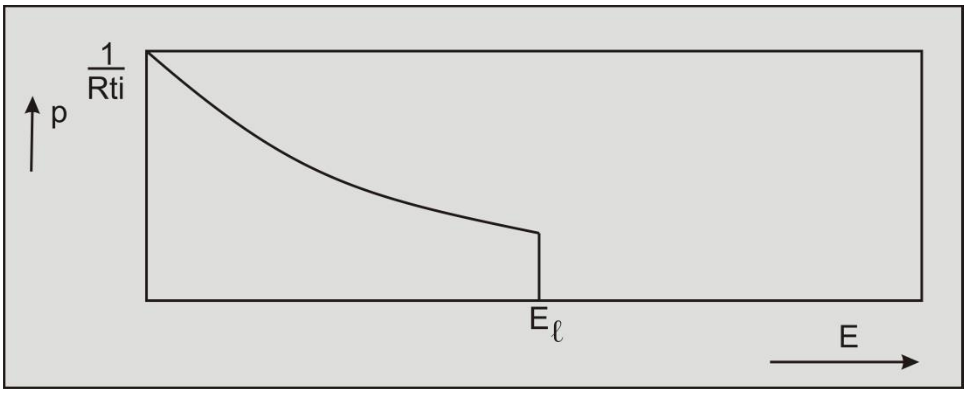

Figure 6-6: The adapted Boltzman probability distribution.

If a probability distribution according to Figure 6-6 is considered, the probability of a particle exceeding a certain activation energy $\mathbf{E_a}$ becomes:

$$p_{E>E_a}=\frac{\exp\left(\frac{-E_a}{R\cdot T}\right)-\exp\left(\frac{-E_\ell}{R\cdot T}\right)}{1-\exp\left(\frac{-E_\ell}{R\cdot T}\right)}\quad \text{if } E_a<E_\ell \text{ and } p_{E>E_a}=0 \quad \text{if } E_a>E_\ell \tag{6-9}$$

If the material is now subjected to an external shear stress, four cases can be distinguished with respect to the strain rate.

Case 1:	The energy level $\mathbf{E_a+\tau\lambda N/2S}$ is smaller than the limiting energy level $\mathbf{E_l}$ (Figure 6-7). The strain rate equation is now: $$\dot{\varepsilon}=2\cdot X\cdot\frac{k\cdot T}{h\cdot i}\cdot\exp\left(\frac{-E_a}{R\cdot T}\right)\cdot\sinh\left(\frac{\tau\cdot\lambda\cdot N}{2\cdot S\cdot R\cdot T}\right) \tag{6-10}$$ with: $i=1-\exp\left(\frac{-E_\ell}{R\cdot T}\right)$ Except for the coefficient **i**, necessary to ensure that the total probability remains 1, equation (6-10) is identical to equation (6-6).

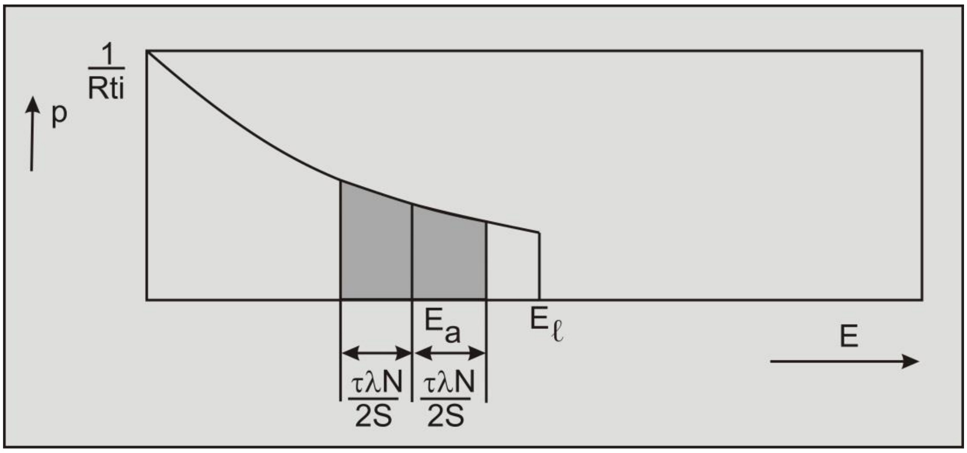

Figure 6-7: The probability of net activation in case 1.

Case 2:	The activation energy $\mathbf{E_a}$ is less than the limiting energy $\mathbf{E_l}$, but the energy level $\mathbf{E+\tau\lambda N/2S}$ is greater than the limiting energy level $\mathbf{E_l}$ (Figure 6-8). The strain rate equation is now: $$\dot{\varepsilon}=X\cdot\frac{k\cdot T}{h\cdot i}\cdot\left\{\exp\left(-\left(\frac{E_a}{R\cdot T}-\frac{\tau\cdot\lambda\cdot N}{2\cdot S\cdot R\cdot T}\right)\right)-\exp\left(\frac{-E_\ell}{R\cdot T}\right)\right\} \tag{6-11}$$

Case 3:	The activation energy $\mathbf{E_a}$ is greater than the limiting energy $\mathbf{E_l}$, but the energy level $\mathbf{E_a-\tau\lambda N/2S}$ is less than the limiting energy level $\mathbf{E_l}$ (Figure 6-9). The strain rate equation is now: $$\dot{\varepsilon}=X\cdot\frac{k\cdot T}{h\cdot i}\cdot\left\{\exp\left(-\left(\frac{E_a}{R\cdot T}-\frac{\tau\cdot\lambda\cdot N}{2\cdot S\cdot R\cdot T}\right)\right)-\exp\left(\frac{-E_\ell}{R\cdot T}\right)\right\} \tag{6-12}$$ Equation (6-12) appears to be identical to equation (6-11), but the boundary conditions differ.

Case 4:	The activation energy $\mathbf{E_a}$ is greater than the limiting energy $\mathbf{E_l}$ and the energy level $\mathbf{E_a-\tau\lambda N/2S}$ is greater than the limiting energy level $\mathbf{E_l}$ (Figure 6-10). The strain rate will be equal to zero in this case.

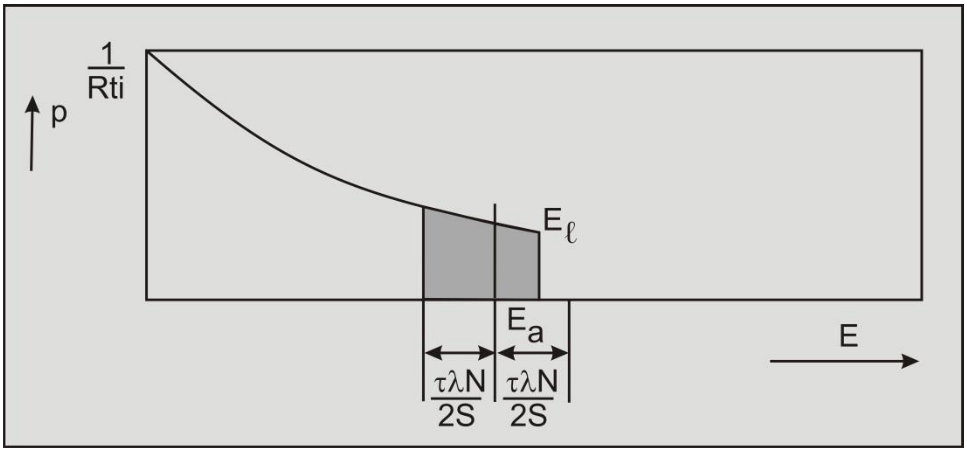

Figure 6-8: The probability of net activation in case 2.

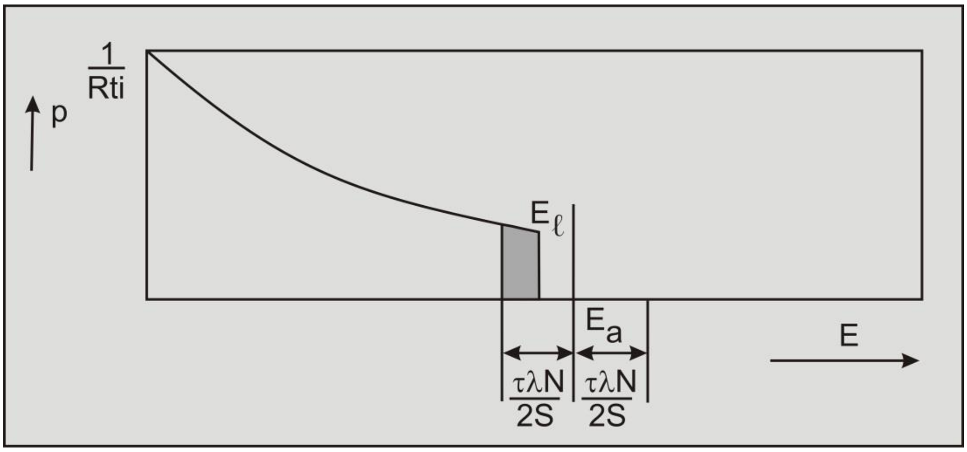

Figure 6-9: The probability of net activation in case 3.

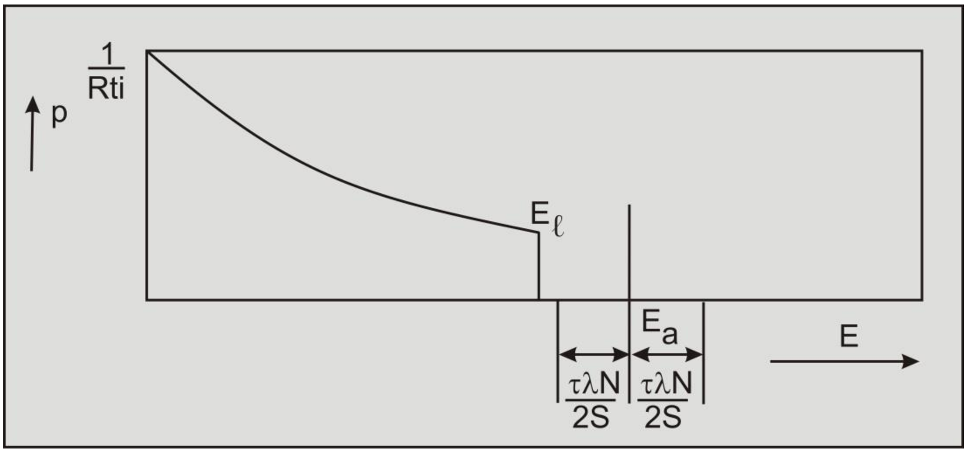

Figure 6-10: The probability of net activation in case 4.

The cases 1 and 2 are similar to the case considered by Mitchell (1976) and still do not permit true cohesion and adhesion. Case 4 considers particles at rest without changing position within the particle matrix. Case 3 considers a material on which an external shear stress of certain magnitude must be applied to allow the particles to cross energy barriers, resulting in a yield stress (true cohesion or adhesion). From equation (6-12) the following equation for the shear stress can be derived:

$$\tau = (\mathbf{E_a} - \mathbf{E_\ell}) \cdot \frac{\mathbf{2 \cdot S}}{\boldsymbol{\lambda \cdot N}} + \mathbf{R \cdot T} \cdot \frac{\mathbf{2 \cdot S}}{\boldsymbol{\lambda \cdot N}} \cdot \boldsymbol{\ell}\mathbf{n}\left(\mathbf{1} + \frac{\dot{\boldsymbol{\varepsilon}}}{\dot{\boldsymbol{\varepsilon}}_\mathbf{0}}\right) \tag{6-13}$$

with: $\dot{\boldsymbol{\varepsilon}}_\mathbf{0} = \frac{\mathbf{X \cdot k \cdot T}}{\mathbf{h \cdot i}} \cdot \mathbf{exp}\left(\frac{-\mathbf{E_\ell}}{\mathbf{R \cdot T}}\right)$

According to Mitchell (1976), if no shattering of particles occurs, the relation between the number of bonds **S** and the effective stress σ_e can be described by the following equation:

$$\mathbf{S = a + b.\sigma_e} \tag{6-14}$$

Lobanov and Joanknecht (1980) confirmed this relation implicitly for pressures up to 10 bars for clay and paraffin wax. At very high pressures they found an exponential relation that might be caused by internal failure of the particles. For the friction between soil and metal Zeng and Yao (1988) also used equation (6-14), but for the internal friction Zeng and Yao (1991) used a logarithmic relationship, which contradicts Lobanov and Joanknecht and Mitchell, although it can be shown by Taylor series approximation that a logarithmic relation can be transformed into a linear relation for values of the argument of the logarithm close to 1. Since equation (6-14) contains the effective stress it is necessary that the clay used, is fully consolidated. Substituting equation (6-14) in equation (6-13) gives:

$$\tau = a \cdot \left\{ (E_a - E_\ell) \cdot \frac{2}{\lambda \cdot N} + R \cdot T \cdot \frac{2}{\lambda \cdot N} \cdot \ell n \left(1 + \frac{\dot{\varepsilon}}{\dot{\varepsilon}_0} \right) \right\} + b \cdot \left\{ (E_a - E_\ell) \cdot \frac{2}{\lambda \cdot N} + R \cdot T \cdot \frac{2}{\lambda \cdot N} \cdot \ell n \left(1 + \frac{\dot{\varepsilon}}{\dot{\varepsilon}} \right) \right\} \cdot \sigma_e \tag{6-15}$$

Equation (6-15) is of the same form as the Mohr-Coulomb failure criterion:

$$\tau = \tau_c + \sigma_e . \tan(\varphi) \tag{6-16}$$

Equation (6-15), however, allows the strain rate to become zero, which is not possible in the equation derived by Mitchell (1976). The Mitchell equation and also the equations derived by Zeng and Yao (1988) and (1991) will result in a negative shear strength at small strain rates.

6.2.4. Comparison of Proposed Theory with some other Theories

The proposed new theory is in essence similar to the theory developed by Mitchell (1976) which was based on the "rate process theory" as proposed by Eyring (1941). It was, however, necessary to use simplifications to obtain the equation in a useful form. The following formulation for the shear stress as a function of the strain rate has been derived by Mitchell by simplification of equation (6-6):

$$\tau = a \cdot \left\{ E_a \cdot \frac{2}{\lambda \cdot N} + R \cdot T \cdot \frac{2}{\lambda \cdot N} \cdot \ell n \left(\frac{\dot{\varepsilon}}{B} \right) \right\} + b \cdot \left\{ E_a \cdot \frac{2}{\lambda \cdot N} + R \cdot T \cdot \frac{2}{\lambda \cdot N} \cdot \ell n \left(\frac{\dot{\varepsilon}}{B} \right) \right\} \cdot \sigma_e \tag{6-17}$$

with: $\mathbf{B = \frac{X.k.T}{h}}$

This equation is not valid for very small strain rates, because this would result in a negative shear stress. It should be noted that for very high strain rates the equations (6-15) and (6-17) will have exactly the same form. Zeng and Yao (1991) derived the following equation by simplification of equation (6-6) and by adding some empirical elements:

$$\ln(\tau) = C_1 + C_2 \cdot \ln(\dot{\varepsilon}) + C_3 \cdot \ln(1 + C_4 \cdot \sigma_e) \tag{6-18}$$

Rewriting equation (6-18) in a more explicit form gives:

$$\tau = \exp(C_1) \cdot (\dot{\varepsilon})^{C_2} \cdot (1 + C_4 \cdot \sigma_e)^{C_3} \tag{6-19}$$

Equation (6-19) is valid for strain rates down to zero, but not for a yield stress. With respect to the strain rate, equation (6-19) is the equation of a fluid behaving according to the power law named "power law fluids". It should be noted however that equation (6-19)(19) cannot be derived from equation (6-6) directly and thus should be considered as an empirical equation. If the coefficient $\mathbf{C_3}$ equals 1, the relation between shear stress and effective stress is similar to the relation found by Mitchell (1976). For the friction between the soil (clay and loam) and metal Zeng and Yao (1988) derived the following equation by simplification of equation (6-6):

$$\tau_b = \tau_{ya} + C_5 \cdot \ln(\dot{\varepsilon}) + \sigma_e \cdot \tan(\delta) = \tau_a + \sigma_e \cdot \tan(\delta) \tag{6-20}$$

Equation (6-20) allows a yield stress, but does not allow the sliding velocity to become zero. An important conclusion of Yao and Zeng is that pasting soil on the metal surface slightly increases the friction meaning that the friction between soil and metal almost equals the shear strength of the soil.
The above-mentioned researchers based their theories on the rate process theory, other researchers derived empirical equations. Turnage and Freitag (1970) observed that for saturated clays the cone resistance varied with the penetration rate according to:

$$F = a.v^b \tag{6-21}$$

With values for the exponent ranging from 0.091 to 0.109 Wismer and Luth (1972B) and (1972A) confirmed this relation and found a value of 0.100 for the exponent, not only for cone penetration tests but also for the relation between the cutting forces and the cutting velocity when cutting clay with straight blades. Hatamura and Chijiiwa (1975), (1976), (1976), (1977) and (1977) also confirmed this relation for clay and loam cutting and found an exponent of 0.089.
Soydemir (1977) derived an equation similar to the Mitchell equation. From the data measured by Soydemir a relation according to equation (6-21) with an exponent of 0.101 can be derived. This confirms both the Mitchell approach and the power law approach.

6.2.5. Verification of the Theory Developed

The theory developed differs from the other theories mentioned in the previous paragraph, because the resulting equation (6-15) allows a yield strength (cohesion or adhesion). At a certain consolidation pressure level equation (6-15) can be simplified to:

$$\tau = \tau_y + \tau_0 \cdot \ln\left(1 + \frac{\dot{\varepsilon}}{\dot{\varepsilon}_0}\right) \tag{6-22}$$

If **(dε/dt)/(dε₀/dt)** << **1**, equation (6-22) can be approximated by:

$$\tau = \tau_y + \tau_0 \cdot \frac{\dot{\varepsilon}}{\dot{\varepsilon}_0} \tag{6-23}$$

This approximation gives the formulation of a Bingham fluid. If the yield strength τ_y is zero, equation (6-23) represents a Newtonian fluid. If **(dε/dt)/(dε₀/dt)** >> **1**, equation (6-22) can be approximated by:

$$\tau = \tau_y + \tau_0 \cdot \ln\left(\frac{\dot{\varepsilon}}{\dot{\varepsilon}_0}\right) \tag{6-24}$$

This approximation is similar to equation (6-17) as derived by Mitchell.
If **(dε/dt)/(dε₀/dt)** >> **1** and $\tau - \tau_y \ll \tau_y$, equation (6-22) can be approximated by:

$$\tau = \tau_y \cdot \left(\frac{\dot{\varepsilon}}{\dot{\varepsilon}_0}\right)^{\tau_0/\tau_y} \tag{6-25}$$

This approximation is similar to equation (6-21) as found empirically by Wismer and Luth (1972B) and many other researchers. The equation (6-15) derived in this paper, the equation (6-17) derived by Mitchell and the empirical equation (6-21) as used by many researchers have been fitted to data obtained by Hatamura and Chijiiwa (1975), (1976), (1976), (1977) and (1977). This is illustrated in Figure 6-11 with a logarithmic horizontal axis. Figure 6-12 gives an illustration with both axis logarithmic. These figures show that the data obtained by Hatamura and Chijiiwa fit well and that the above described approximations are valid.
The values used are τ_y **= 28 kPa,** τ_0 **= 4 kPa** and ε_0 **= 0.03 /s**.

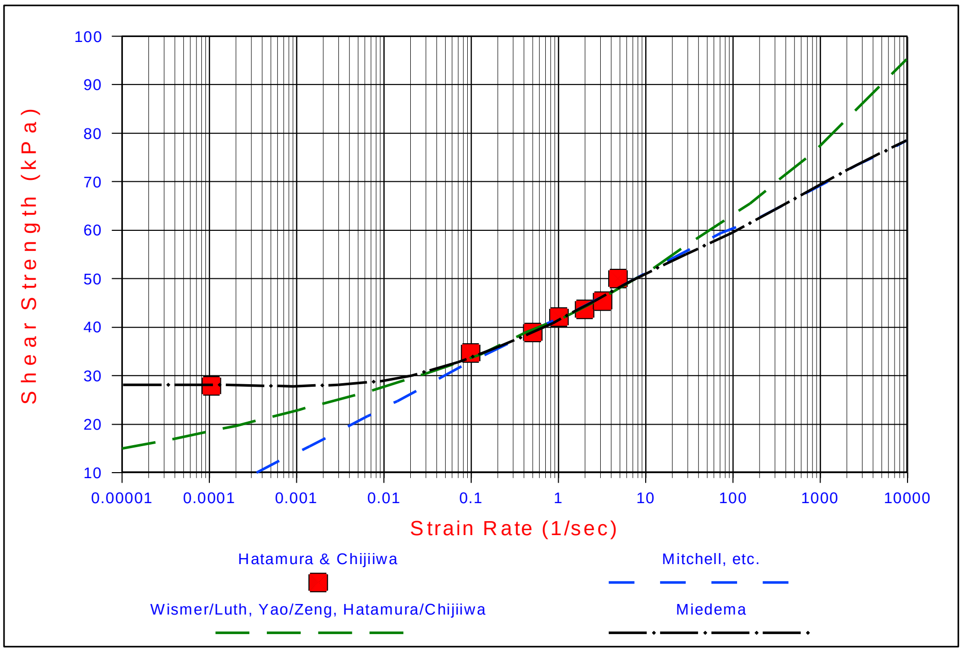

Figure 6-11: Shear stress as a function of strain rate with the horizontal axis logarithmic.

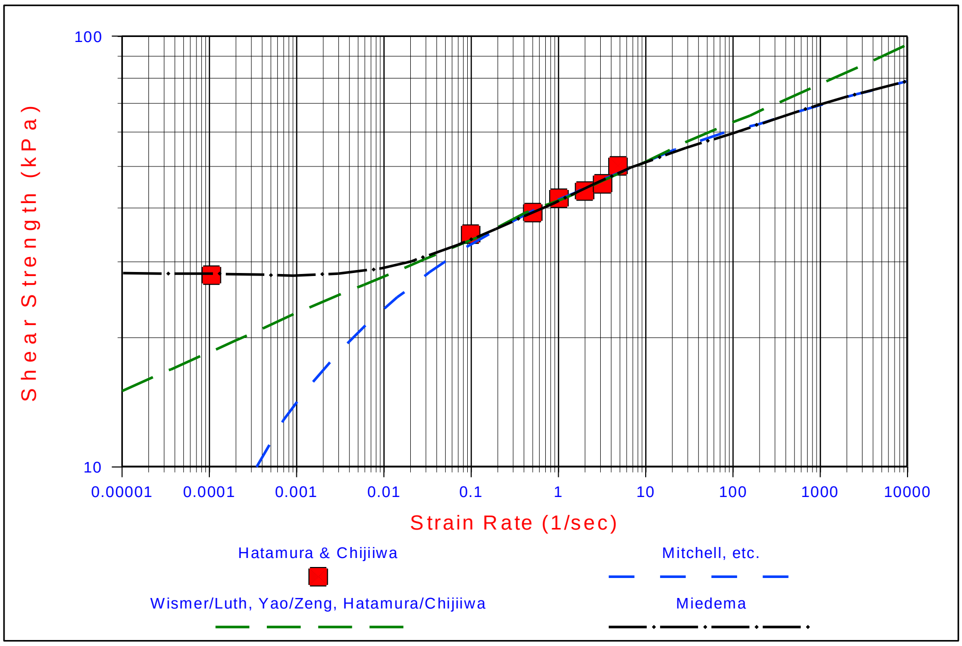

Figure 6-12: Shear stress as a function of strain rate with logarithmic axis

It is assumed that adhesion and cohesion can both be modeled according to equation (6-22). The research carried out by Zeng and Yao (1991) validates the assumption that this is true for adhesion. In more recent research Kelessidis et al. (2007) and (2008) utilizes two rheological models, the Herschel-Bulkley model and the Casson model. The Herschel Bulkley model can be described by the following equation:

$$\tau = \tau_{y,HB} + K \cdot \left(\dot{\varepsilon}\right)^{n} \tag{6-26}$$

The Casson model can be described with the following equation:

$$\sqrt{\tau} = \sqrt{\tau_{y,Ca}} + \sqrt{\mu_{Ca} \cdot \dot{\varepsilon}} \tag{6-27}$$

Figure 6-13 compares these models with the model as derived in this paper. It is clear that for the high strain rates the 3 models give similar results. These high strain rates are relevant for cutting processes in dredging and offshore applications.

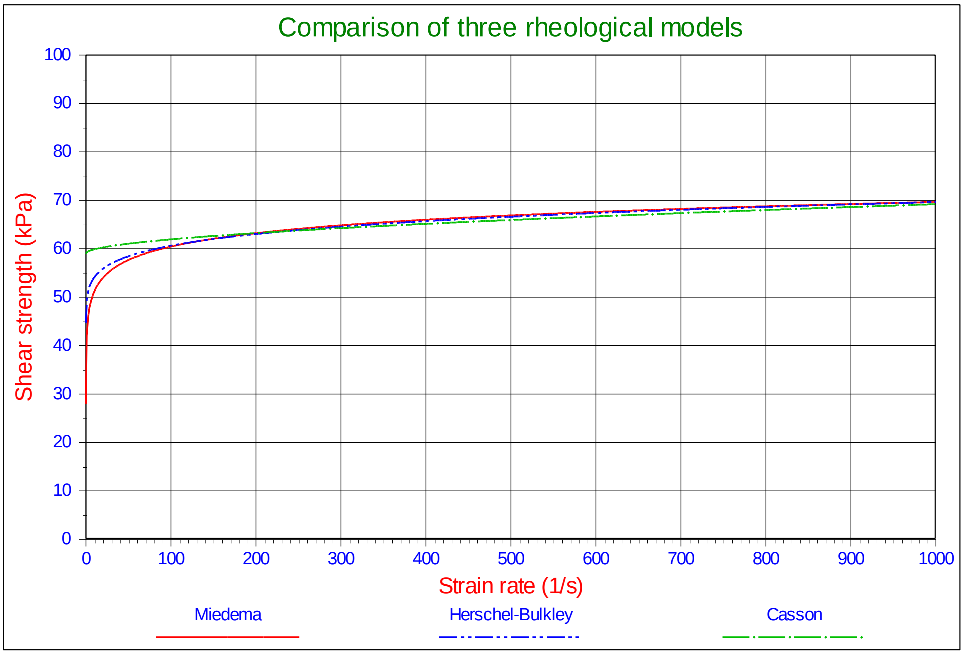

Figure 6-13: Comparison of 3 rheological models.

6.2.6. Resulting Equations

The strain rate is the rate of change of the strain with respect to time and can be defined as a velocity divided by a characteristic length. For the cutting process it is important to relate the strain rate to the cutting (deformation) velocity $\mathbf{v_c}$ and the layer thickness $\mathbf{h_i}$. Since the deformation velocity is different for the cohesion in the shear plane and the adhesion on the blade, two different equations are found for the strain rate as a function of the cutting velocity.

$$\dot{\varepsilon}_c = 1.4 \cdot \frac{v_c}{h_i} \cdot \frac{\sin(\alpha)}{\sin(\alpha+\beta)} \tag{6-28}$$

$$\dot{\varepsilon}_a = 1.4 \cdot \frac{v_c}{h_i} \cdot \frac{\sin(\beta)}{\sin(\alpha+\beta)} \tag{6-29}$$

This results in the following two equations for the multiplication factor for cohesion (internal shear strength) and adhesion (external shear strength). With $\boldsymbol{\tau_y}$ the cohesion at zero strain rate.

$$\lambda_c = 1 + \frac{\tau_0}{\tau_y} \cdot \ln\left(1 + \frac{1.4 \cdot \frac{v_c}{h_i} \cdot \frac{\sin(\alpha)}{\sin(\alpha+\beta)}}{\dot{\varepsilon}_0}\right) \tag{6-30}$$

$$\lambda_a = 1 + \frac{\tau_0}{\tau_y} \cdot \ln\left(1 + \frac{1.4 \cdot \frac{v_c}{h_i} \cdot \frac{\sin(\beta)}{\sin(\alpha+\beta)}}{\dot{\varepsilon}_0}\right) \tag{6-31}$$

With:

$$\tau_0 / \tau_y = 0.1428, \quad \dot{\varepsilon}_0 = 0.03 \tag{6-32}$$

Van der Schrieck (1996) published a graph showing the effect of the deformation rate on the specific energy when cutting clay. Although the shape of the curves found are a bit different from the shape of the curves found with equations (6-30) and (6-31), the multiplication factor for, in dredging common deformation rates, is about 2. This factor matches the factor found with the above equations.

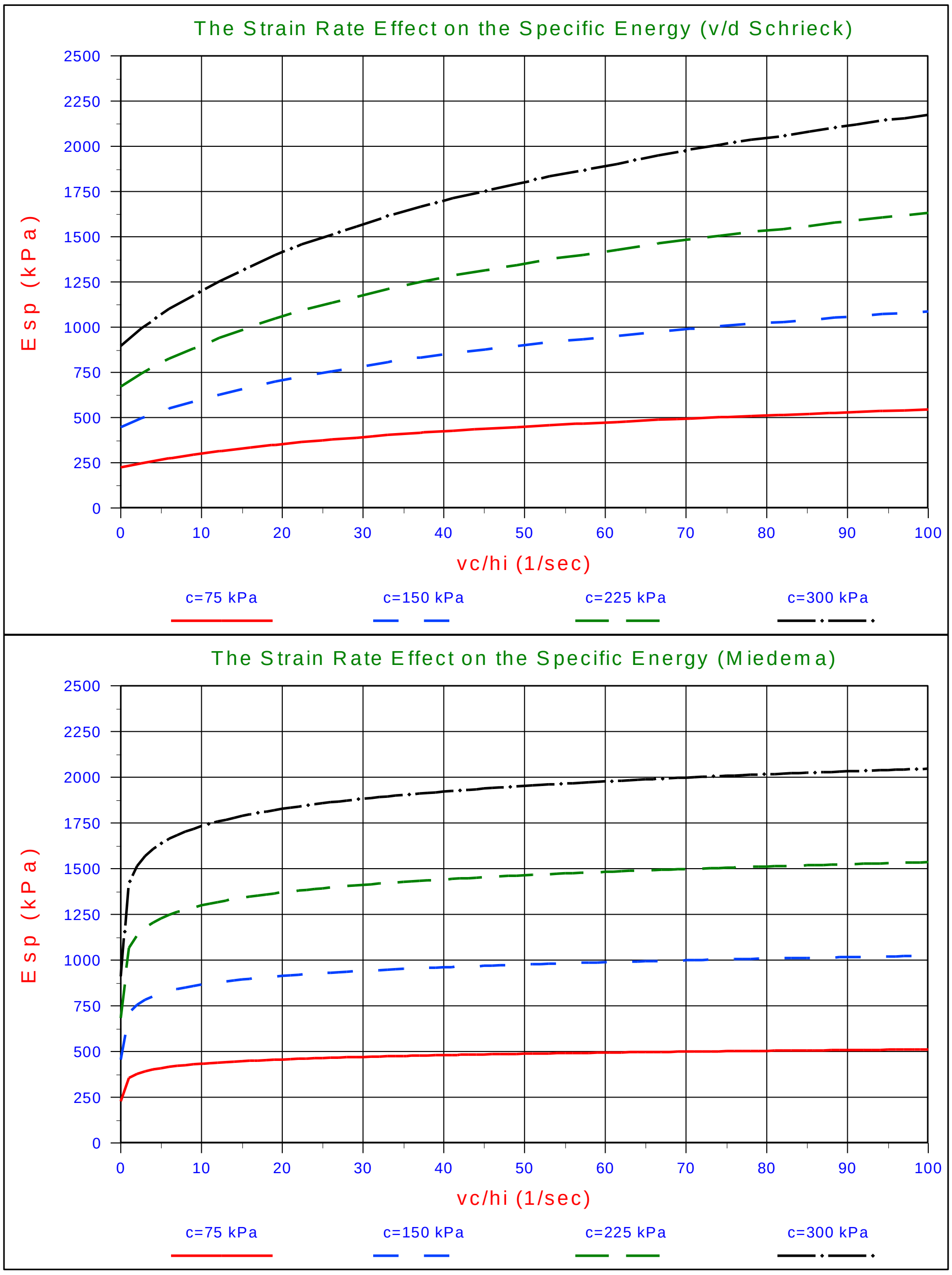

Figure 6-14: Comparison of the model developed with v/d Schriecks (1996) model.

6.3. The Flow Type

6.3.1. The Forces

The most common failure mechanism in clay is the **Flow Type** as is shown in Figure 6-15, which will be considered first. The **Curling Type** and the **Tear Type** may occur under special circumstances and will be derived from the equations of the **Flow Type**.

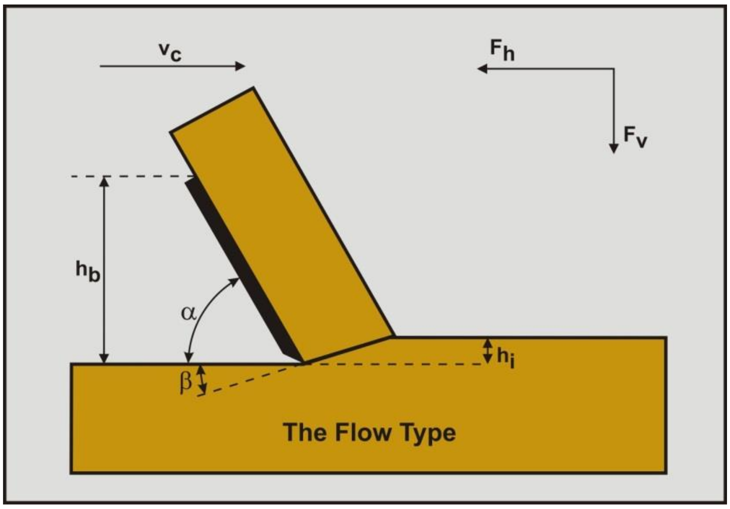

Figure 6-15: The Flow Type cutting mechanism when cutting clay.

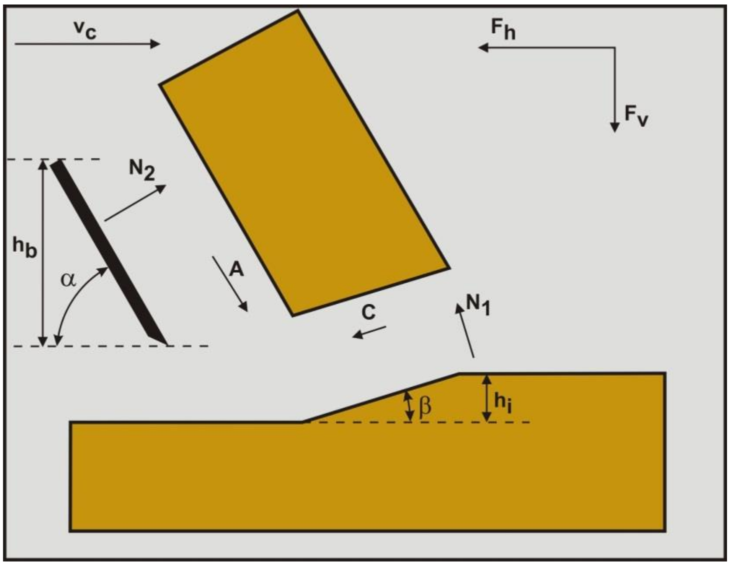

Figure 6-16: The forces on the layer cut in clay.

Figure 6-16 illustrates the forces on the layer of soil cut. The forces shown are valid in general. The forces acting on this layer are:

1. A normal force acting on the shear surface $\mathbf{N_1}$ resulting from the effective grain stresses.
2. A shear force **C** as a result of pure cohesion τ_c. This force can be calculated by multiplying the cohesion **c**/cohesive shear strength τ_c with the area of the shear plane.
3. A force normal to the blade $\mathbf{N_2}$ resulting from the effective grain stresses.
4. A shear force **A** as a result of pure adhesion between the soil and the blade τ_a. This force can be calculated by multiplying the adhesion **a**/adhesive shear strength τ_a of the soil with the contact area between the soil and the blade.

The normal force $\mathbf{N_1}$ and the shear force $\mathbf{S_1}$ can be combined to a resulting grain force $\mathbf{K_1}$.

$$\mathbf{K_1 = \sqrt{N_1^2 + S_1^2}} \tag{6-33}$$

The forces acting on a straight blade when cutting soil, can be distinguished as:

- A force normal to the blade $\mathbf{N_2}$ resulting from the effective grain stresses.
- A shear force **A** as a result of pure adhesion between the soil and the blade $\boldsymbol{\tau_a}$. This force can be calculated by multiplying the adhesive shear strength $\boldsymbol{\tau_a}$ of the soil with the contact area between the soil and the blade.

These forces are shown in Figure 6-17. If the forces $\mathbf{N_2}$ and $\mathbf{S_2}$ are combined to a resulting force $\mathbf{K_2}$ and the adhesive force and the water under pressures are known, then the resulting force $\mathbf{K_2}$ is the unknown force on the blade. By taking the horizontal and vertical equilibrium of forces an expression for the force $\mathbf{K_2}$ on the blade can be derived.

$$\mathbf{K_2 = \sqrt{N_2^2 + S_2^2}} \tag{6-34}$$

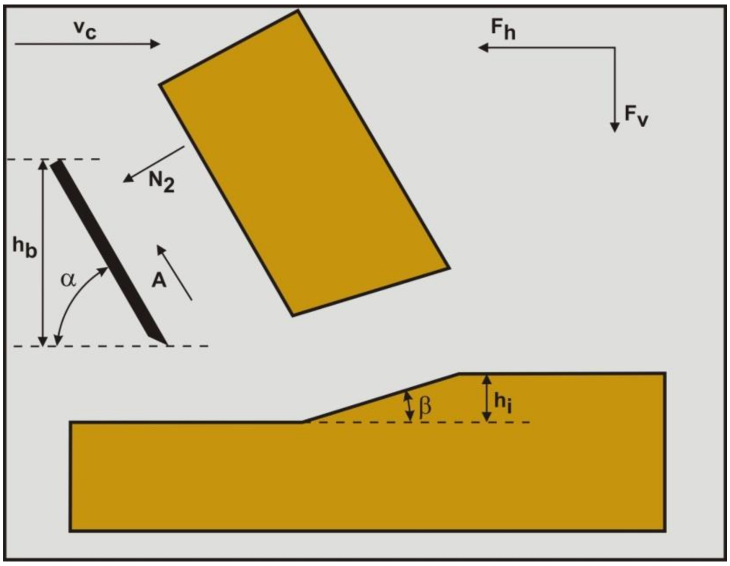

Figure 6-17: The forces on the blade in clay.

Pure clay under undrained conditions follows the **φ=0** concept, meaning that effectively there is no internal friction and thus there is also no external friction. Under drained conditions clay will have some internal friction, although smaller than sand. The reason for this is the very low permeability of the clay. If the clay is compressed with a high strain rate, the water in the pores cannot flow away resulting in the pore water carrying the extra pressure, the grain stresses do not change. If the grain stresses do not change, the shear stresses according to Coulomb friction do not change and effectively there is no relation between the extra normal stresses and the shear stresses, so apparently **φ=0**. At very low strain rates the pore water can flow out and the grains have to carry the extra normal stresses, resulting in extra shear stresses. During the cutting of clay, the strain rates, deformation rates, are so big that the internal and external friction angles can be considered to be zero. The adhesive and cohesive forces play a dominant role, so that gravity and inertia can be neglected.

The horizontal equilibrium of forces:

$$\mathbf{\sum F_h = K_1 \cdot \sin(\beta) + C \cdot \cos(\beta) - A \cdot \cos(\alpha) - K_2 \cdot \sin(\alpha) = 0} \tag{6-35}$$

The vertical equilibrium of forces:

$$\mathbf{\sum F_v = - K_1 \cdot \cos(\beta) + C \cdot \sin(\beta) + A \cdot \sin(\alpha) - K_2 \cdot \cos(\alpha) = 0} \tag{6-36}$$

The force $\mathbf{K_1}$ on the shear plane is now:

$$K_1 = \frac{-C \cdot \cos(\alpha+\beta) + A}{\sin(\alpha+\beta)} \tag{6-37}$$

The force K_2 on the blade is now:

$$K_2 = \frac{C - A \cdot \cos(\alpha+\beta)}{\sin(\alpha+\beta)} \tag{6-38}$$

From equation (6-38) the forces on the blade can be derived. On the blade a force component in the direction of cutting velocity F_h and a force perpendicular to this direction F_v can be distinguished.

$$F_h = K_2 \cdot \sin(\alpha) + A \cdot \cos(\alpha) \tag{6-39}$$

$$F_v = K_2 \cdot \cos(\alpha) - A \cdot \sin(\alpha) \tag{6-40}$$

With the relations for the cohesive force **C**, the adhesive force **A** and the adhesion/cohesion ratio **r** (the ac ratio **r**):

$$C = \frac{\lambda \cdot c \cdot h_i \cdot w}{\sin(\beta)} \tag{6-41}$$

$$A = \frac{\lambda \cdot a \cdot h_b \cdot w}{\sin(\alpha)} \tag{6-42}$$

$$r = \frac{a \cdot h_b}{c \cdot h_i} \tag{6-43}$$

The horizontal F_h and vertical F_v cutting forces can be determined according to:

$$F_h = \frac{C \cdot \sin(\alpha) + A \cdot \sin(\beta)}{\sin(\alpha+\beta)} = \frac{\frac{\lambda \cdot c \cdot h_i \cdot w}{\sin(\beta)} \cdot \sin(\alpha) + \frac{\lambda \cdot a \cdot h_b \cdot w}{\sin(\alpha)} \cdot \sin(\beta)}{\sin(\alpha+\beta)} = \lambda \cdot c \cdot h_i \cdot w \cdot \frac{\frac{\sin(\alpha)}{\sin(\beta)} + r \cdot \frac{\sin(\beta)}{\sin(\alpha)}}{\sin(\alpha+\beta)} \tag{6-44}$$

$$F_v = \frac{C \cdot \cos(\alpha) - A \cdot \cos(\beta)}{\sin(\alpha+\beta)} = \frac{\frac{\lambda \cdot c \cdot h_i \cdot w}{\sin(\beta)} \cdot \cos(\alpha) - \frac{\lambda \cdot a \cdot h_b \cdot w}{\sin(\alpha)} \cdot \cos(\beta)}{\sin(\alpha+\beta)} = \lambda \cdot c \cdot h_i \cdot w \cdot \frac{\frac{\cos(\alpha)}{\sin(\beta)} - r \cdot \frac{\cos(\beta)}{\sin(\alpha)}}{\sin(\alpha+\beta)} \tag{6-45}$$

The normal force on the shear plane is now equal to the force K_1, because the internal friction angle φ is zero:

$$N_1 = \frac{-C \cdot \cos(\alpha+\beta) + A}{\sin(\alpha+\beta)} \tag{6-46}$$

The normal force on the blade is now equal to the force K_2, because the external friction angle δ is zero:

$$N_2 = \frac{C - A \cdot \cos(\alpha+\beta)}{\sin(\alpha+\beta)} \tag{6-47}$$

Equations (6-46) and (6-47) show that both the normal force on the shear plane N_1 and the normal force on the blade N_2 may become negative. This depends on the **ac** ratio between the adhesive and the cohesive forces **r** and on the blade angle α and shear angle β. A negative normal force on the blade will result in the **Curling Type** of cutting mechanism, while a negative normal force on the shear plane will result in the **Tear Type** of cutting mechanism. If both normal forces are positive, the **Flow Type** of cutting mechanism will occur.

6.3.2. Finding the Shear Angle

There is one unknown in the equations and that is the shear angle β**.** This angle has to be known to determine cutting forces, specific energy and power.

$$F_h = \lambda \cdot c \cdot h_i \cdot w \cdot \left(\frac{\frac{\sin(\alpha)}{\sin(\beta)} + r \cdot \frac{\sin(\beta)}{\sin(\alpha)}}{\sin(\alpha+\beta)} \right) \quad \text{with: } r = \frac{a \cdot h_b}{c \cdot h_i} \tag{6-48}$$

Equation (6-48) for the horizontal cutting force F_h can be rewritten as:

$$F_h = \lambda \cdot c \cdot h_i \cdot w \cdot \left(\frac{\sin^2(\alpha) + r \cdot \sin^2(\beta)}{\sin(\alpha+\beta) \cdot \sin(\beta) \cdot \sin(\alpha)} \right) \tag{6-49}$$

The strengthening factor λ, which is not very sensitive for β in the range of cutting velocities v_c as applied in dredging, can be determined by:

$$\lambda = \left(1 + \frac{\tau_0}{\tau_y} \cdot \ln\left(1 + \frac{1.4 \cdot \frac{v_c}{h_i} \cdot \frac{\sin(\alpha)}{\sin(\alpha+\beta)}}{\dot{\varepsilon}_0} \right) \right) \tag{6-50}$$

$$\text{With: } \tau_0 / \tau_y = 0.1428 \text{ and } \dot{\varepsilon}_0 = 0.03$$

The shear angle β is determined by the case where the horizontal cutting force F_h is at a minimum, based on the minimum energy principle (omitting the strengthening factor λ).

$$\frac{\partial F_h}{\partial \beta} = \frac{2 \cdot r \cdot \sin^2(\beta) \cdot \cos(\beta) \cdot \sin(\alpha+\beta) \cdot \sin(\alpha) - \sin(\alpha) \cdot \sin(\alpha + 2 \cdot \beta) \cdot \left(\sin^2(\alpha) + r \cdot \sin^2(\beta) \right)}{\sin^2(\alpha+\beta) \cdot \sin^2(\alpha) \cdot \sin^2(\beta)} = 0 \tag{6-51}$$

In the special case where there is no adhesion **a**, **r=0**, the shear angle β is:

$$\sin(\alpha + 2 \cdot \beta) = 0 \text{ for } \alpha + 2 \cdot \beta = \pi \text{ giving } \beta = \frac{\pi}{2} - \frac{\alpha}{2} \tag{6-52}$$

An approximation equation for β based on curve fitting on equation (6-51) for the range $2 < r < 0.5$ gives:

$$\beta = 1.26 \cdot e^{(-0.174 \cdot \alpha - 0.3148 \cdot r)} \text{ in radians or } \beta = 72.2 \cdot e^{(-0.003 \cdot \alpha - 0.3148 \cdot r)} \text{ in degrees} \tag{6-53}$$

For a clay, with shear strength $c = 1\ kPa$, a layer thickness of $h_i = 0.1\ m$ and a blade height of $h_b = 0.2\ m$, Figure 6-18, Figure 6-19 and Figure 6-20 give the values of the shear angle β, the horizontal cutting force F_h and the vertical cutting force F_v for different values of the adhesion/cohesion (ac) ratio r and as a function of the blade angle.

The horizontal cutting force F_h is at an absolute minimum when:

$$\alpha + \beta = \frac{\pi}{2} \tag{6-54}$$

This is however only useful if the blade angle α is free to choose. For a worst case scenario with an **ac** ratio **r=2**, meaning a high adhesion, a blade angle α of about 55º is found (see Figure 6-19), which matches blade angles as used in dredging. The fact that this does not give an optimum for weaker clays (clays with less adhesion) is not so relevant.

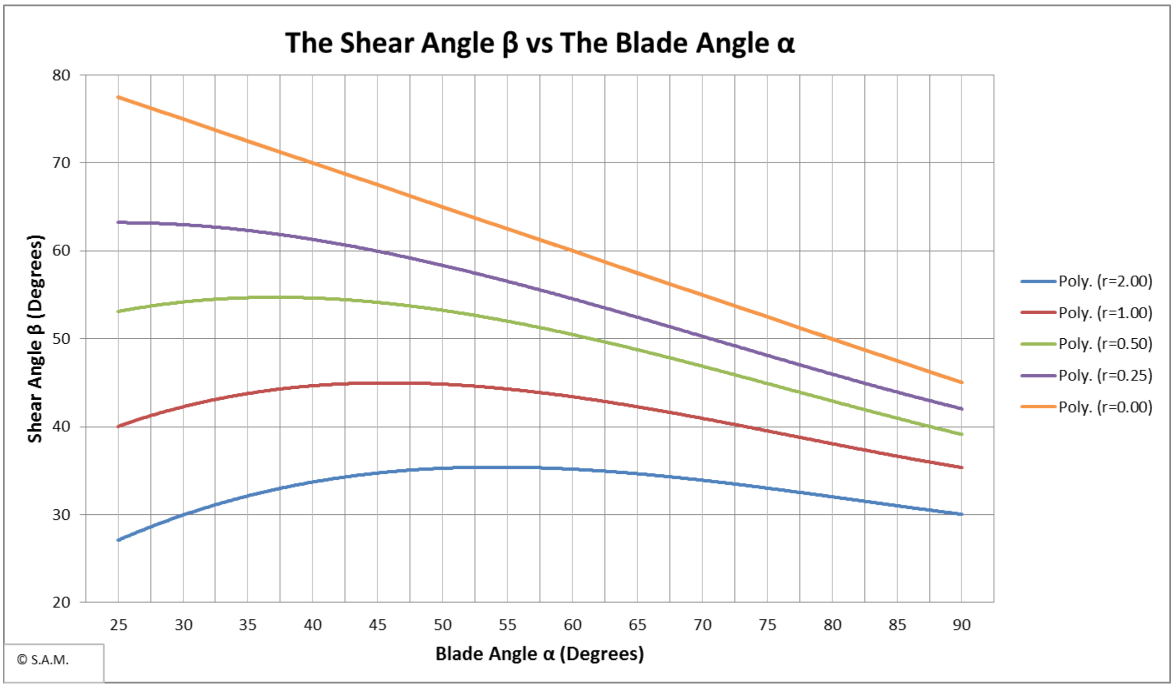

Figure 6-18: The shear angle as a function of the blade angle and the ac ratio r.

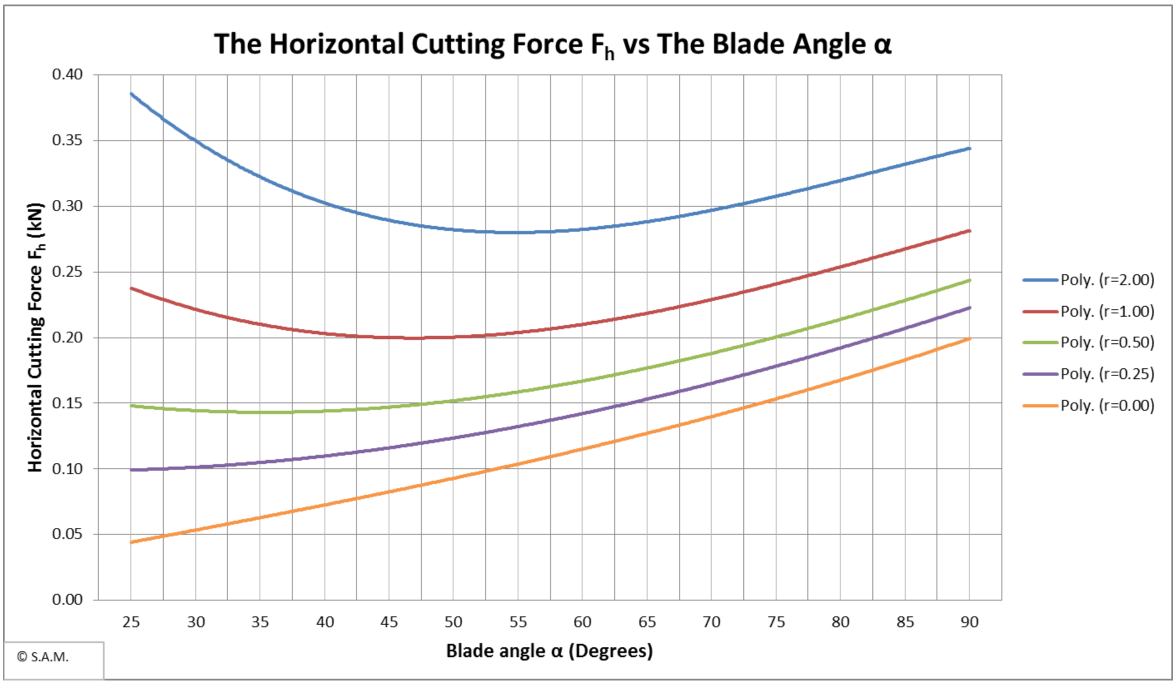

Figure 6-19: The horizontal cutting force as a function of the blade angle and the ac ratio r (c=1 kPa).

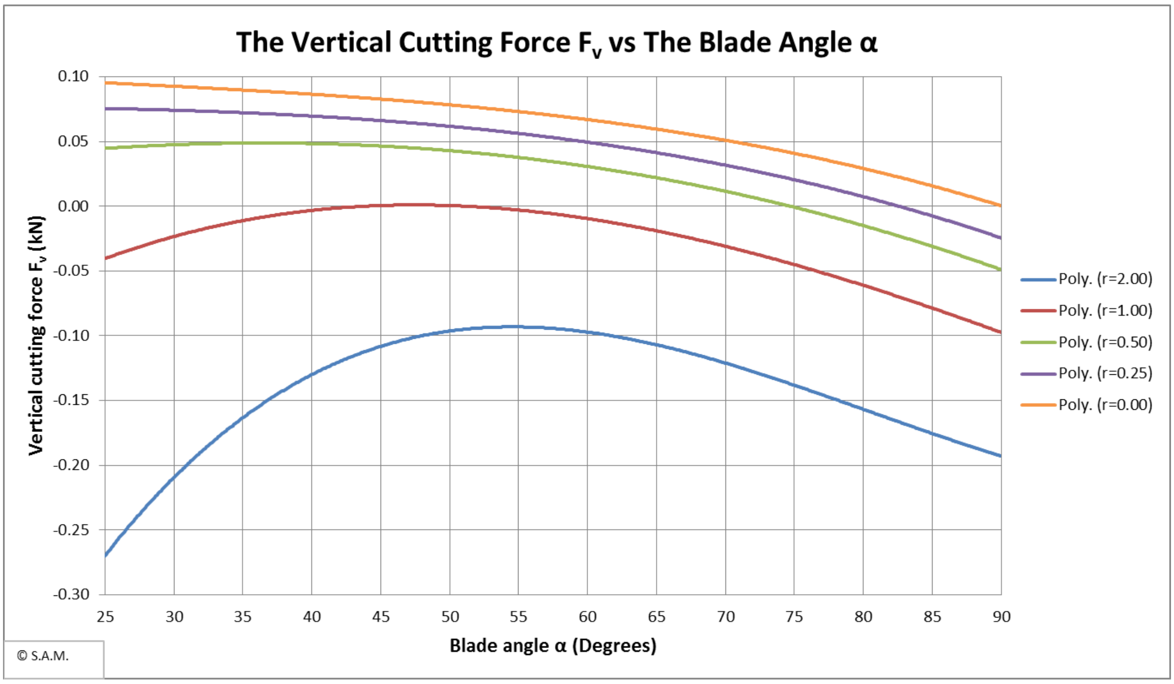

Figure 6-20: The vertical cutting force as a function of the blade angle and the ac ratio r (c=1 kPa).

See Appendix U: Clay Cutting Charts for more and higher resolution charts.

6.3.3. Specific Energy

In the dredging industry, the specific cutting energy $\mathbf{E_{sp}}$ is described as:

The amount of energy, that has to be added to a volume unit of soil (e.g. clay) to excavate the soil.

The dimension of the specific cutting energy is: kN/m² or kPa for sand and clay, while for rock often MN/m² or MPa is used.

For the case as described above, cutting with a straight blade with the direction of the cutting velocity $\mathbf{v_c}$ perpendicular to the blade (edge of the blade), the specific cutting energy $\mathbf{E_{sp}}$ is:

$$\mathbf{E_{sp}=\frac{F_h\cdot v_c}{h_i\cdot w\cdot v_c}=\frac{F_h}{h_i\cdot w}} \tag{6-55}$$

With the following equation for the horizontal cutting force $\mathbf{F_h}$:

$$\mathbf{F_h=\lambda\cdot c\cdot h_i\cdot w\cdot\left(\frac{\sin^2(\alpha)+r\cdot\sin^2(\beta)}{\sin(\alpha+\beta)\cdot\sin(\beta)\cdot\sin(\alpha)}\right)} \tag{6-56}$$

This gives for the specific cutting energy $\mathbf{E_{sp}}$:

$$\mathbf{E_{sp}=\frac{F_h\cdot v_c}{h_i\cdot w\cdot v_c}=\lambda\cdot c\cdot\left(\frac{\sin^2(\alpha)+r\cdot\sin^2(\beta)}{\sin(\alpha+\beta)\cdot\sin(\beta)\cdot\sin(\alpha)}\right)} \tag{6-57}$$

The cohesion **c** is half the UCS value, which can be related to the SPT value of the clay by a factor 12, so the cohesion is related by a factor 6 to the SPT value (see Table 6-1), further, the strengthening **λ** factor will have a value of about 2 at normal cutting velocities of meters per second, this gives:

$$\mathbf{\lambda\cdot c\approx 2\cdot 6\cdot SPT=12\cdot SPT} \tag{6-58}$$

Now a simplified equation for the specific energy $\mathbf{E_{sp}}$ is found by:

$$\mathbf{E_{sp}=12\cdot SPT\cdot\left(\frac{\sin^2(\alpha)+r\cdot\sin^2(\beta)}{\sin(\alpha+\beta)\cdot\sin(\beta)\cdot\sin(\alpha)}\right)} \tag{6-59}$$

Figure 6-21 shows the specific energy $\mathbf{E_{sp}}$ and the production $\mathbf{P_c}$ per 100 kW installed cutting power as a function of the SPT value.

Table 6-1: Guide for Consistency of Fine-Grained Soil (Lambe & Whitman (1979)).

SPT Penetration (blows/ foot)	**Estimated Consistency**	**U.C.S.** (kPa)
<2	Very Soft Clay	<24
2 - 4	Soft Clay	24 - 48
4 - 8	Medium Clay	48 - 96
8 - 16	Stiff Clay	96 – 192
16 - 32	Very Stiff Clay	192 – 384
>32	Hard Clay	>384

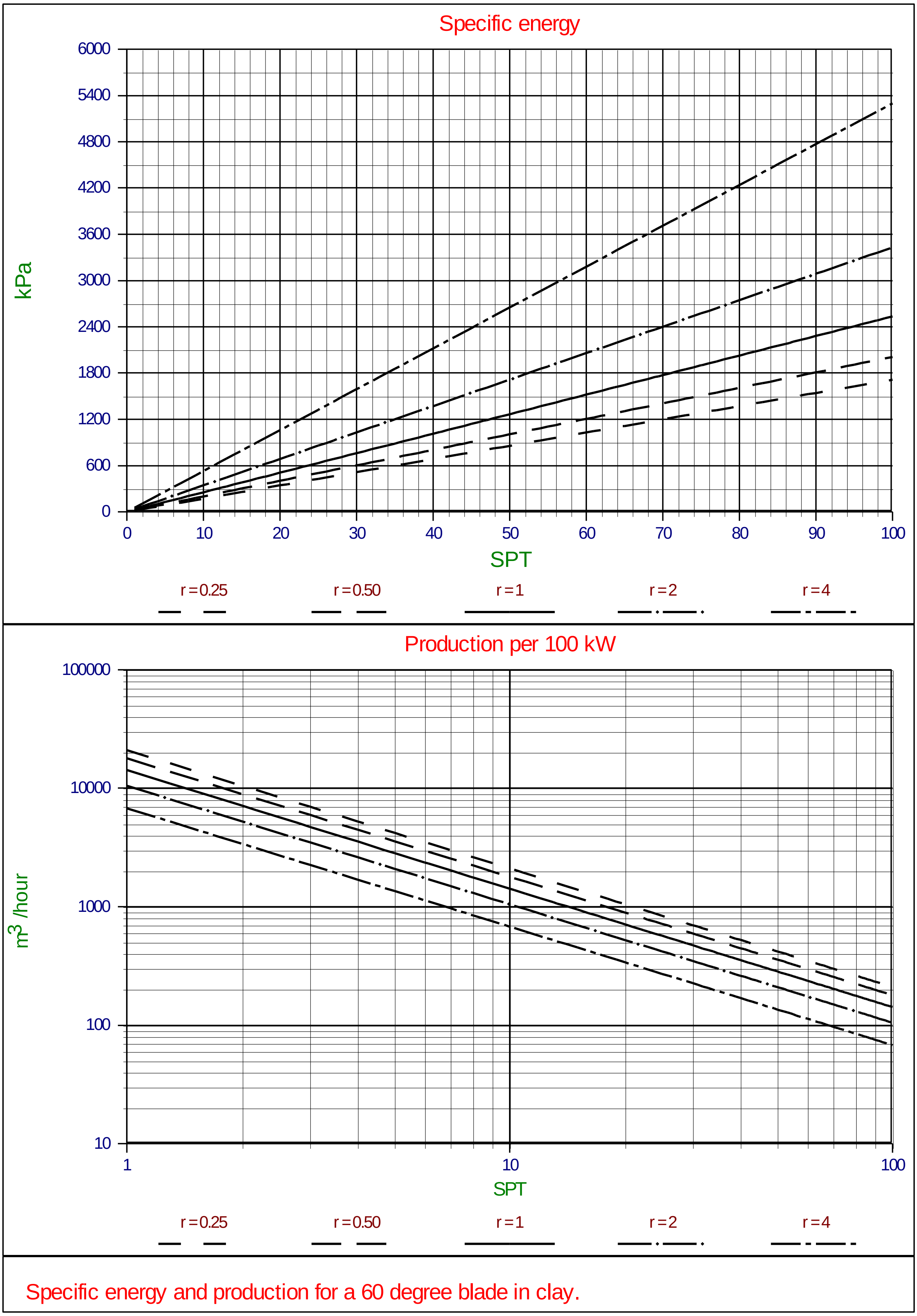

Figure 6-21: Specific energy and production in clay for a 60 degree blade.

See Appendix T: Specific Energy in Clay for more graphs on the specific energy in clay.

6.4. The Tear Type

6.4.1. Introduction

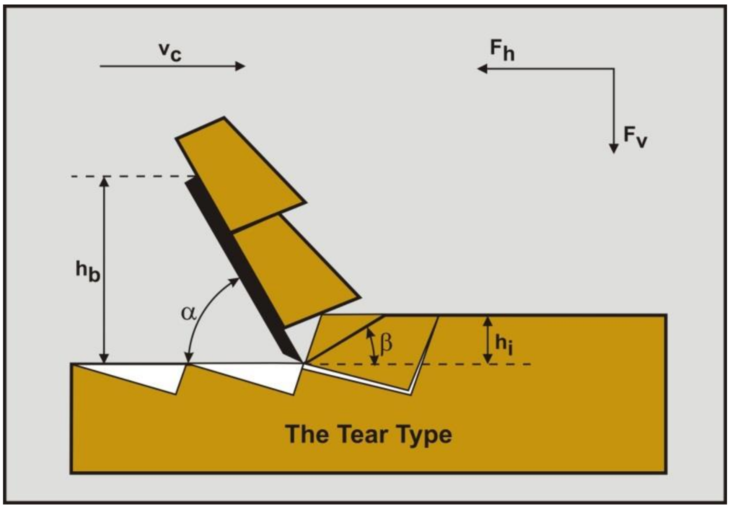

Figure 6-22: The Tear Type cutting mechanism in clay.

6.4.2. The Normal Force on the Shear Plane

$$N_1 = \frac{-C \cdot \cos(\alpha+\beta) + A}{\sin(\alpha+\beta)} \tag{6-60}$$

$$N_1 = \frac{-\dfrac{\lambda \cdot c \cdot h_i \cdot w}{\sin(\beta)} \cdot \cos(\alpha+\beta) + \dfrac{\lambda \cdot a \cdot h_b \cdot w}{\sin(\alpha)}}{\sin(\alpha+\beta)} \tag{6-61}$$

$$\sigma_{N1} = \frac{N_1 \cdot \sin(\beta)}{h_i \cdot w} \tag{6-62}$$

$$\sigma_{N1} = \frac{\sin(\beta)}{h_i \cdot w} \cdot \frac{-\dfrac{\lambda \cdot c \cdot h_i \cdot w}{\sin(\beta)} \cdot \cos(\alpha+\beta) + \dfrac{\lambda \cdot a \cdot h_b \cdot w}{\sin(\alpha)}}{\sin(\alpha+\beta)} = \lambda \cdot c \cdot \frac{-\cos(\alpha+\beta) + r \cdot \dfrac{\sin(\beta)}{\sin(\alpha)}}{\sin(\alpha+\beta)} \tag{6-63}$$

$$\sigma_{N1} - \lambda \cdot c \geq \lambda \cdot \sigma_T \tag{6-64}$$

$$\lambda \cdot c \cdot \frac{-\cos(\alpha+\beta) + r \cdot \dfrac{\sin(\beta)}{\sin(\alpha)}}{\sin(\alpha+\beta)} - \lambda \cdot c \geq \lambda \cdot \sigma_T \tag{6-65}$$

$$c' \cdot \left(\frac{r \cdot \dfrac{\sin(\beta)}{\sin(\alpha)} - \cos(\alpha+\beta) - \sin(\alpha+\beta)}{\sin(\alpha+\beta)} \right) = \sigma_T \tag{6-66}$$

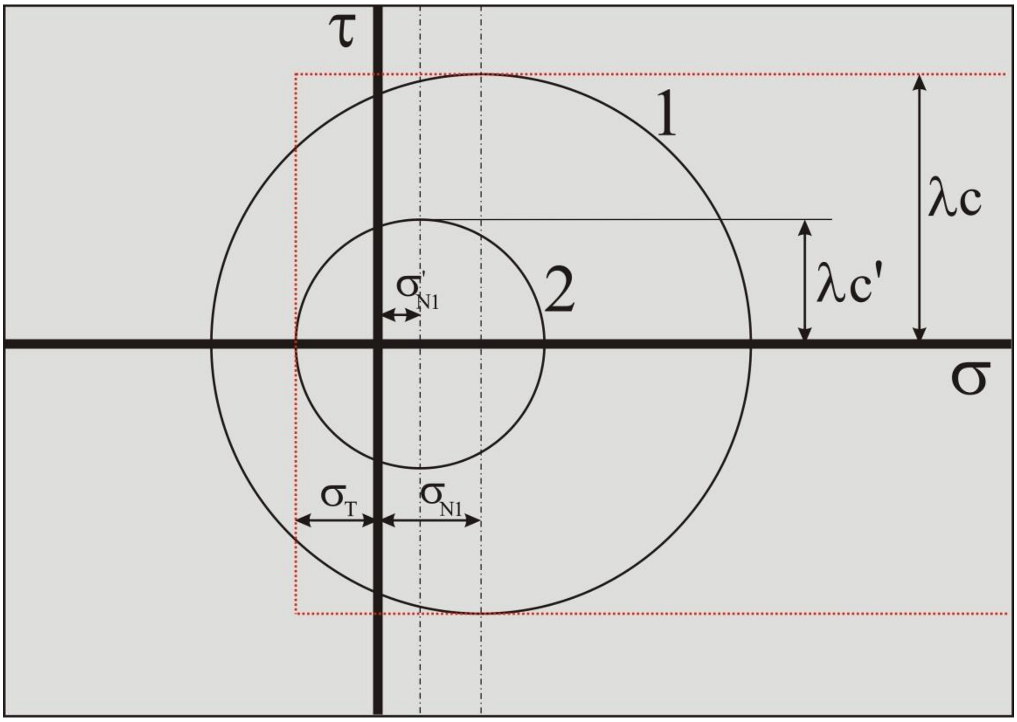

Figure 6-23: The Mohr circles when cutting clay.

$$c^{'} = \sigma_T \cdot \left(\frac{\sin(\alpha+\beta)}{r \cdot \frac{\sin(\beta)}{\sin(\alpha)} - \cos(\alpha+\beta) - \sin(\alpha+\beta)} \right) \tag{6-67}$$

$$\sigma^{'}_{N1} = \lambda \cdot c^{'} \cdot \frac{-\cos(\alpha+\beta) + r^{'} \cdot \frac{\sin(\beta)}{\sin(\alpha)}}{\sin(\alpha+\beta)} \tag{6-68}$$

$$F_h = \lambda \cdot \sigma_T \cdot h_i \cdot w \cdot \frac{\frac{\sin(\alpha)}{\sin(\beta)} + r^{'} \cdot \frac{\sin(\beta)}{\sin(\alpha)}}{r \cdot \frac{\sin(\beta)}{\sin(\alpha)} - \cos(\alpha+\beta) - \sin(\alpha+\beta)} \tag{6-69}$$

$$F_v = \lambda \cdot \sigma_T \cdot h_i \cdot w \cdot \frac{\frac{\cos(\alpha)}{\sin(\beta)} - r^{'} \cdot \frac{\cos(\beta)}{\sin(\alpha)}}{r \cdot \frac{\sin(\beta)}{\sin(\alpha)} - \cos(\alpha+\beta) - \sin(\alpha+\beta)} \tag{6-70}$$

$$r^{'} = \frac{a \cdot h_b}{c^{'} \cdot h_i} = \frac{a \cdot h_b}{\sigma_T \cdot h_i} \cdot \left(\frac{r \cdot \frac{\sin(\beta)}{\sin(\alpha)} - \cos(\alpha+\beta) - \sin(\alpha+\beta)}{\sin(\alpha+\beta)} \right) \tag{6-71}$$

6.5. The Curling Type

6.5.1. Introduction

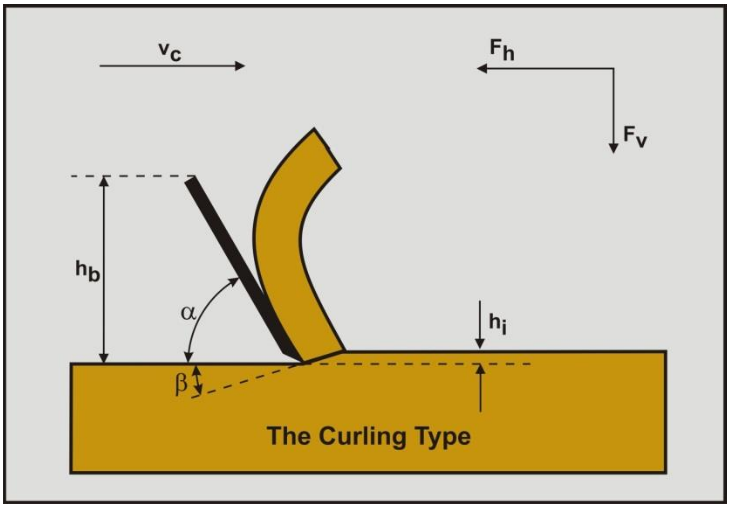

Figure 6-24: The Curling Type cutting mechanism when cutting clay.

6.5.2. The Normal Force on the Blade

$$N_2 = \frac{C - A \cdot \cos(\alpha+\beta)}{\sin(\alpha+\beta)} \tag{6-72}$$

$$N_2 = \frac{\dfrac{\lambda \cdot c \cdot h_i \cdot w}{\sin(\beta)} - \dfrac{\lambda \cdot a \cdot h_b \cdot w}{\sin(\alpha)} \cdot \cos(\alpha+\beta)}{\sin(\alpha+\beta)} = \lambda \cdot c \cdot h_i \cdot w \cdot \frac{\dfrac{1}{\sin(\beta)} - \dfrac{r}{\sin(\alpha)} \cdot \cos(\alpha+\beta)}{\sin(\alpha+\beta)} \tag{6-73}$$

$$\sigma_{N2} = \frac{N_2 \cdot \sin(\alpha)}{h_b \cdot w} \tag{6-74}$$

$$\sigma_{N2} = \frac{\sin(\alpha)}{h_b \cdot w} \cdot \frac{\dfrac{\lambda \cdot c \cdot h_i \cdot w}{\sin(\beta)} - \dfrac{\lambda \cdot a \cdot h_b \cdot w}{\sin(\alpha)} \cdot \cos(\alpha+\beta)}{\sin(\alpha+\beta)} = \lambda \cdot a \cdot \frac{\dfrac{1}{r} \cdot \dfrac{\sin(\alpha)}{\sin(\beta)} - \cos(\alpha+\beta)}{\sin(\alpha+\beta)} \tag{6-75}$$

$$\sigma_{N2} \geq 0 \tag{6-76}$$

$$\lambda \cdot a \cdot \frac{\dfrac{1}{r} \cdot \dfrac{\sin(\alpha)}{\sin(\beta)} - \cos(\alpha+\beta)}{\sin(\alpha+\beta)} \geq 0 \tag{6-77}$$

$$\frac{1}{r} \cdot \frac{\sin(\alpha)}{\sin(\beta)} = \cos(\alpha+\beta) \tag{6-78}$$

$$r' = \frac{\sin(\alpha)}{\sin(\beta)} \cdot \frac{1}{\cos(\alpha+\beta)} \tag{6-79}$$

$$F_h = \lambda \cdot c \cdot h_i \cdot w \cdot \frac{\frac{\sin(\alpha)}{\sin(\beta)} + r' \cdot \frac{\sin(\beta)}{\sin(\alpha)}}{\sin(\alpha+\beta)} = \lambda \cdot c \cdot h_i \cdot w \cdot \frac{\frac{\sin(\alpha)}{\sin(\beta)} + \frac{1}{\cos(\alpha+\beta)}}{\sin(\alpha+\beta)} = \lambda \cdot c \cdot h_i \cdot w \cdot \frac{\frac{\cos(\alpha)}{\sin(\beta)}}{\cos(\alpha+\beta)}$$	**(6-80)**
$$F_v = \lambda \cdot c \cdot h_i \cdot w \cdot \frac{\frac{\cos(\alpha)}{\sin(\beta)} - r' \cdot \frac{\cos(\beta)}{\sin(\alpha)}}{\sin(\alpha+\beta)} = \lambda \cdot c \cdot h_i \cdot w \cdot \frac{\frac{\cos(\alpha)}{\sin(\beta)} - \frac{\cos(\beta)}{\sin(\beta)} \cdot \frac{1}{\cos(\alpha+\beta)}}{\sin(\alpha+\beta)} = -\lambda \cdot c \cdot h_i \cdot w \cdot \frac{\frac{\sin(\alpha)}{\sin(\beta)}}{\cos(\alpha+\beta)}$$	**(6-81)**

6.5.3. The Equilibrium of Moments

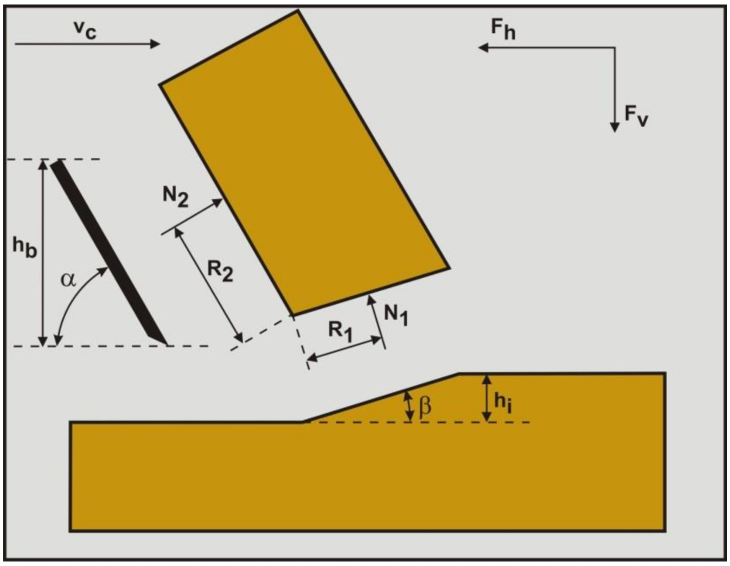

Figure 6-25: The equilibrium of moments on the layer cut in clay.

The normal force on the shear plane is now equal to the force $\mathbf{K_1}$, because the internal friction angle is zero:

$$N_1 = \frac{-C \cdot \cos(\alpha+\beta) + A}{\sin(\alpha+\beta)}$$	**(6-82)**

The normal force on the blade is now equal to the force $\mathbf{K_2}$, because the external friction angle is zero:

$$N_2 = \frac{C - A \cdot \cos(\alpha+\beta)}{\sin(\alpha+\beta)}$$	**(6-83)**

$$N_1 \cdot R_1 = N_2 \cdot R_2$$	**(6-84)**

$$R_1 = \frac{\lambda_1 \cdot h_i}{\sin(\beta)}, \; R_2 = \frac{\lambda_2 \cdot h_b'}{\sin(\alpha)}$$	**(6-85)**

$$\left(\frac{A - C \cdot \cos(\alpha+\beta)}{\sin(\alpha+\beta)}\right) \cdot \frac{\lambda_1 \cdot h_i}{\sin(\beta)} = \left(\frac{C - A \cdot \cos(\alpha+\beta)}{\sin(\alpha+\beta)}\right) \cdot \frac{\lambda_2 \cdot h_b'}{\sin(\alpha)}$$	**(6-86)**

$$\left(\frac{a \cdot h_b'}{\sin(\alpha)} - \frac{c \cdot h_i}{\sin(\beta)} \cdot \cos(\alpha+\beta)\right) \cdot \frac{\lambda_1 \cdot h_i}{\sin(\beta)} = \left(\frac{c \cdot h_i}{\sin(\beta)} - \frac{a \cdot h_b'}{\sin(\alpha)} \cdot \cos(\alpha+\beta)\right) \cdot \frac{\lambda_2 \cdot h_b'}{\sin(\alpha)}$$	**(6-87)**

$\frac{a \cdot h_b'}{\sin(\alpha)} \cdot \frac{\lambda_1 \cdot h_i}{\sin(\beta)} - \frac{c \cdot h_i}{\sin(\beta)} \cdot \frac{\lambda_1 \cdot h_i}{\sin(\beta)} \cdot \cos(\alpha+\beta) = \frac{c \cdot h_i}{\sin(\beta)} \cdot \frac{\lambda_2 \cdot h_b'}{\sin(\alpha)} - \frac{a \cdot h_b'}{\sin(\alpha)} \cdot \frac{\lambda_2 \cdot h_b'}{\sin(\alpha)} \cdot \cos(\alpha+\beta)$	(6-88)

$\frac{a \cdot h_b'}{\sin(\alpha)} \cdot \frac{\lambda_1 \cdot h_i}{\sin(\beta)} + \frac{a \cdot h_b'}{\sin(\alpha)} \cdot \frac{\lambda_2 \cdot h_b'}{\sin(\alpha)} \cdot \cos(\alpha+\beta) = \frac{c \cdot h_i}{\sin(\beta)} \cdot \frac{\lambda_2 \cdot h_b'}{\sin(\alpha)} + \frac{c \cdot h_i}{\sin(\beta)} \cdot \frac{\lambda_1 \cdot h_i}{\sin(\beta)} \cdot \cos(\alpha+\beta)$	(6-89)

$\frac{\lambda_2 \cdot a \cdot \cos(\alpha+\beta)}{\sin(\alpha) \cdot \sin(\alpha)} \cdot h_b' \cdot h_b' + \frac{\lambda_1 \cdot a - \lambda_2 \cdot c}{\sin(\alpha) \cdot \sin(\beta)} \cdot h_i \cdot h_b' - \frac{\lambda_1 \cdot c \cdot \cos(\alpha+\beta)}{\sin(\beta) \cdot \sin(\beta)} \cdot h_i \cdot h_i = 0$	(6-90)

$A \cdot x^2 + B \cdot x + C = 0$ $h_b' = x = \frac{-B - \sqrt{B^2 - 4 \cdot A \cdot C}}{2 \cdot A}$ $A = \frac{\lambda_2 \cdot a \cdot \cos(\alpha+\beta)}{\sin(\alpha) \cdot \sin(\alpha)}$ $B = \frac{\lambda_1 \cdot a - \lambda_2 \cdot c}{\sin(\alpha) \cdot \sin(\beta)} \cdot h_i$ $C = -\frac{\lambda_1 \cdot c \cdot \cos(\alpha+\beta)}{\sin(\beta) \cdot \sin(\beta)} \cdot h_i \cdot h_i$	(6-91)

if $h_b' < h_b$ then use h_b' if $h_b' \geq h_b$ then use h_b	(6-92)

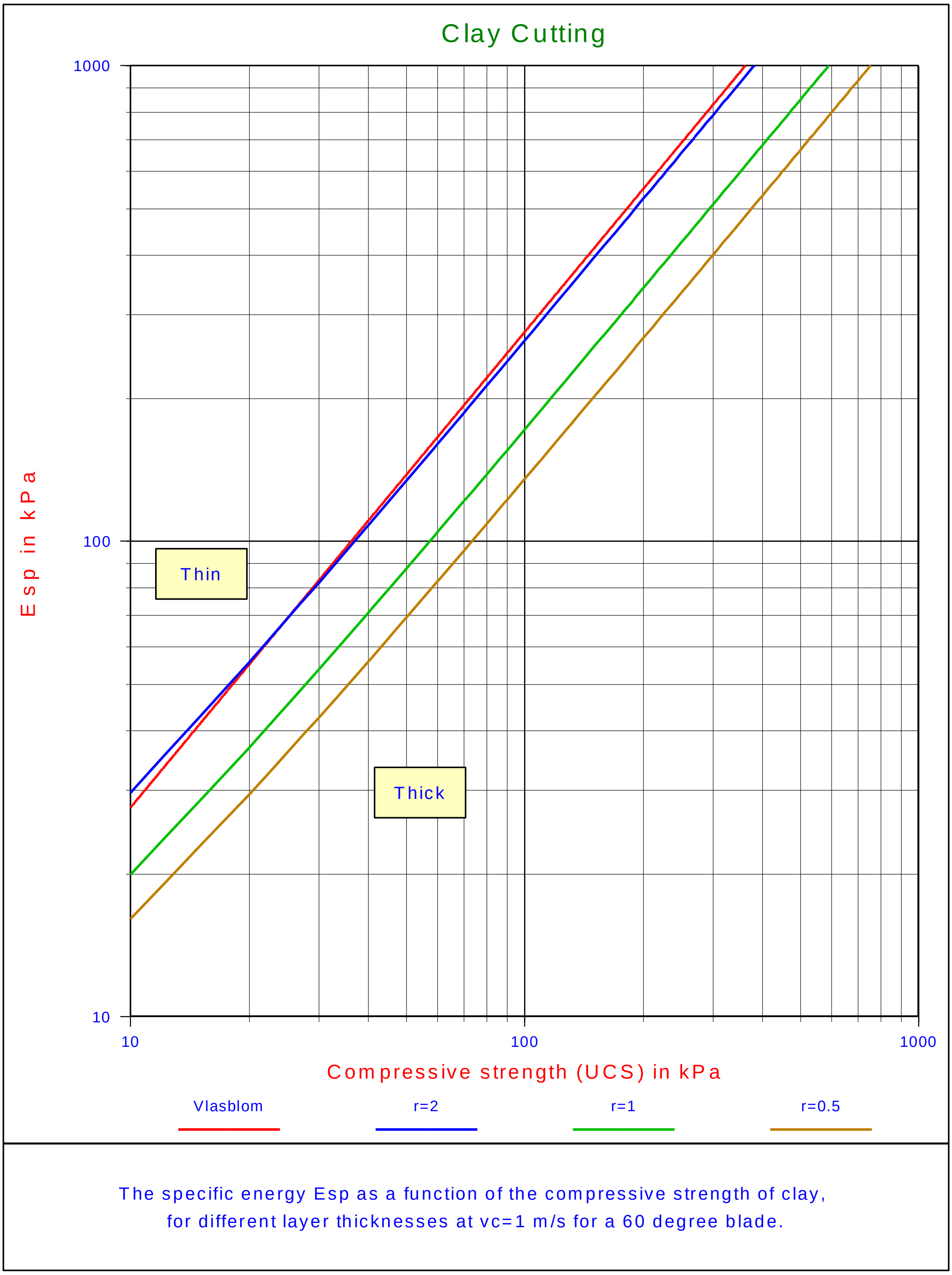

Figure 6-26: The specific energy E_{sp} in clay as a function of the compressive strength (UCS).

6.6. Nomenclature Chapter 6:

A	Adhesive force on the blade	kN
B	Frequency (material property)	1/s
C	Cohesive force on shear plane	kN
E	Energy level	J/kmol
E_a	Activation energy level	J/kmol
E_l	Limiting (maximum) energy level	J/kmol
f	Shear force on flow unit	N
F	Cutting force	kN
G	Gravitational force	kN
h	Planck constant ($6.626 \cdot 10^{-34}$ J·s)	J·s
k	Boltzman constant ($1.3807 \cdot 10^{-23}$ J/K)	J/K
K_1	Grain force on the shear plane	kN
K_2	Grain force on the blade	kN
i	Coefficient	-
I	Inertial force on the shear plane	kN
N	Avogadro constant ($6.02 \cdot 10^{26}$ 1/kmol)	-
N_1	Normal grain force on shear plane	kN
N_2	Normal grain force on blade	kN
p	Probability	-
R	Universal gas constant (8314 J/kmol/K)	J/kmol/K
S	Number of bonds per unit area	1/m²
S_1	Shear force due to internal friction on the shear surface	kN
S_2	Shear force due to soil/steel friction on the blade	kN
T	Absolute temperature	K
T	Tensile force	kN
v_c	Cutting velocity	m/s
W_1	Force resulting from pore under pressure on the shear plane	kN
W_2	Force resulting from pore under pressure on the blade	kN
X	Function	-
α	Blade angle	rad
β	Angle of the shear plane with the direction of cutting velocity	rad
ν	frequency of activation	1/s
λ	Distance between equilibrium positions	m
$d\varepsilon/dt$	Strain rate	1/s
$d\varepsilon_0/dt$	Frequency (material property)	1/s
τ	Shear stress	kPa
τ_a	Adhesive shear strength (strain rate dependent)	kPa
τ_c	Cohesive shear strength (strain rate dependent)	kPa
τ_y	Shear strength (yield stress, material property)	kPa
τ_{ya}	Adhesive shear strength (material property)	kPa
τ_{yc}	Cohesive shear strength (material property)	kPa
τ_0	Dynamical shearing resistance factor (material property)	kPa
σ_e	Effective stress	kPa
σ_n	Normal stress	kPa
σ_t	Tensile strength	kPa
ϕ	Angle of internal friction	rad
δ	Soil/steel friction angle	rad

Chapter 7: Rock Cutting Under Atmospheric Conditions

7.1. Introduction

Merchant (1944), (1945A) and (1945B) derived a model for determining the cutting forces when machining steel. The model was based on elastic-plastic deformation and a continuous chip formation (ductile cutting). The model included internal and external friction and shear strength, but no adhesion, gravity, inertia and pore pressures. Later Miedema (1987 September) extended this model with adhesion, gravity, inertial forces and pore water pressures.

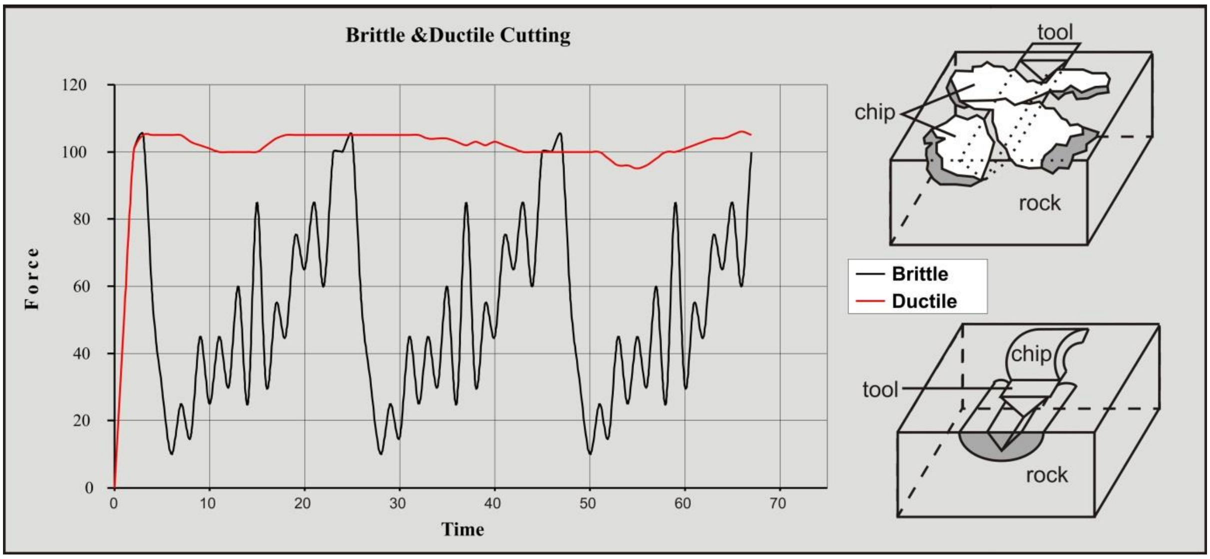

Figure 7-1: Ductile and brittle cutting Verhoef (1997).

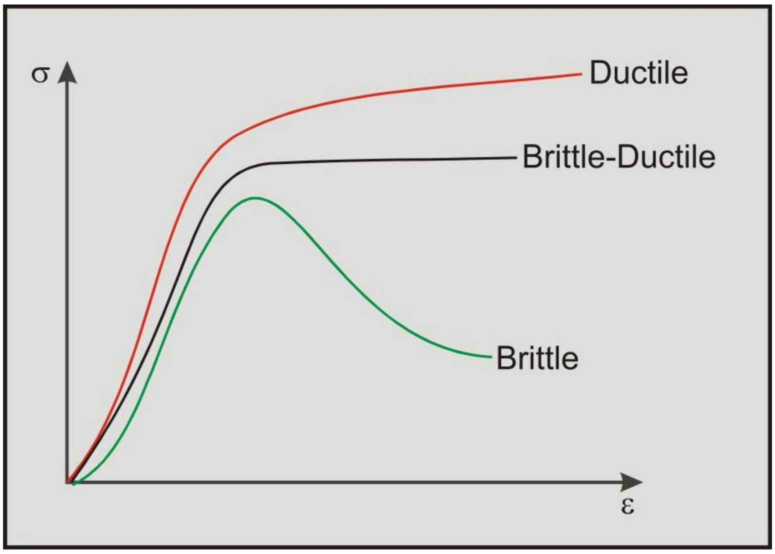

Figure 7-2: The stress-strain curves for ductile and brittle failure.

7.2. Cutting models

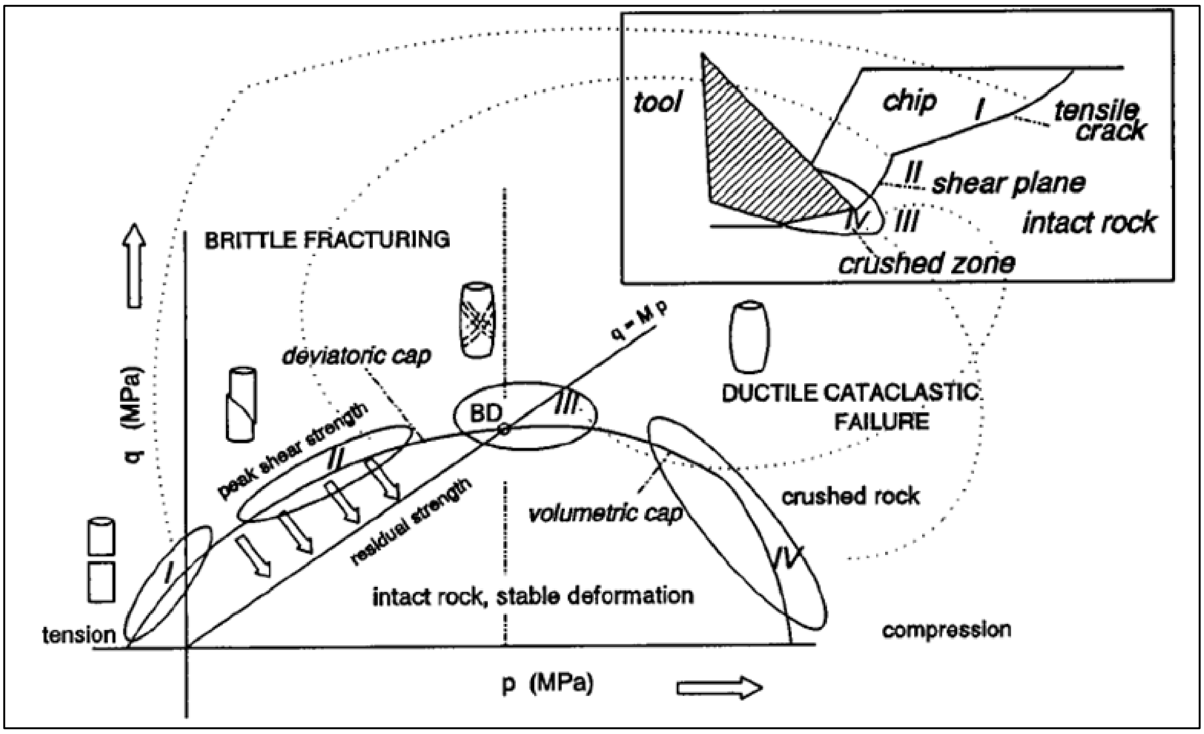

Figure 7-3: Failure during rock cutting involves the entire failure envelope Verhoef (1997).

7.2.1. The Model of Evans

For **brittle rock** the cutting theory of Evans (1964) and (1966) can be used to calculate cutting forces (Figure 7-5). The forces are derived from the geometry of the chisel (width, cutting angle and cutting depth) and the tensile strength (BTS) of the rock. Evans suggested a model on basis of observations on coal breakage by wedges. In this theory it is assumed that:

1. A force **R** is acting under an angle **δ** (external friction angle) with the normal to the surface **A-C** of the wedge.
2. A resultant force **T** of the tensile stresses acting at the center of the arc **C-D**, the line **C-D** is under an angle **β** (the shear angle) with the horizontal.
3. A third force **S** is required to maintain equilibrium in the buttock, but does not play a role in the derivation..
4. The penetration of the wedge is small compared to the layer thickness $\mathbf{h_i}$.

The action of the wedge tends to split the rock and does rotate it about point **D**. It is therefore assumed that the force **S** acts through point **D**. Along the fracture line, it is assumed that a state of plain strain is working and the equilibrium is considered per unit of width **w** of the wedge.

The force due to the tensile strength $\boldsymbol{\sigma_T}$ of the rock is:

$$\mathbf{T = \sigma_T \cdot r \cdot \int_{-\beta}^{\beta} \cos(\omega) \cdot d\omega \cdot w = 2 \cdot \sigma_t \cdot r \cdot \sin(\beta) \cdot w} \qquad \textbf{(7-1)}$$

Where $\mathbf{r \cdot d\omega}$ is an element of the arc **C-D** making an angle $\boldsymbol{\omega}$ with the symmetry axis of the arc. Let $\mathbf{h_i}$ be the depth of the cut and assume that the penetration of the edge may be neglected in comparison with $\mathbf{h_i}$. This means that the force **R** is acting near point **C**. Taking moments about point **D** gives:

$$\mathbf{\frac{R \cdot h_i \cdot w \cdot \cos(\alpha + \beta + \delta)}{\sin(\beta)} = T \cdot r \cdot \sin(\beta) \cdot w} \qquad \textbf{(7-2)}$$

From the geometric relation it follows:

$$\mathbf{r \cdot \sin(\beta) = \frac{h_i}{2 \cdot \sin(\beta)}} \qquad \textbf{(7-3)}$$

Hence:

$$\mathbf{R = \frac{\sigma_T \cdot h_i \cdot w}{2 \cdot \sin(\beta) \cdot \cos(\alpha + \beta + \delta)}} \qquad \textbf{(7-4)}$$

The horizontal component of **R** is $\mathbf{R \cdot \sin(\alpha+\delta)}$ en due to the symmetry of the forces acting on the wedge the total cutting force is:

$$\mathbf{F_c = 2 \cdot R \cdot \sin(\alpha + \delta) = \sigma_T \cdot h_i \cdot w \cdot \frac{\sin(\alpha + \delta)}{\sin(\beta) \cdot \cos(\alpha + \beta + \delta)}} \qquad \textbf{(7-5)}$$

The normal force (⊥ on cutting force) is per side:

$$\mathbf{F_n = R \cdot \cos(\alpha + \delta) = \sigma_T \cdot h_i \cdot w \cdot \frac{\cos(\alpha + \delta)}{2 \cdot \sin(\beta) \cdot \cos(\alpha + \beta + \delta)}} \qquad \textbf{(7-6)}$$

The angle **β** can be determined by using the principle of minimum energy:

$$\mathbf{\frac{dF_c}{d\beta} = 0} \qquad \textbf{(7-7)}$$

Giving:

$$\cos(\beta)\cdot\cos(\alpha+\beta+\delta)-\sin(\beta)\cdot\sin(\alpha+\beta+\delta)=0 \Rightarrow \cos(2\cdot\beta+\alpha+\delta)=0 \tag{7-8}$$

Resulting in:

$$\beta=\frac{1}{2}\cdot\left(\frac{\pi}{2}-\alpha-\delta\right)=\frac{\pi}{4}-\frac{\alpha+\delta}{2} \tag{7-9}$$

With:

$$\sin(\beta)\cdot\cos(\alpha+\beta+\delta)=\frac{1-\sin(\alpha+\delta)}{2} \tag{7-10}$$

This gives for the horizontal cutting force:

$$F_c=\sigma_T\cdot h_i\cdot w\cdot\frac{2\cdot\sin(\alpha+\delta)}{1-\sin(\alpha+\delta)}=\sigma_T\cdot h_i\cdot w\cdot\lambda_{HT} \tag{7-11}$$

For each side of the wedge the normal force is now (the total normal/vertical force is zero):

$$F_n=\sigma_T\cdot h_i\cdot w\cdot\frac{\cos(\alpha+\delta)}{1-\sin(\alpha+\delta)}=\sigma_T\cdot h_i\cdot w\cdot\lambda_{VT} \tag{7-12}$$

Figure 7-4 shows the brittle-tear horizontal force coefficient λ_{HT} as a function of the wedge top angle α and the internal friction angle φ. The internal friction angle φ does not play a role directly, but it is assumed that the external friction angle δ is 2/3 of the internal friction angle φ.

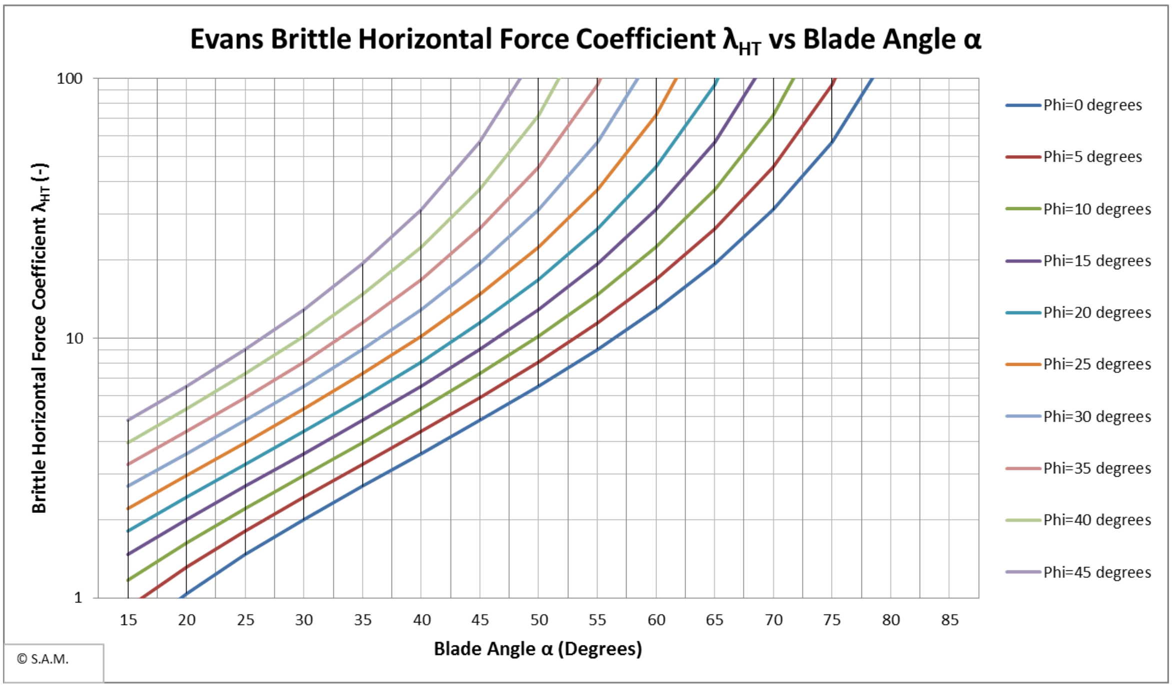

Figure 7-4: The brittle-tear horizontal force coefficient λ_{HT} (Evans).

Comparing Figure 7-4 with Figure 7-20 (the brittle-tear horizontal force coefficient λ_{HT} of the Miedema model) shows that the coefficient λ_{HT} of Evans is bigger than the λ_{HT} coefficient of Miedema. The Miedema model however is based on cutting with a blade, while Evans is based on the penetration with a wedge or chisel, which should give a higher cutting force. The model as is derived in chapter 0 assumes sharp blades however.

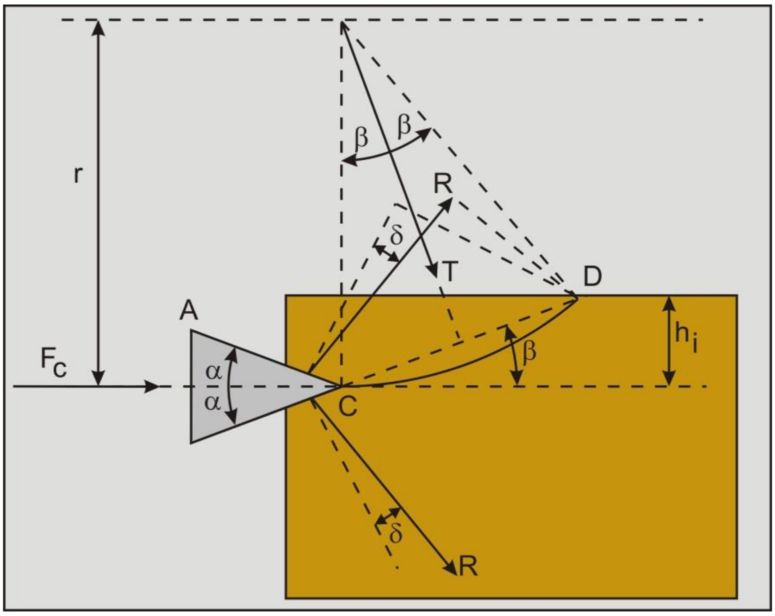

Figure 7-5: The model of Evans.

7.2.2. The Model of Evans under an Angle ε

When it is assumed that the chisel enters the rock under an angle **ε** and the fracture starts in the same direction as the centerline of the chisel as is shown in Figure 7-6, the following can be derived:

$$\mathbf{h = 2 \cdot r \cdot \sin(\beta) \cdot \sin(\beta - \varepsilon) \quad and \quad h_i = 2 \cdot r \cdot \sin^2(\beta)} \tag{7-13}$$

$$\mathbf{h_i = h \cdot \frac{\sin(\beta)}{\sin(\beta - \varepsilon)}} \tag{7-14}$$

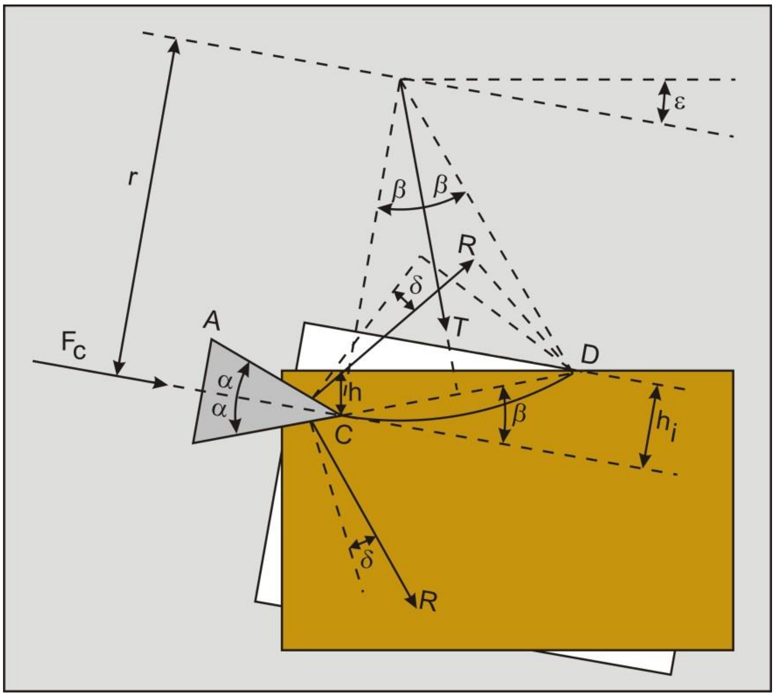

Figure 7-6: The model of Evans under an angle ε.

Substituting equation (7-13) in equation (7-5) for the cutting force gives:

$$F_c = \sigma_T \cdot h_i \cdot w \cdot \frac{2 \cdot \sin(\alpha + \delta)}{1 - \sin(\alpha + \delta)} = \sigma_T \cdot h \cdot w \cdot \frac{\sin(\beta)}{\sin(\beta - \varepsilon)} \cdot \frac{\sin(\alpha + \delta)}{\sin(\beta) \cdot \cos(\alpha + \beta + \delta)}$$

$$= \sigma_T \cdot h \cdot w \cdot \frac{\sin(\alpha + \delta)}{\sin(\beta - \varepsilon) \cdot \cos(\alpha + \beta + \delta)} \qquad \textbf{(7-15)}$$

The horizontal component of the cutting force is now:

$$F_{ch} = \sigma_T \cdot h \cdot w \cdot \frac{\sin(\alpha + \delta)}{\sin(\beta - \varepsilon) \cdot \cos(\alpha + \beta + \delta)} \cdot \cos(\varepsilon) \qquad \textbf{(7-16)}$$

The vertical component of this cutting force is now:

$$F_{cv} = \sigma_T \cdot h \cdot w \cdot \frac{\sin(\alpha + \delta)}{\sin(\beta - \varepsilon) \cdot \cos(\alpha + \beta + \delta)} \cdot \sin(\varepsilon) \qquad \textbf{(7-17)}$$

Note that the vertical force is not zero anymore, which makes sense since the chisel is not symmetrical with regard to the horizontal anymore. Equation (7-18) can be applied to eliminate the shear angle β from the above equations. When the denominator is at a maximum in these equations, the forces are at a minimum. The denominator is at a maximum when the first derivative of the denominator is zero and the second derivative is negative.

The angle **β** can be determined by using the principle of minimum energy:

$$\frac{dF_c}{d\beta} = 0 \qquad \textbf{(7-18)}$$

Giving for the first derevative:

$$\cos(\beta - \varepsilon) \cdot \cos(\alpha + \beta + \delta) - \sin(\beta - \varepsilon) \cdot \sin(\alpha + \beta + \delta) = 0 \;\Rightarrow\; \cos(2 \cdot \beta + \alpha + \delta - \varepsilon) = 0 \qquad \textbf{(7-19)}$$

Resulting in:

$$\beta = \frac{1}{2} \cdot \left(\frac{\pi}{2} - \alpha - \delta + \varepsilon \right) = \frac{\pi}{4} - \frac{\alpha + \delta - \varepsilon}{2} \qquad \textbf{(7-20)}$$

With:

$$\sin(\beta - \varepsilon) \cdot \cos(\alpha + \beta + \delta) = \frac{1 - \sin(\alpha + \delta + \varepsilon)}{2} \qquad \textbf{(7-21)}$$

Substituting equation (7-21) in equation (7-15) gives for the force $\mathbf{F_c}$:

$$F_c = \sigma_T \cdot h \cdot w \cdot \frac{2 \cdot \sin(\alpha + \delta)}{1 - \sin(\alpha + \delta + \varepsilon)} \qquad \textbf{(7-22)}$$

The horizontal component of the cutting force $\mathbf{F_{ch}}$ is now:

$$F_{ch} = \sigma_T \cdot h \cdot w \cdot \frac{2 \cdot \sin(\alpha + \delta)}{1 - \sin(\alpha + \delta + \varepsilon)} \cdot \cos(\varepsilon) \qquad \textbf{(7-23)}$$

The vertical component of this cutting force $\mathbf{F_{cv}}$ is now:

$$F_{cv} = \sigma_T \cdot h \cdot w \cdot \frac{2 \cdot \sin(\alpha + \delta)}{1 - \sin(\alpha + \delta + \varepsilon)} \cdot \sin(\varepsilon) \qquad \textbf{(7-24)}$$

7.2.3. The Model of Evans used for a Pickpoint

In the case where the angle ε equals the angle α, a pickpoint with blade angle $2 \cdot \alpha$ and a wear flat can be simulated as is shown in Figure 7-7. In this case the equations become:

$$F_c = \sigma_T \cdot h \cdot w \cdot \frac{2 \cdot \sin(\alpha + \delta)}{1 - \sin(2 \cdot \alpha + \delta)} \qquad \textbf{(7-25)}$$

The horizontal component of the cutting force F_{ch} is now:

$$F_{ch} = \sigma_T \cdot h \cdot w \cdot \frac{2 \cdot \sin(\alpha + \delta)}{1 - \sin(2 \cdot \alpha + \delta)} \cdot \cos(\alpha) \qquad \textbf{(7-26)}$$

The vertical component of this cutting force F_{cv} is now:

$$F_{cv} = \sigma_T \cdot h \cdot w \cdot \frac{2 \cdot \sin(\alpha + \delta)}{1 - \sin(2 \cdot \alpha + \delta)} \cdot \sin(\alpha) \qquad \textbf{(7-27)}$$

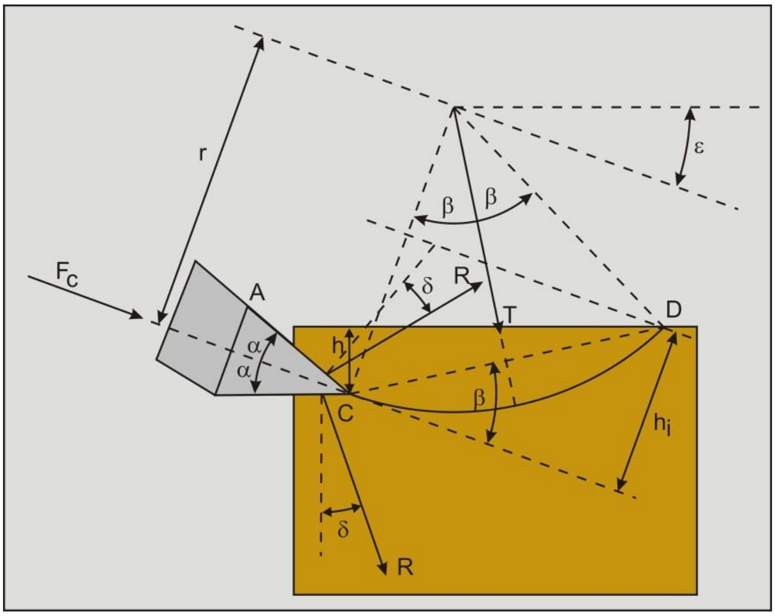

Figure 7-7: The model of Evans used for a pickpoint.

For the force **R** (see equation (7-5)), acting on both sides of the pickpoint the following equation can be found:

$$R = \frac{F_c}{2 \cdot \sin(\alpha + \delta)} = \sigma_T \cdot h \cdot w \cdot \frac{1}{1 - \sin(2 \cdot \alpha + \delta)} \qquad \textbf{(7-28)}$$

In the case of wear calculations the normal and friction forces on the front side and the wear flat can be interesting. According to Evans the normal and friction forces are the same on both sides, since this was the starting point of the derivation, this gives for the normal force R_n:

$$R_n = \sigma_T \cdot h \cdot w \cdot \frac{1}{1 - \sin(2 \cdot \alpha + \delta)} \cdot \cos(\delta) \qquad \textbf{(7-29)}$$

The friction force R_f is now:

$$R_f = \sigma_T \cdot h \cdot w \cdot \frac{1}{1-\sin(2\cdot\alpha+\delta)} \cdot \sin(\delta) \tag{7-30}$$

7.2.4. Summary of the Evans Theory

The Evans theory has been derived for 3 cases:

1. The basic case with a horizontal moving chisel and the centerline of the chisel horizontal.
2. A horizontal moving chisel with the centerline under an angle **ε**.
3. A pickpoint with the centerline angle **ε** equal to half the top angle **α**, horizontally moving.

Table 7-1: Summary of the Evans theory.

Case	Cutting forces and specific energy	
1	$F_c = \sigma_T \cdot h_i \cdot w \cdot \frac{2\cdot\sin(\alpha+\delta)}{1-\sin(\alpha+\delta)}$ $F_{ch} = F_c$ $F_{cv} = 0$ $E_{sp} = \frac{F_{ch}\cdot v_c}{h_i\cdot w\cdot v_c} = \sigma_T \cdot \frac{2\cdot\sin(\alpha+\delta)}{1-\sin(\alpha+\delta)}$	(7-31)
2	$F_c = \sigma_T \cdot h \cdot w \cdot \frac{2\cdot\sin(\alpha+\delta)}{1-\sin(\alpha+\delta+\varepsilon)}$ $F_{ch} = F_c \cdot \cos(\varepsilon)$ $F_{cv} = F_c \cdot \sin(\varepsilon)$ $E_{sp} = \frac{F_{ch}\cdot v_c}{h_i\cdot w\cdot v_c} = \sigma_T \cdot \frac{2\cdot\sin(\alpha+\delta)}{1-\sin(\alpha+\delta+\varepsilon)} \cdot \cos(\varepsilon)$	(7-32)
3	$F_c = \sigma_T \cdot h \cdot w \cdot \frac{2\cdot\sin(\alpha+\delta)}{1-\sin(2\cdot\alpha+\delta)}$ $F_{ch} = F_c \cdot \cos(\alpha)$ $F_{cv} = F_c \cdot \sin(\alpha)$ $E_{sp} = \frac{F_{ch}\cdot v_c}{h_i\cdot w\cdot v_c} = \sigma_T \cdot \frac{2\cdot\sin(\alpha+\delta)}{1-\sin(2\cdot\alpha+\delta)} \cdot \cos(\alpha)$	(7-33)

Once again it should be noted that the angle **α** as used by Evans is half the top angle of the chisel and not the blade angle as **α** is used for in most equations in this book. In case 1 the blade angle would be **α** as used by Evans, in case 2 the blade angle is **α+ε** and in case 3 the blade angle is **2·α**. In all cases it is assumed that the cutting velocity $\mathbf{v_c}$ is horizontal.

7.2.5. The Nishimatsu Model.

For brittle shear rock cutting we may use the equation of Nishimatsu (1972). This theory describes the cutting force of chisels by failure through shear. Figure 7-8 gives the parameters needed to calculate the cutting forces. Nishumatsu (1972) presented a theory similar to Merchant´s (1944), (1945A) and (1945B) only Nishumatsu's theory considered the normal and shear stresses acting on the failure plain (**A-B**) to be proportional to the $\mathbf{n}^{th}$ power of the distance **λ** from point **A** to point **B**. With **n** being the so called stress distribution factor:

$$\mathbf{p} = \mathbf{p_0} \cdot \left(\frac{\mathbf{h_i}}{\sin(\beta)} - \lambda \right)^{\mathbf{n}} \tag{7-34}$$

Nishumatsu made the following assumptions:
1. The rock cutting is brittle, without any accompanying plastic deformation (no ductile crushing zone)
2. The cutting process is under plain stress condition
3. The failure is according a linear Mohr envelope
4. Te cutting speed has no effect on the processes.

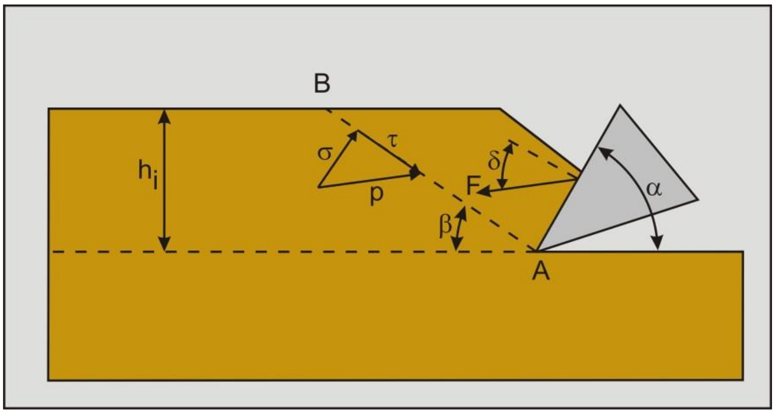

Figure 7-8: Model for shear failure by Nishimatsu (1972).

As a next assumption, let us assume that the direction of the resultant stress **p** is constant along the line **A-B**. The integration of this resultant stress **p** along the line **A-B** should be in equilibrium with the resultant cutting force **F**. Thus, we have:

$$\mathbf{p_0} \cdot \mathbf{w} \cdot \int_0^{\frac{\mathbf{h_i}}{\sin(\beta)}} \left(\frac{\mathbf{h_i}}{\sin(\beta)} - \lambda \right)^{\mathbf{n}} \cdot \mathbf{d}\lambda = \mathbf{F} \quad \Rightarrow \quad \mathbf{p_0} \cdot \frac{\mathbf{1}}{\mathbf{n+1}} \cdot \left(\frac{\mathbf{h_i}}{\sin(\beta)} \right)^{\mathbf{n+1}} = \mathbf{F} \tag{7-35}$$

Integrating the second term of equation (7-35) allows determining the value of the constant $\mathbf{p_0}$.

$$\mathbf{p_0} \cdot \mathbf{w} = (\mathbf{n+1}) \cdot \left(\frac{\mathbf{h_i}}{\sin(\beta)} \right)^{-(\mathbf{n+1})} \cdot \mathbf{F} \tag{7-36}$$

Substituting this in equation (7-34) gives:

$$\mathbf{p} \cdot \mathbf{w} = (\mathbf{n+1}) \cdot \left(\frac{\mathbf{h_i}}{\sin(\beta)} \right)^{-(\mathbf{n+1})} \cdot \left(\frac{\mathbf{h_i}}{\sin(\beta)} - \lambda \right)^{\mathbf{n}} \cdot \mathbf{F} \tag{7-37}$$

The maximum stress **p** is assumed to occur near the tip of the chisel, so **λ=0**, giving:

$$\mathbf{p} \cdot \mathbf{w} = (\mathbf{n+1}) \cdot \left(\frac{\mathbf{h_i}}{\sin(\beta)} \right)^{-\mathbf{1}} \cdot \mathbf{F} \tag{7-38}$$

For the normal stress **σ** and the shear **τ** stress this gives:

$$\sigma_0 \cdot w = -p \cdot w \cdot \cos(\alpha+\beta+\delta) = (n+1)\cdot\left(\frac{h_i}{\sin(\beta)}\right)^{-1} \cdot F \cdot \cos(\alpha+\beta+\delta) \tag{7-39}$$

$$\tau_0 \cdot w = p \cdot w \cdot \sin(\alpha+\beta+\delta) = (n+1)\cdot\left(\frac{h_i}{\sin(\beta)}\right)^{-1} \cdot F \cdot \sin(\alpha+\beta+\delta) \tag{7-40}$$

Rewriting this gives:

$$\sigma_0 \cdot h_i \cdot w = -p \cdot h_i \cdot w \cdot \cos(\alpha+\beta+\delta) = -(n+1)\cdot\sin(\beta)\cdot\cos(\alpha+\beta+\delta)\cdot F \tag{7-41}$$

$$\tau_0 \cdot h_i \cdot w = p \cdot h_i \cdot w \cdot \sin(\alpha+\beta+\delta) = (n+1)\cdot\sin(\beta)\cdot\sin(\alpha+\beta+\delta)\cdot F \tag{7-42}$$

With the Coulomb-Mohr failure criterion:

$$\tau_0 = c + \sigma_0 \cdot \tan(\varphi) \tag{7-43}$$

Substituting equations (7-41) and (7-42) in equation (7-43) gives:

$$(n+1)\cdot\sin(\beta)\cdot\sin(\alpha+\beta+\delta)\cdot\frac{F}{h_i \cdot w} = c - (n+1)\cdot\sin(\beta)\cdot\cos(\alpha+\beta+\delta)\cdot\frac{F}{h_i \cdot w}\cdot\tan(\varphi) \tag{7-44}$$

This can be simplified to:

$$\frac{c \cdot h_i \cdot w \cdot \cos(\varphi)}{(n+1)\cdot\sin(\beta)} = F \cdot \left(\sin(\alpha+\beta+\delta)\cdot\cos(\varphi) + \cos(\alpha+\beta+\delta)\cdot\sin(\varphi)\right) = F \cdot \sin(\alpha+\beta+\delta+\varphi) \tag{7-45}$$

This gives for the force **F**:

$$F = \frac{1}{(n+1)}\cdot\frac{c \cdot h_i \cdot w \cdot \cos(\varphi)}{\sin(\beta)\cdot\sin(\alpha+\beta+\delta+\varphi)} \tag{7-46}$$

For the horizontal force $\mathbf{F_h}$ and the vertical force $\mathbf{F_v}$ we find:

$$F_h = \frac{1}{(n+1)}\cdot\frac{c \cdot h_i \cdot w \cdot \cos(\varphi)\cdot\sin(\alpha+\delta)}{\sin(\beta)\cdot\sin(\alpha+\beta+\delta+\varphi)} \tag{7-47}$$

$$F_v = \frac{1}{(n+1)}\cdot\frac{c \cdot h_i \cdot w \cdot \cos(\varphi)\cdot\cos(\alpha+\delta)}{\sin(\beta)\cdot\sin(\alpha+\beta+\delta+\varphi)} \tag{7-48}$$

To determine the shear angle **β** where the horizontal force $\mathbf{F_h}$ is at the minimum, the denominator of equation (7-46) has to be at a maximum. This will occur when the derivative of $\mathbf{F_h}$ with respect to **β** equals 0 and the double derivative is negative.

$$\frac{\partial \sin(\alpha+\beta+\delta+\varphi)\cdot\sin(\beta)}{\partial\beta} = \sin(\alpha+2\cdot\beta+\delta+\varphi) = 0 \tag{7-49}$$

$$\beta = \frac{\pi}{2} - \frac{\alpha+\delta+\varphi}{2} \tag{7-50}$$

Using this, gives for the force **F**:

$$F = \frac{1}{(n+1)}\cdot\frac{2 \cdot c \cdot h_i \cdot w \cdot \cos(\varphi)}{1+\cos(\alpha+\delta+\varphi)} \tag{7-51}$$

This gives for the horizontal force $\mathbf{F_h}$ and the vertical force $\mathbf{F_v}$:

$$F_h = \frac{1}{(n+1)} \cdot \frac{2 \cdot c \cdot h_i \cdot w \cdot \cos(\varphi) \cdot \sin(\alpha+\delta)}{1+\cos(\alpha+\delta+\varphi)} = \frac{1}{(n+1)} \cdot \lambda_{HF} \cdot c \cdot h_i \cdot w \tag{7-52}$$

$$F_v = \frac{1}{(n+1)} \cdot \frac{2 \cdot c \cdot h_i \cdot w \cdot \cos(\varphi) \cdot \cos(\alpha+\delta)}{1+\cos(\alpha+\delta+\varphi)} = \frac{1}{(n+1)} \cdot \lambda_{VF} \cdot c \cdot h_i \cdot w \tag{7-53}$$

This solution is the same as the Merchant solution (equations (7-68) and (7-69)) that will be derived in the next chapter, if the value of the stress distribution factor **n=0**. In fact the stress distribution factor **n** is just a factor to reduce the forces. From tests it appeared that in a type of rock the value of **n** depends on the rake angle. It should be mentioned that for this particular case **n** is about 1 for a large cutting angle. In that case tensile failure may give way to a process of shear failure, which is observed by other researches as well. For cutting angles smaller than 80 degrees **n** is more or less constant with a value of **n=0.5**.
Figure 7-14 and Figure 7-15 show the coefficients $\boldsymbol{\lambda_{HF}}$ and $\boldsymbol{\lambda_{VF}}$ for the horizontal and vertical forces $\mathbf{F_h}$ and $\mathbf{F_v}$ according to equations (7-68) and (7-69) as a function of the blade angle $\boldsymbol{\alpha}$ and the internal friction angle $\boldsymbol{\varphi}$, where the external friction angle $\boldsymbol{\delta}$ is assumed to be $\mathbf{2/3 \cdot \varphi}$. A positive coefficient $\boldsymbol{\lambda_{VF}}$ for the vertical force means that the vertical force $\mathbf{F_v}$ is downwards directed. Based on equation (7-56) and (7-68) the specific energy $\mathbf{E_{sp}}$ can be determined according to:

$$E_{sp} = \frac{P_c}{Q} = \frac{F_h \cdot v_c}{h_i \cdot w \cdot v_c} = \frac{F_h}{h_i \cdot w} = \frac{1}{(n+1)} \cdot \lambda_{HF} \cdot c \tag{7-54}$$

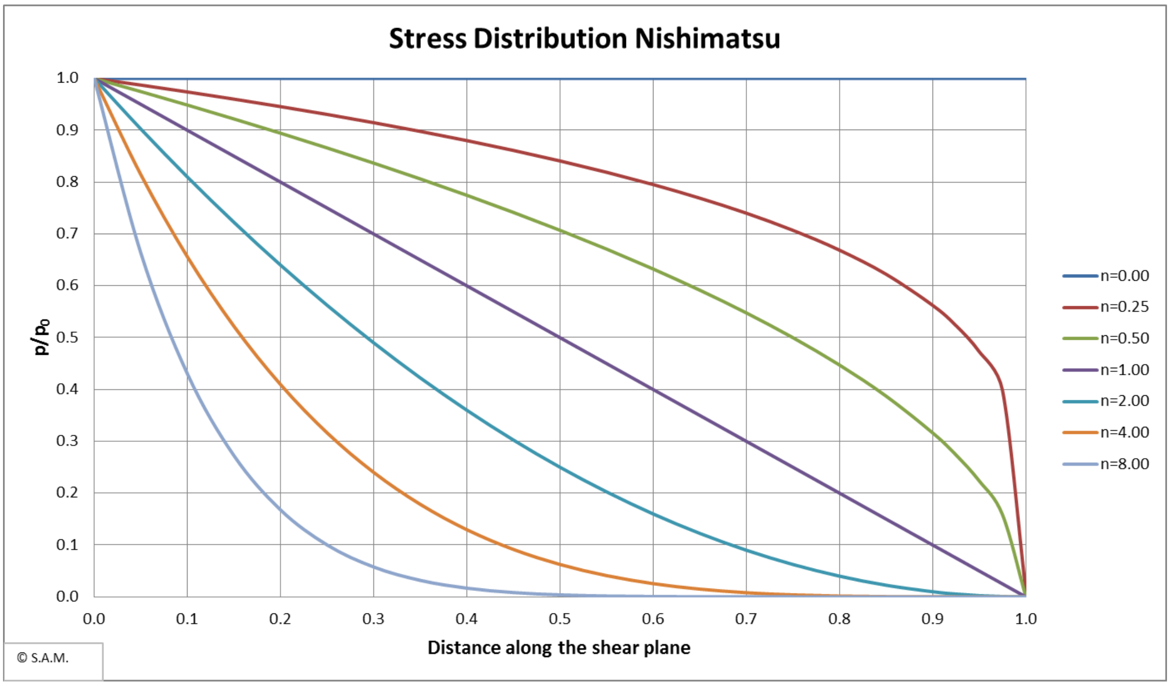

Figure 7-9: The stress distribution along the shear plane.

The difference between the Nishimatsu and the Merchant approach is that Nishimatsu assumes brittle shear failure, while Merchant assumes plastic deformation as can be seen in steel and clay cutting.

7.3. The Flow Type (Based on the Merchant Model)

Rock is the collection of materials where the grains are bonded chemically from very stiff clay, sandstone to very hard basalt. It is difficult to give one definition of rock or stone and also the composition of the material can differ strongly. Still it is interesting to see if the model used for sand and clay, which is based on the Coulomb model, can be used for rock as well. Typical parameters for rock are the compressive strength UCS and the tensile strength BTS and specifically the ratio between those two, which is a measure for how fractured the rock is. Rock also has shear strength and because it consists of bonded grains it will have an internal friction angle and an external friction angle. It can be assumed that the permeability of the rock is very low, so initially the pore pressures do no play a role or cavitation will always occur under atmospheric conditions. But since the absolute hydrostatic pressure, which would result in a cavitation under pressure of the same magnitude can be neglected with respect to the compressive strength of the rock; the pore pressures are usually neglected. This results in a material where gravity, inertia, pore pressures and adhesion can be neglected.
Merchant (1944), (1945A) and (1945B) derived a model for determining the cutting forces when machining steel. The model was based on plastic deformation and a continuous chip formation (ductile cutting). The model included internal and external friction and shear strength, but no adhesion, gravity, inertia and pore pressures. Later Miedema (1987 September) extended this model with adhesion, gravity, inertial forces and pore water pressures.

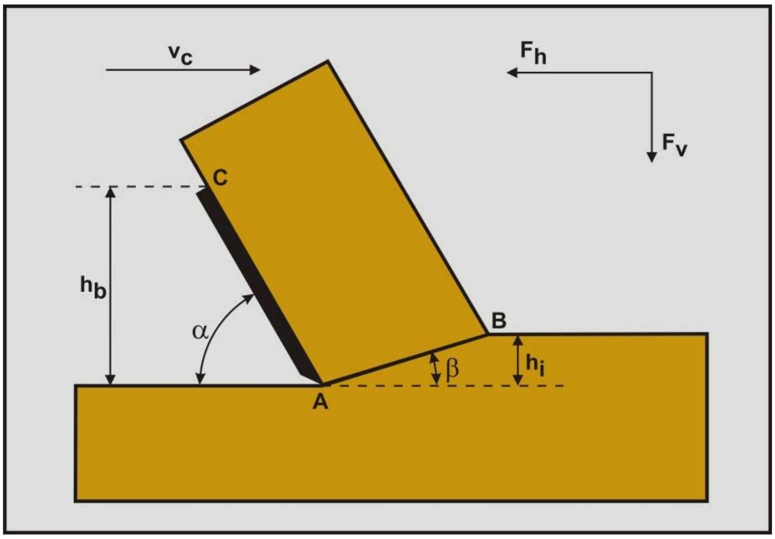

Figure 7-10: The definitions of the cutting process.

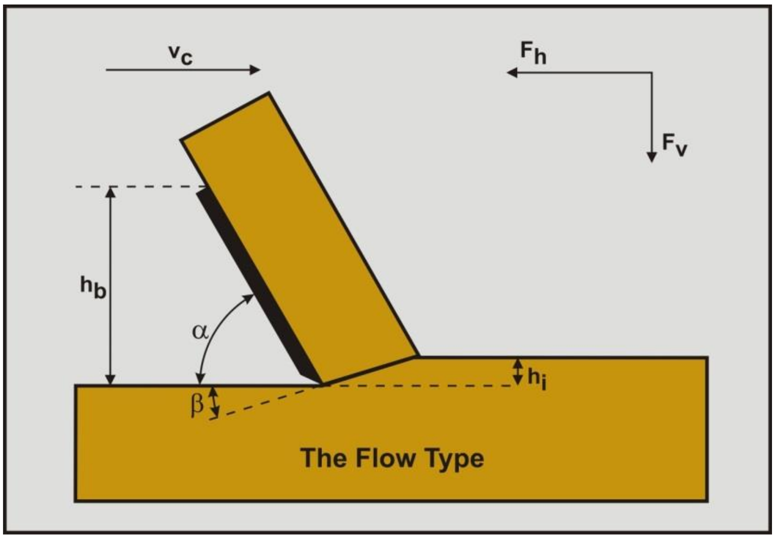

Figure 7-11: The Flow Type cutting mechanism in ductile rock cutting.

Figure 7-10 gives some definitions regarding the cutting process. The line A-B is considered to be the shear plane, while the line A-C is the contact area between the blade and the soil. The blade angle is named $\boldsymbol{\alpha}$ and the shear angle $\boldsymbol{\beta}$. The blade is moving from left to right with a cutting velocity $\mathbf{v_c}$. The thickness of the layer cut is $\mathbf{h_i}$ and the vertical height of the blade h_b. The horizontal force on the blade F_h is positive from right to left always opposite to the direction of the cutting velocity v_c. The vertical force on the blade F_v is positive downwards. Since the vertical force is perpendicular to the cutting velocity, the vertical force does not contribute to the cutting power P_c, which is equal to:

$$P_c = F_h \cdot v_c \tag{7-55}$$

The specific energy E_{sp} is defined as the amount of energy used/required to excavate 1 m^3 of soil/rock. This can be determined by dividing the cutting power P_c by the production Q and results in the cutting force F_h in the direction of the cutting velocity v_c, divided by the cross section cut $h_i \cdot w$:

$$E_{sp} = \frac{P_c}{Q} = \frac{F_h \cdot v_c}{h_i \cdot w \cdot v_c} = \frac{F_h}{h_i \cdot w} \tag{7-56}$$

The model for rock cutting under atmospheric conditions is based on the flow type of cutting mechanism. Although in general rock will encounter a more brittle failure mechanism and the flow type considered represents the ductile failure mechanism, the flow type mechanism forms the basis for all cutting processes. The definitions of the flow type mechanism are shown in Figure 7-11.

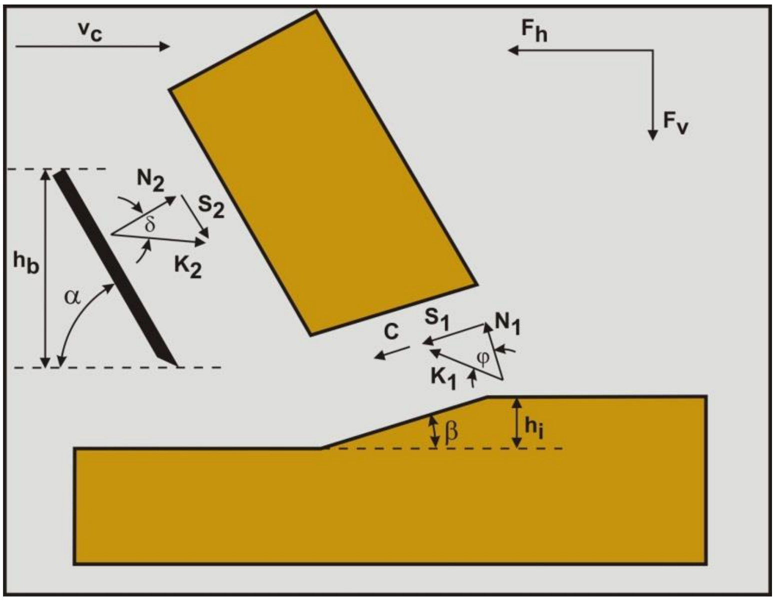

Figure 7-12: The forces on the layer cut in rock (atmospheric).

Figure 7-12 illustrates the forces on the layer of rock cut. The forces shown are valid in general. The forces acting on this layer are:

1. A normal force acting on the shear surface N_1 resulting from the grain stresses.
2. A shear force S_1 as a result of internal fiction $N_1 \cdot \tan(\phi)$.
3. A shear force C as a result of the shear strength (cohesion) τ_c or c. This force can be calculated by multiplying the cohesive shear strength τ_c with the area of the shear plane.
4. A force normal to the blade N_2 resulting from the grain stresses.
5. A shear force S_2 as a result of the soil/steel friction $N_2 \cdot \tan(\delta)$ or external friction.

The normal force N_1 and the shear force S_1 can be combined to a resulting grain force K_1.

The forces acting on a straight blade when cutting rock, can be distinguished as:

6. A force normal to the blade N_2 resulting from the grain stresses.
7. A shear force S_2 as a result of the soil/steel friction $N_2 \cdot \tan(\delta)$ or external friction.

These forces are shown in Figure 7-13. If the forces N_2 and S_2 are combined to a resulting force K_2 the resulting force K_2 is the unknown force on the blade. By taking the horizontal and vertical equilibrium of forces an expression for the force K_2 on the blade can be derived.
The horizontal equilibrium of forces:

$$\sum F_h = K_1 \cdot \sin(\beta + \varphi) + C \cdot \cos(\beta) - K_2 \cdot \sin(\alpha + \delta) = 0 \tag{7-57}$$

The vertical equilibrium of forces:

$$\sum F_v = -K_1 \cdot \cos(\beta + \varphi) + C \cdot \sin(\beta) - K_2 \cdot \cos(\alpha + \delta) = 0 \tag{7-58}$$

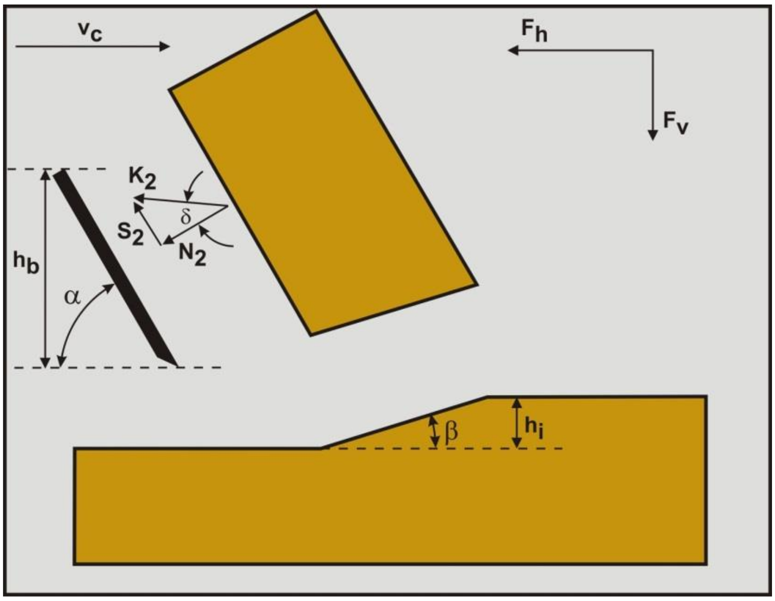

Figure 7-13: The forces on the blade in rock (atmospheric).

The force $\mathbf{K_1}$ on the shear plane is now:

$$K_1 = \frac{-C \cdot \cos(\alpha + \beta + \delta)}{\sin(\alpha + \beta + \delta + \varphi)} \tag{7-59}$$

The force $\mathbf{K_2}$ on the blade is now:

$$K_2 = \frac{C \cdot \cos(\varphi)}{\sin(\alpha + \beta + \delta + \varphi)} \tag{7-60}$$

The force **C** due to the cohesive shear strength **c** is equal to:

$$C = \frac{\lambda \cdot c \cdot h_i \cdot w}{\sin(\beta)} \tag{7-61}$$

The factor λ in equation (7-61) is the velocity strengthening factor, which causes an increase of the cohesive shear strength. In clay (Miedema (1992) and (2010)) this factor has a value of about 2 under normal cutting conditions. In rock the strengthening effect is not reported, so a value of 1 should be used. From equation (7-60) the forces on the blade can be derived. On the blade a force component in the direction of cutting velocity $\mathbf{F_h}$ and a force perpendicular to this direction $\mathbf{F_v}$ can be distinguished.

$$F_h = K_2 \cdot \sin(\alpha + \delta) \tag{7-62}$$

$$F_v = K_2 \cdot \cos(\alpha + \delta) \tag{7-63}$$

Substituting equations (7-61) and (7-60) gives the following equations for the horizontal $\mathbf{F_h}$ and vertical $\mathbf{F_v}$ cutting forces. It should be remarked that the strengthening factor λ in rock is usually 1.

$$F_h = \frac{\lambda \cdot c \cdot h_i \cdot w \cdot \cos(\varphi) \cdot \sin(\alpha + \delta)}{\sin(\beta) \cdot \sin(\alpha + \beta + \delta + \varphi)} \tag{7-64}$$

$$F_v = \frac{\lambda \cdot c \cdot h_i \cdot w \cdot \cos(\varphi) \cdot \cos(\alpha+\delta)}{\sin(\beta) \cdot \sin(\alpha+\beta+\delta+\varphi)} \tag{7-65}$$

7.4. Determining the Angle β

To determine the shear angle **β** where the horizontal force $\mathbf{F_h}$ is at the minimum, the denominator of equation (7-64) has to be at a maximum. This will occur when the derivative of $\mathbf{F_h}$ with respect to **β** equals 0 and the double derivative is negative.

$$\frac{\partial \sin(\alpha+\beta+\delta+\varphi) \cdot \sin(\beta)}{\partial \beta} = \sin(\alpha + 2 \cdot \beta + \delta + \varphi) = 0 \tag{7-66}$$

$$\beta = \frac{\pi}{2} - \frac{\alpha+\delta+\varphi}{2} \tag{7-67}$$

This gives for the cutting forces:

$$F_h = \frac{2 \cdot c \cdot h_i \cdot w \cdot \cos(\varphi) \cdot \sin(\alpha+\delta)}{1+\cos(\alpha+\delta+\varphi)} = \lambda_{HF} \cdot c \cdot h_i \cdot w \tag{7-68}$$

$$F_v = \frac{2 \cdot c \cdot h_i \cdot w \cdot \cos(\varphi) \cdot \cos(\alpha+\delta)}{1+\cos(\alpha+\delta+\varphi)} = \lambda_{VF} \cdot c \cdot h_i \cdot w \tag{7-69}$$

Equations (7-68) and (7-69) are basically the same as the equations found by Merchant (1944), (1945A) and (1945B).

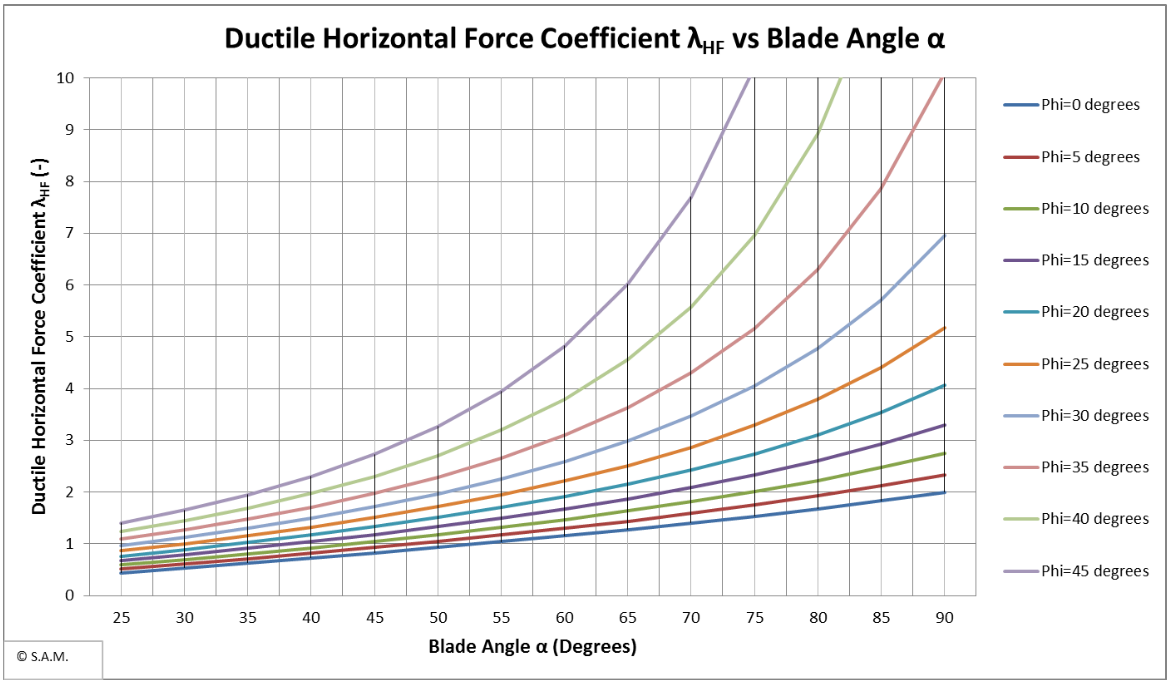

Figure 7-14: The ductile horizontal force coefficient λ_{HF}.

The normal force $\mathbf{N_1}$ and the normal stress $\boldsymbol{\sigma_{N1}}$ on the shear plane are now (with **λ=1**):

$$N_1 = \frac{-C \cdot \cos(\alpha+\beta+\delta)}{\sin(\alpha+\beta+\delta+\varphi)} \cdot \cos(\varphi) \text{ and } \sigma_{N1} = \frac{-c \cdot \cos(\alpha+\beta+\delta)}{\sin(\alpha+\beta+\delta+\varphi)} \cdot \cos(\varphi) \tag{7-70}$$

The normal force $\mathbf{N_2}$ and the normal stress $\boldsymbol{\sigma_{N2}}$ on the blade are now:

$$N_2 = \frac{C \cdot \cos(\varphi)}{\sin(\alpha+\beta+\delta+\varphi)} \cdot \cos(\delta) \text{ and } \sigma_{N2} = c \cdot \frac{h_i \cdot \sin(\alpha)}{h_b \cdot \sin(\beta)} \cdot \frac{\cos(\varphi)}{\sin(\alpha+\beta+\delta+\varphi)} \cdot \cos(\delta) \tag{7-71}$$

Equations (7-70) and (7-71) show that the normal force on the shear plane tends to be negative, unless the sum of the angles **α+β+δ** is greater than 90°. With the use of equation (7-67) the following condition is found:

$$\alpha+\beta+\delta=\alpha+\delta+\left(\frac{\pi}{2}-\frac{\alpha+\delta+\varphi}{2}\right)=\frac{\pi}{2}+\frac{\alpha+\delta-\varphi}{2}>\frac{\pi}{2}\quad \text{so:}\quad \frac{\alpha+\delta-\varphi}{2}>0 \tag{7-72}$$

Because for normal blade angles this condition is always valid, the normal force is always positive.

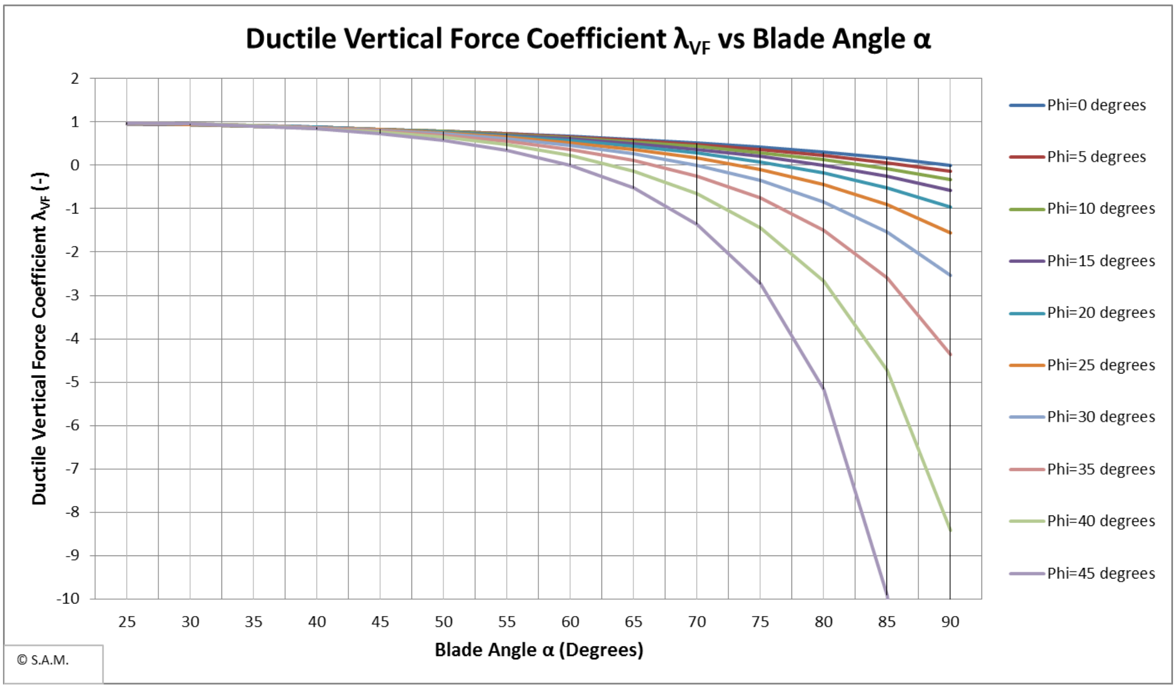

Figure 7-15: The ductile vertical force coefficient λ_{VF}.

Figure 7-14 and Figure 7-15 show the coefficients λ_{HF} and λ_{VF} for the horizontal and vertical forces F_h and F_v according to equations (7-68) and (7-69) as a function of the blade angle **α** and the internal friction angle **φ**, where the external friction angle **δ** is assumed to be **2/3·φ**. A positive coefficient λ_{VF} for the vertical force means that the vertical force F_v is downwards directed. Based on equation (7-56) and (7-68) the specific energy E_{sp} can be determined according to:

$$E_{sp}=\frac{P_c}{Q}=\frac{F_h\cdot v_c}{h_i\cdot w\cdot v_c}=\frac{F_h}{h_i\cdot w}=\lambda_{HF}\cdot c \tag{7-73}$$

The cohesive shear strength c is a function of the Unconfined Compressive Strength UCS and the angle of internal friction **φ** according to (see Figure 7-17):

$$c=\frac{UCS}{2}\cdot\left(\frac{1-\sin(\varphi)}{\cos(\varphi)}\right) \tag{7-74}$$

This gives for the specific energy E_{sp}:

$$E_{sp}=\lambda_{HF}\cdot c=\lambda_{HF}\cdot\frac{UCS}{2}\cdot\left(\frac{1-\sin(\varphi)}{\cos(\varphi)}\right) \tag{7-75}$$

7.5. The Tear Type

Until now only the total normal force on the shear plane N_1 has been taken into consideration, but of course this normal force is the result of integration of the normal stresses σ_{N1} on the shear plane. One could consider that cutting is partly bending the material and it is known that with bending a bar, at the inside (the smallest bending radius) compressive stresses will be developed, while at the outside (the biggest bending radius), tensile stresses are developed. So if the normal force $\mathbf{N_1}$ equals zero, this must mean that near the edge of the blade tensile stresses (negative) stresses develop, while at the outside compressive (positive) stresses develop. So even when the normal force would be slightly positive, still, tensile stresses develop in front of the edge of the blade. The normal force on the blade however is always positive, meaning that the curling type of cutting process will never occur in rock under atmospheric conditions. The previous derivations of the cutting forces are based on the flow type, but in reality rock will fail brittle with either the shear type or the tear type. For the shear type the equations (7-68) and (7-69) can still be used, considering these equations give peak forces. The average forces and thus the average cutting power $\mathbf{P_c}$ and the specific energy $\mathbf{E_{sp}}$ may be 30%-50% of the peak values. The occurrence of the tear type depends on the tensile stress. If somewhere in the rock the tensile stress $\boldsymbol{\sigma_{min}}$ is smaller than the tensile strength $\boldsymbol{\sigma_T}$, a tensile fracture may occur. One should note here that compressive stresses are positive and tensile stresses are negative. So tensile fracture/rupture will occur if the absolute value of the tensile stress $\boldsymbol{\sigma_{min}}$ is bigger than the tensile strength $\boldsymbol{\sigma_T}$.

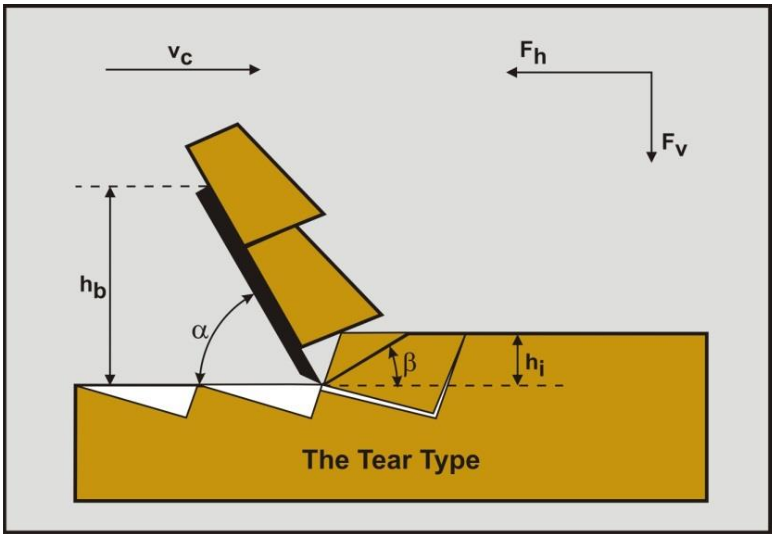

Figure 7-16: The Tear Type cutting mechanism in rock.

If rock is considered, the following condition can be derived with respect to tensile rupture:

The cohesion **c** can be determined from the UCS value and the angle of internal friction according to, as is shown in Figure 7-17:

$$\mathbf{c = \frac{UCS}{2} \cdot \left(\frac{1 - \sin(\varphi)}{\cos(\varphi)} \right)} \qquad \textbf{(7-76)}$$

According to the Mohr-Coulomb failure criterion, the following is valid for the shear stress on the shear plane, as is shown in Figure 7-18.

$$\boldsymbol{\tau_{S1} = c + \sigma_{N1} \cdot \tan(\varphi)} \qquad \textbf{(7-77)}$$

The average stress condition on the shear plane is now $\boldsymbol{\sigma_{N1}}$, $\boldsymbol{\tau_{S1}}$ as is show in Figure 7-18. A Mohr circle (Mohr circle 1) can be drawn through this point, resulting in a minimum stress $\boldsymbol{\sigma_{min}}$ which is negative, so tensile. If this minimum normal stress is smaller than the tensile strength $\boldsymbol{\sigma_T}$ tensile fracture will occur, as is the case in the figure. Now Mohr circle 1 can never exist, but a smaller circle (Mohr circle 2) can, just touching the tensile strength $\boldsymbol{\sigma_T}$. The question is now, how to get from Mohr circle 1 to Mohr circle 2. To find Mohr circle 2 the following steps have to be taken.

The radius **R** of the Mohr circle 1 can be found from the shear stress $\boldsymbol{\tau_{S1}}$ by:

$$\mathbf{R = \frac{\tau_{S1}}{\cos(\varphi)}} \qquad \textbf{(7-78)}$$

The center of the Mohr circle 1, σ_C, now follows from:

$$\sigma_C = \sigma_{N1} + R \cdot \sin(\varphi) = \sigma_{N1} + \tau_{S1} \cdot \tan(\varphi) = \sigma_{N1} + c \cdot \tan(\varphi) + \sigma_{N1} \cdot \tan^2(\varphi) \tag{7-79}$$

The minimum principal stress σ_{min} equals the normal stress in the center of the Mohr circle σ_C minus the radius of the Mohr circle **R**:

$$\sigma_{min} = \sigma_C - R = \sigma_{N1} + c \cdot \tan(\varphi) + \sigma_{N1} \cdot \tan^2(\varphi) - \frac{c}{\cos(\varphi)} - \frac{\sigma_{N1} \cdot \tan(\varphi)}{\cos(\varphi)} \tag{7-80}$$

Rearranging this gives:

$$\sigma_{min} = \sigma_{N1} \cdot \left(1 + \tan^2(\varphi) - \frac{\tan(\varphi)}{\cos(\varphi)}\right) + c \cdot \left(\tan(\varphi) - \frac{1}{\cos(\varphi)}\right) \tag{7-81}$$

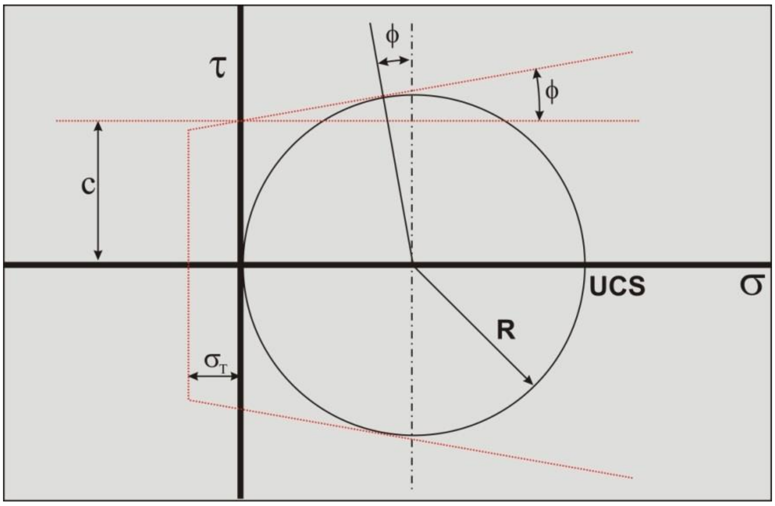

Figure 7-17: The Mohr circle for UCS and cohesion.

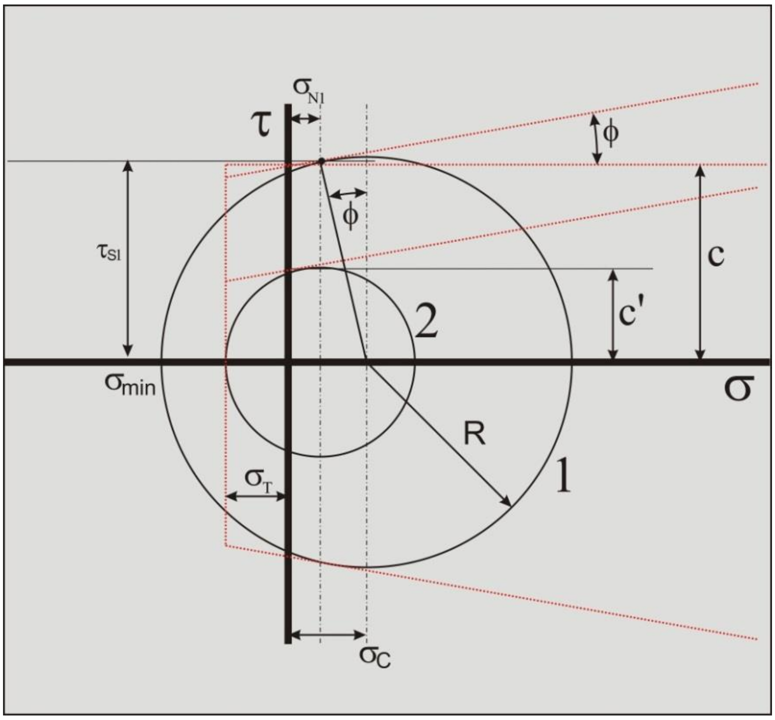

Figure 7-18: The Mohr circles of the Tear Type.

Substituting equation (7-70) for the normal stress on the shear plane gives:

$$\sigma_{min} = \frac{-c \cdot \cos(\alpha+\beta+\delta) \cdot \cos(\varphi)}{\sin(\alpha+\beta+\delta+\varphi)} \cdot \left(1+\tan^2(\varphi) - \frac{\tan(\varphi)}{\cos(\varphi)}\right) + c \cdot \left(\tan(\varphi) - \frac{1}{\cos(\varphi)}\right) > \sigma_T \qquad \textbf{(7-82)}$$

Now ductile failure will occur if the minimum principal stress $\boldsymbol{\sigma_{min}}$ is bigger than then tensile strength $\boldsymbol{\sigma_T}$, thus:

$$\sigma_{min} > \sigma_T \qquad \textbf{(7-83)}$$

If equation (7-83) is true, ductile failure will occur. Keep in mind however, that the tensile strength $\boldsymbol{\sigma_T}$ is a negative number. Of course if the minimum normal stress σ_{min} or in the graph, Figure 7-19, σ_T / c is positive, brittle failure can never occur. Equation (7-83) can be transformed to:

$$\frac{\sigma_T}{c} < -\frac{\cos(\alpha+\beta+\delta)}{\sin(\alpha+\beta+\delta+\varphi)} \cdot \left(\cos(\varphi) - \tan(\varphi) + \tan(\varphi) \cdot \sin(\varphi)\right) + \tan(\varphi) - \frac{1}{\cos(\varphi)} \qquad \textbf{(7-84)}$$

Substituting equation (7-67) for the shear angle $\boldsymbol{\beta}$ gives:

$$\frac{\sigma_T}{c} < \frac{\sin\left(\frac{\alpha+\delta-\varphi}{2}\right)}{\cos\left(\frac{\alpha+\delta+\varphi}{2}\right)} \cdot \left(\cos(\varphi) - \tan(\varphi) + \tan(\varphi) \cdot \sin(\varphi)\right) + \tan(\varphi) - \frac{1}{\cos(\varphi)} \qquad \textbf{(7-85)}$$

This can be transformed to:

$$\frac{\sigma_T}{c} < \left(\frac{\sin\left(\frac{\alpha+\delta-\varphi}{2}\right)}{\cos\left(\frac{\alpha+\delta+\varphi}{2}\right)} - 1\right) \cdot \left(\frac{1-\sin(\varphi)}{\cos(\varphi)}\right) \qquad \textbf{(7-86)}$$

A pseudo cohesive shear strength **c'** can be defined, based on the tensile strength $\boldsymbol{\sigma_T}$, by using the equal sign in equation (7-86). With this pseudo cohesive shear strength Mohr circle 2 can be constructed.

$$c' = \frac{\sigma_T}{\left(\frac{\sin\left(\frac{\alpha+\delta-\varphi}{2}\right)}{\cos\left(\frac{\alpha+\delta+\varphi}{2}\right)} - 1\right) \cdot \left(\frac{1-\sin(\varphi)}{\cos(\varphi)}\right)} \qquad \textbf{(7-87)}$$

Substituting equation (7-87) in the equations (7-68) and (7-69) gives for the cutting forces:

$$F_h = \frac{2 \cdot c' \cdot h_i \cdot w \cdot \cos(\varphi) \cdot \sin(\alpha+\delta)}{1+\cos(\alpha+\delta+\varphi)} = \lambda_{HT} \cdot \sigma_T \cdot h_i \cdot w \qquad \textbf{(7-88)}$$

$$F_v = \frac{2 \cdot c' \cdot h_i \cdot w \cdot \cos(\varphi) \cdot \cos(\alpha+\delta)}{1+\cos(\alpha+\delta+\varphi)} = \lambda_{VT} \cdot \sigma_T \cdot h_i \cdot w \qquad \textbf{(7-89)}$$

Figure 7-19 shows the pseudo cohesive shear strength coefficient σ_T / c from equation (7-86). Below the lines the cutting process is ductile (the flow type) or brittle (the shear type), while above the lines it is brittle (the tear type). It is clear from this figure that an increasing blade angle $\boldsymbol{\alpha}$ and an increasing internal friction angle $\boldsymbol{\varphi}$ surpresses the occurrence of the Tear Type. The coefficients $\boldsymbol{\lambda_{HT}}$ and $\boldsymbol{\lambda_{VT}}$ are shown in Figure 7-20 and Figure 7-21 for a range of blade angles $\boldsymbol{\alpha}$ and internal friction angles $\boldsymbol{\varphi}$.

Equation (7-88) gives for the specific energy $\mathbf{E_{sp}}$:

$$E_{sp} = \lambda_{HT} \cdot \sigma_T \tag{7-90}$$

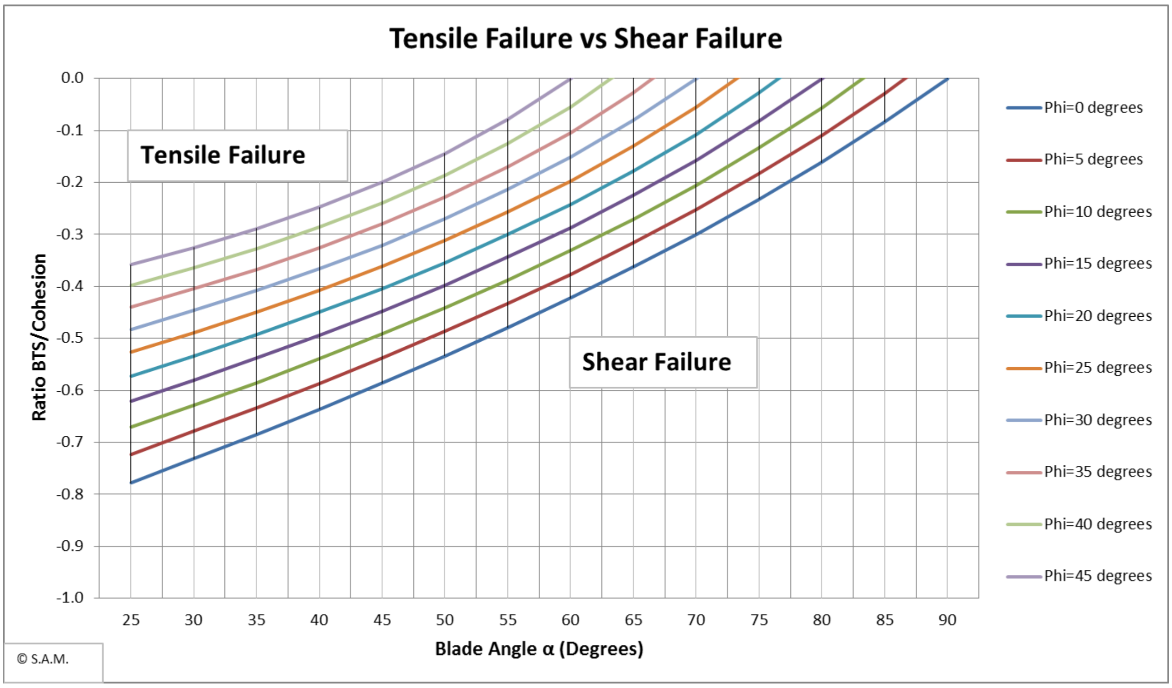

Figure 7-19: Below the lines (equation (7-84)) the cutting process is ductile; above the lines it is brittle.

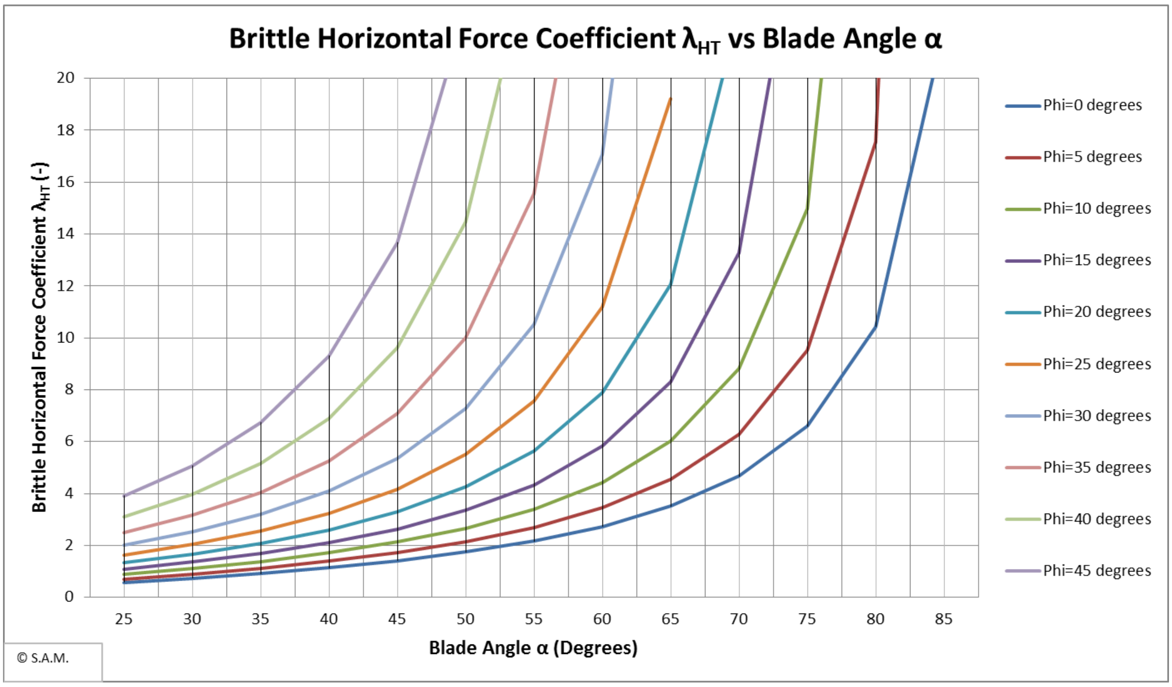

Figure 7-20: The brittle horizontal force coefficient λ_{HT}.

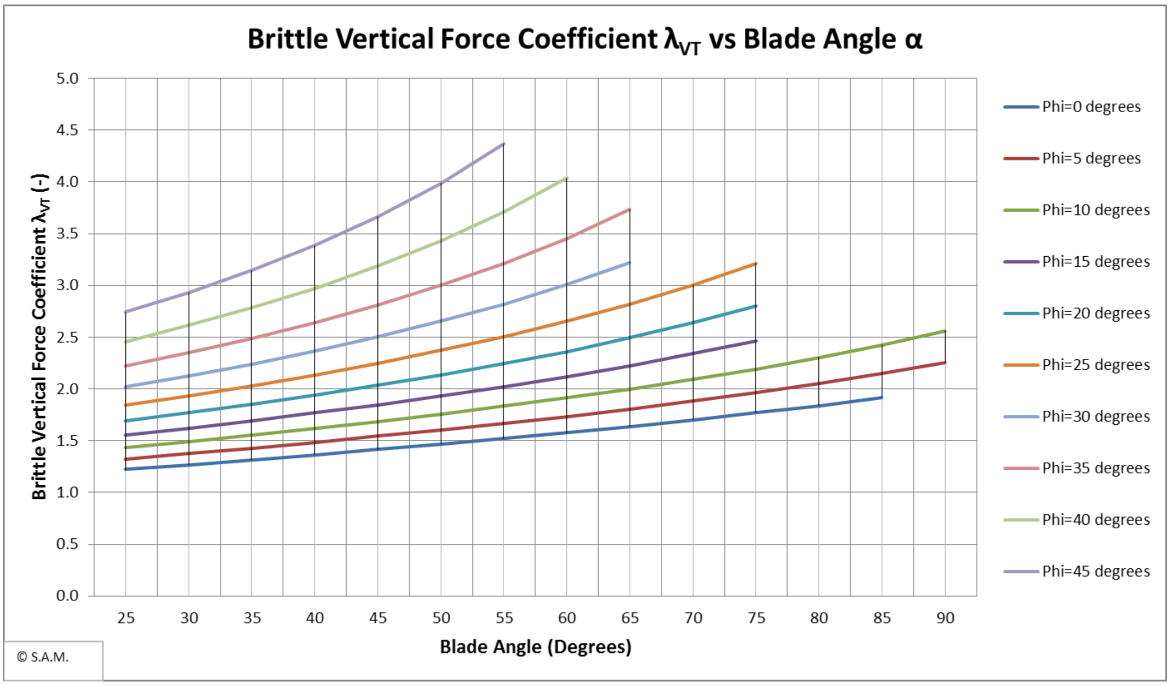

Figure 7-21: The brittle vertical force coefficient λ_{VT}.

To determine the cutting forces in rock under atmospheric conditions the following steps have to be taken:

1. Determine whether the cutting process is based on the Flow Type or the Tear Type, using Figure 7-19.
2. If the cutting process is based on the Flow Type, use Figure 7-14 and Figure 7-15 to determine the coefficients λ_{HF} and λ_{VF}. Use equations (7-68) and (7-69) to calculate the cutting forces. Optionally a factor 0.3-0.5 may be applied in case of brittle shear failure, to account for average forces, power and specific energy.
3. If the cutting process is based on the Tear Type, use Figure 7-20 and Figure 7-21 to determine the coefficients λ_{HT} and λ_{VT}. Use equations (7-88) and (7-89) to calculate the cutting forces. A factor 0.3-0.5 should be applied to account for average forces, power and specific energy.

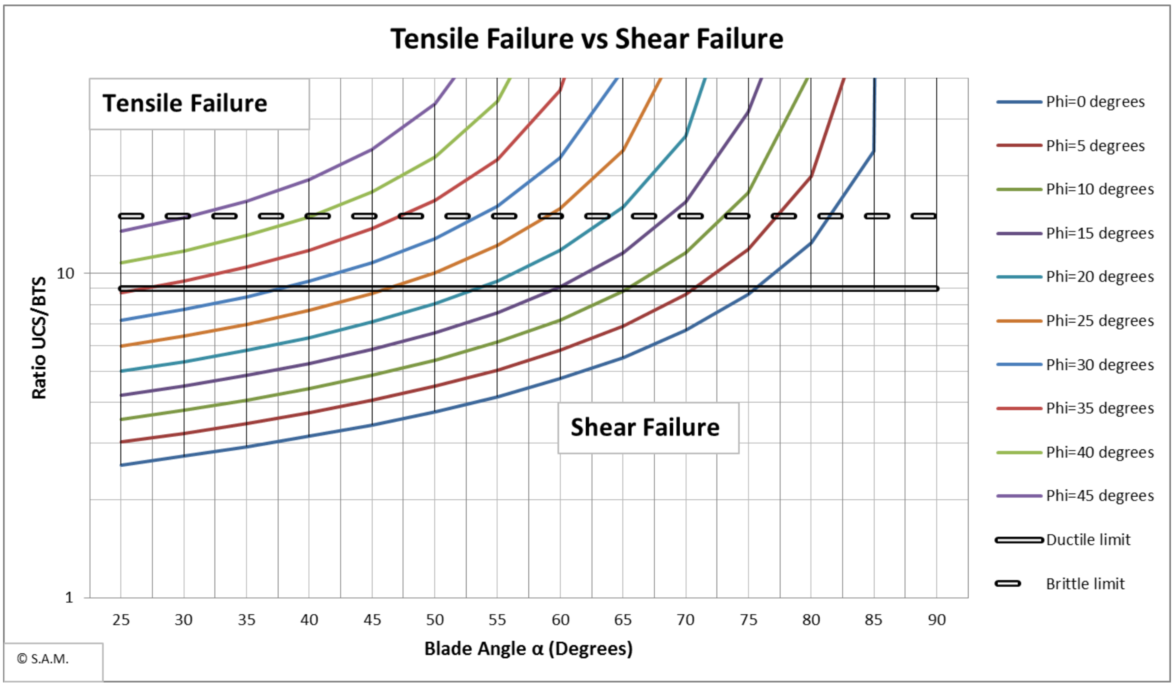

Figure 7-22: The ratio UCS/BTS, below the lines there is ductile failure, above the lines it is brittle.

Based on equation (7-86) and (7-76) the ratio UCS/BTS can also be determined. Gehring (1987) (see Vlasblom (2003-2007)) stated that below a ratio of 9 ductile failure will occur, while above a ratio of 15 brittle failure will occur. In between these limits there is a transition between ductile and brittle failure, which is also in accordance with the findings of Fairhurst (1964). Figure 7-22 shows that the ductile limit of 9 is possible for blade angles **α** between 45º and 60º corresponding with internal friction angles **φ** of 25º and 15º. For the same blade angles, the corresponding internal friction angles **φ** are 35º and 25º at the brittle limit of 15. These values match the blade angles as used in dredging and mining and also match the internal friction angle of commonly dredged rock. Figure 7-22 shows that in general a higher internal friction angle **φ** and a bigger blade angle surpress tensile failure **α**.

$$\frac{UCS}{BTS}=\frac{2}{\left(\frac{\sin\left(\frac{\alpha+\delta-\varphi}{2}\right)}{\cos\left(\frac{\alpha+\delta+\varphi}{2}\right)}-1\right)\cdot\left(\frac{1-\sin(\varphi)}{\cos(\varphi)}\right)^{2}} \tag{7-91}$$

7.6. Nomenclature Chapter 7:

a, τ_a	Adhesive shear strength	kPa
A	Adhesive force on the blade	kN
c, τ_c	Cohesive shear strength	kPa
c'	Pseudo cohesive shear strength	kPa
C	Cohesive force on shear plane	kN
E_{sp}	Specific energy	kPa
F	Force	kN
F_h	Horizontal cutting force	kN
F_v	Vertical cutting force	kN
g	Gavitational constant (9.81)	m/s^2
G	Gravitational force	kN
h_i	Initial thickness of layer cut	m
h_b	Height of the blade	m
h'_b	Contact height of the blade in case **Curling Type**	m
K_1	Grain force on the shear plane	kN
K_2	Grain force on the blade	kN
I	Inertial force on the shear plane	kN
N_1	Normal grain force on shear plane	kN
N_2	Normal grain force on blade	kN
P_c	Cutting power	kW
Q	Production	m^3
r	Adhesion/cohesion ratio	-
r_1	Pore pressure on shear plane/cohesion ratio	-
r_2	Pore pressure on blade/cohesion ratio	-
R	Radius of Mohr circle	kPa
R_1	Acting point on the shear plane	m
R_2	Acting point on the blade	m
S_1	Shear force due to internal friction on the shear plane	kN
S_2	Shear force due to external friction on the blade	kN
T	Tensile force	kN
UCS	Unconfined Compressive Stress	kPa
v_c	Cutting velocity	m/s
w	Width of the blade	m
W_1	Force resulting from pore under pressure on the shear plane	kN
W_2	Force resulting from pore under pressure on the blade	kN
α	Blade angle	rad
β	Angle of the shear plane with the direction of cutting velocity	rad
τ	Shear stress	kPa
τ_a, a	Adhesive shear strength (strain rate dependent)	kPa
τ_c, c	Cohesive shear strength (strain rate dependent)	kPa
τ_{S1}	Average shear stress on the shear plane	kPa
τ_{S2}	Average shear stress on the blade	kPa
σ	Normal stress	kPa
σ_C	Center of Mohr circle	kPa
σ_T	Tensile strength	kPa
σ_{min}	Minimum principal stress in Mohr circle	kPa
σ_{N1}	Average normal stress on the shear plane	kPa
σ_{N2}	Average normal stress on the blade	kPa
φ	Angle of internal friction	rad
δ	Angle of external friction	rad
λ	Strengthening factor	-

λ_1	Acting point factor on the shear plane	-
λ_2	Acting point factor on the blade	-
λ_{HF}	Ductile horizontal force coefficient	-
λ_{VF}	Ductile vertical force coefficient	-
λ_{HT}	Brittle horizontal force coefficient	-
λ_{VT}	Brittle vertical force coefficient	-

Chapter 8: Rock Cutting Under Hyperbaric Conditions

8.1. Introduction

For rock cutting in dredging and mining under hyperbaric conditions not much is known yet. The data available are from drilling experiments under very high pressures (a.o. Zijsling (1987), Kaitkay and Lei (2005) and Rafatian et al. (2009)). The main difference between dredging and mining applications on one side and drilling experiments on the other side is that in dredging and mining the thickness of the layer cut is relatively big, like 5-10 cm, while in drilling the process is more like scraping with a thickness less than a mm. From the drilling experiments it is known that under high pressures there is a transition from a brittle-shear cutting process to a ductile-flow cutting process. Figure 8-1 and Figure 8-2 from Rafatian et al. (2009) show clearly that with increasing confining pressure, first the specific energy $\mathbf{E_{sp}}$ increases with a steep curve, which is the transition brittle-ductile, after which the curve for ductile failure is reached which is less steep. The transition is completed at 690 kPa-1100 kPa, matching a waterdepth of 69-110 m.

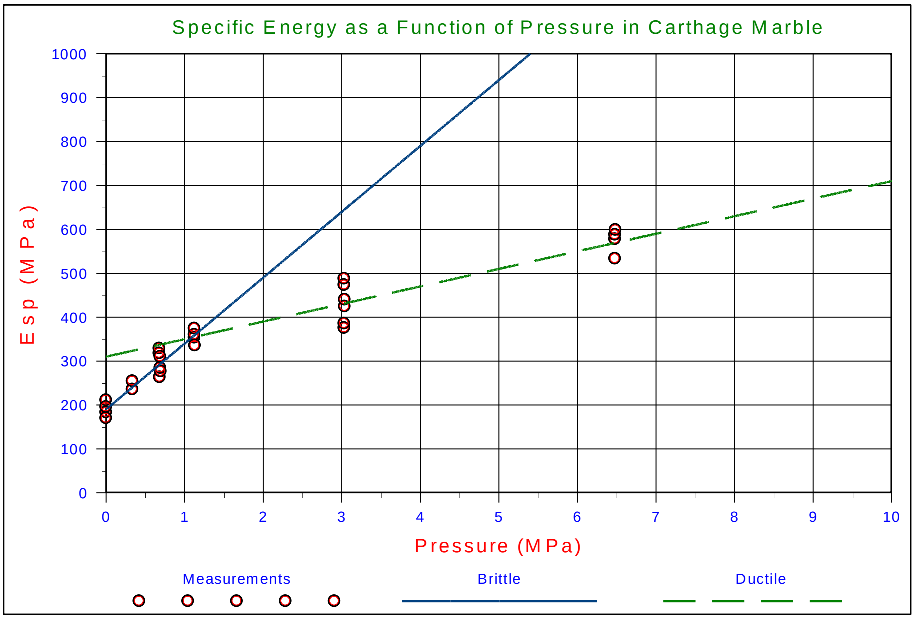

Figure 8-1: MSE versus confining pressure for Carthage marble in light and viscous mineral oil, Rafatian et al. (2009).

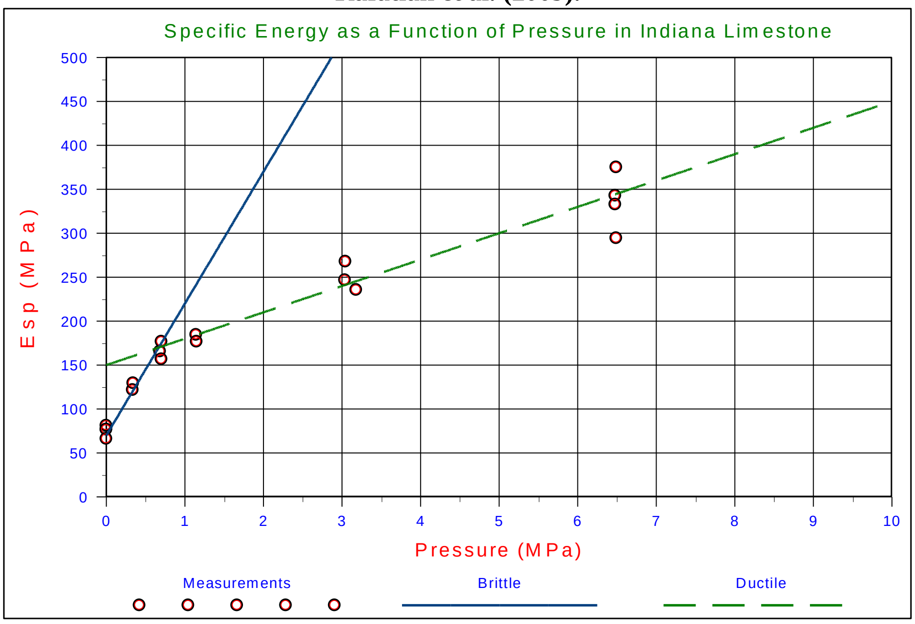

Figure 8-2: MSE versus confining pressure for Indiana limestone in light mineral oil, Rafatian et al. (2009).

The Carthage Marble has a UCS value of about 100 MPa and the Indiana Limestone a UCS value of 48 MPa. The cutter had a blade angle **α** of 110º. Figure 8-13 shows the specific energy (according to the theory as developed in this chapter) as a function of the UCS value and the confining pressure (water depth). For the Carthage Marble a specific energy of about 400 MPa is found under atmospheric conditions for the ductile cutting process. For the brittle shear process 25%-50% of this value should be chosen, matching Figure 8-1 at 0 MPa. For a waterdepth of 65 m, matching 6.5 MPa the graph gives about 500 MPa specific energy, which is a bit lower than the measurements. For the Indiana Limestone a specific energy of about 200 MPa is found under atmospheric conditions for the ductile cutting process. Also here, for the brittle shear process, 25%-50% of this value should be chosen, matching Figure 8-2 at 0 MPa confining pressure. For a waterdepth of 65 m, matching 6.5 MPa the graph gives about 280 MPa specific energy, which is a bit lower than the measurements.
For deep sea mining applications this is still shallow water. Both graphs show an increase of the $\mathbf{E_{sp}}$ by a factor 2-2.5 during the transition brittle-shear to ductile-flow, which matches a reduction factor of 0.25-0.5 for the average versus the maximum cutting forces as mentioned before. Figure 8-11 and Figure 8-12 show the results of Zijsling (1987) in Mancos Shale and Figure 8-3 shows the results of Kaitkay & Lei (2005) in Carthage Marble.

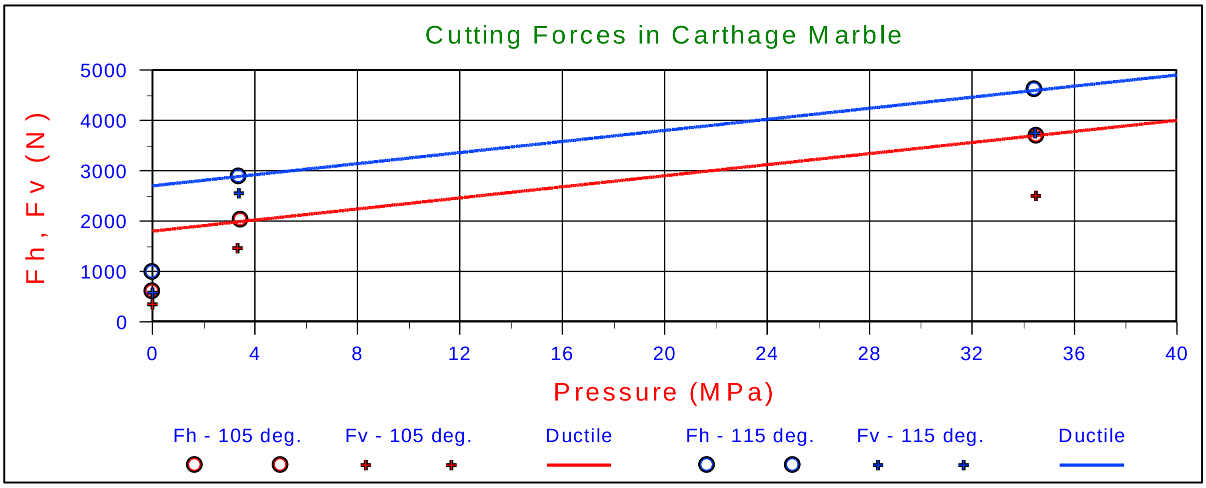

Figure 8-3: Variations of average cutting forces with hydrostatic pressure, Kaitkay & Lei (2005).

The experiments of Kaitkay & Lei (2005) also show that the transition from brittle-shear to ductile-flow takes place in the first few hundreds of meters of waterdepth (from 0 to about 2.5 MPa). They also show a multiplication factor of about 3 during this transition. The experiments of Zijsling (1987) are not really suitable for determining the transition brittle-shear to ductile-flow because there are only measurements at 0 MPa and about 10 MPa, so they do not show when the transition is completed, but they do show the increase in forces and $\mathbf{E_{sp}}$. The explanation for the transition from brittle-shear to ductile-flow is, according to Zijsling (1987), the dilatation due to shear stress in the shear plane resulting in pore under pressures, similar to the cutting process in water saturated sand as has been described by Miedema (1987 September). Zijsling however did not give any mathematical model. Detournay & Atkinson (2000) use the same explanation and use the Merchant (1944) model (equations (7-68) and (7-69) for the flow type cutting process) to quantify the cutting forces and specific energy by adding the pore pressures to the basic equations:

$$\mathbf{F_h} = \frac{2 \cdot h_i \cdot w \cdot \cos(\varphi) \cdot \sin(\alpha + \delta)}{1 + \cos(\alpha + \delta + \varphi)} \cdot \left(c + p_{1m} \cdot \tan(\varphi)\right) \qquad \textbf{(8-1)}$$

The difference between the bottom hole pressure (or hydrostatic pressure) and the average pressure $\mathbf{p_{1m}}$ in the shear plane has to be added to the effective stress between the particles in the shear plane **A-B.** Multiplying this with the tangent of the internal friction angle gives the additional shear stress in the shear plane **A-B**, see Figure 8-4.
So in the vision of Detournay & Atkinson (2000) the effect of pore water under pressures $\mathbf{p_{1m}}$ is like an apparent additional cohesion. Based on this they find a value of the external friction angle which is almost equal to the internal friction angle of 23º for the experiments of Zijsling (1987). Detournay & Atkinson (2000) however forgot that, if there is a very large pore water under pressure in the shear plane, this pore water under pressure has not disappeared when the layer cut moves over the blade or cutter. There will also be a very large pore water under pressures on the blade as has been explained by Miedema (1987 September) for water saturated sand in dredging applications. In the next paragraph this will be explained.

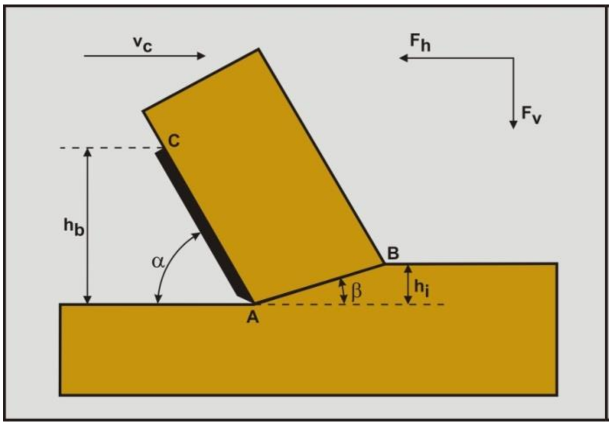

Figure 8-4: The definitions of the cutting process.

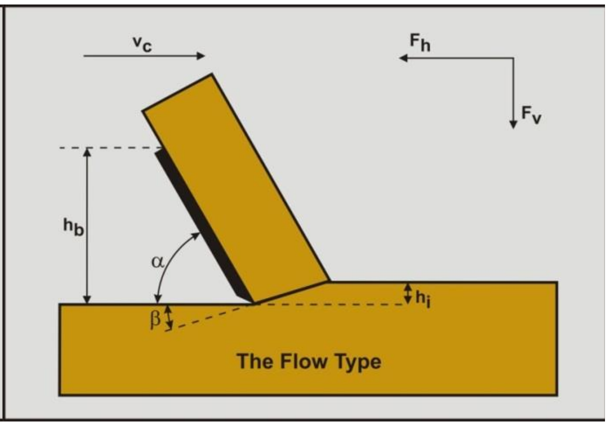

Figure 8-5: The Flow Type cutting mechanism in ductile hyperbaric rock cutting.

8.2. The Flow Type

First of all it is assumed that the hyperbaric cutting mechanism is similar to the **Flow Type** as is shown in Figure 8-5. There may be 3 mechanisms that might explain the influence of large hydrostatic pressures:

1. When a tensile failure occurs, water has to flow into the crack, but the formation of the crack goes so fast that cavitation will occur.
2. A second possible mechanism that might occur is an increase of the pore volume due to the elasticity of the rock and the pore water. If high tensile stresses exist in the rock, then the pore volume will increase due to elasticity. Because of the very low permeability of the rock, the compressibility of the pore water will have to deal with this. Since the pore water is not very compressible, at small volume changes this will already result in large under pressures in the pores. Whether this will lead to full cavitation of the pore water is still a question.
3. Due to the high effective grain stresses, the particles are removed from the matrix which normally keeps them together and makes it a rock. This will happen near the shear plane. The loose particles will be subject to dilatation, resulting in an increase of the pore volume. This pore volume increase results in water flow to the shear plane, which can only occur if there is an under pressure in the pores in the shear plane. If this under pressure reaches the water vapor pressure, cavitation will occur, which is the lower limit for the absolute pressures and the upper limit for the pressure difference between the bottom hole or hydrostatic pressure and the pore water pressure. The pressure difference is proportional to the cutting velocity and the dilatation, squared proportional to the layer thickness and reversely proportional to the permeability of the rock. If the rock is very impermeable, cavitation will always occur and the cutting forces will match the upper limit.

Now under atmospheric conditions, the compressive strength of the rock will be much bigger than the atmospheric pressure; usually the rock will have a compressive strength of 1 MPa or more while the atmospheric pressure is just 100 kPa. Strong rock may have compressive strengths of 100’s of MPa’s, so the atmospheric pressure and thus the effect of cavitation in the pores or the crack can be neglected. However in oil drilling and deep sea mining at water depths of 3000 m nowadays plus a few 1000’s m into the seafloor (in case of oil drilling), the hydrostatic pressure could easily increase to values higher than 10 MPa up to 100 MPa causing softer rock to behave ductile, where it would behave brittle under low hydrostatic pressures.
It should be noted that brittle-tear failure, which is tensile failure, will only occur under atmospheric conditions and small blade angles as used in dredging and mining. With blade angles larger than 90 brittle-tear will never occur (see Figure 7-19). Brittle-shear may occur in all cases under atmospheric conditions.
Now what is the difference between rock cutting under atmospheric conditions and under hyperbaric conditions? The difference is the extra pore pressure forces $\mathbf{W_1}$ and $\mathbf{W_2}$ on the shear plane and on the blade as will be explained next.

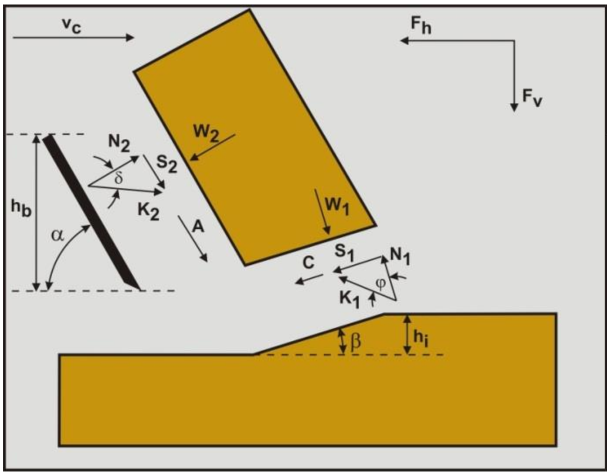

Figure 8-6: The forces on the layer cut in rock (hyperbaric).

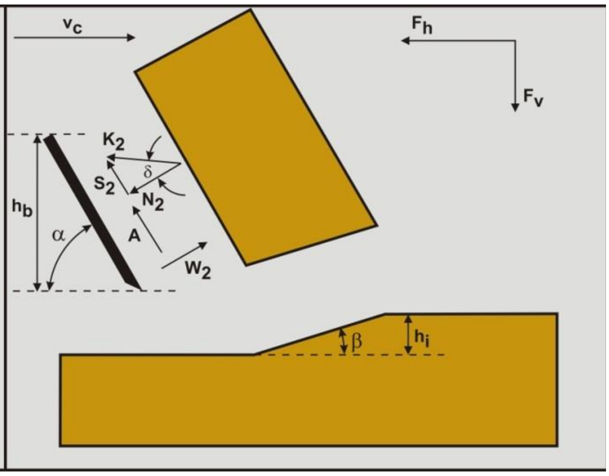

Figure 8-7: The forces on the blade in rock (hyperbaric).

Figure 8-6 illustrates the forces on the layer of rock cut. The forces acting on this layer are:

1. A normal force acting on the shear surface $\mathbf{N_1}$ resulting from the grain stresses.
2. A shear force $\mathbf{S_1}$ as a result of internal fiction $\mathbf{N_1 \cdot tan(\phi)}$.
3. A force $\mathbf{W_1}$ as a result of water under pressure in the shear zone.
4. A shear force **C** as a result of the cohesive shear strength $\boldsymbol{\tau_c}$ or **c**. This force can be calculated by multiplying the cohesive shear strength $\boldsymbol{\tau_c}$/**c** with the area of the shear plane.
5. A force normal to the blade $\mathbf{N_2}$ resulting from the grain stresses.
6. A shear force $\mathbf{S_2}$ as a result of the external friction $\mathbf{N_2 \cdot tan(\delta)}$.
7. A shear force **A** as a result of pure adhesion between the rock and the blade $\boldsymbol{\tau_a}$ or **a**. This force can be calculated by multiplying the adhesive shear strength $\boldsymbol{\tau_a}$/**a** of the rock with the contact area between the rock and the blade. In most rocks this force will be absent.
8. A force $\mathbf{W_2}$ as a result of water under pressure on the blade

The normal force $\mathbf{N_1}$ and the shear force $\mathbf{S_1}$ on the shear plane can be combined to a resulting grain force $\mathbf{K_1}$.

$$\mathbf{K_1 = \sqrt{N_1^2 + S_1^2}} \tag{8-2}$$

The forces acting on a straight blade when cutting rock, can be distinguished as:

9. A force normal to the blade $\mathbf{N_2}$ resulting from the grain stresses.
10. A shear force $\mathbf{S_2}$ as a result of the external friction $\mathbf{N_2 \cdot tan(\delta)}$.
11. A shear force **A** as a result of pure adhesion between the rock and the blade $\boldsymbol{\tau_a}$ or **c**. This force can be calculated by multiplying the adhesive shear strength $\boldsymbol{\tau_a}$/**a** of the rock with the contact area between the rock and the blade. In most rocks this force will be absent.
12. A force $\mathbf{W_2}$ as a result of water under pressure on the blade

These forces are shown in Figure 8-7. If the forces $\mathbf{N_2}$ and $\mathbf{S_2}$ are combined to a resulting force $\mathbf{K_2}$ and the adhesive force and the water under pressures are known, then the resulting force $\mathbf{K_2}$ is the unknown force on the blade. By taking the horizontal and vertical equilibrium of forces an expression for the force $\mathbf{K_2}$ on the blade can be derived.

$$\mathbf{K_2 = \sqrt{N_2^2 + S_2^2}} \tag{8-3}$$

The horizontal equilibrium of forces:

$$\sum \mathbf{F_h} = \mathbf{K_1 \cdot \sin(\beta + \varphi) - W_1 \cdot \sin(\beta) + C \cdot \cos(\beta) - A \cdot \cos(\alpha) + W_2 \cdot \sin(\alpha) - K_2 \cdot \sin(\alpha + \delta) = 0} \tag{8-4}$$

The vertical equilibrium of forces:

$$\sum \mathbf{F_v} = \mathbf{-K_1 \cdot \cos(\beta + \varphi) + W_1 \cdot \cos(\beta) + C \cdot \sin(\beta) + A \cdot \sin(\alpha) + W_2 \cdot \cos(\alpha) - K_2 \cdot \cos(\alpha + \delta) = 0} \tag{8-5}$$

The force K_1 on the shear plane is now:

$$K_1 = \frac{W_2 \cdot \sin(\delta) + W_1 \cdot \sin(\alpha+\beta+\delta) - C \cdot \cos(\alpha+\beta+\delta) + A \cdot \cos(\delta)}{\sin(\alpha+\beta+\delta+\varphi)} \tag{8-6}$$

The force K_2 on the blade is now:

$$K_2 = \frac{W_2 \cdot \sin(\alpha+\beta+\varphi) + W_1 \cdot \sin(\varphi) + C \cdot \cos(\varphi) - A \cdot \cos(\alpha+\beta+\varphi)}{\sin(\alpha+\beta+\delta+\varphi)} \tag{8-7}$$

From equation (8-7) the forces on the blade can be derived. On the blade a force component in the direction of cutting velocity F_h and a force perpendicular to this direction F_v can be distinguished.

$$F_h = -W_2 \cdot \sin(\alpha) + K_2 \cdot \sin(\alpha+\delta) \tag{8-8}$$

$$F_v = -W_2 \cdot \cos(\alpha) + K_2 \cdot \cos(\alpha+\delta) \tag{8-9}$$

The normal force on the shear plane is now:

$$N_1 = \frac{W_2 \cdot \sin(\delta) + W_1 \cdot \sin(\alpha+\beta+\delta) - C \cdot \cos(\alpha+\beta+\delta) + A \cdot \cos(\delta)}{\sin(\alpha+\beta+\delta+\varphi)} \cdot \cos(\varphi) \tag{8-10}$$

The normal force on the blade is now:

$$N_2 = \frac{W_2 \cdot \sin(\alpha+\beta+\varphi) + W_1 \cdot \sin(\varphi) + C \cdot \cos(\varphi) - A \cdot \cos(\alpha+\beta+\varphi)}{\sin(\alpha+\beta+\delta+\varphi)} \cdot \cos(\delta) \tag{8-11}$$

The pore pressure forces can be determined in the case of full-cavitation or the case of no cavitation according to:

$$W_1 = \frac{\rho_w \cdot g \cdot (z+10) \cdot h_i \cdot w}{\sin(\beta)} \quad \text{or} \quad W_1 = \frac{p_{1m} \cdot h_i \cdot w}{\sin(\beta)} \tag{8-12}$$

$$W_2 = \frac{\rho_w \cdot g \cdot (z+10) \cdot h_b \cdot w}{\sin(\alpha)} \quad \text{or} \quad W_2 = \frac{p_{2m} \cdot h_b \cdot w}{\sin(\alpha)} \tag{8-13}$$

The forces **C** and **A** are determined by the cohesive shear strength **c** and the adhesive shear strength **a** according to:

$$C = \frac{c \cdot h_i \cdot w}{\sin(\beta)} \tag{8-14}$$

$$A = \frac{a \cdot h_b \cdot w}{\sin(\alpha)} \tag{8-15}$$

The ratio’s between the adhesive shear strength and the pore pressures with the cohesive shear strength can be found according to:

$$r = \frac{a \cdot h_b}{c \cdot h_i}, \ r_1 = \frac{p_{1m} \cdot h_i}{c \cdot h_i} \quad \text{or} \quad r_1 = \frac{\rho_w \cdot g \cdot (z+10) \cdot h_i}{c \cdot h_i}, r_2 = \frac{p_{2m} \cdot h_b}{c \cdot h_i} \quad \text{or} \quad r_2 = \frac{\rho_w \cdot g \cdot (z+10) \cdot h_b}{c \cdot h_i} \tag{8-16}$$

8.3. The Tear Type

Similar to the derivation of equation (7-86) for the occurrence of tensile failure under atmospheric conditions, equation (8-17) can be derived for the occurrence of tensile failure under hyperbaric conditions. Under hyperbaric conditions equation (8-17) will almost always be true, because of the terms with $\mathbf{r_1}$ and $\mathbf{r_2}$ which may become very big (positive). So tensile failure will not be considered for hyperbaric conditions.

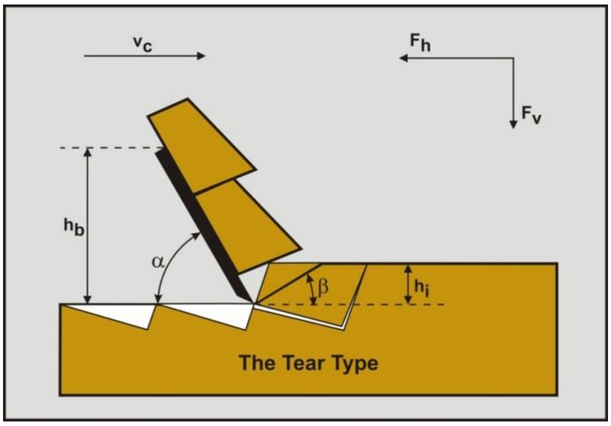

Figure 8-8: The Tear Type cutting mechanism in rock under hyperbaric conditions.

$$c \cdot \left(\frac{r \cdot \dfrac{\sin(\beta) \cdot \cos(\delta)}{\sin(\alpha)} + r_2 \cdot \dfrac{\sin(\beta) \cdot \sin(\delta)}{\sin(\alpha)} + r_1 \cdot \sin(\alpha+\beta+\delta) - \cos(\alpha+\beta+\delta) - \sin(\alpha+\beta+\delta+\varphi)}{\sin(\alpha+\beta+\delta+\varphi)} \right) \cdot \left(\frac{1-\sin(\varphi)}{\cos(\varphi)} \right) > \sigma_T \tag{8-17}$$

8.4. The Curling Type

When cutting or scraping a very thin layer of rock, the **Curling Type** may occur. In dredging and mining usually the layer thickness is such that this will not occur, but in drilling practices usually the layer thickness is very small compared with the height of the blade. In the Zijsling (1987) experiments layer thicknesses of 0.15 mm and 0.30 mm were applied with a PDC bit with a height and width of about 10 mm. Under these conditions the **Curling Type** will occur, which is also named balling. Figure 8-9 shows this type of cutting mechanism.

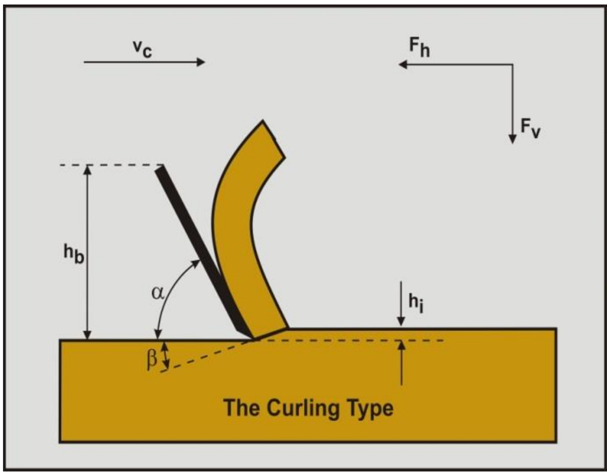

Figure 8-9: The Curling Type or balling.

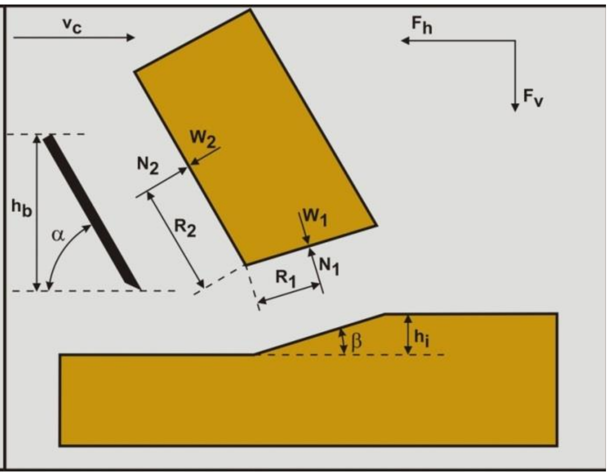

Figure 8-10: The equilibrium of moments on the layer cut in hyperbaric rock.

Now the question is, what is the effective blade height $\mathbf{h'_b}$? In other words, along which distance will the rock cut be in contact with the blade? To solve this problem an additional condition has to be found. This condition is the equilibrium of moments around the blade tip as is shown in Figure 8-10. The only forces that contribute to the equilibrium of moments are the normal forces $\mathbf{N_1}$ and $\mathbf{N_2}$ and the pore pressure forces $\mathbf{W_1}$ and $\mathbf{W_2}$. The acting points of these forces are chosen as fractions of the length of the shear plane $\boldsymbol{\lambda_1}$ and the blade length $\boldsymbol{\lambda_2}$.
The equilibrium of moments around the blade tip is:

$$(N_1 - W_1) \cdot R_1 = (N_2 - W_2) \cdot R_2 \tag{8-18}$$

For the acting points the following can be derived:

$$R_1 = \frac{\lambda_1 \cdot h_i}{\sin(\beta)}, \quad R_2 = \frac{\lambda_2 \cdot h_b^{'}}{\sin(\alpha)} \tag{8-19}$$

Substituting equations (8-10) and (8-11) into equation (8-18) gives:

$$\begin{aligned}&\left(\frac{W_2 \cdot \sin(\delta) + W_1 \cdot \sin(\alpha+\beta+\delta) - C \cdot \cos(\alpha+\beta+\delta) + A \cdot \cos(\delta)}{\sin(\alpha+\beta+\delta+\varphi)} \cdot \cos(\varphi) - W_1\right) \cdot \frac{\lambda_1 \cdot h_i}{\sin(\beta)}\\ &= \left(\frac{W_2 \cdot \sin(\alpha+\beta+\varphi) + W_1 \cdot \sin(\varphi) + C \cdot \cos(\varphi) - A \cdot \cos(\alpha+\beta+\varphi)}{\sin(\alpha+\beta+\delta+\varphi)} \cdot \cos(\delta) - W_2\right) \cdot \frac{\lambda_2 \cdot h_b^{'}}{\sin(\alpha)}\end{aligned} \tag{8-20}$$

This can be written as a second degree function of the effective blade height **h'b**:

$$A \cdot x^2 + B \cdot x + C = 0$$

$$h_b^{'} = x = \frac{-B - \sqrt{B^2 - 4 \cdot A \cdot C}}{2 \cdot A}$$

$$A = \frac{\lambda_2 \cdot p_{2m} \cdot \sin(\alpha+\beta+\delta+\varphi) - \lambda_2 \cdot p_{2m} \cdot \sin(\alpha+\beta+\varphi) \cdot \cos(\delta) + a \cdot \lambda_2 \cdot \cos(\alpha+\beta+\varphi) \cdot \cos(\delta)}{\sin(\alpha) \cdot \sin(\alpha)} \tag{8-21}$$

$$B = \frac{\lambda_1 \cdot p_{2m} \cdot \sin(\delta) \cdot \cos(\varphi) - \lambda_2 \cdot p_{1m} \cdot \cos(\delta) \cdot \sin(\varphi) - c \cdot \lambda_2 \cdot \cos(\delta) \cdot \cos(\varphi) + a \cdot \lambda_1 \cdot \cos(\varphi) \cdot \cos(\delta)}{\sin(\alpha) \cdot \sin(\beta)} \cdot h_i$$

$$C = \frac{\lambda_1 \cdot p_{1m} \cdot \sin(\alpha+\beta+\delta) \cdot \cos(\varphi) - \lambda_1 \cdot p_{1m} \cdot \sin(\alpha+\beta+\delta+\varphi) - c \cdot \lambda_1 \cdot \cos(\alpha+\beta+\delta) \cdot \cos(\varphi)}{\sin(\beta) \cdot \sin(\beta)} \cdot h_i \cdot h_i$$

If **h'b**<**hb** then the **Curling Type** will occur, but if **h'b**>**hb** the normal **Flow Type** will occur.

$$\begin{aligned}&\text{if } h_b^{'} < h_b \text{ then use } h_b^{'}\\ &\text{if } h_b^{'} \geq h_b \text{ then use } h_b\end{aligned} \tag{8-22}$$

8.5. Conclusions and Discussion

The theory developed here, which basically is the theory of Miedema (1987 September) extended with the **Curling Type**, has been applied on the cutting tests of Zijsling (1987). Zijsling conducted cutting tests with a PDC bit with a width and height of 10 mm in Mancos Shale. This type of rock has a UCS value of about 65 MPa, a cohesive shear strength **c** of about 25 MPa, an internal friction angle **φ** of 23º, according to Detournay & Atkinson (2000), a layer thickness **hi** of 0.15 mm and 0.30 mm and a blade angle **α** of 110º. The external friction angle **δ** is chosen at 2/3 of the internal friction angle **φ**. Based on the principle of minimum energy a shear angle **β** of 12º has been derived. Zijsling already concluded that balling would occur. Using equation (8-21) an effective blade height **h'b** = 4.04·**hi** has been found**.** Figure 8-11 shows the cutting forces as measured by Zijsling compared with the theory derived here. The force **FD** is the force **Fh** in the direction of the cutting velocity and the force **FN** is the force **Fv** normal to the velocity direction. Figure 8-12 shows the specific energy **Esp** and the so called drilling strength **S**. Figure 8-13 and Figure 8-14 show the specific energy **Esp** as a function of the UCS value of a rock for different UCS/BTS ratio's and different water depths. Figure 8-13 shows this for a 110º blade as in the experiments of Zijsling (1987) . The UCS value of the Mancos Shale is about 65 MPa. It is clear that in this graph the UCS/BTS value has no influence, since there will be no tensile failure at a blade angle of 110º. There could however be brittle shear failure under atmospheric conditions resulting in a specific energy of 30%-50% of the lowest line in the graph. Figure 8-13 gives a good indication of the specific energy for drilling purposes.

Figure 8-14 and Figure 8-15 show this for a 45º and a 60 º blade as may be used in dredging and mining. From this figure it is clear that under atmospheric conditions tensile failure may occur. The lines for the UCS/BTS ratios give the specific energy based on the peak forces. This specific energy should be multiplied with 30%-50% to get the average value. Roxborough (1987) found that for all sedimentary rocks and some sandstone, the specific energy is about 25% of the UCS value (both have the dimension kPa or MPa). In Figure 8-14 and Figure 8-15 this would match brittle-shear failure with a factor of 30%-50% (R=2). In dredging and mining the blade angle would normally be in a range of 45º to 60º. Vlasblom (2003-2007) uses a percentage of 40% of the UCS value for the specific energy based on the experience of the dredging industry, which is close to the value found by Roxborough (1987). The percentage used by Vlasblom has the purpose of production estimation and is on the safe side (a bit too high). Both the percentages of Roxborough (1987) and Vlasblom (2003-2007) are based on the brittle shear failure. In the case of brittle tensile failure the specific energy may be much lower.

Resuming it can be stated that the theory developed here matches the measurements of Zijsling (1987) well. It has been proven that the approach of Detournay & Atkinson (2000) misses the pore pressure force on the blade and thus leads to some wrong conclusions. It can further be stated that brittle tensile failure will only occur with relatively small blade angles under atmospheric conditions. Brittle shear failure may also occur with large blade angles under atmospheric conditions. The measurements of Zijsling show clearly that at 0 MPa bottomhole pressure, the average cutting forces are 30%-50% of the forces that would be expected based on the trend. The conclusions are valid for the experiments they are based on. In other types of rock or with other blade angles the theory may have to be adjusted.

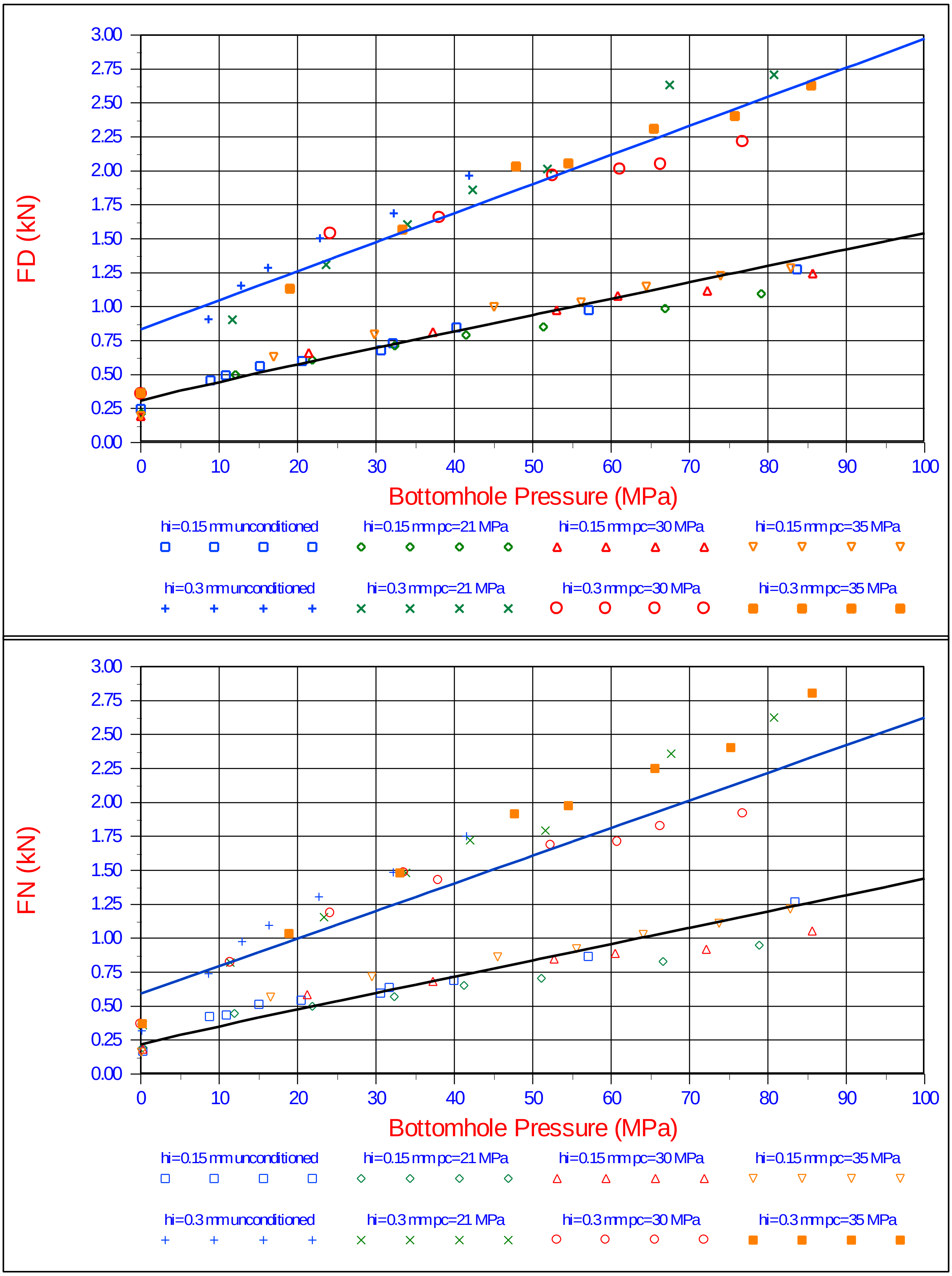

Figure 8-11: The theory of hyperbaric cutting versus the Zijsling (1987) experiments.

Blade angle **α** = 110º, blade width **w** = 10 mm, internal friction angle **φ** = 23.8º, external friction angle **δ** = 15.87º, shear strength **c** = 24.82 MPa, shear angle **β** = 12.00º, layer thickness $\mathbf{h_i}$ = 0.15 mm and 0.30 mm, effective blade height $\mathbf{h_b} = 4.04 \cdot \mathbf{h_i}$.

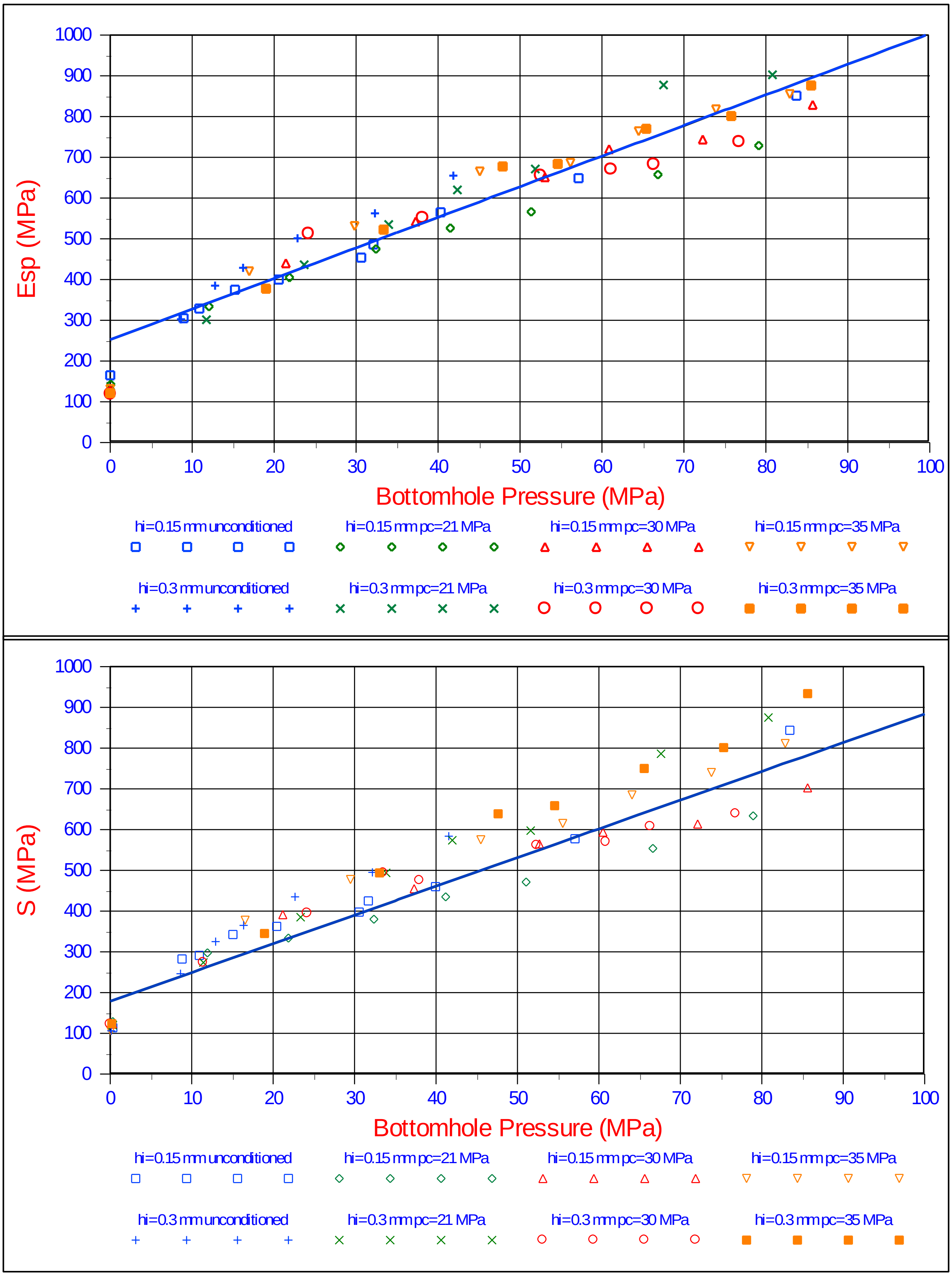

Figure 8-12: The specific energy E_{sp} and the drilling strength S, theory versus the Zijsling (1987) experiments.

Blade angle **α** = 110º, blade width **w** = 10 mm, internal friction angle **φ** = 23.8º, external friction angle **δ** = 15.87º, shear strength **c** = 24.82 MPa, shear angle **β** = 12.00º, layer thickness $\mathbf{h_i}$ = 0.15 mm and 0.30 mm, effective blade height $\mathbf{h_b} = 4.04 \cdot \mathbf{h_i}$.

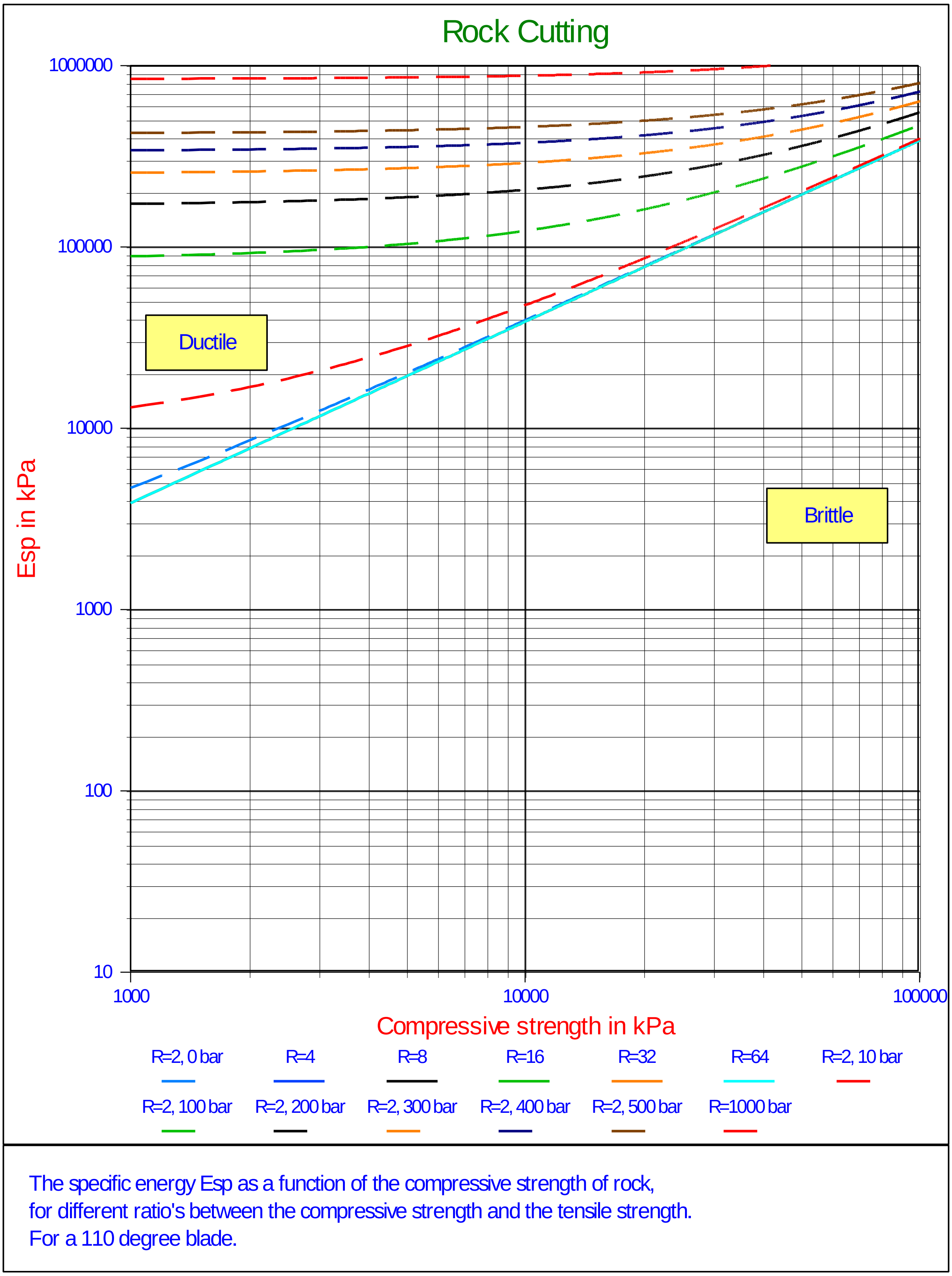

Figure 8-13: The specific energy E_{sp} in rock versus the compressive strength (UCS) for a 110° blade.

Blade angle $\boldsymbol{\alpha}$ = 110°, layer thickness $\mathbf{h_i}$ = 0.00015 m, blade height $\mathbf{h_b}$ = 0.01 m, angle of internal friction $\boldsymbol{\varphi}$ = 23.80°, angle of external friction $\boldsymbol{\delta}$ = 15.87°, shear angle $\boldsymbol{\beta}$ = 12.00°.

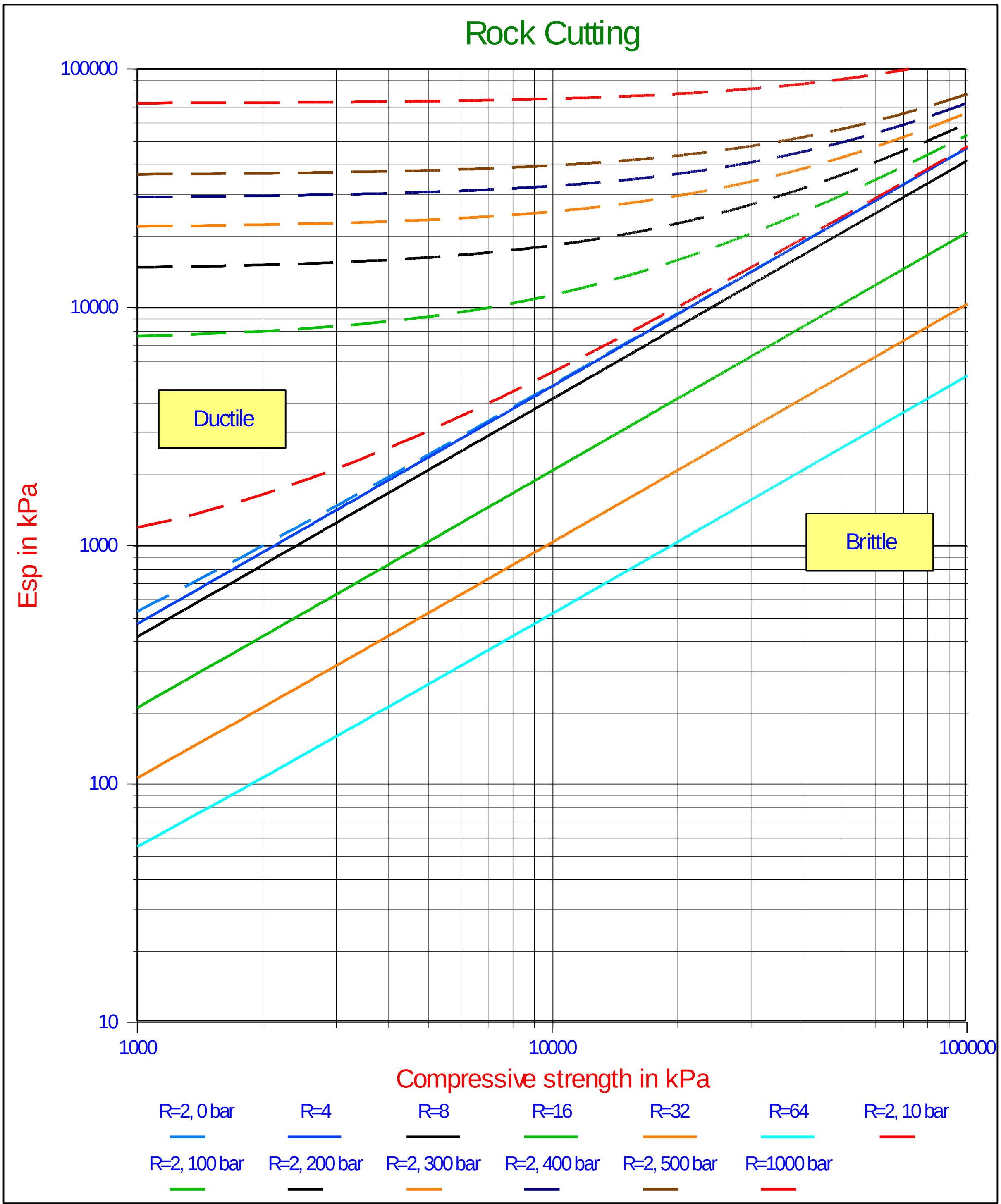

The specific energy Esp as a function of the compressive strength of rock,
for different ratio's between the compressive strength and the tensile strength.
For a 45 degree blade.

Figure 8-14: The specific energy E_{sp} in rock versus the compressive strength (UCS) for a 45º blade.

Blade angle **α** = 45º, layer thickness $\mathbf{h_i}$ = 0.05 m, blade height $\mathbf{h_b}$ = 0.1 m, angle of internal friction **φ** = 20.00º, angle of external friction **δ** = 13.33º, shear angle **β** = 40.00º.

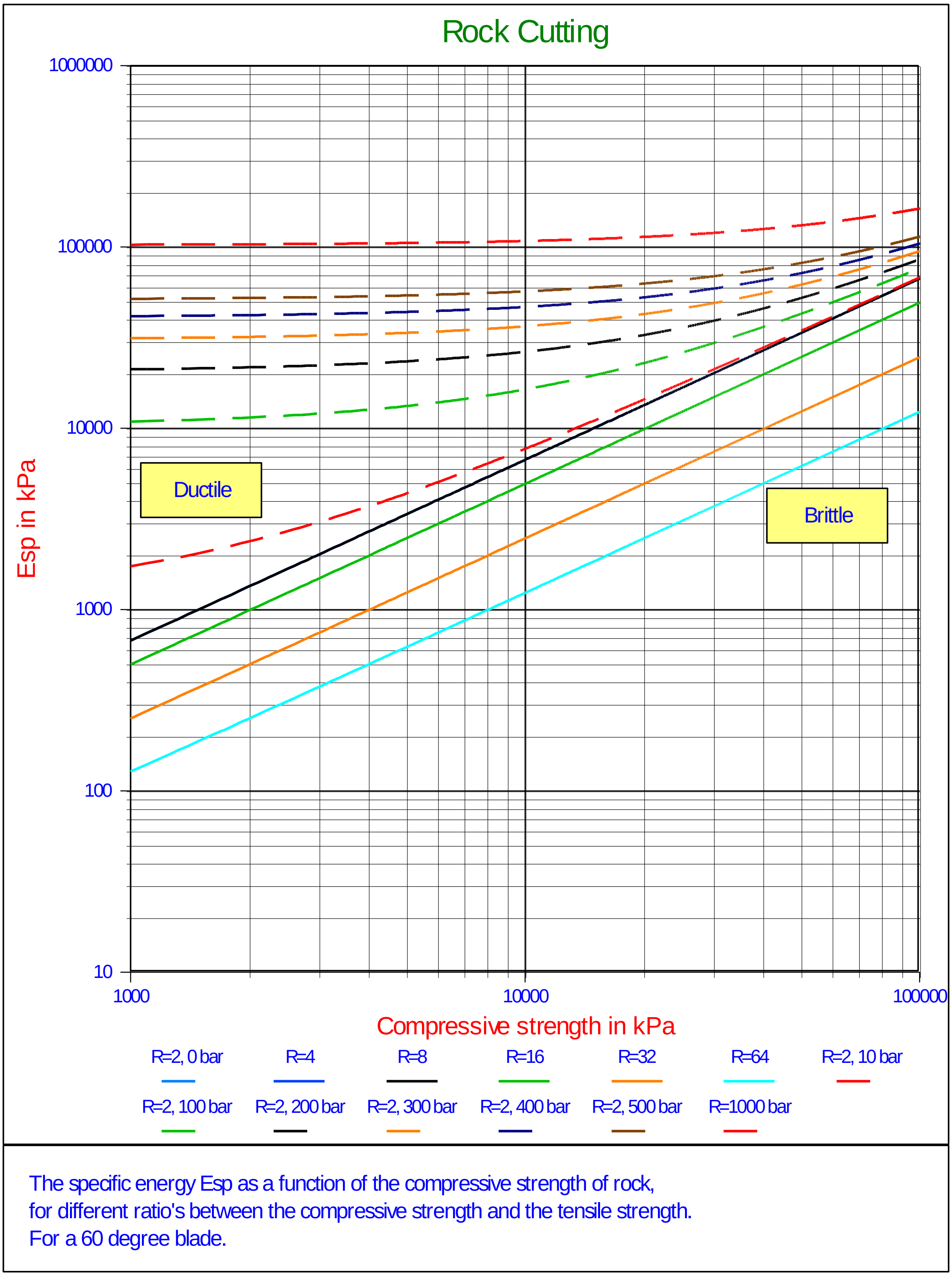

Figure 8-15 The specific energy E_{sp} in rock versus the compressive strength (UCS) for a 60° blade.

Blade angle $\boldsymbol{\alpha}$ = 60°, layer thickness $\mathbf{h_i}$ = 0.05 m, blade height $\mathbf{h_b}$ = 0.1 m, angle of internal friction $\boldsymbol{\varphi}$ = 20.00°, angle of external friction $\boldsymbol{\delta}$ = 13.33°, shear angle $\boldsymbol{\beta}$ = 40.00°.

8.6. Nomenclature Chapter 8:

a, τ_a	Adhesive shear strength	kPa
A	Adhesive force on the blade	kN
c, τ_c	Cohesive shear strength	kPa
c'	Pseudo cohesive shear strength	kPa
C	Cohesive force on shear plane	kN
E_{sp}	Specific energy	kPa
F	Force	kN
F_h	Horizontal cutting force	kN
F_v	Vertical cutting force	kN
g	Gavitational constant (9.81)	m/s^2
G	Gravitational force	kN
h_i	Initial thickness of layer cut	m
h_b	Height of the blade	m
h'_b	Contact height of the blade in case **Curling Type**	m
K_1	Grain force on the shear plane	kN
K_2	Grain force on the blade	kN
I	Inertial force on the shear plane	kN
N_1	Normal grain force on shear plane	kN
N_2	Normal grain force on blade	kN
P_c	Cutting power	kW
Q	Production	m^3
r	Adhesion/cohesion ratio	-
r_1	Pore pressure on shear plane/cohesion ratio	-
r_2	Pore pressure on blade/cohesion ratio	-
R	Radius of Mohr circle	kPa
R_1	Acting point on the shear plane	m
R_2	Acting point on the blade	m
S_1	Shear force due to internal friction on the shear plane	kN
S_2	Shear force due to external friction on the blade	kN
T	Tensile force	kN
UCS	Unconfined Compressive Stress	kPa
v_c	Cutting velocity	m/s
w	Width of the blade	m
W_1	Force resulting from pore under pressure on the shear plane	kN
W_2	Force resulting from pore under pressure on the blade	kN
α	Blade angle	rad
β	Angle of the shear plane with the direction of cutting velocity	rad
τ	Shear stress	kPa
τ_a, a	Adhesive shear strength (strain rate dependent)	kPa
τ_c, c	Cohesive shear strength (strain rate dependent)	kPa
τ_{S1}	Average shear stress on the shear plane	kPa
τ_{S2}	Average shear stress on the blade	kPa
σ	Normal stress	kPa
σ_C	Center of Mohr circle	kPa
σ_T	Tensile strength	kPa
σ_{min}	Minimum principal stress in Mohr circle	kPa
σ_{N1}	Average normal stress on the shear plane	kPa
σ_{N2}	Average normal stress on the blade	kPa
φ	Angle of internal friction	rad
δ	Angle of external friction	rad
λ	Strengthening factor	-

λ_1	Acting point factor on the shear plane	-
λ_2	Acting point factor on the blade	-
λ_{HF}	Ductile horizontal force coefficient	-
λ_{VF}	Ductile vertical force coefficient	-
λ_{HT}	Brittle horizontal force coefficient	-
λ_{VT}	Brittle vertical force coefficient	-

Chapter 9: The Occurrence of a Wedge

9.1. Introduction

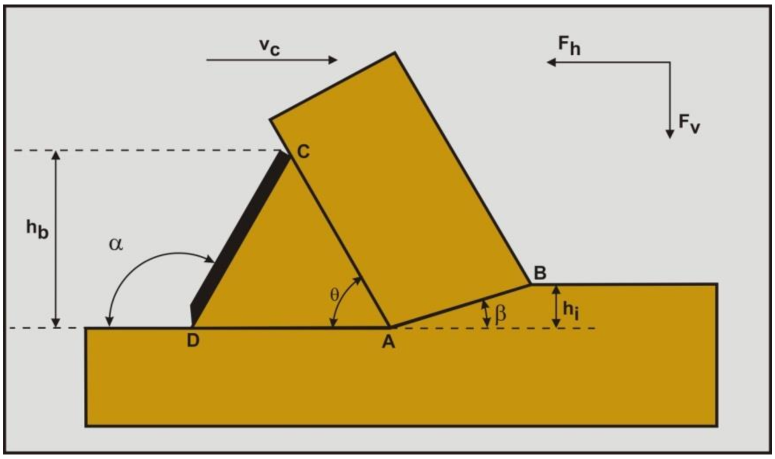

Figure 9-1: The occurrence of a wedge.

9.2. The Force Equilibrium

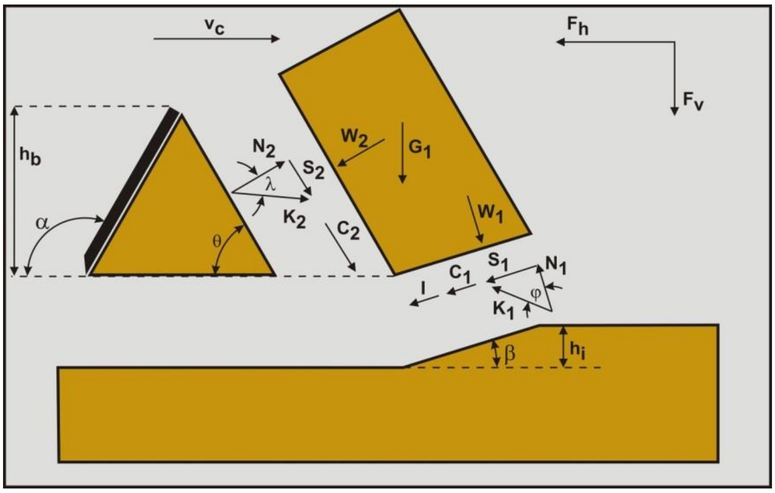

Figure 9-2: The forces on the layer cut when a wedge is present.

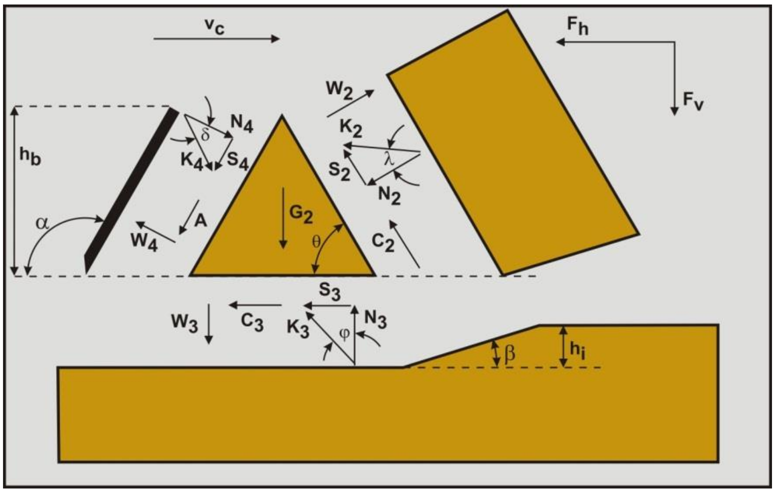

Figure 9-3: The forces on the wedge.

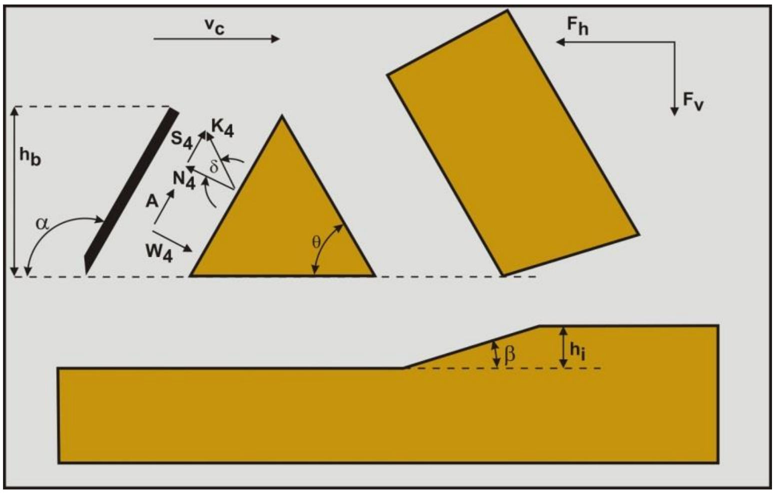

Figure 9-4: The forces on the blade when a wedge is present.

Figure 9-2 illustrates the forces on the layer of soil cut. The forces shown are valid in general for each type of soil. The forces acting on the layer **A-B** are:

1. A normal force acting on the shear surface $\mathbf{N_1}$, resulting from the effective grain stresses.
2. A shear force $\mathbf{S_1}$ as a result of internal fiction $\mathbf{N_1 \cdot tan(\varphi)}$.
3. A force $\mathbf{W_1}$ as a result of water under pressure in the shear zone.
4. A shear force $\mathbf{C_1}$ as a result of pure cohesion $\boldsymbol{\tau_c}$ or shear strength. This force can be calculated by multiplying the cohesive shear strength $\boldsymbol{\tau_c}$ with the area of the shear plane.
5. A gravity force $\mathbf{G_1}$ as a result of the weight of the layer cut.
6. An inertial force **I**, resulting from acceleration of the soil.
7. A force normal to the pseudo blade $\mathbf{N_2}$, resulting from the effective grain stresses.
8. A shear force $\mathbf{S_2}$ as a result of the soil/soil friction $\mathbf{N_2 \cdot tan(\lambda)}$ between the layer cut and the wedge pseudo blade. The friction angle $\boldsymbol{\lambda}$ does not have to be equal to the internal friction angle $\boldsymbol{\varphi}$ in the shear plane, since the soil has already been deformed.
9. A shear force $\mathbf{C_2}$ as a result of the mobilized cohesion between the soil and the wedge $\boldsymbol{\tau_c}$. This force can be calculated by multiplying the cohesive shear strength $\boldsymbol{\tau_c}$ of the soil with the contact area between the soil and the wedge.
10. A force $\mathbf{W_2}$ as a result of water under pressure on the wedge.

The normal force $\mathbf{N_1}$ and the shear force $\mathbf{S_1}$ can be combined to a resulting grain force $\mathbf{K_1}$.

$$\mathbf{K_1 = \sqrt{N_1^2 + S_1^2}} \tag{9-1}$$

The forces acting on the wedge front or pseudo blade **A-C** when cutting soil, can be distinguished as:

11. A force normal to the blade $\mathbf{N_2}$, resulting from the effective grain stresses.
12. A shear force $\mathbf{S_2}$ as a result of the soil/soil friction $\mathbf{N_2 \cdot tan(\lambda)}$) between the layer cut and the wedge pseudo blade. The friction angle $\boldsymbol{\lambda}$ does not have to be equal to the internal friction angle $\boldsymbol{\varphi}$ in the shear plane, since the soil has already been deformed.
13. A shear force $\mathbf{C_2}$ as a result of the cohesion between the layer cut and the pseudo blade $\boldsymbol{\tau_c}$. This force can be calculated by multiplying the cohesive shear strength $\boldsymbol{\tau_c}$ of the soil with the contact area between the soil and the pseudo blade.
14. A force $\mathbf{W_2}$ as a result of water under pressure on the pseudo blade **A-C**.

These forces are shown in Figure 9-3. If the forces $\mathbf{N_2}$ and $\mathbf{S_2}$ are combined to a resulting force $\mathbf{K_2}$ and the adhesive force and the water under pressures are known, then the resulting force $\mathbf{K_2}$ is the unknown force on the blade. By taking the horizontal and vertical equilibrium of forces an expression for the force $\mathbf{K_2}$ on the blade can be derived.

$$\mathbf{K_2 = \sqrt{N_2^2 + S_2^2}} \tag{9-2}$$

The forces acting on the wedge bottom **A-D** when cutting soil, can be distinguished as:

15. A force normal to the blade $\mathbf{N_3}$, resulting from the effective grain stresses.

16. A shear force S_3 as a result of the soil/soil friction $N_3 \cdot \tan(\varphi)$) between the wedge bottom and the undisturbed soil.
17. A shear force C_3 as a result of the cohesion between the wedge bottom and the undisturbed soil τ_c. This force can be calculated by multiplying the cohesive shear strength τ_c of the soil with the contact area between the wedge bottom and the undisturbed soil.
18. A force W_3 as a result of water under pressure on the wedge bottom **A-D**.

The normal force N_3 and the shear force S_3 can be combined to a resulting grain force K_3.

$$K_3 = \sqrt{N_3^2 + S_3^2} \tag{9-3}$$

The forces acting on a straight blade **C-D** when cutting soil (see Figure 9-4), can be distinguished as:
19. A force normal to the blade N_4, resulting from the effective grain stresses.
20. A shear force S_4 as a result of the soil/steel friction $N_4 \cdot \tan(\delta)$.
21. A shear force **A** as a result of pure adhesion between the soil and the blade τ_a. This force can be calculated by multiplying the adhesive shear strength τ_a of the soil with the contact area between the soil and the blade.
22. A force W_4 as a result of water under pressure on the blade.

The normal force N_4 and the shear force S_4 can be combined to a resulting grain force K_4.

$$K_4 = \sqrt{N_4^2 + S_4^2} \tag{9-4}$$

The horizontal equilibrium of forces:

$$\sum F_h = K_1 \cdot \sin(\beta+\varphi) - W_1 \cdot \sin(\beta) + C_1 \cdot \cos(\beta) + I \cdot \cos(\beta) - C_2 \cdot \cos(\alpha) + W_2 \cdot \sin(\alpha) - K_2 \cdot \sin(\alpha+\lambda) = 0 \tag{9-5}$$

The vertical equilibrium of forces:

$$\sum F_v = -K_1 \cdot \cos(\beta+\varphi) + W_1 \cdot \cos(\beta) + C_1 \cdot \sin(\beta) + I \cdot \sin(\beta) + G_1 + C_2 \cdot \sin(\alpha) + W_2 \cdot \cos(\alpha) - K_2 \cdot \cos(\alpha+\lambda) = 0 \tag{9-6}$$

The force K_1 on the shear plane is now:

$$K_1 = \frac{W_2 \cdot \sin(\lambda) + W_1 \cdot \sin(\alpha+\beta+\lambda) + G_1 \cdot \sin(\alpha+\lambda) - I \cdot \cos(\alpha+\beta+\lambda) - C_1 \cdot \cos(\alpha+\beta+\lambda) + C_2 \cdot \cos(\lambda)}{\sin(\alpha+\beta+\lambda+\varphi)} \tag{9-7}$$

The force K_2 on the blade is now:

$$K_2 = \frac{W_2 \cdot \sin(\alpha+\beta+\varphi) + W_1 \cdot \sin(\varphi) + G_1 \cdot \sin(\beta+\varphi) + I \cdot \cos(\varphi) + C_1 \cdot \cos(\varphi) - C_2 \cdot \cos(\alpha+\beta+\varphi)}{\sin(\alpha+\beta+\lambda+\varphi)} \tag{9-8}$$

From equation (2-7) the forces on the pseudo blade can be derived. On the blade a force component in the direction of cutting velocity F_h and a force perpendicular to this direction F_v can be distinguished.

$$F_h = -W_2 \cdot \sin(\alpha) + K_2 \cdot \sin(\alpha+\lambda) + C_2 \cdot \cos(\alpha) \tag{9-9}$$

$$F_v = -W_2 \cdot \cos(\alpha) + K_2 \cdot \cos(\alpha+\lambda) - C_2 \cdot \sin(\alpha) \tag{9-10}$$

The normal force on the shear plane is now:

$$N_1 = \frac{W_2 \cdot \sin(\lambda) + W_1 \cdot \sin(\alpha+\beta+\lambda) + G_1 \cdot \sin(\alpha+\lambda) - I \cdot \cos(\alpha+\beta+\lambda) - C_1 \cdot \cos(\alpha+\beta+\lambda) + C_2 \cdot \cos(\lambda)}{\sin(\alpha+\beta+\lambda+\varphi)} \cdot \cos(\varphi) \tag{9-11}$$

The normal force on the blade is now:

$$N_2 = \frac{W_2 \cdot \sin(\alpha+\beta+\varphi) + W_1 \cdot \sin(\varphi) + G_1 \cdot \sin(\beta+\varphi) + I \cdot \cos(\varphi) + C_1 \cdot \cos(\varphi) - C_2 \cdot \cos(\alpha+\beta+\varphi)}{\sin(\alpha+\beta+\lambda+\varphi)} \cdot \cos(\lambda) \tag{9-12}$$

$$\sum F_h = -A \cdot \cos(\alpha) + W_4 \cdot \sin(\alpha) - K_4 \cdot \sin(\alpha+\delta) + K_3 \cdot \sin(\varphi) + C_3 - W_2 \cdot \sin(\theta) + C_2 \cdot \cos(\theta) + K_2 \cdot \sin(\theta+\lambda) = 0 \tag{9-13}$$

$$\sum F_v = A \cdot \sin(\alpha) + W_4 \cdot \cos(\alpha) - K_4 \cdot \cos(\alpha+\delta) + W_3 - K_3 \cdot \cos(\varphi) - W_2 \cdot \cos(\theta) - C_2 \cdot \sin(\theta) + K_2 \cdot \cos(\theta+\lambda) + G_2 = 0 \tag{9-14}$$

$$K_3 = \frac{-W_2 \cdot \sin(\alpha+\delta-\theta) + K_2 \cdot \sin(\alpha+\delta-\theta-\lambda) + W_3 \cdot \sin(\alpha+\delta) + W_4 \cdot \sin(\delta)}{\sin(\alpha+\delta+\varphi)} \quad \frac{A \cdot \cos(\delta) + C_3 \cdot \cos(\alpha+\delta) - C_2 \cdot \cos(\alpha+\delta-\theta) + G_2 \cdot \sin(\alpha+\delta)}{\sin(\alpha+\delta+\varphi)} \tag{9-15}$$

$$K_4 = \frac{-W_2 \cdot \sin(\theta+\varphi) + K_2 \cdot \sin(\theta+\lambda+\varphi) + W_3 \cdot \sin(\varphi) + W_4 \cdot \sin(\alpha+\varphi)}{\sin(\alpha+\delta+\varphi)} \quad \frac{-A \cdot \cos(\alpha+\varphi) + C_3 \cdot \cos(\varphi) + C_2 \cdot \cos(\theta+\varphi) + G_2 \cdot \sin(\varphi)}{\sin(\alpha+\delta+\varphi)} \tag{9-16}$$

$$F_h = -W_4 \cdot \sin(\alpha) + K_4 \cdot \sin(\alpha+\delta) + A \cdot \cos(\alpha) \tag{9-17}$$

$$F_v = -W_4 \cdot \cos(\alpha) + K_4 \cdot \cos(\alpha+\delta) - A \cdot \sin(\alpha) \tag{9-18}$$

9.3. The Equilibrium of Moments

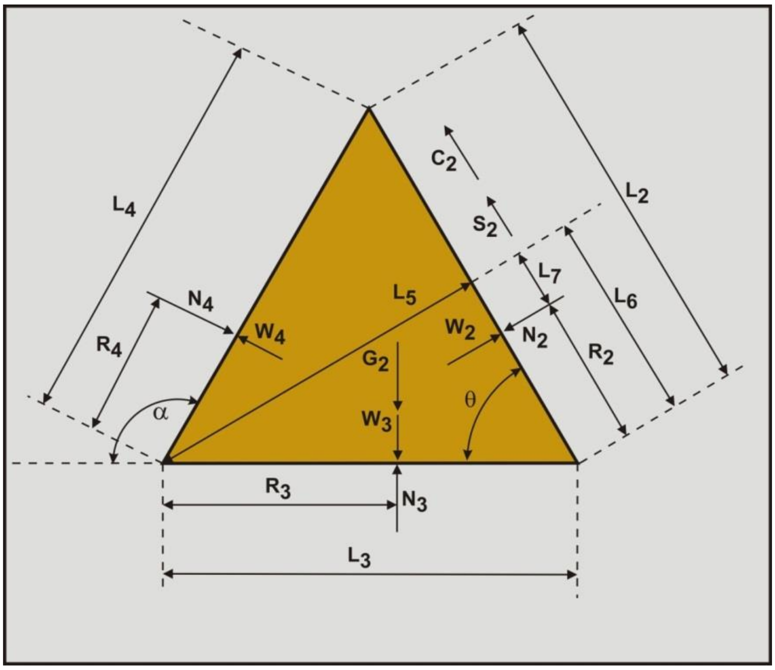

Figure 9-5: The moments on a wedge.

The equilibrium of moments:

$$\mathbf{L_1 = \frac{h_i}{\sin(\beta)}}$$

$$\mathbf{L_2 = \frac{h_b}{\sin(\theta)}}$$

$$\mathbf{L_3 = h_b \cdot \left(\frac{1}{\tan(\theta)} - \frac{1}{\tan(\alpha)}\right)}$$

$$\mathbf{L_4 = \frac{h_b}{\sin(\alpha)}}$$

$$\mathbf{L_5 = L_3 \cdot \sin(\theta)}$$

$$\mathbf{L_6 = L_3 \cdot \cos(\theta)}$$

$$\mathbf{L_7 = L_6 - R_2}$$

$$\mathbf{\sum M = (N_4 - W_4) \cdot R_4 - (N_3 - W_3 - G_2) \cdot R_3 + (N_2 - W_2) \cdot L_7 - (S_2 + C_2) \cdot L_5 = 0}$$

Chapter 10: The Occurrence of a Wedge in Dry Sand

Chapter 11: The Occurrence of a Wedge in Saturated Sand

11.1. Introduction

In the last decennia extensive research has been carried out into the cutting of water saturated sand. In the cutting of water-saturated sand, the phenomenon of dilatation plays an important role. In fact the effects of gravity, inertia, cohesion and adhesion can be neglected at cutting speeds in the range of 0.5 – 10 m/s. In the cutting equations, as published by Miedema (1987 September), there is a division by the sine of the sum of the blade angle, the shear angle, the angle of internal friction and the soil/interface friction angle. When the sum of these angle approaches 180°, a division by zero is the result, resulting in infinite cutting forces. This may occur for example for α=80°, β=30°, ϕ=40° and δ=30°. When this sum is greater than 180 degrees, the cutting forces become negative. It is obvious that this cannot be the case in reality and that nature will look for another cutting mechanism.
Hettiaratchi and Reece (1975) found a mechanism, which they called boundary wedges for dry soil. At large cutting angles a triangular wedge will exist in front of the blade, not moving relative to the blade. This wedge acts as a blade with a smaller blade angle. In fact, this reduces the sum of the 4 angles mentioned before to a value much smaller than 180°. The existence of a dead zone (wedge) in front of the blade when cutting at large cutting angles will affect the value and distribution of vacuum water pressure on the interface. He et al. (1998) proved experimentally that also in water saturated sand at large cutting angles a wedge will occur. A series of tests with rake angles 90, 105 and 120 degrees under fully saturated and densely compacted sand condition was performed by He et al. (1998) at the Dredging Technology Laboratory of Delft University of Technology. The experimental results showed that the failure pattern with large rake angles is quite different from that with small rake angles. For large rake angles a dead zone is formed in front of the blade, but not for small rake angles. In the tests he carried out, both a video camera and film camera were used to capture the failure pattern. The video camera was fixed on the frame which is mounted on the main carriage, translates with the same velocity as the testing cutting blade. Shown in the static slide of the video record, as in Figure 11-1, the boundary wedges exist during the cutting test. The assumption of an alternative failure mechanism is based on a small quantity of picture material, see Figure 11-1. It is described as a static wedge in front of the blade, which serves as a new virtual blade over which the sand flows away.

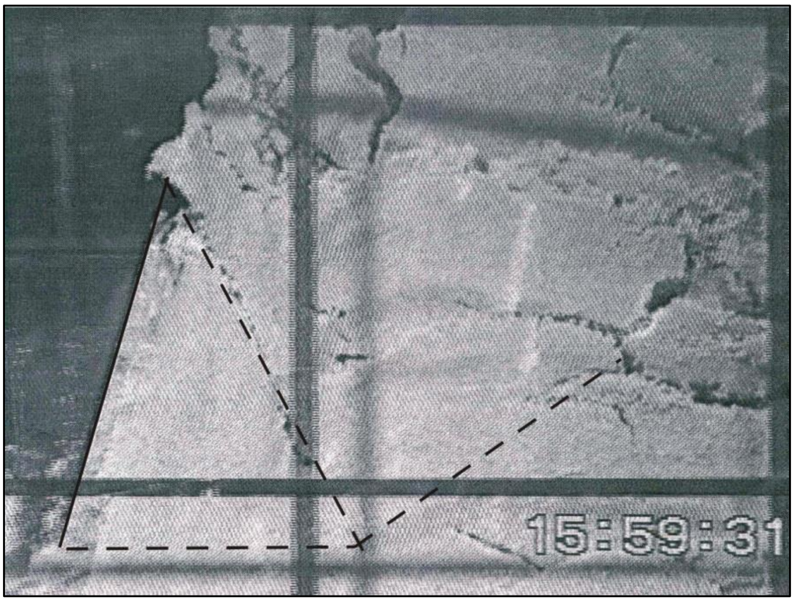

Figure 11-1: Failure pattern with rake angle of 120°.

Although the number of experiments published is limited, the research is valuable as a starting point to predict the shape of the wedge. At small cutting angles the cutting forces are determined by the horizontal and vertical force equilibrium equations of the sand cut in front of the blade. These equations contain 3 unknowns, so a third equation/condition had to be found. The principle of minimum energy is used as a third condition to solve the 3 unknowns. This has proved to give very satisfactory results finding the shear angle and the horizontal and vertical cutting forces at small cutting angles. At large cutting angles, a 4^{th} unknown exists, the wedge angle or virtual blade angle. This means that a 4^{th} equation/condition must be found in order to determine the wedge angle. There are 3 possible conditions that can be used: The principle of minimum energy, The circle of Mohr, The equilibrium of moments of the wedge. In fact, there is also a 5^{th} unknown, the mobilized friction on the blade. New research carried out in the Dredging Engineering Laboratory shows that a wedge exists, but not always a static wedge. The sand inside the wedge is still moving, but with a much lower velocity then the sand outside the wedge. This results in fully mobilized friction on the blade. The bottom boundary of the wedge, which is horizontal for a static wedge, may have a small angle with respect to the horizontal in the new case considered.

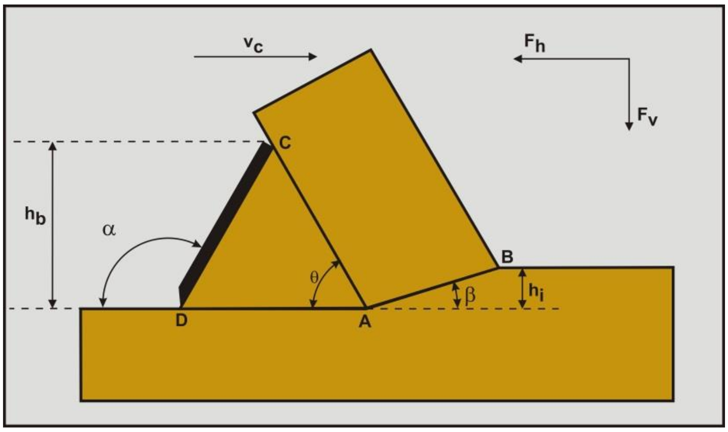

Figure 11-2: Sand cutting with a wedge, definitions.

Figure 11-2 shows the definitions of the cutting process with a static wedge. A-B is the shear plane where dilatation occurs. A-C is the front of the static wedge and forms a pseudo cutting blade. A-C-D is the static wedge, where C-D is the blade, A-D the bottom of the wedge and A-C the pseudo blade or the front of the wedge.
The sand wedge theory is based on publications of Hettiaratchi and Reece (1975), Miedema (1987 September), He et al. (1998), Yi (2000), Miedema et al. (2001), Yi et al. (2001), Ma (2001), Miedema et al. (2002A), Miedema et al. (2002B), Yi et al. (2002), Miedema (2003), Miedema et al. (2003), Miedema (2004), Miedema et al. (2004), He et al. (2005), Ma et al. (2006A), Ma et al. (2006B), Miedema (2005), Miedema (2006A), Miedema (2006B).

11.2. Forces

Figure 11-3, Figure 11-4 and Figure 11-5 show the forces occurring at the layer cut, the wedge and the blade, while Figure 11-17 shows the moments occurring on the wedge. The forces are:

The forces acting on the layer **A-B** are:
1. A normal force acting on the shear surface $\mathbf{N_1}$, resulting from the effective grain stresses.
2. A shear force $\mathbf{S_1}$ as a result of internal fiction $\mathbf{N_1 \cdot tan(\varphi)}$.
3. A force $\mathbf{W_1}$ as a result of water under pressure in the shear zone.
4. A force normal to the pseudo blade $\mathbf{N_2}$, resulting from the effective grain stresses.
5. A shear force $\mathbf{S_2}$ as a result of the soil/soil friction $\mathbf{N_2 \cdot tan(\lambda)}$ between the layer cut and the wedge pseudo blade. The friction angle λ does not have to be equal to the internal friction angle φ in the shear plane, since the soil has already been deformed.
6. A force $\mathbf{W_2}$ as a result of water under pressure on the wedge.

The forces acting on the wedge front or pseudo blade **A-C** when cutting soil, can be distinguished as:
7. A force normal to the blade $\mathbf{N_2}$, resulting from the effective grain stresses.
8. A shear force $\mathbf{S_2}$ as a result of the soil/soil friction $\mathbf{N_2 \cdot tan(\lambda)}$) between the layer cut and the wedge pseudo blade. The friction angle λ does not have to be equal to the internal friction angle φ in the shear plane, since the soil has already been deformed.
9. A force $\mathbf{W_2}$ as a result of water under pressure on the pseudo blade **A-C**.

The forces acting on the wedge bottom **A-D** when cutting soil, can be distinguished as:
10. A force normal to the blade $\mathbf{N_3}$, resulting from the effective grain stresses.
11. A shear force $\mathbf{S_3}$ as a result of the soil/soil friction $\mathbf{N_3 \cdot tan(\varphi)}$) between the wedge bottom and the undisturbed soil.
12. A force $\mathbf{W_3}$ as a result of water under pressure on the wedge bottom **A-D**.

The forces acting on a straight blade **C-D** when cutting soil, can be distinguished as:
13. A force normal to the blade $\mathbf{N_4}$**,** resulting from the effective grain stresses.
14. A shear force $\mathbf{S_4}$ as a result of the soil/steel friction $\mathbf{N_4 \cdot tan(\delta)}$ between the wedge and the blade.

15. A force W_4 as a result of water under pressure on the blade.

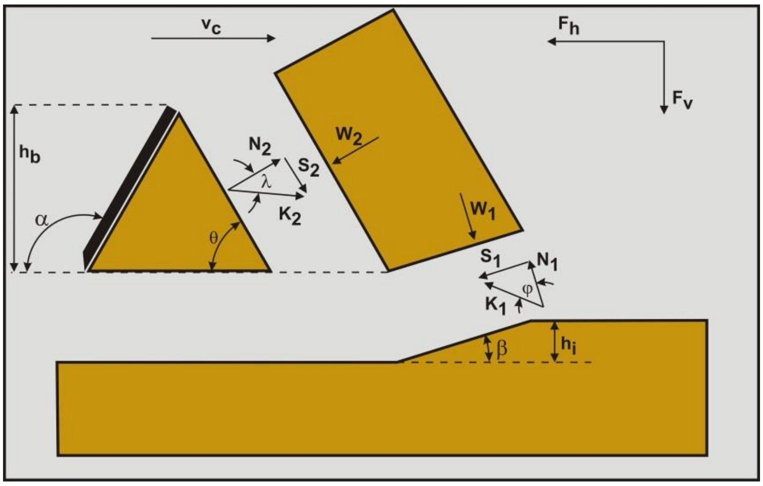

Figure 11-3: The forces on the layer cut in saturated sand with a wedge.

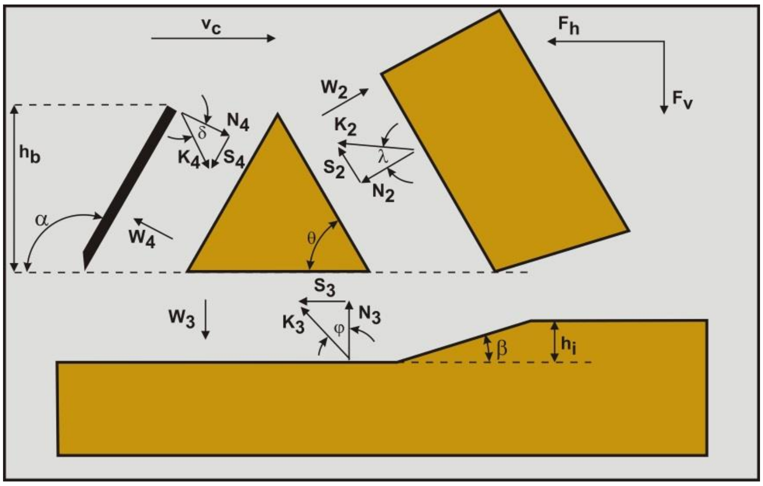

Figure 11-4: The forces on the wedge in saturated sand.

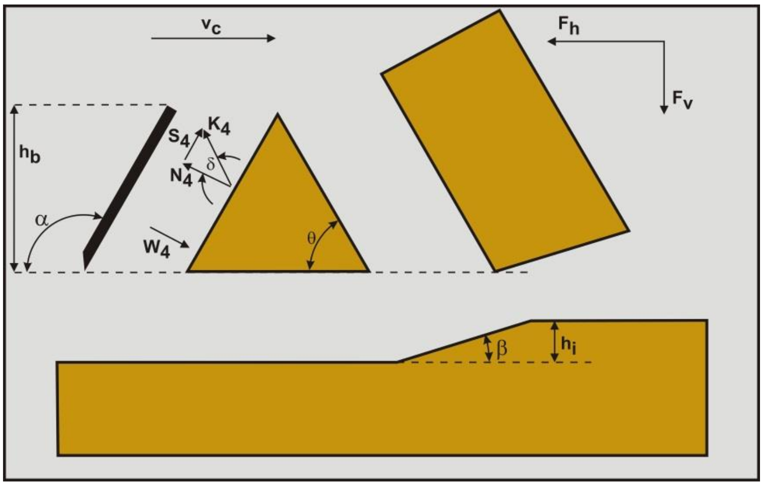

Figure 11-5: The forces on the blade in saturated sand with a wedge.

To determine the cutting forces on the blade, first the cutting forces on the pseudo blade have to be determined by taking the horizontal and vertical equilibrium of forces on the layer cut **B-A-C**. The shear angle **β** is determined by minimizing the cutting energy.

The horizontal equilibrium of forces:

$$\sum F_h = K_1 \cdot \sin(\beta+\varphi) - W_1 \cdot \sin(\beta) + W_2 \cdot \sin(\alpha) - K_2 \cdot \sin(\alpha+\lambda) = 0 \quad (11\text{-}1)$$

The vertical equilibrium of forces:

$$\sum F_v = -K_1 \cdot \cos(\beta+\varphi) + W_1 \cdot \cos(\beta) + W_2 \cdot \cos(\alpha) - K_2 \cdot \cos(\alpha+\lambda) = 0 \quad (11\text{-}2)$$

The force **K_1** on the shear plane is now:

$$K_1 = \frac{W_2 \cdot \sin(\lambda) + W_1 \cdot \sin(\alpha+\beta+\lambda)}{\sin(\alpha+\beta+\lambda+\varphi)} \quad (11\text{-}3)$$

The force **K_2** on the pseudo blade is now:

$$K_2 = \frac{W_2 \cdot \sin(\alpha+\beta+\varphi) + W_1 \cdot \sin(\varphi)}{\sin(\alpha+\beta+\lambda+\varphi)} \quad (11\text{-}4)$$

From equation (11-4) the forces on the pseudo blade can be derived. On the pseudo blade a force component in the direction of cutting velocity **F_h** and a force perpendicular to this direction **F_v** can be distinguished.

$$F_h = -W_2 \cdot \sin(\alpha) + K_2 \cdot \sin(\alpha+\lambda) \quad (11\text{-}5)$$

$$F_v = -W_2 \cdot \cos(\alpha) + K_2 \cdot \cos(\alpha+\lambda) \quad (11\text{-}6)$$

The normal force on the shear plane **A-B** is now:

$$N_1 = \frac{W_2 \cdot \sin(\lambda) + W_1 \cdot \sin(\alpha+\beta+\lambda)}{\sin(\alpha+\beta+\lambda+\varphi)} \cdot \cos(\varphi) \quad (11\text{-}7)$$

The normal force on the pseudo blade **A-C** is now:

$$N_2 = \frac{W_2 \cdot \sin(\alpha+\beta+\varphi) + W_1 \cdot \sin(\varphi)}{\sin(\alpha+\beta+\lambda+\varphi)} \cdot \cos(\lambda) \quad (11\text{-}8)$$

Now the force equilibrium on the wedge has to be solved. This is done by first taking the horizontal and vertical force equilibrium on the wedge **A-C-D**.

The horizontal equilibrium of forces:

$$\sum F_h = +W_4 \cdot \sin(\alpha) - K_4 \cdot \sin(\alpha+\delta_e) + K_3 \cdot \sin(\varphi) - W_2 \cdot \sin(\theta) + K_2 \cdot \sin(\theta+\lambda) = 0 \quad (11\text{-}9)$$

The vertical equilibrium of forces:

$$\sum F_v = +W_4 \cdot \cos(\alpha) - K_4 \cdot \cos(\alpha+\delta_e) + W_3 - K_3 \cdot \cos(\varphi) - W_2 \cdot \cos(\theta) + K_2 \cdot \cos(\theta+\lambda) = 0 \quad (11\text{-}10)$$

The grain force **K_3** on the bottom of the wedge is now:

$$K_3 = \frac{-W_2 \cdot \sin(\alpha+\delta_e-\theta) + K_2 \cdot \sin(\alpha+\delta_e-\theta-\lambda) + W_3 \cdot \sin(\alpha+\delta_e) + W_4 \cdot \sin(\delta_e)}{\sin(\alpha+\delta_e+\varphi)} \quad (11\text{-}11)$$

The grain force **K_4** on the blade is now:

$$K_4 = \frac{-W_2 \cdot \sin(\theta+\varphi) + K_2 \cdot \sin(\theta+\lambda+\varphi) + W_3 \cdot \sin(\varphi) + W_4 \cdot \sin(\alpha+\varphi)}{\sin(\alpha+\delta_e+\varphi)} \quad (11\text{-}12)$$

From equation (11-12) the forces on the pseudo blade can be derived. On the pseudo blade a force component in the direction of cutting velocity **F_h** and a force perpendicular to this direction **F_v** can be distinguished.

$$F_h = -W_4 \cdot \sin(\alpha) + K_4 \cdot \sin(\alpha + \delta_e) \tag{11-13}$$

$$F_v = -W_4 \cdot \cos(\alpha) + K_4 \cdot \cos(\alpha + \delta_e) \tag{11-14}$$

11.3. Pore Pressures

If the cutting process is assumed to be stationary, the water flow through the pores of the sand can be described in a blade motions related coordinate system. The determination of the water vacuum pressures in the sand around the blade is then limited to a mixed boundary conditions problem. The potential theory can be used to solve this problem. For the determination of the water vacuum pressures it is necessary to have a proper formulation of the boundary condition in the shear zone. Miedema (1985A) derived the basic equation for this boundary condition. In later publications a more extensive derivation is published. If it is assumed that no deformations take place outside the deformation zone, then:

$$\left|\frac{\partial^2 p}{\partial x^2}\right| + \left|\frac{\partial^2 p}{\partial y^2}\right| = 0 \tag{11-15}$$

Making the boundary condition in the shear plane dimensionless is similar to that of the breach equation of Meijer and Van Os (1976). In the breach problem the length dimensions are normalized by dividing them by the breach height, while in the cutting of sand they are normalized by dividing them by the cut layer thickness. Equation (11-15) is the same as the equation without a wedge. In the shear plane **A-B** the following equation is valid:

$$\frac{k_i}{k_{max}} \cdot \left|\frac{\partial p}{\partial n'}\right|_1 + \left|\frac{\partial p}{\partial n'}\right|_2 = \frac{\rho_w \cdot g \cdot v_c \cdot \varepsilon \cdot h_i \cdot \sin(\beta)}{k_{max}} \quad \text{with:} \quad n' = \frac{n}{h_i} \tag{11-16}$$

This equation is made dimensionless with:

$$\left|\frac{\partial p}{\partial n}\right|' = \frac{\left|\dfrac{\partial p}{\partial n'}\right|}{\rho_w \cdot g \cdot v_c \cdot \varepsilon \cdot h_i / k_{max}} \tag{11-17}$$

The accent indicates that a certain variable or partial derivative is dimensionless. The next dimensionless equation is now valid as a boundary condition in the deformation zone:

$$\frac{k_i}{k_{max}} \cdot \left|\frac{\partial p}{\partial n}\right|_1' + \left|\frac{\partial p}{\partial n}\right|_2' = \sin(\beta) \tag{11-18}$$

The storage equation also has to be made dimensionless, which results in the next equation:

$$\left|\frac{\partial^2 p}{\partial x^2}\right|' + \left|\frac{\partial^2 p}{\partial y^2}\right|' = 0 \tag{11-19}$$

Because this equation equals zero, it is similar to equation (11-15). The water under-pressures distribution in the sand package can now be determined using the storage equation and the boundary conditions. Because the calculation of the water under-pressures is dimensionless the next transformation has to be performed to determine the real water under-pressures. The real water under-pressures can be determined by integrating the derivative of the water under-pressures in the direction of a flow line, along a flow line, so:

$$P_{calc} = \int_{s'} \left|\frac{\partial p}{\partial s}\right|' \cdot ds' \tag{11-20}$$

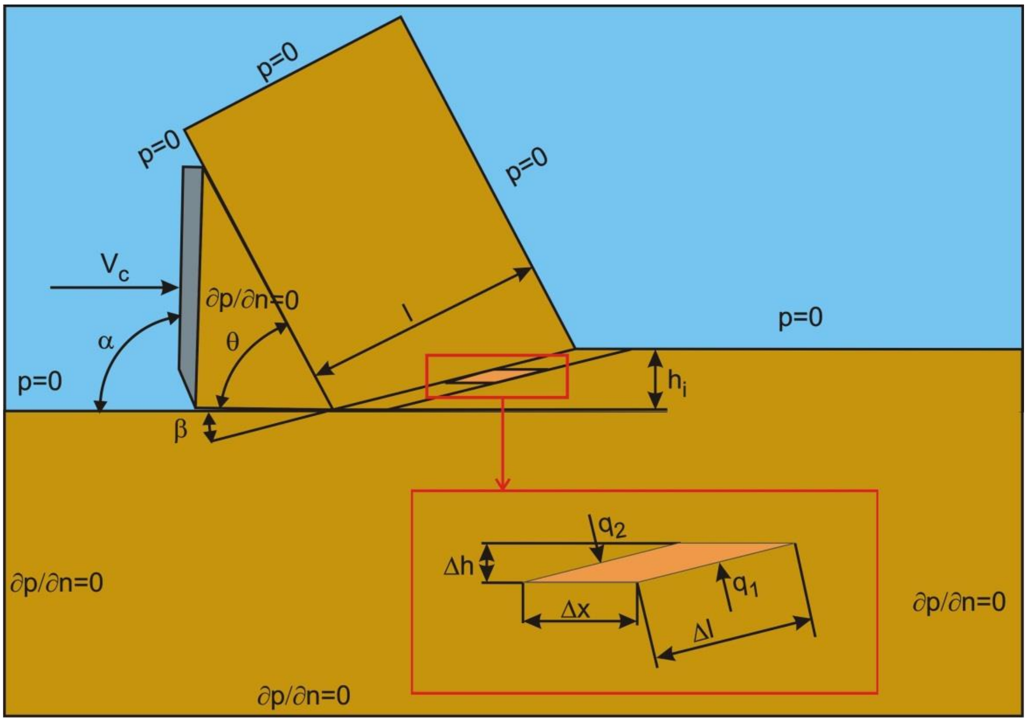

Figure 11-6: The volume balance over the shear zone.

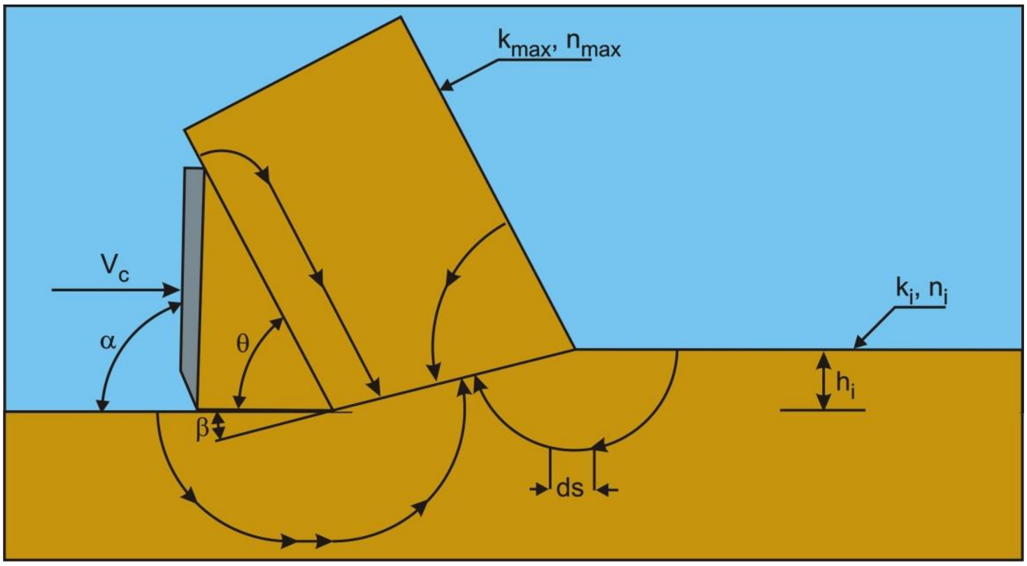

Figure 11-7: Possible flow lines.

This is illustrated in Figure 11-6 and Figure 11-7. Using equation (11-20) this is written as:

$$\mathbf{P_{real}} = \int_{s} \left| \frac{\partial \mathbf{p}}{\partial \mathbf{s}} \right| \cdot \mathbf{ds} = \int_{s'} \frac{\rho_w \cdot \mathbf{g} \cdot \mathbf{v_c} \cdot \varepsilon \cdot \mathbf{h_i}}{\mathbf{k_{max}}} \cdot \left| \frac{\partial \mathbf{p}}{\partial \mathbf{s}} \right|' \cdot \mathbf{ds}' \quad \text{with:} \quad \mathbf{s}' = \frac{\mathbf{s}}{\mathbf{h_i}} \qquad \mathbf{(11\text{-}21)}$$

This gives the next relation between the real emerging water under pressures and the calculated water under pressures:

$$\mathbf{P_{real}} = \frac{\rho_w \cdot \mathbf{g} \cdot \mathbf{v_c} \cdot \varepsilon \cdot \mathbf{h_i}}{\mathbf{k_{max}}} \cdot \mathbf{P_{calc}} \qquad \mathbf{(11\text{-}22)}$$

To be independent of the ratio between the initial permeability $\mathbf{k_i}$ and the maximum permeability $\mathbf{k_{max}}$, $\mathbf{k_{max}}$ has to be replaced with the weighted average permeability $\mathbf{k_m}$ before making the measured water under pressures dimensionless.

The water vacuum pressures in the sand package on and around the blade are numerically determined using the finite element method. A standard FEM software package is used (Segal (2001)). Within this package and the use of the available "subroutines" a program is written, with which water vacuum pressures can be calculated and be output graphically and numerically. As shown in Figure 11-8, the SEPRAN model is made of three parts, the original sand layer, the cut sand layer, and the wedge. The solution of such a calculation is however not only dependent on the physical model of the problem, but also on the next points:

1. The size of the area in which the calculation takes place.
2. The size and distribution of the elements
3. The boundary conditions

The choices for these three points have to be evaluated with the problem that has to be solved in mind. These calculations are about the values and distribution of the water under-pressures in the shear zone and on the blade, on the interface between wedge and cut sand, between wedge and the original sand layer. A variation of the values for point 1 and 2 may therefore not influence this part of the solution. This is achieved by on one hand increasing the area in which the calculations take place in steps and on the other hand by decreasing the element size until the variation in the solution was less than 1%. The distribution of the elements is chosen such that a finer mesh is present around the blade tip, the shear zone and on the blade, also because of the blade tip problem. A number of boundary conditions follow from the physical model of the cutting process, these are:

- For the hydrostatic pressure it is valid to take a zero pressure as the boundary condition.
- The boundary conditions along the boundaries of the area where the calculation takes place that are located in the sand package are not determined by the physical process. For this boundary condition there is a choice among:
  1. A hydrostatic pressure along the boundary.
  2. A boundary as an impermeable wall.
  3. A combination of a known pressure and a known specific flow rate.

None of these choices complies with the real process. Water from outside the calculation area will flow through the boundary. This also implies, however, that the pressure along this boundary is not hydrostatic. If, however, the boundary is chosen with enough distance from the real cutting process the boundary condition may not have an influence on the solution. The impermeable wall is chosen although this choice is arbitrary. Figure 11-13 and Figure 11-15 give an impression of the equi-potential lines and the stream lines in the model area. Figure 11-9 show the dimensionless pore pressure distributions on the lines **A-B**, **A-C**, **A-D** and **D-C**. The average dimensionless pore pressures on these lines are named $\mathbf{p_{1m}}$, $\mathbf{p_{2m}}$, $\mathbf{p_{3m}}$ and $\mathbf{p_{4m}}$.

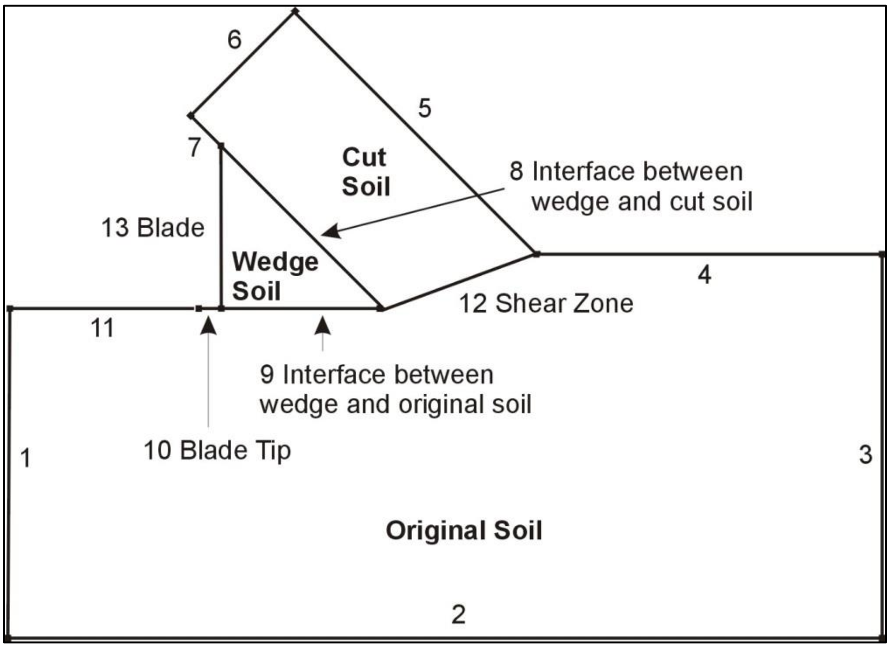

Figure 11-8: The boundaries of the FEM model.

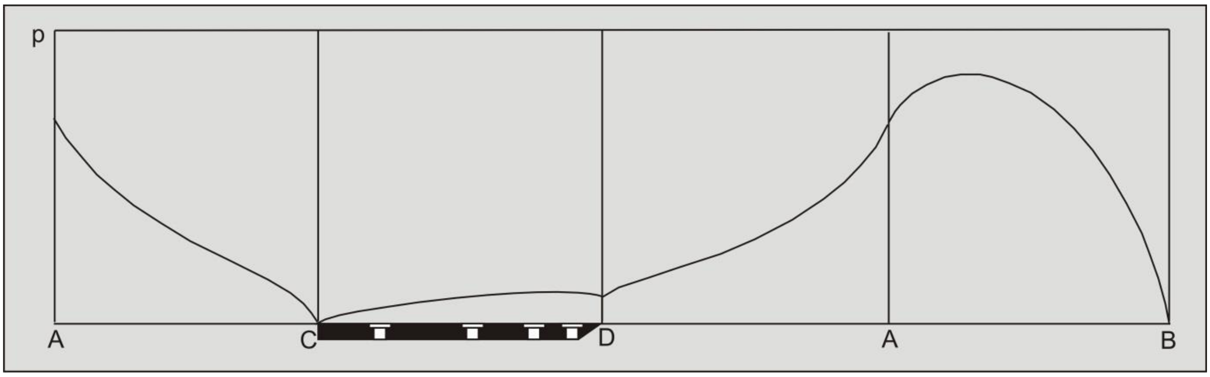

Figure 11-9: Pore pressure distribution on the shear plane A-B, the bottom of the wedge A-D, the blade D-C and the front of the wedge A-C.

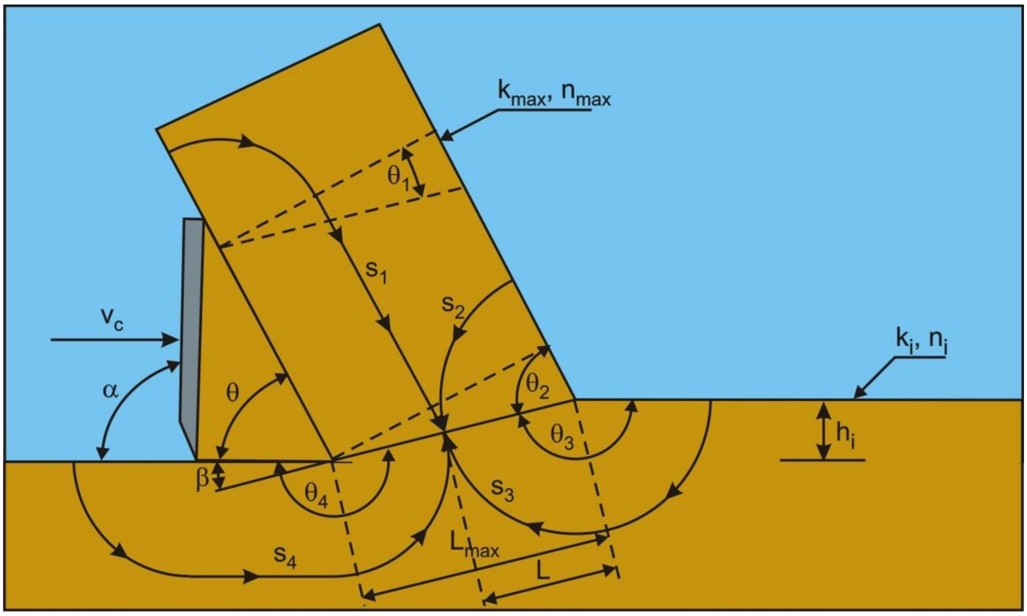

Figure 11-10: The parallel resistor method.

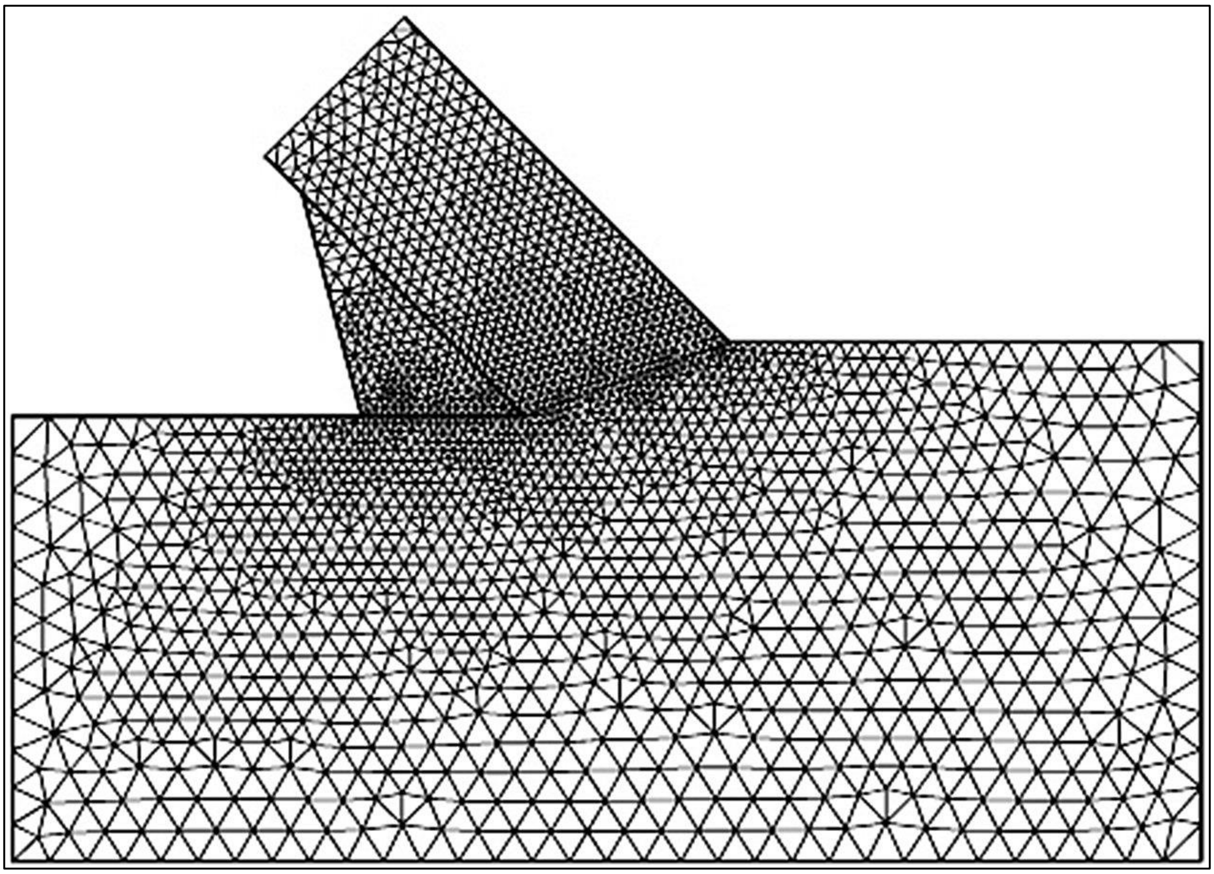

Figure 11-11: The coarse mesh.

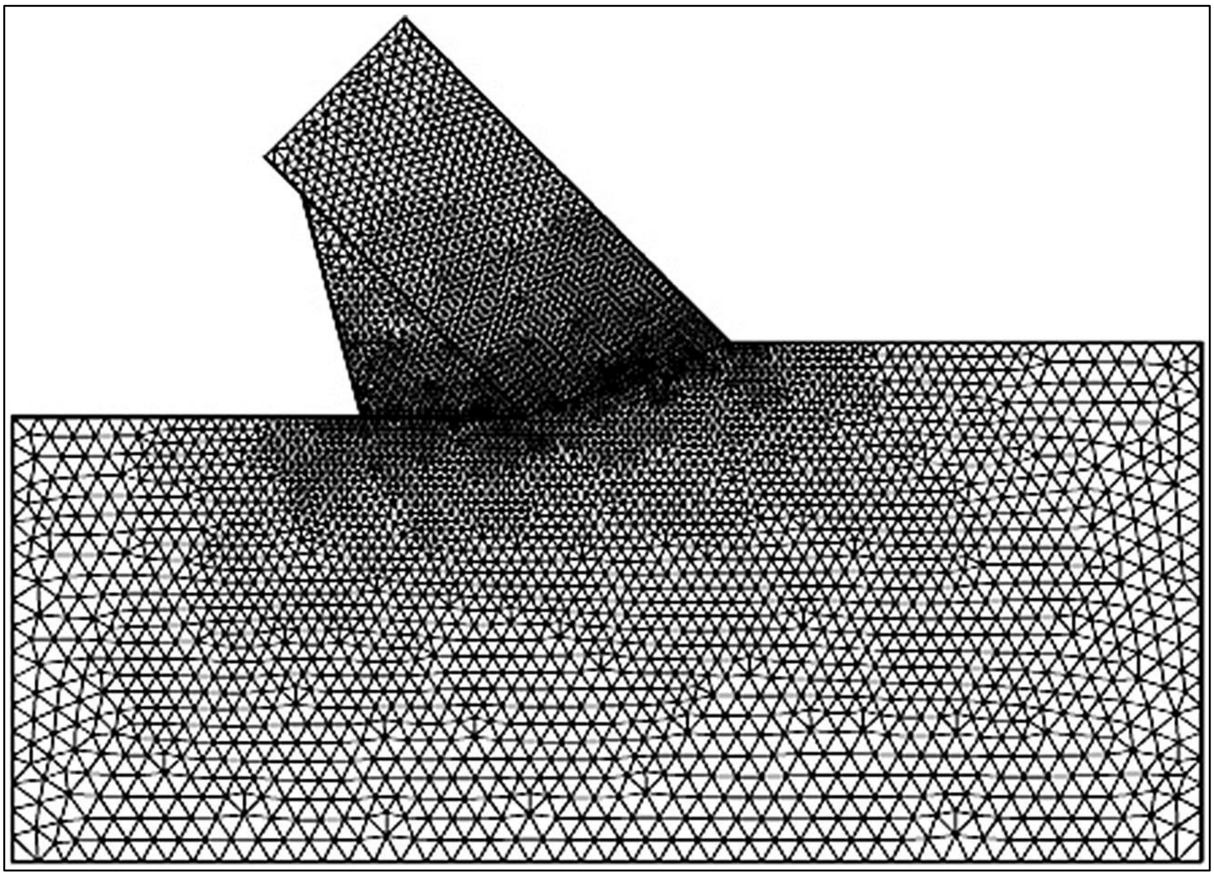

Figure 11-12: The fine mesh.

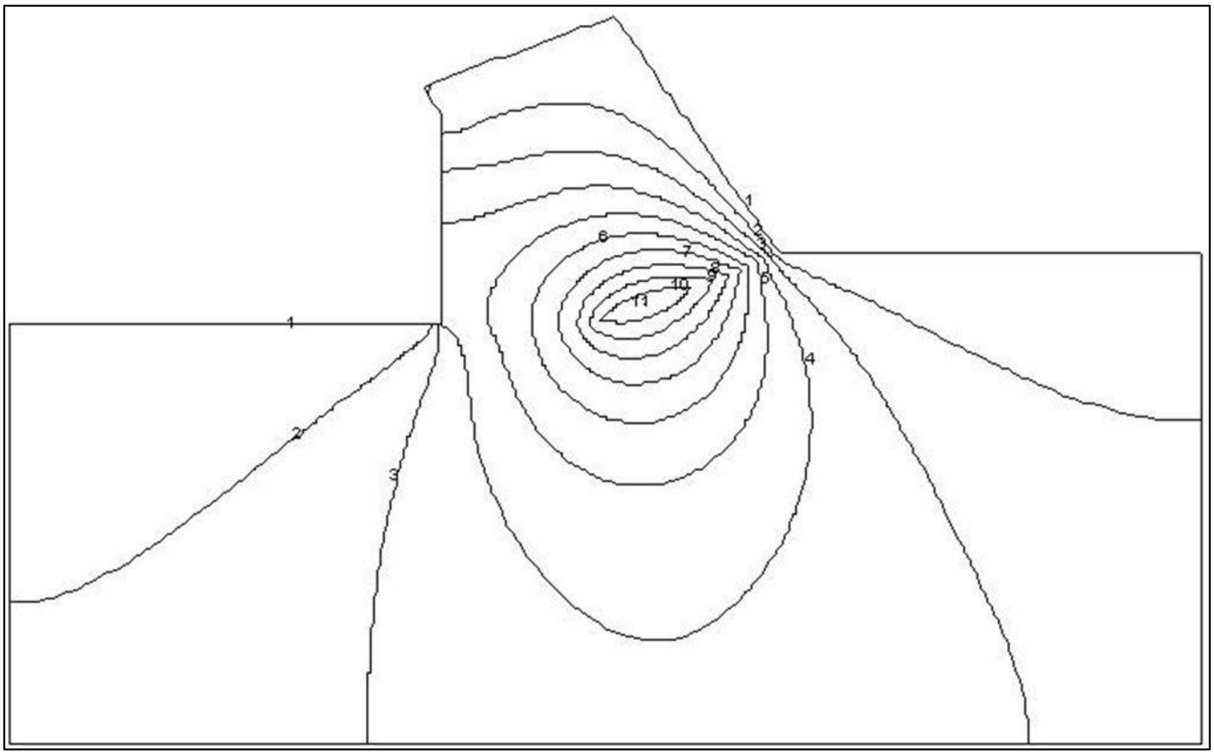

Figure 11-13: Equipotential lines of pore pressures.

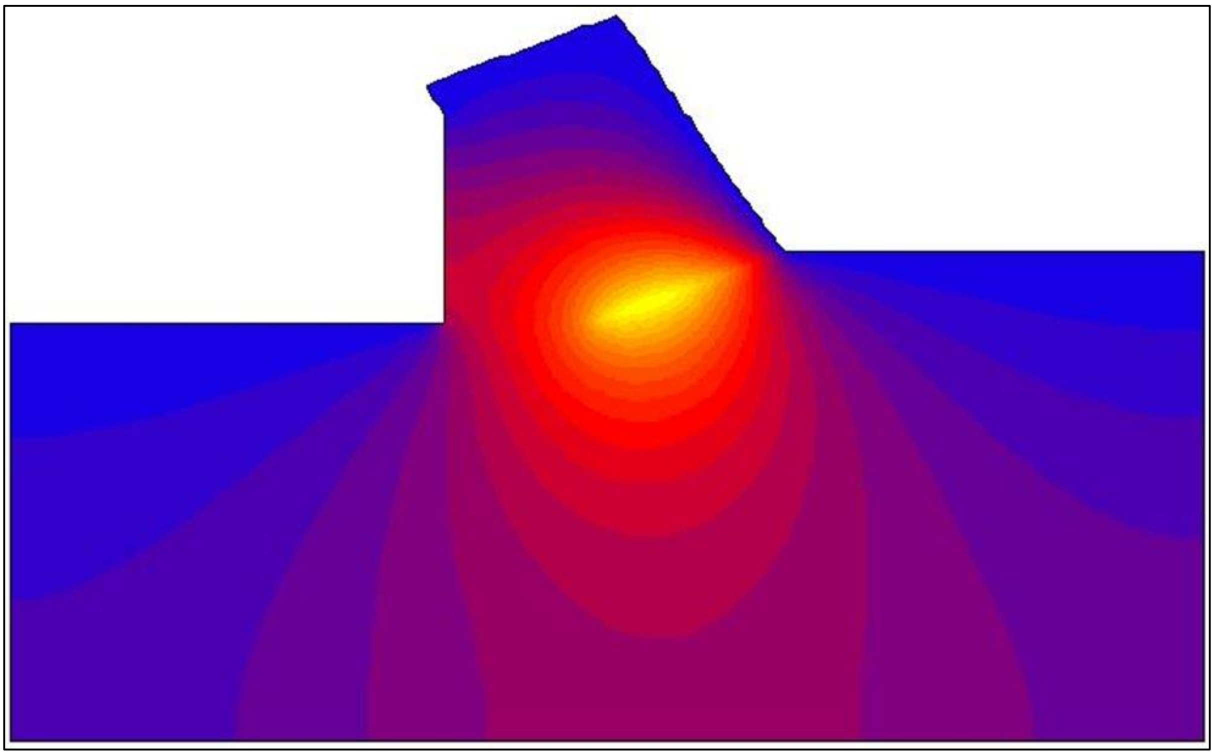

Figure 11-14: Equi-potential distribution in color.

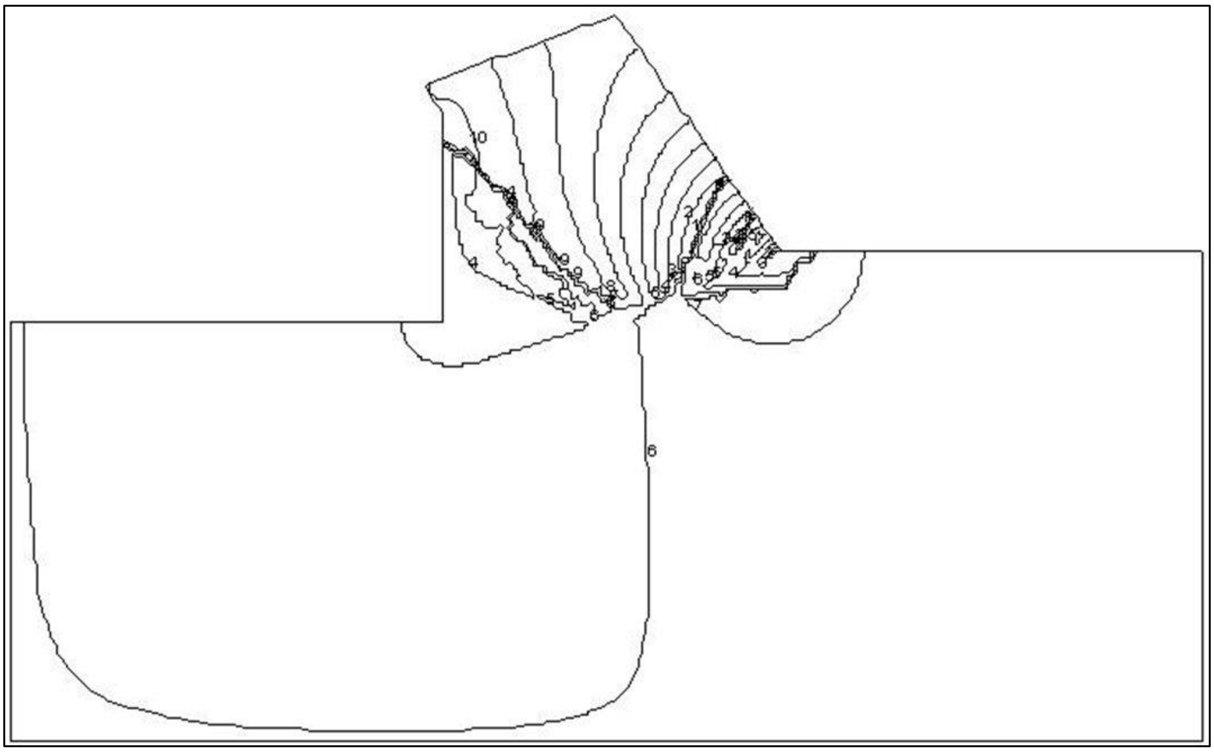

Figure 11-15: The flow lines or stream function.

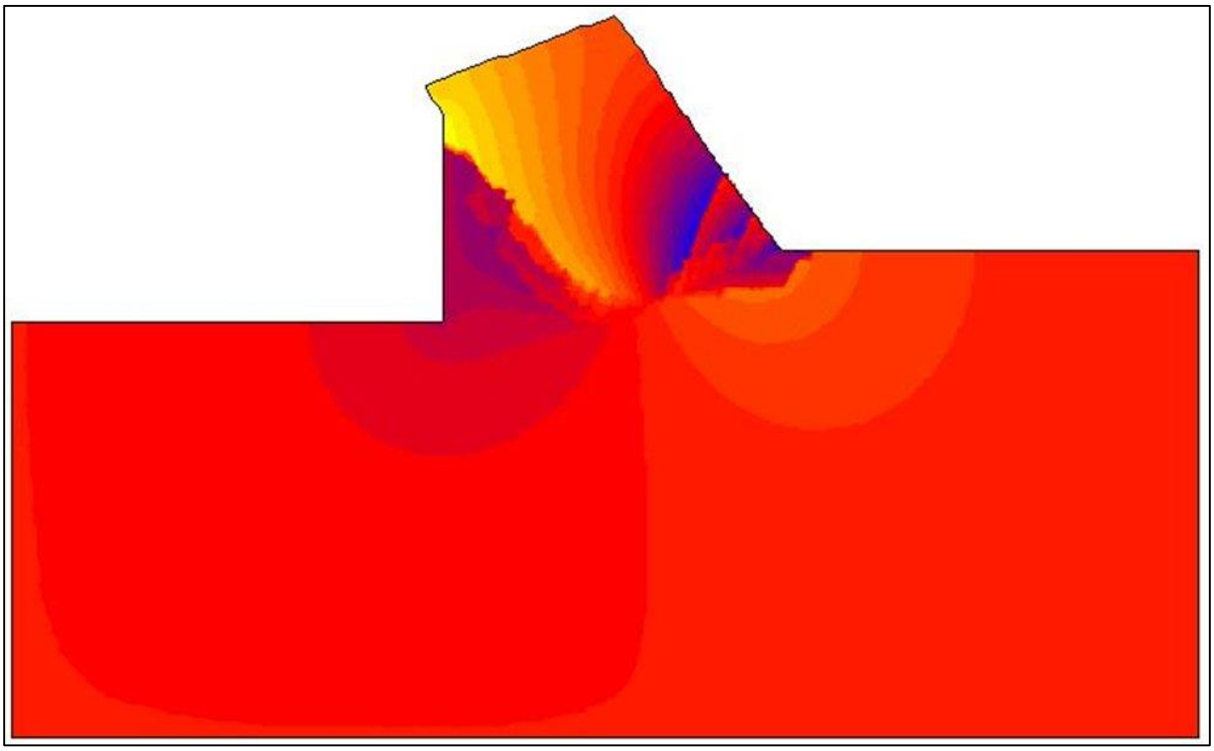

Figure 11-16: The stream function in colors.

11.4. Moments

Based on the equilibrium of forces on the layer cut **B-A-C**, FEM calculations of pore water pressures and the minimum of cutting energy the forces $\mathbf{N_2}$, $\mathbf{S_2}$ and $\mathbf{W_2}$ are determined; see Miedema (1987 September). To determine the forces on the blade there are still a number of unknowns. $\mathbf{W_3}$ and $\mathbf{W_4}$ can be determined using FEM calculations of pore water pressures, given the wedge angle $\boldsymbol{\theta}$. Assuming $\boldsymbol{\lambda=\varphi}$ as a first estimate, the forces $\mathbf{K_3}$ and $\mathbf{K_4}$ depend on the wedge angle $\boldsymbol{\theta}$ and on the effective external friction angle $\boldsymbol{\delta_e}$. For a static wedge, meaning that there is no movement between the wedge and the blade, the effective external friction angle can have a value between + and – the maximum external friction angle $\boldsymbol{\delta}$, so $\boldsymbol{-\delta<\delta_e<\delta}$. Combining this with the minimum energy principle results in a varying $\boldsymbol{\delta_e}$ and a force $\mathbf{N_3}$ being equal to zero for a static wedge. The value of $\boldsymbol{\delta_e}$ follows from the equilibrium of moments. For small values of the blade angle $\boldsymbol{\alpha}$, smaller than about 60º, the effective external friction angle $\boldsymbol{\delta_e=\delta}$ and most probably there will not be a wedge. For intermediate values of the blade angle $\boldsymbol{\alpha}$ around 90º, there will be a static wedge and the effective external friction angle $\boldsymbol{\delta_e}$ will decrease from $\boldsymbol{+\delta}$ to $\boldsymbol{-\delta}$. For very large values of $\boldsymbol{\alpha}$, larger than about 120º, the effective external friction angle $\boldsymbol{\delta_e=-\delta}$ and $\mathbf{N_3}$ will have a positive value, meaning an upwards direction. Probably there will be a movement of soil under the blade. To find the value of the effective external friction angle first the equilibrium of moments has to be solved. Figure 11-17 shows the moments that occur on the wedge as a result of the forces and their acting points.

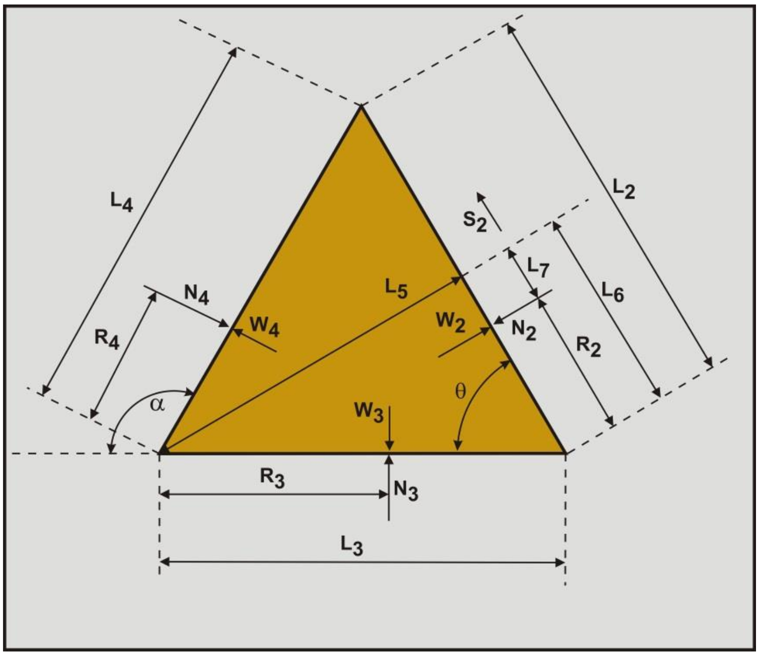

Figure 11-17: The equilibrium of moments on the wedge in water saturated sand.

To determine the moment on the wedge, first the different lengths and distances have to be determined. The length of the shear plane **A-B** is:

$$\mathbf{A-B=L_1=\frac{h_i}{\sin(\beta)}} \qquad \mathbf{(11\text{-}23)}$$

The length of the pseudo blade or front of the wedge **A-C** is:

$$\mathbf{A-C=L_2=\frac{h_b}{\sin(\theta)}} \qquad \mathbf{(11\text{-}24)}$$

The length of the bottom of the wedge **A-D** is:

$$\mathbf{A-D=L_3=h_b\cdot\left(\frac{1}{\tan(\theta)}-\frac{1}{\tan(\alpha)}\right)} \qquad \mathbf{(11\text{-}25)}$$

The length of the blade **D-C** is:

$$\mathbf{D-C=L_4=\frac{h_b}{\sin(\alpha)}} \tag{11-26}$$

The distance between the blade edge and the wedge side **A-C** (perpendicular) is:

$$\mathbf{L_5=L_3\cdot\sin(\theta)} \tag{11-27}$$

The distance from point **A** and the line $\mathbf{L_5}$ is:

$$\mathbf{L_6=L_3\cdot\cos(\theta)} \tag{11-28}$$

The arm of the acting point of $\mathbf{N_2}$ and $\mathbf{W_2}$ is now:

$$\mathbf{L_7=L_6-R_2} \tag{11-29}$$

The equilibrium of moments can be determined using all those distances:

$$\sum\mathbf{M=(N_4-W_4)\cdot R_4-(N_3-W_3)\cdot R_3+(N_2-W_2)\cdot L_7-S_2\cdot L_5=0} \tag{11-30}$$

Equation (11-30) still contains the unknown arms $\mathbf{R_2}$, $\mathbf{R_3}$ and $\mathbf{R_4}$. Based on the FEM calculations for the pore pressures, values of $\mathbf{0.35\cdot L_2}$, $\mathbf{0.55\cdot L_3}$ and $\mathbf{0.32\cdot L_4}$ are found, Ma (2001). Figure 11-18 shows the moments on the wedge with respect to the cutting edge as a function of the wedge angle $\boldsymbol{\theta}$ for different values of the shear angle $\boldsymbol{\beta}$ and a blade angle $\boldsymbol{\alpha}$ of 90º. The moment is zero for a wedge angle $\boldsymbol{\theta}$ between 50º and 55º.

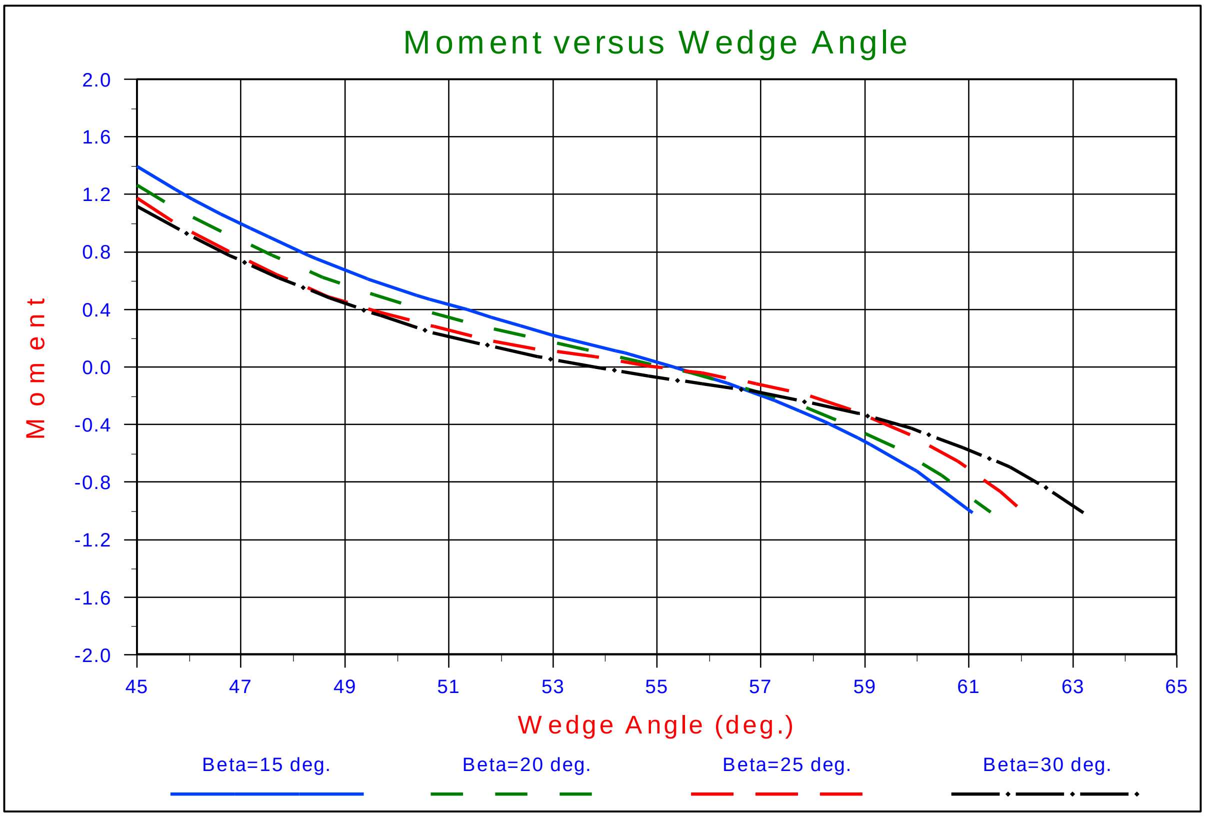

Figure 11-18: Moment versus wedge angle θ by using polynomial regression for: $\boldsymbol{\alpha=90^0}$; $\boldsymbol{\beta=15^0,20^0,25^0,30^0}$; $\boldsymbol{\delta=28^0}$; $\boldsymbol{\varphi=42^0}$; $\mathbf{h_i=1}$; $\mathbf{h_b=3}$; $\mathbf{k_i/k_{max}=0.25}$

Figure 11-19 shows the moments as a function of the shear angle $\boldsymbol{\beta}$ for 4 values of the wedge angle $\boldsymbol{\theta}$. The moment is zero for the wedge angle $\boldsymbol{\theta=55^o}$ at a shear angle $\boldsymbol{\beta=18^o}$. It is clear from these figures that the shear angle where the moment is zero is not very sensitive for the shear angle and the wedge angle.

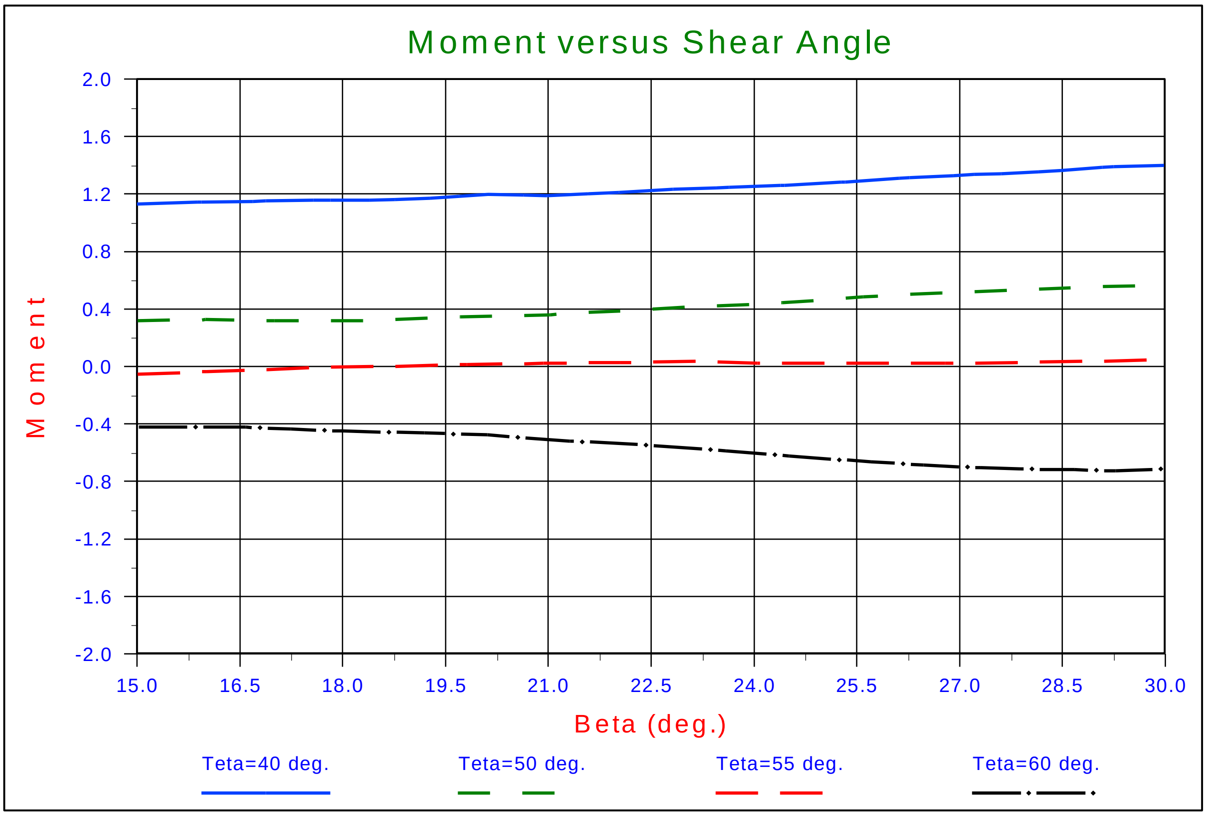

Figure 11-19: The moment versus the shear angle for 4 different wedge angles for: $\alpha=90^0$; $\delta=28^0$; $\varphi=42^0$; $h_i=1$; $h_b=3$; $k_i/k_{max}=0.25$

Figure 11-20 shows the force triangles on the 3 sides of the wedges for cutting angles from 60 to 120 degrees. From the calculations it appeared that the pore pressures on interface between the soil cut and the wedge and in the shear plane do not change significantly when the blade angle changes. These pore pressures $\mathbf{p_{1m}}$ and $\mathbf{p_{2m}}$, resulting in the forces $\mathbf{W_1}$ and $\mathbf{W_2}$, are determined by the shear angle $\boldsymbol{\beta}$, the wedge angle $\boldsymbol{\theta}$ and other soil mechanical properties like the permeability.
The fact that the pore pressures do not significantly change, also results in forces $\mathbf{K_2}$, acting on the wedge that do not change a significantly, according to equations (11-4), (11-5) and (11-6). These forces are shown in Figure 11-20 on the right side of the wedges and the figure shows that these forces are almost equal for all blade angles. These forces are determined by the conventional theory as published by Miedema (1987 September). Figure 11-20 also shows that for the small blade angles the friction force on the wedge is directed downwards, while for the bigger blade angles this friction force is directed upwards.

$$\mathbf{R_2 = e_2 \cdot L_2, \quad R_3 = e_3 \cdot L_3, \quad R_4 = e_4 \cdot L_4} \qquad \textbf{(11-31)}$$

Now the question is, what is the solution for the cutting of water saturated sand at large cutting angles? From many calculations and an analysis of the laboratory research is described by He (1998), Ma (2001) and Miedema (2005), it appeared that the wedge can be considered a static wedge, although the sand inside the wedge still may have velocity, the sand on the blade is not moving. The main problem in finding acceptable solutions was finding good values for the acting points on the 3 sides of the wedge, $\mathbf{e_2}$, $\mathbf{e_3}$ and $\mathbf{e_4}$. If these values are chosen right, solutions exist based on the equilibrium of moments, but if they are chosen wrongly, no solution will be found. So the choice of these parameters is very critical. The statement that the sand on the blade is not moving is based on two things, first of all if the sand is moving with respect to the blade, the soil interface friction is fully mobilized and the bottom of the wedge requires to have a small angle with respect to the horizontal in order to make a flow of sand possible. This results in much bigger cutting forces, while often no solution can be found or unreasonable values for $\mathbf{e_2}$, $\mathbf{e_3}$ and $\mathbf{e_4}$ have to be used to find a solution.

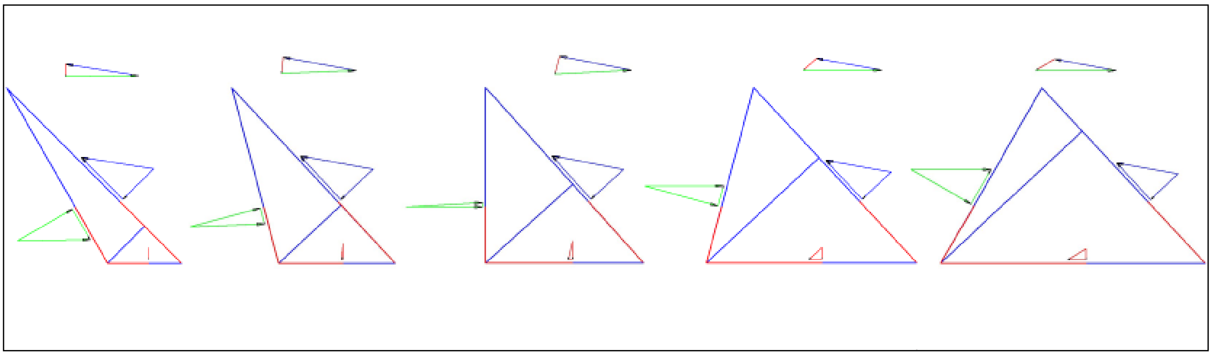

Figure 11-20: The forces on the wedges at 60°, 75°, 90°, 105° and 120° cutting angles.

So the solution is, using the equilibrium equations for the horizontal force, the vertical force and the moments on the wedge. The recipe to determine the cutting forces seems not to difficult now, but it requires a lot of calculations and understanding of the processes, because one also has to distinguish between the theory for small cutting angles and the wedge theory.

The following steps have to be taken to find the correct solution:

1. Determine the dimensionless pore pressures $\mathbf{p_{1m}}$, $\mathbf{p_{2m}}$, $\mathbf{p_{3m}}$ and $\mathbf{p_{4m}}$ using a finite element calculation or the method described by Miedema (2006B), for a variety of shear angles $\boldsymbol{\beta}$ and wedge angles $\boldsymbol{\theta}$ around the expected solution.
2. Determine the shear angle $\boldsymbol{\beta}$ based on the equilibrium equations for the horizontal and vertical forces, a given wedge angle $\boldsymbol{\theta}$ and the principle of minimum energy, which is equivalent to the minimum horizontal force. This also gives a value for the resulting force $\mathbf{K_2}$ acting on the wedge.
3. Determine values of $\mathbf{e_2}$, $\mathbf{e_3}$ and $\mathbf{e_4}$ based on the results from the pore pressure calculations.
4. Determine the solutions of the equilibrium equations on the wedge and find the solution which has the minimum energy dissipation, resulting in the minimum horizontal force on the blade.
5. Determine the forces without a wedge with the theory for small cutting angles.
6. Determine which horizontal force is the smallest, with or without the wedge.

11.5. The Non-Cavitating Wedge

To illustrate the results of the calculation method, a non-cavitating case will be discussed. Calculations are carried out for blade angles $\boldsymbol{\alpha}$ of 65°, 70°, 75°, 80°, 85°, 90°, 95°, 100°, 105°, 110°, 115° and 120°, while the smallest angle is around 60° depending on the possible solutions. Also the cutting forces are determined with and without a wedge, so it's possible to carry out step 6.

The case concerns a sand with an internal friction angle $\boldsymbol{\varphi}$ of 30°, a soil interface friction angle $\boldsymbol{\delta}$ of 20° fully mobilized, a friction angle λ between the soil cut and the wedge equal to the internal friction angle, an initial permeability $\mathbf{k_i}$ of 6.2*10^{-5} m/s and a residual permeability $\mathbf{k_{max}}$ of 17*10^{-5} m/s. The blade dimensions are a width of 0.25 m and a height of 0.2 m, while a layer of sand of 0.05 m is cut with a cutting velocity of 0.3 m/s at a water depth of 0.6 m, matching the laboratory conditions. The values for the acting points of the forces, are $\mathbf{e_2=0.35}$, $\mathbf{e_3=0.55}$ and $\mathbf{e_4=0.32}$, based on the finite element calculations carried out by Ma (2001).

Figure 11-21 and Figure 11-22 show the results of the calculations. Figure 11-21 shows the wedge angle $\boldsymbol{\theta}$, the shear angle $\boldsymbol{\beta}$, the mobilized internal friction angle $\boldsymbol{\lambda}$ and the mobilized external friction angle $\boldsymbol{\delta_e}$ as a function of the blade angle $\boldsymbol{\alpha}$. Figure 11-22 shows the horizontal and vertical cutting forces, with and without a wedge.

The wedge angles found are smaller than $\mathbf{90°\text{-}\varphi}$, which would match the theory of Hettiaratchi and Reece (1975). The shear angle $\boldsymbol{\beta}$ is around 20°, but it is obvious that a larger internal friction angle gives a smaller shear angle $\boldsymbol{\beta}$. The mobilized external friction angle varies from plus the maximum mobilized external friction angle to minus the maximum mobilized external friction angle as is also shown in the force diagrams in Figure 11-20.

Figure 11-22 shows clearly how the cutting forces become infinite when the sum of the 4 angles involved is 180° and become negative when this sum is larger then 180°. So the transition from the small cutting angle theory to the wedge theory occurs around a cutting angle of 70°, depending on the soil mechanical parameters and the geometry of the cutting process.

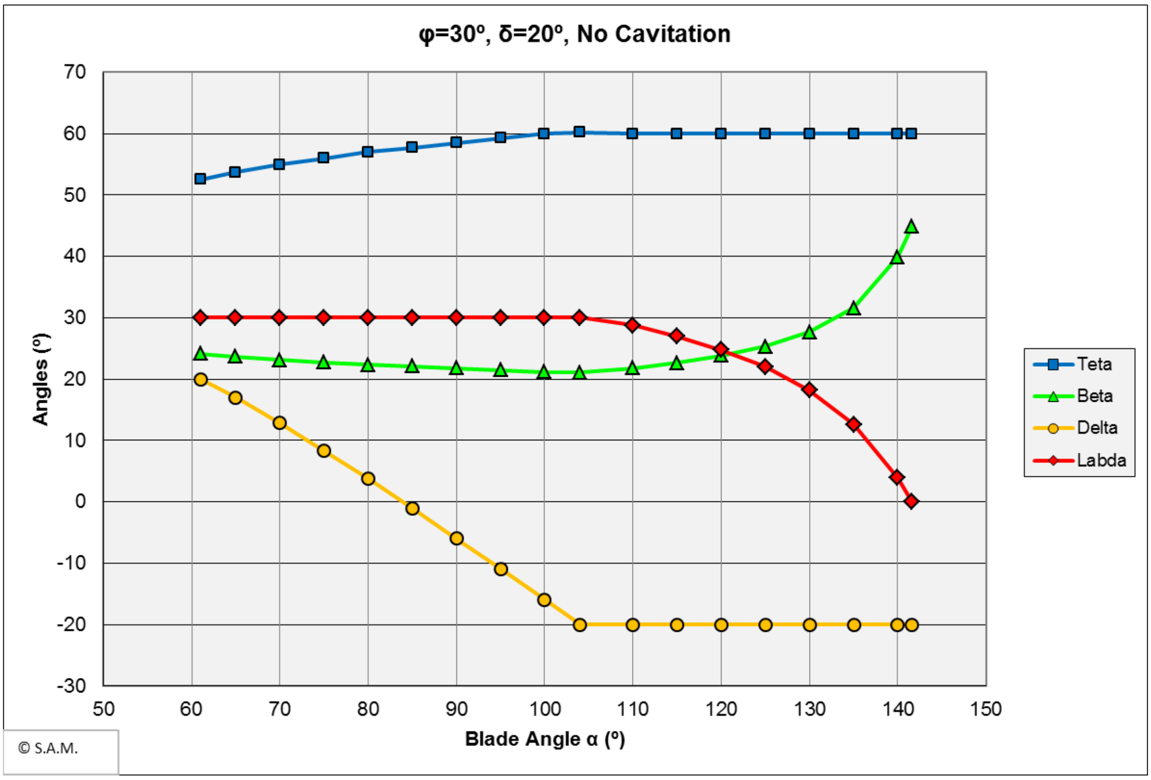

Figure 11-21: No cavitation, the angles θ, β, δ_m and λ as a function of the blade angle α for φ=30º and δ=20º.

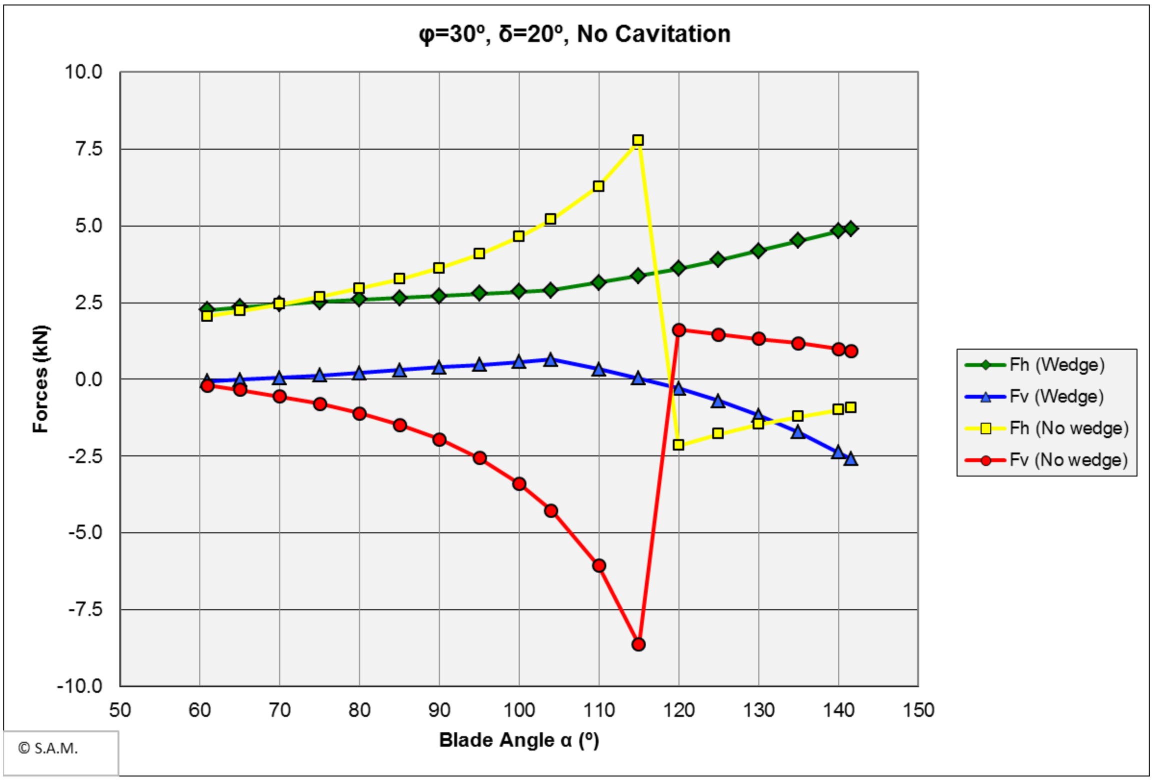

Figure 11-22: No cavitation, the cutting forces as a function of the blade angle α for φ=30º and δ=20º.

11.6. The Cavitating Wedge

Also for the cavitating process, a case will be discussed. The calculations are carried out for blade angles **α** of 65°, 70°, 75°, 80°, 85°, 90°, 95°, 100°, 105°, 110°, 115° and 120°, while the smallest angle is around 60º depending on the possible solutions. Also the cutting forces are determined with and without a wedge, so its possible to carry out step 6.

The case concerns a sand with an internal friction angle **φ** of 30°, a soil interface friction angle **δ** of 20° fully mobilized, a friction angle **λ** between the soil cut and the wedge equal to the internal friction angle, an initial permeability $\mathbf{k_i}$ of $6.2*10^{-5}$ m/s and a residual permeability $\mathbf{k_{max}}$ of $17*10^{-5}$ m/s. The blade dimensions are a width of 0.25 m and a height of 0.2 m, while a layer of sand of 0.05 m is cut with a cutting velocity of 0.3 m/s at a water depth of 0.6 m, matching the laboratory conditions. The values for the acting points of the forces, are $\mathbf{e_2=0.35}$, $\mathbf{e_3=0.55}$ and $\mathbf{e_4=0.32}$, based on the finite element calculations carried out by Ma (2001).

Figure 11-23 and Figure 11-24 show the results of the calculations. Figure 11-23 shows the wedge angle **θ**, the shear angle **β**, the mobilized internal friction angle **λ** and the mobilized external friction angle $\mathbf{\delta_e}$ as a function of the blade angle **α**. Figure 11-24 shows the horizontal and vertical cutting forces, with and without a wedge.

With the cavitating cutting process, the wedge angle **θ** always results in an angle of **90°-φ**, which matches the theory of Hettiaratchi and Reece (1975). The reason of this is that in the full cavitation situation, the pore pressures are equal on each side of the wedge and form equilibrium in itself. So the pore pressures do not influence the ratio between the grain stresses on the different sides of the wedge. From Figure 11-24 it can be concluded that the transition point between the conventional cutting process and the wedge process occurs at a blade angle of about 77 degrees.

In the non-cavitating cases this angle is about 70 degrees. A smaller angle of internal friction results in a higher transition angle, but in the cavitating case this influence is bigger. In the cavitating case, the horizontal force is a constant as long as the external friction angle is changing from a positive maximum to the negative minimum. Once this minimum is reached, the horizontal force increases a bit. At the transition angle where the horizontal forces with and without the wedge are equal, the vertical forces are not equal, resulting in a jump of the vertical force, when the wedge starts to occur.

11.7. Limits

Instead of carrying out the calculations for each different case, the limits of the occurrence of the wedge can be summarized in a few graphs. Figure 11-25 shows the upper and lower limit of the wedge for the non-cavitating case as a function of the angle of internal friction **φ**. It can be concluded that the upper and lower limits are not symmetrical around 90º, but a bit lower than that. An increasing angle of internal friction results in a larger bandwidth for the occurrence of the wedge. For blade angles above the upper limit most probably subduction will occur, although there is no scientific evidence for this. The theory developed should not be used for blade angles above the upper limit yet. Further research is required. The lower limit is not necessarily the start of the occurrence of the wedge. This depends on whether the cutting forces with the wedge are smaller than the cutting forces without the wedge. Figure 11-27 shows the blade angle where the wedge will start to occur, based on the minimum of the horizontal cutting forces with and without the wedge. It can be concluded that the blade angle where the wedge starts to occur is larger than the minimum where the wedge can exist, which makes sense. For high angles of internal friction, the starting blade angle is about equal to the lower limit.

For the cavitating case the upper and lower limit are shown in Figure 11-26. In this case the limits are symmetrical around 90º and with an external friction angle of 2/3 of the internal friction angle it can be concluded that these limits are **90º+δ** and **90º-δ**. The blade anle where the wedge will start to occur is again shown in Figure 11-27.

The methodology applied gives satisfactory results to determine the cutting forces at large cutting angles. The results shown in this paper are valid for the non-cavitating and the cavitating cutting process and for the soils and geometry as used in this paper. The wedge angles found are, in general, a bit smaller then **90°-φ** for the non-cavitating case and exactly **90°-φ** for the cavitating case, so as a first approach this can be used.

The mobilized external friction angle δ_e varies from plus the maximum for small blade angles to minus the maximum for large blade angles, depending on the blade angle.

The cutting forces with the wedge do not increase much in the non-cavitating case and not at all in the cavitating case, when the cutting angle increases from 60° to 120°.

If the ratio between the thickness of the layer cut and the blade height changes, also the values of the acting points $\mathbf{e_2}$, $\mathbf{e_3}$ and $\mathbf{e_4}$ will change slightly.

It is not possible to find an explicit analytical solution for the wedge problem and it's even difficult to automate the calculation method, since the solution depends strongly on the values of the acting points.

Figure 11-25, Figure 11-26 and Figure 11-27 are a great help determining whether or not a wedge will occur and at which blade angle it will start to occur.

The theory developed can be applied to cutting processes of bulldozers, in front of the heel of a drag head, ice scour, tunnel boring machines and so on.

Figure 11-23: Cavitating, the angles θ, β, δ_m and λ as a function of the blade angle α for φ=30º and δ=20º.

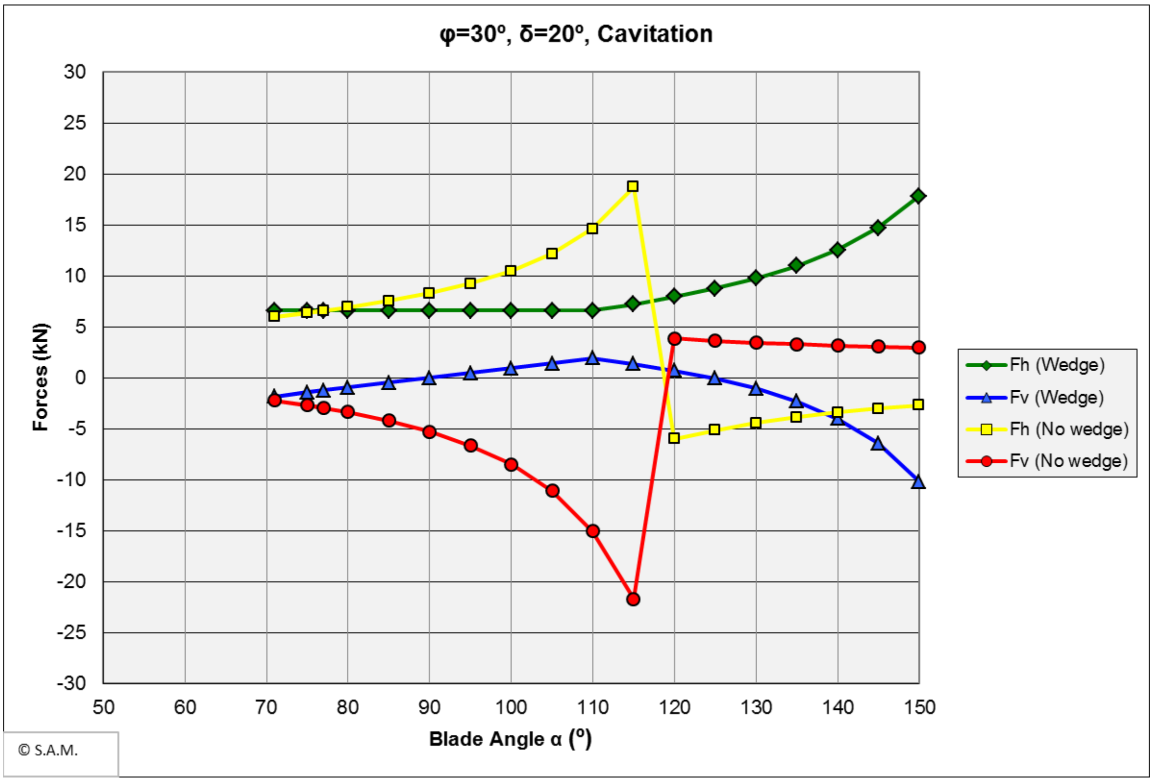

Figure 11-24: Cavitating, the cutting forces as a function of the blade angle α for φ=30º and δ=20º.

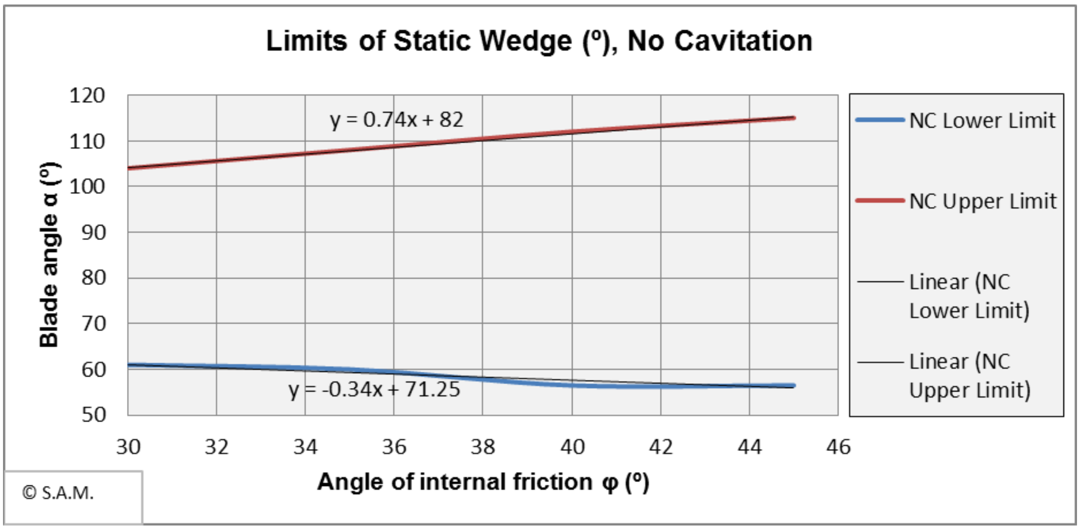

Figure 11-25: The lower and upper limit where a static wedge can exist for the non-cavitating cutting process.

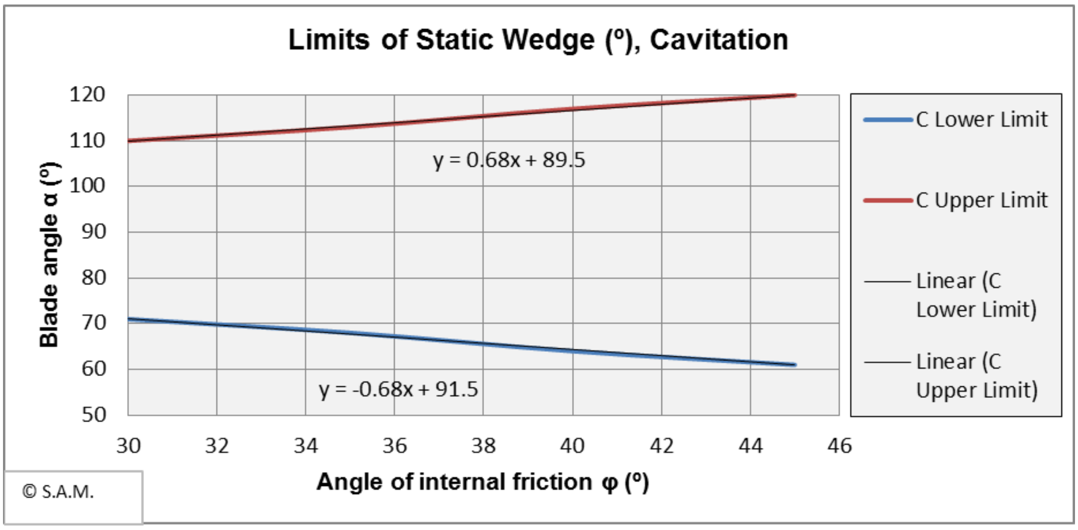

Figure 11-26: The lower and upper limit where a static wedge can exist for the cavitating cutting process.

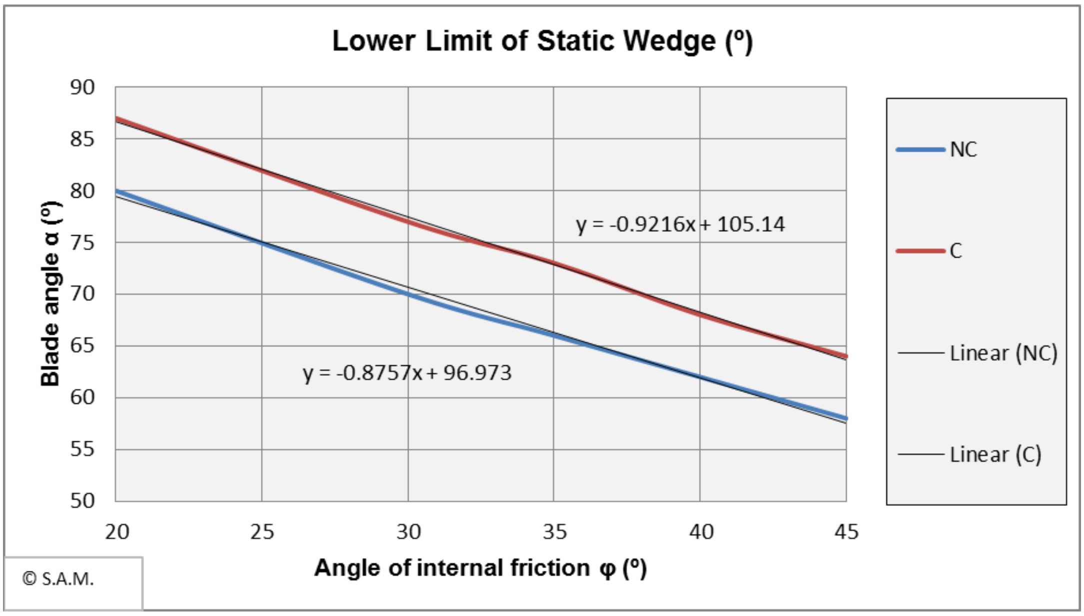

Figure 11-27: The lower limit where the wedge starts to occur.

11.8. Experiments

Ssand cutting tests have been carried out in the Laboratory of Dredging Engineering at the Delft University.

The cutting tank is a concrete tank with a length of 35 m, a width of 3 m and a depth of 1.5 m. The bottom of the tank is covered with a drainage system. Above the drainage system is a layer of about 0.7 m sand (0.110 mm). On top of the sand is a layer of 0.5 m water. Other soils than the 0.110 mm sand can be used in the tank. On top of the tank rails are mounted on which a carriage can ride with speeds of up to 1.25 m/s with a pulling force of up to 15 kN, or 2.5 m/s with a pulling force of 7.5 kN. On the carriage an auxilary carriage is mounted that can be moved transverse to the velocity of the main carriage. On this carriage a hydraulic swell simulating system is mounted, thus enabling the cutting tools to be subjected to specific oscillations. Under the carriage dredging equipment such as cutterheads and dragheads can be mounted. The dredging equipment can be instrumented with different types of transducers such as force, speed, density, etc. transducers. The signals from these transducers will be conditioned before they go to a computer via an A/D converter. On the carriage a hydraulic system is available, including velocity and density transducers. A 25 kW hydraulic drive is available for cutterheads and dredging wheels. The dredge pump is driven by a 15 kW electric drive with speed control. With the drainage system the pore water pressures can be controlled. Dredged material is dumped in an adjacent hopper tank to keep the water clean for under water video recordings. In the cutting tank research is carried out on cutting processes, mixture forming, offshore dredging, but also jet-cutting, the removal of contaminated silt, etc.

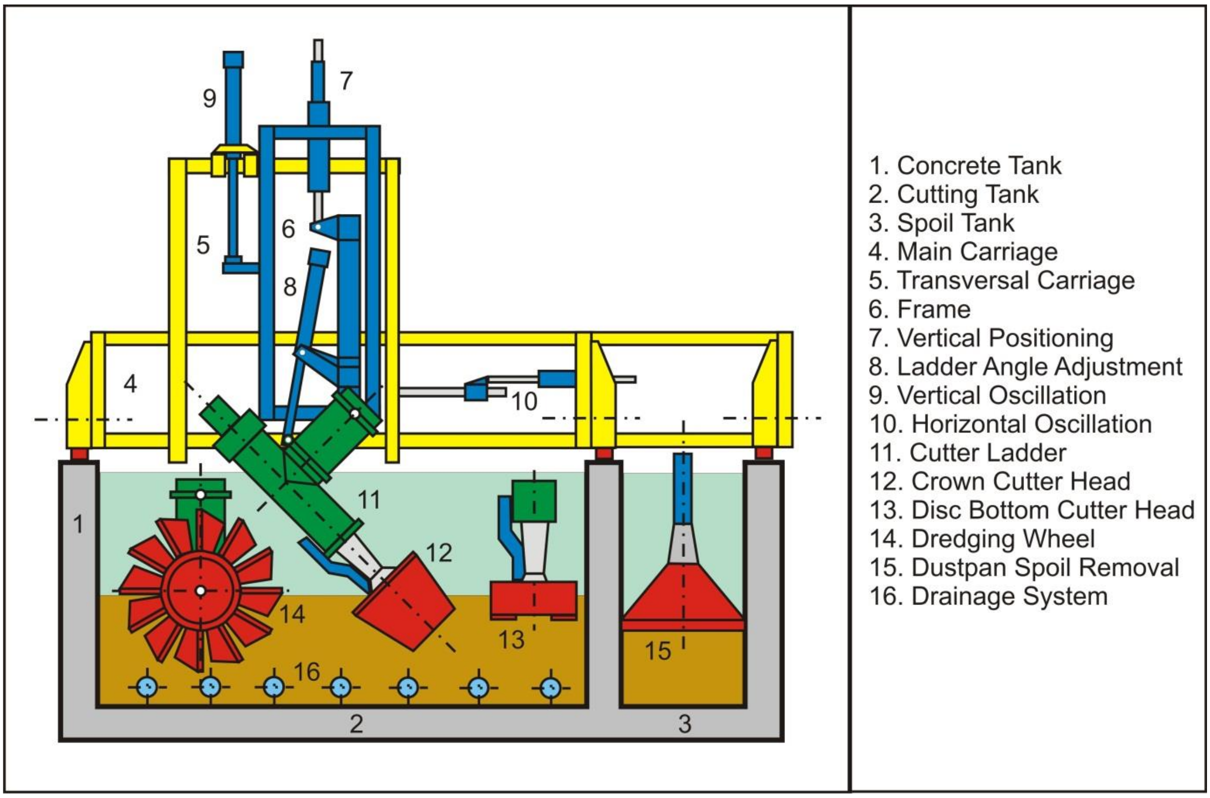

Figure 11-28: Cross section of the cutting tank.

Figure 11-29: Front view of the test facility.

The tests carried out in the Dredging Engineering Laboratory had the objective to find the failure mechanisms of a sand package under large cutting angles of 60°, 75° and 90°. Main goal of the tests was to visualize the total process in a 2-dimensional view. Besides, the behaviour of sand in front of the blade was to be investigated. As mentioned before, some wedge exists in front of the blade, but it was not clear until now whether this was a kinematic wedge or a dynamic wedge. Visualising the cutting process and visualising the velocity of the sand on the blade has to improve the understanding of the processes involved.

The existing testing facilities have been used to carry out the cutting tests. With these facilities cutting depths from 3 till 7 cm are tested, resulting in an (effective blade height)/(cutting depth) ratio of 2.5 to 6, for the various angles. Cutting velocities of the tests were from 0,1 m/s to 0,4 m/s for smaller and 0,2 m/s for the larger cutting depths. These maximum velocities are limited by the maximum electrical power of the testing facility. In the first series of tests the 2-dimensional cutting process is made visual by doing tests near the window in the cutting tank. The process is not completely 2-dimensional here, because the water pressures and sand friction are influenced by the window, but it gives a good indication of the appearing failure mechanism of the sand package. Figure 11-28 shows a cross-section of the cutting tank and the carriage under which the cutting tools are mounted, while Figure 11-29 shows a front view and Figure 11-30 shows the blades mounted under the carriage.

To visualise the behaviour of the sand package in front of the blade a perspex window is made in the middle one of the 3 cutting blades. Here we expect the least side influences. The middle blade measures a height of 20 cm and a width of 25 cm. The camera is mounted at the back of the blade, in a cover, as seen in Figure 11-32. In Figure 11-31 you can see an underwater light, which is also mounted in the cover, shining on the camera. This construction gives a view of the process as can be seen in Figure 11-33 and Figure 11-34, at a height of 8 till 9 cm in the blade. The camera records with a frame rate of 25/sec. In the perspex window, Figure 11-34, a scale of 1 cm is engraved. By tracing sand grains along the window a ratio is determined between the cutting velocity and the velocity along the window at the recorded height, for the angles of 75° and 90°. These ratios are respectively 0.3 and 0.15. At 60° this ratio can hardly be determined because it lies in the range of the cutting velocity and out of the range of the recorded frame rate.

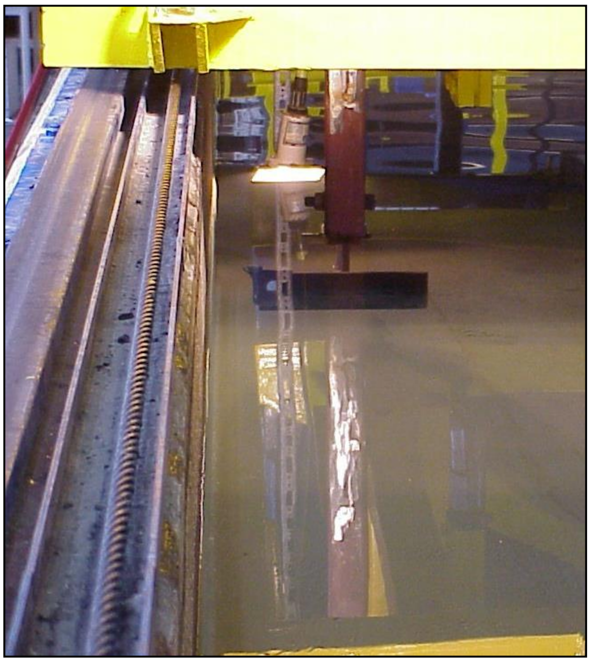

Figure 11-30: The blade mounted under the carriage

Figure 11-31: The camera in front of the window.

With a dynamometer forces on the middle blade are measured. The horizontal cutting forces for the various angles are roughly in a ratio of 1:1.5:2, for 60°, 75°, 90° respectively. This indicates a changing failure mechanism for the 3 tested angles, which the videos from the tests along the glass also confirm.
Figures 9, 10 and 11 show the horizontal cutting forces as obtained from the experiments.
From the above results two main conclusions can be drawn. First of all, the sand is moving relative to the blade on the blade and secondly the cutting forces at a 90° blade are much smaller then would be expected from the cutting theory, Miedema (1987 September). As shown in Figure 11-1, He et al. (1998) and also observed according to Figure 11-38, a wedge exists in front of the blade, but apparently this is not a kinematic wedge, but a dynamic wedge.

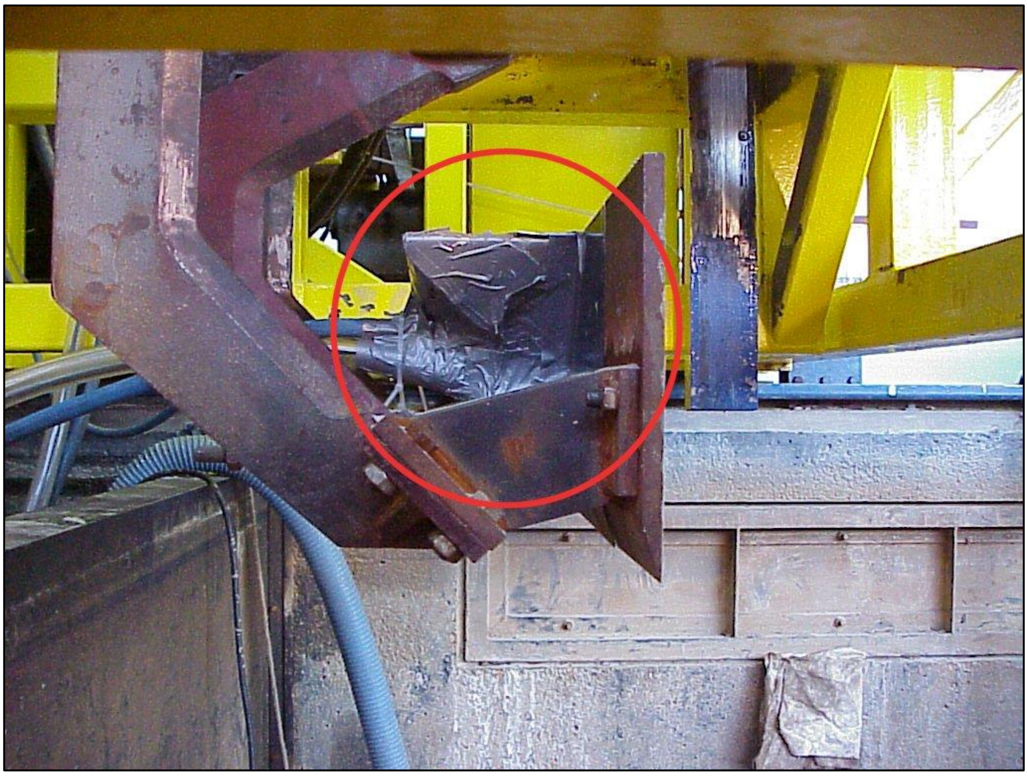

Figure 11-32: Cover with camera behind the blade.

To determine the flow pattern of the sand in the dynamic wedge, vertical bars of colored sand grains were inserted in the sand. These vertical bars had a length of about 10 cm. Since the maximum cutting depth was 7 cm, the full cutting process was covered by these bars. Figure 12 shows the cutting process with the vertical bars and it shows how the bars are deformed by the cutting process.

Unfortunately the recorded video's of these cutting tests cannot be shown in this paper, but they are shown at the conference.

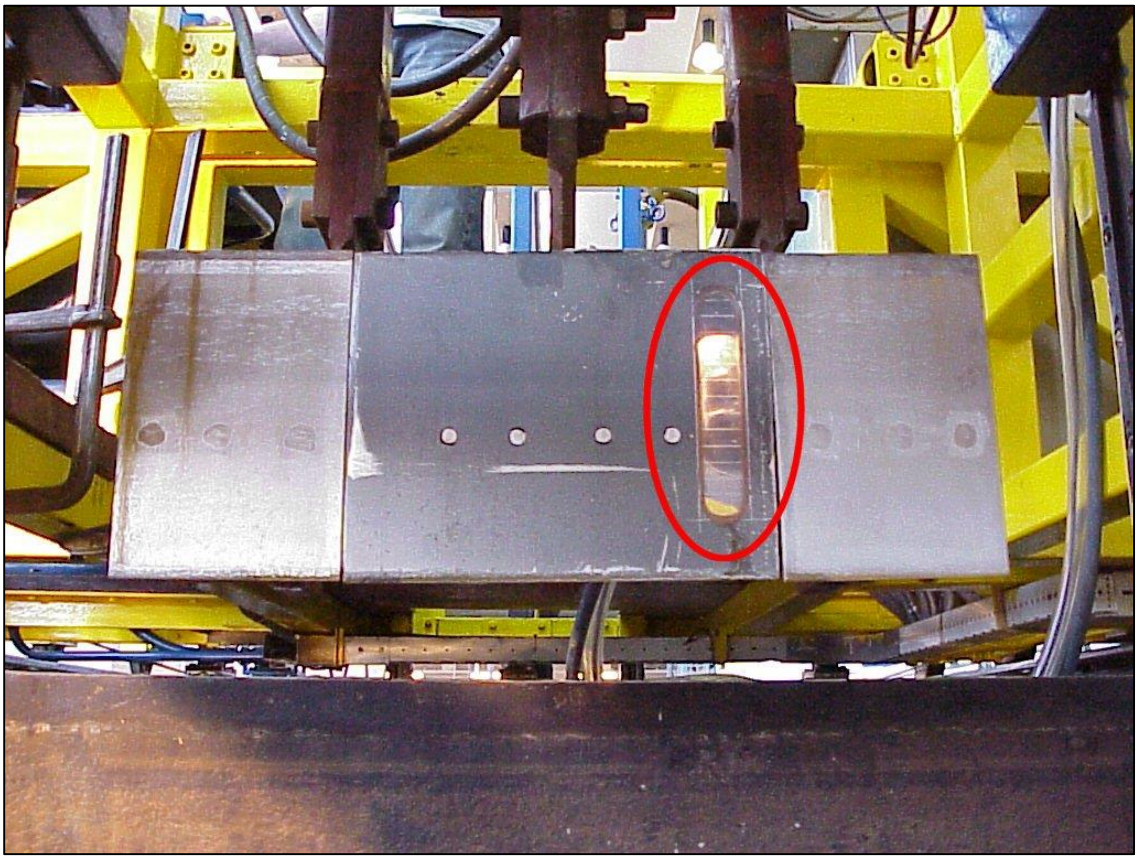

Figure 11-33: The perspex window in the blade.

Figure 11-34: View of the cutting process through the perspex window.

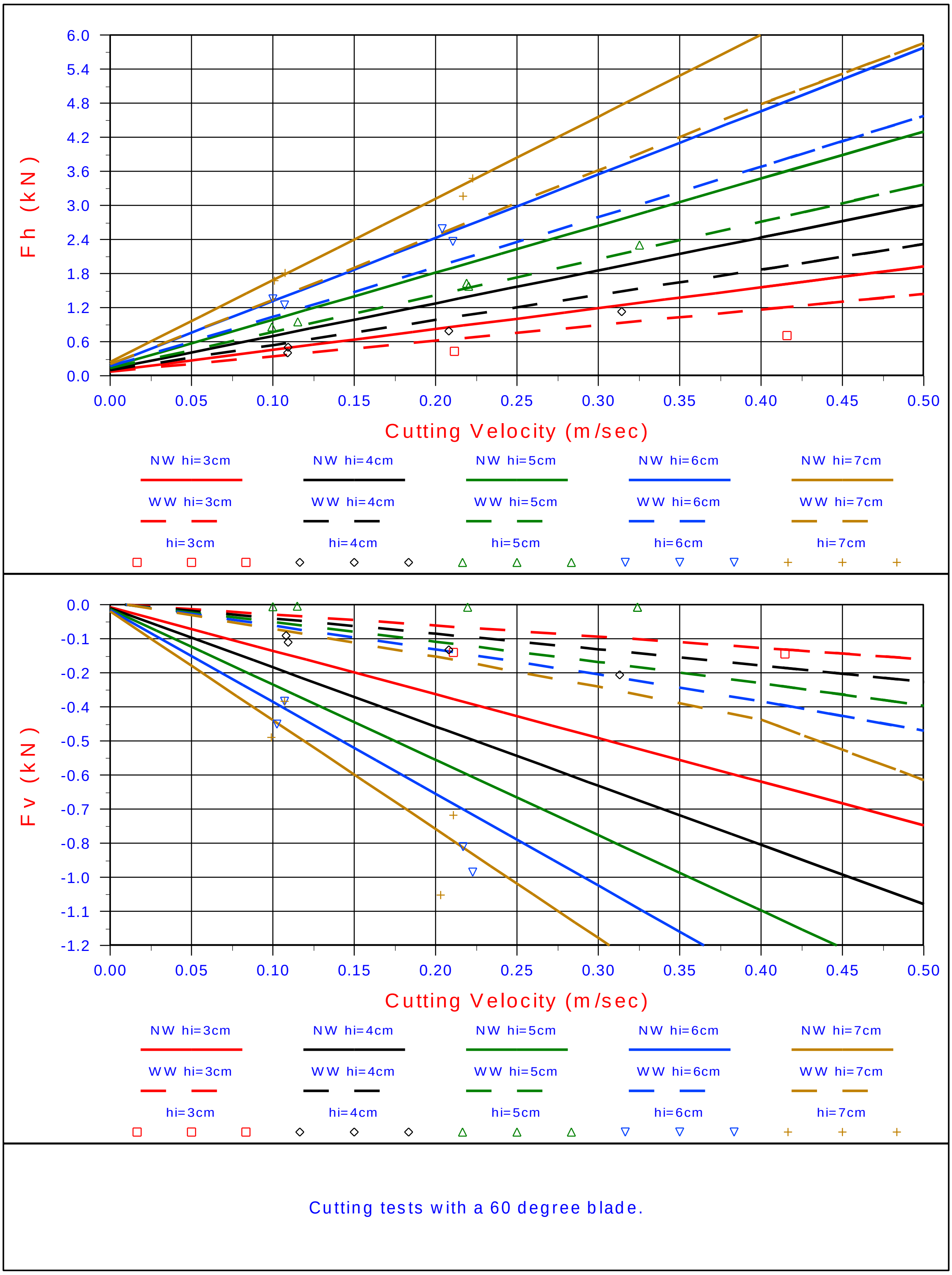

Figure 11-35: Cutting forces for cutting depths (h_i) from 3 to 7 cm; blade angle 60°.

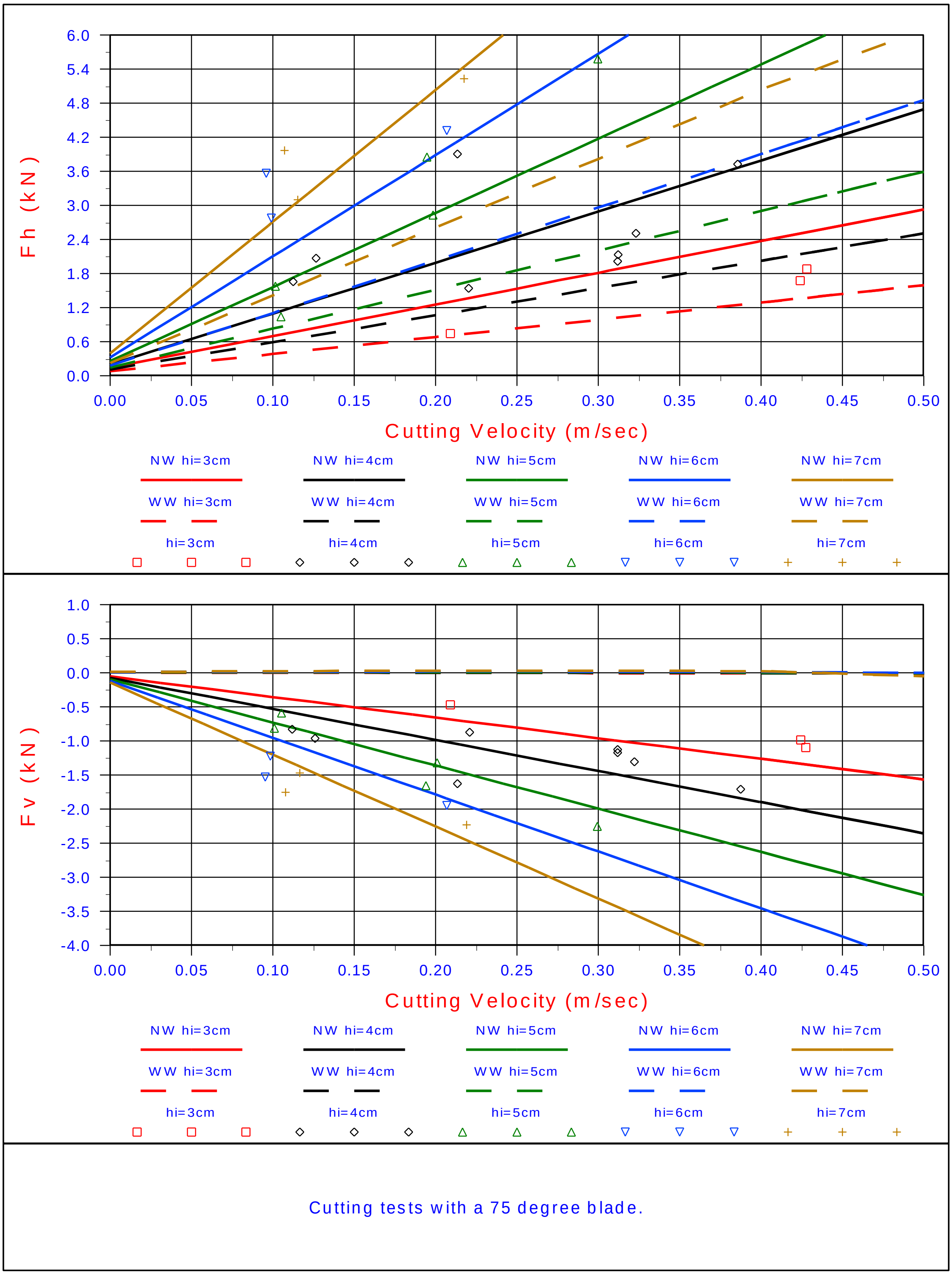

Figure 11-36: Cutting forces for cutting depths (h_i) from 3 to 7 cm; blade angle 75°.

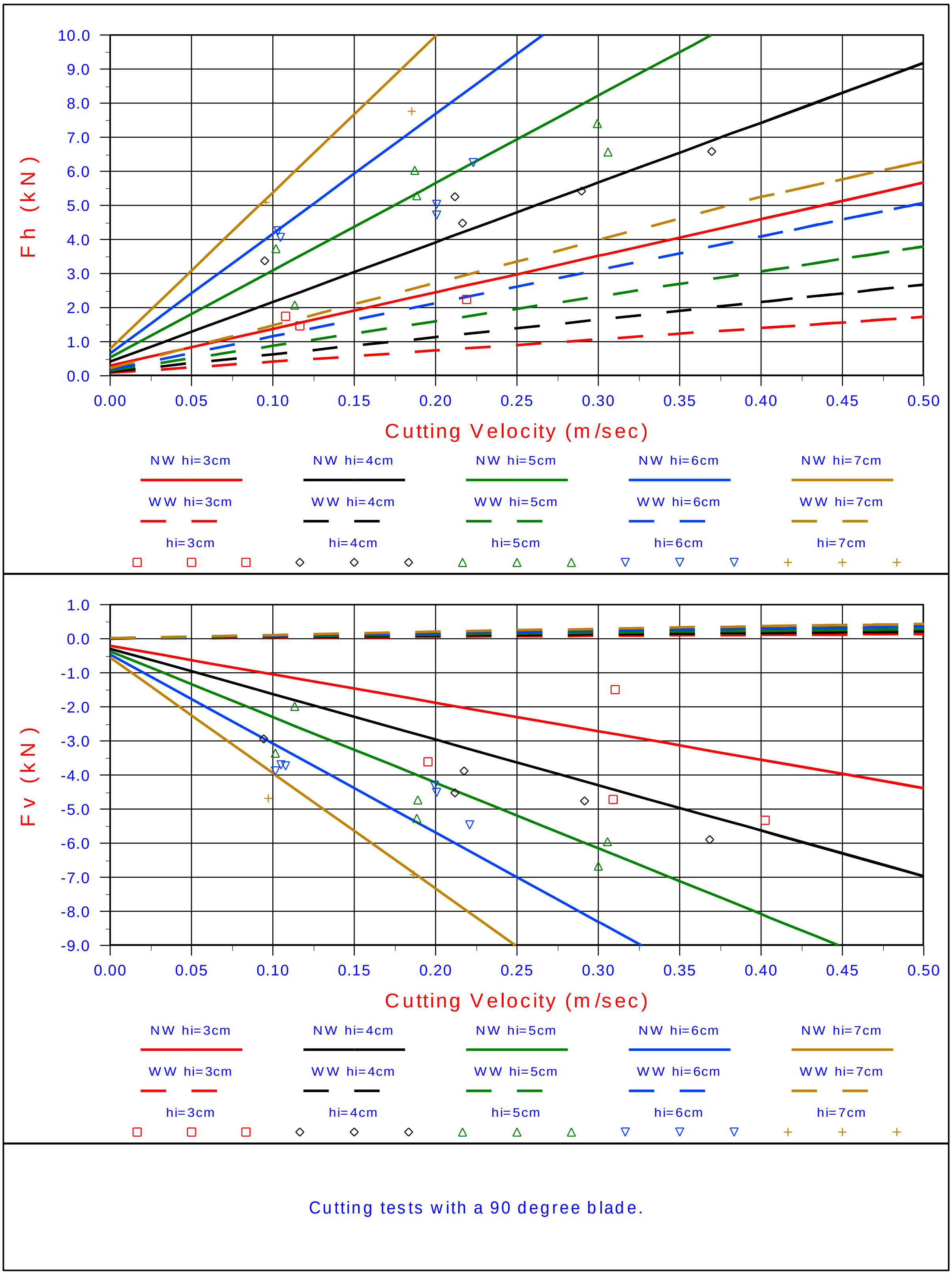

Figure 11-37: Cutting forces for cutting depths (h_i) from 3 to 7 cm; blade angle 90°.

11.9. The Dynamic Wedge

As discussed in the above paragraphs, the new research has led to the insight that the wedge in front of the blade is not static but dynamic. The aim of the new research was to get a good understanding of the mechanisms involved in the cutting at large cutting angles. To achieve this, vertical bars of about 10 cm deep with colored sand grains were inserted in the sand as is shown in Figure 11-38. When these bars are cut they will be deformed. If the wedge in front of the blade is a static wedge, meaning that the grains in the wedge have no velocity relative to the blade, then the colored grains from the bars will not enter the wedge. If however the colored grains enter the wedge, this means that the grains in the wedge move with respect to the blade. The research has shown that the colored grains have entered the wedge according to Figure 11-38. In the layer cut, the colored grains show a straight line, which is obvious, because of the velocity distribution in the layer cut. In fact the layer cut moves as a rigid body. In the wedge the colored grains show a curved line. Because of the velocity distribution in the wedge, the grains near the blade move much slower then the grains in the layer cut. Although Figure 11-38 shows a line between the layer cut and the wedge, in reality there does not exist a clear boundary between these two surfaces. The grains on both sides of the drawn boundary line will have (almost) the same velocity, resulting in an internal friction angle λ, which is not fully mobilized. The external friction angle on the blade however is fully mobilized. This contradicts the findings of Miedema et al. (2002A), from previous research. The value of this internal friction angle is between $\mathbf{0<\lambda<\varphi}$. Further research will have to show the value of $\boldsymbol{\lambda}$.

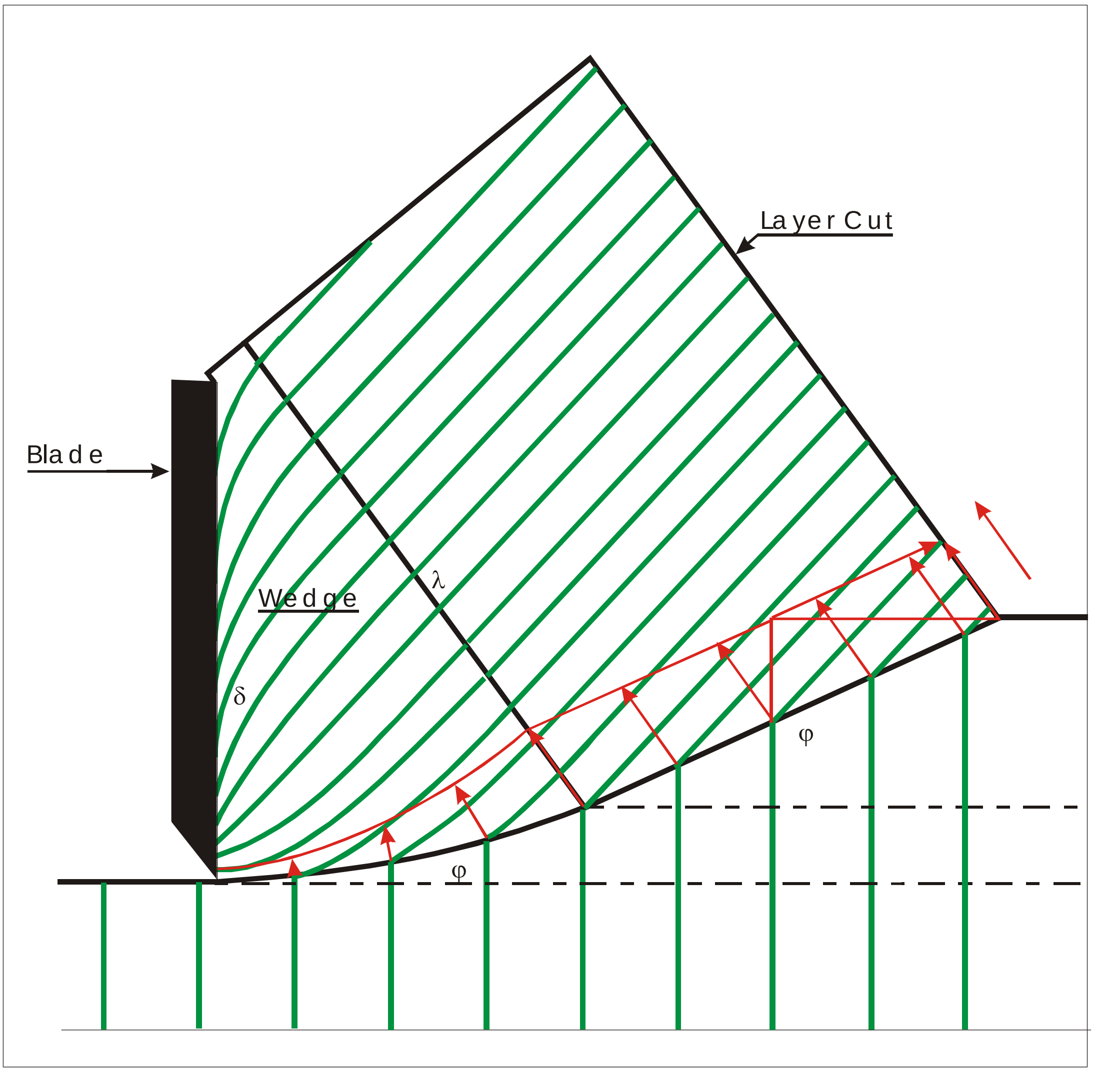

Figure 11-38: The dynamic wedge.

11.10. Nomenclature Chapter 11:

e_2, e_3, e_4	Acting point of cutting forces	-
F, F_h, F_v	Cutting force (general)	kN
g	Gravitation acceleration	m/s²
h_i	Initial layer thickness	m
h_b	Blade height	m
k_i	Initial permeability	m/s
k_{max}	Maximum permeability	m/s
$K_{1, 2, 3, 4}$	Grain force caused by grain stresses	kN
n_i	Initial pore percentage	%
n_{max}	Maximum pore percentage	%
$N_{1, 2, 3, 4}$	Normal force caused by grain stresses	kN
$p_{1m, 2m, 3m, 4m}$	Average pore pressure on a surface	-
$S_{1, 2, 3, 4}$	Force caused by shear stresses	kN
v_c	Cutting velocity perpendicular on the blade edge	m/s
w	Width of the blade of blade element	m
$W_{1, 2, 3, 4}$	Pore pressure forces	kN
z	Water depth	m
α	Blade angle	rad
β	Shear angle	rad
θ	Wedge angle	rad
ε	Volume strain	%
φ	Internal friction angle	rad
δ, δ_e	External friction angle, mobilized effective external friction angle	rad
ρ_w	Water density	ton/m³
λ	Angle of internal friction between wedge and layer cut	rad

Chapter 12: The Occurrence of a Wedge in Clay Cutting

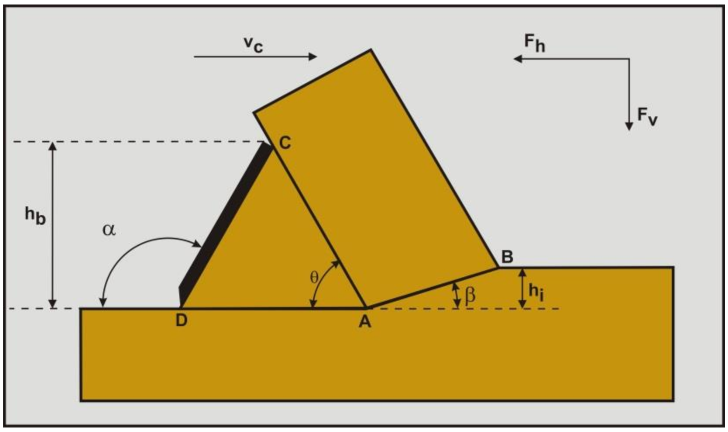

Figure 12-1: The occurrence of a wedge in clay cutting.

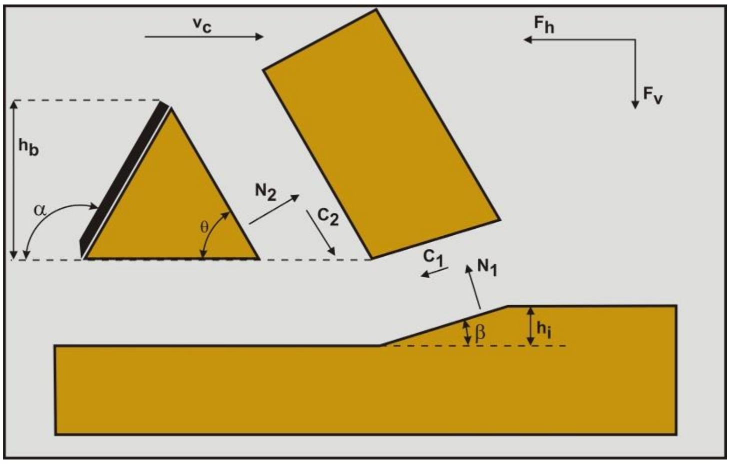

Figure 12-2: The forces on the layer cut in clay cutting with a wedge.

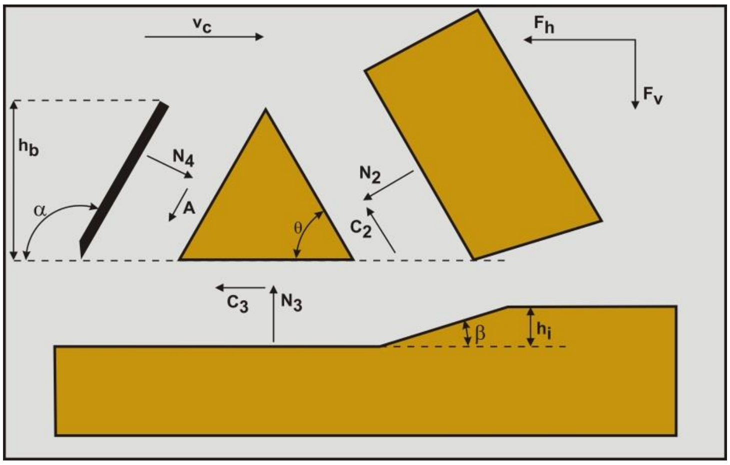

Figure 12-3: The forces on the wedge in clay cutting.

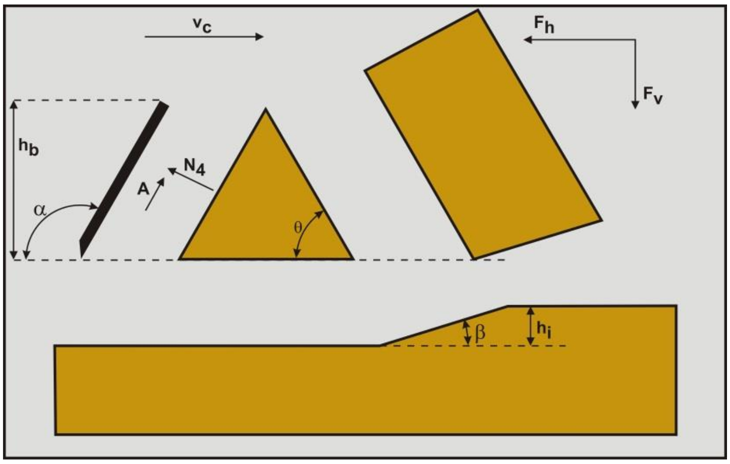

Figure 12-4: The forces on the blade when cutting clay with a wedge.

The horizontal equilibrium of forces on the wedge:

$$\sum F_h = N_4 \cdot \sin(\alpha) + A_m \cdot \cos(\alpha) - C_2 \cdot \cos(\theta) - N_2 \cdot \sin(\theta) - C_3 = 0 \tag{12-1}$$

The vertical equilibrium of forces on the wedge:

$$\sum F_v = N_4 \cdot \cos(\alpha) - A_m \cdot \sin(\alpha) - C_2 \cdot \sin(\theta) + N_2 \cdot \cos(\theta) - N_3 = 0 \tag{12-2}$$

To derive **N_4**:

$$\begin{aligned} & N_4 \cdot \sin(\alpha) \cdot \sin(\alpha) + A_m \cdot \cos(\alpha) \cdot \sin(\alpha) - C_2 \cdot \cos(\theta) \cdot \sin(\alpha) \\ & -N_2 \cdot \sin(\theta) \cdot \sin(\alpha) - C_3 \cdot \sin(\alpha) = 0 \end{aligned} \tag{12-3}$$

$$\begin{aligned} & N_4 \cdot \cos(\alpha) \cdot \cos(\alpha) - A_m \cdot \sin(\alpha) \cdot \cos(\alpha) - C_2 \cdot \sin(\theta) \cdot \cos(\alpha) \\ & +N_2 \cdot \cos(\theta) \cdot \cos(\alpha) - N_3 \cdot \cos(\alpha) = 0 \end{aligned} \tag{12-4}$$

$$N_4 = C_2 \cdot \sin(\alpha + \theta) - N_2 \cdot \cos(\alpha + \theta) + C_3 \cdot \sin(\alpha) + N_3 \cdot \cos(\alpha) \tag{12-5}$$

To derive **A_m**:

$$\begin{aligned} & N_4 \cdot \sin(\alpha) \cdot \cos(\alpha) + A_m \cdot \cos(\alpha) \cdot \cos(\alpha) - C_2 \cdot \cos(\theta) \cdot \cos(\alpha) \\ & -N_2 \cdot \sin(\theta) \cdot \cos(\alpha) - C_3 \cdot \cos(\alpha) = 0 \end{aligned} \tag{12-6}$$

$$\begin{aligned} & N_4 \cdot \cos(\alpha) \cdot \sin(\alpha) - A_m \cdot \sin(\alpha) \cdot \sin(\alpha) - C_2 \cdot \sin(\theta) \cdot \sin(\alpha) \\ & +N_2 \cdot \cos(\theta) \cdot \sin(\alpha) - N_3 \cdot \sin(\alpha) = 0 \end{aligned} \tag{12-7}$$

$$A_m = C_2 \cdot \cos(\alpha + \theta) + N_2 \cdot \sin(\alpha + \theta) + C_3 \cdot \cos(\alpha) - N_3 \cdot \sin(\alpha) \tag{12-8}$$

$$N_3 = N_4 \cdot \cos(\alpha) - A_m \cdot \sin(\alpha) - C_2 \cdot \sin(\theta) + N_2 \cdot \cos(\theta) \tag{12-9}$$

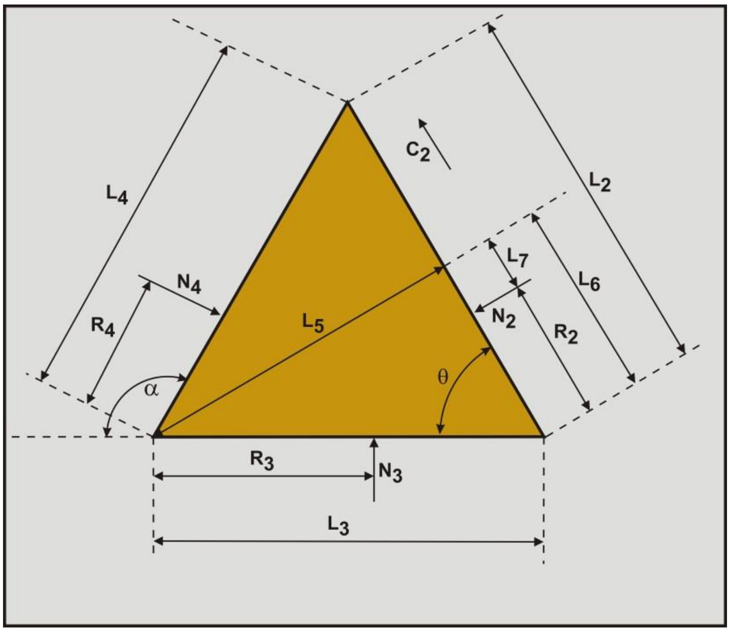

Figure 12-5: The equilibrium of moments on the wedge when cutting clay.

The equilibrium of moments:

$$\mathbf{L_1 = \frac{h_i}{\sin(\beta)}} \tag{12-10}$$

$$\mathbf{L_2 = \frac{h_b}{\sin(\theta)}} \tag{12-11}$$

$$\mathbf{L_3 = h_b \cdot \left(\frac{1}{\tan(\theta)} - \frac{1}{\tan(\alpha)}\right)} \tag{12-12}$$

$$\mathbf{L_4 = \frac{h_b}{\sin(\alpha)}} \tag{12-13}$$

$$\mathbf{L_5 = L_3 \cdot \sin(\theta)} \tag{12-14}$$

$$\mathbf{L_6 = L_3 \cdot \cos(\theta)} \tag{12-15}$$

$$\mathbf{L_7 = L_6 - R_2} \tag{12-16}$$

$$\mathbf{\sum M = \frac{N_4 \cdot L_4}{2} - \frac{N_3 \cdot L_3}{2} + N_2 \cdot L_7 - C_2 \cdot L_5 = 0} \tag{12-17}$$

If there is a static wedge, the normal force $\mathbf{N_3}$ has to be zero.

$$\mathbf{N_4 = C_2 \cdot \sin(\alpha+\theta) - N_2 \cdot \cos(\alpha+\theta) + C_3 \cdot \sin(\alpha)} \tag{12-18}$$

From the equilibrium of moments it follows that:

$$\mathbf{N_4 = \frac{2 \cdot (-N_2 \cdot L_7 + C_2 \cdot L_5)}{L_4}} \tag{12-19}$$

The mobilized adhesive force on the blade $\mathbf{A_m}$ has to be between the positive and negative maximum value.

$$\mathbf{A_m = C_2 \cdot \cos(\alpha + \theta) + N_2 \cdot \sin(\alpha + \theta) + C_3 \cdot \cos(\alpha)} \quad \textbf{(12-20)}$$

Chapter 13: The Occurrence of a Wedge in Atmospheric Rock Cutting

Chapter 14: The Occurrence of a Wedge in Hyperbaric Rock Cutting

Chapter 15: Nomenclature

15.1. Nomenclature Chapter 1:

a	Adhesion or external shear strength	kPa
c	Cohesion or internal shear strength	kPa
f	Function	-
F	Horizontal force	kN
g	Gravitational constant (9.81)	m/s^2
G	Gravitational vertical force	kN
h	Height of the dam/soil	m
K_a	Coefficient of active failure	-
K_p	Coefficient of passive failure	-
N	Force normal to the shear plane	kN
S	Shear force on the shear plane	kN
α	Orientation of shear plane (Mohr circle)	rad
β	Angle of the shear plane (active & passive failure)	rad
δ	External friction angle	rad
φ	Internal friction angle	rad
σ	Normal stress	kPa
σ_h	Horizontal normal stress (principal stress)	kPa
σ_v	Vertical normal stress (principal stress)	kPa
τ	Shear stress	kPa
ρ_g	Density of the soil	ton/m^3

15.2. Nomenclature Chapter 2:

a_1, a_2	Coefficients for weighted permeability	-
a, τ_a	Adhesion or external shear strength	kPa
A	Adhesive force on the blade	kN
c, τ_c	Cohesion or internal shear strength	kPa
C, C_1	Force due to cohesion in the shear plane	kN
C_2	Force due to cohesion on the front of the wedge	kN
C_3	Force due to cohesion at the bottom of the wedge	kN
F_h	Horizontal cutting force	kN
F_{f1}	Friction force on the shear surface	kN
F_{f2}	Friction force on the blade	kN
F_{n1}	Normal force on the shear surface	kN
F_{n2}	Normal force on the blade	kN
F_v	Vertical cutting force	kN
F_{d1}	Deviation force on the shear surface	kN
$F_{d,\,d2}$	Deviation force on the blade	kN
$F_{x1,\,2}$	Cutting force in x-direction	kN
$F_{y1,\,2}$	Cutting force in y-direction	kN
$F_{z1,\,2}$	Cutting force in z-direction	kN
g	Gravitational constant (9.81)	m/s^2
G, G_1	Gravitational force on the layer cut	kN
G_2	Gravitational force on the wedge	kN
h_i	Initial thickness of layer cut	m
h_b	Height of blade	m
h'_b	Effective height of the blade in case **Curling Type**	m
I	Inertial force on the shear plane	kN
k_i	Initial permeability	m/s
k_{max}	Maximum permeability	m/s
k_m	Average permeability	m/s
K_1	Grain force on the shear plane	kN

K_2	Grain force on the blade or the front of the wedge	kN
K_3	Grain force on the bottom of the wedge	kN
K_4	Grain force on the blade (in case a wedge exists)	kN
n_i	Initial porosity	%
n_{max}	Maximum porosity	%
N_1	Normal force on the shear plane	kN
N_2	Normal force on the blade or the front of the wedge	kN
N_3	Normal force on the bottom of the wedge	kN
N_4	Normal force on the blade (in case a wedge exists)	kN
p_{1m}	Average pore pressure on the shear surface	kPa
p_{2m}	Average pore pressure on the blade	kPa
P_c	Cutting power	kW
R_1	Acting point of resulting forces on the shear plane	m
R_2	Acting point of resulting forces on the blade	m
R_3	Acting point of resulting forces on the bottom of the wedge	m
R_4	Acting point of resulting forces on the blade (in case a wedge exists)	m
S_1	Shear force due to friction on the shear plane	kN
S_2	Shear force due to friction on the blade or the front of the wedge	kN
S_3	Shear force due to friction at the bottom of the wedge	kN
S_4	Shear force due to friction on the blade (in case a wedge exists)	kN
v_c	Cutting velocity component perpendicular to the blade	m/s
v_d	Cutting velocity, drag velocity	m/s
v_{r1}	Velocity of grains in the shear surface	m/s
v_{r2}	Relative velocity of grains on the blade	m/s
v_{d1}	Deviation velocity of grains in the shear surface	m/s
v_{d2}	Deviation velocity of grains on the blade	m/s
$v_{x1,2}$	Velocity of grains in the x-direction	m/s
$v_{y1,2}$	Velocity of grains in the y-direction	m/s
$v_{z1,2}$	Velocity of grains in the z-direction	m/s
w	Width of blade	m
W_1	Force resulting from pore underpressure on the shear plane	kN
W_2	Force resulting from pore underpressure on the blade or on the front of the wedge	kN
W_3	Force resulting from pore underpressure on the bottom of the wedge	kN
W_4	Force resulting from pore underpressures on the blade (in case a wedge exists)	
z	Water depth	m
α	Cutting angle blade	rad
β	Shear angle	rad
ε	Dilatation	-
ϕ	Angle of internal friction	rad
ϕ_e	Angle of internal friction perpendicular to the cutting edge	rad
λ	Angle of internal friction on the front of the wedge	rad
λ_1	Acting point factor for resulting forces on the shear plane	-
λ_2	Acting point factor for resulting forces on the blade or front of wedge	-
λ_3	Acting point factor for resulting forces on the bottom of the wedge	-
λ_4	Acting point factor for resulting forces on the blade	-
δ	External friction angle	rad
δ_e	External friction angle perpendicular to the cutting edge	rad
ι	Deviation angle blade	rad
ρ_g	Density of the soil	ton/m³
ρ_w	Density water	ton/m³
θ	Wedge angle	rad

15.3. Nomenclature Chapter 3:

a	Adhesion or external shear strength	kPa
c	Cohesion or internal shear strength	kPa
h_i	Thickness of the layer cut	m
h_b	Height of the blade	m
α	Blade angle	rad
φ	Angle of internal friction	rad

15.4. Nomenclature Chapter 4:

F_h	Horizontal cutting force	kN
F_v	Vertical cutting force	kN
g	Gravitational constant (9.81)	m/s^2
G	Gravitational force on the layer cut	kN
h_i	Initial thickness of layer cut	m
h_b	Height of blade	m
I	Inertial force on the shear plane	kN
K_1	Grain force on the shear plane	kN
K_2	Grain force on the blade or the front of the wedge	kN
N_1	Normal force on the shear plane	kN
N_2	Normal force on the blade or the front of the wedge	kN
Pc	Cutting power	kW
S_1	Shear force due to friction on the shear plane	kN
S_2	Shear force due to friction on the blade or the front of the wedge	kN
v_c	Cutting velocity component perpendicular to the blade	m/s
w	Width of blade	m
W_1	Force resulting from pore underpressure on the shear plane	kN
W_2	Force resulting from pore underpressure on the blade or on the front of the wedge	kN
α	Cutting angle blade	rad
β	Shear angle	rad
ϕ	Angle of internal friction	rad
δ	External friction angle	rad
ρ_g	Density of the soil	ton/m^3
ρ_w	Density water	ton/m^3

15.5. Nomenclature Chapter 5:

a_1, a_2	Weight factors k-value (permeability)	-
A	Surface	m^2
b_{pr}	Projected width of the blade perpendicular to the velocity direction	m
c_i , c_1 , c_2	Coefficients (non-cavitating cutting process)	-
c_r	Coefficient side effects	-
c_s	Wear coefficient	-
c_t	Coefficient total cutting force (non-cavitating cutting process)	-
c_{ts}	Coefficient total cutting force including wear effects	-
c_{tr}	Coefficient total cutting force including side effects	-
d_i , d_1 , d_2	Coefficients (cavitating cutting process)	-
d_r	Coefficient side effects	-
d_s	Wear coefficient	-
d_t	Coefficient total cutting force (cavitating cutting process)	-
d_{ts}	Coefficient total cutting force including wear	-
d_{tr}	Coefficient total cutting force including side effects	-
E_{sp}	Specific cutting energy	kN/m^2

E_{gc}	Specific cutting energy (no cavitation)	kN/m²
E_{ca}	Specific cutting energy (full cavitation)	kN/m²
F_{ci}	Cutting force (general)	kN
F_{cit}	Total cutting force (general)	kN
F_h	Horizontal cutting force (parallel to the cutting speed)	kN
F_l	Cutting force parallel to the edge of the blade	kN
F_n	Normal force	kN
F_v	Vertical cutting force (perpendicular to the cutting velocity)	kN
F_w	Friction force	kN
F_x	Cutting force in x-direction (longitudinal)	kN
F_{xt}	Total cutting force in x-direction (longitudinal)	kN
F_y	Cutting force in y-direction (transversal)	kN
F_{yt}	Total cutting force in y-direction (transversal)	kN
F_z	Cutting force in z-direction (vertical)	kN
g	Gravitational acceleration	m/s²
h_i	Initial layer thickness	m
h_b	Blade height	m
k	Permeability	m/s
k_i	Initial permeability	m/s
k_{max}	Maximum permeability	m/s
k_m	Effective permeability	m/s
K_1	Grain force on the shear zone	kN
K_2	Grain force on the blade	kN
l	Length of the shear zone	m
n	Normal on an edge	m
n	Porosity	-
n_i	Initial pore percentage	%
n_{max}	Maximum pore percentage	%
N_1	Normal force on the shear zone	kN
N_2	Normal force on the blade	kN
p	Number of blades excavating element	-
p	Pressure (water pressure)	kPa
p_{atm}	Atmosferic pressure	kPa
P_{calc}	Calculated dimensionless pressure (water pore pressure)	-
p_{damp}	Saturated water pore pressure (12 cm w.k.)	kPa
P_{real}	Real pore pressure (water pore pressure)	kPa
p_{1m}	Average pore pressure in the shear zone	-
p_{2m}	Average pore pressure on the blade	-
P_c	Drive power excavating element	kW
q, q_1, q_2	Specific flow	m/s
Q	Flow per unit of blade width	m²/s
s	Length of a stream line	m
s	Measure for the layer thickness	m
S_1	Shear force on the shear zone	kN
S_2	Shear force on the blade	kN
v_c	Cutting velocity perpendicular to the edge of the blade	m/s
V	Volume strain per unit of blade width	m²
w	Width of blade of blade element	m
W_1	Pore pressure force on the shear zone	kN
W_2	Pore pressure force on the blade	kN
x	Coordinate	m
y	Coordinate	m
z	Coordinate	m
z	Water depth	m

α	Blade angle	rad
β	Shear angle	rad
ε	Volume strain	-
φ	Angle of internal friction	rad
δ	Soil/steel interface friction angle	rad
ρ_g	Wet density of the sand	ton/m³
ρ_s	Dry density of the sand	ton/m³
ρ_w	Density of water	ton/m³
θ_r	Angular displacement force vector as a result of side effects	rad
θ_s	Angular displacement force vector as a result of wear	rad
θ_t	Angle force vector angle in relation to cutting velocity vector	rad
θ_{ts}	Angle force vector angle in relation to velocity vector including wear	rad
θ_{tr}	Angle force vector angle in relation to velocity vector including side effects	rad
Θ_r	Angular displacement force vector as a result of side effects	rad
Θ_s	Angular displacement force vector as a result of wear	rad
Θ_t	Angle force vector angle in relation to cutting velocity vector	rad
Θ_{ts}	Angle force vector angle in relation to velocity vector including wear	rad
Θ_{tr}	Angle force vector angle in relation to velocity vector including side effects	rad

15.6. Nomenclature Chapter 6:

A	Adhesive force on the blade	kN
B	Frequency (material property)	1/s
C	Cohesive force on shear plane	kN
E	Energy level	J/kmol
E_a	Activation energy level	J/kmol
E_l	Limiting (maximum) energy level	J/kmol
f	Shear force on flow unit	N
F	Cutting force	kN
G	Gravitational force	kN
h	Planck constant ($6.626 \cdot 10^{-34}$ J·s)	J·s
k	Boltzman constant ($1.3807 \cdot 10^{-23}$ J/K)	J/K
K_1	Grain force on the shear plane	kN
K_2	Grain force on the blade	kN
i	Coefficient	-
I	Inertial force on the shear plane	kN
N	Avogadro constant ($6.02 \cdot 10^{26}$ 1/kmol)	-
N_1	Normal grain force on shear plane	kN
N_2	Normal grain force on blade	kN
p	Probability	-
R	Universal gas constant (8314 J/kmol/K)	J/kmol/K
S	Number of bonds per unit area	1/m²
S_1	Shear force due to internal friction on the shear surface	kN
S_2	Shear force due to soil/steel friction on the blade	kN
T	Absolute temperature	K
T	Tensile force	kN
v	Cutting velocity	m/s
W_1	Force resulting from pore under pressure on the shear plane	kN
W_2	Force resulting from pore under pressure on the blade	kN
X	Function	-
α	Blade angle	rad
β	Angle of the shear plane with the direction of cutting velocity	rad
ν	frequency of activation	1/s
λ	Distance between equilibrium positions	m

$d\varepsilon/dt$	Strain rate	1/s
$d\varepsilon_0/dt$	Frequency (material property)	1/s
τ	Shear stress	kPa
τ_a	Adhesive shear strength (strain rate dependent)	kPa
τ_c	Cohesive shear strength (strain rate dependent)	kPa
τ_y	Shear strength (yield stress, material property)	kPa
τ_{ya}	Adhesive shear strength (material property)	kPa
τ_{yc}	Cohesive shear strength (material property)	kPa
τ_0	Dynamical shearing resistance factor (material property)	kPa
σ_e	Effective stress	kPa
σ_n	Normal stress	kPa
σ_t	Tensile strength	kPa
ϕ	Angle of internal friction	rad
δ	Soil/steel friction angle	rad

15.7. Nomenclature Chapter 7:

a, τ_a	Adhesive shear strength	kPa
A	Adhesive force on the blade	kN
c, τ_c	Cohesive shear strength	kPa
c'	Pseudo cohesive shear strength	kPa
C	Cohesive force on shear plane	kN
E_{sp}	Specific energy	kPa
F	Force	kN
F_h	Horizontal cutting force	kN
F_v	Vertical cutting force	kN
g	Gavitational constant (9.81)	m/s^2
G	Gravitational force	kN
h_i	Initial thickness of layer cut	m
h_b	Height of the blade	m
h'_b	Contact height of the blade in case **Curling Type**	m
K_1	Grain force on the shear plane	kN
K_2	Grain force on the blade	kN
I	Inertial force on the shear plane	kN
N_1	Normal grain force on shear plane	kN
N_2	Normal grain force on blade	kN
P_c	Cutting power	kW
Q	Production	m^3
r	Adhesion/cohesion ratio	-
r_1	Pore pressure on shear plane/cohesion ratio	-
r_2	Pore pressure on blade/cohesion ratio	-
R	Radius of Mohr circle	kPa
R_1	Acting point on the shear plane	m
R_2	Acting point on the blade	m
S_1	Shear force due to internal friction on the shear plane	kN
S_2	Shear force due to external friction on the blade	kN
T	Tensile force	kN
UCS	Unconfined Compressive Stress	kPa
v_c	Cutting velocity	m/s
w	Width of the blade	m
W_1	Force resulting from pore under pressure on the shear plane	kN
W_2	Force resulting from pore under pressure on the blade	kN
α	Blade angle	rad

β	Angle of the shear plane with the direction of cutting velocity	rad
τ	Shear stress	kPa
τ_a, a	Adhesive shear strength (strain rate dependent)	kPa
τ_c, c	Cohesive shear strength (strain rate dependent)	kPa
τ_{S1}	Average shear stress on the shear plane	kPa
τ_{S2}	Average shear stress on the blade	kPa
σ	Normal stress	kPa
σ_C	Center of Mohr circle	kPa
σ_T	Tensile strength	kPa
σ_{min}	Minimum principal stress in Mohr circle	kPa
σ_{N1}	Average normal stress on the shear plane	kPa
σ_{N2}	Average normal stress on the blade	kPa
φ	Angle of internal friction	rad
δ	Angle of external friction	rad
λ	Strengthening factor	-
λ_1	Acting point factor on the shear plane	-
λ_2	Acting point factor on the blade	-
λ_{HF}	Ductile horizontal force coefficient	-
λ_{VF}	Ductile vertical force coefficient	-
λ_{HT}	Brittle horizontal force coefficient	-
λ_{VT}	Brittle vertical force coefficient	-

15.8. Nomenclature Chapter 8:

a, τ_a	Adhesive shear strength	kPa
A	Adhesive force on the blade	kN
c, τ_c	Cohesive shear strength	kPa
c'	Pseudo cohesive shear strength	kPa
C	Cohesive force on shear plane	kN
E_{sp}	Specific energy	kPa
F	Force	kN
F_h	Horizontal cutting force	kN
F_v	Vertical cutting force	kN
g	Gavitational constant (9.81)	m/s^2
G	Gravitational force	kN
h_i	Initial thickness of layer cut	m
h_b	Height of the blade	m
h'_b	Contact height of the blade in case **Curling Type**	m
K_1	Grain force on the shear plane	kN
K_2	Grain force on the blade	kN
I	Inertial force on the shear plane	kN
N_1	Normal grain force on shear plane	kN
N_2	Normal grain force on blade	kN
P_c	Cutting power	kW
Q	Production	m^3
r	Adhesion/cohesion ratio	-
r_1	Pore pressure on shear plane/cohesion ratio	-
r_2	Pore pressure on blade/cohesion ratio	-
R	Radius of Mohr circle	kPa
R_1	Acting point on the shear plane	m
R_2	Acting point on the blade	m
S_1	Shear force due to internal friction on the shear plane	kN
S_2	Shear force due to external friction on the blade	kN

T	Tensile force	kN
UCS	Unconfined Compressive Stress	kPa
v_c	Cutting velocity	m/s
w	Width of the blade	m
W_1	Force resulting from pore under pressure on the shear plane	kN
W_2	Force resulting from pore under pressure on the blade	kN
α	Blade angle	rad
β	Angle of the shear plane with the direction of cutting velocity	rad
τ	Shear stress	kPa
τ_a, a	Adhesive shear strength (strain rate dependent)	kPa
τ_c, c	Cohesive shear strength (strain rate dependent)	kPa
τ_{S1}	Average shear stress on the shear plane	kPa
τ_{S2}	Average shear stress on the blade	kPa
σ	Normal stress	kPa
σ_C	Center of Mohr circle	kPa
σ_T	Tensile strength	kPa
σ_{min}	Minimum principal stress in Mohr circle	kPa
σ_{N1}	Average normal stress on the shear plane	kPa
σ_{N2}	Average normal stress on the blade	kPa
φ	Angle of internal friction	rad
δ	Angle of external friction	rad
λ	Strengthening factor	-
λ_1	Acting point factor on the shear plane	-
λ_2	Acting point factor on the blade	-
λ_{HF}	Ductile horizontal force coefficient	-
λ_{VF}	Ductile vertical force coefficient	-
λ_{HT}	Brittle horizontal force coefficient	-
λ_{VT}	Brittle vertical force coefficient	-

15.9. Nomenclature Chapter 11:

e_2, e_3, e_4	Acting point of cutting forces	-
F, F_h, F_v	Cutting force (general)	kN
g	Gravitation acceleration	m/s²
h_i	Initial layer thickness	m
h_b	Blade height	m
k_i	Initial permeability	m/s
k_{max}	Maximum permeability	m/s
$K_{1, 2, 3, 4}$	Grain force caused by grain stresses	kN
n_i	Initial pore percentage	%
n_{max}	Maximum pore percentage	%
$N_{1, 2, 3, 4}$	Normal force caused by grain stresses	kN
$p_{1m, 2m, 3m, 4m}$	Average pore pressure on a surface	-
$S_{1, 2, 3, 4}$	Force caused by shear stresses	kN
v_c	Cutting velocity perpendicular on the blade edge	m/s
w	Width of the blade of blade element	m
$W_{1, 2, 3, 4}$	Pore pressure forces	kN
z	Water depth	m
α	Blade angle	rad
β	Shear angle	rad
θ	Wedge angle	rad
ε	Volume strain	%
φ	Internal friction angle	rad
δ, δ_e	External friction angle, mobilized effective external friction angle	rad

ρ_w	Water density	ton/m³
λ	Angle of internal friction between wedge and layer cut	rad

Chapter 16: Bibliography

Becker, S., Miedema, S., Jong, P., & Wittekoek, S. (1992). On the Closing Process of Clamshell Dredges in Water Saturated Sand. *WODCON XIII* (p. 22 pages). Bombay, India: WODA.

Becker, S., Miedema, S., Jong, P., & Wittekoek, S. (1992, September). The Closing Process of Clamshell Dredges in Water Saturated Sand. *Terra et Aqua, No. 49* , pp. 22 pages.

Biot, M. (1941). General theory of three dimensional consolidation. *Journal of Applied Physics, vol. 12.* , pp. 155-164.

Bishop, A. (1966). The strength of soils as engineering materials. *Geotechnique, vol. 16, no. 2.* , pp. 91-128.

Brakel, J. (1981). *Mathematisch model voor de krachten op een roterende snijkop van een in zeegang werkende snijkopzuiger.* Delft, Netherlands: Delft University of Technology - ScO/80/96.

Butterfield, R., & Andrawes, K. (1972). On the angles of friction between sand and plane surfaces. *Journal of Terramechanics, vol. 8, no. 4.* , pp. 15-23.

Carman, P. (1937). Fluid flow through granular beds. *Transactions Institute Chemical Engineering, 15, 150.*

Carman, P. (1956). *Flow of gases through porous media.* London: Butterworths Scientific Publications.

Coulomb, C. (1776). Essai sur une application des regles des maximis et minimis a quelques problemes de statique relatifs a l'architecture. *Academie royale des sciences, Paris, Memoires de mathematique et de physique, vol. 7.* , pp. 343-382.

Detournay, E., & Atkinson, C. (2000). Influence of pore pressure on the drilling response in low permeability shear dilatant rocks. *International Journal of Rock Mechanics & Mining Sciences, vol. 37.* , pp. 1091-1101.

Evans, I. (1964). The force required to cut coal with blunt wedges. *Mining Research Establishment Isleworth* .

Evans, I., & Pomeroy, C. (1966). *The strength, fracture and workability of coal.* Pergamon Press.

Fairhurst, C. (1964). On the validity of the Brazilian test for brittle materials. *International Journal of Rock Mechanics & Mining Sciences, vol. 1.* , pp. 535-546.

Glasstone, S., Laidler, K., & Eyring, H. (1941). *The theory of rate processes.* New York: McGraw Hill.

Hansen, B. (1958). Line ruptures regarded as narrow rupture zones. *Earth Pressure Problems*, (pp. 39-48). Brussels.

Hatamura, Y., & Chijiiwa, K. (1975). Analyses of the mechanism of soil cutting, 1st report. *Bulletin of JSME, vol. 18, no. 120* , pp. 619-626.

Hatamura, Y., & Chijiiwa, K. (1976). Analyses of the mechanism of soil cutting, 2nd report. *Bulletin of the JSME, vol. 19, no. 131.* , pp. 555-563.

Hatamura, Y., & Chijiiwa, K. (1976). Analyses of the mechanism of soil cutting, 3rd report. *Bulletin of the JSME, vol. 19, no. 139.* , pp. 1376-1384.

Hatamura, Y., & Chijiiwa, K. (1977). Analyses of the mechanism of soil cutting, 4th report. *Bulletin of the JSME, vol. 20, no. 139.* , pp. 130-137.

Hatamura, Y., & Chijiiwa, K. (1977). Analyses of the mechanism of soil cutting, 5th report. *Bulletin of the JSME, vol. 20, no. 141.* , pp. 388-395.

Hazen, A. (1982). Some physical properties of sands and gravels with special reference to their use in filtration. *24th Annual Report, Massachusetts State Board of Health, Pub. Doc. No. 34.* , pp. 539-556.

He, J., & Vlasblom, W. (1998). Modelling of saturated sand cutting with large rake angles. *WODCON XV.* Las Vegas, USA: WODA.

He, J., Miedema, S., & Vlasblom, W. (2005). FEM Analyses Of Cutting Of Anisotropic Densely Compacted and Saturated Sand. *WEDAXXV/TAMU37.* New Orleans, Louisiana, USA: WEDA/TAMU.

Hettiaratchi, D. (1967A). The mechanics of soil cultivation. *AES, no. 3/245/C/28.*

Hettiaratchi, D., & Reece, A. (1967B). Symmetrical three-dimensional soil failure. *Journal of Terramechanics 4 (3).* , pp. 45-67.

Hettiaratchi, D., & Reece, A. (1974). The calculation of passive soil rtesistance. *Geotechnique 24, no. 3.* , pp. 289-310.

Hettiaratchi, D., & Reece, A. (1975). Boundary wedges in two dimensional passive soil failure. *Geotechnique 25, no. 2.* , pp. 197-220.

Hettiaratchi, D., Witney, B., & Reece, A. (1966). The calculation of passive pressure in two dimensional soil failure. *Journal of Agriculture Engineering Resources 11 (2)* , pp. 89-107.

Joanknecht, L. (1973). *Mechanisch graaf onderzoek onder water.* Delft, Netherlands: Delft University of Technology.

Joanknecht, L. (1974). *Cutting forces in submerged soils.* Delft, Netherlands: Delft University of Technology.

Josselin de Jong, G. (1976). Rowe's stress dilatancy relation based on friction. *Geotechnique 26, no. 3* , pp. 527-534.

Kaitkay, P., & Lei, S. (2005). Experimental study of rock cutting under external hydrostatic pressure. *Journal of Materials Processing Technology, vol. 159.* , pp. 206-213.

Kelessidis, V., & Maglione, R. (2008). Yield stress of water bentonite dispersions. *Colloids and Surfaces A: Physicochemical Engineering Aspects 318.* , pp. 217-226.

Kelessidis, V., Tsamantaki, C., & Dalamarinis, P. (2007). Effect of pH and electrolyte on the rheology of aqueous Wyoming bentonite dispersions. *Applied Clay Science 38.* , pp. 86-96.

Koning, J. d., Miedema, S., & Zwartbol, A. (1983). Soil/Cutterhead Interaction under Wave Conditions. *WODCON X.* Singapore: WODA.

Kozeny, J. (1927). *Uber kapillare leitung des wassers in boden.* Wien: Sitzungsber. Akad. Wiss. Wien, Math. Naturwiss. Kl. Abt. 2a, 136, 271-306.

Lambe, T., & Whitman, R. (1979). *Soil mechanics, SI version.* New York: John Wiley & Sons.

Leussen, W. v., & Os, A. v. (1987 December). Basic research on cutting forces in saturated sand. *Journal of Geotechnical Engineering, vol. 113, no. 12.* , pp. 1501-1516.

Leussen, W., & Nieuwenhuis, J. (1984). Soil mechanics aspects of dredging. *Geotechnique 34, no. 3.* , pp. 359-381.

Lobanov, V., & Joanknecht, L. (1980). The cutting of soil under hydrostatic pressure. *WODCON IX.* Vancouver, Canada: WODA.

Ma, Y. (2001). *Mathematical model analysis for the saturated sand cutting with large cutting angles in the non-vavitation situation.* Delft, Netherlands: Delft University of Technology, Report: 2001.BT.5581.

Ma, Y., Ni, F., & Miedema, S. (2006A). Calculation of the Blade Cutting Force for small Cutting Angles based on MATLAB. *The 2nd China Dredging Association International Conference & Exhibition, themed Dredging and Sustainable Development.* Guangzhou, China: CHIDA.

Ma, Y., Ni, F., & Miedema, S. (2006B). Mechanical Model of Water Saturated Sand Cutting at Blade Large Cutting Angles. *Journal of Hohai University, ISSN 1009-1130, CN 32-1591* .

Meijer, K. (1981). *Berekening van spanningen en deformaties in verzadigde grond.* Delft, Netherlands: Delft Hydraulics Laboratory, Report R914 part 1.

Meijer, K. (1985). *Computation of stresses and strains in saturated soil, PhD Thesis.* Delft, Netherlands: Delft University of Technology.

Meijer, K., & Os, A. (1976). Pore pressures near a moving under water slope. *Geotechnical Engineering Division ASCE 102, no. GT4.* , pp. 361-372.

Merchant, M. (1944). Basic mechanics of the metal cutting process. *Journal of Applied Mechanics, vol. 11A.* , pp. 168-175.

Merchant, M. (1945A). Mechanics of metal cutting process, orthogonal cutting and a type 2 chip. *Journal of Applied Physics, vol. 16, no. 5.* , pp. 267-275.

Merchant, M. (1945B). Mechanics of metal cutting, plasticity conditions in orthogonal cutting. *Journal of Applied Physics, vol. 16, no. 6.* , pp. 318-324.

Miedema, S. (1981). *The soil reaction forces on a crown cutterhead on a swell compensated ladder.* Delft, The Netherlands: Delft University of Technology.

Miedema, S. (1982). The Interaction between Cutterhead and Soil at Sea. *Dredging Day November 19th* (p. 25 pages in Dutch). Delft, The Netherlands: Delft University of Technology.

Miedema, S. (1982). *The mathematical modeling of the soil reaction forces on a cutterhead and the development of the computer program DREDMO.* Delft, The Netherlands: Delft University of Technology.

Miedema, S. (1984A). *Mathematical Modeling of a Seagoing Cutter Suction Dredge*. Delft, The Netherlands: Delft University of Technology/KIVI.

Miedema, S. (1984B, October). The Cutting of Densely Compacted Sand under Water. *Terra et Aqua, No. 28* , pp. 4-10.

Miedema, S. (1985A, September). Derivation of the Differential Equation for Sand Pore Pressures. *Dredging and Port Construction* , pp. 35.

Miedema, S. (1985B, July). Mathematical Modeling of the Cutting of Densely Compacted Sand Under Water. *Dredging and Port Construction* , pp. 22-26.

Miedema, S. (1986A). The Application of a Cutting Theory on a Dredging Wheel. *WODCON XI* (p. 14 pages). Brighton, UK: WODA.

Miedema, S. (1986B, June). Underwater Soil Cutting: a Study in Continuity. *Dredging and Port Construction* , pp. 47-53.

Miedema, S. (1987 September). *The Calculation of the Cutting Forces when Cutting Water Saturated Sand, PhD Thesis.* Delft: Delft University of Technology.

Miedema, S. (1989). On the Cutting Forces in Saturated Sand of a Seagoing Cutter Suction Dredge. *WODCON XII* (p. 27 pages). Orlando, Florida, USA: WODA.

Miedema, S. (1989, December). On the Cutting Forces in Saturated Sand of a Seagoing Cutter Suction Dredge. *Terra et Aqua, No. 41* , pp. 27 pages.

Miedema, S. (1992). New developments of cutting theories with respect to dredging, the cutting of clay. *WODCON XIII.* Bombay, India: World Dredging Association (WODA).

Miedema, S. (1994). On the Snow-Plough Effect when Cutting Water Saturated Sand with Inclined Straight Blades. *ASCE Dredging 94* (p. 24 pages). Orlando, Florida, USA: ASCE.

Miedema, S. (1995). Production Estimation Based on Cutting Theories for Cutting Water Saturated Sand. *WODCON IV* (p. 30 pages). Amsterdam, The Netherlands: WODA.

Miedema, S. (1999). Considerations on limits of dredging processes. *19th Annual Meeting & Technical Conference of the Western Dredging Association.* Louisville, Kentucky, USA: WEDA/TAMU.

Miedema, S. (2000). The modelling of the swing winches of a cutter dredge in relation with simulators. *Texas A/M 32nd Annual Dredging Seminar.* Warwick, Rhode Island, USA: WEDA/TAMU.

Miedema, S. (2003). The Existence of Kinematic Wedges at Large Cutting Angles. *CHIDA Dredging Days.* Shanghai, China: CHIDA.

Miedema, S. (2004). The Cutting Mechanisms of Water Saturated Sand at Small and Large Cutting Angles. *International Conference on Coastal Infrastructure Development - Challenges in the 21st Century.* Hongkong: ICCD.

Miedema, S. (2005). The Cutting of Water Saturated Sand, the FINAL Solution. *WEDAXXV/TAMU37.* New Orleans, Louisiana, USA: WEDA/TAMU.

Miedema, S. (2006A). The Cutting of Water Saturated Sand, the Solution. *CEDA African Section: Dredging Days.* Tangiers, Morocco: CEDA.

Miedema, S. (2006B). The Cutting of Water Saturated Sand, the Solution. *The 2nd China Dredging Association International Conference & Exhibition, themed Dredging and Sustainable Development.* Guangzhou, China: CHIDA.

Miedema, S. (2009). New Developments Of Cutting Theories With Respect To Dredging, The Cutting Of Clay And Rock. *WEDA XXIX/Texas A/M 40.* Phoenix, Arizona, USA: WEDA/TAMU.

Miedema, S. (2010). New Developments of Cutting Theories with respect to Offshore Applications. *ISOPE* (p. 8). Beijing, China.: ISOPE.

Miedema, S., & Becker, S. (1993). The Use of Modeling and Simulation in the Dredging Industry, in Particular the Closing Process of Clamshell Dredges. *CEDA Dredging Days* (p. 26 pages). Amsterdam, The Netherlands: CEDA.

Miedema, S., & Frijters, D. (2003). The Mechanism of Kinematic Wedges at Large Cutting Angles - Velocity and Friction Measurements. *23rd WEDA Technical Conference/35th TAMU Dredging Seminar* (p. 14 pages). Chicago, Illinois, USA: WEDA/TAMU.

Miedema, S., & Frijters, D. (2004). The wedge mechanism for cutting of water saturated sand at large cutting angles. *WODCON XVII.* Hamburg, Germany: WODA.

Miedema, S., & He, J. (2002B). The Existance of Kinematic Wedges at Large Cutting Angles. *WEDA XXII Technical Conference/34th Texas A/M Dredging Seminar* (p. 20 pages). Denver, Colorado, USA: WEDA/TAMU.

Miedema, S., & Ma, Y. (2002A). The Cutting of Water Saturated Sand at Large Cutting Angles. *ASCE Dredging 02* (p. 16 pages). Orlando, Florida, USA: ASCE.

Miedema, S., & Yi, Z. (2001). An Analytical Method of Pore Pressure Calculations when Cutting Water Saturated Sand. *Texas A/M 33nd Annual Dredging Seminar* (p. 18 pages). Houston, USA: WEDA/TAMU.

Mitchell, J. (1976). *Fundamentals of soil behavior.* John Wiley & Sons, Inc.

Mitchell, J., Campanella, R., & Singh, A. (1968). Soil creep as a rate process. *Journal SMFD, vol. 94, no. 1, ASCE.*

Nishimatsu, Y. (1972). The mechanics of rock cutting. *International Journal of Rock Mechanics & Mining Science, vol. 9.* , pp. 261-270.

Os, A. (1977A). Behavior of soil when excavated under water. In *International course on modern dredging.* The Hague, Netherlands.

Os, A. (1977B). Snelle deformatie van korrelvormig materiaal onder water. *PT-B32, no. 8.* , pp. 461-467.

Os, A. v. (1976). Snelle deformatie van korrelvormig materiaal onder water. *PT-P31, no. 12* , pp. 735-741.

Osman, M. (1964). The mechanics of soil cutting blades. *J.A.E.R. 9 (4)* , pp. 313-328.

Palmer, A. (1999). Speed effects in cutting and ploughing. *Geotechnique 49, no. 3.* , pp. 285-294.

Raalte, G., & Zwartbol, A. (1986). Disc bottom cutterhead, a report on laboratory and field tests. *WODCON XI.* Brighton, UK: WODA.

Rafatian, N., Miska, S., Ledgerwood III, L., Hughes, B., Ahmed, R., Yu, M., et al. (2009). Experimental study of MSE of a single PDC cutter under simulated pressurized conditions. *SPE/IADC 119302 Drilling Conference & Exhibition.* Amsterdam, Netherlands: SPE International.

Reece, A. (1965). The fundamental equation of earth moving machinery. *Symposium Earth Moving Machinery.* London: Institute of Mechanical Engineering.

Rhee, C., & Steeghs, H. (1991 June). Multi blade ploughs in saturated sand, model cutting tests. *Dredging & Port Construction* .

Rowe, P. (1962). The stress dilatancy relation for static equilibrium of an assembly of particles in contact. *Proceedings Royal Society A269.* (pp. 500-527). Royal Society.

Roxborough, F. (1987). The role of some basic rock properties in assessing cuttability. *Seminar on Tunnels - Wholly Engineered Structures* (pp. 1-21). Canberra, Australia: AFCC.

Schrieck, G. (1996). *Introduction to Dredging Engineering.* Delft, the Netherlands: Delft University of Technology.

Segal, G. (2001). *Sepra analysis programmers guide, standard problems and users manual.* Leidschendam, Netherlands: Ingenieursbureau Sepra.

Sohne, W. (1956). Some basic considerations of soil mechanics as applied to agricultural engineering. *Grundlagen der landtechnik (7).* , pp. 11-27.

Soydemir, C. (1977). Potential models for shear strength generation in soft marine clays. *International Symposium on Soft Clay*. Bangkok, Thailand.

Stam, P. (1983). *Analyse ten behoeve van het ontwerp van een klei snijdende sleepkop, CO/82/129.* Delft, Netherlands: Delft University of Technology.

Steeghs, H. (1985A). Snijden van zand onder water, part I. *Ports & Dredging no. 121* .

Steeghs, H. (1985B). Snijden van zand onder water, part II. *Ports & Dredging no. 123.*

Terzaghi, K., & Peck, R. (1964). *Soil mechanics in engineering practise.* New York: John Wiley & Sons.

Turnage, G., & Freitag, D. (1970). Effects of cone velocity and size on soil penetration resistance. *ASEA 69-670.*

Verhoef, P. (1997). *Wear of rock cutting tools: Implications for site investigation of rock dredging projects.* Delft, Netherlands: Balkema Rotterdam.

Verruijt, A. (1983). *Soil Mechanics.* Delft: DUM, Netherlands.

Vlasblom, W. (2003-2007). *Rock Cutting, Lecture Notes.* Delft, Netherlands: Delft University of Technology.

Vukovic, M., & Soro, A. (1992). Determination of hydraulic conductivity of porous media from grain size composition. *Water Resources Publications, Littleton, Colorado.*

Wismer, R., & Luth, H. (1972A). Performance of Plane Soil Cutting Blades. *Transactions of ASEA* .

Wismer, R., & Luth, H. (1972B). Rate effects in soil cutting. *Journal of Terramechanics, vol. 8, no. 3.* , pp. 11-21.

Yi, Z. (2000). *The FEM calculation of pore water pressure in sand cutting process by SEPRAN.* Delft, Netherlands: Delft University of Technology, Report: 2001.BT.5455.

Yi, Z., & Miedema, S. (2001). Finite Element Calculations To Determine The Pore Pressures When Cutting Water Saturated Sand At Large Cutting Angles. *CEDA Dredging Days* (p. 20 pages). Amsterdam, The Netherlands: CEDA.

Yi, Z., & Miedema, S. (2002). Finite Element Calculations To Determine The Pore Pressures When Cutting Water Saturated Sand At Large Cutting Angles. *CEDA Dredging Days* (p. 20 pages). Amsterdam, The Netherlands: CEDA.

Zeng, D., & Yao, Y. (1988). Investigation on the relationship between soil metal friction and sliding speed. *2nd Asian Pacific Conference of ISTVS.* Bangkok, Thailand.

Zeng, D., & Yao, Y. (1991). Investigation on the relationship between soil shear strength and shear rate. *Journal of Terramechanics, 28 (1).*

Zijsling, D. (1987). Single cutter testing - a key for PDC bit development (SPE 16529). *Offshore Europe 87.* Aberdeen, Scotland.

Chapter 17: Figures & Tables

17.1. List of Figures

17.2. List of Figures in Appendices

17.3. List of Tables

17.4. List of Tables in Appendices

Appendix A: Appendices

Appendix B: The Dimensionless Pore Pressures p_{1m} & p_{2m}

Table B-1: The dimensionless pore pressures.

	h_b/h_i	k_i/k_{max}=1			k_i/k_{max}=0.25		
		β =30 º	37.5 º	45 º	30 º	37.5 º	45 º
α =15 º	1 (s)	0.156	0.168	0.177	0.235	0.262	0.286
	2 (s)	0.157	0.168	0.177	0.236	0.262	0.286
	3 (s)	0.158	0.168	0.177	0.237	0.262	0.286
	1 (b)	0.031	0.033	0.035	0.054	0.059	0.063
	2 (b)	0.016	0.017	0.018	0.028	0.030	0.032
	3 (b)	0.011	0.011	0.012	0.019	0.020	0.021
		β =25º	30º	35º	25º	30º	35º
α =30 º	1 (s)	0.178	0.186	0.193	0.274	0.291	0.308
	2 (s)	0.179	0.187	0.193	0.276	0.294	0.310
	3 (s)	0.179	0.187	0.193	0.277	0.294	0.310
	1 (b)	0.073	0.076	0.078	0.126	0.133	0.139
	2 (b)	0.049	0.049	0.049	0.084	0.085	0.086
	3 (b)	0.034	0.034	0.033	0.059	0.059	0.059
		β =20º	25º	30º	20º	25º	30º
α =45 º	1 (s)	0.185	0.193	0.200	0.289	0.306	0.325
	2 (s)	0.190	0.198	0.204	0.304	0.322	0.339
	3 (s)	0.192	0.200	0.205	0.308	0.325	0.340
	1 (b)	0.091	0.097	0.104	0.161	0.174	0.187
	2 (b)	0.081	0.082	0.083	0.146	0.148	0.151
	3 (b)	0.067	0.065	0.063	0.120	0.116	0.114
		β =15º	20º	25º	15º	20º	25º
α =60 º	1 (s)	0.182	0.192	0.200	0.278	0.303	0.324
	2 (s)	0.195	0.204	0.211	0.314	0.339	0.359
	3 (s)	0.199	0.208	0.214	0.327	0.350	0.368
	1 (b)	0.091	0.103	0.112	0.158	0.184	0.205
	2 (b)	0.100	0.106	0.109	0.182	0.196	0.204
	3 (b)	0.094	0.095	0.093	0.174	0.176	0.174

The dimensionless pore pressures $\mathbf{p_{1m}}$ in the shear zone (s) and $\mathbf{p_{2m}}$ on the blade surface (b) as a function of the blade angle $\boldsymbol{\alpha}$, de shear angle $\boldsymbol{\beta}$, the ratio between the blade height $\mathbf{h_b}$ and the layer thickness $\mathbf{h_i}$ and the ratio between the permeability of the situ sand $\mathbf{k_i}$ and the permeability of the sand cut $\mathbf{k_{max}}$, with a wear zone behind the edge of the blade of $0.2\cdot\mathbf{h_i}$.

Appendix C: The Shear Angle β Non-Cavitating

Table C-1: β for hb/hi=1, non-cavitating

h_b/h_i=1	φ	32 º	37 º	42 º	47 º	52 º
α	δ					
15	15 º	40.892	40.152	39.169	38.012	36.727
	18 º	39.024	38.380	37.483	36.402	35.184
	21 º	37.355	36.781	35.947	34.924	33.756
	24 º	35.847	35.321	34.534	33.552	32.423
	27 º	34.468	33.975	33.220	32.269	31.166
	30 º	33.196	32.723	31.989	31.058	29.973
30	15 º	37.967	36.937	35.707	34.334	32.854
	18 º	36.187	35.250	34.100	32.795	31.372
	21 º	34.564	33.696	32.606	31.353	29.974
	24 º	33.072	32.255	31.209	29.994	28.648
	27 º	31.690	30.907	29.893	28.705	27.382
	30 º	30.401	29.640	28.646	27.476	26.166
45	15 º	33.389	32.254	30.936	29.481	27.919
	18 º	31.792	30.726	29.467	28.061	26.539
	21 º	30.326	29.310	28.092	26.720	25.224
	24 º	28.969	27.984	26.793	25.442	23.963
	27 º	27.700	26.733	25.557	24.218	22.745
	30 º	26.503	25.543	24.373	23.036	21.562
60	15 º	28.220	26.928	25.482	23.917	22.253
	18 º	26.813	25.569	24.160	22.623	20.978
	21 º	25.500	24.287	22.901	21.379	19.742
	24 º	24.264	23.067	21.692	20.174	18.535
	27 º	23.091	21.897	20.522	18.999	17.350
	30 º	21.967	20.767	19.382	17.845	16.177

The shear angle β as a function of the blade angle α, the angle of internal friction φ, the soil/interface friction angle δ, for the non-cavitating cutting process, for $\mathbf{h_b/h_i=1}$.

Table C-2: β for hb/hi=2, non-cavitating

h_b/h_i=2	φ	32 °	37 °	42 °	47 °	52 °
α	δ					
15 °	15 °	41.128	40.402	39.427	38.273	36.986
	18 °	39.239	38.609	37.720	36.643	35.424
	21 °	37.554	36.993	36.167	35.147	33.979
	24 °	36.030	35.517	34.738	33.760	32.630
	27 °	34.638	34.158	33.410	32.462	31.358
	30 °	33.354	32.893	32.167	31.238	30.152
30 °	15 °	39.129	37.939	36.562	35.056	33.457
	18 °	37.223	36.144	34.859	33.429	31.894
	21 °	35.458	34.468	33.258	31.891	30.408
	24 °	33.820	32.899	31.748	30.432	28.992
	27 °	32.293	31.425	30.320	29.043	27.637
	30 °	30.864	30.035	28.965	27.718	26.336
45 °	15 °	33.483	32.334	30.991	29.508	27.918
	18 °	31.743	30.679	29.408	27.985	26.444
	21 °	30.142	29.141	27.925	26.547	25.043
	24 °	28.660	27.704	26.527	25.182	23.705
	27 °	27.278	26.353	25.202	23.879	22.420
	30 °	25.982	25.074	23.939	22.630	21.179
60 °	15 °	27.692	26.533	25.186	23.694	22.085
	18 °	26.156	25.057	23.759	22.307	20.729
	21 °	24.744	23.683	22.418	20.991	19.432
	24 °	23.432	22.394	21.147	19.733	18.180
	27 °	22.203	21.173	19.932	18.520	16.965
	30 °	21.039	20.008	18.763	17.344	15.776

The shear angle β as a function of the blade angle α, the angle of internal friction ϕ, the soil/interface friction angle δ, for the non-cavitating cutting process, for $\mathbf{h_b/h_i=2}$.

Table C-3: β for hb/hi=3, non-cavitating

h_b/h_i=3	φ	32 º	37 º	42 º	47 º	52 º
α	δ					
15 º	15 º	42.346	41.502	40.418	39.164	37.786
	18 º	40.414	39.674	38.681	37.507	36.198
	21 º	38.673	38.010	37.086	35.973	34.718
	24 º	37.087	36.481	35.609	34.542	33.328
	27 º	35.631	35.064	34.230	33.197	32.013
	30 º	34.283	33.742	32.934	31.926	30.763
30 º	15 º	40.176	38.793	37.257	35.619	33.909
	18 º	38.242	36.978	35.537	33.977	32.331
	21 º	36.421	35.258	33.900	32.407	30.817
	24 º	34.711	33.631	32.341	30.906	29.364
	27 º	33.103	32.090	30.858	29.470	27.968
	30 º	31.590	30.631	29.444	28.095	26.625
45 º	15 º	35.406	33.895	32.248	30.509	28.703
	18 º	33.548	32.142	30.578	28.907	27.156
	21 º	31.788	30.472	28.981	27.368	25.665
	24 º	30.126	28.885	27.455	25.891	24.230
	27 º	28.557	27.376	25.996	24.474	22.845
	30 º	27.075	25.941	24.600	23.111	21.509
60 º	15 º	28.252	26.972	25.516	23.930	22.241
	18 º	26.613	25.406	24.010	22.472	20.823
	21 º	25.094	23.940	22.588	21.086	19.464
	24 º	23.677	22.560	21.238	19.760	18.156
	27 º	22.348	21.253	19.950	18.485	16.890
	30 º	21.092	20.008	18.713	17.254	15.600

The shear angle β as a function of the blade angle α, the angle of internal friction φ, the soil/interface friction angle δ, for the non-cavitating cutting process, for **h_b/h_i=3**.

Appendix D: The Coefficient c_1

Table D-1: c_1 for hb/hi=1

h_b/h_i=1	ϕ	32 º	37 º	42 º	47 º	52 º
α	δ					
15 º	15 º	0.104	0.118	0.132	0.146	0.162
	18 º	0.119	0.134	0.150	0.167	0.186
	21 º	0.133	0.150	0.169	0.189	0.210
	24 º	0.147	0.167	0.188	0.211	0.236
	27 º	0.162	0.184	0.209	0.235	0.264
	30 º	0.177	0.202	0.229	0.259	0.292
30 º	15 º	0.175	0.203	0.234	0.268	0.306
	18 º	0.195	0.227	0.261	0.300	0.343
	21 º	0.215	0.251	0.290	0.334	0.384
	24 º	0.236	0.276	0.320	0.370	0.427
	27 º	0.257	0.302	0.352	0.409	0.474
	30 º	0.279	0.329	0.385	0.450	0.525
45 º	15 º	0.254	0.304	0.360	0.425	0.502
	18 º	0.279	0.334	0.398	0.472	0.560
	21 º	0.305	0.367	0.438	0.523	0.624
	24 º	0.332	0.401	0.482	0.578	0.695
	27 º	0.360	0.437	0.529	0.639	0.774
	30 º	0.390	0.477	0.580	0.706	0.863
60 º	15 º	0.360	0.445	0.547	0.671	0.826
	18 º	0.393	0.488	0.604	0.746	0.928
	21 º	0.428	0.535	0.666	0.831	1.045
	24 º	0.466	0.587	0.736	0.928	1.180
	27 º	0.507	0.643	0.815	1.039	1.341
	30 º	0.553	0.707	0.905	1.169	1.534

The dimensionless force c_1, in the direction of the cutting velocity, as a function of the blade angle α, the angle of internal friction ϕ, the soil/interface friction angle δ, for h_b/h_i**=1.**

Table D-2: c_1 for hb/hi=2

h_b/h_i=2	ϕ	32 º	37 º	42 º	47 º	52 º
α	δ					
15 º	15 º	0.106	0.119	0.133	0.148	0.163
	18 º	0.120	0.135	0.152	0.169	0.187
	21 º	0.135	0.152	0.171	0.191	0.213
	24 º	0.149	0.169	0.191	0.214	0.239
	27 º	0.164	0.187	0.211	0.237	0.267
	30 º	0.179	0.205	0.232	0.262	0.296
30 º	15 º	0.185	0.214	0.246	0.281	0.320
	18 º	0.207	0.240	0.276	0.317	0.362
	21 º	0.230	0.267	0.308	0.354	0.407
	24 º	0.254	0.296	0.342	0.395	0.455
	27 º	0.278	0.325	0.378	0.437	0.507
	30 º	0.303	0.356	0.415	0.483	0.563
45 º	15 º	0.282	0.335	0.396	0.466	0.547
	18 º	0.313	0.373	0.441	0.521	0.616
	21 º	0.345	0.412	0.490	0.582	0.692
	24 º	0.379	0.454	0.543	0.648	0.775
	27 º	0.414	0.499	0.600	0.721	0.869
	30 º	0.452	0.547	0.662	0.801	0.974
60 º	15 º	0.415	0.509	0.622	0.760	0.932
	18 º	0.458	0.565	0.693	0.853	1.056
	21 º	0.504	0.625	0.772	0.958	1.197
	24 º	0.554	0.690	0.860	1.077	1.362
	27 º	0.607	0.762	0.958	1.213	1.556
	30 º	0.665	0.843	1.070	1.372	1.787

The dimensionless force $\mathbf{c_1}$, in the direction of the cutting velocity, as a function of the blade angle α, the angle of internal friction ϕ, the soil/interface friction angle δ, for $\mathbf{h_b/h_i=2}$.

Table D-3: c_1 for hb/hi=3

h_b/h_i=3	ϕ	32 º	37 º	42 º	47 º	52 º
α	δ					
15 º	15 º	0.105	0.119	0.133	0.148	0.164
	18 º	0.120	0.135	0.152	0.169	0.188
	21 º	0.135	0.152	0.171	0.192	0.214
	24 º	0.150	0.170	0.191	0.215	0.240
	27 º	0.165	0.188	0.212	0.239	0.268
	30 º	0.180	0.206	0.234	0.264	0.298
30 º	15 º	0.185	0.215	0.247	0.282	0.322
	18 º	0.208	0.241	0.278	0.318	0.364
	21 º	0.232	0.269	0.310	0.357	0.410
	24 º	0.256	0.298	0.345	0.398	0.459
	27 º	0.280	0.328	0.381	0.441	0.511
	30 º	0.306	0.359	0.419	0.488	0.569
45 º	15 º	0.290	0.345	0.408	0.480	0.565
	18 º	0.324	0.386	0.457	0.541	0.640
	21 º	0.359	0.429	0.511	0.607	0.722
	24 º	0.396	0.476	0.568	0.679	0.813
	27 º	0.436	0.525	0.631	0.758	0.914
	30 º	0.478	0.579	0.699	0.846	1.029
60 º	15 º	0.439	0.538	0.657	0.802	0.983
	18 º	0.489	0.601	0.737	0.906	1.120
	21 º	0.542	0.670	0.826	1.024	1.278
	24 º	0.599	0.744	0.926	1.157	1.461
	27 º	0.660	0.827	1.037	1.310	1.676
	30 º	0.728	0.918	1.163	1.487	1.933

The dimensionless force c_1, in the direction of the cutting velocity, as a function of the blade angle α, the angle of internal friction ϕ, the soil/interface friction angle δ, for h_b/h_i**=3.**

Appendix E: The Coefficient c_2

Table E-1: c_2 for hb/hi=1

h_b/h_i=1	ϕ	32 º	37 º	42 º	47 º	52 º
α	δ					
15 º	15 º	0.113	0.137	0.161	0.187	0.215
	18 º	0.110	0.134	0.159	0.186	0.215
	21 º	0.106	0.130	0.156	0.184	0.214
	24 º	0.101	0.126	0.152	0.181	0.213
	27 º	0.096	0.121	0.148	0.178	0.211
	30 º	0.090	0.116	0.143	0.174	0.208
30 º	15 º	0.117	0.146	0.177	0.211	0.249
	18 º	0.110	0.139	0.171	0.206	0.246
	21 º	0.103	0.132	0.164	0.200	0.241
	24 º	0.094	0.123	0.156	0.193	0.235
	27 º	0.084	0.114	0.147	0.184	0.228
	30 º	0.074	0.103	0.136	0.174	0.218
45 º	15 º	0.101	0.130	0.164	0.202	0.247
	18 º	0.090	0.119	0.152	0.191	0.237
	21 º	0.078	0.106	0.139	0.178	0.224
	24 º	0.064	0.092	0.124	0.162	0.208
	27 º	0.049	0.075	0.106	0.143	0.188
	30 º	0.032	0.056	0.085	0.120	0.164
60 º	15 º	0.060	0.084	0.112	0.146	0.189
	18 º	0.041	0.063	0.088	0.120	0.160
	21 º	0.021	0.039	0.061	0.088	0.124
	24 º	-0.003	0.011	0.028	0.050	0.078
	27 º	-0.030	-0.021	-0.011	0.003	0.021
	30 º	-0.061	-0.059	-0.057	-0.055	-0.053

The dimensionless force c_2, perpendicular to the cutting velocity, as a function of the blade angle α, the angle of internal friction ϕ, the soil/interface friction angle δ, for h_b/h_i=1.

Table E-2: c_2 for hb/hi=2

h_b/h_i=2	φ	32 °	37 °	42 °	47 °	52 °
α	δ					
15 °	15 °	0.113	0.136	0.161	0.187	0.215
	18 °	0.109	0.133	0.159	0.186	0.216
	21 °	0.105	0.130	0.156	0.184	0.215
	24 °	0.101	0.126	0.153	0.182	0.214
	27 °	0.095	0.121	0.148	0.178	0.212
	30 °	0.089	0.115	0.143	0.174	0.209
30 °	15 °	0.113	0.143	0.174	0.209	0.249
	18 °	0.105	0.135	0.168	0.204	0.245
	21 °	0.096	0.126	0.160	0.197	0.239
	24 °	0.086	0.116	0.150	0.188	0.232
	27 °	0.075	0.105	0.139	0.178	0.223
	30 °	0.062	0.092	0.127	0.166	0.212
45 °	15 °	0.092	0.123	0.158	0.199	0.247
	18 °	0.078	0.109	0.144	0.185	0.234
	21 °	0.062	0.092	0.127	0.168	0.217
	24 °	0.044	0.073	0.107	0.148	0.197
	27 °	0.023	0.051	0.084	0.124	0.173
	30 °	0.001	0.027	0.058	0.096	0.143
60 °	15 °	0.042	0.068	0.099	0.137	0.184
	18 °	0.017	0.040	0.069	0.104	0.148
	21 °	-0.012	0.008	0.033	0.063	0.103
	24 °	-0.044	-0.029	-0.010	0.015	0.046
	27 °	-0.081	-0.071	-0.060	-0.045	-0.025
	30 °	-0.123	-0.121	-0.120	-0.118	-0.116

The dimensionless force c_2, perpendicular to the cutting velocity, as a function of the blade angle α, the angle of internal friction ϕ, the soil/interface friction angle δ, for h_b/h_i**=2.**

Table E-3: c_2 for hb/hi=3

h_b/h_i=3	ϕ	32 º	37 º	42 º	47 º	52 º
α	δ					
15 º	15 º	0.113	0.137	0.161	0.188	0.216
	18 º	0.110	0.134	0.159	0.187	0.216
	21 º	0.105	0.130	0.156	0.185	0.216
	24 º	0.101	0.126	0.153	0.182	0.214
	27 º	0.096	0.121	0.149	0.179	0.212
	30 º	0.090	0.116	0.144	0.175	0.210
30 º	15 º	0.113	0.142	0.174	0.209	0.248
	18 º	0.105	0.135	0.167	0.204	0.244
	21 º	0.096	0.126	0.159	0.196	0.239
	24 º	0.085	0.116	0.149	0.188	0.231
	27 º	0.074	0.104	0.138	0.177	0.222
	30 º	0.061	0.091	0.125	0.165	0.211
45 º	15 º	0.089	0.121	0.156	0.197	0.246
	18 º	0.073	0.105	0.140	0.182	0.232
	21 º	0.056	0.086	0.122	0.163	0.214
	24 º	0.035	0.065	0.100	0.141	0.192
	27 º	0.012	0.041	0.074	0.115	0.164
	30 º	-0.013	0.013	0.045	0.083	0.131
60 º	15 º	0.032	0.058	0.090	0.129	0.177
	18 º	0.002	0.026	0.055	0.091	0.136
	21 º	-0.031	-0.011	0.014	0.045	0.085
	24 º	-0.069	-0.054	-0.035	-0.011	0.021
	27 º	-0.112	-0.104	-0.093	-0.079	-0.059
	30 º	-0.162	-0.162	-0.162	-0.162	-0.162

The dimensionless force $\mathbf{c_2}$, perpendicular to the cutting velocity, as a function of the blade angle α, the angle of internal friction ϕ, the soil/interface friction angle δ, for $\mathbf{h_b/h_i=3}$.

Appendix F: The Coefficient a_1

Table F-1: a_2 for hb/hi=1

h_b/h_i=1	ϕ	32 °	37 °	42 °	47 °	52 °
α	δ					
15 °	15 °	0.525	0.520	0.515	0.509	0.503
	18 °	0.520	0.516	0.510	0.505	0.498
	21 °	0.516	0.511	0.506	0.500	0.494
	24 °	0.511	0.507	0.502	0.496	0.490
	27 °	0.507	0.503	0.498	0.492	0.485
	30 °	0.503	0.498	0.493	0.487	0.481
30 °	15 °	0.526	0.522	0.517	0.512	0.506
	18 °	0.523	0.519	0.514	0.509	0.503
	21 °	0.520	0.516	0.511	0.506	0.500
	24 °	0.517	0.512	0.508	0.502	0.497
	27 °	0.514	0.509	0.504	0.499	0.493
	30 °	0.510	0.506	0.501	0.496	0.490
45 °	15 °	0.534	0.530	0.525	0.520	0.514
	18 °	0.531	0.527	0.522	0.517	0.511
	21 °	0.528	0.524	0.519	0.514	0.508
	24 °	0.525	0.521	0.516	0.511	0.505
	27 °	0.523	0.518	0.513	0.508	0.501
	30 °	0.520	0.515	0.510	0.504	0.498
60 °	15 °	0.535	0.528	0.521	0.513	0.505
	18 °	0.530	0.524	0.517	0.509	0.500
	21 °	0.526	0.519	0.512	0.504	0.494
	24 °	0.521	0.515	0.507	0.498	0.489
	27 °	0.517	0.510	0.502	0.493	0.483
	30 °	0.512	0.505	0.497	0.487	0.477

The weigh factor $\mathbf{a_1}$, for the determination of the weighted average permeability $\mathbf{k_m}$, as a function of the blade angle **α**, the angle of internal friction **φ**, the soil/interface friction angle **δ**, for $\mathbf{h_b/h_i=1}$.

Table F-2: a_2 for hb/hi=2

h_b/h_i=2	ϕ	32 º	37 º	42 º	47 º	52 º
α	δ					
15 º	15 º	0.522	0.518	0.513	0.507	0.501
	18 º	0.518	0.514	0.509	0.503	0.497
	21 º	0.514	0.510	0.505	0.499	0.493
	24 º	0.510	0.506	0.501	0.495	0.489
	27 º	0.506	0.502	0.497	0.491	0.485
	30 º	0.502	0.498	0.493	0.487	0.481
30 º	15 º	0.531	0.526	0.521	0.516	0.511
	18 º	0.527	0.523	0.518	0.513	0.508
	21 º	0.524	0.520	0.515	0.510	0.505
	24 º	0.521	0.517	0.512	0.507	0.501
	27 º	0.518	0.514	0.509	0.504	0.498
	30 º	0.514	0.510	0.506	0.500	0.495
45 º	15 º	0.554	0.550	0.546	0.541	0.536
	18 º	0.552	0.548	0.544	0.539	0.534
	21 º	0.550	0.546	0.542	0.537	0.532
	24 º	0.548	0.544	0.539	0.535	0.529
	27 º	0.546	0.542	0.537	0.532	0.527
	30 º	0.544	0.540	0.535	0.530	0.524
60 º	15 º	0.575	0.569	0.563	0.556	0.549
	18 º	0.571	0.566	0.559	0.552	0.545
	21 º	0.568	0.562	0.556	0.549	0.541
	24 º	0.565	0.559	0.552	0.545	0.536
	27 º	0.561	0.555	0.548	0.541	0.532
	30 º	0.558	0.552	0.544	0.536	0.527

The weigh factor $\mathbf{a_1}$, for the determination of the weighted average permeability $\mathbf{k_m}$, as a function of the blade angle **α**, the angle of internal friction **φ**, the soil/interface friction angle **δ**, for $\mathbf{h_b/h_i=2}$.

Table F-3: a_2 for hb/hi=3

h_b/h_i=3	ϕ	32 º	37 º	42 º	47 º	52 º
α	δ					
15 º	15 º	0.522	0.517	0.512	0.507	0.501
	18 º	0.518	0.513	0.508	0.503	0.497
	21 º	0.514	0.509	0.504	0.499	0.493
	24 º	0.510	0.505	0.500	0.495	0.489
	27 º	0.506	0.501	0.497	0.491	0.485
	30 º	0.502	0.498	0.493	0.487	0.480
30 º	15 º	0.534	0.529	0.524	0.519	0.514
	18 º	0.531	0.526	0.521	0.516	0.511
	21 º	0.528	0.523	0.519	0.513	0.508
	24 º	0.525	0.520	0.516	0.511	0.505
	27 º	0.522	0.517	0.513	0.508	0.502
	30 º	0.519	0.514	0.510	0.504	0.499
45 º	15 º	0.552	0.548	0.544	0.540	0.536
	18 º	0.550	0.547	0.543	0.539	0.534
	21 º	0.549	0.545	0.541	0.537	0.532
	24 º	0.547	0.543	0.539	0.535	0.531
	27 º	0.545	0.542	0.538	0.533	0.529
	30 º	0.544	0.540	0.536	0.531	0.527
60 º	15 º	0.580	0.575	0.570	0.565	0.559
	18 º	0.578	0.573	0.568	0.563	0.557
	21 º	0.576	0.571	0.566	0.560	0.554
	24 º	0.573	0.569	0.564	0.558	0.551
	27 º	0.571	0.566	0.561	0.555	0.548
	30 º	0.569	0.564	0.558	0.552	0.545

The weigh factor $\mathbf{a_1}$, for the determination of the weighted average permeability $\mathbf{k_m}$, as a function of the blade angle **α**, the angle of internal friction **φ**, the soil/interface friction angle **δ**, for $\mathbf{h_b/h_i=3}$.

Appendix G: The Shear Angle β Cavitating

Table G-1: β for hb/hi=1, cavitating

h_b/h_i=1	φ	32 °	37 °	42 °	47 °	52 °
α	δ					
15 °	15 °	37.217	37.520	37.355	36.831	36.026
	18 °	34.461	34.854	34.790	34.370	33.669
	21 °	32.163	32.598	32.594	32.243	31.613
	24 °	30.212	30.661	30.689	30.379	29.796
	27 °	28.530	28.973	29.012	28.726	28.173
	30 °	27.060	27.483	27.520	27.243	26.707
30 °	15 °	39.766	39.060	38.014	36.718	35.232
	18 °	37.341	36.757	35.823	34.628	33.233
	21 °	35.196	34.696	33.844	32.725	31.399
	24 °	33.280	32.837	32.041	30.977	29.704
	27 °	31.554	31.145	30.387	29.363	28.127
	30 °	29.985	29.593	28.859	27.860	26.650
45 °	15 °	36.853	35.599	34.097	32.412	30.591
	18 °	34.768	33.616	32.202	30.594	28.839
	21 °	32.866	31.789	30.441	28.892	27.188
	24 °	31.119	30.094	28.794	27.288	25.623
	27 °	29.502	28.512	27.246	25.770	24.132
	30 °	27.996	27.026	25.781	24.325	22.705
60 °	15 °	31.992	30.395	28.608	26.683	24.654
	18 °	30.155	28.634	26.911	25.039	23.055
	21 °	28.444	26.979	25.303	23.471	21.520
	24 °	26.841	25.414	23.772	21.968	20.040
	27 °	25.330	23.927	22.306	20.520	18.605
	30 °	23.897	22.506	20.896	19.118	17.208

The shear angle β as a function of the blade angle α, the angle of internal friction ϕ, the soil/interface friction angle δ, for the cavitating cutting process. for **h_b/h_i=1.**

Table G-2: β for hb/hi=2, cavitating

h_b/h_i=2	ϕ	32 º	37 º	42 º	47 º	52 º
α	δ					
15 º	15 º	28.724	29.560	29.957	29.994	29.733
	18 º	26.332	27.162	27.586	27.670	27.472
	21 º	24.420	25.221	25.643	25.747	25.582
	24 º	22.849	23.608	24.014	24.120	23.968
	27 º	21.528	22.240	22.621	22.716	22.566
	30 º	20.396	21.059	21.407	21.485	21.329
30 º	15 º	33.398	33.367	32.937	32.198	31.215
	18 º	30.972	31.019	30.677	30.027	29.134
	21 º	28.922	29.011	28.721	28.131	27.299
	24 º	27.161	27.265	27.004	26.451	25.659
	27 º	25.622	25.725	25.476	24.944	24.177
	30 º	24.259	24.349	24.101	23.576	22.823
45 º	15 º	32.378	31.721	30.741	29.516	28.100
	18 º	30.207	29.642	28.751	27.610	26.271
	21 º	28.308	27.801	26.970	25.887	24.605
	24 º	26.624	26.149	25.357	24.314	23.070
	27 º	25.110	24.652	23.881	22.862	21.643
	30 º	23.736	23.280	22.518	21.512	20.306
60 º	15 º	28.906	27.806	26.445	24.886	23.174
	18 º	26.993	25.974	24.686	23.194	21.540
	21 º	25.276	24.309	23.072	21.626	20.014
	24 º	23.716	22.781	21.576	20.159	18.574
	27 º	22.283	21.364	20.176	18.776	17.204
	30 º	20.955	20.038	18.855	17.461	15.892

The shear angle β as a function of the blade angle α, the angle of internal friction ϕ, the soil/interface friction angle δ, for the cavitating cutting process. for **h_b/h_i=2.**

Table G-3: β for hb/hi=3, cavitating

h_b/h_i=3	ϕ	32 º	37 º	42 º	47 º	52 º
α	δ					
15 º	15 º	24.046	25.019	25.609	25.872	25.856
	18 º	21.976	22.900	23.476	23.751	23.765
	21 º	20.350	21.217	21.763	22.030	22.053
	24 º	19.031	19.838	20.348	20.596	20.615
	27 º	17.932	18.680	19.150	19.374	19.381
	30 º	16.996	17.687	18.117	18.313	18.303
30 º	15 º	29.286	29.575	29.466	29.038	28.353
	18 º	26.992	27.319	27.267	26.908	26.297
	21 º	25.100	25.435	25.410	25.090	24.525
	24 º	23.504	23.828	23.811	23.511	22.973
	27 º	22.130	22.433	22.410	22.116	21.592
	30 º	20.928	21.202	21.165	20.867	20.346
45 º	15 º	29.236	28.919	28.257	27.325	26.179
	18 º	27.101	26.853	26.266	25.411	24.339
	21 º	25.277	25.065	24.524	23.719	22.699
	24 º	23.690	23.493	22.977	22.203	21.215
	27 º	22.288	22.091	21.584	20.825	19.857
	30 º	21.031	20.823	20.315	19.561	18.600
60 º	15 º	26.619	25.832	24.754	23.450	21.967
	18 º	24.711	23.995	22.987	21.750	20.329
	21 º	23.037	22.362	21.398	20.206	18.826
	24 º	21.543	20.889	19.951	18.785	17.431
	27 º	20.193	19.545	18.617	17.464	16.121
	30 º	18.958	18.303	17.374	16.222	14.880

The shear angle β as a function of the blade angle α, the angle of internal friction ϕ, the soil/interface friction angle δ, for the cavitating cutting process. for h_b/h_i**=3.**

Appendix H: The Coefficient d_1

Table H-1: d_1 for hb/hi=1

h_b/h_i=1	ϕ	32 º	37 º	42 º	47 º	52 º
α	δ					
15 º	15 º	1.390	1.505	1.625	1.753	1.890
	18 º	1.626	1.766	1.913	2.069	2.238
	21 º	1.860	2.028	2.205	2.393	2.597
	24 º	2.092	2.291	2.501	2.726	2.970
	27 º	2.324	2.557	2.803	3.068	3.358
	30 º	2.556	2.826	3.112	3.423	3.764
30 º	15 º	1.206	1.374	1.559	1.766	2.000
	18 º	1.381	1.575	1.791	2.033	2.309
	21 º	1.559	1.783	2.033	2.315	2.638
	24 º	1.741	1.998	2.286	2.613	2.991
	27 º	1.928	2.222	2.552	2.930	3.370
	30 º	2.121	2.455	2.833	3.269	3.781
45 º	15 º	1.419	1.688	2.000	2.365	2.800
	18 º	1.598	1.905	2.262	2.685	3.192
	21 º	1.784	2.133	2.543	3.032	3.625
	24 º	1.980	2.376	2.846	3.411	4.105
	27 º	2.186	2.636	3.174	3.829	4.642
	30 º	2.404	2.916	3.533	4.292	5.249
60 º	15 º	1.879	2.331	2.883	3.570	4.444
	18 º	2.099	2.615	3.252	4.054	5.090
	21 º	2.336	2.925	3.661	4.602	5.837
	24 º	2.593	3.267	4.120	5.228	6.711
	27 º	2.872	3.645	4.639	5.952	7.746
	30 º	3.179	4.069	5.232	6.798	8.991

The dimensionless force $\mathbf{d_1}$, in the direction of the cutting velocity, as a function of the blade angle α, the angle of internal friction ϕ, the soil/interface friction angle δ, for $\mathbf{h_b/h_i=1}$.

Table H-2: d_1 for hb/hi=2

h_b/h_i=2	ϕ	32 º	37 º	42 º	47 º	52 º
α	δ					
15 º	15 º	2.295	2.460	2.627	2.801	2.984
	18 º	2.683	2.889	3.098	3.315	3.545
	21 º	3.062	3.313	3.569	3.836	4.119
	24 º	3.435	3.735	4.042	4.364	4.707
	27 º	3.803	4.156	4.520	4.903	5.313
	30 º	4.169	4.579	5.005	5.455	5.941
30 º	15 º	1.729	1.934	2.156	2.401	2.674
	18 º	1.997	2.239	2.503	2.794	3.122
	21 º	2.267	2.550	2.860	3.205	3.593
	24 º	2.539	2.868	3.230	3.634	4.093
	27 º	2.815	3.195	3.614	4.085	4.625
	30 º	3.097	3.532	4.015	4.563	5.195
45 º	15 º	1.836	2.142	2.492	2.898	3.377
	18 º	2.093	2.447	2.854	3.330	3.897
	21 º	2.357	2.765	3.238	3.794	4.462
	24 º	2.631	3.100	3.646	4.296	5.084
	27 º	2.917	3.454	4.085	4.843	5.772
	30 º	3.217	3.830	4.558	5.442	6.541
60 º	15 º	2.269	2.764	3.364	4.104	5.038
	18 º	2.567	3.139	3.837	4.710	5.827
	21 º	2.883	3.543	4.357	5.388	6.728
	24 º	3.221	3.982	4.933	6.154	7.771
	27 º	3.586	4.464	5.578	7.031	8.995
	30 º	3.982	4.998	6.306	8.047	10.453

The dimensionless force $\mathbf{d_1}$, in the direction of the cutting velocity, as a function of the blade angle α, the angle of internal friction ϕ, the soil/interface friction angle δ , for $\mathbf{h_b/h_i=2}$.

Table H-3: d_1 for hb/hi=3

h_b/h_i=3	ϕ	32 °	37 °	42 °	47 °	52 °
α	δ					
15 °	15 °	3.145	3.362	3.578	3.799	4.028
	18 °	3.672	3.945	4.218	4.497	4.789
	21 °	4.185	4.519	4.855	5.200	5.562
	24 °	4.687	5.087	5.492	5.910	6.351
	27 °	5.180	5.652	6.132	6.631	7.159
	30 °	5.667	6.216	6.778	7.366	7.993
30 °	15 °	2.216	2.458	2.717	3.000	3.312
	18 °	2.567	2.858	3.169	3.510	3.889
	21 °	2.919	3.262	3.632	4.038	4.492
	24 °	3.272	3.673	4.107	4.587	5.127
	27 °	3.629	4.093	4.599	5.162	5.799
	30 °	3.991	4.525	5.110	5.766	6.515
45 °	15 °	2.222	2.566	2.954	3.402	3.925
	18 °	2.549	2.951	3.408	3.938	4.562
	21 °	2.883	3.350	3.885	4.509	5.252
	24 °	3.228	3.768	4.391	5.123	6.004
	27 °	3.585	4.207	4.929	5.788	6.831
	30 °	3.958	4.671	5.508	6.513	7.750
60 °	15 °	2.632	3.170	3.817	4.610	5.605
	18 °	2.999	3.627	4.387	5.329	6.526
	21 °	3.387	4.116	5.008	6.128	7.572
	24 °	3.799	4.645	5.692	7.025	8.774
	27 °	4.240	5.222	6.453	8.044	10.175
	30 °	4.717	5.856	7.307	9.217	11.833

The dimensionless force $\mathbf{d_1}$, in the direction of the cutting velocity, as a function of the blade angle α, the angle of internal friction ϕ, the soil/interface friction angle δ , for $\mathbf{h_b/h_i=3}$.

Appendix I: The Coefficient d_2

Table I-1: d_2 for hb/hi=1

h_b/h_i=1	ϕ	32 °	37 °	42 °	47 °	52 °
α	δ					
15 °	15 °	0.409	0.608	0.816	1.037	1.274
	18 °	0.312	0.528	0.754	0.995	1.255
	21 °	0.205	0.436	0.680	0.939	1.220
	24 °	0.087	0.333	0.592	0.870	1.172
	27 °	-0.040	0.219	0.493	0.788	1.110
	30 °	-0.175	0.095	0.382	0.692	1.034
30 °	15 °	0.474	0.642	0.828	1.035	1.269
	18 °	0.412	0.588	0.782	1.000	1.249
	21 °	0.341	0.523	0.725	0.954	1.216
	24 °	0.261	0.447	0.657	0.895	1.169
	27 °	0.171	0.361	0.576	0.822	1.108
	30 °	0.071	0.264	0.483	0.735	1.031
45 °	15 °	0.398	0.553	0.733	0.945	1.196
	18 °	0.325	0.481	0.664	0.879	1.138
	21 °	0.241	0.396	0.579	0.797	1.061
	24 °	0.145	0.298	0.478	0.696	0.962
	27 °	0.037	0.183	0.358	0.572	0.836
	30 °	-0.086	0.051	0.217	0.421	0.678
60 °	15 °	0.195	0.317	0.465	0.650	0.885
	18 °	0.083	0.193	0.329	0.500	0.721
	21 °	-0.047	0.047	0.164	0.313	0.510
	24 °	-0.198	-0.126	-0.036	0.081	0.238
	27 °	-0.372	-0.331	-0.278	-0.208	-0.113
	30 °	-0.575	-0.574	-0.573	-0.572	-0.570

The dimensionless force $\mathbf{d_2}$, perpendicular to the cutting velocity, as a function of the blade angle α, the angle of internal friction ϕ, the soil/interface friction angle δ, for $\mathbf{h_b/h_i=1}$.

Table I-2: d_2 for hb/hi=2

h_b/h_i=2	φ	32 º	37 º	42 º	47 º	52 º
α	δ					
15 º	15 º	-0.024	0.262	0.552	0.853	1.170
	18 º	-0.253	0.064	0.387	0.722	1.076
	21 º	-0.496	-0.151	0.202	0.569	0.959
	24 º	-0.752	-0.381	-0.001	0.396	0.820
	27 º	-1.018	-0.626	-0.221	0.204	0.660
	30 º	-1.294	-0.884	-0.458	-0.007	0.479
30 º	15 º	0.266	0.471	0.693	0.938	1.211
	18 º	0.136	0.354	0.592	0.854	1.149
	21 º	-0.008	0.222	0.473	0.752	1.067
	24 º	-0.165	0.074	0.337	0.631	0.965
	27 º	-0.336	-0.089	0.183	0.490	0.841
	30 º	-0.520	-0.268	0.011	0.327	0.693
45 º	15 º	0.216	0.393	0.595	0.830	1.107
	18 º	0.087	0.267	0.475	0.718	1.007
	21 º	-0.059	0.123	0.334	0.582	0.880
	24 º	-0.221	-0.040	0.170	0.420	0.723
	27 º	-0.401	-0.226	-0.020	0.227	0.529
	30 º	-0.600	-0.435	-0.240	-0.002	0.293
60 º	15 º	-0.009	0.124	0.285	0.484	0.735
	18 º	-0.182	-0.060	0.089	0.275	0.513
	21 º	-0.379	-0.274	-0.145	0.019	0.233
	24 º	-0.603	-0.523	-0.422	-0.293	-0.122
	27 º	-0.859	-0.812	-0.753	-0.676	-0.571
	30 º	-1.151	-1.151	-1.150	-1.148	-1.146

The dimensionless force $\mathbf{d_2}$, perpendicular to the cutting velocity, as a function of the blade angle α, the angle of internal friction φ, the soil/interface friction angle δ, for $\mathbf{h_b/h_i=2}$.

Table I-3: d_2 for hb/hi=3

h_b/h_i=3	ϕ	32 °	37 °	42 °	47 °	52 °
α	δ					
15 °	15 °	-0.552	-0.177	0.198	0.581	0.979
	18 °	-0.921	-0.501	-0.080	0.350	0.800
	21 °	-1.306	-0.846	-0.384	0.092	0.590
	24 °	-1.703	-1.208	-0.708	-0.191	0.353
	27 °	-2.111	-1.586	-1.053	-0.498	0.090
	30 °	-2.528	-1.979	-1.417	-0.828	-0.201
30 °	15 °	0.020	0.263	0.522	0.805	1.118
	18 °	-0.182	0.079	0.360	0.667	1.009
	21 °	-0.402	-0.124	0.176	0.505	0.873
	24 °	-0.638	-0.346	-0.030	0.319	0.711
	27 °	-0.890	-0.588	-0.259	0.107	0.521
	30 °	-1.158	-0.850	-0.511	-0.132	0.301
45 °	15 °	0.017	0.215	0.440	0.698	1.001
	18 °	-0.171	0.034	0.267	0.537	0.856
	21 °	-0.379	-0.171	0.068	0.346	0.677
	24 °	-0.608	-0.400	-0.160	0.122	0.460
	27 °	-0.858	-0.656	-0.420	-0.141	0.199
	30 °	-1.133	-0.941	-0.717	-0.447	-0.114
60 °	15 °	-0.221	-0.076	0.097	0.310	0.578
	18 °	-0.455	-0.321	-0.159	0.042	0.298
	21 °	-0.718	-0.602	-0.460	-0.282	-0.052
	24 °	-1.014	-0.925	-0.814	-0.673	-0.488
	27 °	-1.349	-1.297	-1.231	-1.147	-1.034
	30 °	-1.728	-1.727	-1.726	-1.724	-1.722

The dimensionless force $\mathbf{d_2}$, perpendicular to the cutting velocity, as a function of the blade angle α, the angle of internal friction ϕ, the soil/interface friction angle δ, for $\mathbf{h_b/h_i=3}$.

Appendix J: The Properties of the 200 μm Sand

The sand in the old laboratory DE, with a $\mathbf{d_{50}}$ of 200 μm, is examined for the following soil mechanical parameters:

1. The minimum and the maximum density, Table J-1: Pore percentages.
2. The dry critical density, Table J-1: Pore percentages.
3. The saturated critical density, Table J-1: Pore percentages.
4. The permeability as a function of the density, Table J-2: Permeability as a function of the porosity.
5. The angle of internal friction as a function of the density, Table J-4: The angle of internal friction as function of the pore percentage.
6. The $\mathbf{d_{50}}$ as a function of the time, Table J-3: The **d50** of the sand as function of the time.
7. The cone resistance per experiment.
8. The density in the test stand in combination with the cone resistance.

The points 7 and 8 need some explanation. With the aid of a Troxler density measuring set density measurements are performed in situ, that is in the test stand. During each measurement the cone resistance is determined at the same position. In this way it is possible to formulate a calibration formula for the density as a function of the cone resistance. The result is:

$$\mathbf{n = \frac{65.6}{C_p^{0.082}} \quad with:\ n\ in\ \%,\ C_p\ in\ kPa} \tag{J-1}$$

In which the cone resistance is determined in a top layer of 18 cm, where the cone resistance was continuously increasing and almost proportional with the depth. The value to be used in this equation is the cone resistance for the 18 cm depth.

With the aid of this equation it was possible to determine the density for each cutting test from the cone resistance measurements. The result was an average pore percentage of 38.53% over 367 tests.
By interpolating in Table J-2 it can be derived that a pore percentage of 38.53% corresponds to a permeability of 0.000165 m/s. By extrapolating in this table it can also be derived that the maximum pore percentage of 43.8% corresponds to a permeability of approximately 0.00032 m/s. At the start of the cutting tests the pore percentage was averaged 38%, which corresponds to a permeability of 0.00012 m/s.

Table J-1: Pore percentages.

Minimum density	43.8%
Maximum density	32.7%
Dry critical density	39.9%
Saturated critical density	40.7%-41.7%
Initial density	38.5%

Table J-2: Permeability as a function of the porosity.

Pore percentage	Permeability (m/s)
36.97%	0.000077
38.48%	0.000165
38.98%	0.000206
39.95%	0.000240
40.88%	0.000297
41.84%	0.000307
43.07%	0.000289
43.09%	0.000322

Table J-3: The d_{50} of the sand as function of the time.

Date	d_{50} (mm)
22-09-1982	0.175
17-12-1984	0.180
02-01-1985	0.170
08-01-1985	0.200
14-01-1985	0.200
21-01-1985	0.200
28-01-1985	0.195
04-02-1985	0.205
26-02-1985	0.210

Table J-4: The angle of internal friction as function of the pore percentage.

Pore percentage	Cell pressure kPa	Angle of internal friction
Dry		
43.8%	50	35.1º
41.2%	50	36.0º
39.9%	50	38.3º
Saturated undrained		
43.8%	100	30.9º
42.1%	10	31.2º
42.1%	50	31.2º
42.1%	100	31.6º
42.2%	100	32.0º
41.8%	10	33.1º
41.3%	10	31.9º
41.2%	50	32.2º
41.1%	50	30.1º
41.1%	100	31.3º
41.1%	100	33.7º
41.0%	100	35.2º
40.5%	10	33.8º
40.3%	50	33.7º
40.4%	100	33.1º
39.8%	10	34.1º
39.2%	10	33.8º
39.2%	50	33.8º
39.2%	100	33.9º
38.2%	10	35.2º
38.1%	50	35.3º
38.1%	100	35.0º
37.3%	10	37.4º
37.0%	10	38.6º
37.0%	50	37.3º
36.9%	100	36.8º
36.2%	100	38.0º

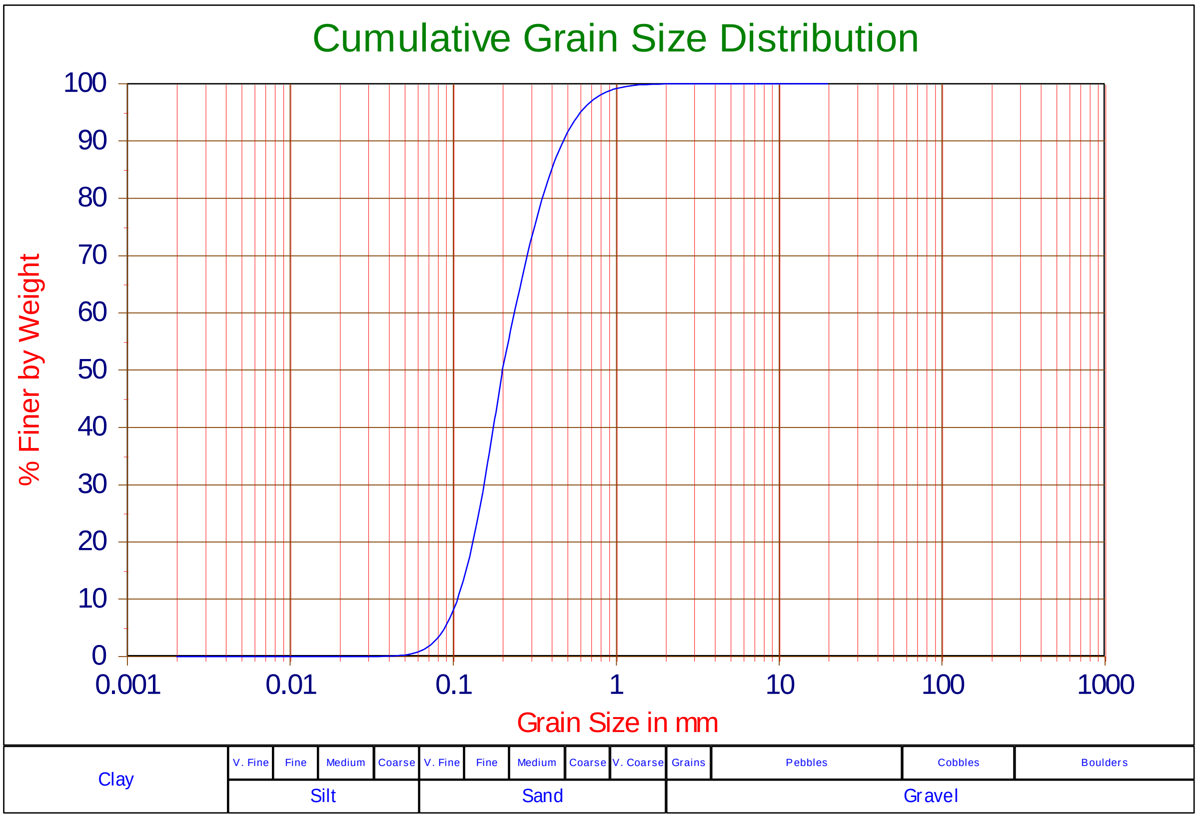

Figure J-1: The PSD of the 200 µm sand.

Appendix K: The Properties of the 105 μm Sand

The sand in the new laboratory DE, with a $\mathbf{d_{50}}$ of 105 μm, is examined for the following soil mechanical parameters:

1. The minimum and the maximum density, Table K-1: Pore percentages, indicated are the average measured densities for the various blade angles.
2. The saturated critical density, Table K-1: Pore percentages, indicated are the average measured densities for the various blade angles.
3. The permeability as a function of the density, Table K-2: Permeabilities, indicated are the average permeabilities for the various blade angles.
4. The angle of internal friction as a function of the density, Table K-4: The angle of internal friction as a function of the pore percentage.
5. The d_{50} as a function of the time, Table K-3: The **d50** of the sand as a function of time.
6. The cone resistance per test.
7. The density in the test stand in combination with the cone resistance.

The points 6 and 7 need some explanation. As with the 200 μm sand density measurements are performed in situ with the aid of a Troxler density measuring set. The calibration formula for the 105 μm sand is:

$$\mathbf{n = \frac{69.9}{C_p^{0.068}} \quad with: \; n \; in \; \%, \; C_p \; in \; kPa} \tag{K-1}$$

In which the cone resistance is determined in a top layer of 12 cm, where the cone resistance was continuously increasing and almost proportional with the depth. The value to be used in this equation is the cone resistance for the 12 cm depth.

With the aid of this equation it was possible to determine the density for each cutting test from the cone resistance measurements. As, however, new sand was used, the density showed changed in time. The sand was looser in the first tests than in the last tests. This resulted in different average initial densities for the different test series. The tests with a 45° blade were performed first with an average pore percentage of 44.9%. The tests with the 60° blade were performed with an average pore percentage of 44.2%. The tests with the 30° blade were performed with an average pore percentage of 43.6%. Because of the consolidation of the sand a relatively large spread was found in the first tests. Table K-2 lists the permeabilities corresponding to the mentioned pore percentages. By extrapolation in Table K-2 a permeability of 0.00017 m/s is derived for the maximum pore percentage of 51.6%. The sandbed is flushed after the linear tests because of the visibility in the water above the sand. In the tables it is indicated which soil mechanical parameters are determined after the flushing of the sandbed.

Table K-1: Pore percentages, indicated are the average measured densities for the various blade angles.

Minimum density	51.6%
Maximum density	38.3%
Initial density 30 º	43.6%
Initial density 45 º	44.9%
Initial density 60 º	44.2%
After the flushing	
Minimum density	50.6%
Maximum density	37.7%
Saturated critical density	44.5%

Table K-2: Permeabilities, indicated are the average permeabilities for the various blade angles.

Pore percentage	Permeability (m/s)
42.2%	0.000051
45.6%	0.000082
47.4%	0.000096
49.4%	0.000129
Initial	
43.6%	0.000062
44.2%	0.000067
44.9%	0.000075
After the flushing	
39.6%	0.000019
40.7%	0.000021
41.8%	0.000039
43.8%	0.000063
45.7%	0.000093
48.3%	0.000128

Table K-3: The d_{50} of the sand as a function of time.

Date	d_{50} (mm)
06-08-1986	0.102
06-08-1986	0.097
06-08-1986	0.104
06-08-1986	0.129
06-08-1986	0.125
06-08-1986	0.123
29-08-1986	0.105
29-08-1986	0.106
29-08-1986	0.102
16-09-1986	0.111
16-09-1986	0.105
16-09-1986	0.107

Table K-4: The angle of internal friction as a function of the pore percentage.

Pore percentage	Cell pressure kPa	Angle of internal friction
Saturated undrained		After the flushing
44.7%	100	33.5º
44.9%	200	33.3º
44.5%	400	32.8º
42.6%	100	35.0º
42.1%	200	35.5º
42.2%	400	34.8º
39.8%	100	38.6º
39.9%	200	38.3º
39.6%	400	37.9º

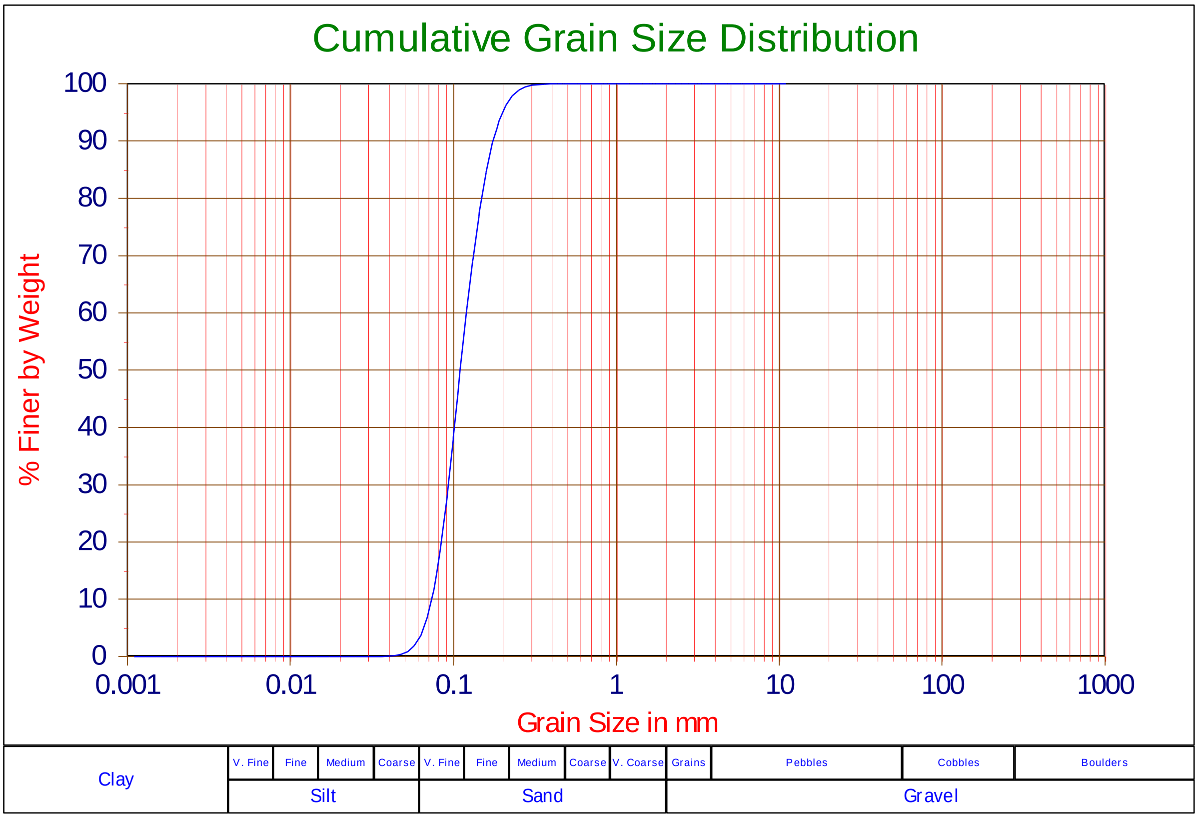

Figure K-1: The PSD of the 105 µm sand.

Appendix L: Experiments in Water Saturated Sand

L.1 Pore pressures and cutting forces in 105 μm Sand

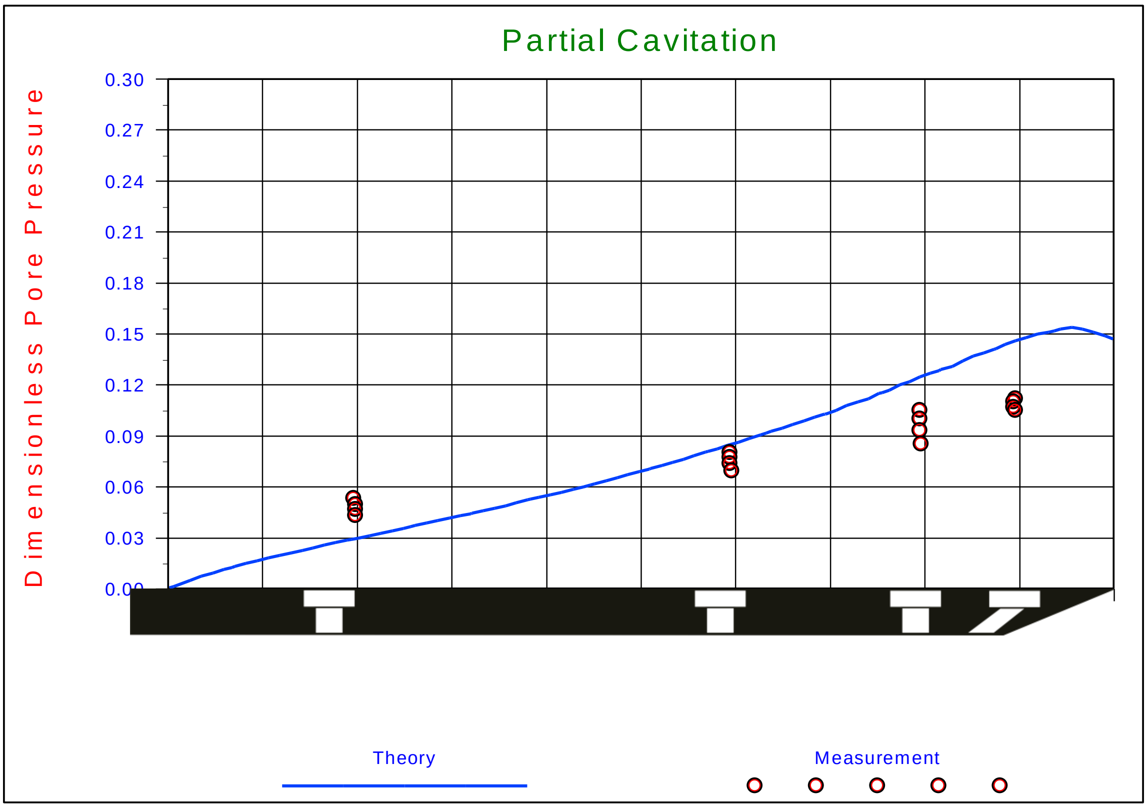

Figure L-1: Dimensionless pore pressures, theory versus measurements.

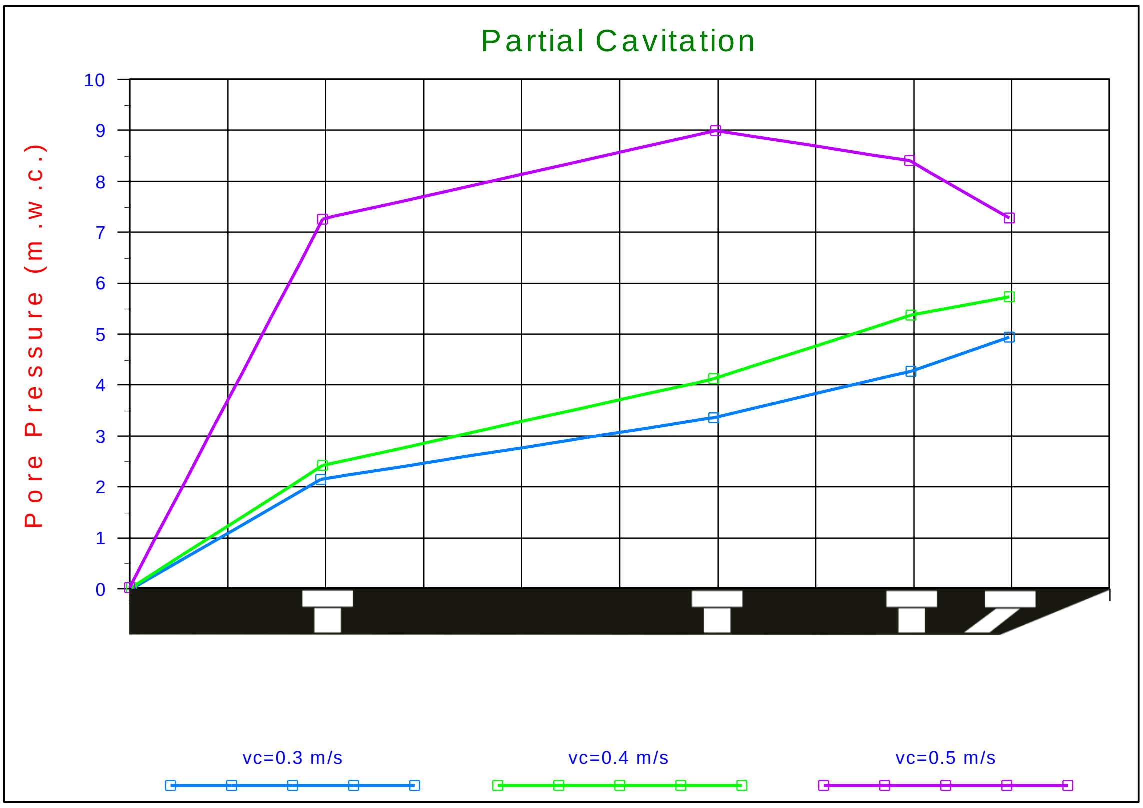

Figure L-2: Measured absolute pore pressures.

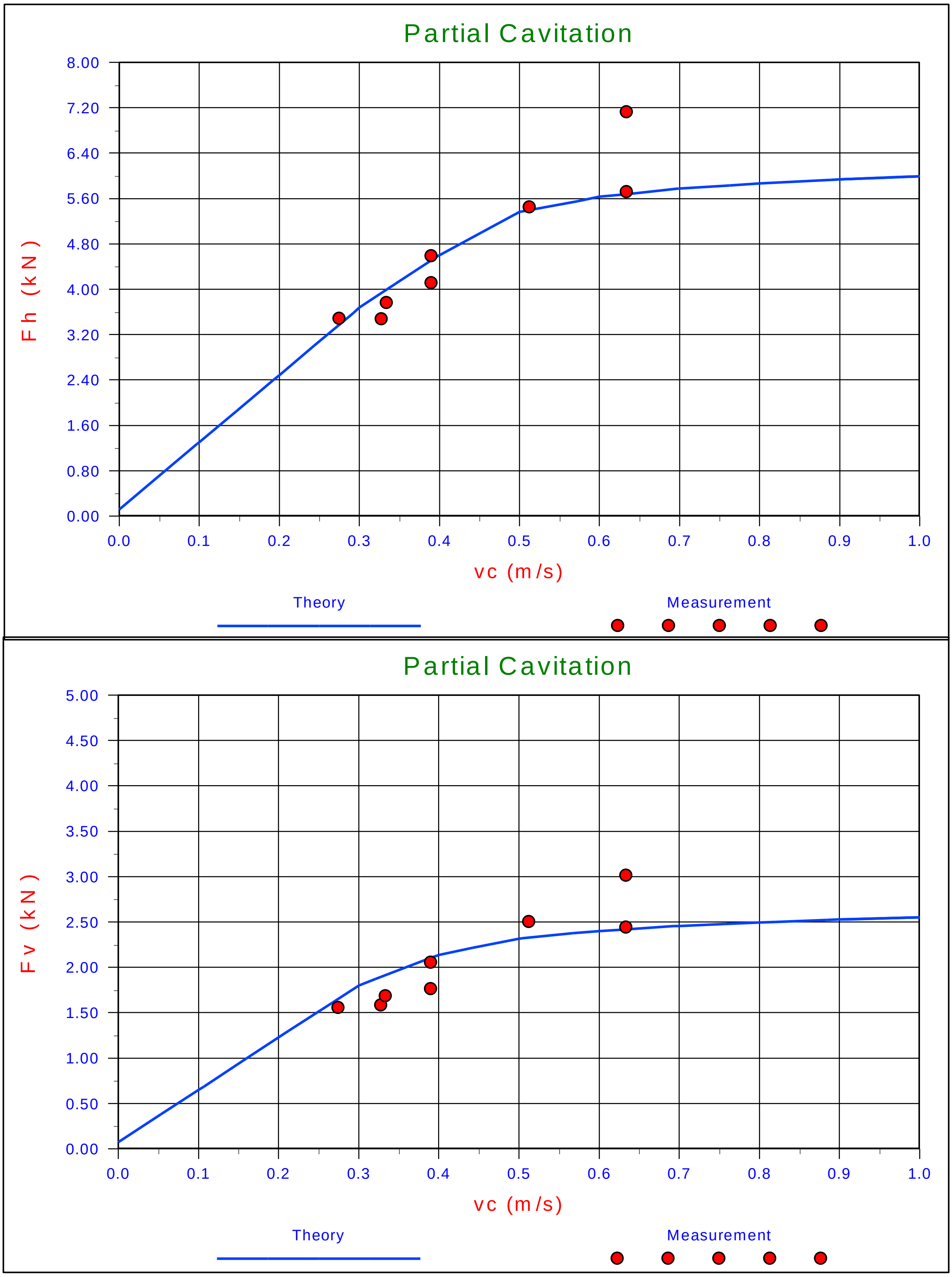

Figure L-3: The cutting forces F_h and F_v, theory versus measurement.

The cutting forces on the blade. Experiments in 105 μm sand, with **α**=30°, **β**=30°, **φ**=41°, **δ**=27°, $\mathbf{n_i}$=43.6%, $\mathbf{n_{max}}$=51.6%, $\mathbf{k_i}$=0.000062 m/s, $\mathbf{k_{max}}$=0.000170 m/s, $\mathbf{h_i}$=100 mm, $\mathbf{h_b}$=100 mm, **w**=0.2 m, **z**=0.6 m and a partial cavitating cutting process.

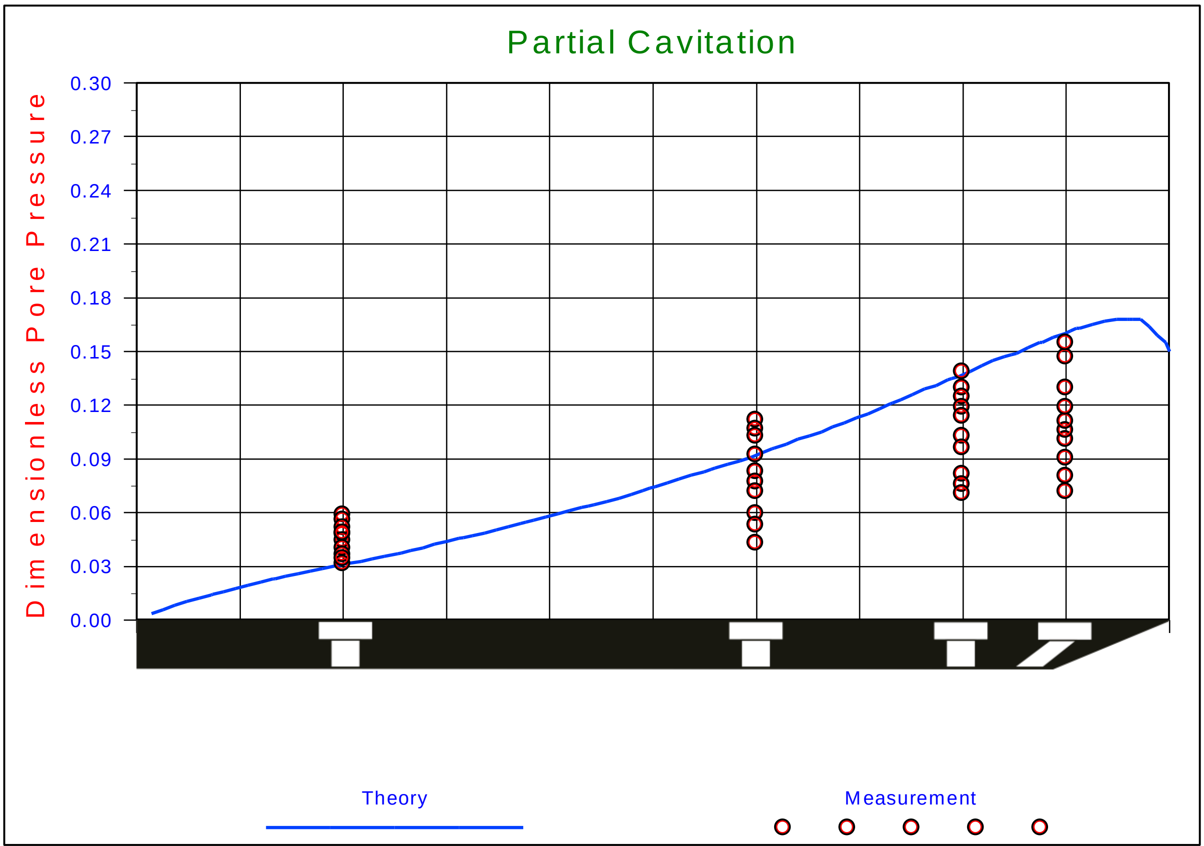

Figure L-4: Dimensionless pore pressures, theory versus measurements.

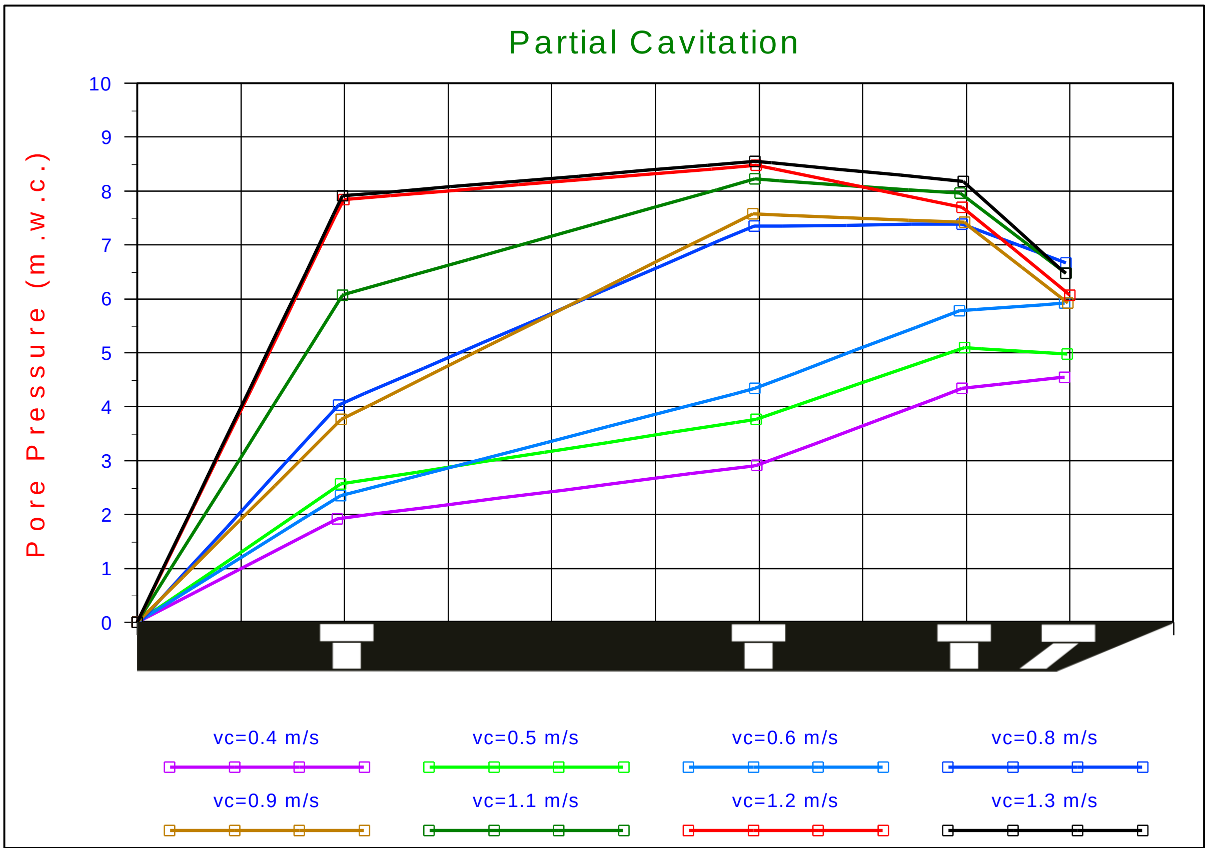

Figure L-5: Measured absolute pore pressures.

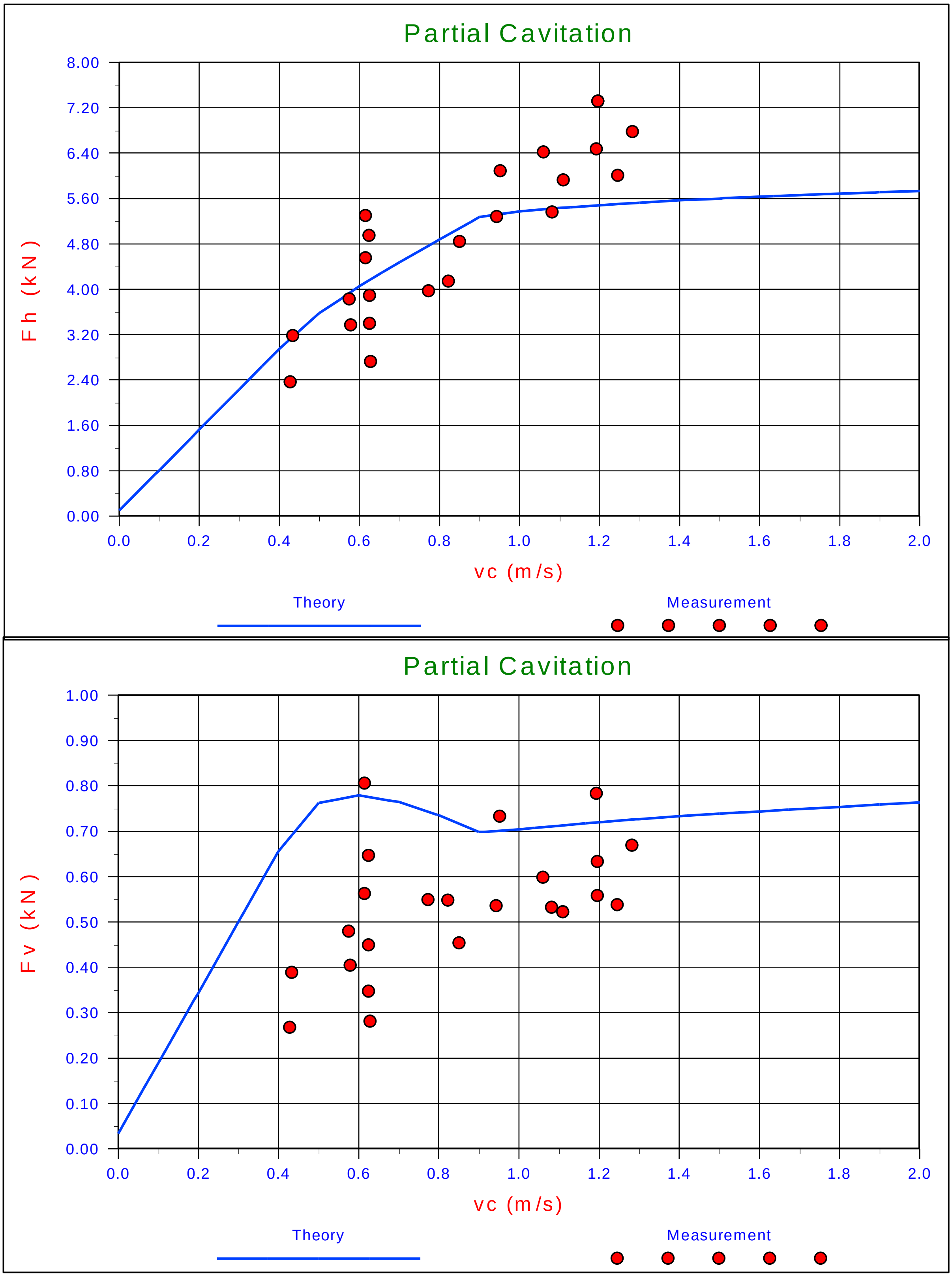

Figure L-6: The cutting forces F_h and F_v, theory versus measurement.

The cutting forces on the blade. Experiments in 105 μm sand, with **α**=45°, **β**=30º, **φ**=38º, **δ**=25º, $\mathbf{n_i}$=45.0%, $\mathbf{n_{max}}$=51.6%, $\mathbf{k_i}$=0.000075 m/s, $\mathbf{k_{max}}$=0.000170 m/s, $\mathbf{h_i}$=70 mm, $\mathbf{h_b}$=100 mm, **w**=0.2 m, **z**=0.6 m and a partial cavitating cutting process.

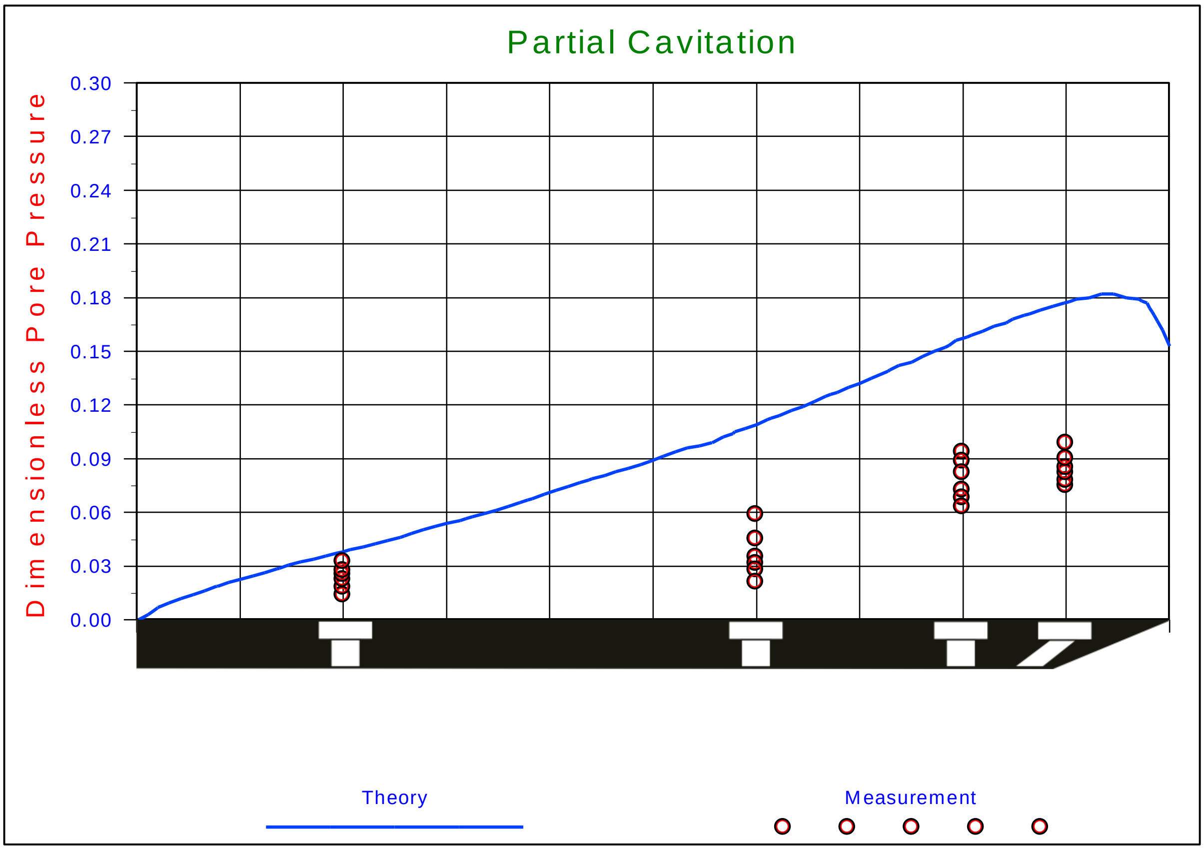

Figure L-7: Dimensionless pore pressures, theory versus measurements.

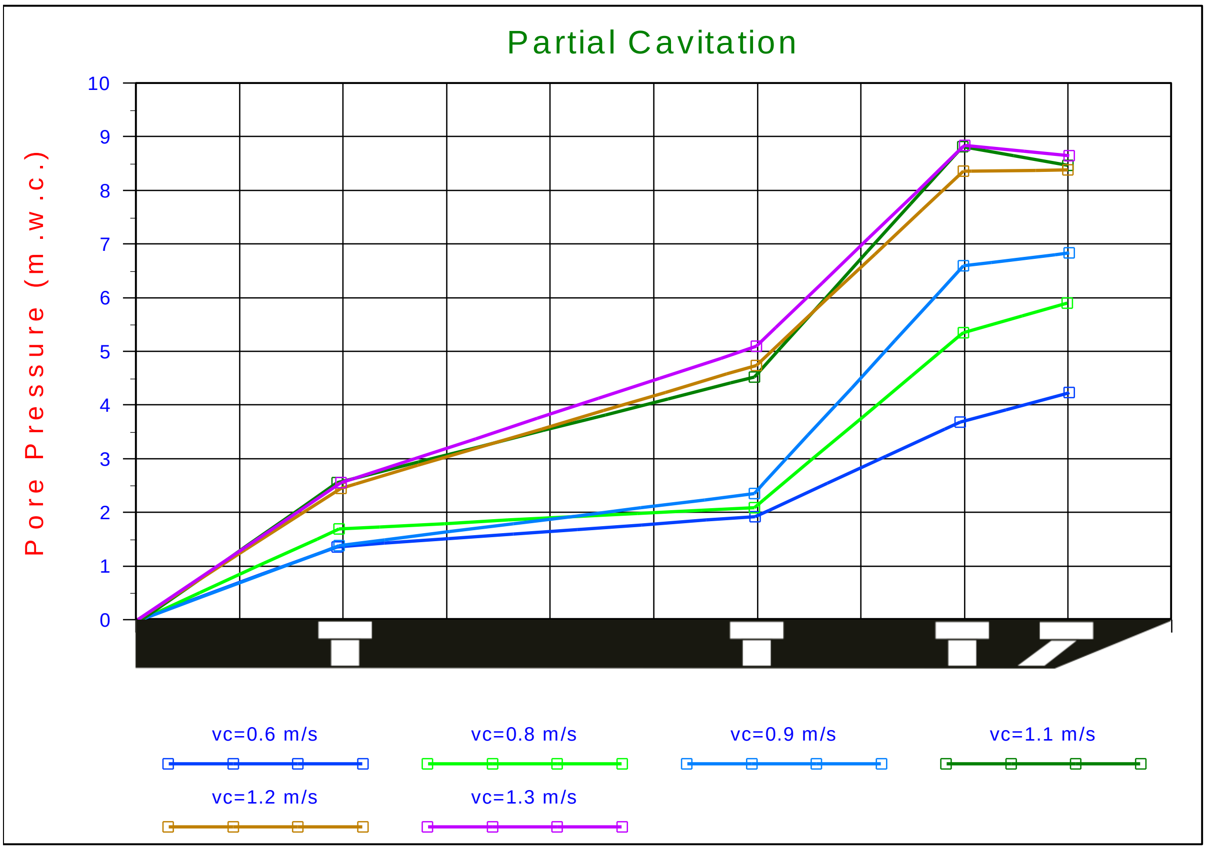

Figure L-8: Measured absolute pore pressures.

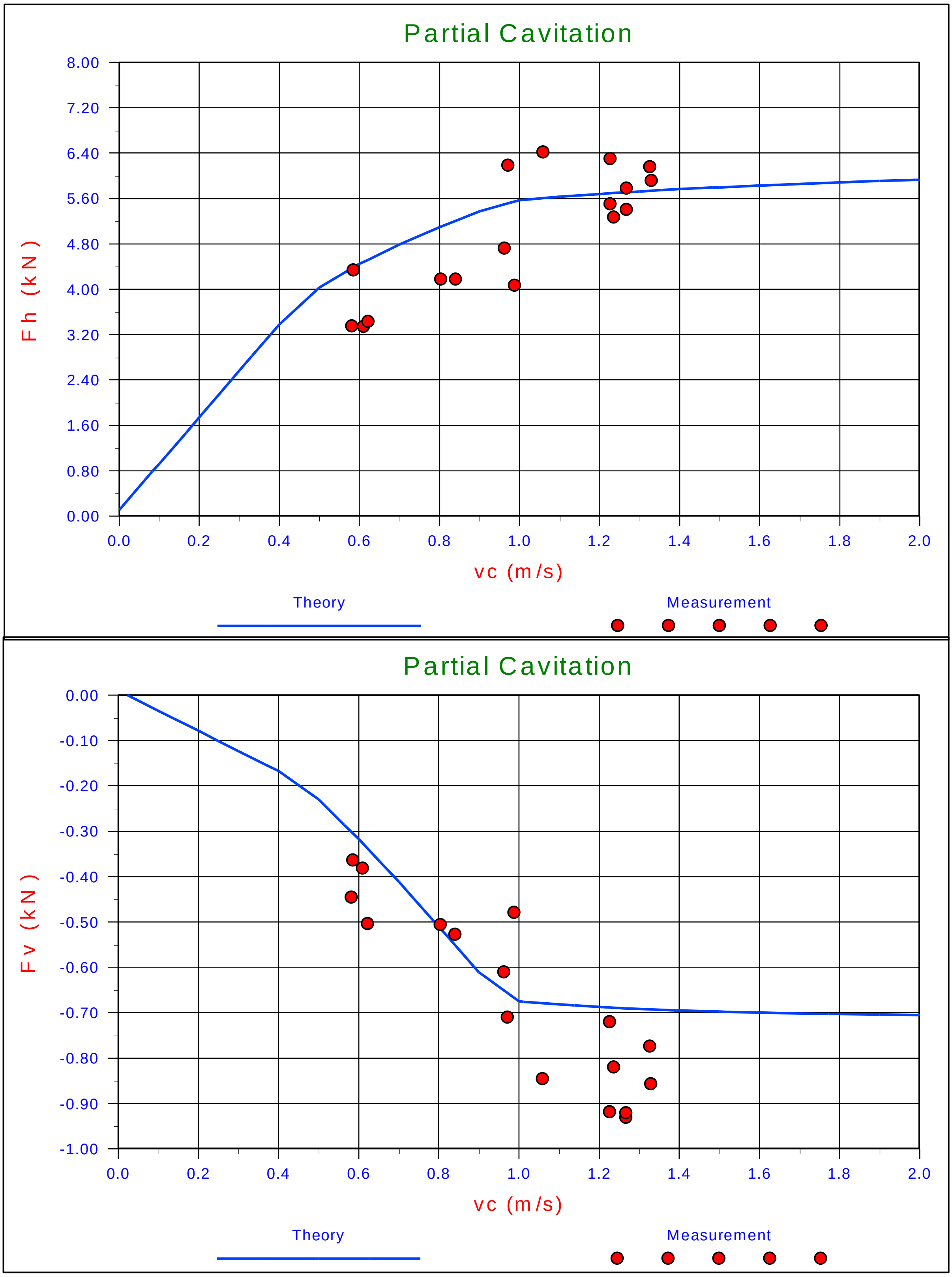

Figure L-9: The cutting forces F_h and F_v, theory versus measurement.

The cutting forces on the blade. Experiments in 105 μm sand, with **α**=60°, **β**=30º, **φ**=36º, **δ**=24º, $\mathbf{n_i}$=44.3%, $\mathbf{n_{max}}$=51.6%, $\mathbf{k_i}$=0.000067 m/s, $\mathbf{k_{max}}$=0.000170 m/s, $\mathbf{h_i}$=58 mm, $\mathbf{h_b}$=100 mm, **w**=0.2 m, **z**=0.6 m and a partial cavitating cutting process.

L.2 Pore Pressures in 200 μm Sand

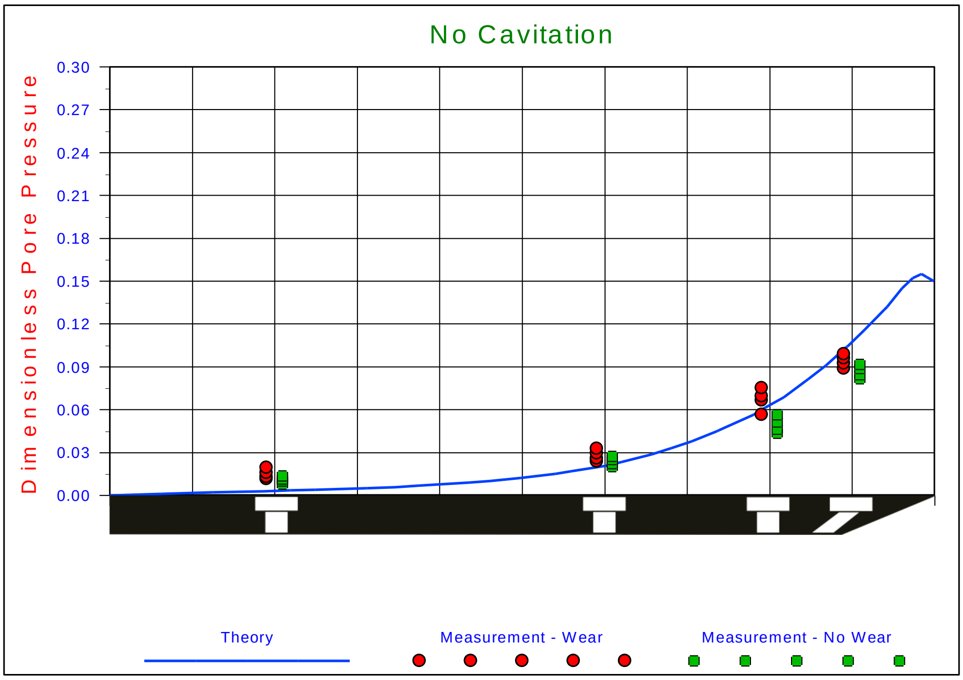

Figure L-10: α=30º, h_i=33 mm, h_b=100 mm.

The dimensionless water pore pressures on the blade. Experiments in 200 μm sand, with **α**=30°, **β**=30º, **φ**=38º, **δ**=30º, $\mathbf{n_i}$=38.53%, $\mathbf{n_{max}}$=43.88%, $\mathbf{k_i}$=0.000165 m/s, $\mathbf{k_{max}}$=0.000320 m/s, $\mathbf{h_i}$=33 mm, $\mathbf{h_b}$=100 mm, **w**=0.2 m, **z**=0.6 m and a non-cavitating cutting process.

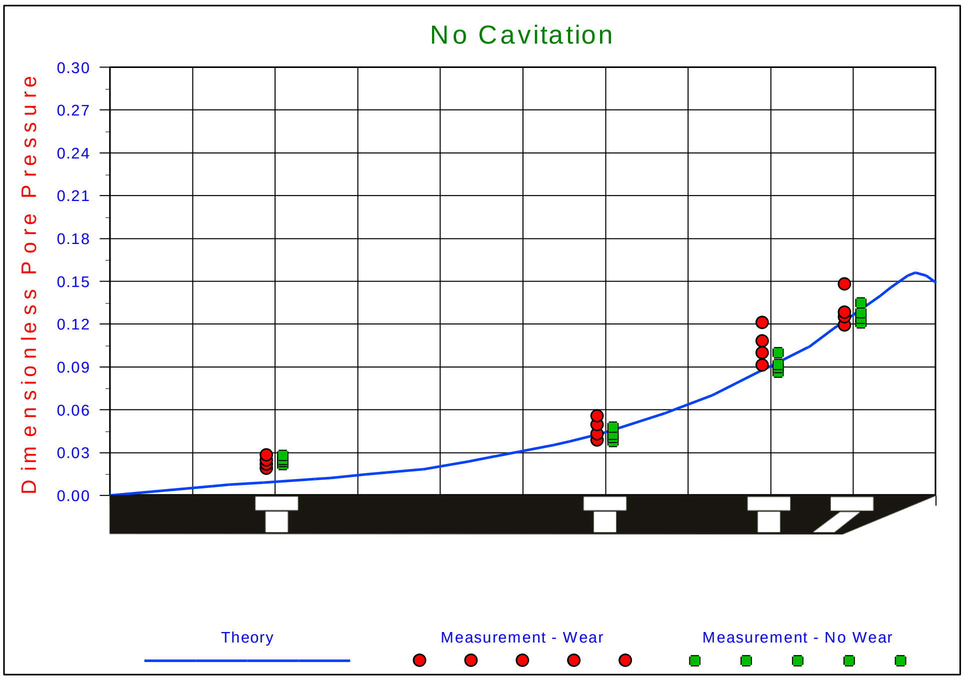

Figure L-11: α=30º, h_i=50 mm, h_b=100 mm.

The dimensionless water pore pressures on the blade. Experiments in 200 μm sand, with **α**=30°, **β**=29º, **φ**=38º, **δ**=30º, $\mathbf{n_i}$=38.53%, $\mathbf{n_{max}}$=43.88%, $\mathbf{k_i}$=0.000165 m/s, $\mathbf{k_{max}}$=0.000320 m/s, $\mathbf{h_i}$=50 mm, $\mathbf{h_b}$=100 mm, **w**=0.2 m, **z**=0.6 m and a non-cavitating cutting process.

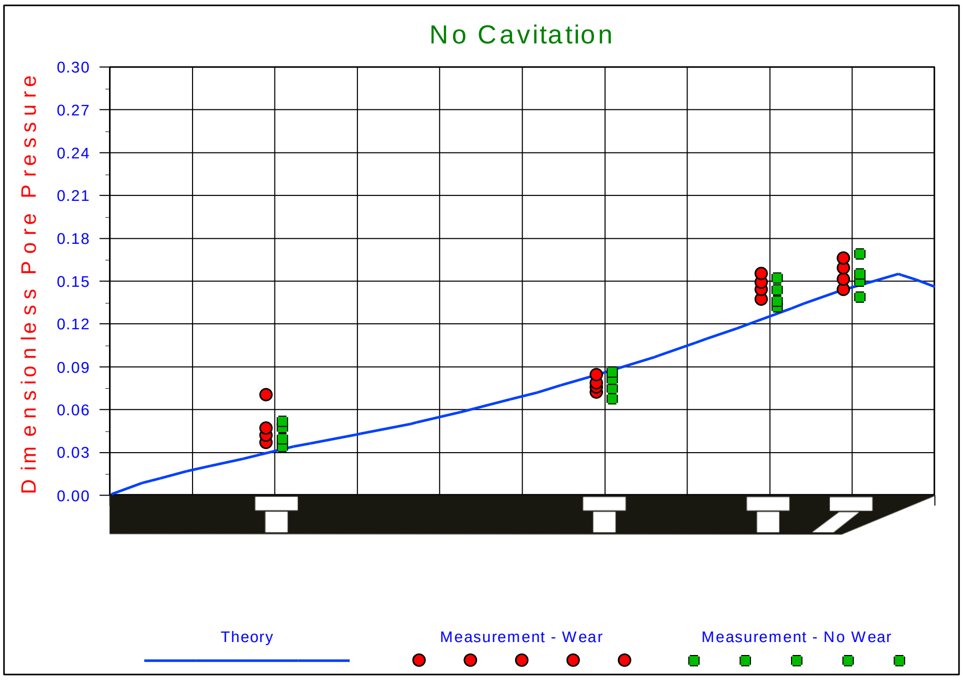

Figure L-12: α=30°, h_i=100 mm, h_b=100 mm.

The dimensionless water pore pressures on the blade. Experiments in 200 μm sand, with **α**=30°, **β**=29°, **φ**=38°, **δ**=30°, $\mathbf{n_i}$=38.53%, $\mathbf{n_{max}}$=43.88%, $\mathbf{k_i}$=0.000165 m/s, $\mathbf{k_{max}}$=0.000320 m/s, $\mathbf{h_i}$=100 mm, $\mathbf{h_b}$=100 mm, **w**=0.2 m, **z**=0.6 m and a non-cavitating cutting process.

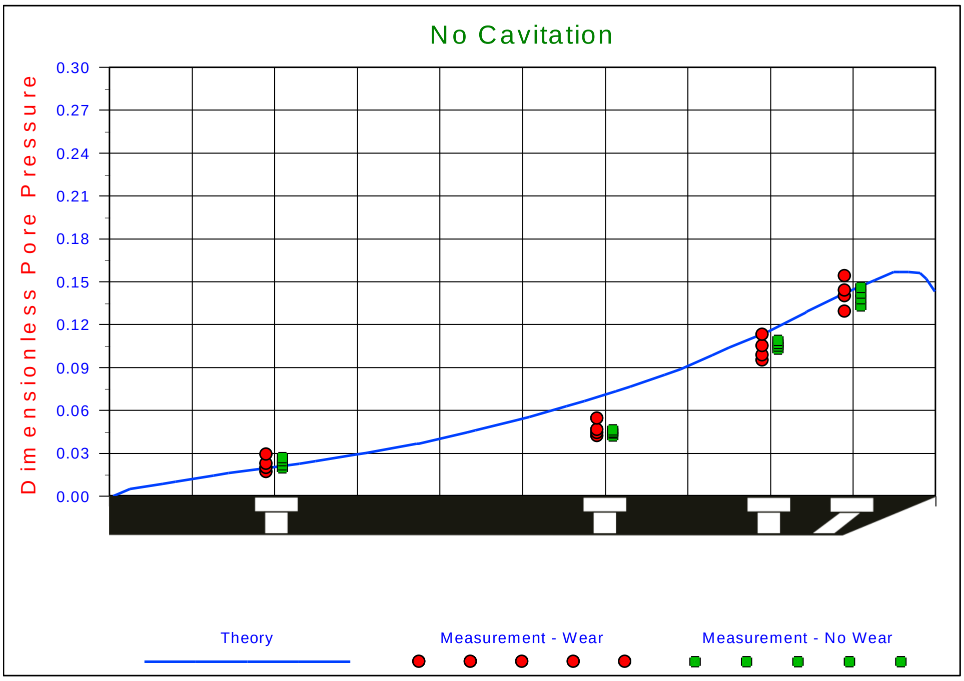

Figure L-13: α=45°, h_i=47 mm, h_b=141 mm.

The dimensionless water pore pressures on the blade. Experiments in 200 μm sand, with **α**=45°, **β**=25°, **φ**=38°, **δ**=30°, $\mathbf{n_i}$=38.53%, $\mathbf{n_{max}}$=43.88%, $\mathbf{k_i}$=0.000165 m/s, $\mathbf{k_{max}}$=0.000320 m/s, $\mathbf{h_i}$=47 mm, $\mathbf{h_b}$=141 mm, **w**=0.2 m, **z**=0.6 m and a non-cavitating cutting process.

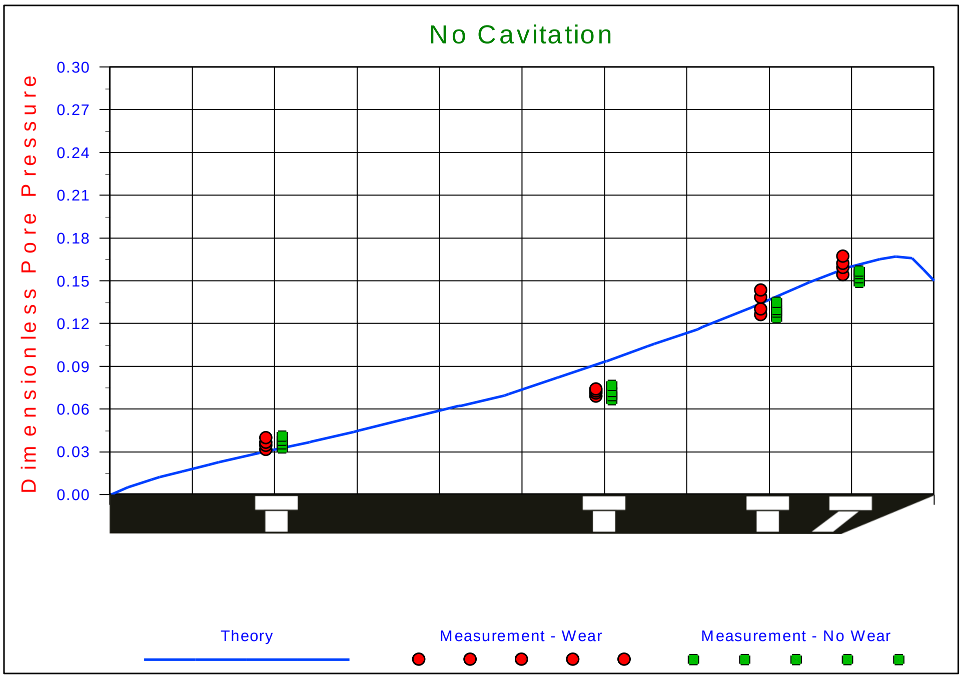

Figure L-14: α=45°, h_i=70 mm, h_b=141 mm.

The dimensionless water pore pressures on the blade. Experiments in 200 μm sand, with **α**=45°, **β**=24°, **φ**=38°, **δ**=30°, $\mathbf{n_i}$=38.53%, $\mathbf{n_{max}}$=43.88%, $\mathbf{k_i}$=0.000165 m/s, $\mathbf{k_{max}}$=0.000320 m/s, $\mathbf{h_i}$=70 mm, $\mathbf{h_b}$=141 mm, **w**=0.2 m, **z**=0.6 m and a non-cavitating cutting process.

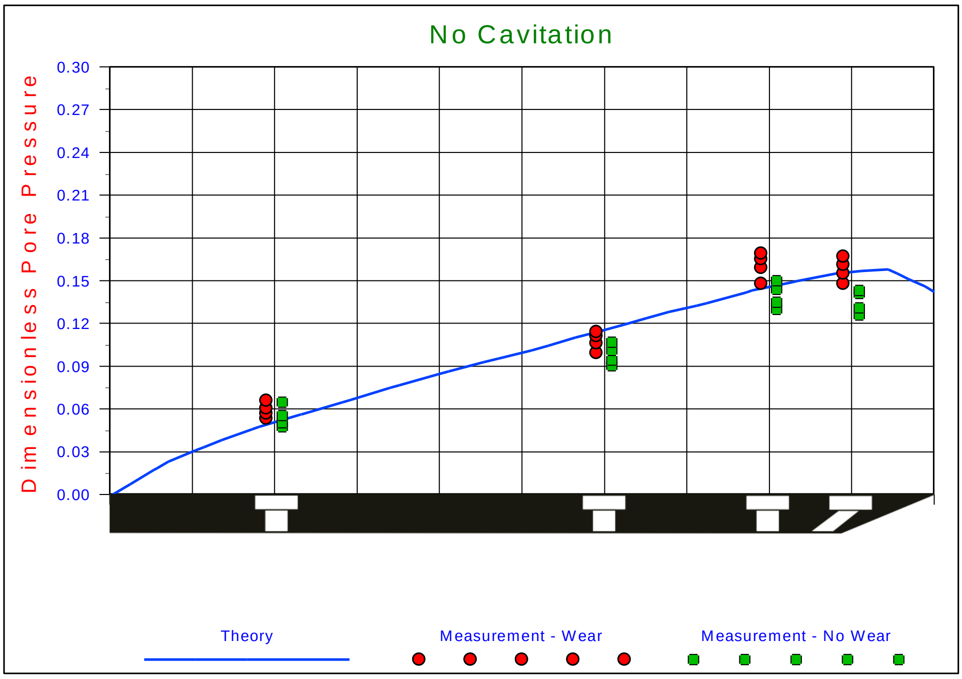

Figure L-15: α=45°, h_i=141 mm, h_b=141 mm.

The dimensionless water pore pressures on the blade. Experiments in 200 μm sand, with **α**=45°, **β**=25°, **φ**=38°, **δ**=30°, $\mathbf{n_i}$=38.53%, $\mathbf{n_{max}}$=43.88%, $\mathbf{k_i}$=0.000165 m/s, $\mathbf{k_{max}}$=0.000320 m/s, $\mathbf{h_i}$=141 mm, $\mathbf{h_b}$=141 mm, **w**=0.2 m, **z**=0.6 m and a non-cavitating cutting process.

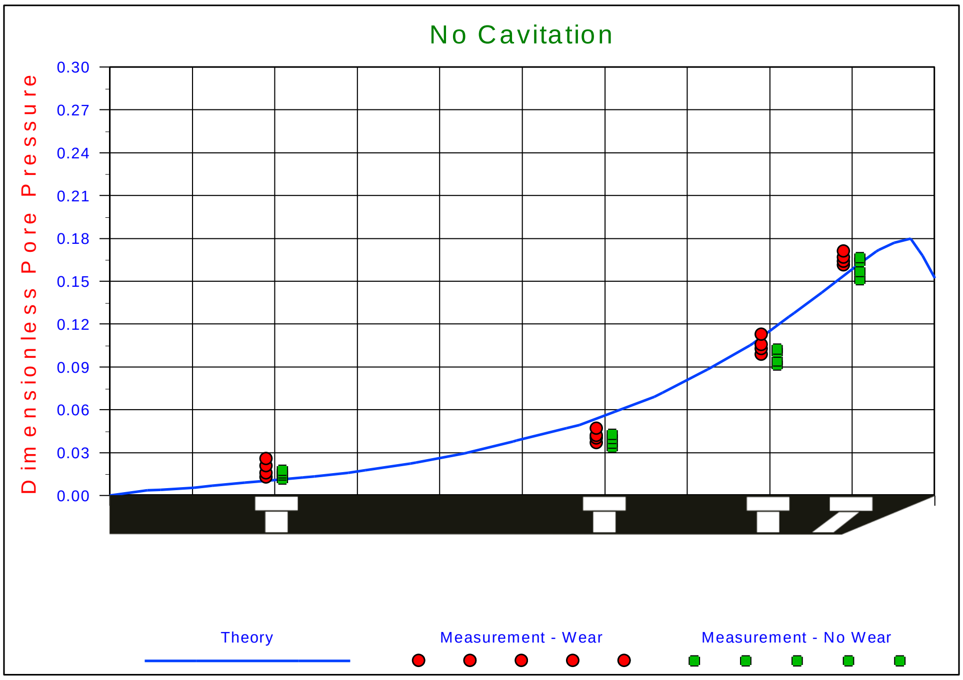

Figure L-16: α=60º, h_i=30 mm, h_b=173 mm.

The dimensionless water pore pressures on the blade. Experiments in 200 μm sand, with **α**=60°, **β**=19º, **φ**=38º, **δ**=30º, $\mathbf{n_i}$=38.53%, $\mathbf{n_{max}}$=43.88%, $\mathbf{k_i}$=0.000165 m/s, $\mathbf{k_{max}}$=0.000320 m/s, $\mathbf{h_i}$=30 mm, $\mathbf{h_b}$=173 mm, **w**=0.2 m, **z**=0.6 m and a non-cavitating cutting process.

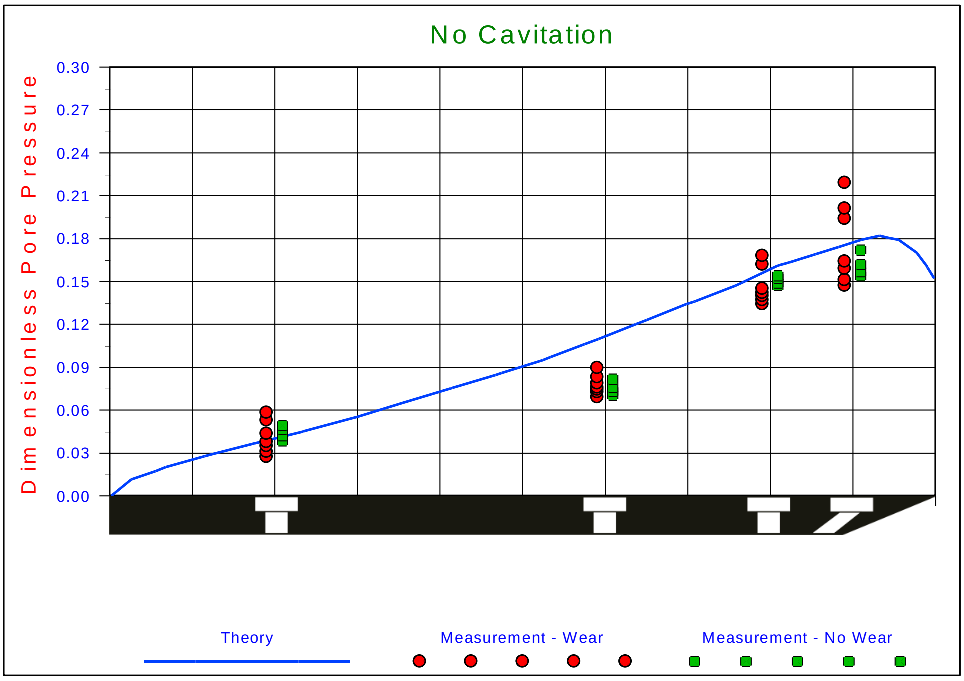

Figure L-17: α=60º, h_i=58 mm, h_b=173 mm.

The dimensionless water pore pressures on the blade. Experiments in 200 μm sand, with **α**=60°, **β**=19º, **φ**=38º, **δ**=30º, $\mathbf{n_i}$=38.53%, $\mathbf{n_{max}}$=43.88%, $\mathbf{k_i}$=0.000165 m/s, $\mathbf{k_{max}}$=0.000320 m/s, $\mathbf{h_i}$=58 mm, $\mathbf{h_b}$=173 mm, **w**=0.2 m, **z**=0.6 m and a non-cavitating cutting process.

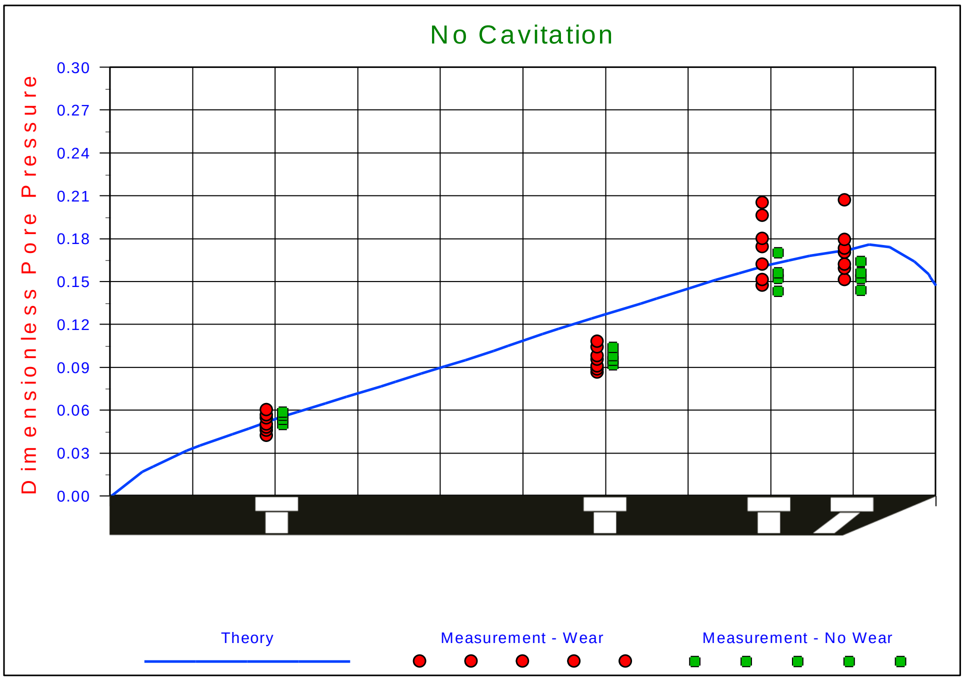

Figure L-18: α=60º, h_i=87 mm, h_b=173 mm.

The dimensionless water pore pressures on the blade. Experiments in 200 μm sand, with **α**=60°, **β**=19º, **φ**=38º, **δ**=30º, $\mathbf{n_i}$=38.53%, $\mathbf{n_{max}}$=43.88%, $\mathbf{k_i}$=0.000165 m/s, $\mathbf{k_{max}}$=0.000320 m/s, $\mathbf{h_i}$=87 mm, $\mathbf{h_b}$=173 mm, **w**=0.2 m, **z**=0.6 m and a non-cavitating cutting process.

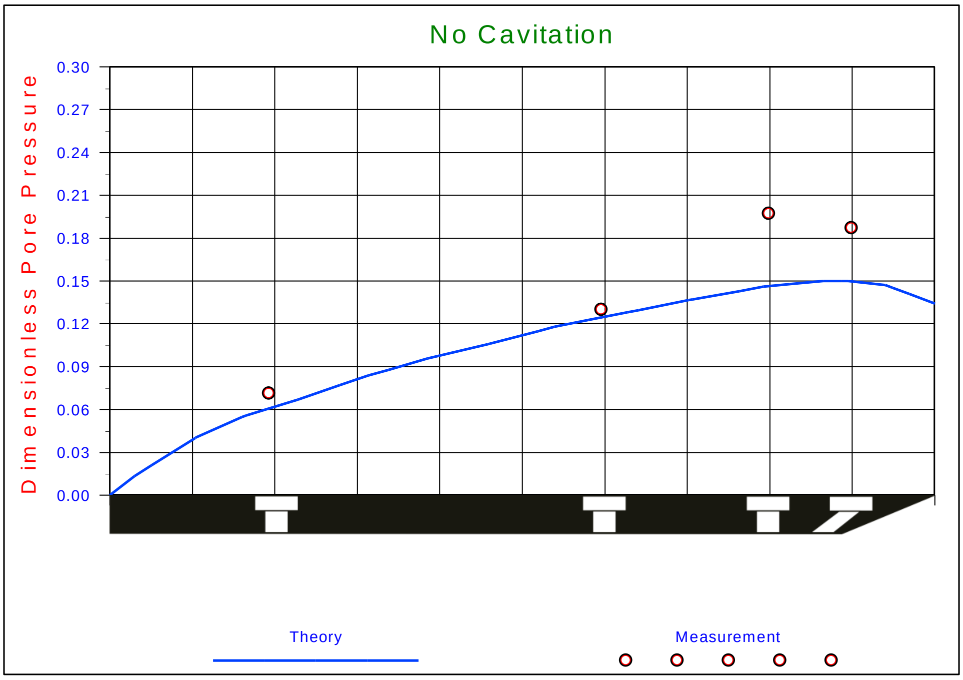

Figure L-19: α=60º, h_i=173 mm, h_b=173 mm.

The dimensionless water pore pressures on the blade. Experiments in 200 μm sand, with **α**=60°, **β**=20º, **φ**=38º, **δ**=30º, $\mathbf{n_i}$=38.53%, $\mathbf{n_{max}}$=43.88%, $\mathbf{k_i}$=0.000165 m/s, $\mathbf{k_{max}}$=0.000320 m/s, $\mathbf{h_i}$=173 mm, $\mathbf{h_b}$=173 mm, **w**=0.2 m, **z**=0.6 m and a non-cavitating cutting process.

L.3 Cutting Forces in 200 μm Sand

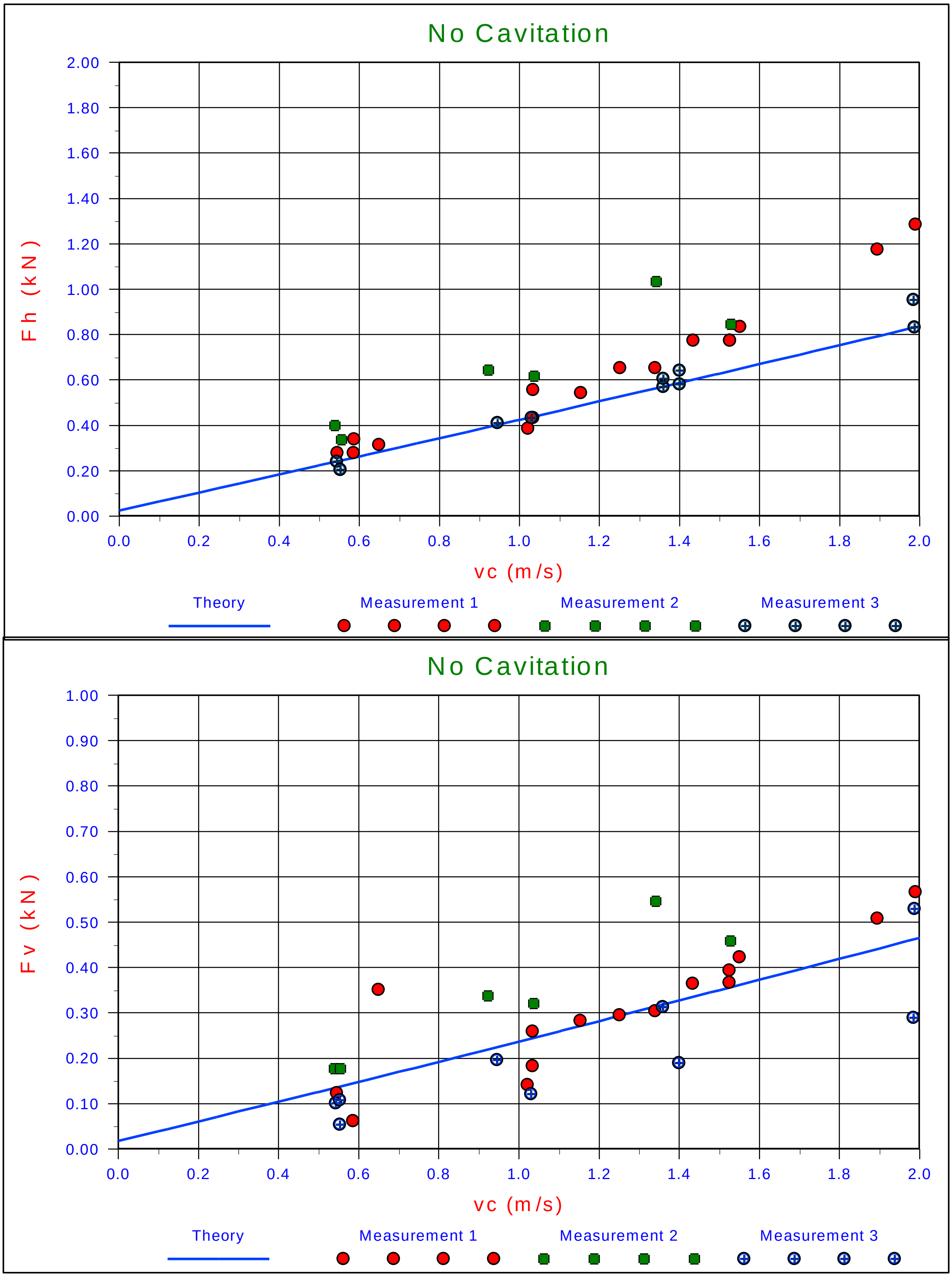

Figure L-20: α=30°, h_i=33 mm, h_b=100 mm.

The cutting forces $\mathbf{F_h}$ and $\mathbf{F_v}$ on the blade. Experiments in 200 μm sand, with **α**=30°, **β**=30º, **φ**=38º, **δ**=30º, $\mathbf{n_i}$=38.53%, $\mathbf{n_{max}}$=43.88%, $\mathbf{k_i}$=0.000165 m/s, $\mathbf{k_{max}}$=0.000320 m/s, $\mathbf{h_i}$=33 mm, $\mathbf{h_b}$=100 mm, **w**=0.2 m, **z**=0.6 m and a non-cavitating cutting process.

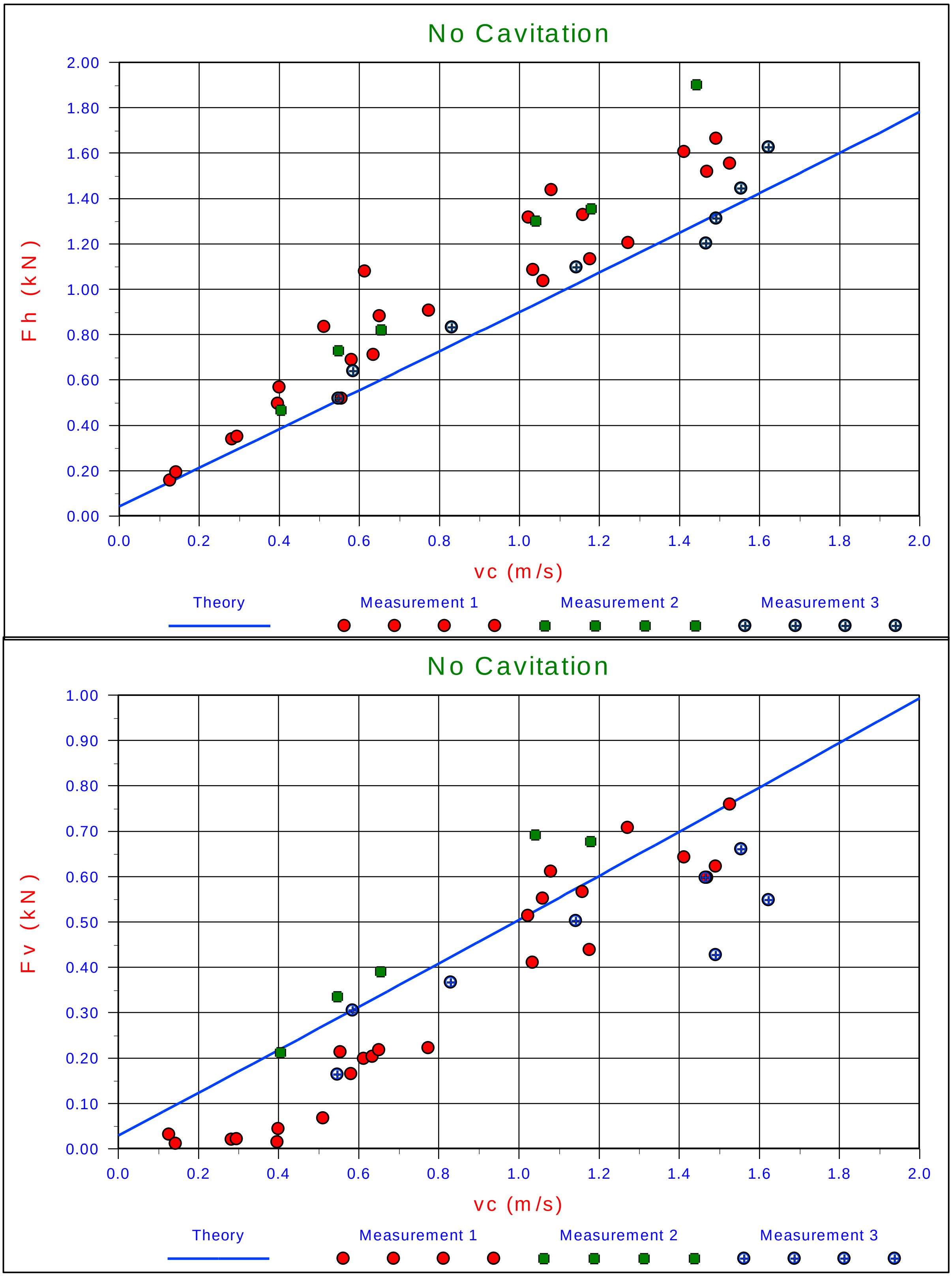

Figure L-21: α=30°, h_i=50 mm, h_b=100 mm.

The cutting forces $\mathbf{F_h}$ and $\mathbf{F_v}$ on the blade. Experiments in 200 μm sand, with $\boldsymbol{\alpha}$=30°, $\boldsymbol{\beta}$=30º, $\boldsymbol{\varphi}$=38º, $\boldsymbol{\delta}$=30º, $\mathbf{n_i}$=38.53%, $\mathbf{n_{max}}$=43.88%, $\mathbf{k_i}$=0.000165 m/s, $\mathbf{k_{max}}$=0.000320 m/s, $\mathbf{h_i}$=50 mm, $\mathbf{h_b}$=100 mm, **w**=0.2 m, **z**=0.6 m and a non-cavitating cutting process.

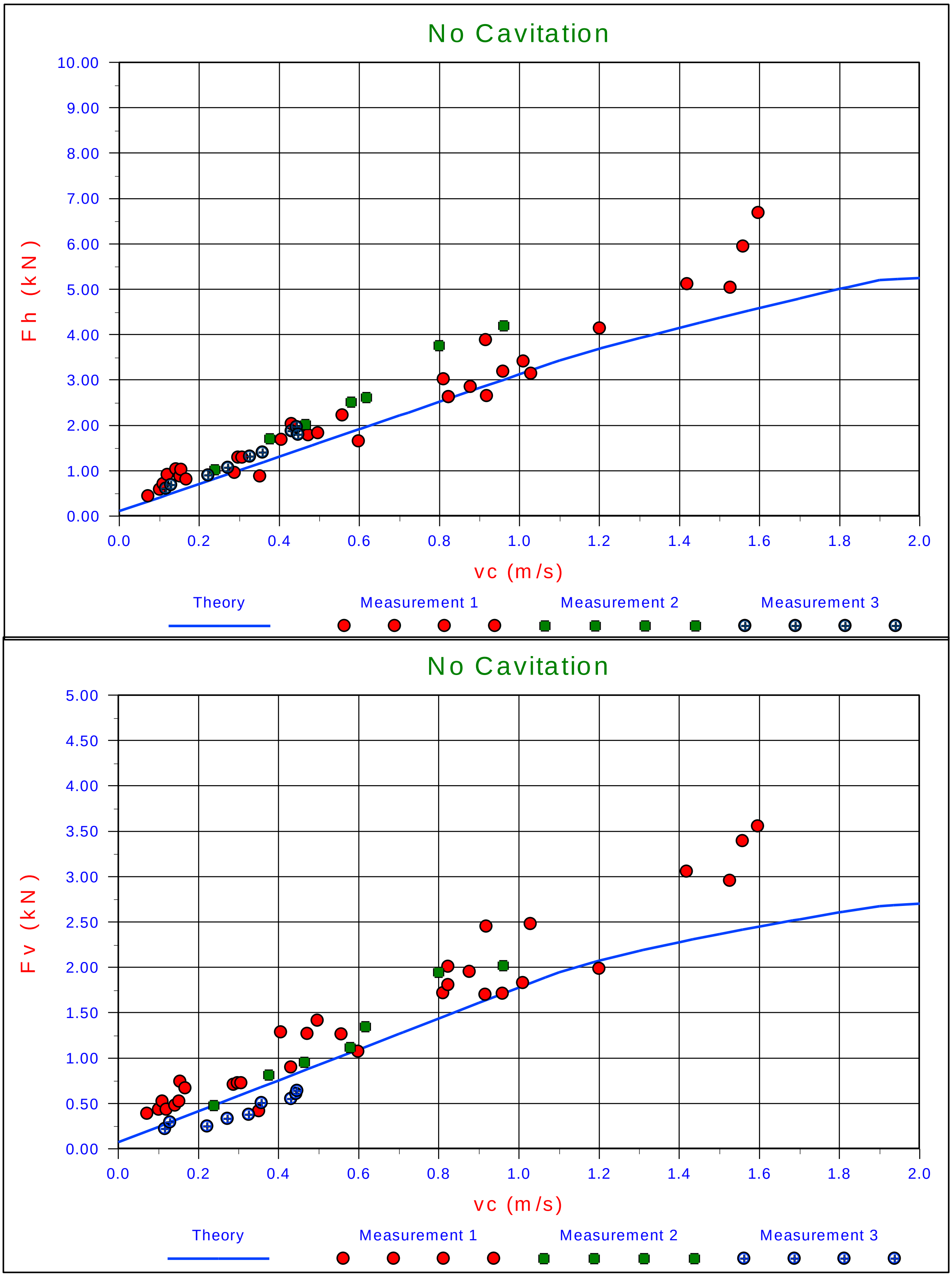

Figure L-22: α=30°, h_i=100 mm, h_b=100 mm.

The cutting forces $\mathbf{F_h}$ and $\mathbf{F_v}$ on the blade. Experiments in 200 µm sand, with **α**=30°, **β**=30º, **φ**=38º, **δ**=30º, $\mathbf{n_i}$=38.53%, $\mathbf{n_{max}}$=43.88%, $\mathbf{k_i}$=0.000165 m/s, $\mathbf{k_{max}}$=0.000320 m/s, $\mathbf{h_i}$=100 mm, $\mathbf{h_b}$=100 mm, **w**=0.2 m, **z**=0.6 m and a non-cavitating cutting process.

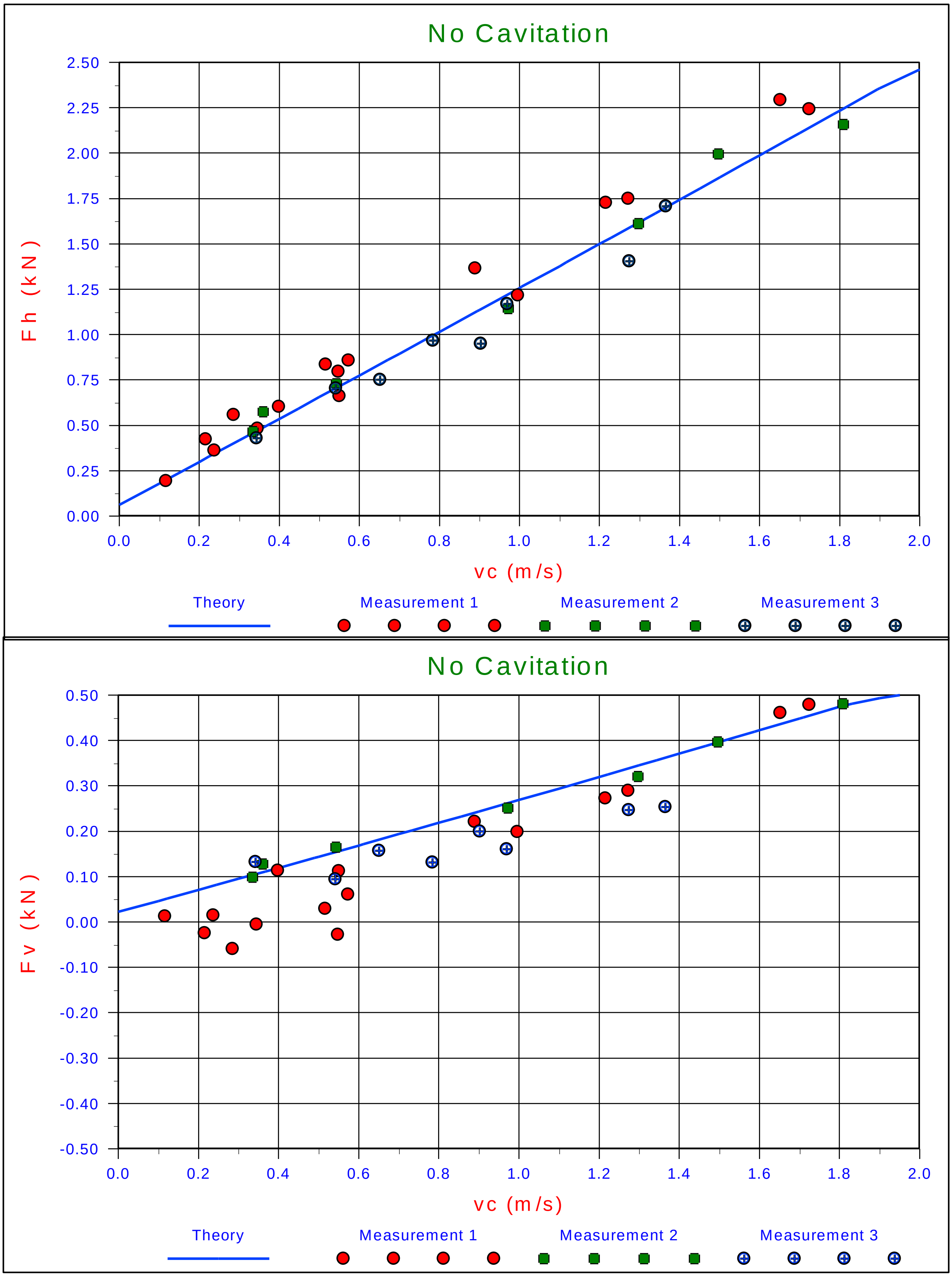

Figure L-23: α=45°, h_i=47 mm, h_b=141 mm.

The cutting forces F_h and F_v on the blade. Experiments in 200 μm sand, with **α**=45°, **β**=30°, **φ**=38°, **δ**=30°, n_i=38.53%, n_{max}=43.88%, k_i=0.000165 m/s, k_{max}=0.000320 m/s, h_i=47 mm, h_b=141 mm, **w**=0.2 m, **z**=0.6 m and a non-cavitating cutting process.

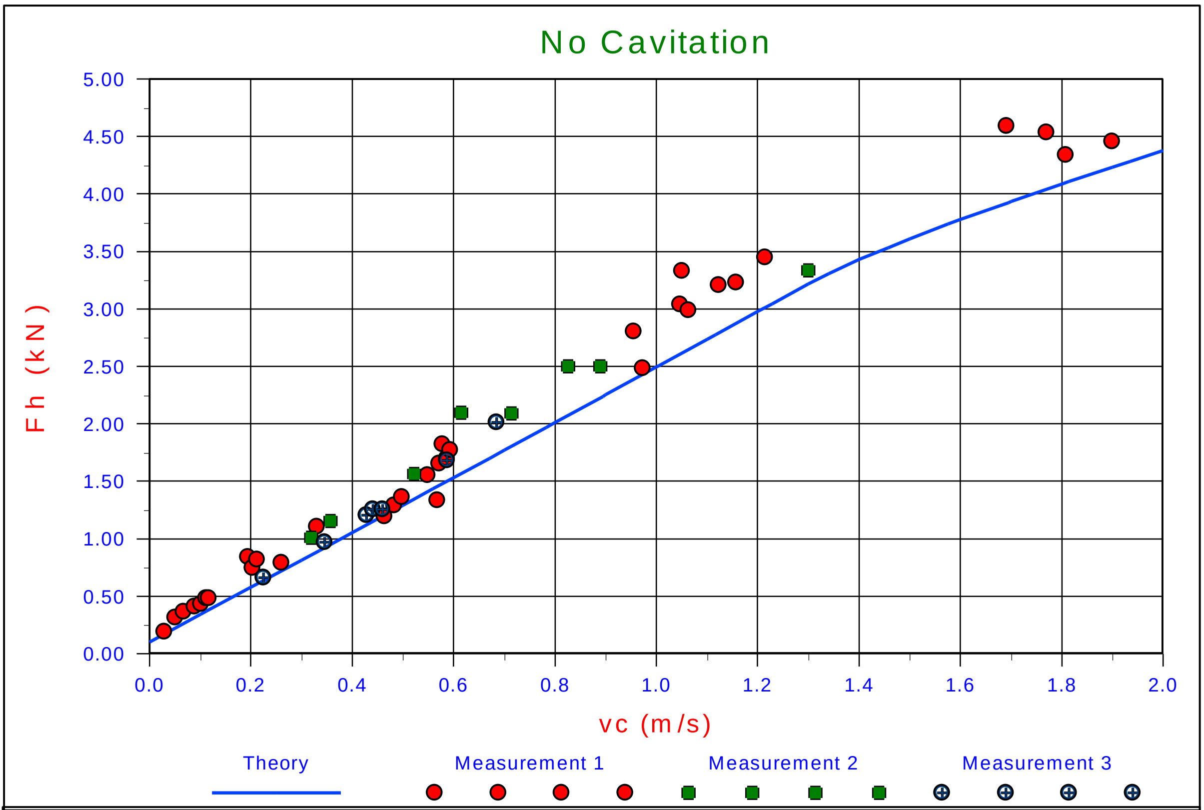

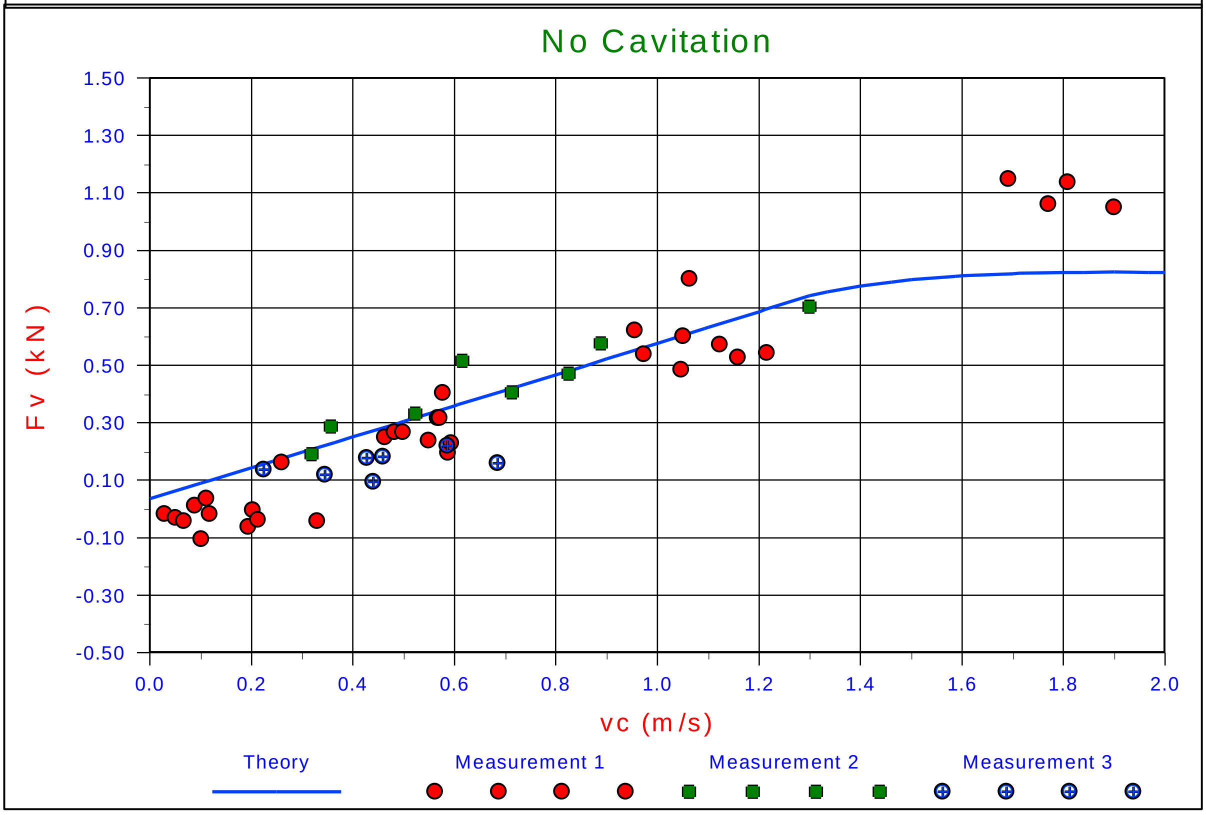

Figure L-24: α=45°, h_i=70 mm, h_b=141 mm.

The cutting forces $\mathbf{F_h}$ and $\mathbf{F_v}$ on the blade. Experiments in 200 μm sand, with **α**=45°, **β**=30º, **φ**=38º, **δ**=30º, $\mathbf{n_i}$=38.53%, $\mathbf{n_{max}}$=43.88%, $\mathbf{k_i}$=0.000165 m/s, $\mathbf{k_{max}}$=0.000320 m/s, $\mathbf{h_i}$=70 mm, $\mathbf{h_b}$=141 mm, **w**=0.2 m, **z**=0.6 m and a non-cavitating cutting process.

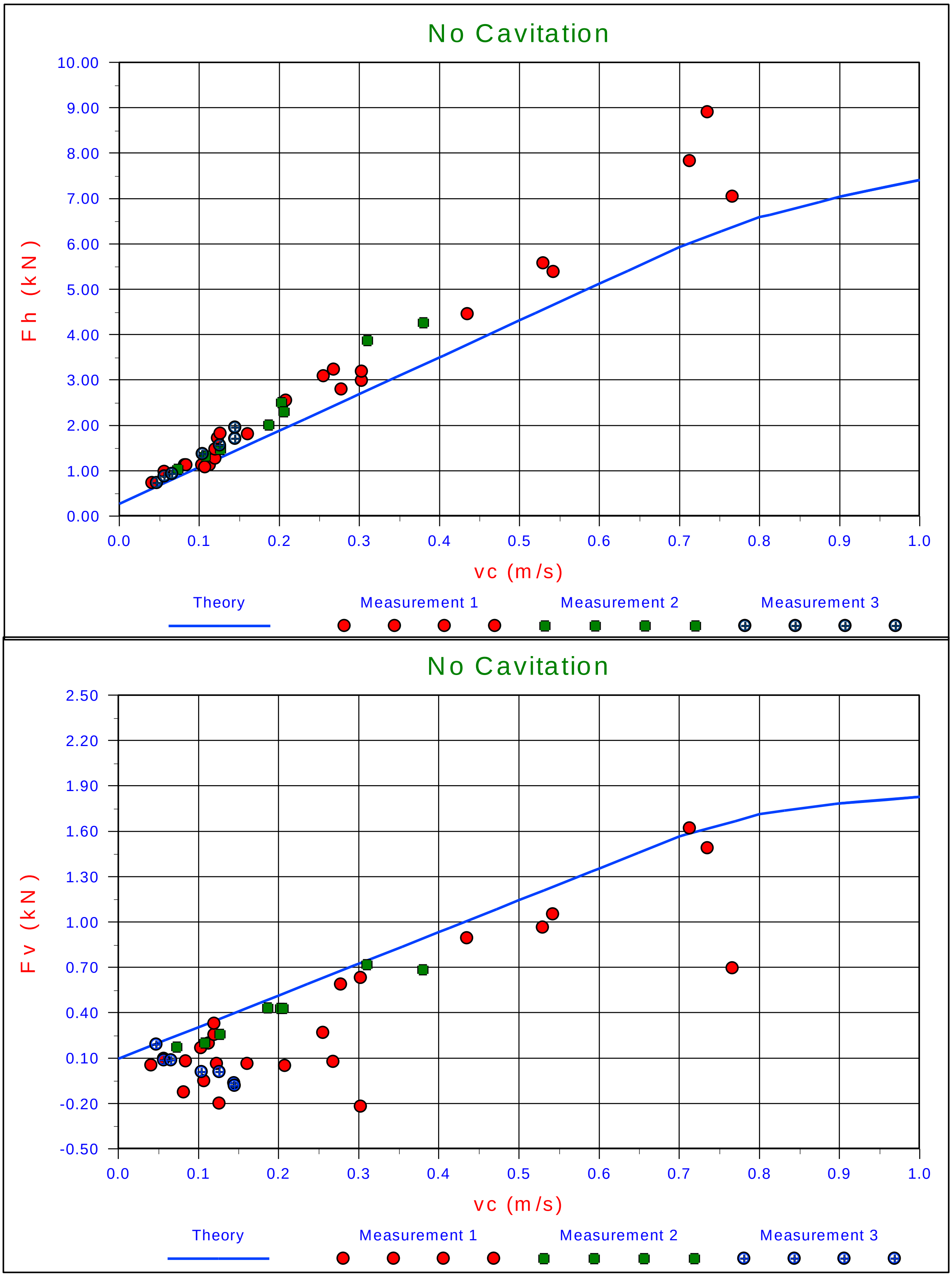

Figure L-25: α=45°, h_i=141 mm, h_b=141 mm.

The cutting forces $\mathbf{F_h}$ and $\mathbf{F_v}$ on the blade. Experiments in 200 µm sand, with **α**=45°, **β**=30º, **φ**=38º, **δ**=30º, $\mathbf{n_i}$=38.53%, $\mathbf{n_{max}}$=43.88%, $\mathbf{k_i}$=0.000165 m/s, $\mathbf{k_{max}}$=0.000320 m/s, $\mathbf{h_i}$=141 mm, $\mathbf{h_b}$=141 mm, **w**=0.2 m, **z**=0.6 m and a non-cavitating cutting process.

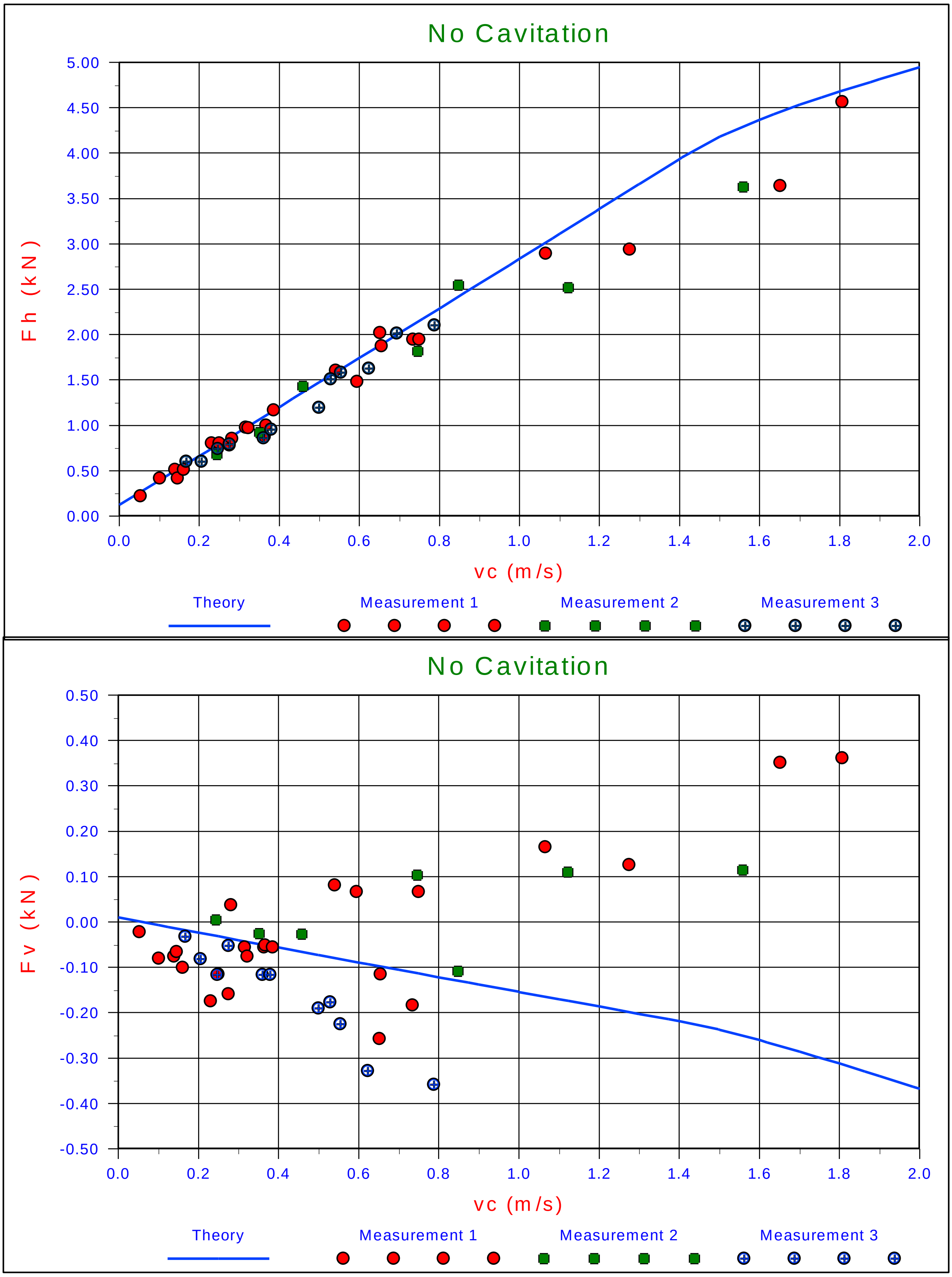

Figure L-26: α=60°, h_i=58 mm, h_b=173 mm.

The cutting forces $\mathbf{F_h}$ and $\mathbf{F_v}$ on the blade. Experiments in 200 μm sand, with **α**=45°, **β**=30º, **φ**=38º, **δ**=30º, $\mathbf{n_i}$=38.53%, $\mathbf{n_{max}}$=43.88%, $\mathbf{k_i}$=0.000165 m/s, $\mathbf{k_{max}}$=0.000320 m/s, $\mathbf{h_i}$=58 mm, $\mathbf{h_b}$=173 mm, **w**=0.2 m, **z**=0.6 m and a non-cavitating cutting process.

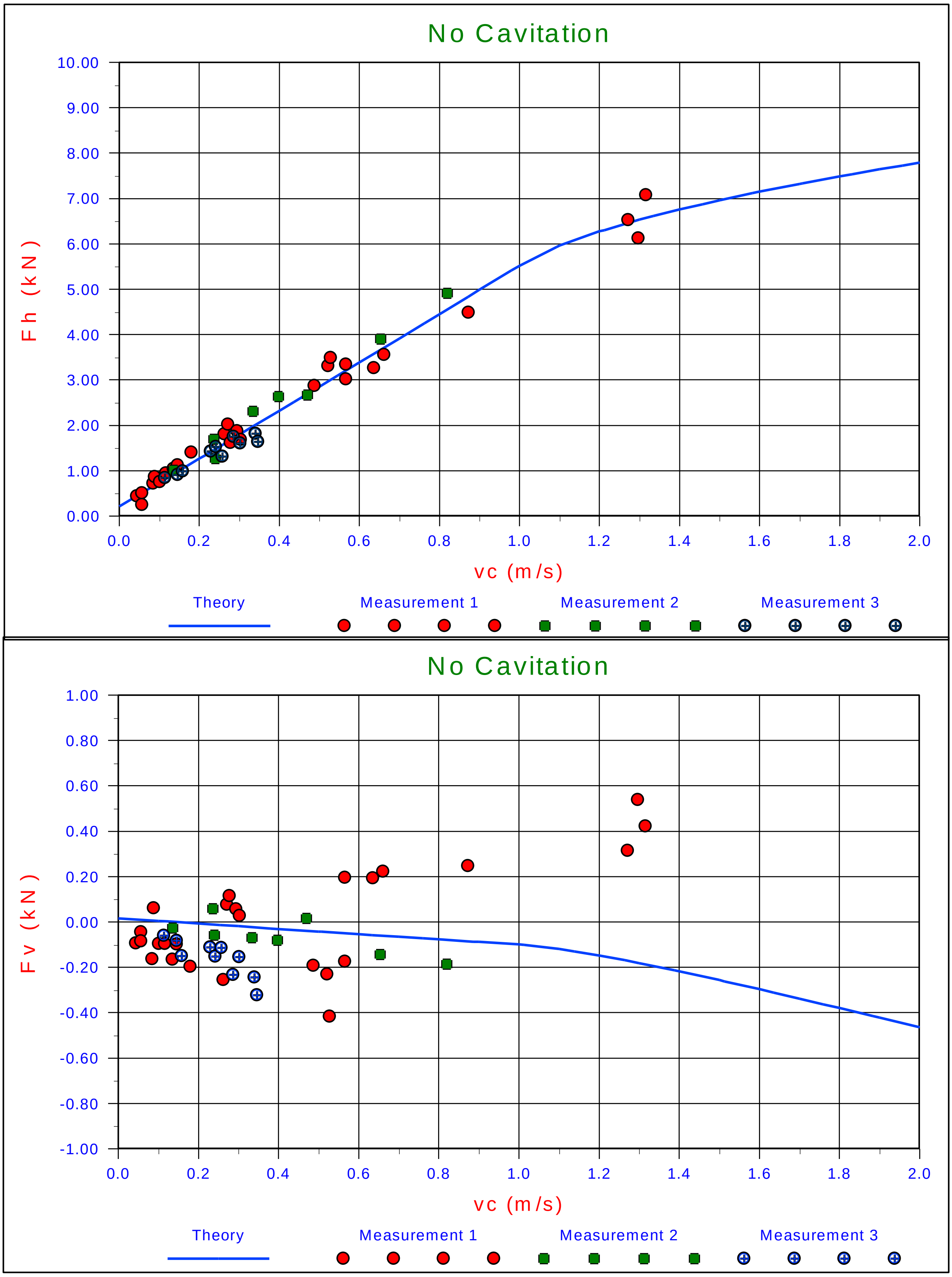

Figure L-27: α=60°, h_i=87 mm, h_b=173 mm.

The cutting forces $\mathbf{F_h}$ and $\mathbf{F_v}$ on the blade. Experiments in 200 μm sand, with **α**=45°, **β**=30º, **φ**=38º, **δ**=30º, $\mathbf{n_i}$=38.53%, $\mathbf{n_{max}}$=43.88%, $\mathbf{k_i}$=0.000165 m/s, $\mathbf{k_{max}}$=0.000320 m/s, $\mathbf{h_i}$=87 mm, $\mathbf{h_b}$=173 mm, **w**=0.2 m, **z**=0.6 m and a non-cavitating cutting process.

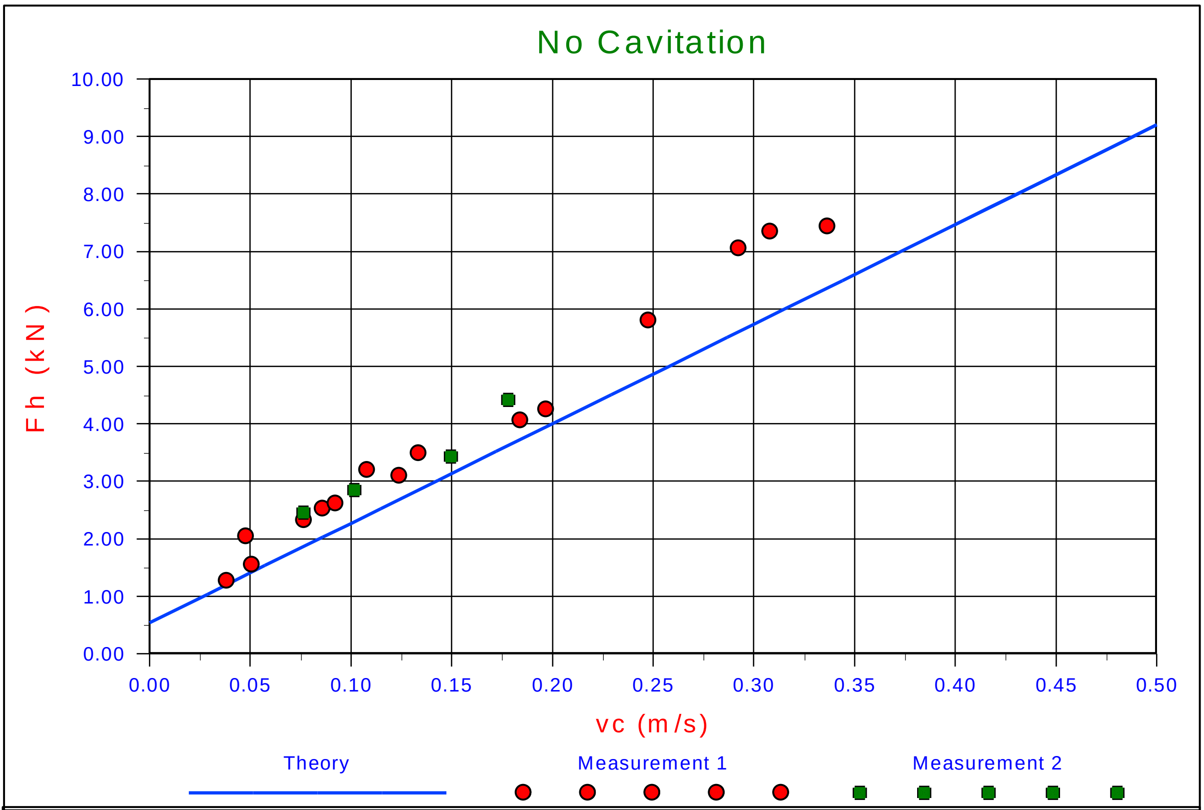

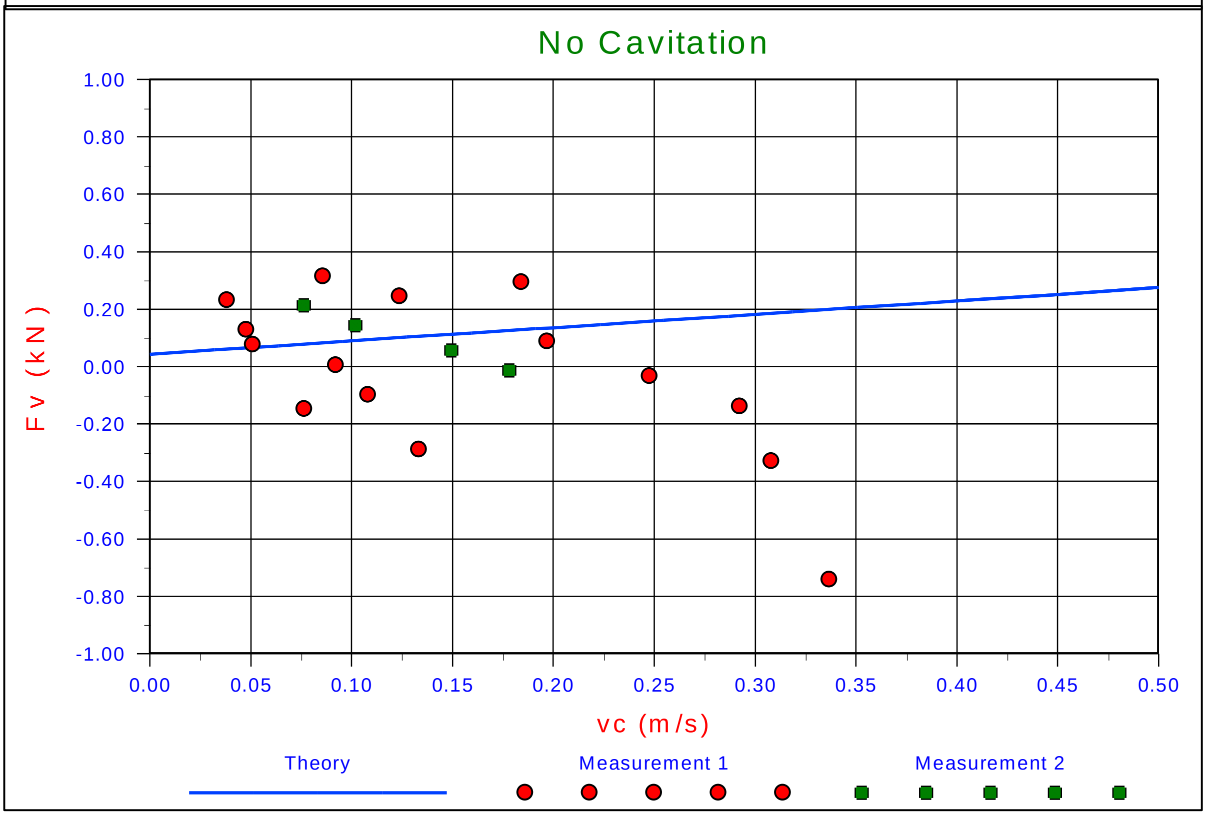

Figure L-28: α=60°, h_i=173 mm, h_b=173 mm.

The cutting forces $\mathbf{F_h}$ and $\mathbf{F_v}$ on the blade. Experiments in 200 μm sand, with **α**=45°, **β**=30º, **φ**=38º, **δ**=30º, $\mathbf{n_i}$=38.53%, $\mathbf{n_{max}}$=43.88%, $\mathbf{k_i}$=0.000165 m/s, $\mathbf{k_{max}}$=0.000320 m/s, $\mathbf{h_i}$=173 mm, $\mathbf{h_b}$=173 mm, **w**=0.2 m, **z**=0.6 m and a non-cavitating cutting process.

Appendix M: The Snow Plough Effect

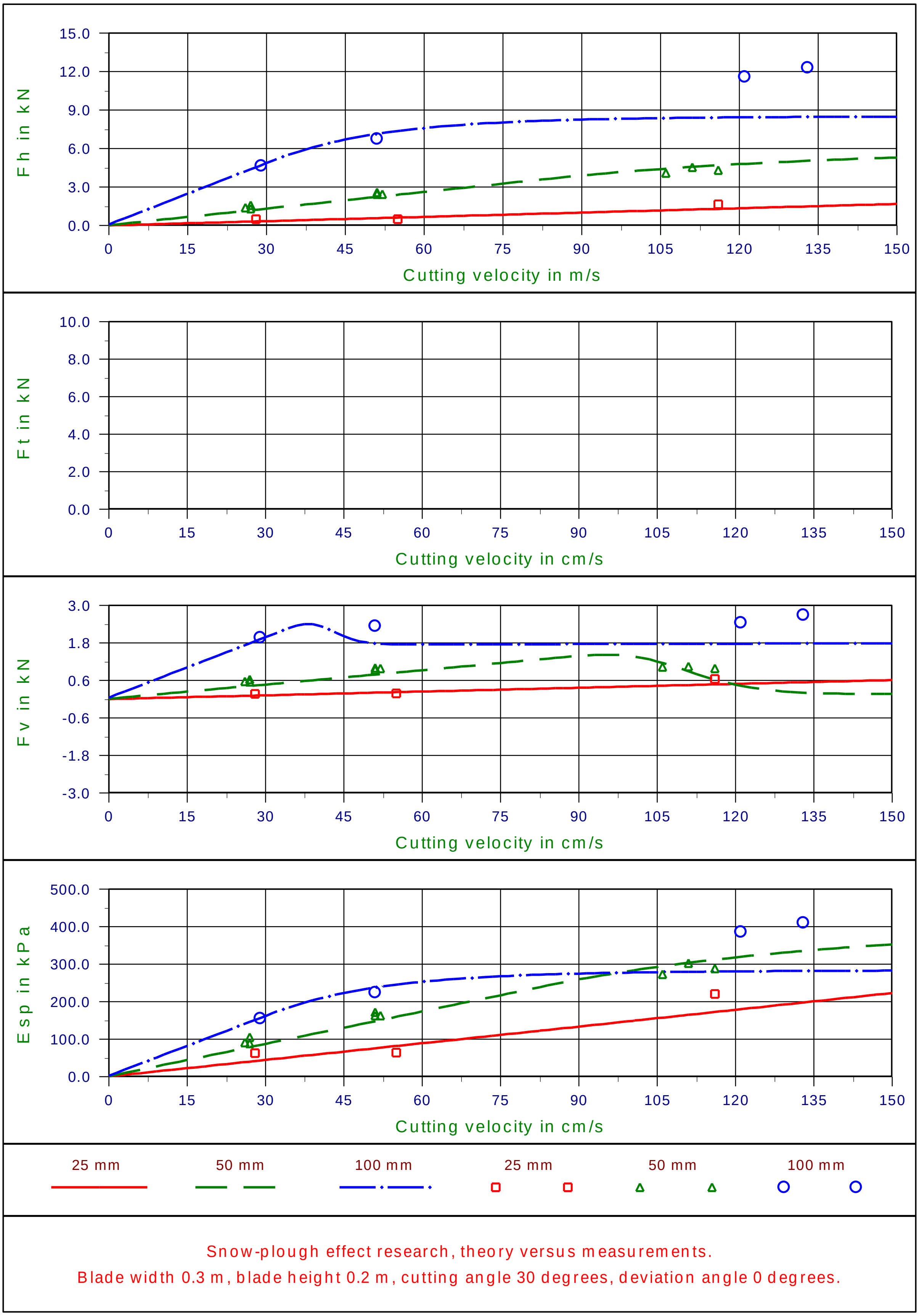

Figure M-1: Blade angle 30 degrees – Deviation angle 00 degrees

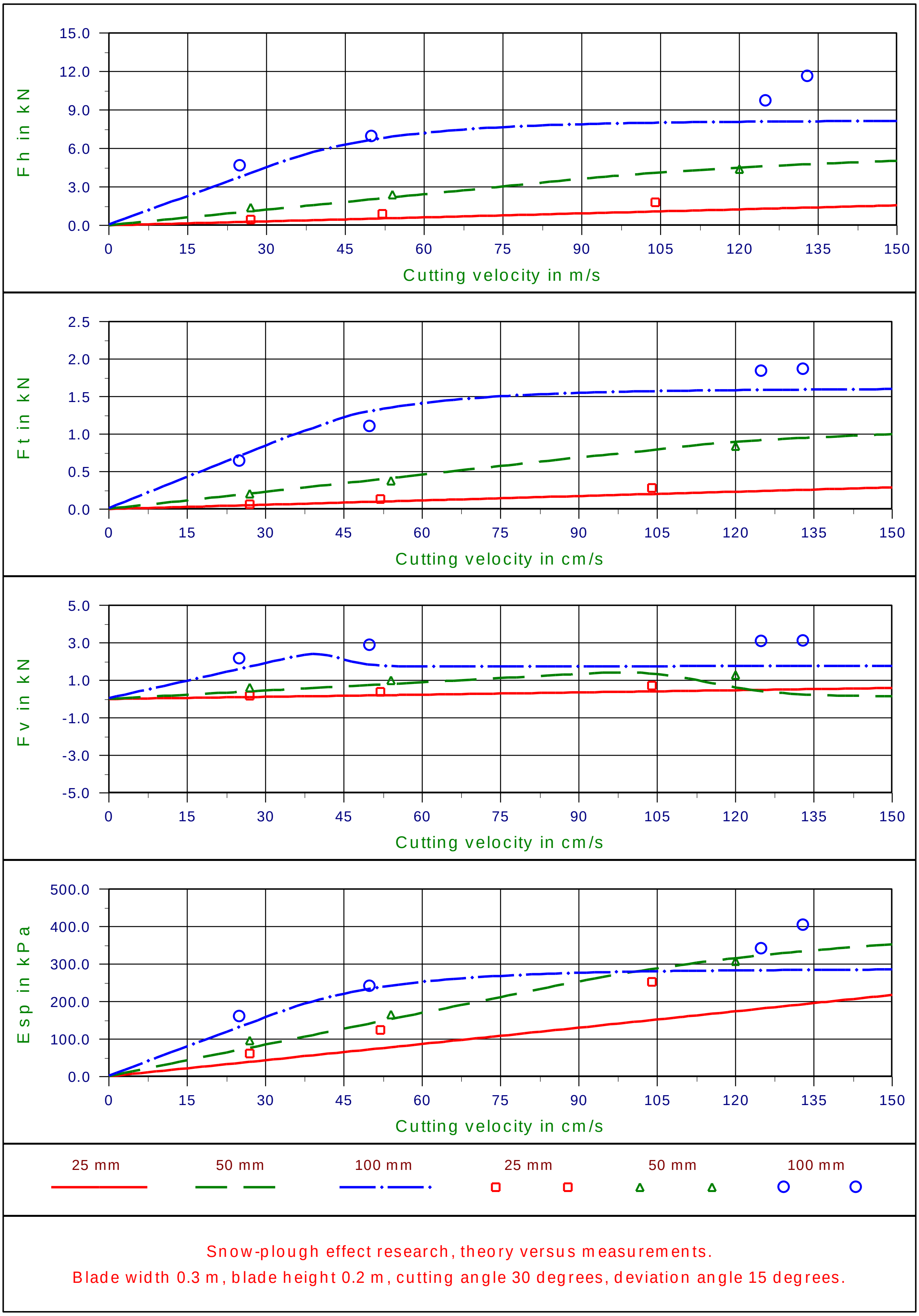

Figure M-2: Blade angle 30 degrees – Deviation angle 15 degrees

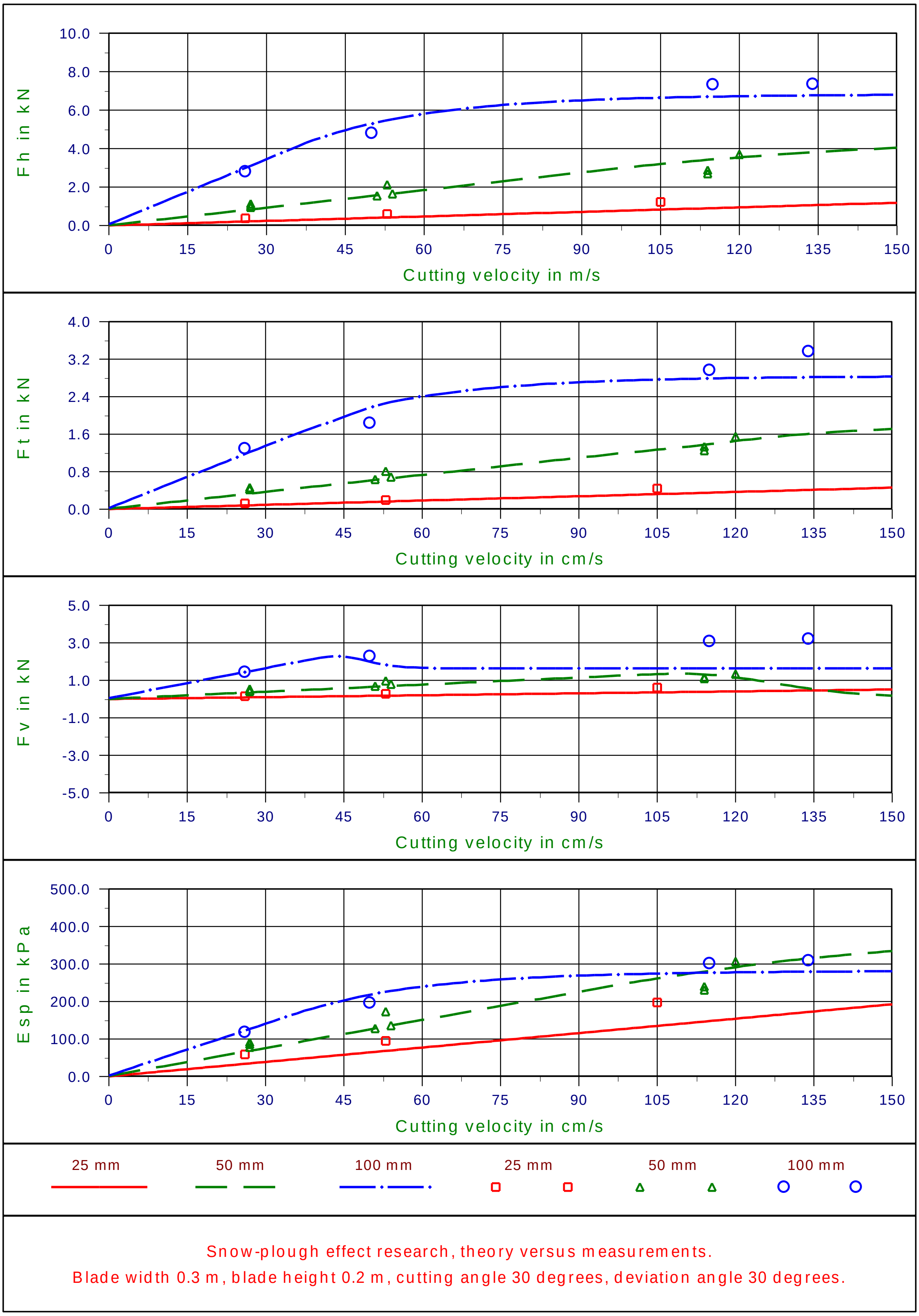

Figure M-3: Blade angle 30 degrees – Deviation angle 30 degrees

In the snow-plough experiments the blade was 0.3 m wide and 0.2 m heigh, so the blade height $\mathbf{h_b=0.2\cdot sin(\alpha)}$. The 105 μm sand from Appendix K: The Properties of the 105 μm Sand was used.

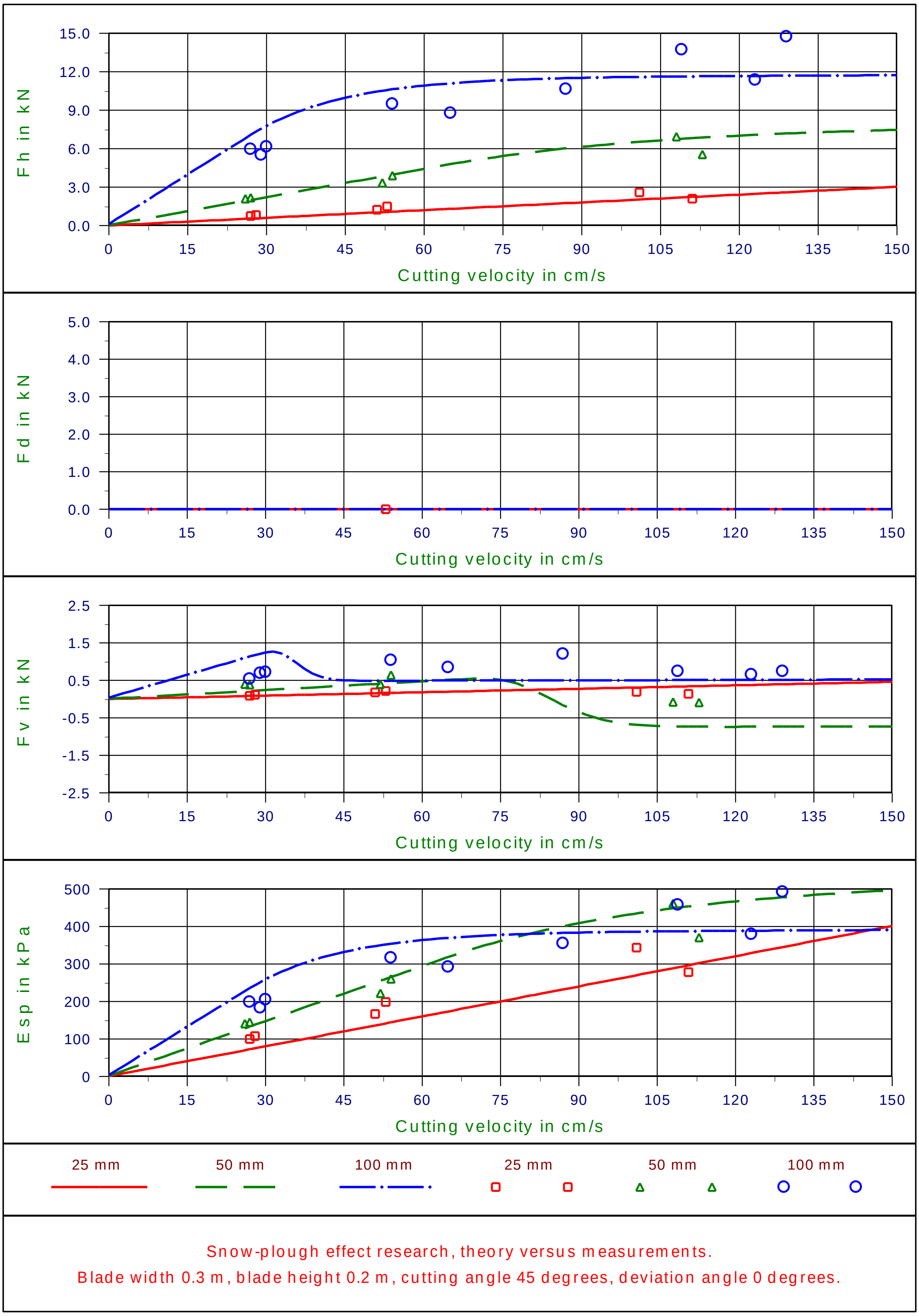

Figure M-4: Blade angle 45 degrees – Deviation angle 00 degrees

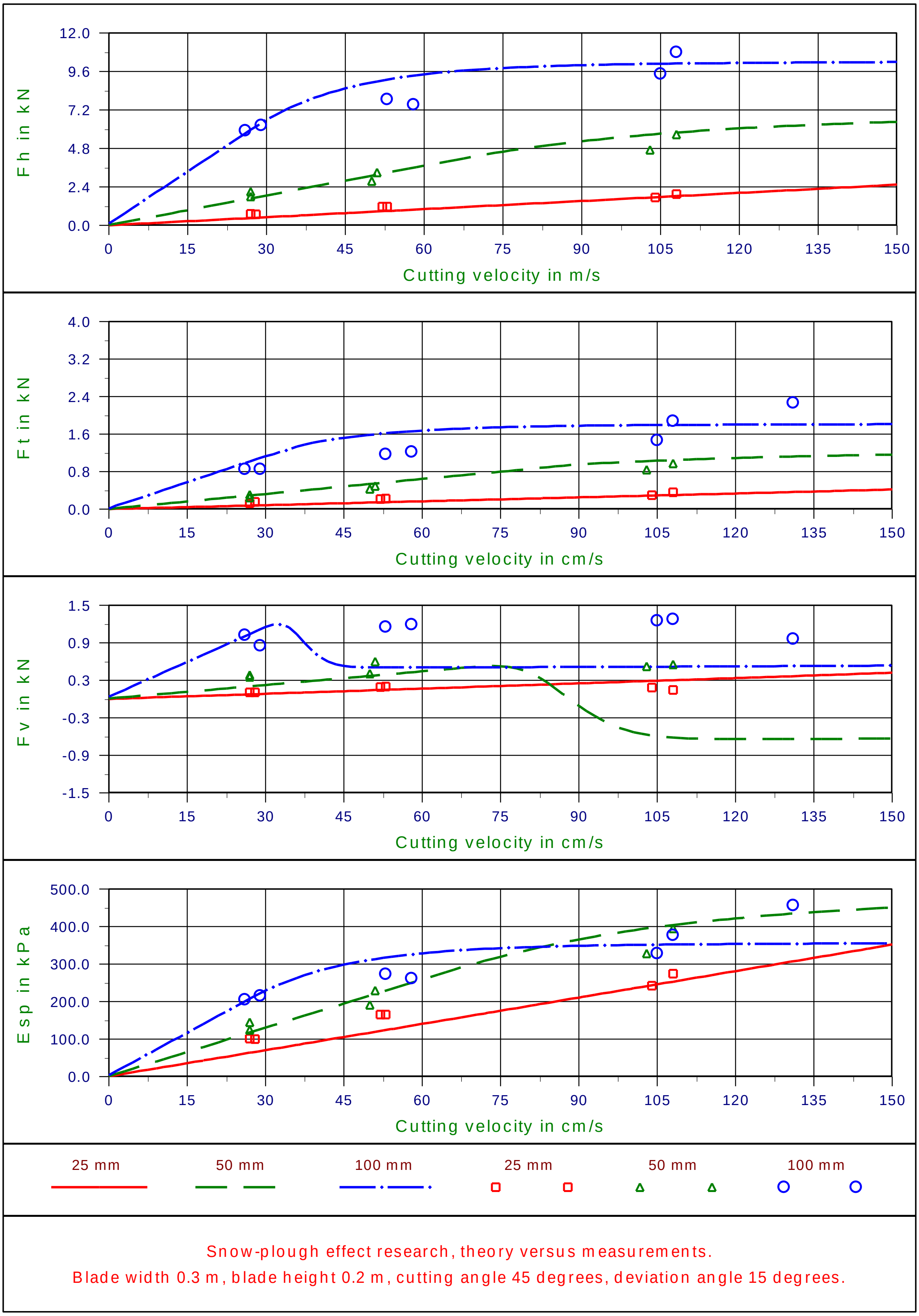

Figure M-5: Blade angle 45 degrees – Deviation angle 15 degrees

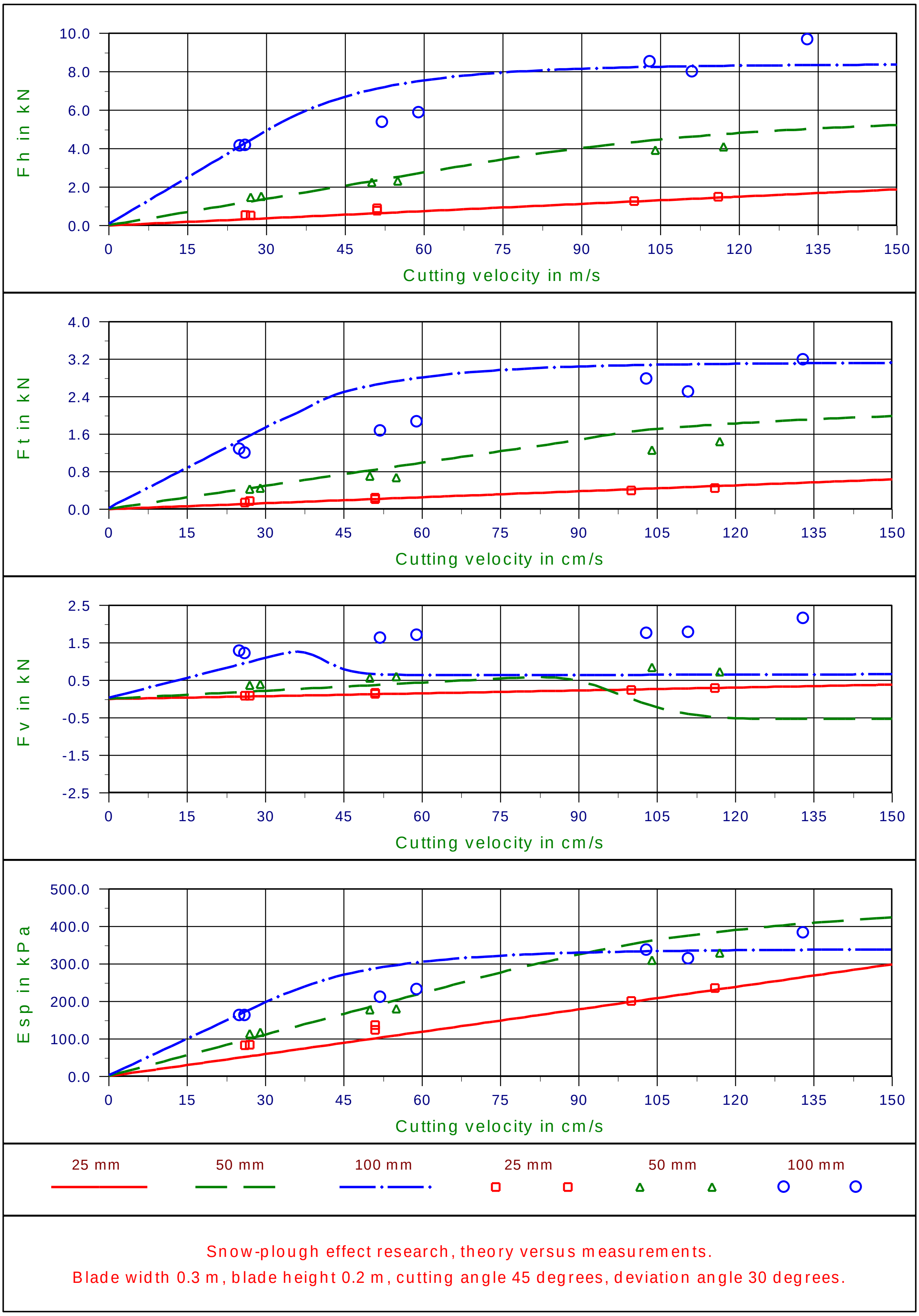

Figure M-6: Blade angle 45 degrees – Deviation angle 30 degrees

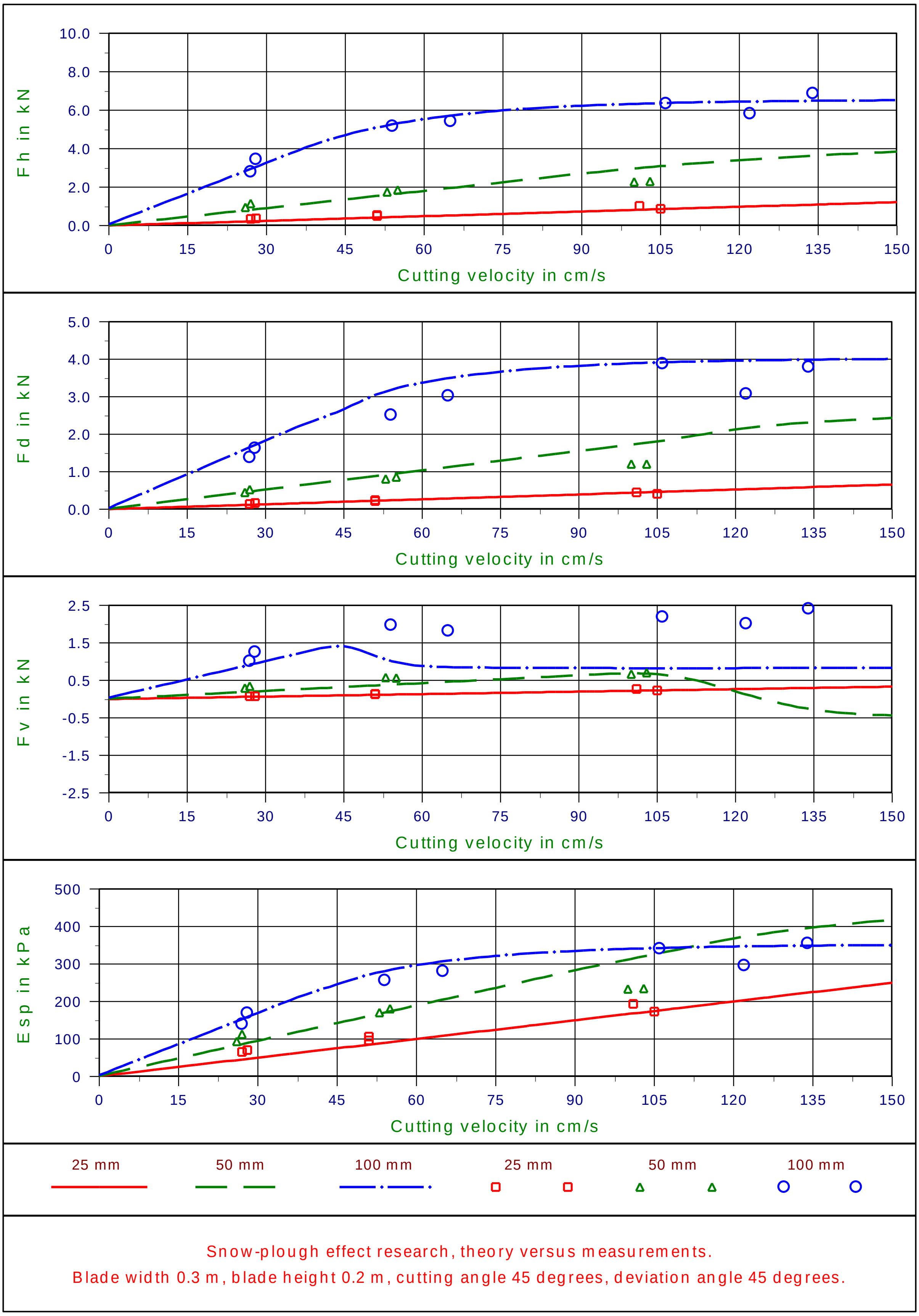

Figure M-7: Blade angle 45 degrees – Deviation angle 45 degrees

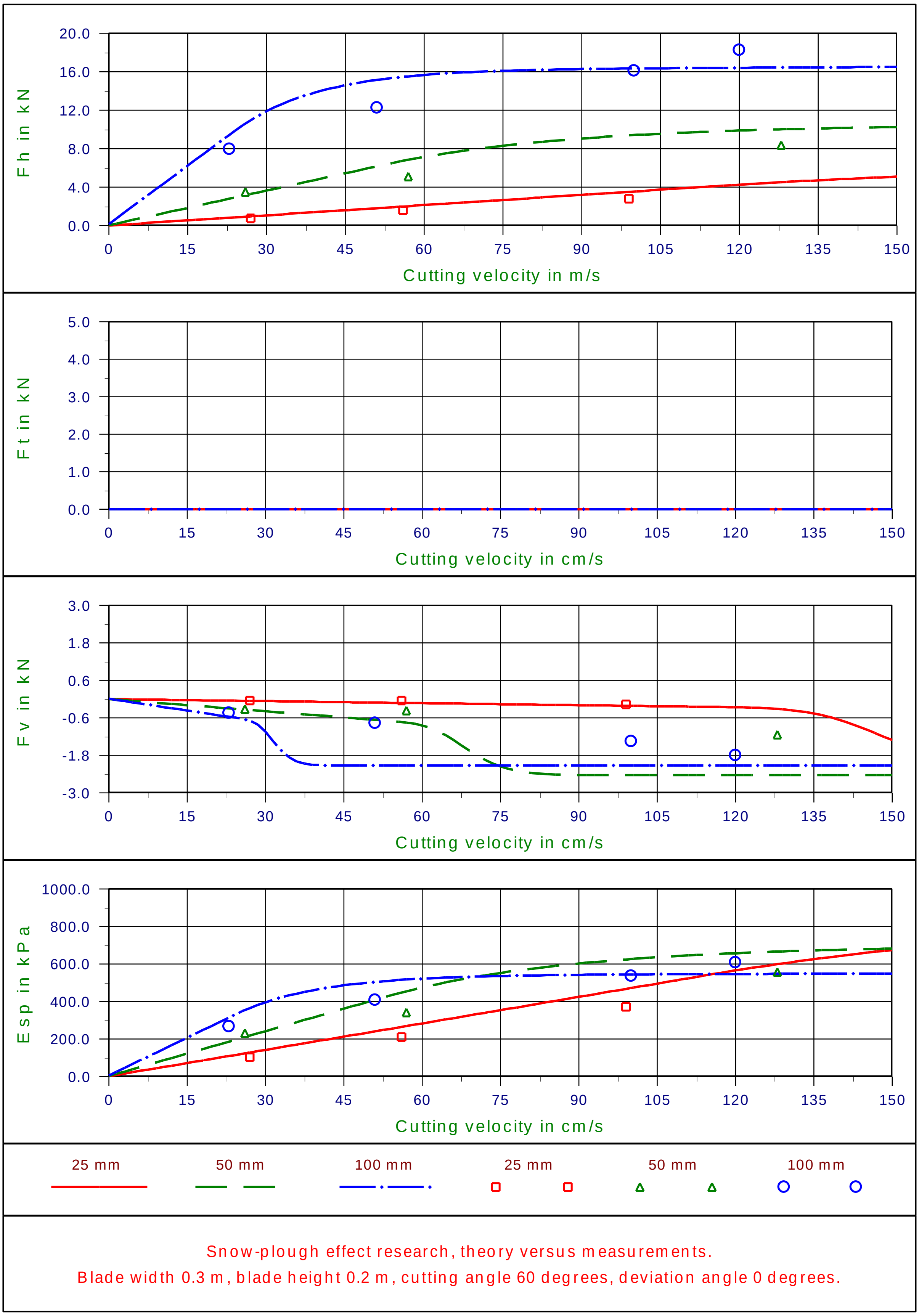

Figure M-8: Blade angle 60 degrees – Deviation angle 00 degrees

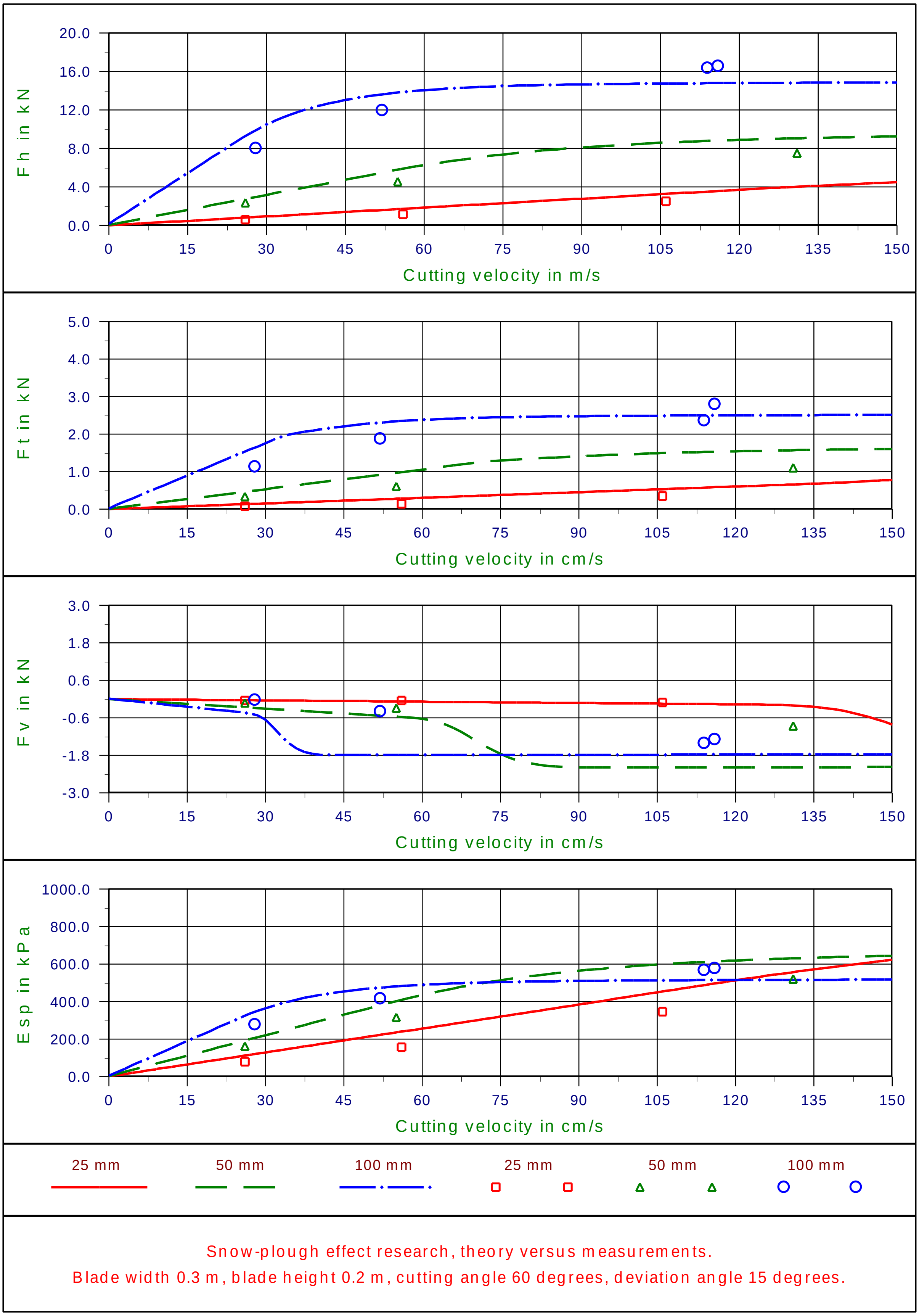

Figure M-9: Blade angle 60 degrees – Deviation angle 15 degrees

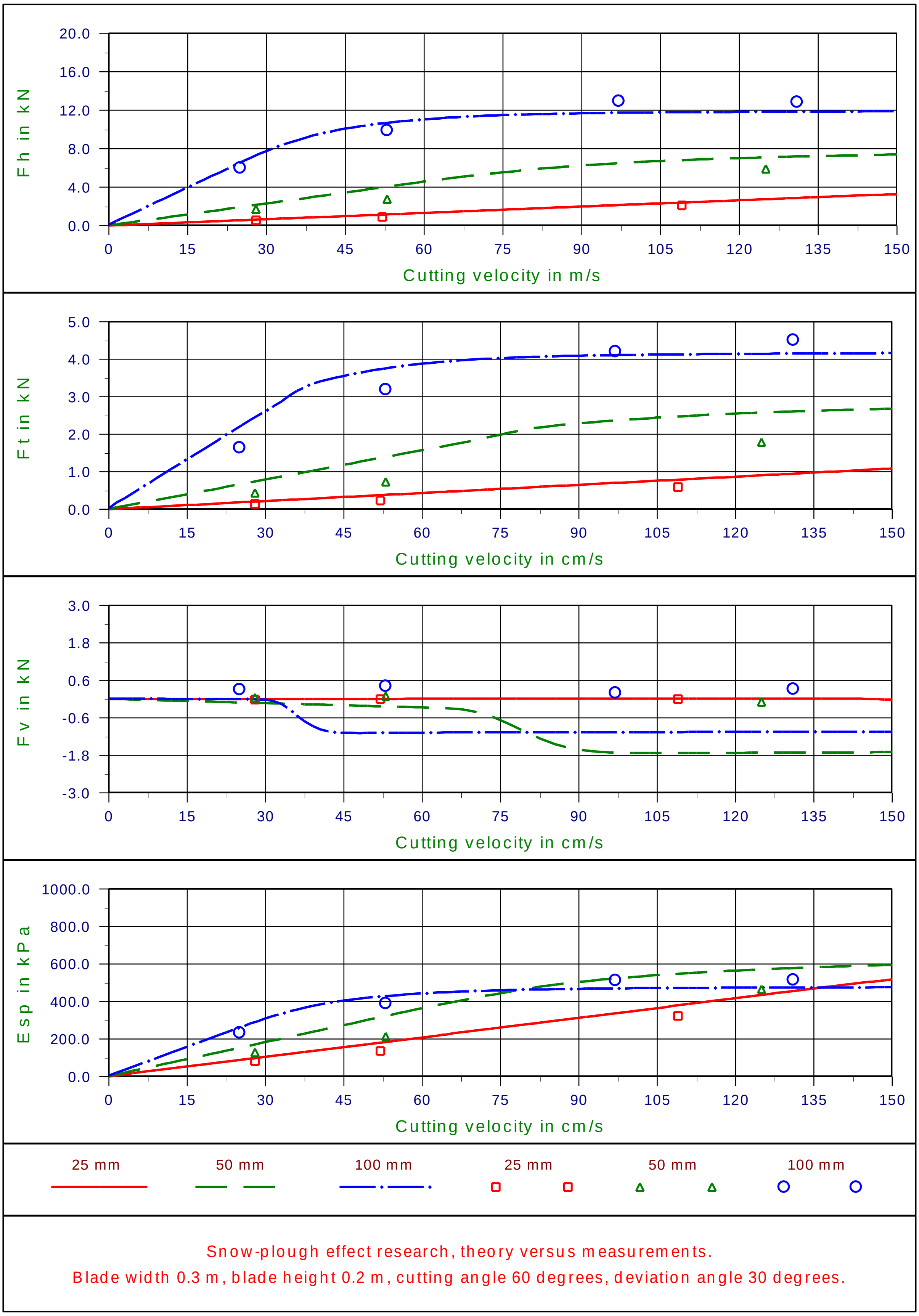

Figure M-10: Blade angle 60 degrees – Deviation angle 30 degrees

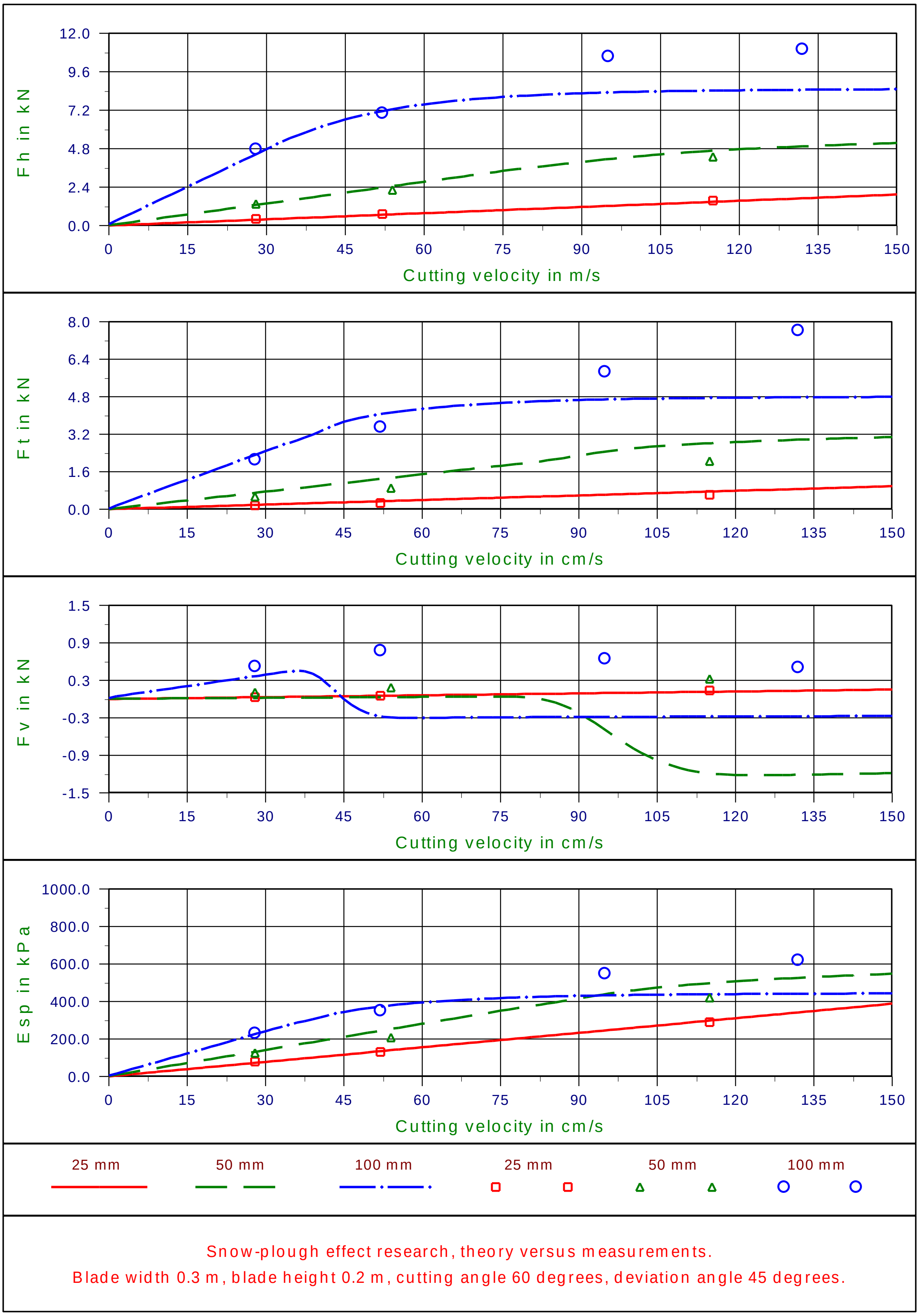

Figure M-11: Blade angle 60 degrees – Deviation angle 45 degrees

Appendix N: Specific Energy in Sand

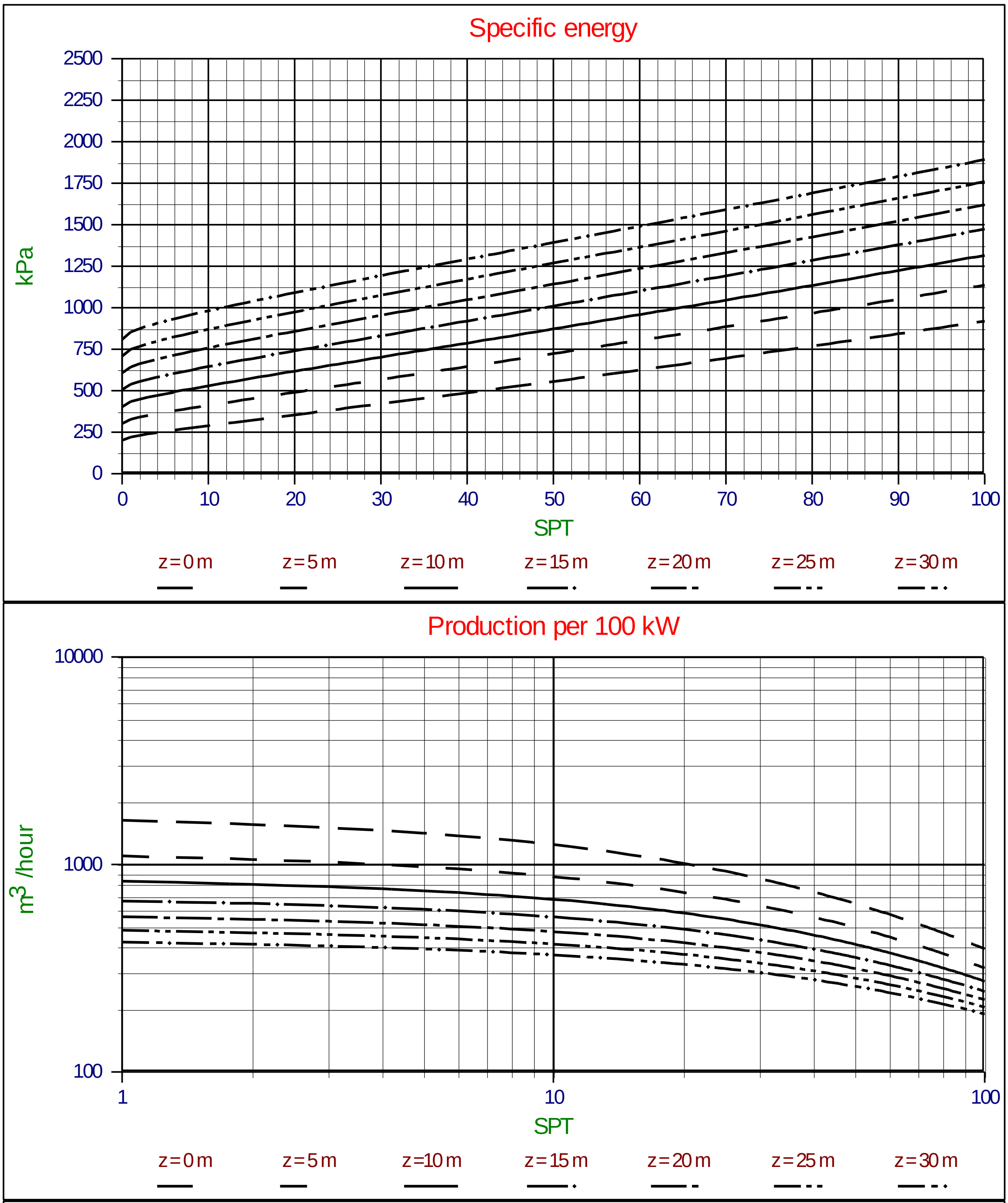

Specific energy and production for a 30 degree blade and a cavitating cutting process in sand as a function of the reduced SPT value.

Figure N-1: Specific energy and production in sand for a 30 degree blade.

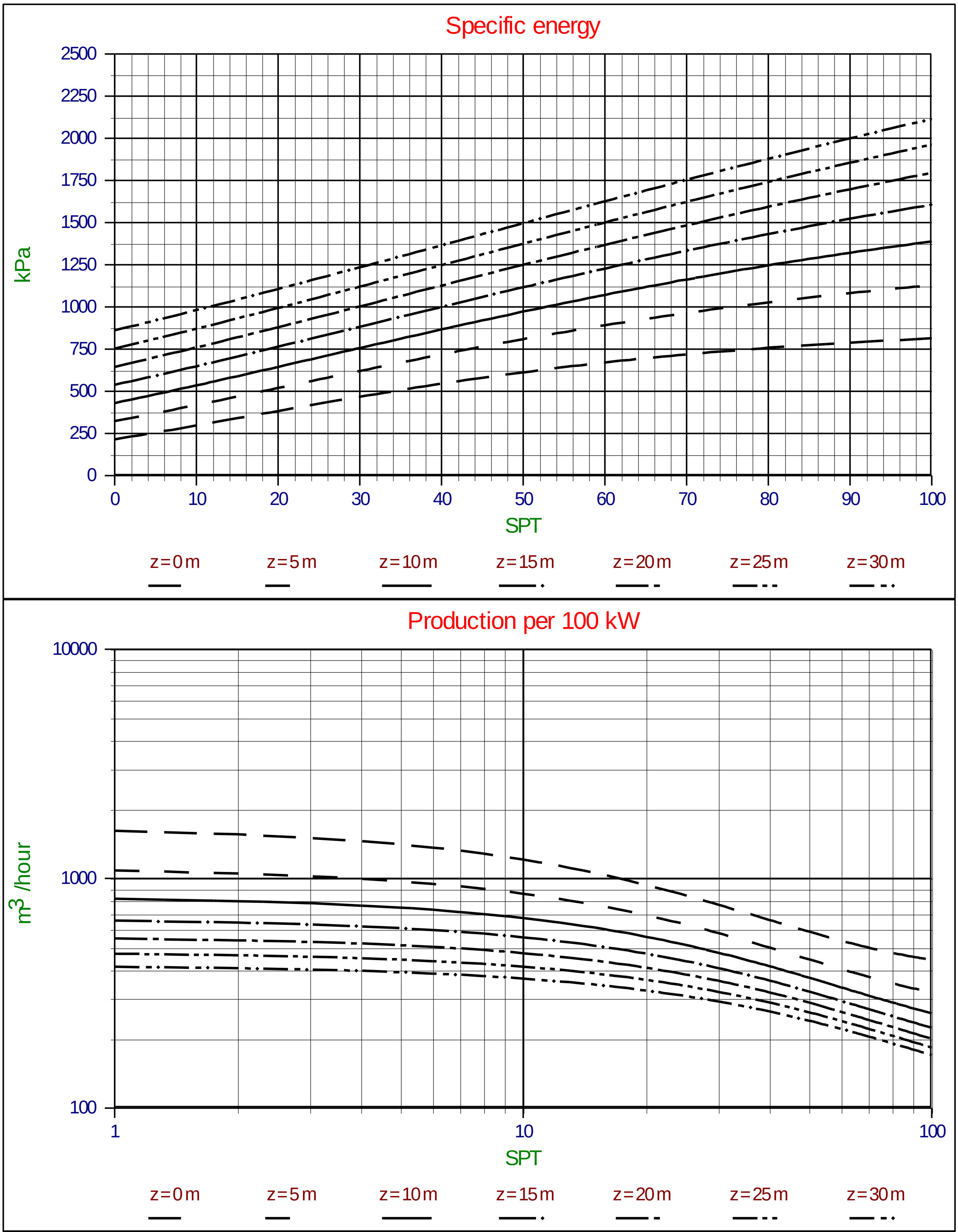

Specific energy and production for a 45 degree blade and a cavitating cutting process in sand as a function of the reduced SPT value.

Figure N-2: Specific energy and production in sand for a 45 degree blade.

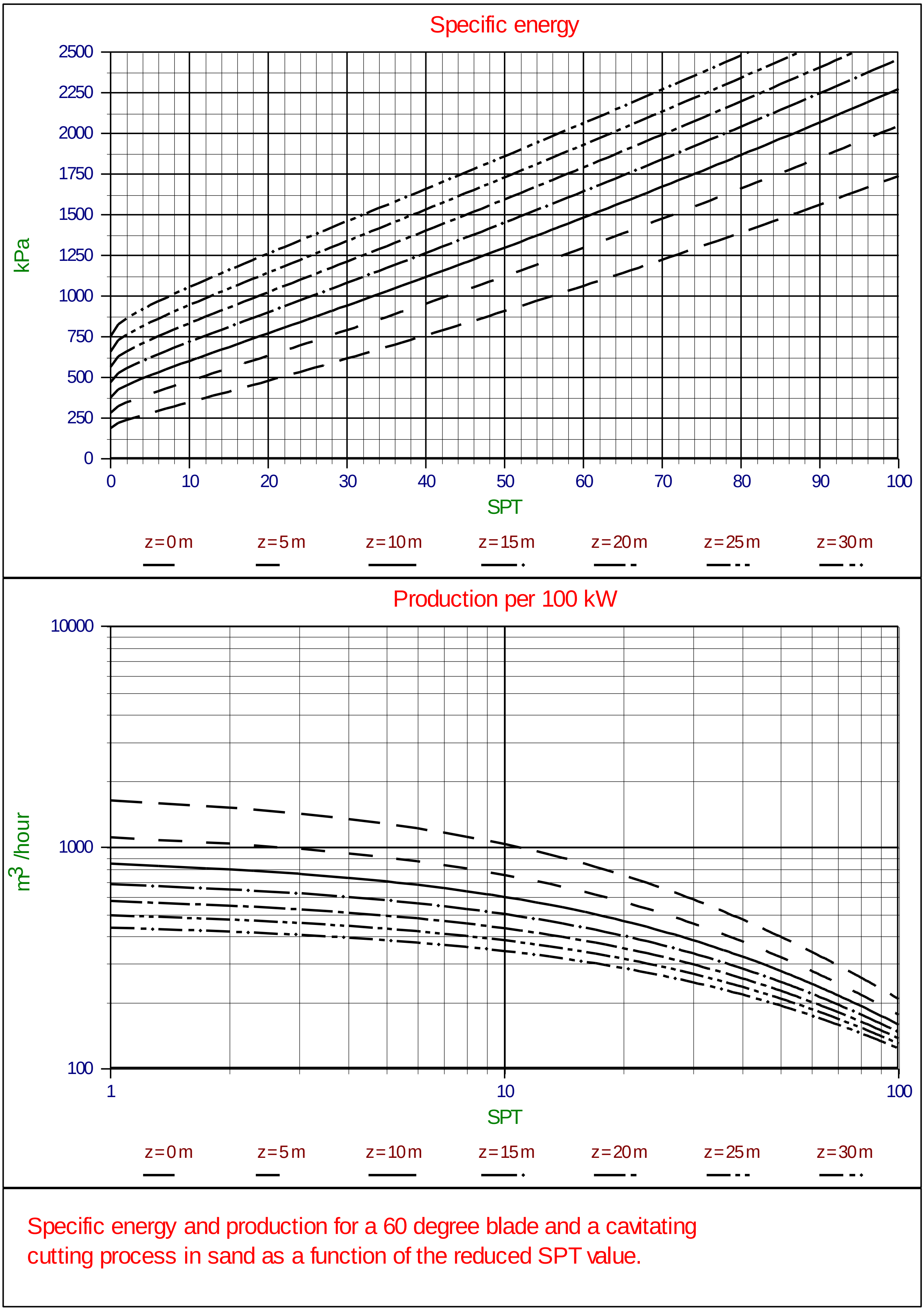

Figure N-3: Specific energy and production in sand for a 60 degree blade.

Appendix O: The Occurrence of a Wedge, Non-Cavitating

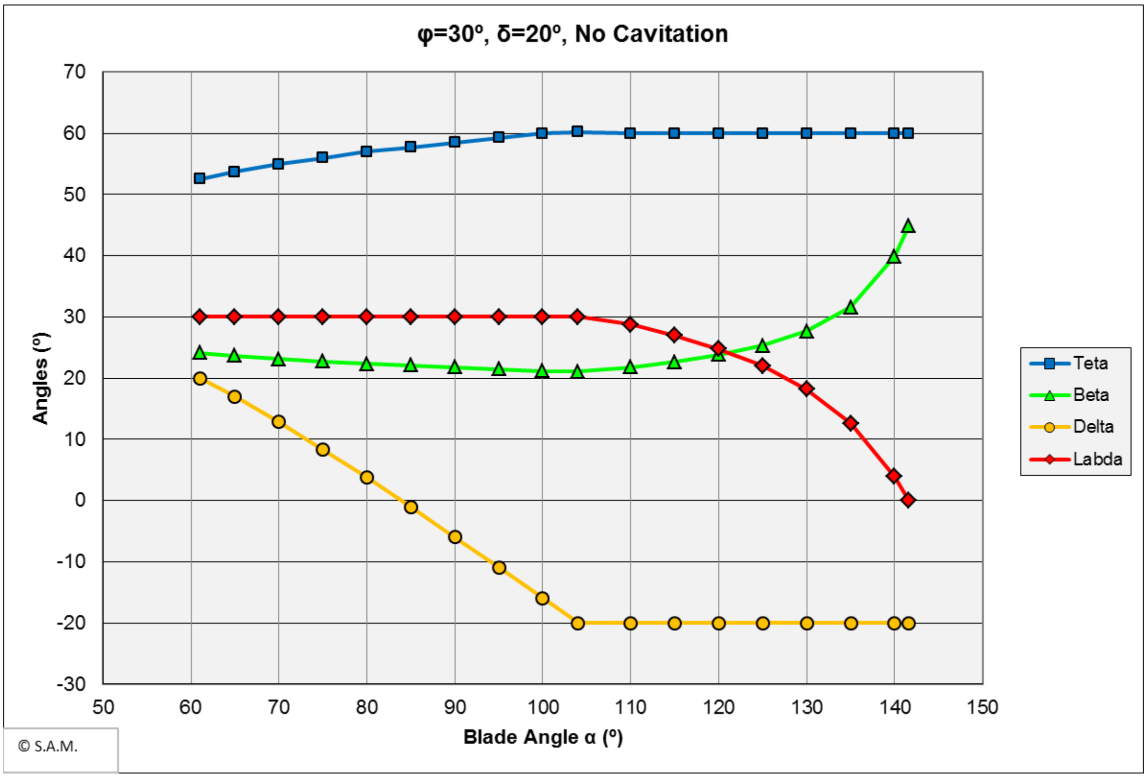

Figure O-1: No cavitation, the angles θ, β, δ_m and λ as a function of the blade angle α for φ=30° and δ=20°.

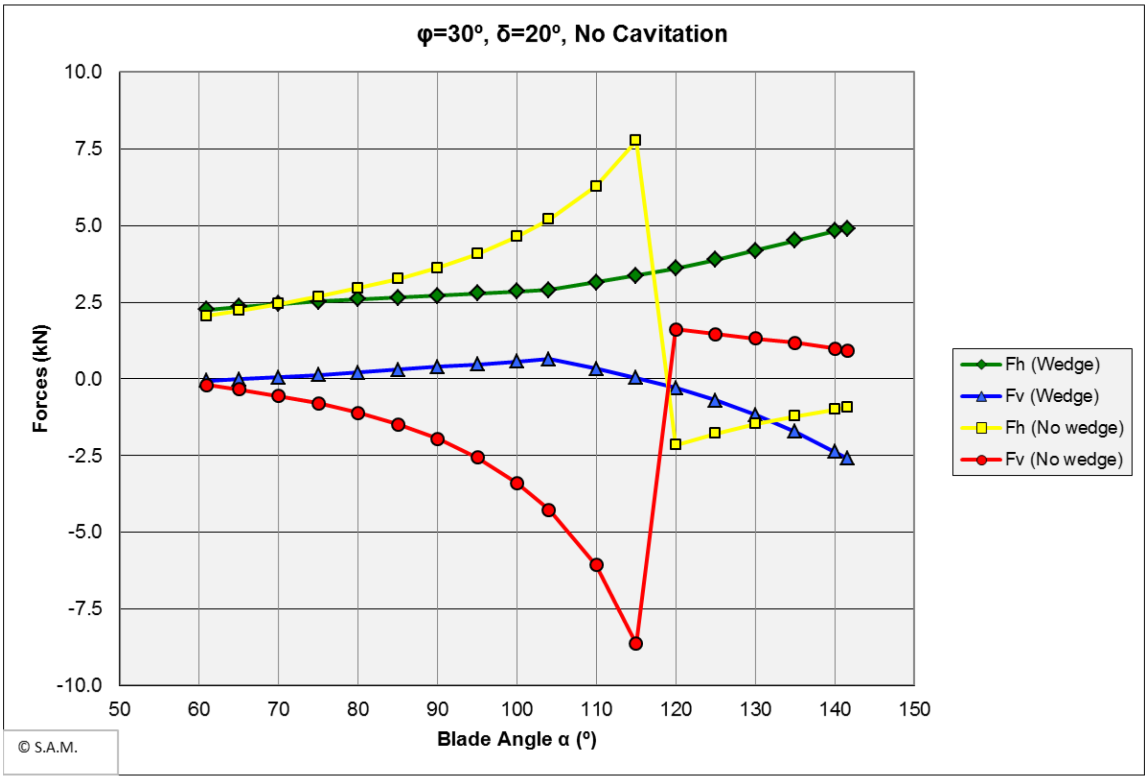

Figure O-2: No cavitation, the cutting forces as a function of the blade angle α for φ=30° and δ=20°.

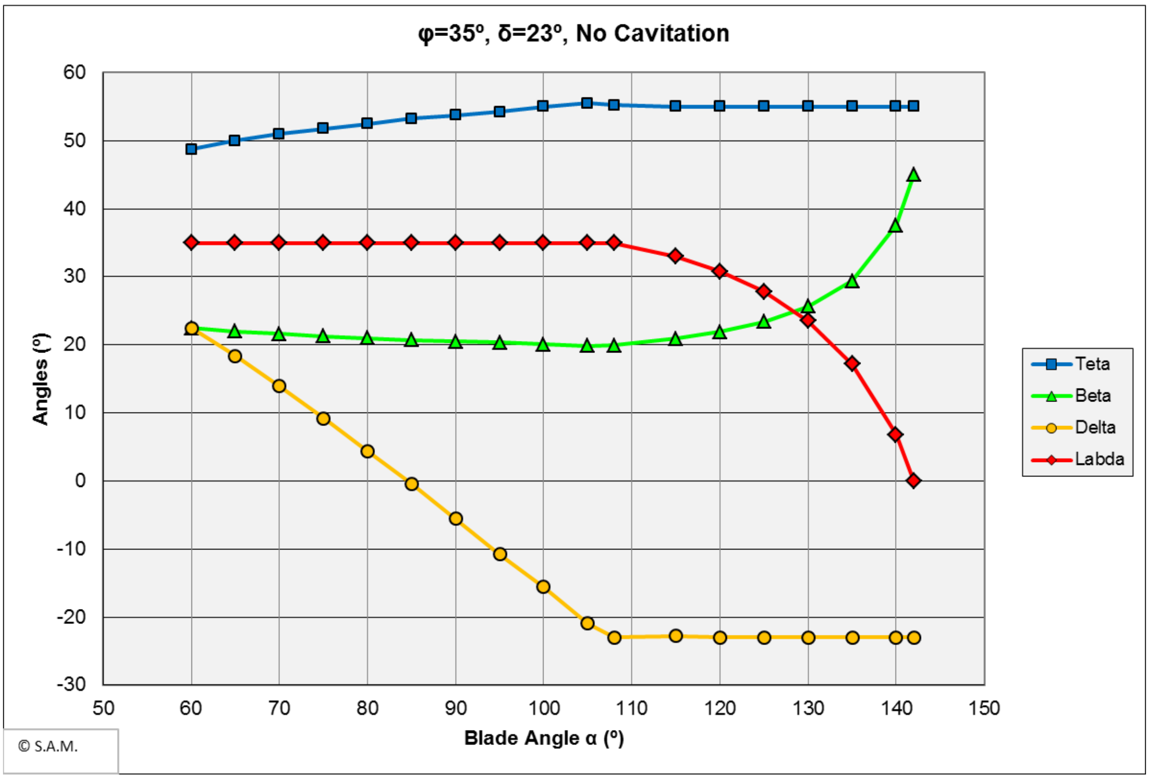

Figure O-3: No cavitation, the angles θ, β, δ_m and λ as a function of the blade angle α for φ=35° and δ=23°.

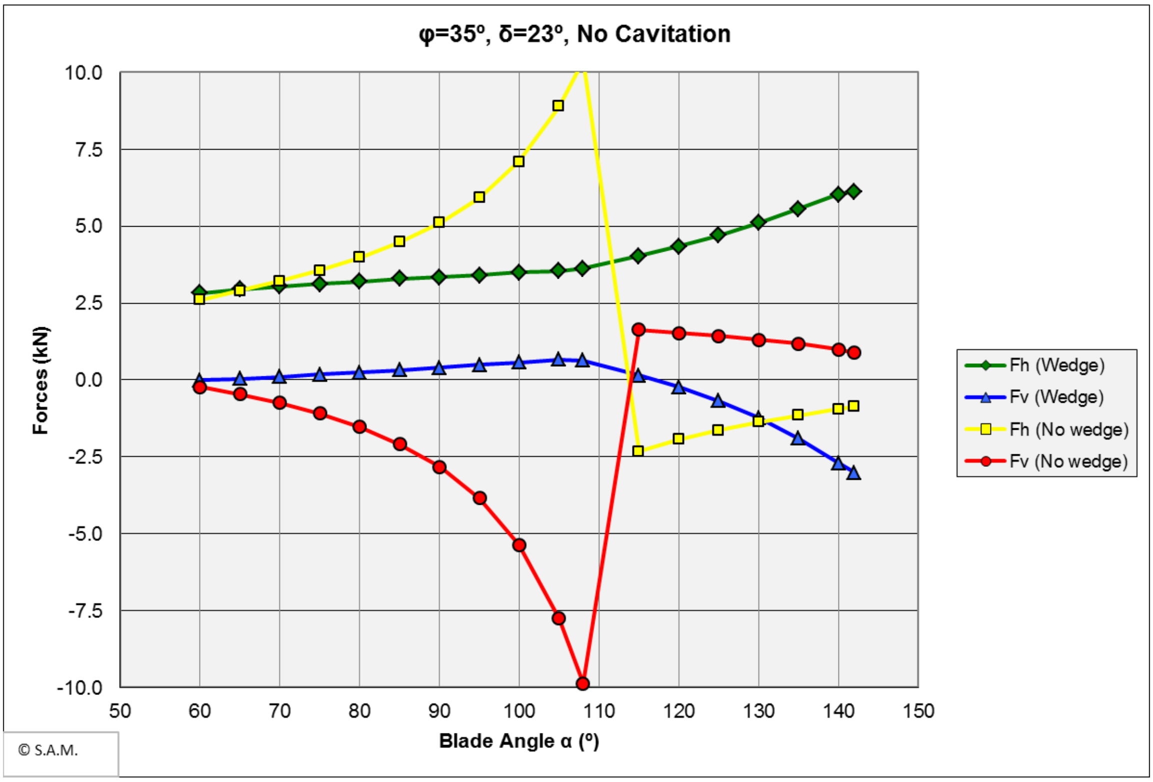

Figure O-4: No cavitation, the cutting forces as a function of the blade angle α for φ=35° and δ=23°.

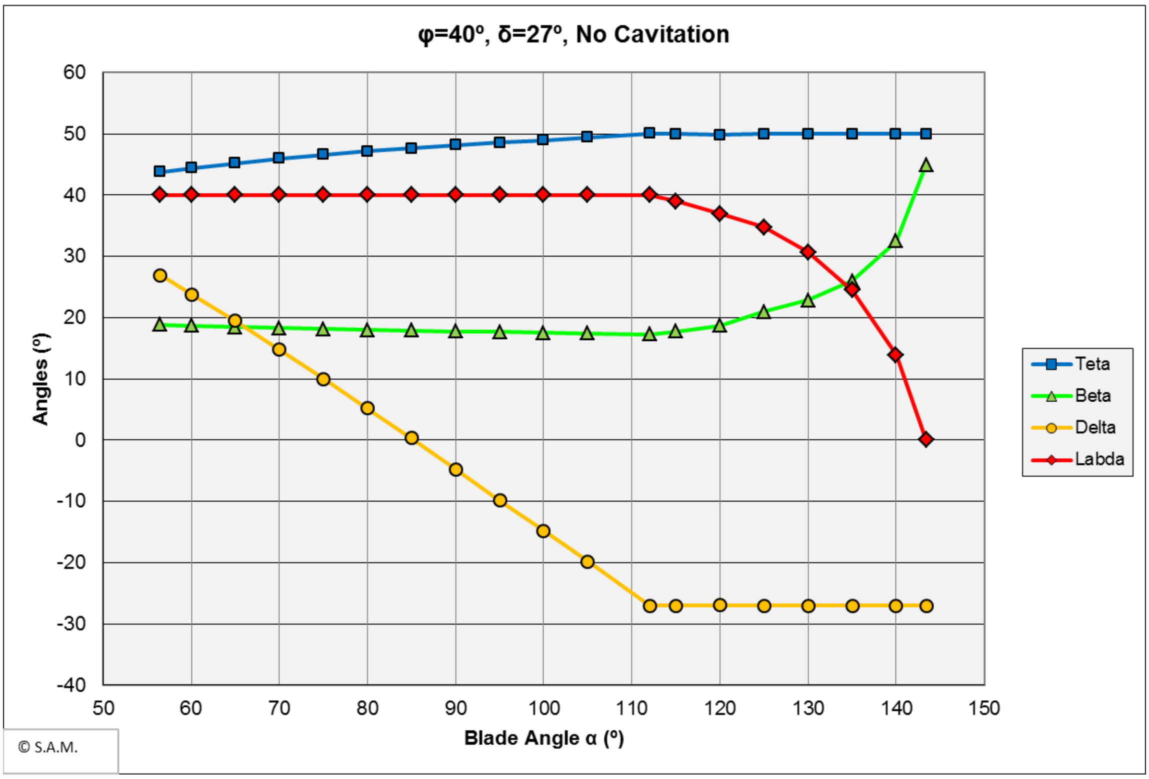

Figure O-5: No cavitation, the angles θ, β, δ_m and λ as a function of the blade angle α for φ=40° and δ=27°.

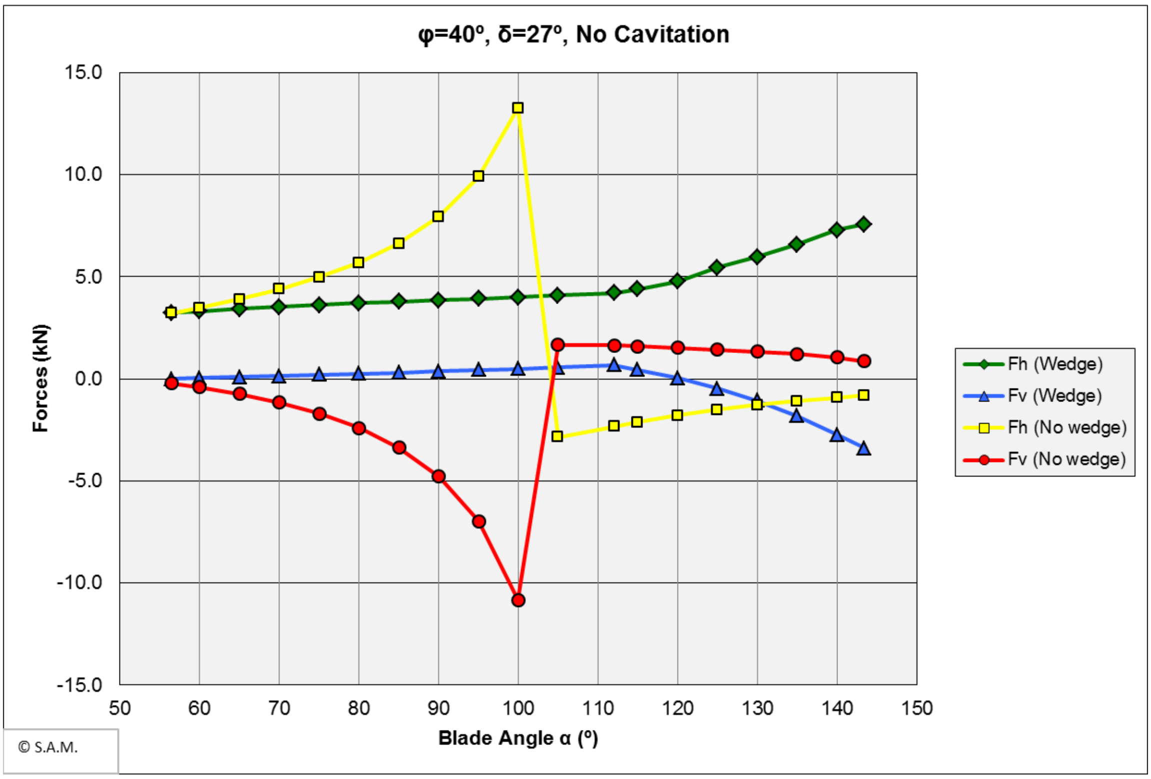

Figure O-6: No cavitation, the cutting forces as a function of the blade angle α for φ=40° and δ=27°.

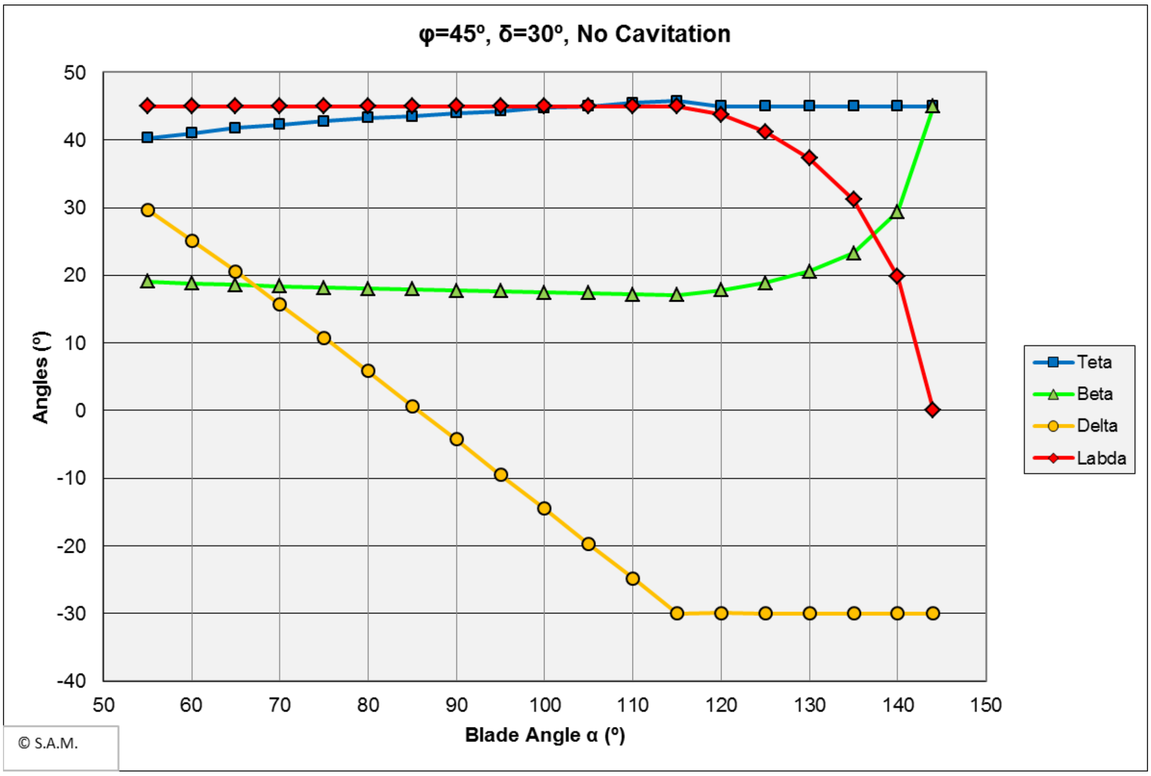

Figure O-7: No cavitation, the angles θ, β, δ_m and λ as a function of the blade angle α for φ=45º and δ=30º.

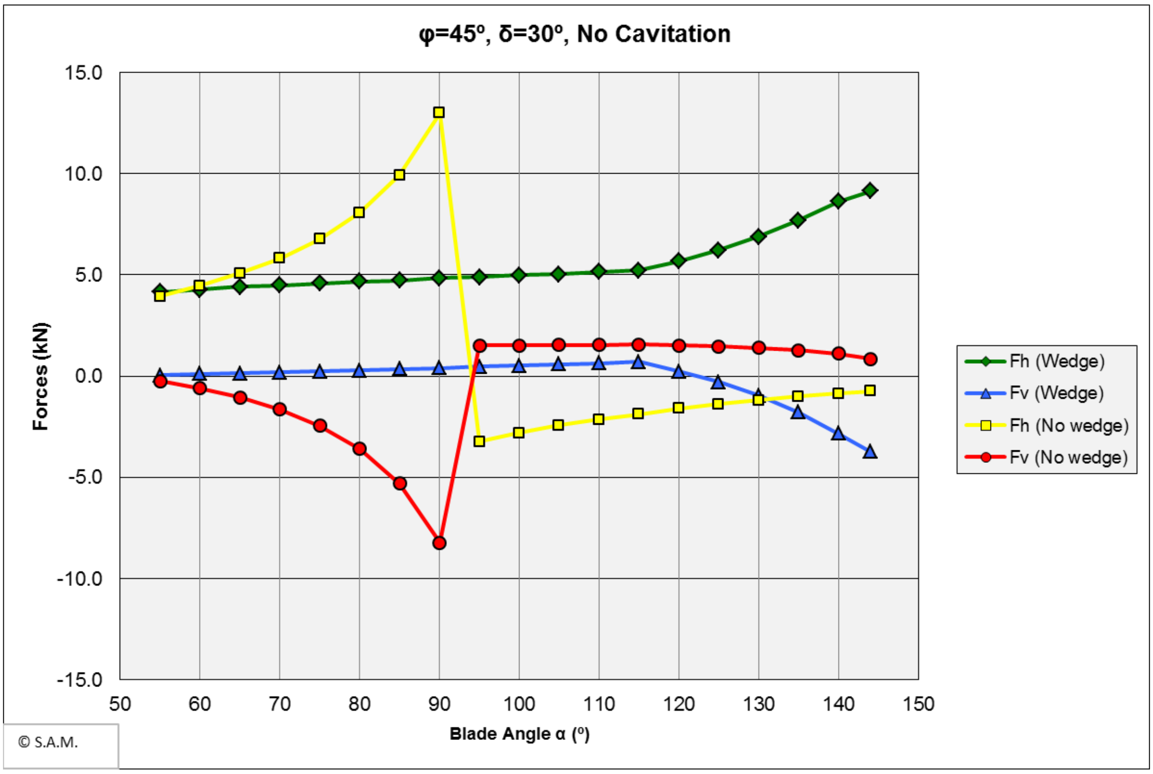

Figure O-8: No cavitation, the cutting forces as a function of the blade angle α for φ=45º and δ=30º.

Appendix P: The Occurrence of a Wedge, Cavitating

Figure P-1: Cavitating, the angles θ, β, δ_m and λ as a function of the blade angle α for φ=30° and δ=20°

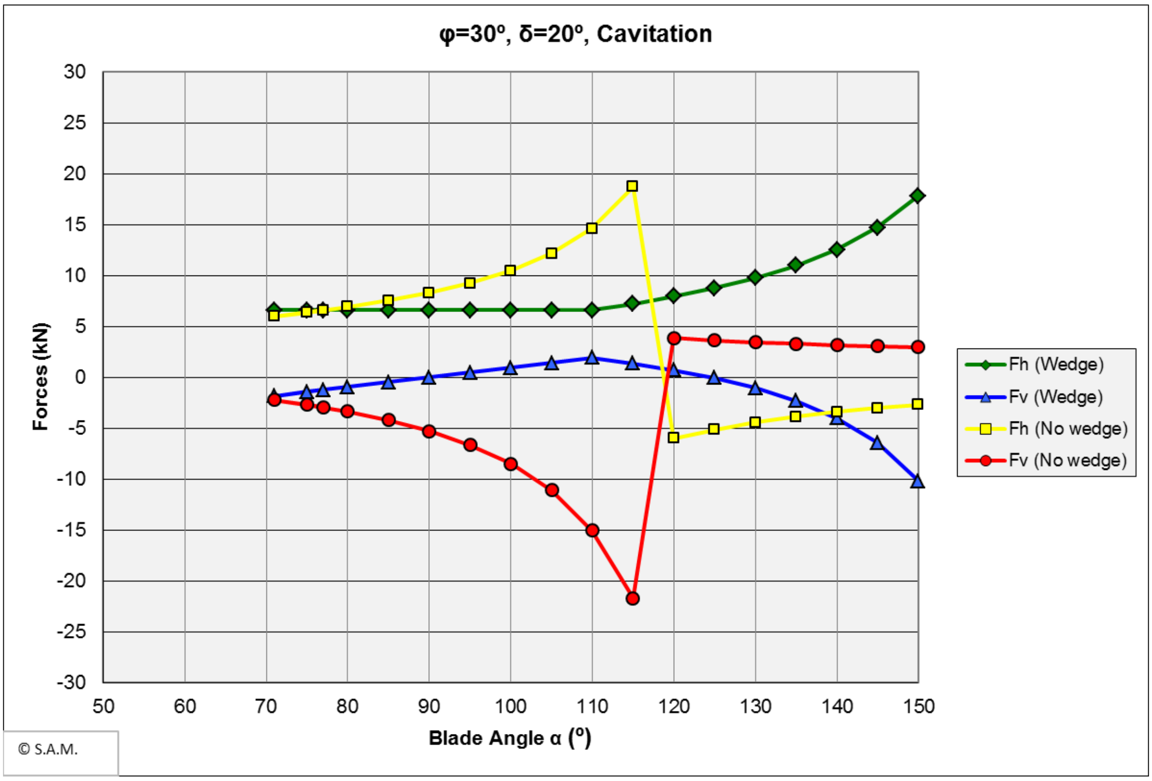

Figure P-2: Cavitating, the cutting forces as a function of the blade angle α for φ=30° and δ=20°.

.

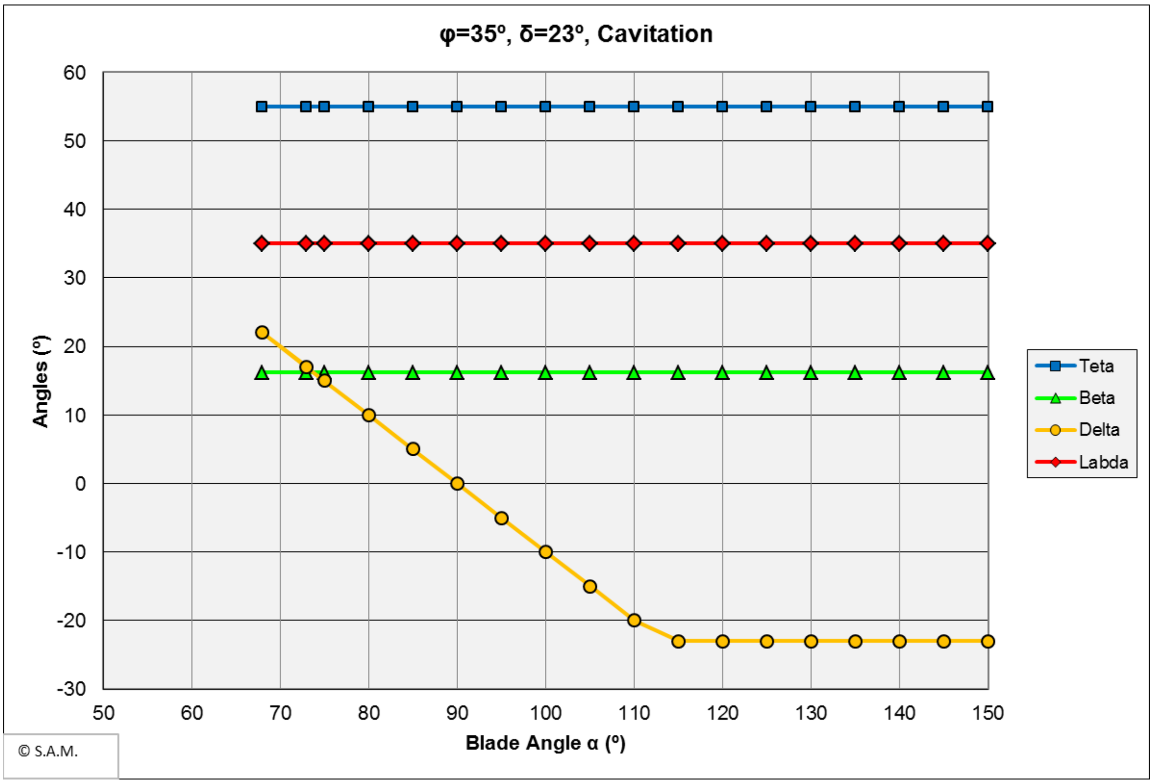

Figure P-3: Cavitating, the angles θ, β, δ_m and λ as a function of the blade angle α for φ=35° and δ=23°.

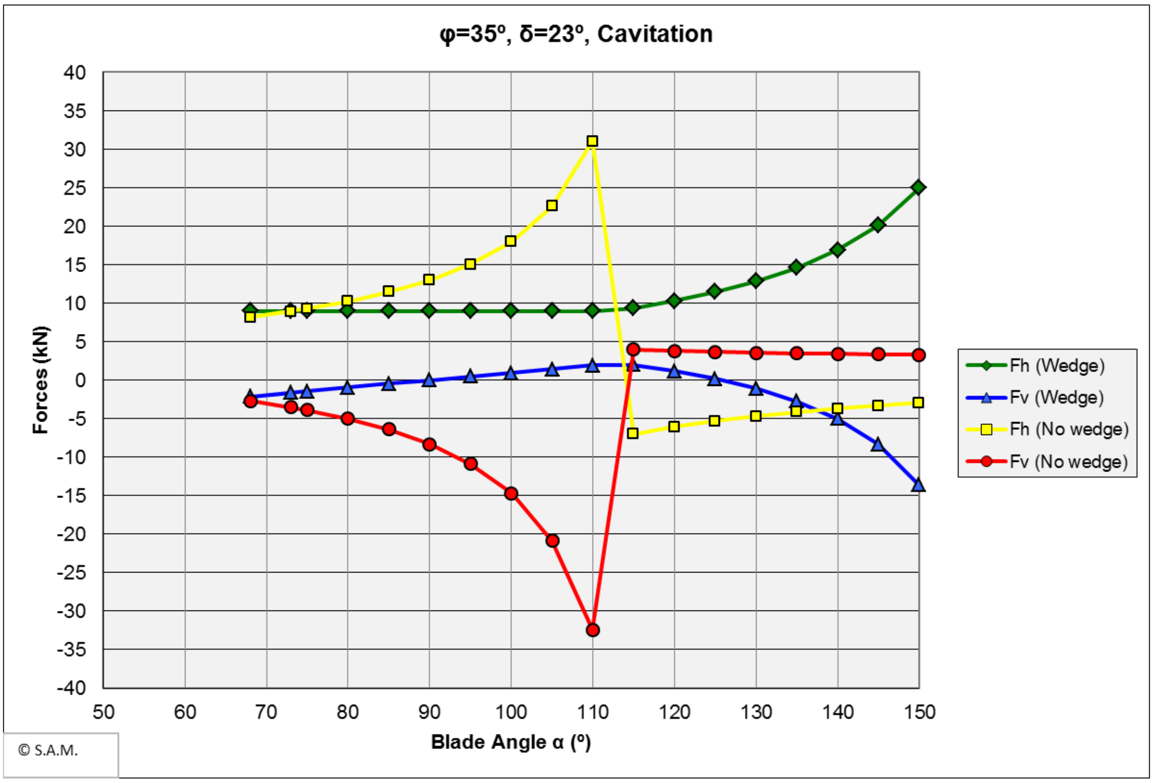

Figure P-4: Cavitating, the cutting forces as a function of the blade angle α for φ=35° and δ=23°.

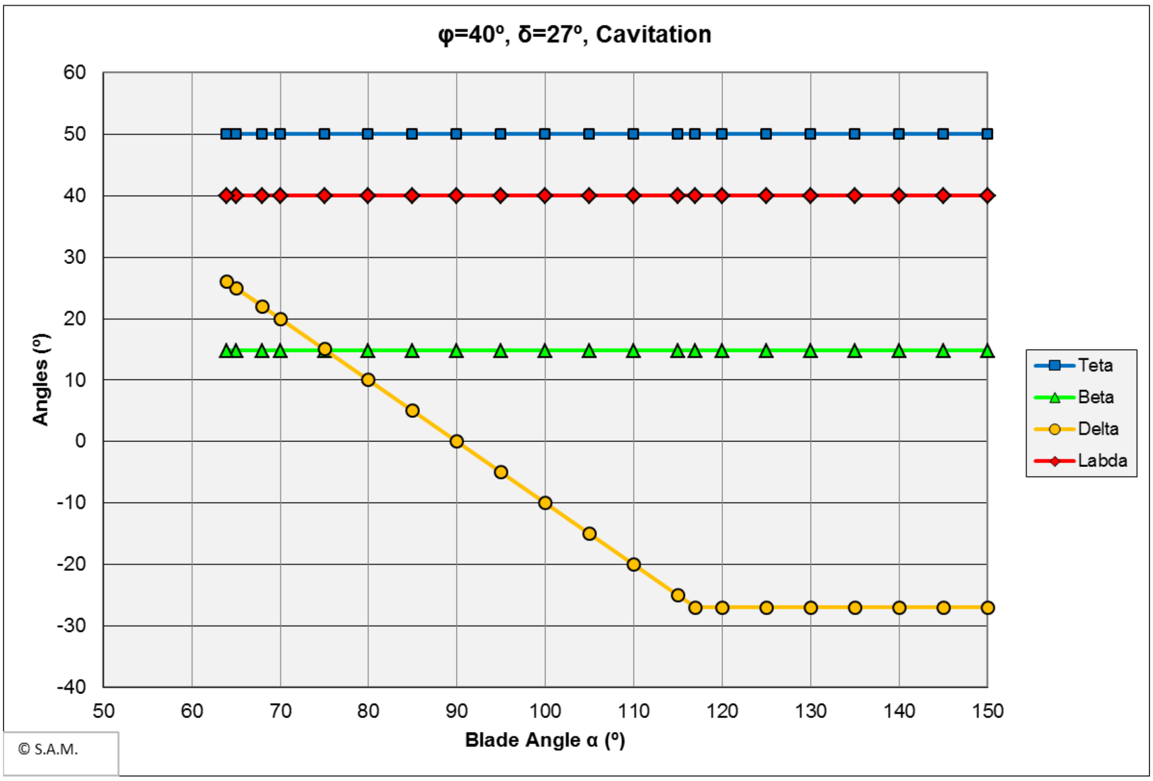

Figure P-5: Cavitating, the angles θ, β, δ_m and λ as a function of the blade angle α for φ=40° and δ=27°.

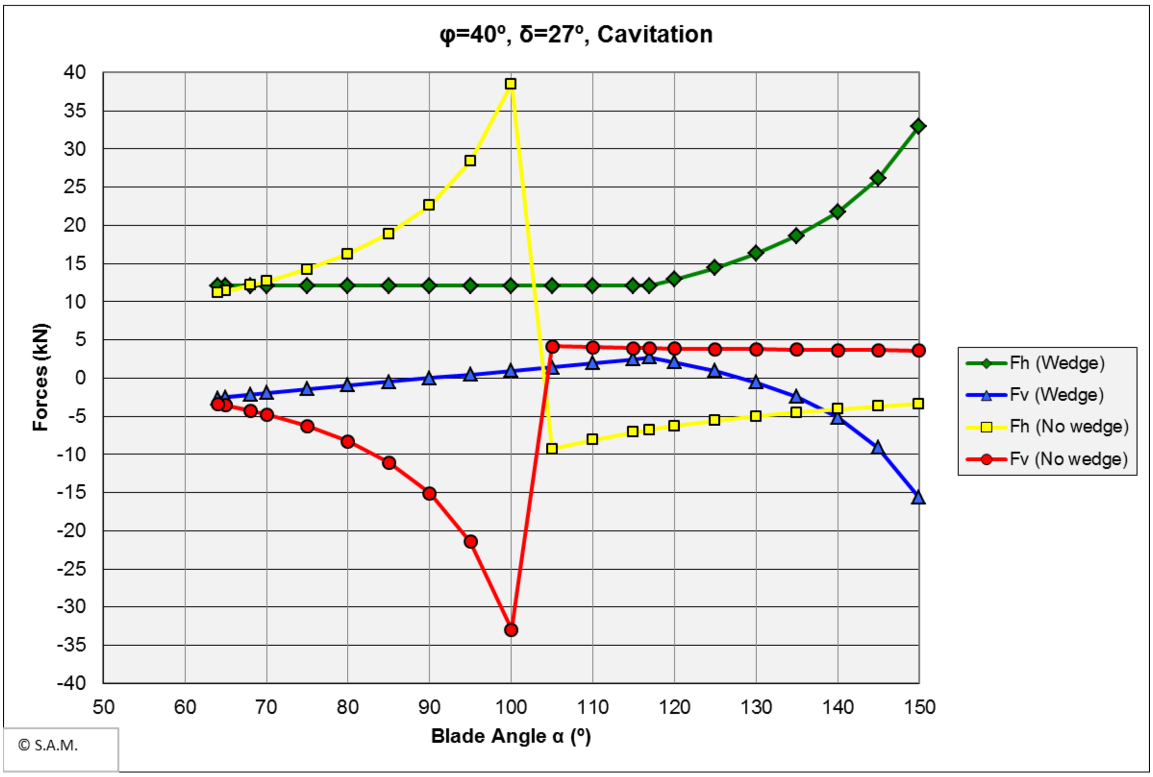

Figure P-6: Cavitating, the cutting forces as a function of the blade angle α for φ=40° and δ=27°.

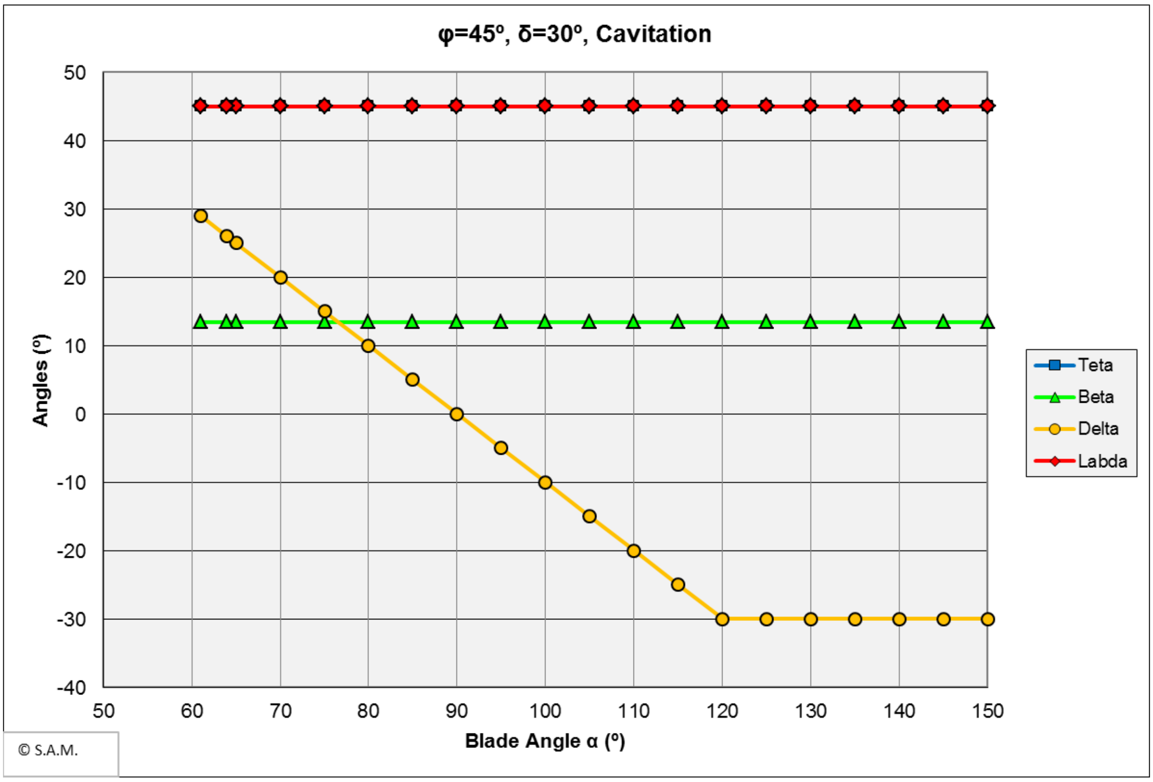

Figure P-7: Cavitating, the angles θ, β, δ_m and λ as a function of the blade angle α for φ=45º and δ=30º.

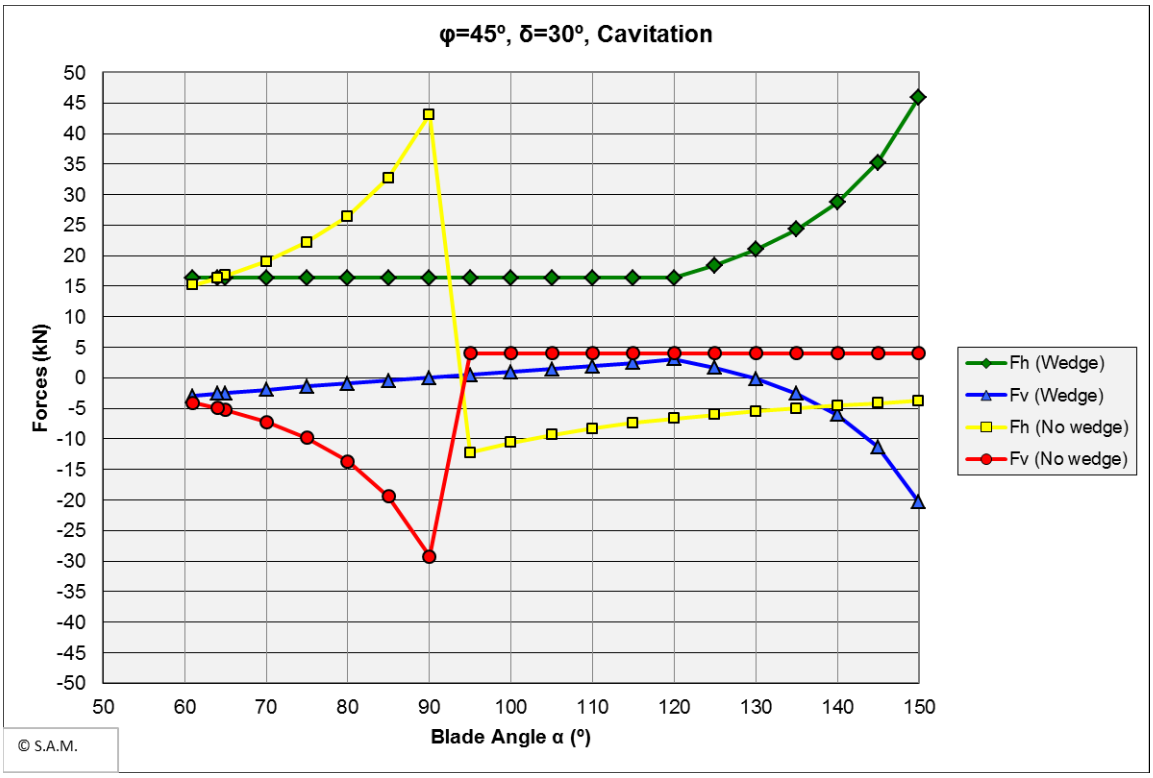

Figure P-8: Cavitating, the cutting forces as a function of the blade angle α for φ=45º and δ=30º.

Appendix Q: Pore Pressures with Wedge

Table Q-1: The average water pore pressure and total pressure along the four sides, for $\alpha=60^0$; $h_i=1$; $h_b=3$; $k_i/k_{max}=0.25$

	β	p_{1m}	p_{2m}	p_{3m}	p_{4m}
$\theta=30^0$	15^0	0.2489	0.0727	0.1132	0.0313
	20^0	0.2675	0.0713	0.1133	0.0290
	25^0	0.2852	0.0702	0.1139	0.0268
	30^0	0.3014	0.0695	0.1149	0.0249
	β	p_{1m}	p_{2m}	p_{3m}	p_{4m}
$\theta=40^0$	15^0	0.2798	0.1040	0.1728	0.0688
	20^0	0.2980	0.1047	0.1788	0.0672
	25^0	0.3145	0.1036	0.1827	0.0640
	30^0	0.3291	0.1022	0.1859	0.0607
	β	p_{1m}	p_{2m}	p_{3m}	p_{4m}
$\theta=50^0$	15^0	0.3043	0.1338	0.2357	0.1141
	20^0	0.3240	0.1377	0.2523	0.1158
	25^0	0.3404	0.1373	0.2635	0.1134
	30^0	0.3544	0.1353	0.2722	0.1096
	β	p_{1m}	p_{2m}	p_{3m}	p_{4m}
$\theta=55^0$	15^0	0.3152	0.1492	0.2720	0.1392
	20^0	0.3367	0.1549	0.2967	0.1435
	25^0	0.3540	0.1549	0.3143	0.1422
	30^0	0.3684	0.1526	0.3284	0.1388
	β	p_{1m}	p_{2m}	p_{3m}	p_{4m}
$\theta=59^0$	15^0	0.3242	0.1626	0.3089	0.1607
	20^0	0.3481	0.1699	0.3436	0.1676
	25^0	0.3675	0.1705	0.3707	0.1679
	30^0	0.3838	0.1683	0.3922	0.1654

Table Q-2: The average water pore pressure and total pressure along the four sides, for $\alpha=70^0$; $h_i=1$; $h_b=3$; $k_i/k_{max}=0.25$

$\theta=30^0$	β	p_{1m}	p_{2m}	p_{3m}	p_{4m}
	15^0	0.2499	0.0773	0.1071	0.0339
	20^0	0.2679	0.0735	0.1048	0.0292
	25^0	0.2854	0.0715	0.1041	0.0261
	30^0	0.3015	0.0704	0.1043	0.0240
$\theta=40^0$	β	p_{1m}	p_{2m}	p_{3m}	p_{4m}
	15^0	0.2825	0.1127	0.1622	0.0712
	20^0	0.2992	0.1088	0.1625	0.0651
	25^0	0.3152	0.1060	0.1634	0.0603
	30^0	0.3297	0.1039	0.1646	0.0564
$\theta=50^0$	β	p_{1m}	p_{2m}	p_{3m}	p_{4m}
	15^0	0.3088	0.1438	0.2160	0.1129
	20^0	0.3259	0.1422	0.2230	0.1086
	25^0	0.3414	0.1399	0.2283	0.1038
	30^0	0.3549	0.1373	0.2325	0.0992
$\theta=55^0$	β	p_{1m}	p_{2m}	p_{3m}	p_{4m}
	15^0	0.3175	0.1496	0.1994	0.1104
	20^0	0.3382	0.1556	0.2103	0.1128
	25^0	0.3547	0.1563	0.2156	0.1110
	30^0	0.3682	0.1548	0.2184	0.1076
$\theta=60^0$	β	p_{1m}	p_{2m}	p_{3m}	p_{4m}
	15^0	0.3300	0.1719	0.2720	0.1562
	20^0	0.3498	0.1745	0.2907	0.1567
	25^0	0..3664	0.1736	0.3043	0.1540
	30^0	0.3803	0.1710	0.3150	0.1497
$\theta=69^0$	B	p_{1m}	p_{2m}	p_{3m}	p_{4m}
	15^0	0.3474	0.1984	0.3369	0.1970
	20^0	0.3737	0.2066	0.3760	0.2050
	25^0	0.3953	0.2081	0.4060	0.2063
	30^0	0.4134	0.2062	0.4306	0.2041

Table Q-3: The average water pore pressure and total pressure along the four sides, for $\alpha=80^0$; $h_i=1$; $h_b=3$; $k_i/k_{max}=0.25$

$\theta=30^0$	β	p_{1m}	p_{2m}	p_{3m}	p_{4m}
	15^0	0.2493	0.0738	0.0973	0.0279
	20^0	0.2679	0.0723	0.0966	0.0260
	25^0	0.2856	0.0712	0.0962	0.0242
	30^0	0.3018	0.0705	0.0964	0.0226
$\theta=40^0$	β	p_{1m}	p_{2m}	p_{3m}	p_{4m}
	15^0	0.2810	0.1058	0.1450	0.0595
	20^0	0.2992	0.1065	0.1481	0.0581
	25^0	0.3156	0.1055	0.1493	0.0555
	30^0	0.3302	0.1042	0.1501	0.0527
$\theta=50^0$	β	p_{1m}	p_{2m}	p_{3m}	p_{4m}
	15^0	0.3062	0.1352	0.1917	0.0967
	20^0	0.3257	0.1393	0.2010	0.0978
	25^0	0.3420	0.1393	0.2057	0.0954
	30^0	0.3557	0.1378	0.2085	0.0919
$\theta=55^0$	β	p_{1m}	p_{2m}	p_{3m}	p_{4m}
	15^0	0.3170	0.1495	0.2153	0.1167
	20^0	0.3378	0.1554	0.2284	0.1195
	25^0	0.3542	0.1560	0.2355	0.1176
	30^0	0.3678	0.1544	0.2400	0.1140
$\theta=60^0$	β	p_{1m}	p_{2m}	p_{3m}	p_{4m}
	15^0	0.3271	0.1639	0.2398	0.1375
	20^0	0.3493	0.1716	0.2572	0.1422
	25^0	0.3663	0.1728	0.2672	0.1411
	30^0	0.3799	0.1712	0.2739	0.1375
$\theta=70^0$	β	p_{1m}	p_{2m}	p_{3m}	p_{4m}
	15^0	0.3465	0.1944	0.2946	0.1820
	20^0	0.3727	0.2057	0.3231	0.1914
	25^0	0.3922	0.2082	0.3419	0.1923
	30^0	0.4070	0.2062	0.3549	0.1890

Table Q-4: The average water pore pressure and total pressure along the four sides, for $\theta=90^0$; $h_i=1$; $h_b=3$; $k_i/k_{max}=0.25$

	β	p_{1m}	p_{2m}	p_{3m}	p_{4m}
$\theta=30^0$	15^0	0.2494	0.0740	0.0917	0.0270
	20^0	0.2680	0.0726	0.0908	0.0252
	25^0	0.2857	0.0715	0.0902	0.0235
	30^0	0.3018	0.0708	0.0901	0.0220
$\theta=40^0$	β	p_{1m}	p_{2m}	p_{3m}	p_{4m}
	15^0	0.2813	0.1062	0.1358	0.0569
	20^0	0.2995	0.1070	0.1381	0.0556
	25^0	0.3159	0.1060	0.1387	0.0530
	30^0	0.3305	0.1047	0.1389	0.0504
$\theta=50^0$	β	p_{1m}	p_{2m}	p_{3m}	p_{4m}
	15^0	0.3067	0.1355	0.1782	0.0917
	20^0	0.3262	0.1397	0.1860	0.0926
	25^0	0.3424	0.1397	0.1893	0.0904
	30^0	0.3561	0.1383	0.1910	0.0871
$\theta=55^0$	β	p_{1m}	p_{2m}	p_{3m}	p_{4m}
	15^0	0.3175	0.1496	0.1994	0.1104
	20^0	0.3382	0.1556	0.2103	0.1128
	25^0	0.3547	0.1563	0.2156	0.1110
	30^0	0.3682	0.1548	0.2184	0.1076
$\theta=60^0$	β	p_{1m}	p_{2m}	p_{3m}	p_{4m}
	15^0	0.3276	0.1637	0.2209	0.1296
	20^0	0.3497	0.1713	0.2353	0.1338
	25^0	0.3666	0.1727	0.2428	0.1327
	30^0	0.3800	0.1713	0.2471	0.1292
$\theta=70^0$	β	p_{1m}	p_{2m}	p_{3m}	p_{4m}
	15^0	0.3464	0.1927	0.2670	0.1706
	20^0	0.3719	0.2038	0.2894	0.1780
	25^0	0.3907	0.2065	0.3027	0.1793
	30^0	0.4047	0.2049	0.3110	0.1759
$\theta=80^0$	β	p_{1m}	p_{2m}	p_{3m}	p_{4m}
	15^0	0.3658	0.2253	0.3216	0.2157
	20^0	0.3965	0.2400	0.3556	0.2289
	25^0	0.4185	0.2435	0.3776	0.2311
	30^0	0.4347	0.2411	0.3930	0.2277

Table Q-5: Acting points for $\alpha=90^0$; $h_i=1$; $h_b=3$; $k_i/k_{max}=0.25$

θ	β	E_2	E_3	E_4
60^0	15^0	0.36	0.56	0.40
60^0	20^0	0.36	0.56	0.40
60^0	25^0	0.35	0.56	0.39
60^0	30^0	0.34	0.57	0.39
55^0	15^0	0.35	0.56	0.40
55^0	20^0	0.34	0.56	0.40
55^0	25^0	0.33	0.57	0.39
55^0	30^0	0.33	0.57	0.39
50^0	15^0	0.34	0.58	0.40
50^0	20^0	0.34	0.58	0.40
50^0	25^0	0.33	0.59	0.40
50^0	30^0	0.33	0.59	0.40
40^0	15^0	0.32	0.61	0.40
40^0	20^0	0.31	0.62	0.40
40^0	25^0	0.30	0.62	0.40
40^0	30^0	0.29	0.63	0.39

Table Q-6: Acting points for $\alpha=80^0$; $h_i=1$; $h_b=3$; $k_i/k_{max}=0.25$

θ	β	E_2	E_3	E_4
60^0	15^0	0.36	0.54	0.39
60^0	20^0	0.35	0.54	0.39
60^0	25^0	0.35	0.55	0.38
60^0	30^0	0.34	0.56	0.37
55^0	15^0	0.35	0.55	0.40
55^0	20^0	0.34	0.55	0.39
55^0	25^0	0.33	0.56	0.39
55^0	30^0	0.33	0.57	0.38
50^0	15^0	0.35	0.57	0.40
50^0	20^0	0.34	0.57	0.40
50^0	25^0	0.33	0.58	0.39
50^0	30^0	0.32	0.58	0.39

Table Q-7: Acting points for $\alpha=70^0$; $h_i=1$; $h_b=3$; $k_i/k_{max}=0.25$

θ	β	E_2	E_3	E_4
60^0	15^0	0.36	0.53	0.36
60^0	20^0	0.35	0.53	0.35
60^0	25^0	0.34	0.54	0.34
60^0	30^0	0.34	0.54	0.34
55^0	15^0	0.35	0.54	0.37
55^0	20^0	0.34	0.54	0.37
55^0	25^0	0.33	0.54	0.36
55^0	30^0	0.33	0.54	0.35
50^0	15^0	0.34	0.55	0.38
50^0	20^0	0.33	0.55	0.38
50^0	25^0	0.32	0.56	0.37
50^0	30^0	0.31	0.56	0.36

Table Q-8: Acting points for $\alpha=60^0$; $h_i=1$; $h_b=3$; $k_i/k_{max}=0.25$

θ	β	E_2	E_3	E_4
55^0	15^0	0.34	0.52	0.34
55^0	20^0	0.32	0.52	0.33
55^0	25^0	0.31	0.52	0.32
55^0	30^0	0.30	0.52	0.31
50^0	15^0	0.33	0.54	0.35
50^0	20^0	0.32	0.54	0.34
50^0	25^0	0.31	0.54	0.34
50^0	30^0	0.31	0.54	0.33

Appendix R: FEM Calculations with Wedge.

R.1 The Boundaries of the FEM Model

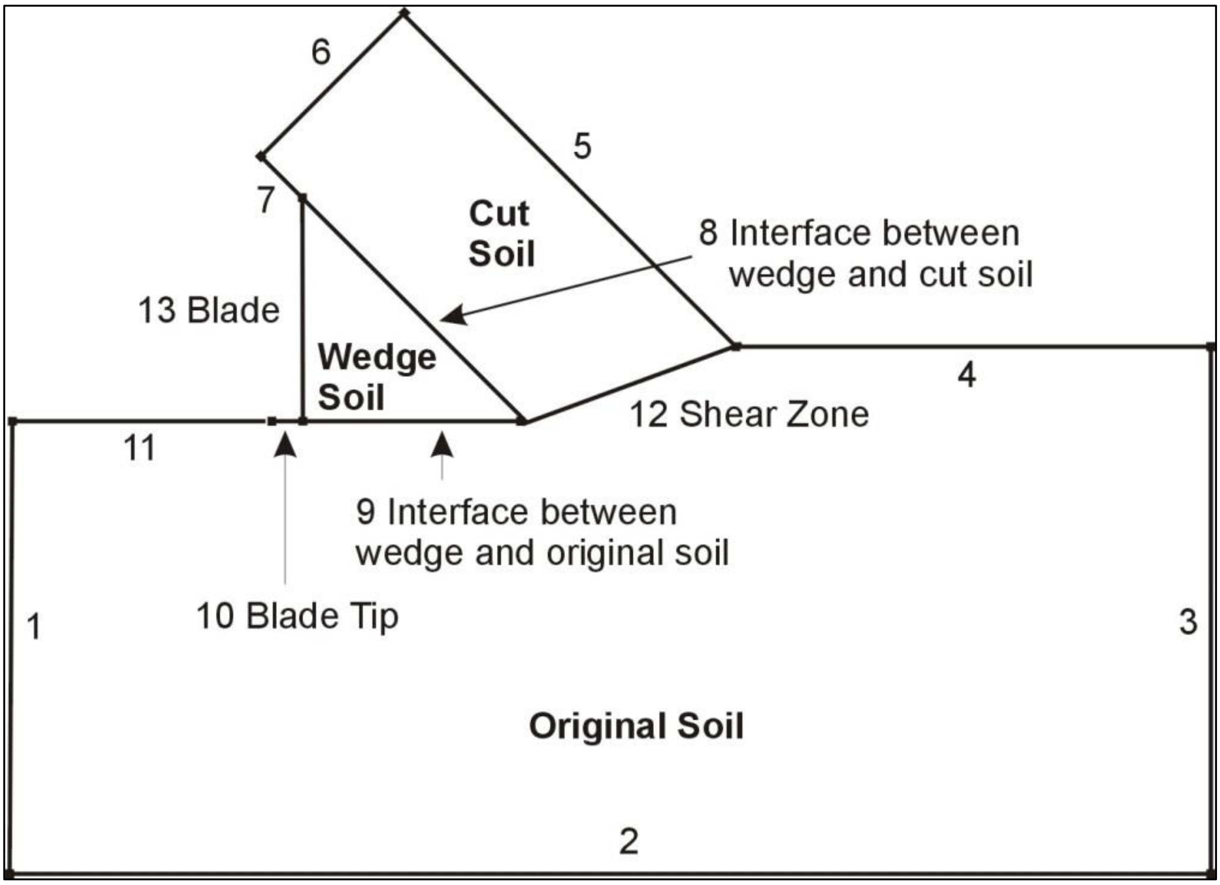

Figure R-1: The boundaries of the FEM model.

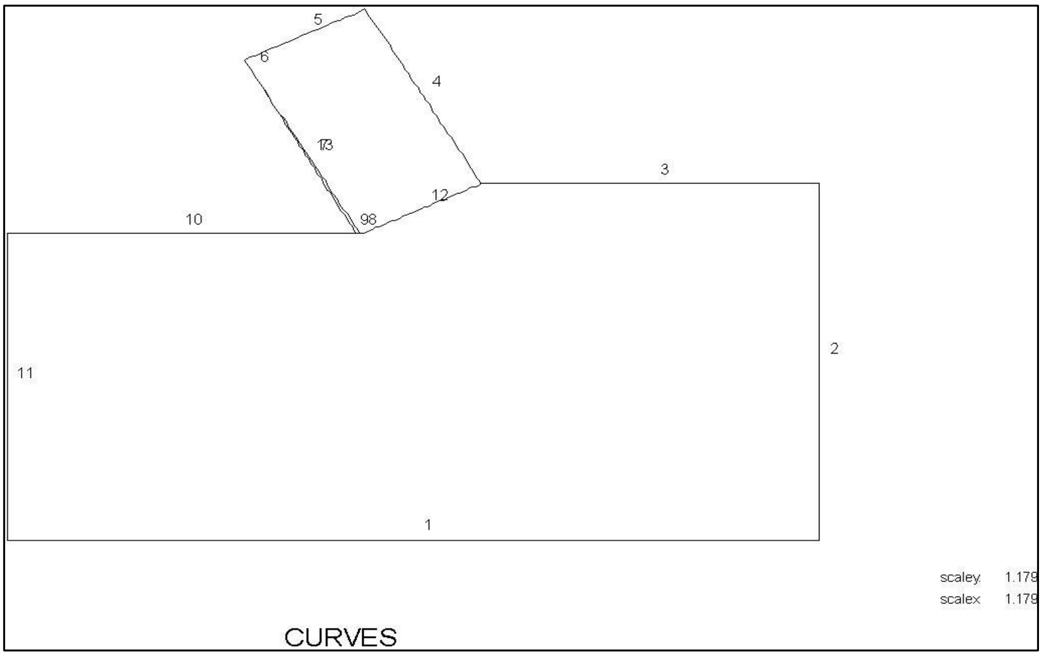

Figure R-2: The boundaries of the 60/59 degree calculations.

R.2 The 60 Degree Blade

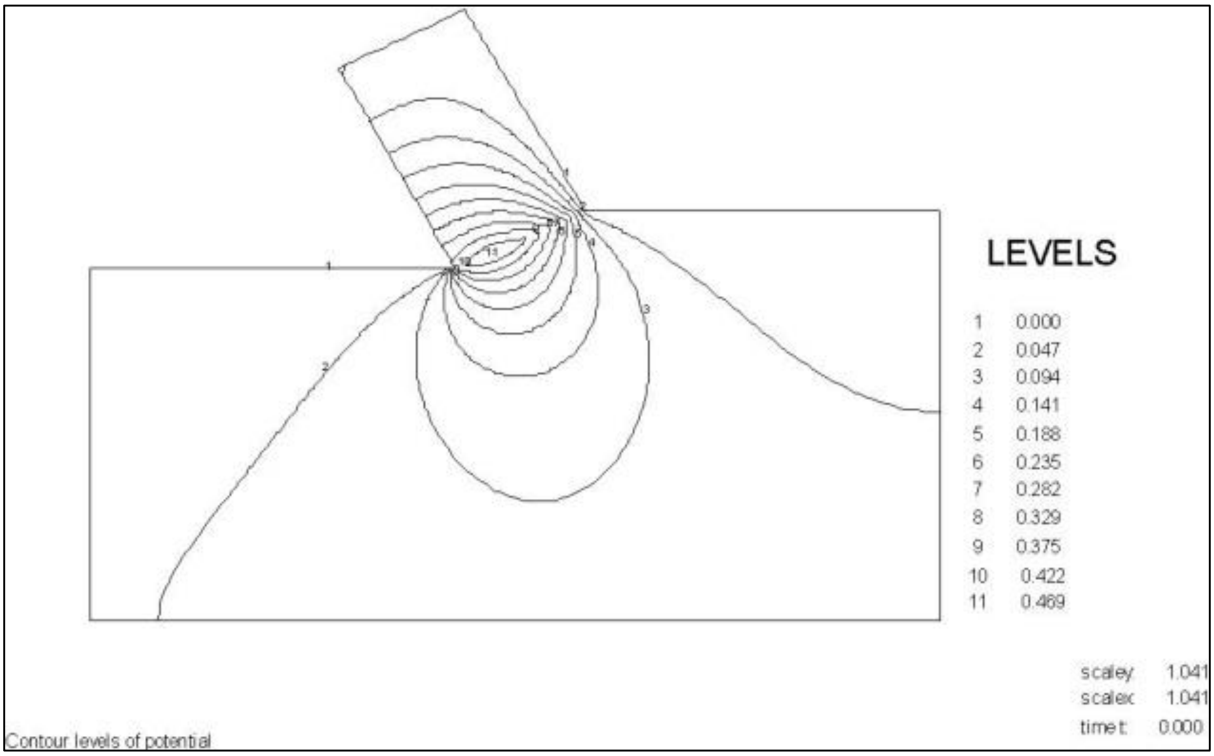

Figure R-3: The equipotential lines.

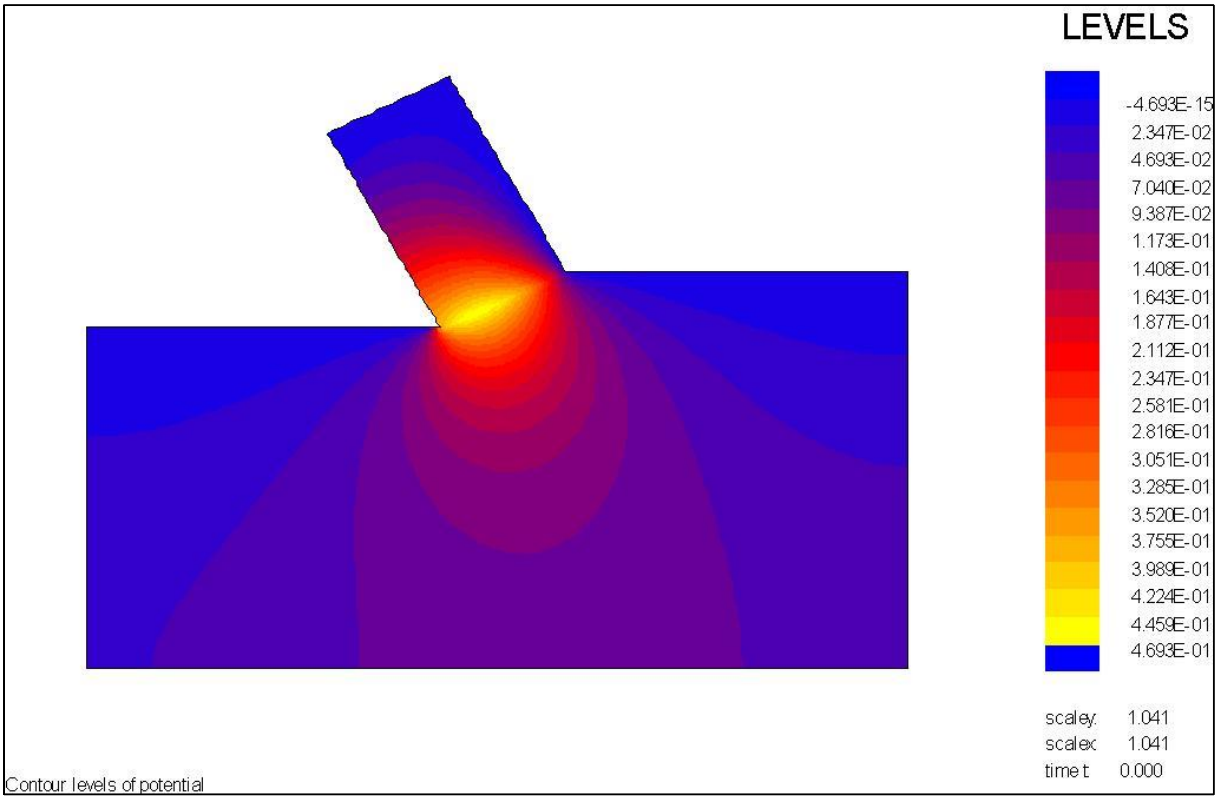

Figure R-4: The equipotential lines in color.

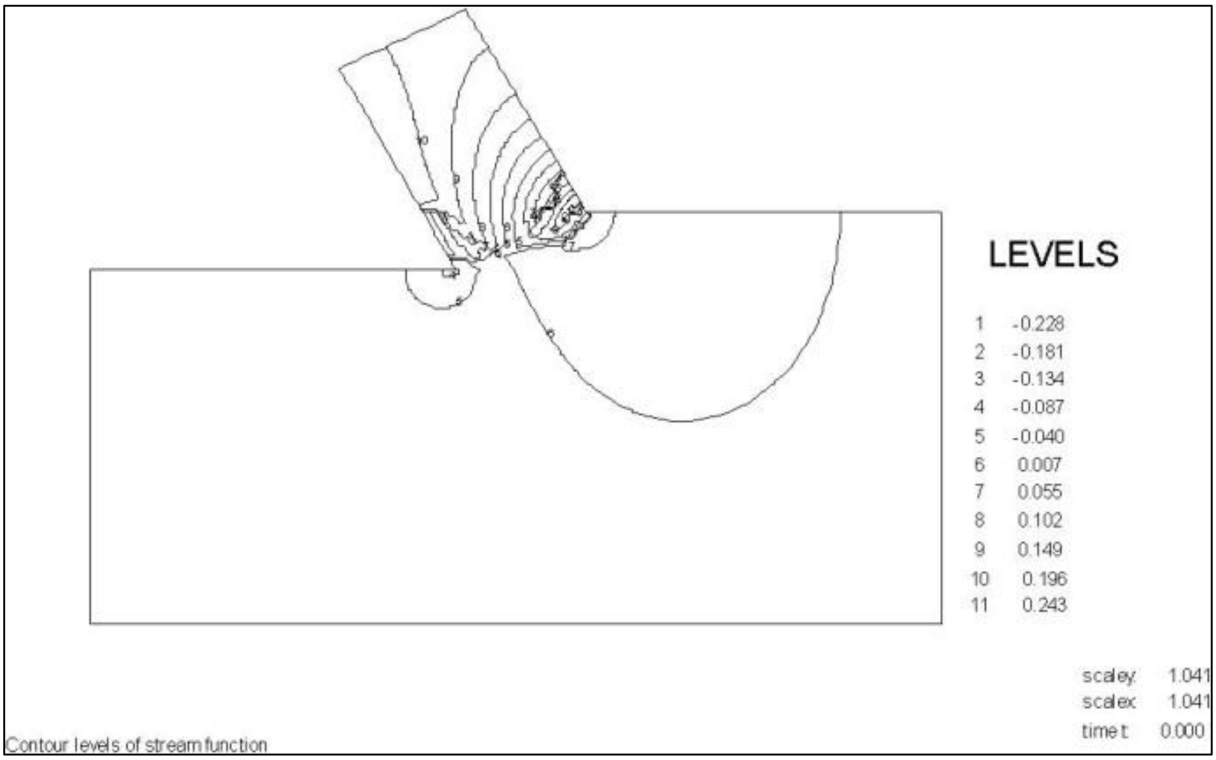

Figure R-5: The flow lines or stream function.

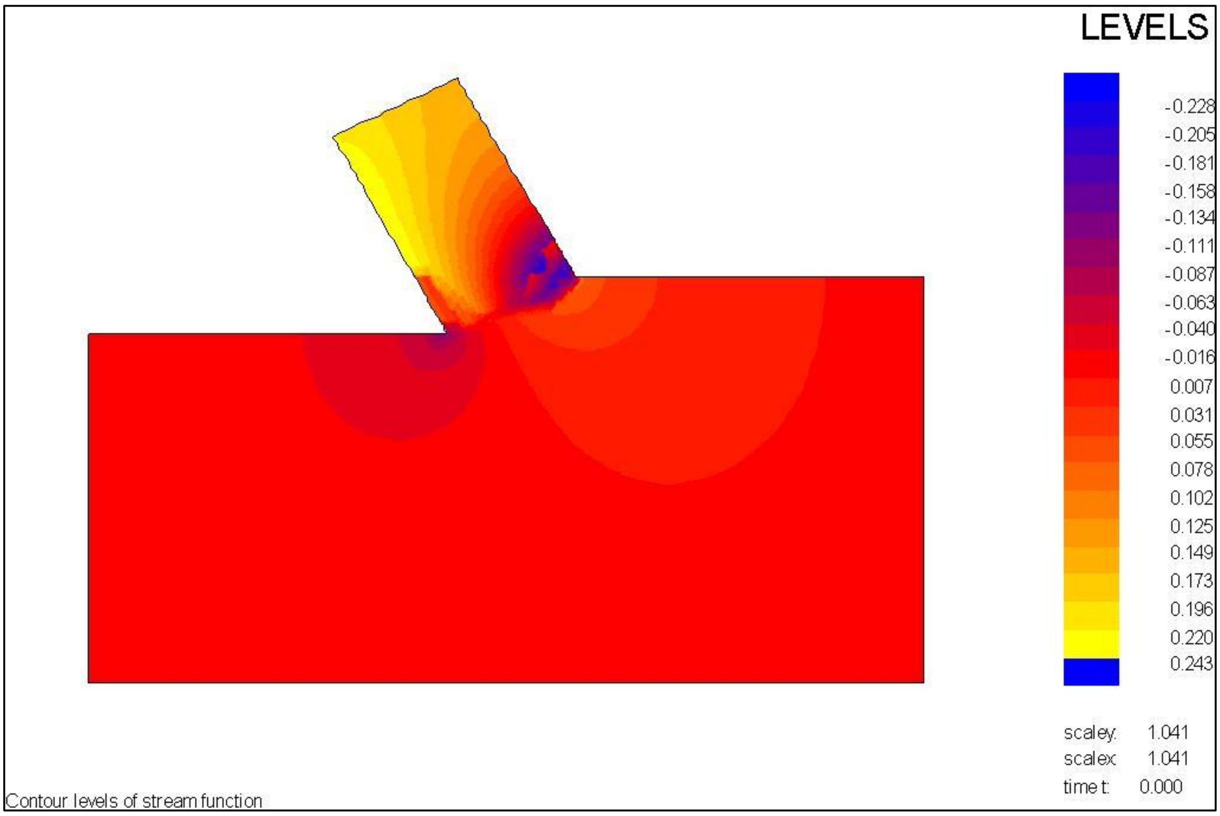

Figure R-6: The stream function in colors.

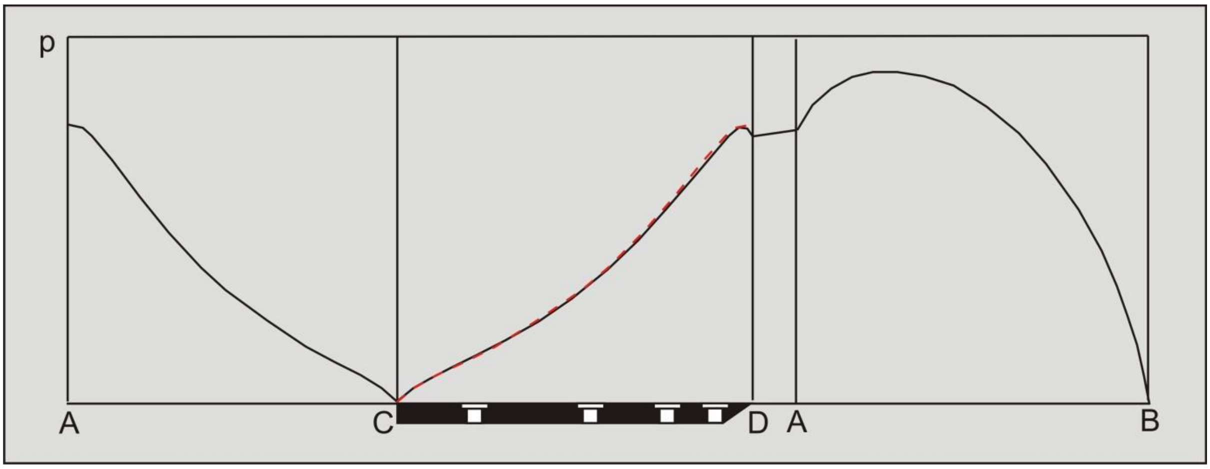

Figure R-7: The pore pressures in the shear zone A-B, at the bottom of the wedge A-D, on the front of the wedge C-A and on the blade C-D

The wedge angle in these calculations is 59 degrees. The pore pressures on the blade C-D are almost equal to the pore pressures on the front of the wedge A-C, which they should be with a blade angle of 60 degrees and a wedge angle of 59 degrees. The pore pressures on the front of the wedge C-A are drawn in red on top of the pore pressures on the blade C-A and match almost exactly.

R.3 The 75 Degree Blade

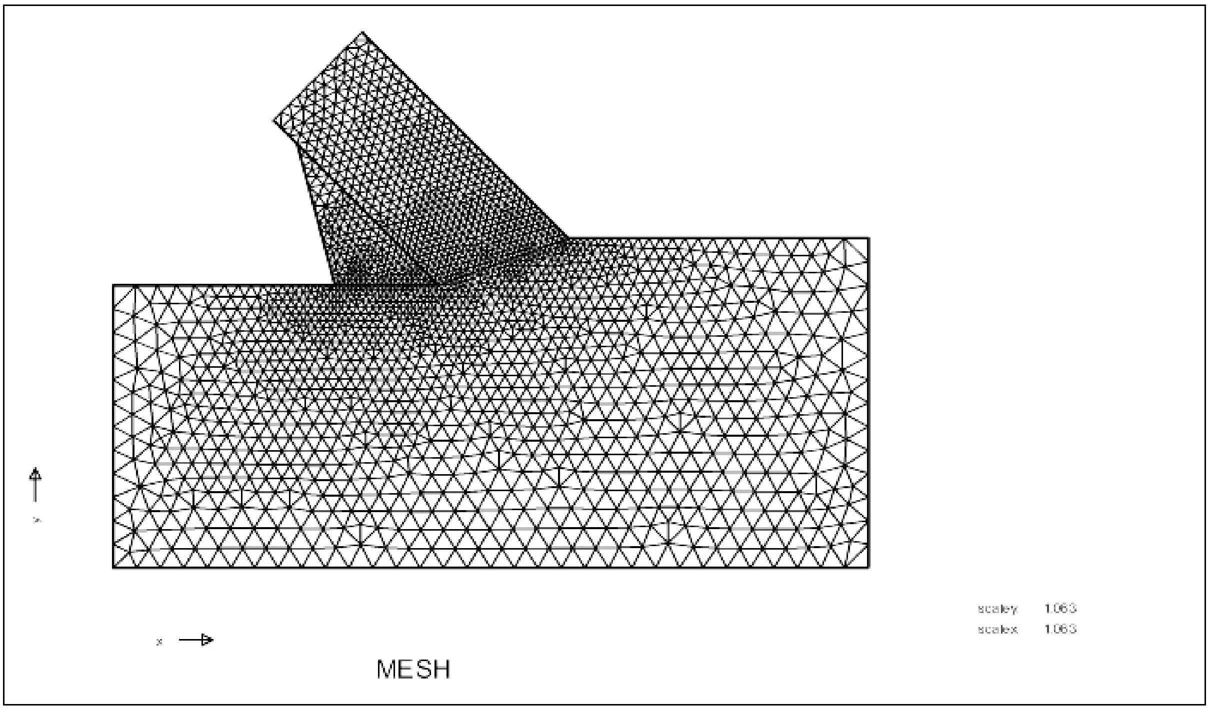

Figure R-8: The coarse mesh.

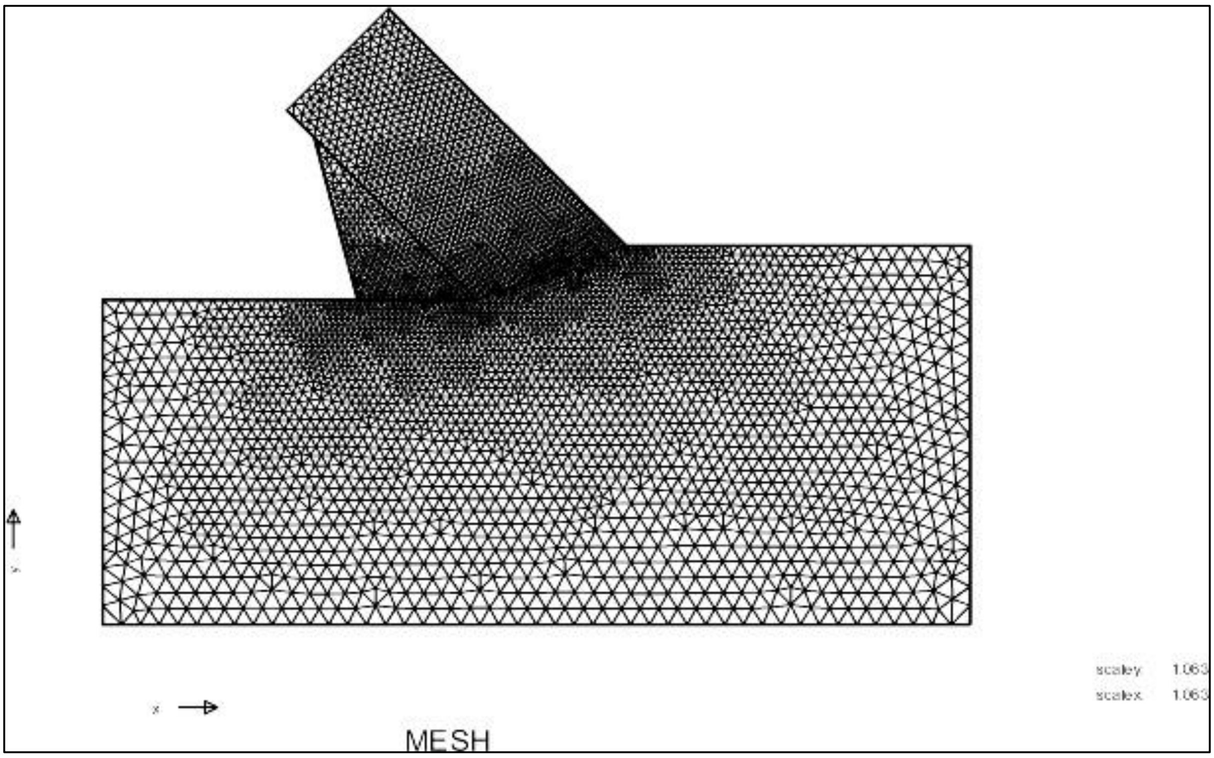

Figure R-9: The fine mesh.

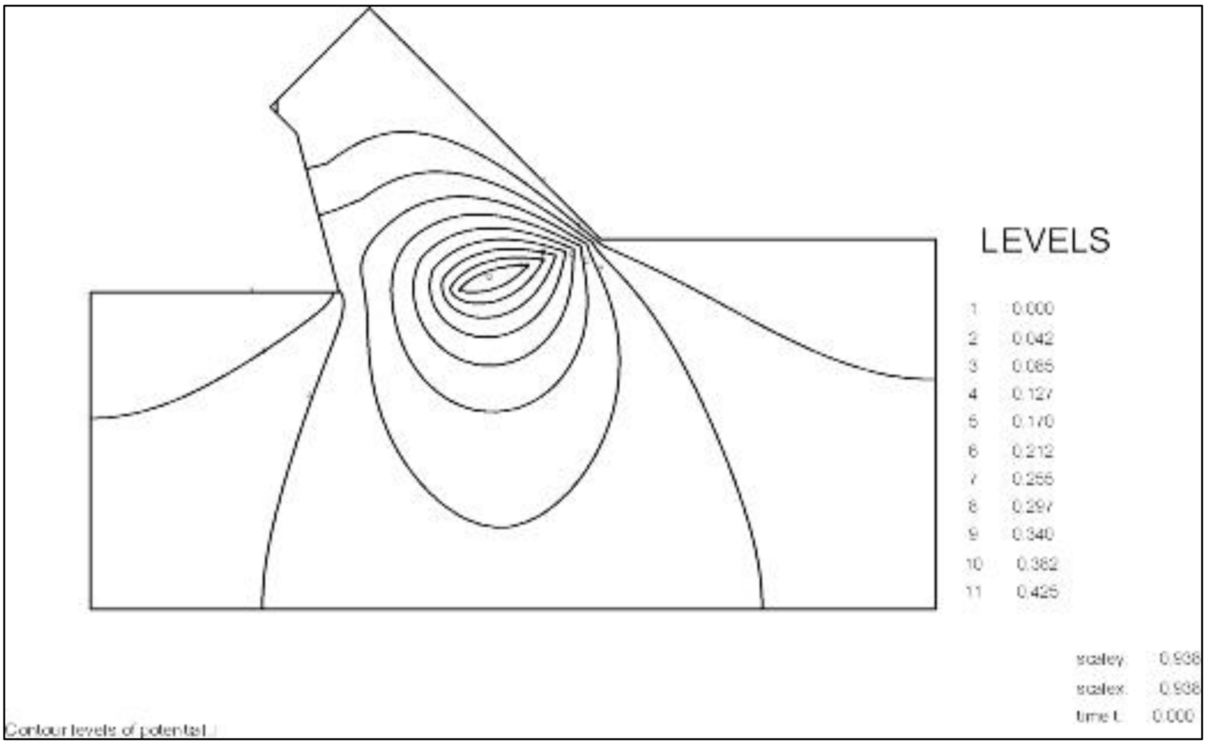

Figure R-10: The equipotential lines.

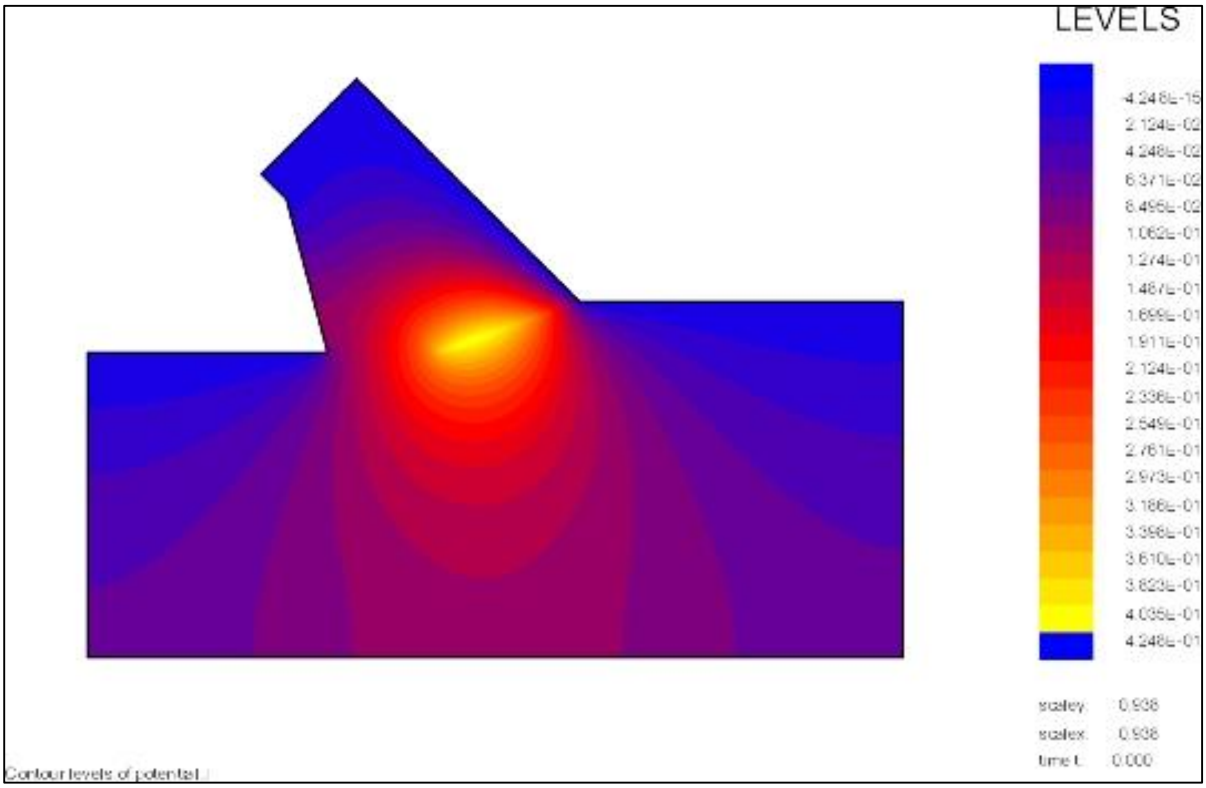

Figure R-11: The equipotential lines in color.

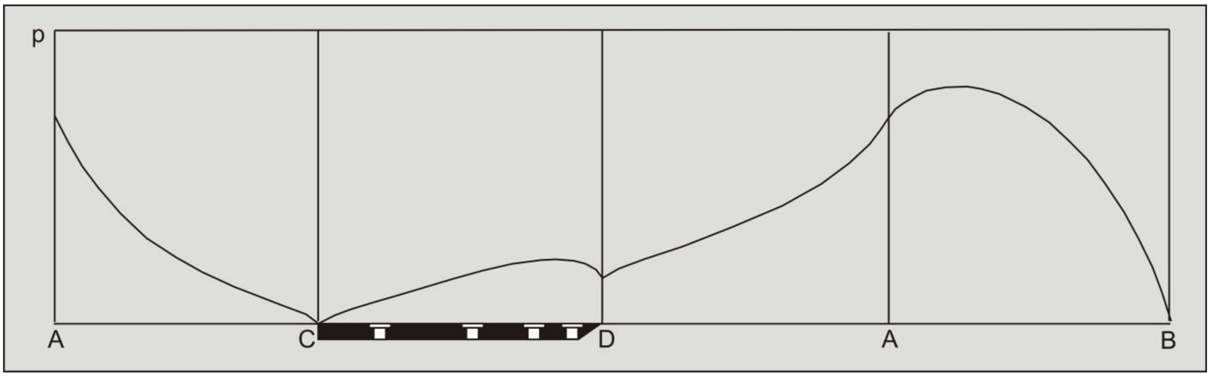

Figure R-12: Pore pressure distribution on the shear plane A-B, the bottom of the wedge A-D, the blade D-C and the front of the wedge A-C.

R.4 The 90 Degree Blade

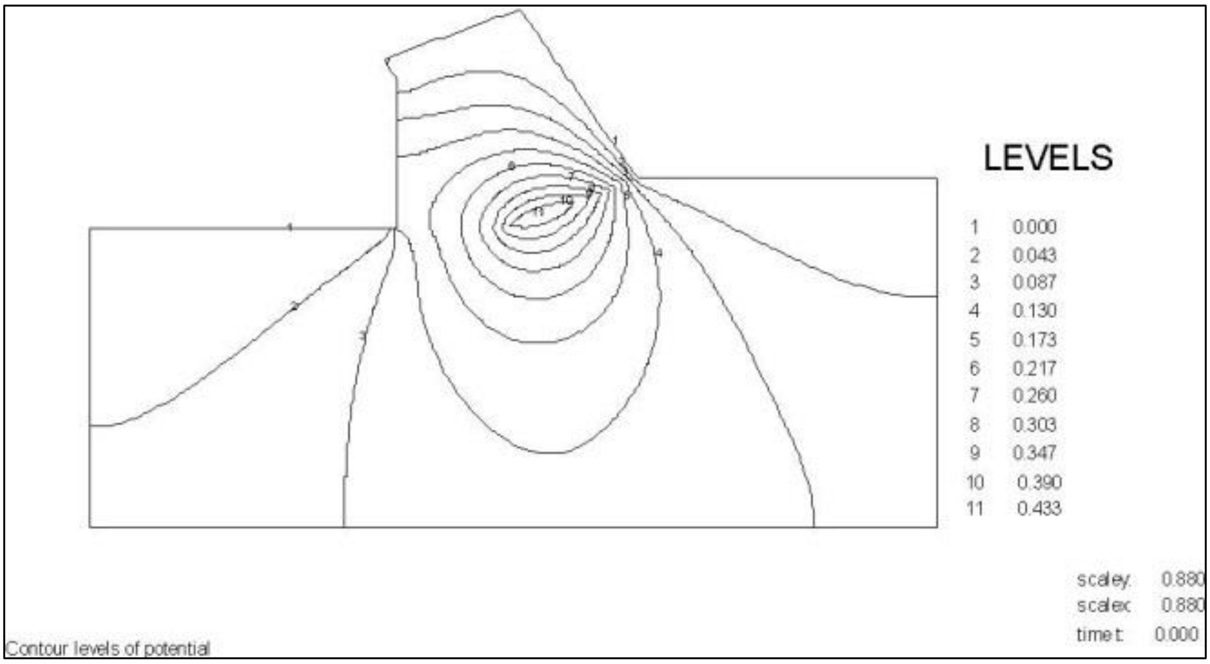

Figure R-13: Equipotential lines of pore pressures.

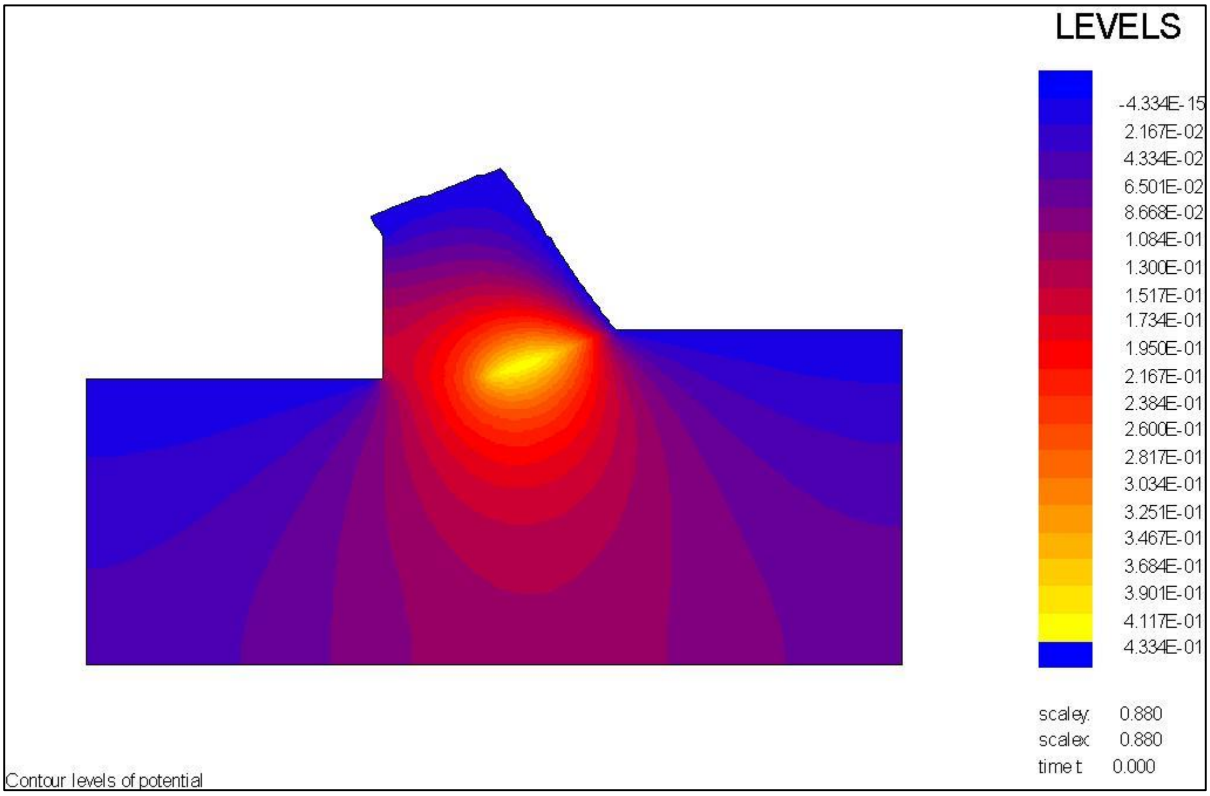

Figure R-14: Equi-potential distribution in color.

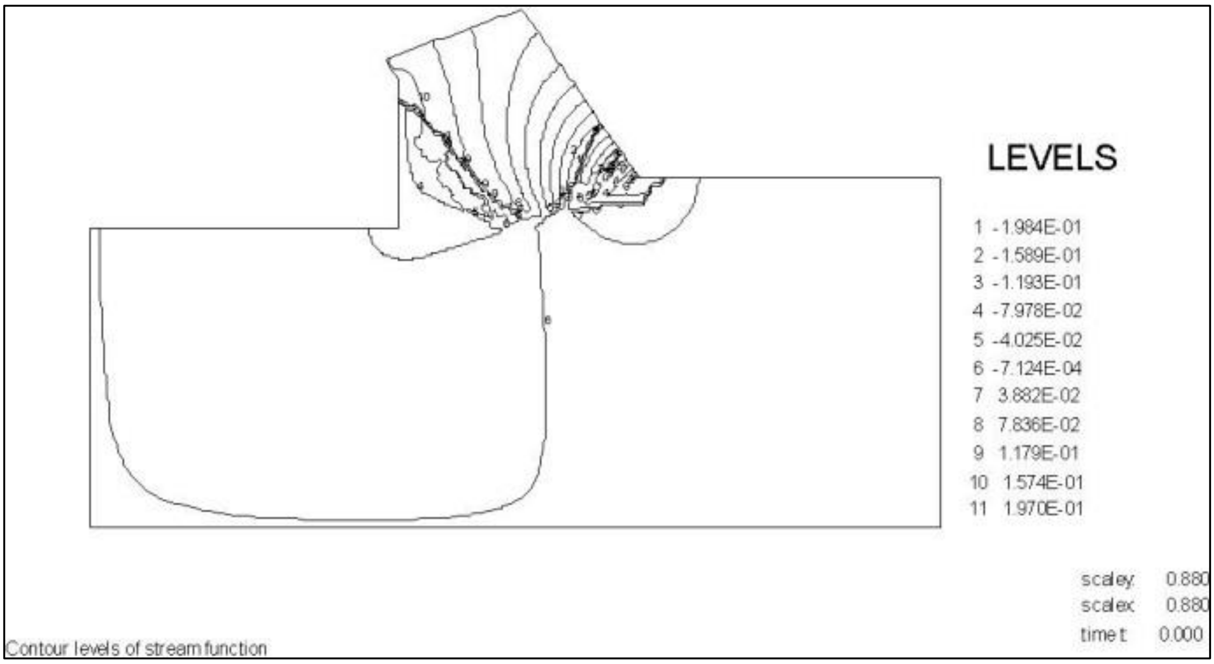

Figure R-15: The flow lines or stream function.

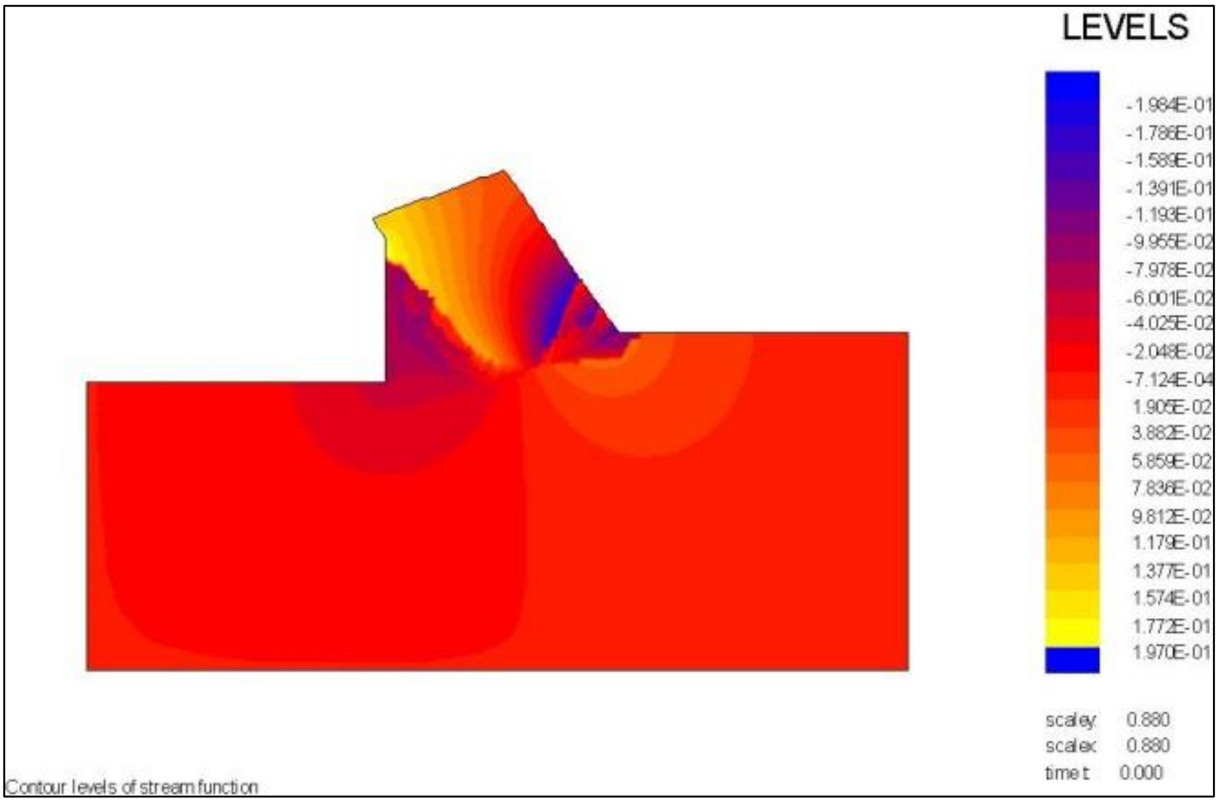

Figure R-16: The stream function in colors.

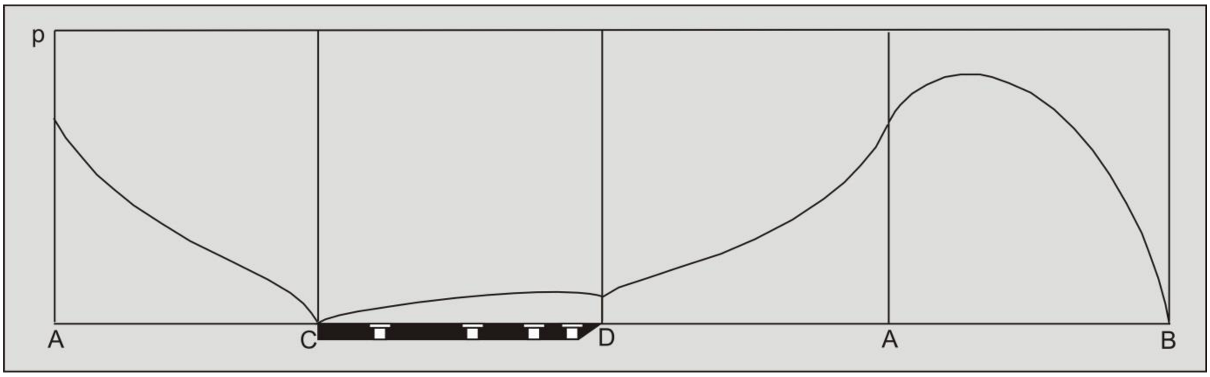

Figure R-17: Pore pressure distribution on the shear plane A-B, the bottom of the wedge A-D, the blade D-C and the front of the wedge A-C.

Appendix S: Force Triangles

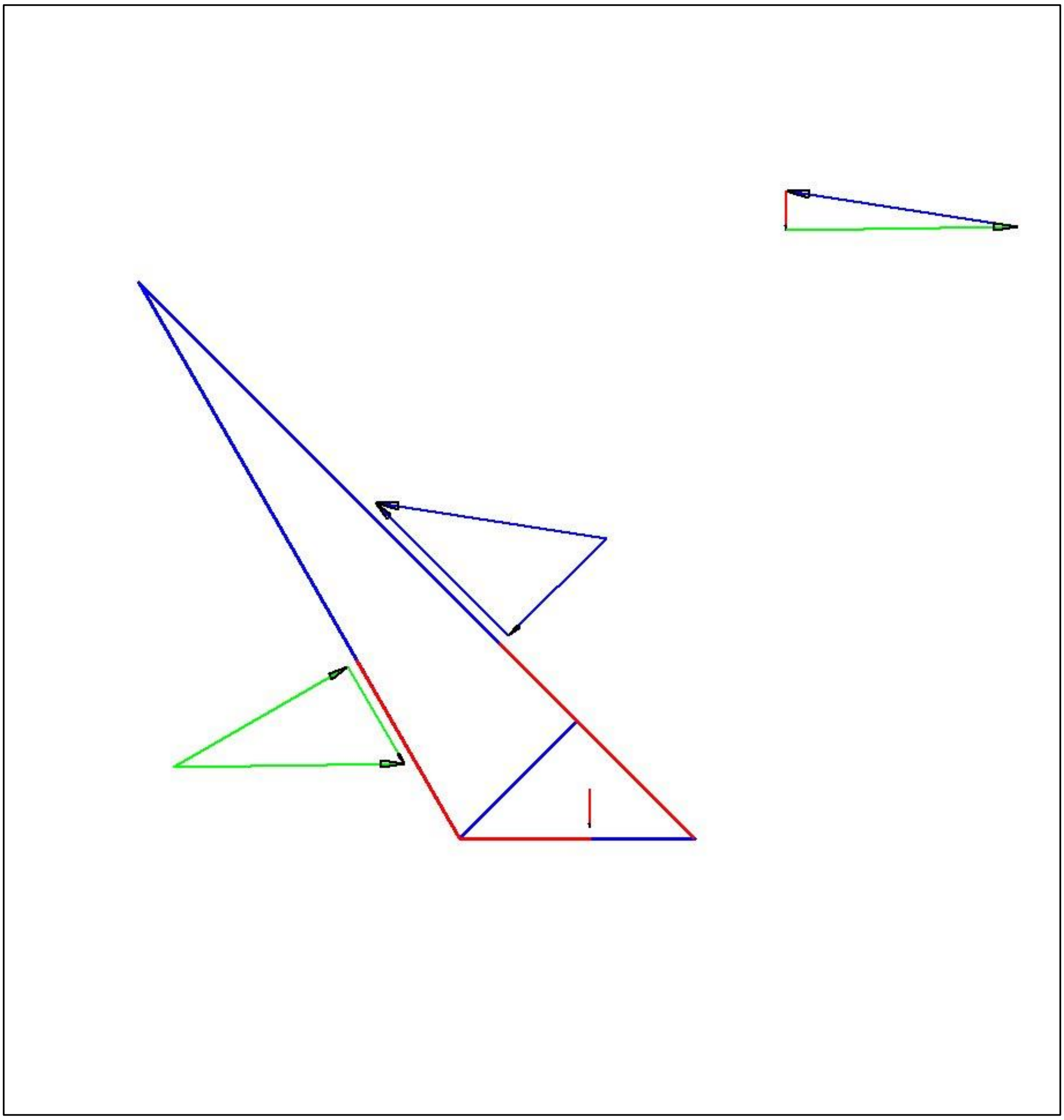

Figure S-1: The forces on the wedge for a 60º blade.

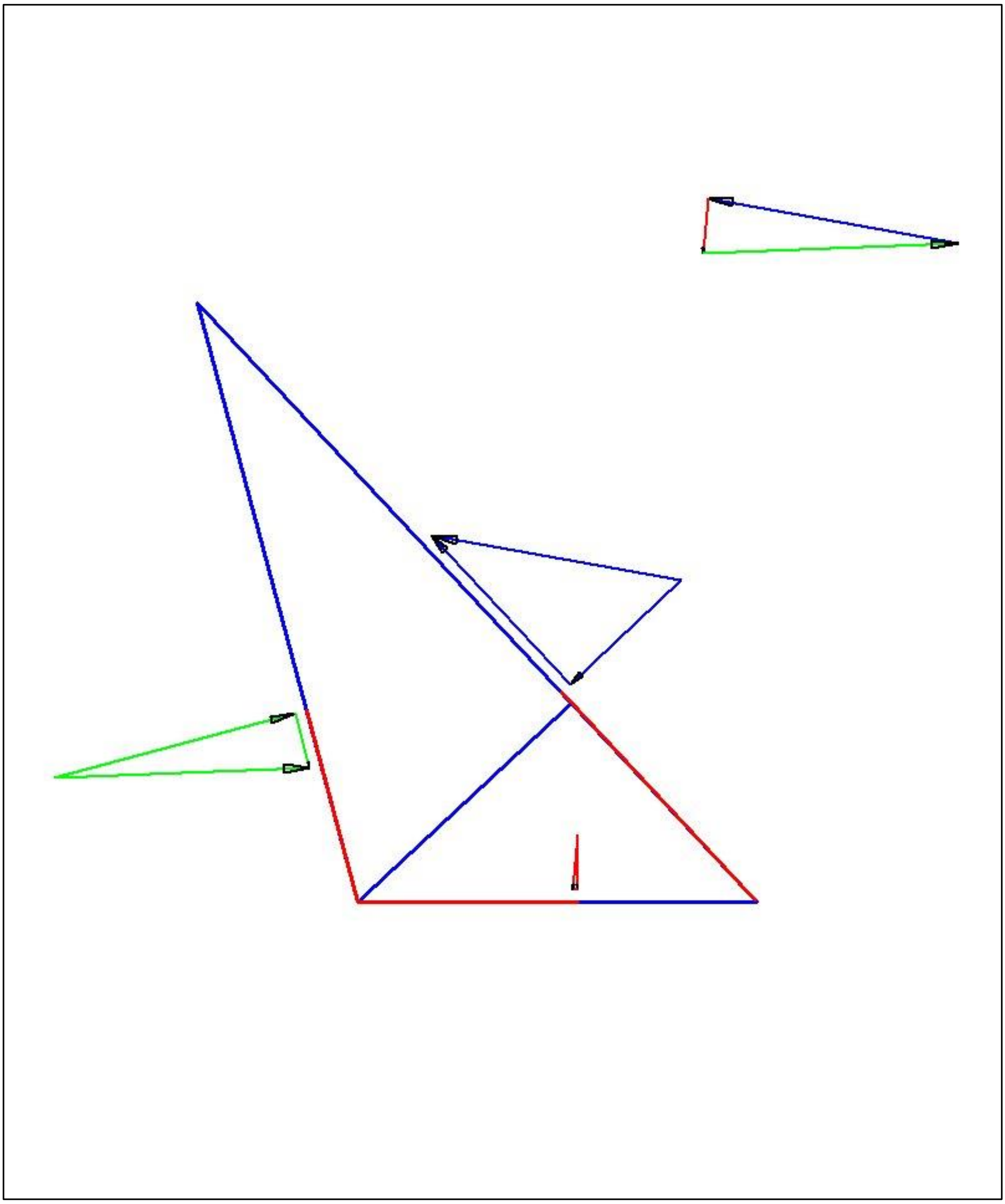

Figure S-2: The forces on the wedge for a 75º blade.

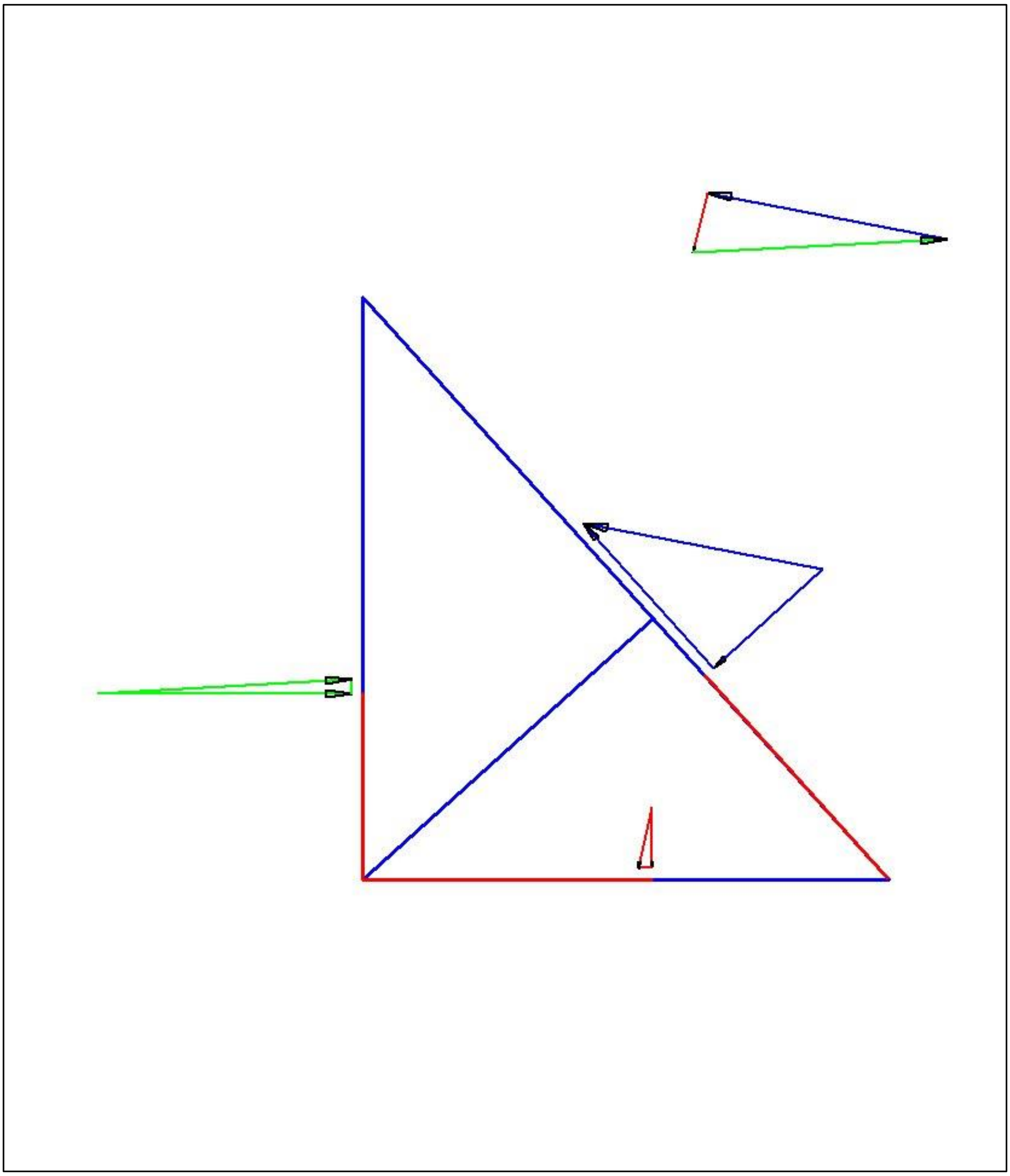

Figure S-3: The forces on the wedge for a 90º blade.

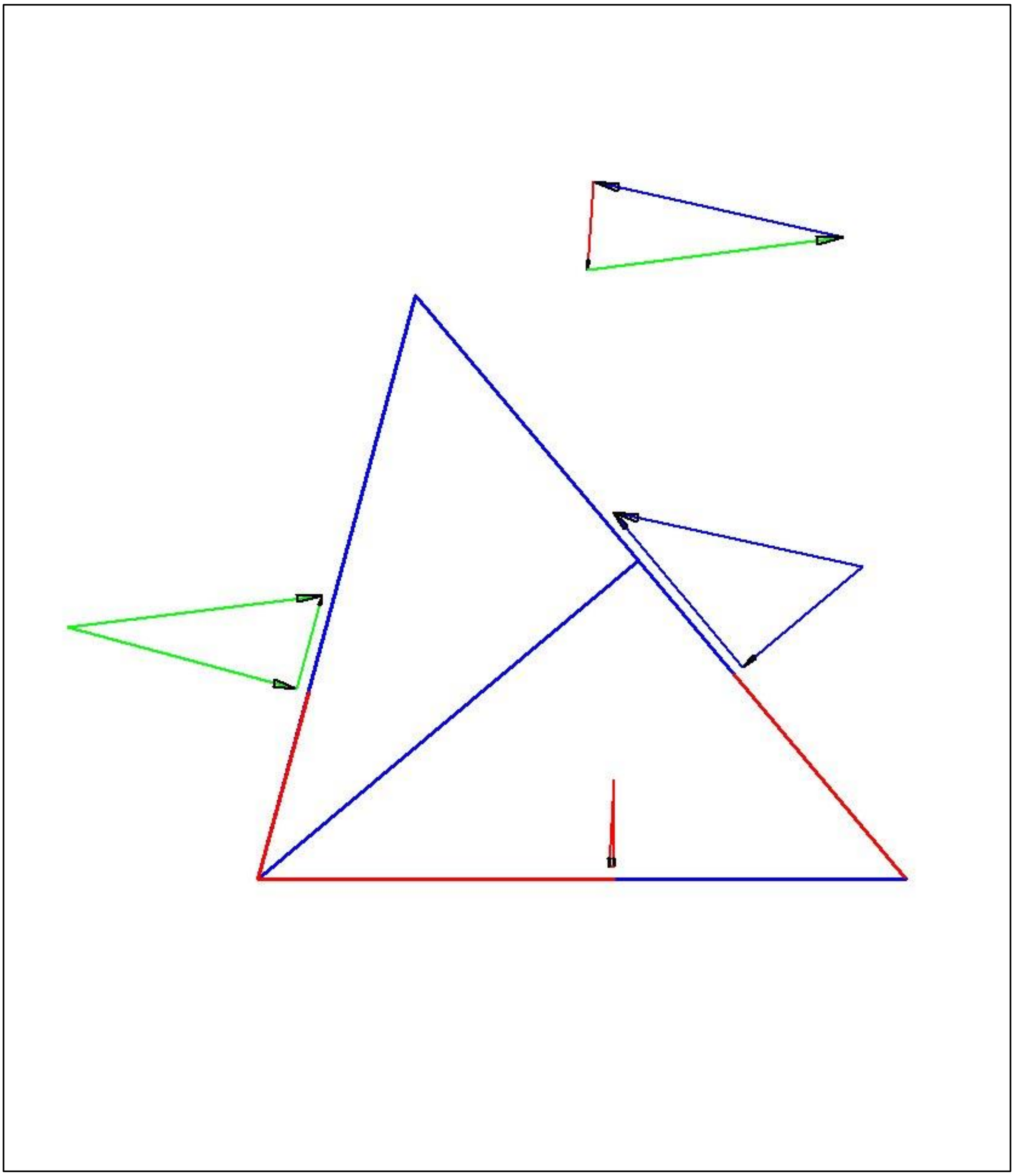

Figure S-4: The forces on the wedge for a 105° blade.

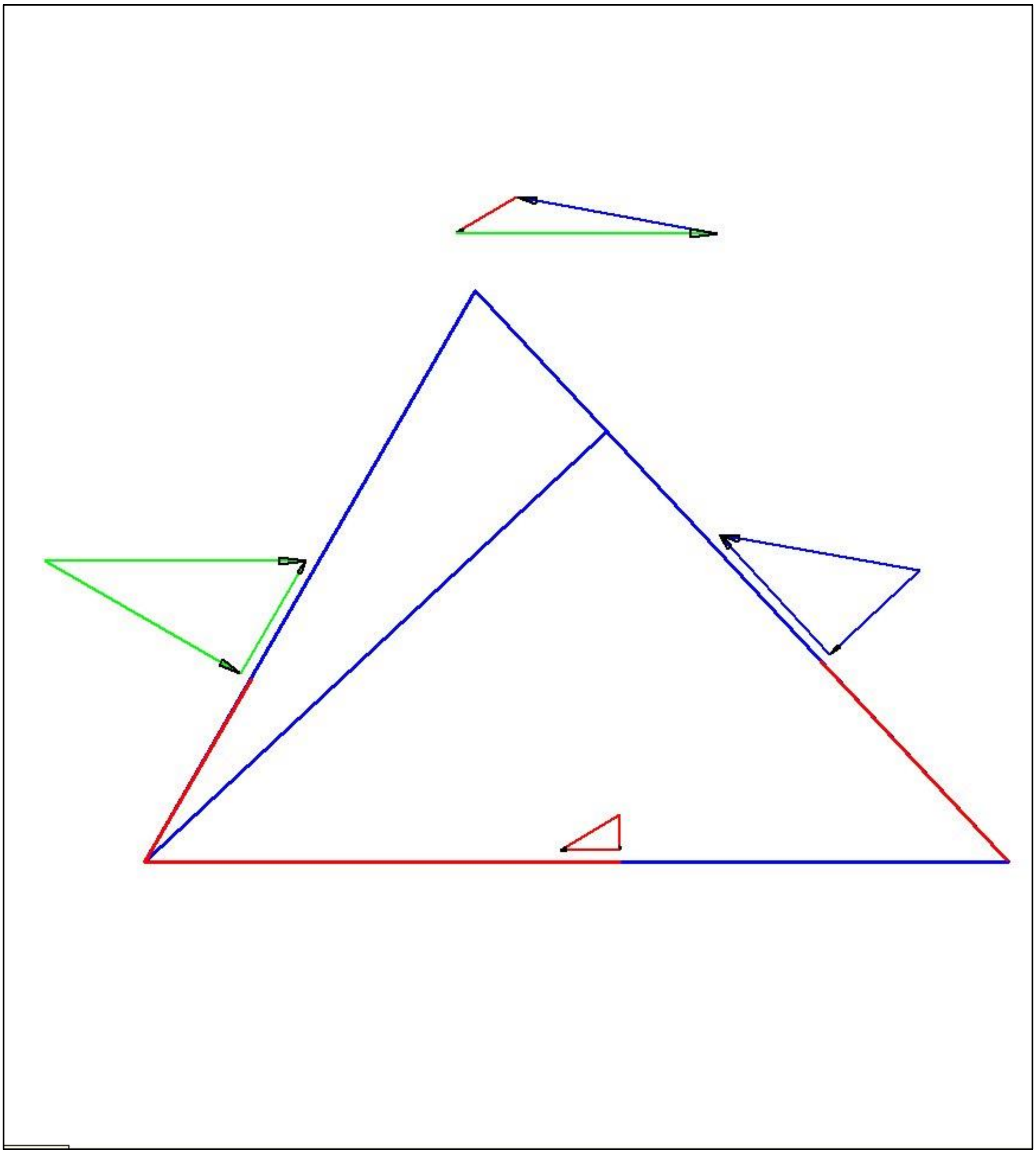

Figure S-5: The forces on the wedge for a 120° blade.

Appendix T: Specific Energy in Clay

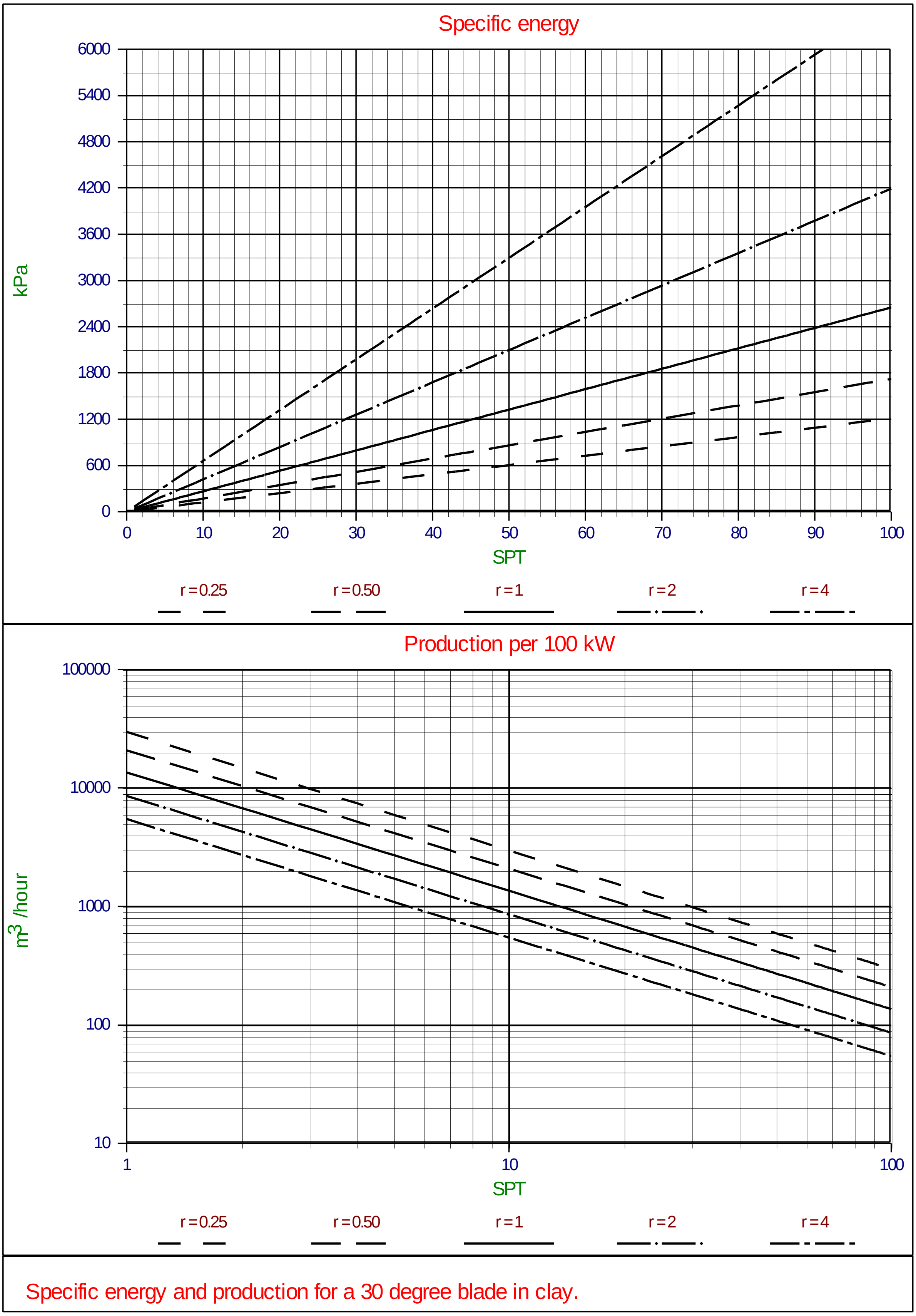

Figure T-1: Specific energy and production in clay for a 30 degree blade.

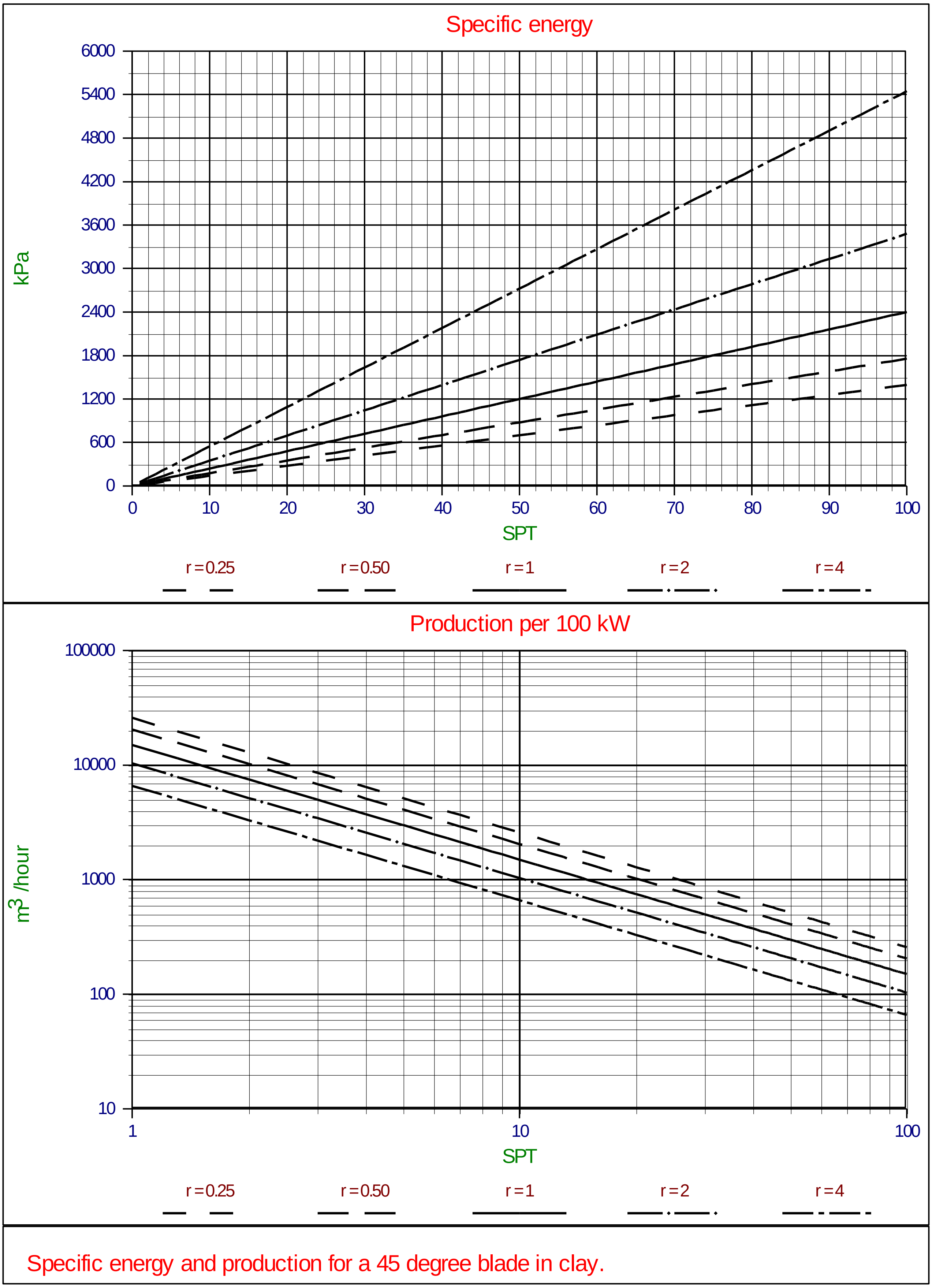

Figure T-2: Specific energy and production in clay for a 45 degree blade.

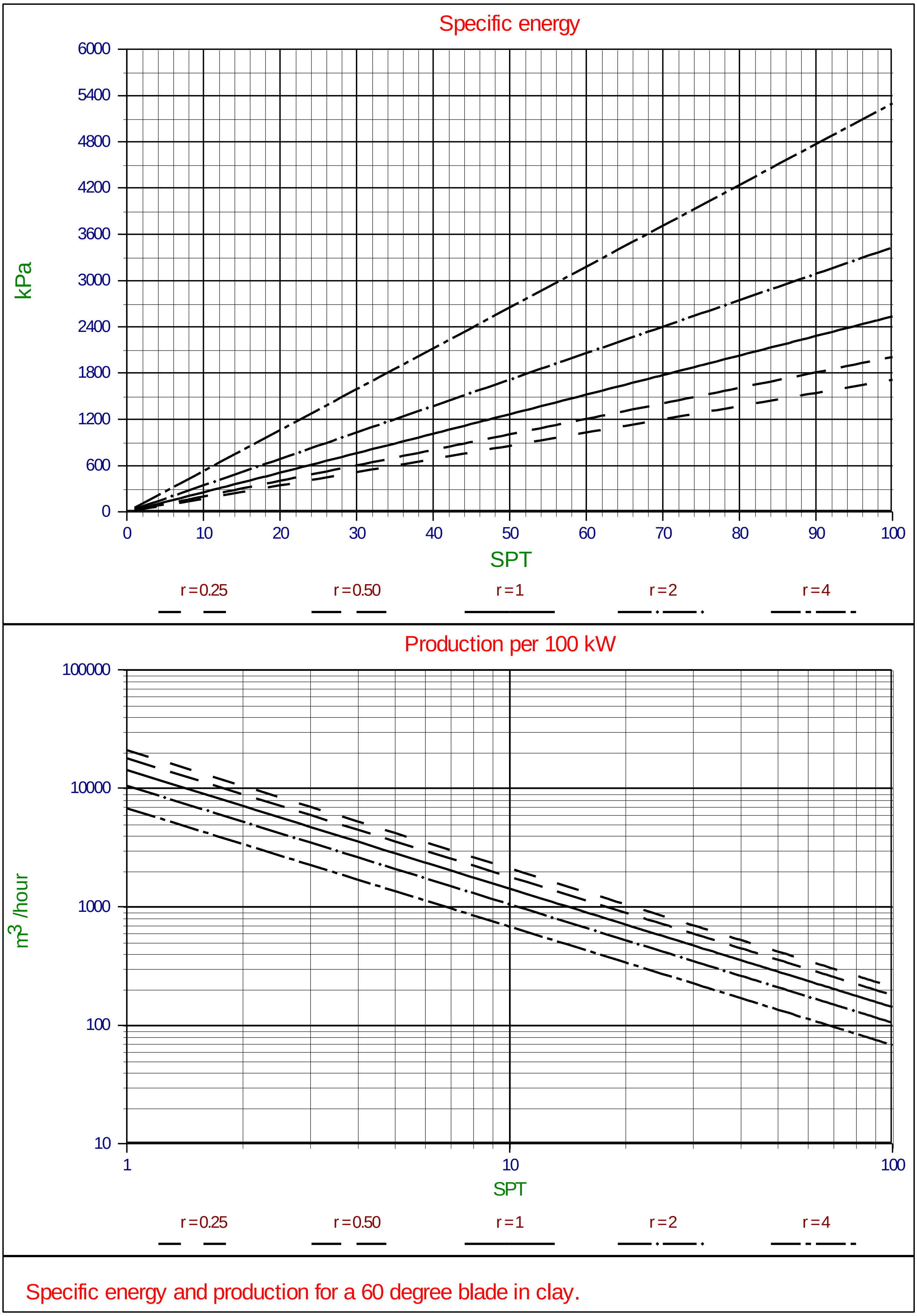

Figure T-3: Specific energy and production in clay for a 60 degree blade.

Appendix U: Clay Cutting Charts

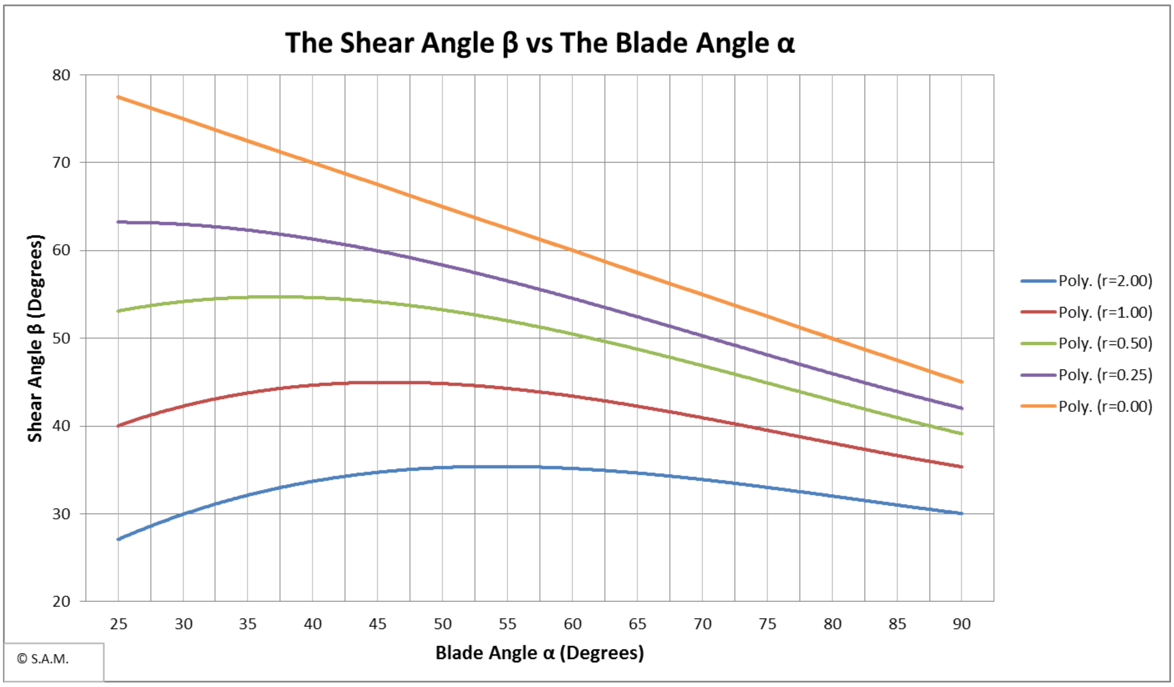

Figure U-1: The shear angle β as a function of the blade angle α and the ac ratio r.

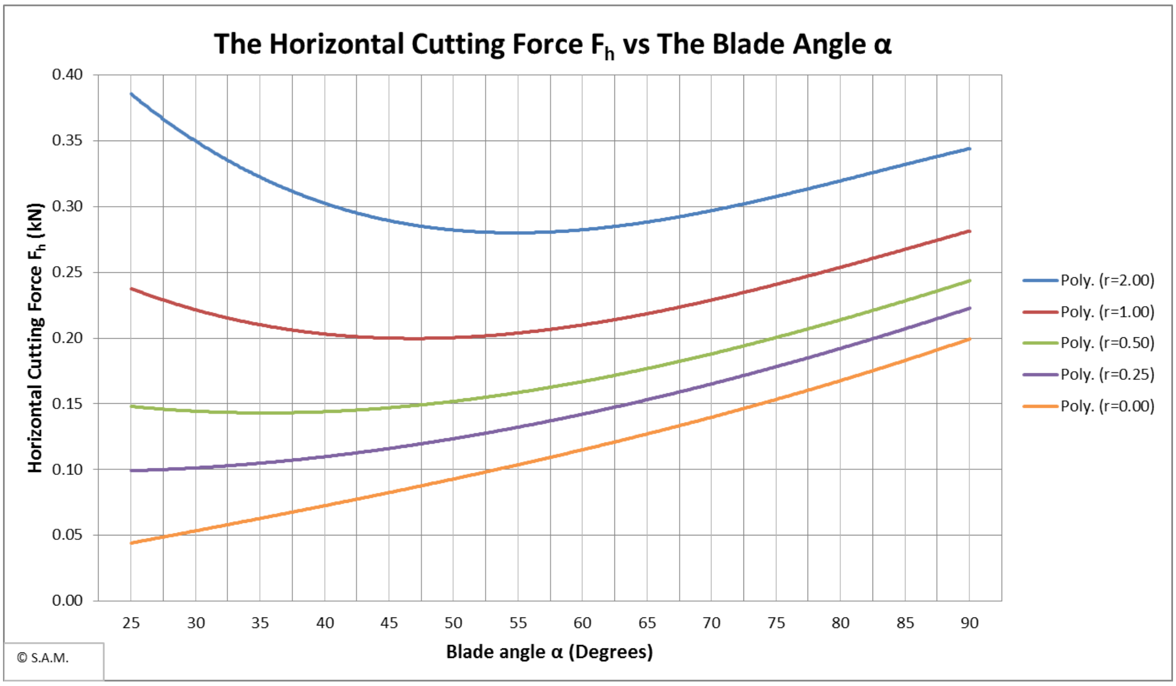

Figure U-2: The horizontal cutting force as a function of the blade angle α and the ac ratio r (c=1 kPa).

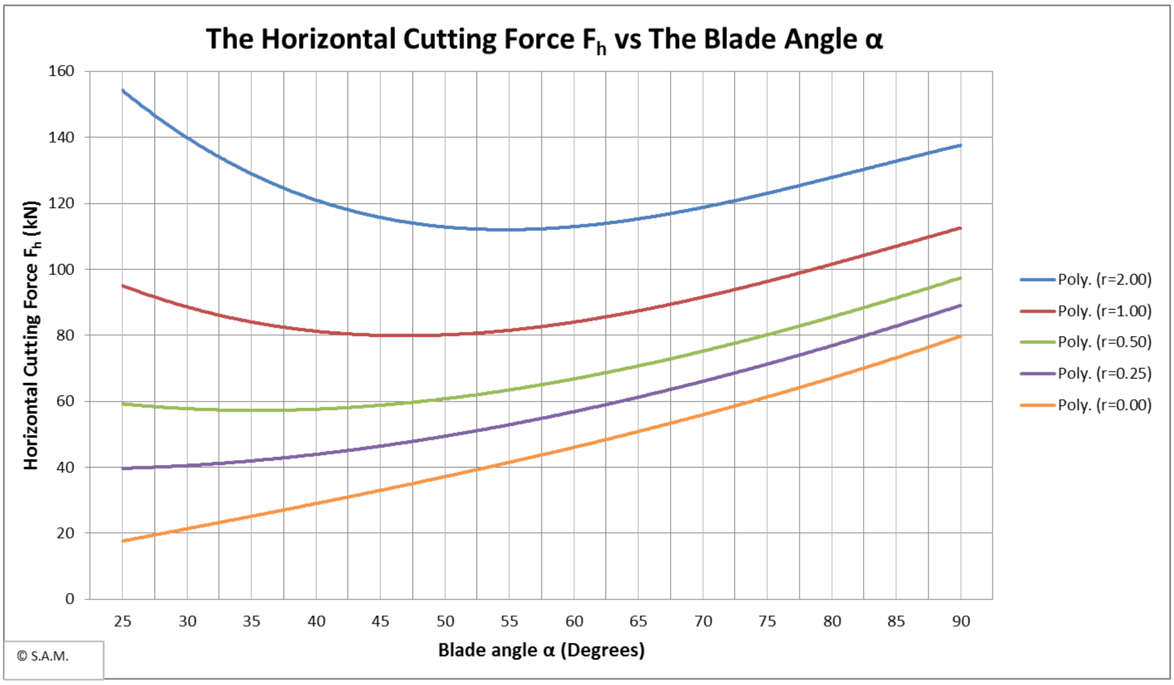

Figure U-3: The horizontal cutting force as a function of the blade angle α and the ac ratio r (c=400 kPa).

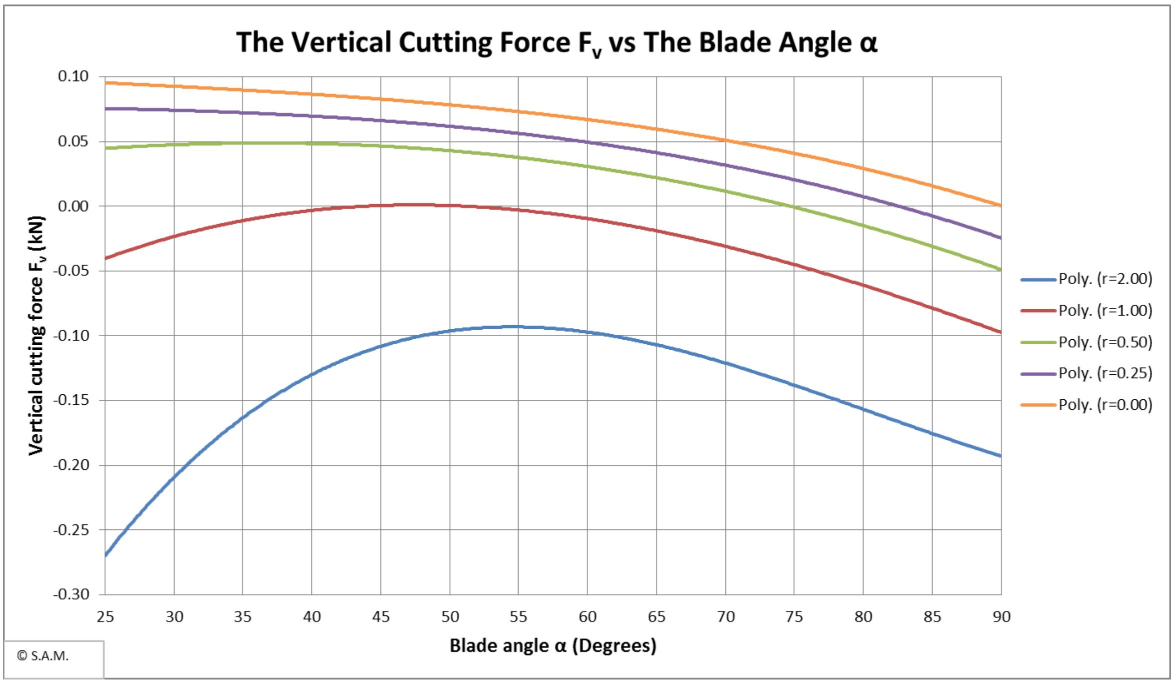

Figure U-4: The vertical cutting force as a function of the blade angle α and the ac ratio r (c=1 kPa).

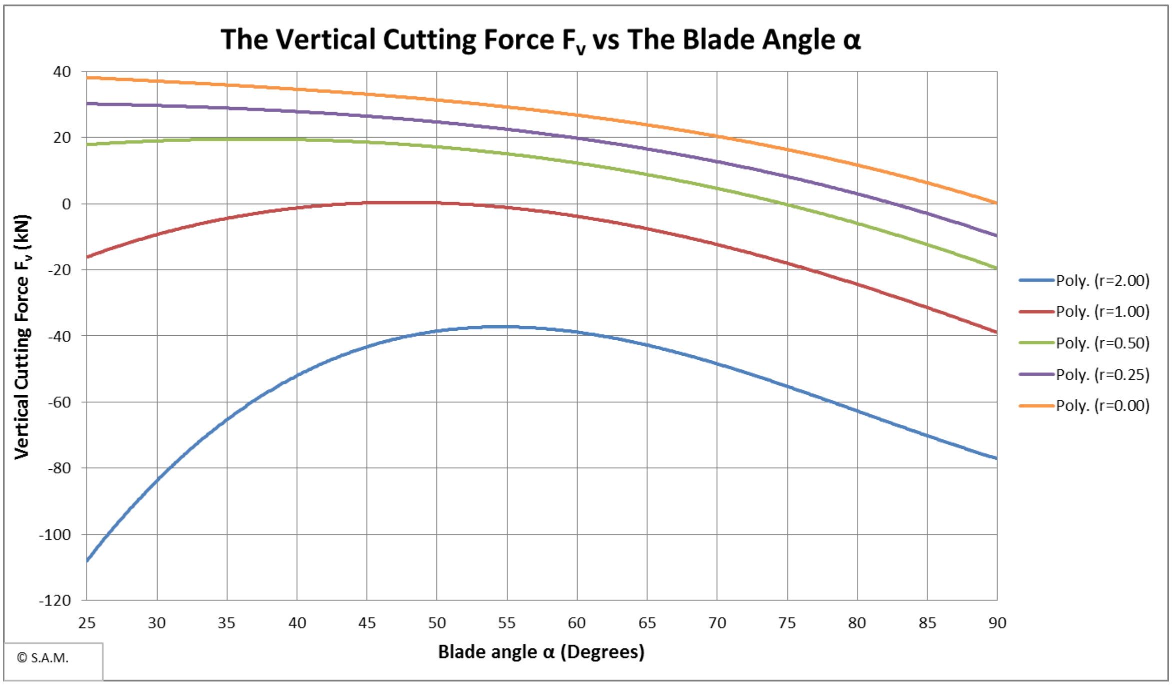

Figure U-5: The vertical cutting force as a function of the blade angle α and the ac ratio r (c=400 kPa).

Appendix V: Rock Cutting Charts

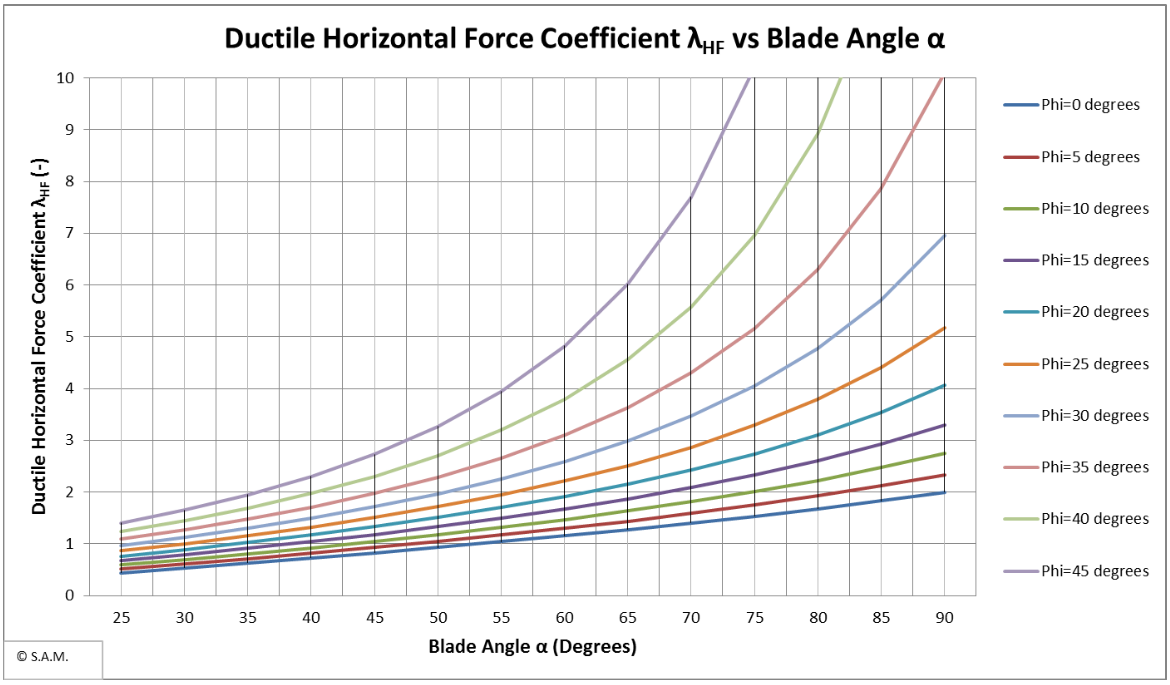

Figure V-1: The ductile horizontal force coefficient λ_{HF} (Miedema/Merchant).

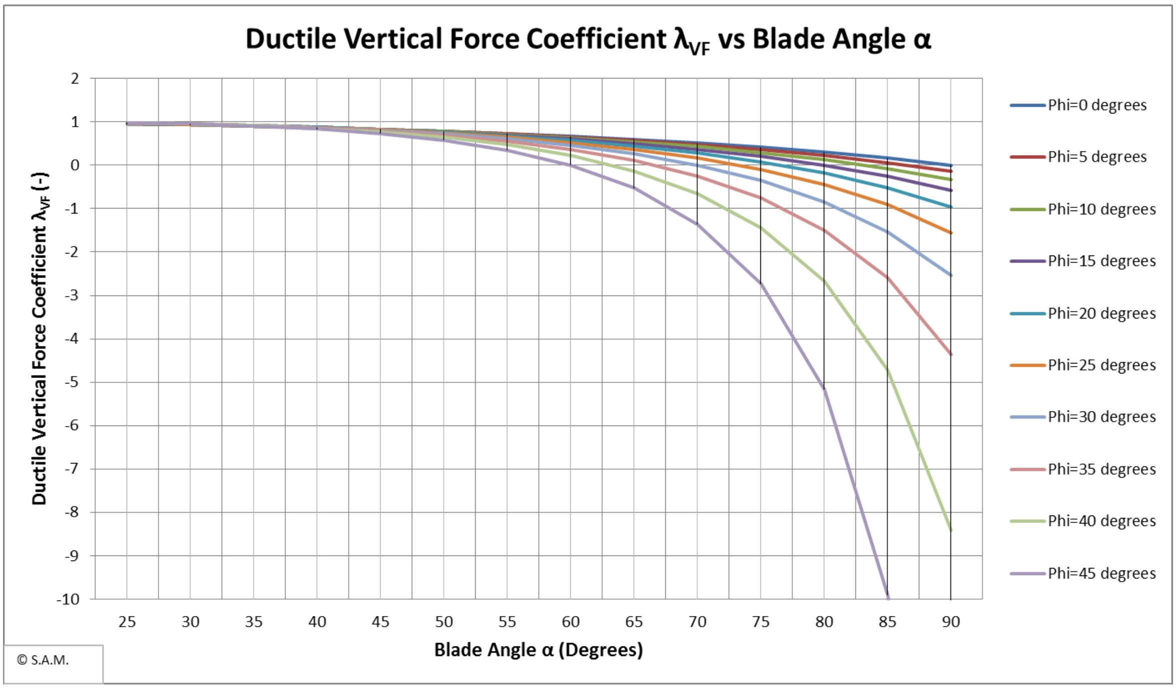

Figure V-2: The ductile horizontal force coefficient λ_{VF} (Miedema/Merchant).

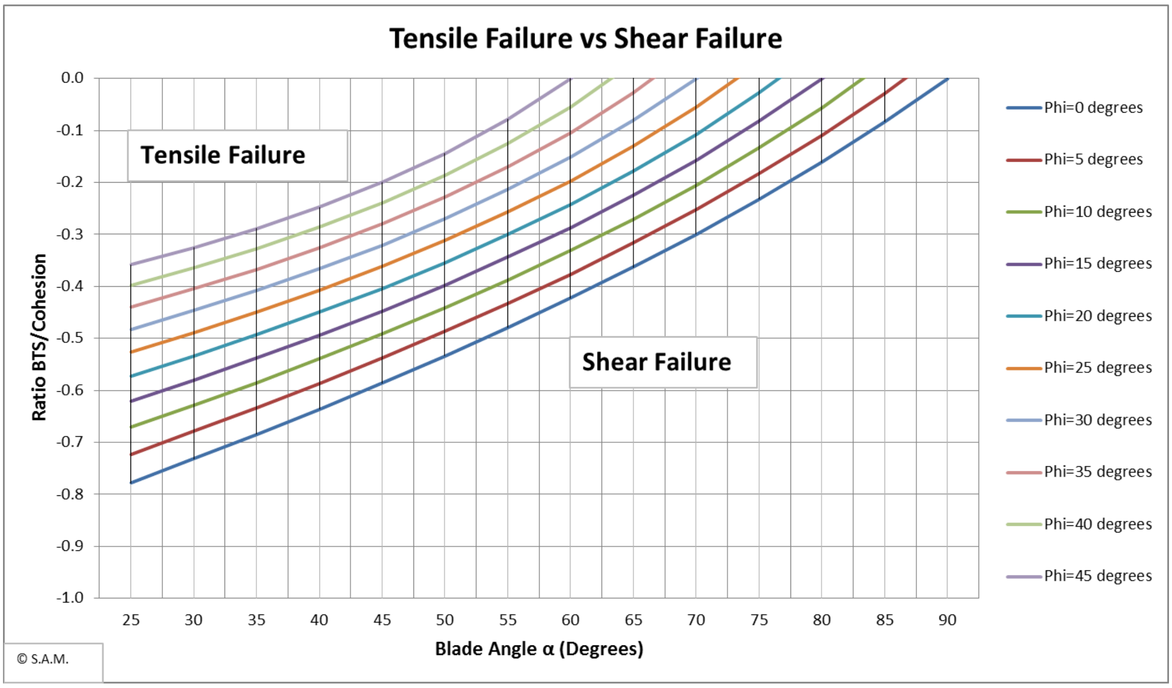

Figure V-3: The ductile/brittle criterion based on BTS/Cohesion (Miedema).

Below the lines the cutting process is ductile.

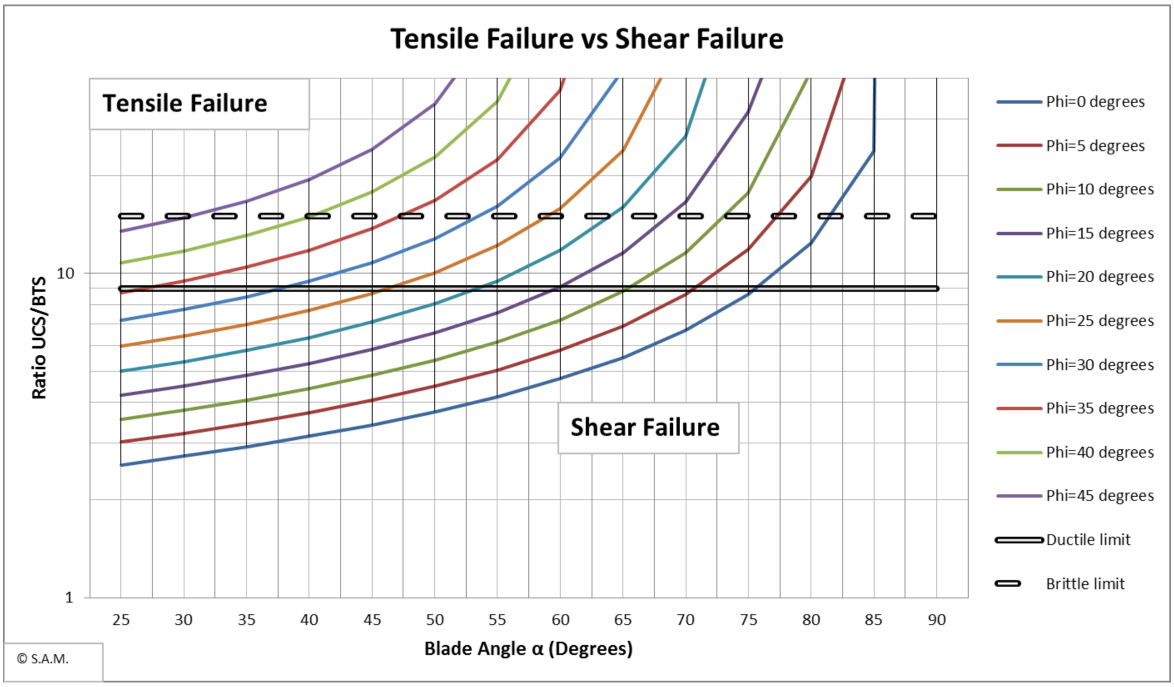

Figure V-4: The ductile/brittle criterion based on UCS/BTS (Miedema).

Below the lines the cutting process is ductile.

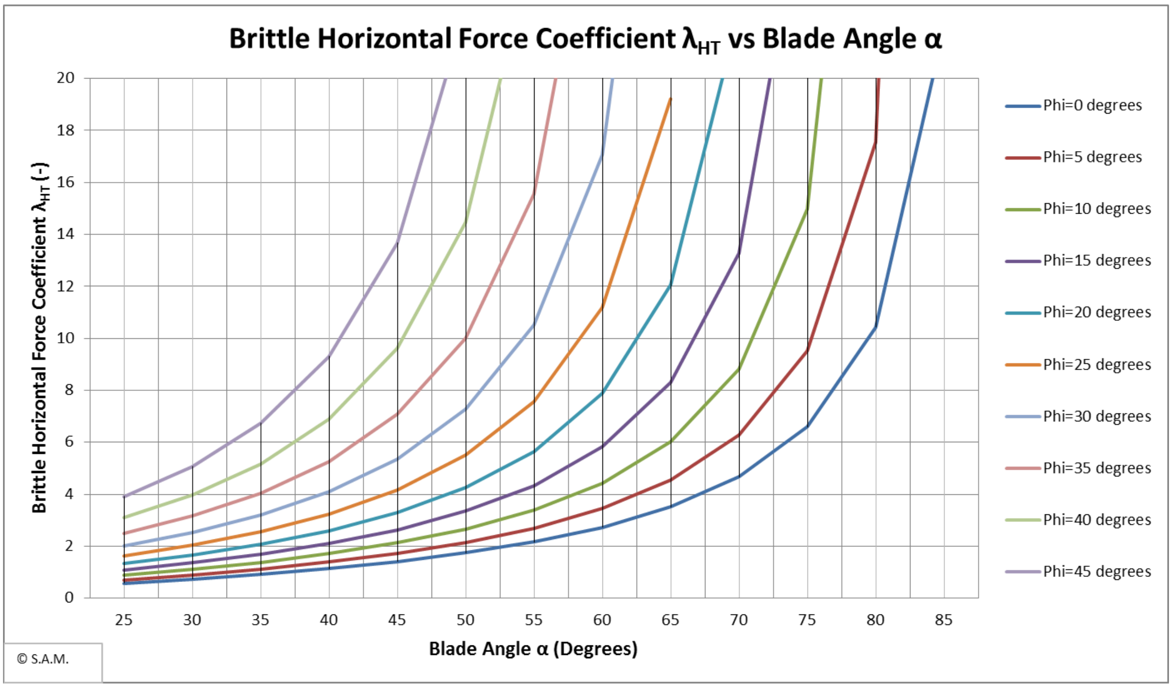

Figure V-5: The brittle tensile horizontal force coefficient λ_{HT} (Miedema).

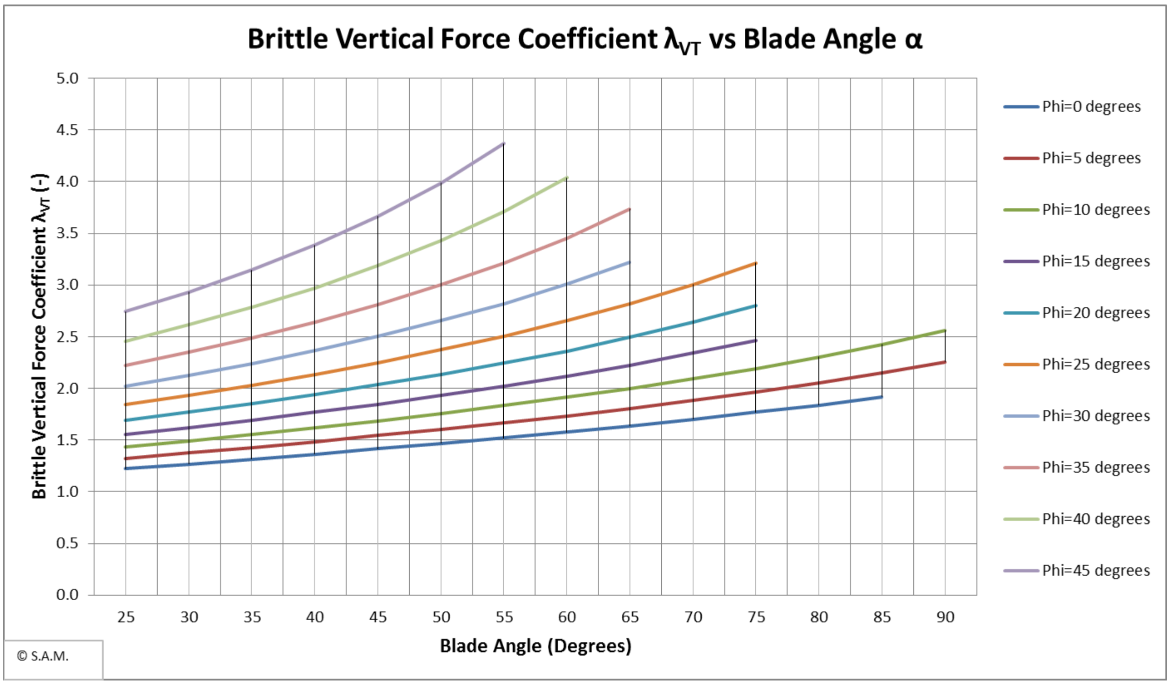

Figure V-6: The brittle tensile vertical force coefficient λ_{VT} (Miedema).

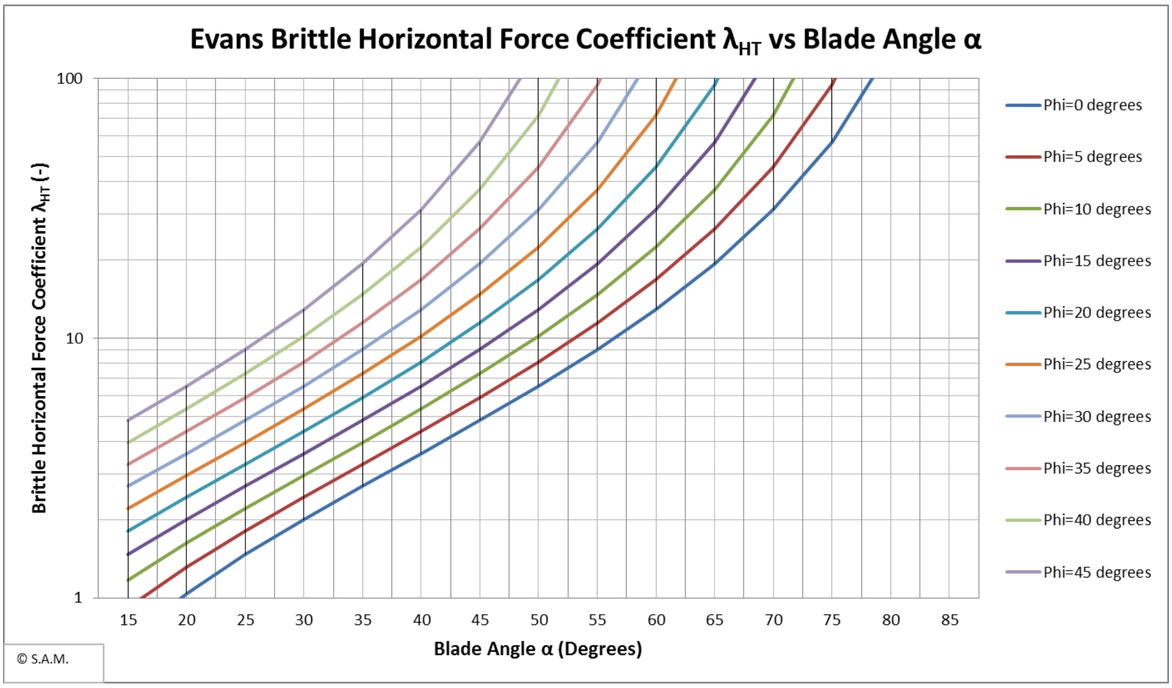

Figure V-7: The brittle tensile horizontal force coefficient λ_{HT} (Evans, logaritmic).

Figure V-8: The brittle tensile horizontal force coefficient λ_{HT} (Miedema, logaritmic).

Appendix W: Manual

W.1 Input Properties General

- .Soiltype (Sand, Clay or Rock, default Sand)
- .Description (Default: Default Sand)
- .Iterations (Number of iterations in calculation, default 100)
- .RhoWater (Water density, default 1.025 ton/m^3)
- .Labda (If deviation angle not zero, default 1)
- .NumberOfSoils (Default 1)
- .NumberOfBlades (Default 1)

W.2 Input Properties Soil Mechanics

- .RhoGrain (Grain density, default 2.65 ton/m^3)
- .Phi (Angle of internal friction, default 45 degrees)
- .PhiNR (Angle of natural repose, default 30 degrees)
- .Delta (Angle of external friction, default 30 degrees)
- .Ki (Initial permeability, situ permeability, default 0.0001 m/s)
- .Kmax (Maximum permeability, after shearing, default 0.0004 m/s)
- .Ni (Initial porosity, situ porosity, default 40%)
- .Nmin (Minimum porosity, default 32%)
- .Nmax (Maximum porosity, porosity after shearing, default 50%)
- .Cohesion (Internal shear strength, default 0 kPa)
- .Adhesion (External shear strength, default 0 kPa)
- .Tensile (Tensile strength of the soil, default 0 kPal)
- .Compressive (Compressive strength of rock, default 0 kPa)
- .D15 (d15 of the soil, 15% of the grains is smaller, default 0.1 mm)
- .D50 (d50 of the soil, 50% of the grains is smaller, default 0.2 mm)
- .D85 (d85 of the soil, 85% of the grains is smaller, default 0.3 mm)
- .PsiGrain (Shape factor of the grains, for normal sand 0.26)
- .Tau0 (Clay strengthening coefficient, default 0.15)
- .Epsilon0 (Clay strengthening coefficient, default 0.15)
- .PsiClayBall (Shape factor of clayballs, default 0.54)
- .RhoClayBall (Clayball density, default 1.8 ton/m^3)
- .WallFriction (Wall friction factor for Wilson model, default 0.4)
- .ClayBallConcentration (Bulked concentration, default 0.6)

W.3 Input Properties Geometry

- .BladeDescription (Default: Default Blade)
- .Alpha (Blade angle in degrees, default 45)
- .Iota (Deviation angle of the blade in degrees, default 0)
- .Hb (Height of the blade in m, default 0.2)
- .B (Width of the blade in m, default 0.5)
- .WearFactor (Increase of force due to wear, default 1)
- .WearAngle (Directional change of cutting force due to wear, default 0)
- .Vc (Cutting velocity in m/s, default 0.2)
- .Hi (Thickness of the layer cut in m, default 0.1)
- .Z (Waterdepth in m, default 10)
- .Labda1 (Point of action on shearplane)
- .Labda2 (Point of action on blade)
- .Labda3 (Point of action on bottom of wedge)
- .Labda4 (Point of action on blade if there is a wedge)

W.4 Output Properties

- .Fh (Horizontal cutting force in kN)
- .Fv (Vertical cutting force in kN)
- .Fd (Deviation force resulting from snow plough effect in kN)

- .K1 (Force on the shear plane in kN)
- .K2 (Force on the blade or pseudo blade in case of wedge in kN)
- .K3 (Force on the bottom of the wedge in kN)
- .K4 (Force on the blade in case of wedge in kN)
- .P1m (Underpressure on the shear plane in kPa)
- .P2m (Underpressure on the blade or pseudo blade in kPa)
- .P3m (Underpressure on the bottom of the wedge in kPa)
- .P4m (Underpressure on the blade in case of wedge in kPa)
- .C1 (Coefficient horizontal force no cavitation)
- .C2 (Coefficient vertical force no cavitation)
- .D1 (Coefficient horizontal force cavitation)
- .D2 (Coefficient vertical force cavitation)
- .Beta (Shear angle in degrees)
- .E (Dilatation as a fraction)
- .RD (Relative density in %)
- .Esp (Specific energy in kPa)
- .Kmean (Average permeability in m/s)
- .Percentage (Percentage of cavitation in case sand cutting)
- .Mechanism (Shows the cutting mechanism)
- .Labda1 (Point of action on shear plane)
- .Labda2 (Point of action on pseudo blade)
- .Labda3 (Point of action on bottom wedge)
- .Labda4 (Point of action on blade)

W.5 Methods

- .CuttingOfSand(Vc, Hi, Z) (Calculates the sand forces)
- .CuttingOfClay(Vc, Hi, Z) (Calculates the clay forces)
- .CuttingOfRock(Vc, Hi, Z) (Calculates the rock forces)
- .SaveSoil(SoilName, Optional Overwrite)
- .OpenSoilByName(SoilName)
- .OpenSoilByIndex(Index)
- .GetSoilName(Index)
- .ShowAvailableSoils
- .SaveBlade(BladeName, Optional Overwrite)
- .OpenBladeByName(BladeName)
- .OpenBladeByIndex(Index)
- .GetBladeName(Index)
- .ShowAvailableBlades
- .GetDefaultBlade
- .GetSharpBlade
- .GetWornBlade
- .GetBluntBlade
- .GetDefaultSand
- .GetVerySoftClay
- .GetSoftClay
- .GetMediumClay
- .GetStiffClay
- .GetVeryStiffClay
- .GetHardClay
- .GetVeryLooseSand
- .GetLooseSand
- .GetMediumSand
- .GetDenseSand
- .GetVeryDenseSand
- .ShowSandProperties
- .ShowClayProperties
- .ShowRockProperties
- .ShowGeometryProperties

- .CohesionFactor (Factor between compressive strength (UCS) and cohesion)
- .SandWedgeLowerLimitC (Lower limit where a wedge can exist based on equilibrium of moments, cavitating)
- . SandWedgeLowerLimitNC (Lower limit where a wedge can exist based on equilibrium of moments, non cavitating)
- .SandWedgeLowerLimitT (Lower limit where a wedge can exist based on equilibrium of moments, transition)
- . SandWedgeUpperLimitC (Upper limit where a wedge can exist based on equilibrium of moments, cavitating)
- . SandWedgeUpperLimitNC (Upper limit where a wedge can exist based on equilibrium of moments, non cavitating)
- . SandWedgeUpperLimitT (Upper limit where a wedge can exist based on equilibrium of moments, transition)
- . SandStartWedgeC (Lower limit where a wedge will occur, cavitating)
- . SandStartWedgeNC (Lower limit where a wedge will occur, non cavitating)
- . SandStartWedgeT (Lower limit where a wedge will occur, transition)
- .SandWedgeAngleC (Wedge angle Teta, cavitating)
- .SandWedgeAngleNC (Wedge angle Teta, non cavitating)
- .SandWedgeAngleT (Wedge angle Teta, transition)
- .SandWedgeFrictionAngleC (Mobilized external friction angle Delta, cavitating)
- .SandWedgeFrictionAngleNC (Mobilized external friction angle Delta, non cavitating)
- .SandWedgeFrictionAngleT (Mobilized external friction angle Delta, transition)

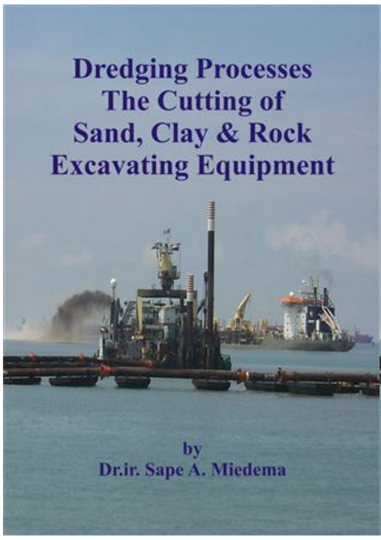
Dredging Processes
The Cutting of
Sand, Clay & Rock
Excavating Equipment
by
Dr.ir. Sape A. Miedema

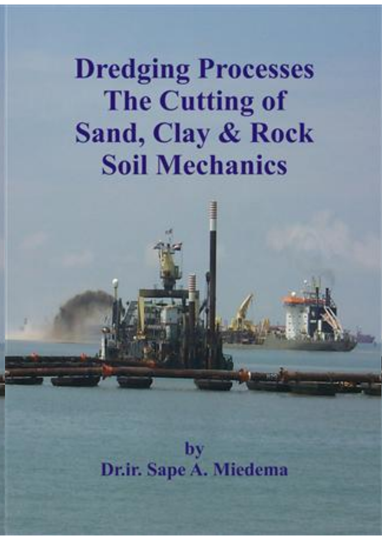
Dredging Processes
The Cutting of
Sand, Clay & Rock
Soil Mechanics
by
Dr.ir. Sape A. Miedema

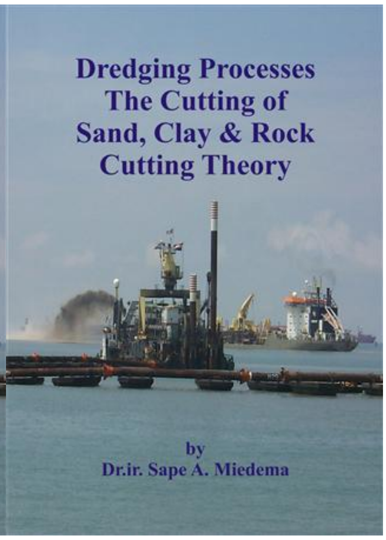
Dredging Processes
The Cutting of
Sand, Clay & Rock
Cutting Theory
by
Dr.ir. Sape A. Miedema

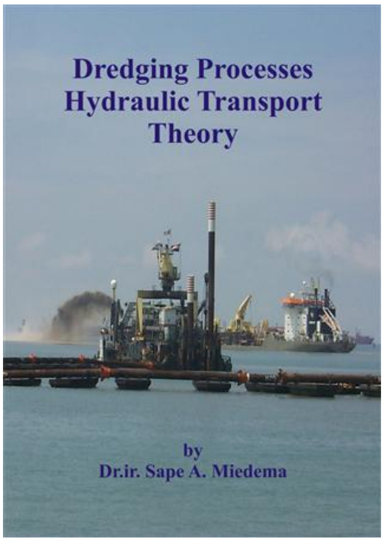
Dredging Processes
Hydraulic Transport
Theory
by
Dr.ir. Sape A. Miedema

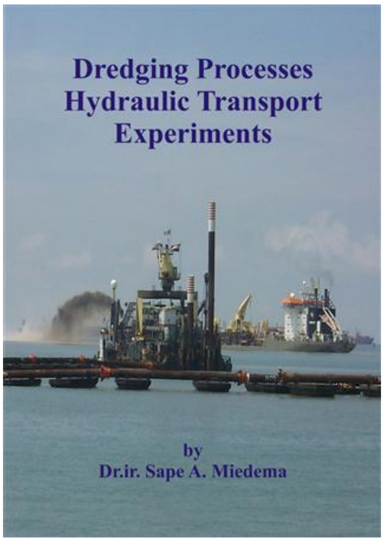
Dredging Processes
Hydraulic Transport
Experiments
by
Dr.ir. Sape A. Miedema

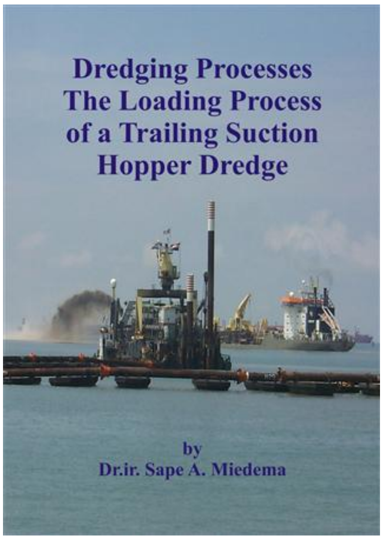
Dredging Processes
The Loading Process
of a Trailing Suction
Hopper Dredge
by
Dr.ir. Sape A. Miedema

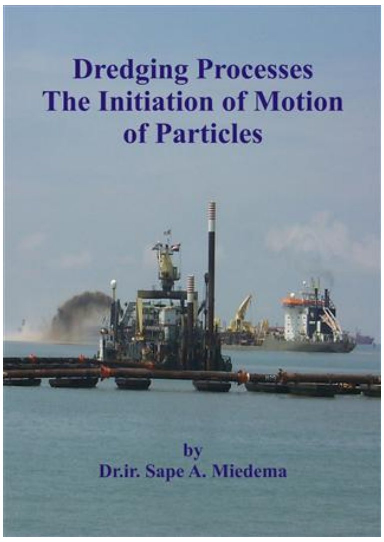
Dredging Processes
The Initiation of Motion
of Particles
by
Dr.ir. Sape A. Miedema

Chapter 18: About the Author.

Dr.ir. Sape A. Miedema (November 8th 1955) obtained his M.Sc. degree in Mechanical Engineering with honours at the Delft University of Technology (DUT) in 1983. He obtained his Ph.D. degree on research into the basics of soil cutting in relation with ship motions, in 1987. From 1987 to 1992 he was assistant professor at the chair of Dredging Technology. In 1992 and 1993 he was a member of the management board of Mechanical Engineering & Marine Technology of the DUT. In 1992 he became associate professor at the DUT with the chair of Dredging Technology. From 1996 to 2001 he was appointed educational director of Mechanical Engineering and Marine Technology at the DUT, but still remaining associate professor of Dredging Engineering. In 2005 he was appointed Educational Director/Director of Studies of the MSc program of Offshore & Dredging Engineering and he is also still Associate Professor of Dredging Engineering. In 2013 he was also appointed as Director of Studies of the MSc program Marine Technology of the DUT.

Dr.ir. S.A. Miedema teaches (or has taught) courses on soil mechanics and soil cutting, hopper sedimentation, mechatronics, applied thermodynamics, drive system design principles, mooring systems and mathematics. His research focuses on the mathematical modeling of dredging systems like, cutter suction dredges, hopper dredges, clamshell dredges, backhoe dredges and trenchers. The fundamental part of the research focuses on the cutting processes of sand, clay and rock, sedimentation processes in Trailing Suction Hopper Dredges and the associated erosion processes. Lately the research focuses on hyperbaric rock cutting in relation with deep sea mining and on hydraulic transport of sand/water slurries.

Dredging Processes
The Cutting of Sand, Clay & Rock
Theory

By

Dr.ir. Sape A. Miedema

In dredging, trenching, (deep sea) mining, drilling, tunnel boring and many other applications, sand, clay or rock has to be excavated. The productions (and thus the dimensions) of the excavating equipment range from mm^3/sec - cm^3/sec to m^3/sec. In oil drilling layers with a thickness of a magnitude of 0.2 mm are cut, while in dredging this can be of a magnitude of 0.1 m with cutter suction dredges and meters for clamshells and backhoe's. Some equipment is designed for dry soil, while others operate under water saturated conditions. Installed cutting powers may range up to 10 MW. For both the design, the operation and production estimation of the excavating equipment it is important to be able to predict the cutting forces and powers. After the soil has been excavated it is usually transported hydraulically as a slurry over a short (TSHD's) or a long distance (CSD's). Estimating the pressure losses and determining whether or not a bed will occur in the pipeline is of great importance. Fundamental processes of sedimentation, initiation of motion and ersosion of the soil particles determine the transport process and the flow regimes. In TSHD's the soil has to settle during the loading process, where also sedimentation and erosion will be in equilibrium. In all cases we have to deal with soil and high density soil water mixtures and its fundamental behavior.

This book gives an overview of cutting theories. It starts with a generic model, which is valid for all types of soil (sand, clay and rock) after which the specifics of dry sand, water saturated sand, clay, rock and hyperbaric rock are covered. For each soil type small blade angles and large blade angles, resulting in a wedge in front of the blade, are discussed. The failure mechanism of sand, dry and water saturated, is the so called Shear Type. The failure mechanism of clay is the so called Flow Type, but under certain circumstances also the Curling Type and the Tear Type are possible. Rock will usually fail in a brittle way. This can be brittle tensile failure, the Tear Type, for small blade angles, but it can also be brittle shear failure, which is of the Shear Type of failure mechanism for larger blade angles. Under hyperbaric conditions rock may also fail in a more ductile way according to the Flow Type of failure mechanism.

For each case considered, the equations/model for the cutting forces, power and specific energy are given. The models are verified with laboratory research, mainly at the Delft University of Technology, but also with data from literature.